INVESTIGATION OF LOW DISCHARGE VOLTAGE HALL THRUSTER CHARACTERISTICS AND EVALUATION OF LOSS MECHANISMS

by

Daniel Lucas Brown

A dissertation submitted in partial fulfillment
of the requirements for the degree of
Doctor of Philosophy
(Aerospace Engineering)
in The University of Michigan
2009

Doctoral Committee:

Professor Alec D. Gallimore, Chair
Professor Iain D. Boyd
Associate Professor John E. Foster
James M. Haas, Air Force Research Laboratory

"When nothing seems to help, I go and look at a stonecutter hammering away at his rock, perhaps a hundred times without as much as a crack showing in it. Yet at the hundred and first blow it will split in two, and I know it was not that blow that did it, but all that had gone before."

Jacob Riis (1849-1914) – Danish-American Photographer, Journalist, Social Reformer

Acknowledgements

My path through undergraduate and graduate school has definitely been the road less traveled. I rarely envisioned what the next step would bring, yet found new opportunities, guidance, and support at each turn. Each mentor along the way provided unique experiences, challenges, and wisdom. I've been fortunate to have their leadership, and develop good friends along the way.

First and foremost, I'd like to thank my advisor at Michigan, Professor Alec Gallimore. Alec, these last five years have been an honor. While I've spent a majority of my time in the desert at AFRL, you've always been available when I needed direction and granted the latitude when I needed room to grow (i.e. learn from mistakes). Alec attracts students who are highly motivated and assert themselves to not only achieve, but to excel in graduate school. His rare ability to harness that drive and allow each of us to create a unique scientific contribution with the right mix of guidance and independence is unparalleled. It's been the privilege and opportunity of a lifetime. Thanks Sensei!

Of course, the next thanks goes to James Haas. James, it's been a long haul and I couldn't have done it without you. I'm looking forward to working with you in the years ahead and drinking a few JC's along the way.

I'd also like to thank the other members of my committee, Professor Iain Boyd and Professor John Foster. Their advice and instruction over the years has been truly appreciated.

A true testament of Alec's leadership and the remarkable learning environment he has established was in meeting and working with his past students (aka the Michigan Mafia). In addition to James and John, I'm grateful for the opportunity to work closely with Brain Beal and Rich Hofer, whose teachings have been invaluable. As for the rest of the older crowd I've become friends with over the years, the support for less seasoned members of the Michigan Mafia is truly appreciated. Thanks to Jesse Linnell, Josh Rovey, Mitchell Walker, Alan Victor, Tim Smith, Pete Peterson, Frank Gulczinski, Brad King, and even Dan Herman, who told me there were too many Dans when I first joined the lab.

Then there are the peers who I've grown along with over the years, including Rob Lobbia, Kristina Lemmer, Prashant Patel, Brian Reid, Sonca Nguyen, Tom Liu, and Bailo Ngom. Bryan was my cohort in crime building a certain 6-kW thruster that will remain un-named for all eternity. Rob and Kristina in particular shared the growing pains of pre-lims. One of my few regrets from graduate school is spending so much time away from everyone in Ann Arbor.

Of course there's Dave "Floppy" Kirtley. We've been through a lot in a few short years, from traveling to the highest point in Africa to getting robbed at knife-point in the streets of Peru, starting a business, and maintaining sanity at Domingo's. Good times.

To the younger PEPL crew: Rohit Shastry, Mike McDonald, David Huang, Ray Liang, Adam Shabshelowitz, Laura Spencer, and Roland Florenz, the PEPL tradition you inherit is truly exceptional. I've enjoyed getting to know you on my brief stints back in Ann Arbor, and hope I can help future PEPL generations as well as my predecessors have helped me.

None of this would have been possible without the long-distance administrative help from a few hard-working ladies back in Michigan. I'd like to thank Denise Phelps for keeping me on course, and especially helping me get a Ph.D. in Aerospace Engineering as opposed to Aerospace Science. Denise Edmund went above and beyond in helping me complete the final Rackham degree requirements. Colleen Root is much appreciated for all her work scheduling meetings with Alec. Last but not least is Margaret Fillion, who is one of a kind.

Previous PEPL graduates have described their time at AFRL as filled with freedom and frustration, or more succinctly as "purgatory". All are true descriptions, but the group of friends and colleagues help overshadow most of the shortcomings. A special thanks to Bill Larson, Justin Koo, and Michelle Scharfe for many fruitful discussions and patience when I used you as a sounding board. Bill also deserves tribute for his vital contributions to the Hall thruster efficiency architecture in Chapter 2. Garrett Reed deserves special recognition for developing an automated DAQ system for Chamber 3. Thanks to Bill Hargus and Mike Nakles for assistance with Chamber 1, and to Daron Bromaghim for advice on STINFO related issues.

Then there's the AFRL support staff. I gratefully acknowledge "Skip" Skipworth, John Morrow, Bob Gregory, and Tom Glover for their continual maintenance and resuscitation of Chamber 3. Linda Skipworth, Rosa Ritter, Eva Lawson, and Lynn Hutchison, I can't imagine where this place would be without you. Thanks for all the things that you do to keep us going on a daily basis.

I express gratitude to my advisors and mentors at the University of Washington, specifically Denice Denton and Mark Campbell. Denice gave me the opportunity to

begin experimental research during my first quarter as a freshman, and was instrumental in my early undergraduate years. She was a special advisor who continually provided pathways for further growth and did everything in her means to enable students to realize their full potential. Mark is a mentor who gave his students the same trust and respect he would to a professor, and in the process makes people want to work harder for him. Thanks for allowing a 20 year old kid to play with flight hardware, even if it never got off the ground. In addition, I'd like to thank my good friends at the University of Washington, Ruchi and Nels, whose support and guidance was beyond measure.

My family has shown tremendous support over the years, each in their own way. I'm not sure any of you understand what I do, but your love and encouragement made all the difference. I'm grateful to my Mom and Dad for the love, the foundation, and the freedom they have always provided. I can't express in words what it's meant to me. I'd like to thank my brother, Steve, for his sound advice and always keeping things in perspective. There are too many people to name, but thank you all.

Lastly, I want to thank my wife, Katie. She's dedicated these last months to helping me focus solely on finishing this degree, and I can't imagine how much more difficult it would be without her enduring love and support. Katie, I told you I had "about" a year left when we started dating…. It's taken a slightly longer than that, but I can't wait to begin the next phase of our lives together. Thank you.

Daniel Lucas Brown

aka: "DB", "Bearded", "Oso de la Noche"

May 2009

Table of Contents

Acknowledgements ..... **ii**

List of Figures ..... **x**

List of Tables ..... **xxii**

List of Appendices ..... **xxiii**

Nomenclature ..... **xxiv**

Abstract ..... **xxxii**

Chapter 1. Introduction **1**

1.1 Fundamentals of Space Propulsion 2
1.2 Electric Propulsion Thruster Technologies 6
1.2.1 Electrothermal Propulsion 6
1.2.2 Electromagnetic Propulsion 6
1.2.3 Electrostatic Propulsion 7
1.3 Hall Effect Thruster Overview 9
1.3.1 Hall Thruster Physics 10
1.3.2 Hall Thruster Design Considerations and Operation 11
1.4 Motivation 13
1.5 Contributions of Research 15
1.6 Organization 19

Chapter 2. Hall Thruster Efficiency Architecture **22**

2.1 Historical Perspective and Recent Methodologies 23
2.2 Development of a Hall Thruster Efficiency Architecture 26
2.2.1 Formulation of Thrust 27
2.2.2 Decomposing Total Thruster Efficiency 31
2.2.3 Propellant Efficiency 32
2.2.3.1 Charge Utilization 33
2.2.3.2 Mass Utilization 35
2.2.3.3 Neutral-gain Utilization 37
2.2.4 Energy Efficiency 39
2.2.4.1 Voltage Utilization 40
2.2.4.2 Current Utilization 42
2.2.5 Beam Efficiency 44
2.3 Performance Parameters 49

2.3.1 Voltage Exchange and Mass Exchange Parameters 49
2.3.2 Specific Impulse and Thrust to Power Ratio 51
2.3.3 Energy Losses and Ionization Cost of a Multiply-Charged Plasma 51
2.4 Application to Experimental Results 53
2.5 Summary 54

Chapter 3. Experimental Apparatus 56

3.1 Vacuum Facilities 57
3.1.1 Chamber 1 at AFRL 57
3.1.1.1 Power Electronics and Propellant Hardware 59
3.1.1.2 Diagnostic Positioning System 60
3.1.2 Chamber 3 at AFRL 61
3.1.2.1 Power Electronics and Propellant Hardware 64
3.1.2.2 Thruster Telemetry and Data Acquisition System 66
3.1.2.3 Diagnostic Positioning Systems 67
3.2 Laboratory Hall Effect Thruster 69
3.3 Performance and Plume Diagnostics 71
3.3.1 Inverted Pendulum Thrust Stand 71
3.3.2 Langmuir Probe 73
3.3.3 Retarding Potential Analyzer 76
3.3.4 ExB Probe 83
3.3.5 Faraday Probes 93
3.3.5.1 Nude Faraday Probe 93
3.3.5.2 Nested Faraday Probe 95
3.4 Summary 102

Chapter 4. Evaluation of Faraday Probe Design and Scattering Effects 103

4.1 Past Investigations 104
4.2 Measurement Coordinate System Effects and Correction Factors 107
4.2.1 Angle of Beam Ions to Probe Face 108
4.2.2 Distance of Beam Ions to Probe Face 113
4.2.3 Faraday Probe Angle and Distance Correction Factors 117
4.2.4 Additional Spatial Measurement Uncertainty 119
4.3 Examination of Faraday Probe Design and Geometry 120
4.3.1 Comparison of Nested Faraday Probe Current Density Profiles 120
4.3.2 Gap Correction Factor for the Effective Projected Collection Area 124
4.3.3 Effects of Non-uniform Bias Potential 131
4.3.4 Applying the Gap Correction Factor to Past Results 138
4.4 Analysis of Ion Plume Scattering and Facility Effects 145
4.4.1 Determination of Vacuum Current Density Profiles 146
4.4.2 Analysis of Ion Migration in the Plume 155
4.4.3 Comparison of Ion Migration Results With Numerical Simulations 161
4.4.4 Calculation of Vacuum Beam Divergence 164
4.5 Recommendations for High Accuracy Current Density Profiles 169
4.6 Summary and Conclusions 172

Chapter 5. Characterization of Low-Voltage Hall Thruster Operation 176
5.1 Facility Effects on Thruster Performance and Beam Formation 177
5.1.1 Thrust and Discharge Current 178
5.1.2 Ion Current and Plume Expansion 184
5.2 Thruster Performance Measurements 199
5.2.1 Current-Voltage Characteristics 199
5.2.2 Thrust and Performance 200
5.2.3 Thruster Discharge Oscillations 203
5.3 Far-field Plume Measurements 209
5.3.1 Current Density Profiles and Ion Beam Current 209
5.3.2 Ion Energy per Charge Distributions 213
5.3.3 Ion Species Current Fractions and Mass Flow Fractions 216
5.4 Low Discharge Voltage Hall Thruster Loss Mechanisms 220
5.4.1 Evaluation of Performance Parameters 220
5.4.2 Performance Utilization Efficiencies 225
5.4.2.1 Beam Efficiency 227
5.4.2.2 Propellant Efficiency 231
5.4.2.3 Energy Efficiency 235
5.4.3 Ionization Processes and Joule Heating Losses 237
5.5 Summary 247

Chapter 6. Low Discharge Voltage Thruster Operating Regimes 251
6.1 Visualization of Low Discharge Voltage Operating Regimes 253
6.2 Mapping Thruster Operation for Anode and Cathode Flow Rate 255
6.3 Discharge Oscillations of Low-Voltage Operating Regimes 261
6.4 Far-field Plume Measurements 267
6.4.1 Ion Beam Current and Plume Divergence 267
6.4.2 Plasma Potential and Electron Temperature 270
6.4.3 Distributions of Ion Energy and Ion Energy per Charge 275
6.5 Variation in Near-field Neutral Density 284
6.6 Potential Causes of Low Discharge Voltage Operating Regimes 290
6.6.1 Thruster Ionization Instabilities 290
6.6.2 Cathode Induced Discharge Oscillations 291
6.6.3 Discharge Power Supply Oscillations 294
6.7 Summary 294

Chapter 7. Summary and Concluding Remarks 296
7.1 Low Discharge Voltage Hall Thruster Loss Mechanisms 297
7.2 Low Discharge Voltage Hall Thruster Operating Regimes 299
7.3 Facility Effects and Formation of the Jet-mode Plume Structure 300
7.4 Evaluation of Faraday Probe Design and Analysis 302
7.5 Development of a Hall Thruster Efficiency Architecture 305
7.6 Recommendations for Future Work 307
7.6.1 Analysis of Joule Heating Discharge Loss Mechanisms 307

7.6.2 Interpretation of Low Discharge Voltage Operating Regimes ……. 308
7.6.3 Validation of Faraday Probe Experimental Methods and Analysis ….. 310
7.6.4 Improvements in Characterization of Global Performance Quantities.. 311

Appendices ……..…… 313

Bibliography …..……..…… 333

List of Figures

Figure 1-1 Trade-space of payload mass fraction as a function of exhaust velocity with variations in propulsion system metrics for a maneuver with ΔV=4000 m/s, (theoretical LEO to GEO transfer). Variations in maneuver time, specific power, and thruster efficiency are studied for the rocket equation 4

Figure 1-2 Cross-sectional illustration of a conventional magnetic layer Hall thruster with a centrally mounted cathode 12

Figure 2-1 Ionization number fraction as a function of mass utilization with lines of constant neutral velocity ratio, y_0, for a singly-charged plasma ($Q = 1, f_2^* = f_3^* = 0$) 37

Figure 2-2 Neutral-gain utilization as a function of mass utilization with variations in reduced neutral speed from y_0=0.01 to y_0=0.06 for Q=1 and Q=3, which are limiting cases for a trimodal ion population. 39

Figure 2-3 Illustration of electron-impact cascade ionization of singly-charged and doubly-charged ions in the Hall thruster discharge 43

Figure 2-4 Variation in γ due to ion species composition for Φ_m=1. Lines of constant f_2^*=0 and f_3^*=0 bound γ for a trimodal ion population, and are compared with the approximation $\gamma \approx Q^{-1/2}$ 47

Figure 2-5 Representative distribution of beam current and current density at 1-meter radius as a function of angular position in the plume of a nominal 6-kW laboratory Hall thruster at 300-V, 20-mg/s described in Chapter 3. 49

Figure 3-1 Chamber 1 schematic (not to scale) 58

Figure 3-2 Diagnostic positioning system in Chamber 1 with R,θ-coordinate axis control 60

Figure 3-3 Chamber 3 at AFRL/RZSS 61

Figure 3-4 Chamber 3 schematic (not to scale) 63

Figure 3-5 Electrical diagram of power electronics in Chamber 3 for the 6-kW Hall thruster and LaB6 cathode 64

Figure 3-6 Schematic of the Chamber 3 propellant distribution system 65

Figure 3-7 Diagnostic positioning system in Chamber 3 with θ-coordinate axis control. ……..... 67

Figure 3-8 Diagnostic positioning system in Chamber 3 with X,Y,θ-coordinate axis control. ……..... 68

Figure 3-9 Photograph of the 6-kW laboratory Hall thruster with a centrally mounted LaB6 cathode. ……..... 70

Figure 3-10 Photograph of the 6-kW laboratory Hall thruster (courtesy of JPL). ……. 70

Figure 3-11 Schematic of the 6-kW laboratory model Hall thruster illustrating locations of propellant injection at the anode, cathode, and auxiliary port. ……..... 71

Figure 3-12 Photograph of a 6-kW Hall thruster mounted on the inverted pendulum thrust stand at AFRL/RZSS ..…..... 72

Figure 3-13 Langmuir probe trace comparing data analysis techniques used to determine plasma potential. The measurement was taken on thruster centerline 1 meter downstream of the 6-kW HET operating at 105-V, 20-mg/s in Chamber 3. ……..... 76

Figure 3-14 Cross-sectional illustration of the RPA showing the multi-grid design and particle filtration process. …..…..... 77

Figure 3-15 RPA trace showing the data analysis technique used to determine the most probable ion potential. The measurement was taken on thruster centerline 1-meter downstream of the 6-kW HET operating at 300-V, 20-mg/s in Chamber 3 ……...……..... 79

Figure 3-16 Potential diagram illustrating the relationship between measured voltages (V_d, V_{cg}), plume measurements (V_{mp}, V_p) and calculated potentials (V_a, V_{loss}) …..……..... 80

Figure 3-17 Electrical diagram of RPA grid power electronics and DAQ system. ……... 82

Figure 3-18 Photograph of the ExB probe build by Plasma Controls, LLC. The top cover is removed to illustrate the electromagnetic fields in ion velocity filter and regions of ion collimation, drift, and collection. ……..... 86

Figure 3-19 Electrical diagram of ExB probe power electronics and DAQ system. …..…. 87

Figure 3-20 Normalized ExB probe trace showing the data analysis technique used to determine ion species fractions. The measurement was taken on thruster centerline 1-meter downstream of the 6-kW HET operating at 300-V, 20-mg/s in Chamber 3 …..……..... 88

Figure 3-21 Normalized ExB probe traces on thruster centerline from 1.0 to 1.3-meters downstream of the 6-kW HET operating at 300-V, 10-mg/s and 150-V, 20-mg/s in Chamber 3 ……..... 91

Figure 3-22 Electrical diagram of the nude Faraday probe power electronics and DAQ system. ……..……...…. 94

Figure 3-23 Top-view and cross-sectional diagrams of the AFRL nested Faraday probe. .. 95

Figure 3-24 Top view of the four collection area configurations of AFRL nested Faraday probe. Regions of blue are the current collecting surfaces orthogonal to the beam. The gap between Collector 1 and Collector 2 is equal to the gap between Collector 2 and the guard ring. ……...……... 96

Figure 3-25 Photograph of the AFRL nested Faraday probe shown in the 0.5 mm gap width configuration ..……...…….. 98

Figure 3-26 Electrical diagram of the nested Faraday probe power electronics and DAQ system ..……...…….. 99

Figure 3-27 Nested Faraday probe bias voltage characterization of the inner collector (left) and the outer collector (right) for the 0.5 mm and 1.5 mm gap configurations at $3.1x10^{-6}$ and $3.4x10^{-5}$ torr. Normalized current is shown at the location of largest Debye length in the plume at θ=0 degrees and the location of smallest Debye length in the plume at θ=90 degrees at 8 CCDD and 20 CCDD …….……...……. 101

Figure 4-1 Coordinate system for probe distance and angular location with the thruster modeled as two point sources ..……...…… 108

Figure 4-2 Diagram of ion angles of incidence and relevant distances for the probe angular orientation in a two point source system. ……...…… 109

Figure 4-3 Ion angle of incidence from the left and right point sources as a function of probe angular position with contours of constant $R/2R_{CL}$ = 4, 8, 12, 16, and 20 CCDD …..……...…… 111

Figure 4-4 Correction factor, κ_A, accounting for cosine losses in the probe collection area as a function of angular position with contours of constant $R/2R_{CL}$ = 4, 8, 12, 16, and 20 CCDD …..……...…. 111

Figure 4-5 Correction factor, κ_A, accounting for cosine losses in the probe collection area on channel centerline (θ=90°) as a function of downstream thruster diameters ($R/2R_{CL}$) ..……...…. 112

Figure 4-6 Diagram of the relevant angles and distances to characterize probe distance to the left and right ion point sources ..……...…. 114

Figure 4-7 Probe distance from the left and right point sources relative to the measurement radius, R, as a function of probe angular position with contours of constant $R/2R_{CL}$ = 4, 8, 12, 16, and 20 CCDD. ……...…. 115

Figure 4-8 Correction factor, κ_D, accounting for the probe distance to the left and right ion point sources as a function of angular position with contours of constant $R/2R_{CL}$ = 4, 8, 12, 16, and 20 CCDD. ……..…...…. 115

Figure 4-9 Probe distance from the left and right ion point sources relative to the measurement radius, R, as a function of downstream thruster diameters ($R/2R_{CL}$) at $\theta=0°$ and $\theta=90°$ 116

Figure 4-10 Combined effect of correction factors (κ_D/κ_A) accounting for the probe distance and angle with respect to the left and right ion point sources as a function of angular position with contours of constant $R/2R_{CL}$ = 4, 8, 12, 16, and 20 CCDD 117

Figure 4-11 Combined effect of the correction factors (κ_D/κ_A) on channel centerline ($\theta=90°$) as a function of downstream thruster diameters ($R/2R_{CL}$). 118

Figure 4-12 Normalized current density profiles from Collector 1 and Collector 1+2 for the 0.5 mm and 1.5 mm gap configurations measured at 8, 12, 16, and 20 CCDD with a facility background pressure of $3.1x10^{-6}$ torr 121

Figure 4-13 Comparison of collector area ratios and collected current ratios of the 0.5 mm configuration (top), 1.5 mm configuration (middle), and Collector 1 (bottom) at $3.1x10^{-6}$, $1.0x10^{-5}$, and $3.4x10^{-5}$ torr measured at 8, 12, 16, and 20 CCDD as a function of probe angular position. 123

Figure 4-14 Illustration of ions collected by the side walls of the nested Faraday probe and the increase in projected collection area. 125

Figure 4-15 Diagram of the nude Faraday probe collector (outer radius R_c, height h_C), guard ring (inner radius R_{GR}, height h_{GR}) and gap width (g) 126

Figure 4-16 Comparison of corrected and uncorrected collector area ratios and collected current ratios of the 0.5 mm configuration (top), 1.5 mm configuration (middle), and Collector 1 (bottom) at $3.1x10^{-6}$, $1.0x10^{-5}$, and $3.4x10^{-5}$ torr measured at 8, 12, 16, and 20 CCDD as a function of probe angular position 129

Figure 4-17 Normalized current density profiles, corrected with κ_G, from Collector 1 and Collector 1+2 for the 0.5 mm and 1.5 mm gap configurations measured at 8, 12, 16, and 20 CCDD with a facility background pressure of $3.1x10^{-6}$ torr 130

Figure 4-18 Normalized current to Collector 1 in the 0.5 mm gap configuration (Configuration 1) as a function of bias potential on Collector 2 and the guard ring. Measurements are normalized to the maximum centerline current for 0 V on the guard ring, and are shown from $\theta=50°$ to 130° in 10° increments at 20 CCDD with a facility background pressure of $3.1x10^{-6}$ torr 134

Figure 4-19 Normalized current to Collector 1+2 in the 0.5 mm gap configuration (Configuration 2) as a function of bias potential on the guard ring. Measurements are normalized to the maximum centerline current for 0 V on the guard ring, and are shown from $\theta=50°$ to 130° in 10° increments at 20 CCDD with a facility background pressure of $3.1x10^{-6}$ torr 135

Figure 4-20 Normalized current density profiles of the 0.5 mm and 1.5 mm gap configurations with -15 V on the collector and 0 V, -15 V, and -25 V on the guard ring at 20 CCDD. Measurements are normalized to the maximum centerline current of Configuration 1 with -15 V on the guard ring. 137

Figure 4-21 Diagram of the JPL nude Faraday probe 139

Figure 4-22 Diagram of the GRC nude Faraday probe 140

Figure 4-23 Total ion beam current of the NASA173M-v1 as a function of background pressure for the JPL and GRC nude Faraday probes from Walker, *et al*. 140

Figure 4-24 Ratio of total ion beam current of the JPL nude Faraday probe relative to the GRC nude Faraday probe with variations in facility pumping speed for the case of no area corrections (Case 1, top), both probe collection areas corrected (Case 2, middle), and only the GRC probe collection area corrected (Case 3, bottom) 143

Figure 4-25 Illustration of the distribution of ions in the gap volume of the JPL Faraday probe for high and low facility background pressure 144

Figure 4-26 Normalized collected ion current of the nested Faraday probe Configuration 1 as a function of background pressure at discrete angular locations in the plume at 20 CCDD. Measurements are normalized to the maximum collected current of the profile at 3.4×10^{-5} torr 148

Figure 4-27 Residuals and slope of the extrapolated collected ion current of the nested Faraday probe Configuration 1 as a function of angular position at 8, 12, 16, and 20 CCDD 149

Figure 4-28 Residuals and slope of the extrapolated collected ion current of the nested Faraday probe Configuration 1 as a function of angular position at 8, 12, 16, and 20 CCDD. A superposition of two Gaussian curves is fit to the experimental slope. Note the differences in scale of the Slope axes. 152

Figure 4-29 Normalized ion current density profiles of the nested Faraday probe Configuration 1 as a function of angular position at 8, 12, 16, and 20 CCDD. The extrapolated vacuum profiles are compared to measurements at background pressures of 3.1×10^{-6}, 1.0×10^{-5}, and 3.4×10^{-5} torr. Current density profiles are normalized to the maximum extrapolated vacuum current density at 8 CCDD 153

Figure 4-30 Normalized ion current density profiles at vacuum conditions of the nested Faraday probe Configurations 1, 2, 3, and 4 as a function of angular position at 8, 12, 16, and 20 CCDD. Current density profiles are normalized to the maximum extrapolated vacuum current density of Configuration 1 at 8 CCDD. 154

Figure 4-31 Normalized profiles of ion current density per solid angle at vacuum conditions and residuals of the nested Faraday probe Configuration 1 as a function of angular position at 8, 12, 16, and 20 CCDD. Profiles are normalized to the maximum extrapolated vacuum current per steradian at 8 CCDD 155

Figure 4-32 Diagram of the axisymmetric spherical stripe coordinate geometry for analysis of angular ion beam current distribution in the plume. 156

Figure 4-33 Normalized vacuum profiles of ion beam current per unit stripe and relative difference in ion beam current distributions with variation in downstream distance and pressures as a function of angular position. All profiles are normalized to the maximum extrapolated vacuum beam current at 8 CCDD 158

Figure 4-34 Distributions of the relative difference in ion beam current per unit stripe with variation in downstream distance and pressures as a function of angular position. All profiles are normalized to the maximum extrapolated vacuum beam current at 8 CCDD 159

Figure 4-35 Normalized difference in vacuum ion beam current at 12, 16, and 20 CCDD relative to the profile at 8 CCDD as a function of angular position. All profiles are normalized to the maximum extrapolated vacuum beam current at 8 CCDD 160

Figure 4-36 Comparison of the simulated and experimental normalized differences in vacuum ion beam current at 12, 16, and 20 CCDD relative to the profile at 8 CCDD as a function of angular position. All profiles are normalized to the maximum extrapolated experimental vacuum beam current at 8 CCDD. The simulated and experimental normalized current density profiles are shown in the small window for reference 163

Figure 4-37 Diagram of the axial component of beam current relative to channel centerline 165

Figure 4-38 Experimental data (markers) and 2nd order polynomial trendlines (lines) of the ratio of the axial component of ion beam current relative to the total ion beam current of the nested Faraday probe Configurations 1, 2, 3, and 4 as a function of downstream distance at background pressures of 3.1×10^{-6} torr, 1.0×10^{-5} torr, 3.4×10^{-5} torr, and the ratio extrapolated to vacuum. Experimental data deviates from the trendlines by less than ±0.1%. 167

Figure 5-1 Experimental and modeled thrust and discharge current of the 6-kW Hall thruster as a function of facility background pressure for 300-V, 7-CFF and 150-V, 16-CFF operation at 10-mg/s and 20-mg/s anode flow rate. 182

Figure 5-2 Experimental parameters E_1 and E_2 with increasing background pressure for 300-V, 7-CFF and 150-V, 16-CFF operation at 10-mg/s and 20-mg/s anode flow rate. Arrows of decreasing pressure illustrate facility effects on total thruster efficiency, and extrapolated vacuum conditions are labeled as p=0 183

Figure 5-3 Angular distributions of ion current density (top) and ion beam current (bottom) with increasing background pressure for 300-V, 7-CFF and 150-V, 16-CFF operation at 20-mg/s anode flow rate 185

Figure 5-4 Angular distributions of current density and ion beam current extrapolated to vacuum (top) and the angular difference in ion beam current from vacuum (bottom) with increasing background pressure for 300-V, 7-CFF at 10-mg/s and 20-mg/s anode flow rate 186

Figure 5-5 Angular distributions of current density and ion beam current extrapolated to vacuum (top) and the angular difference in ion beam current from vacuum (bottom) increasing background pressure for 105-V, 16-CFF at 10-mg/s and 20-mg/s anode flow rate 188

Figure 5-6 Illustration of facility effects on the low-power Hall thruster in Chamber 1. Increased pressure alters the location of ionization of facility neutrals near the thruster exit and varies the effect of the external potential field on ionized facility neutral. Potential field contours from the near-field of the P5 HET[60] are included to display a characteristic external figure structure ... 189

Figure 5-7 Illustration of facility effects on the 6-kW Hall thruster in Chamber 3. Increased pressure has minimal effect on the location of ionization of facility neutrals near the thruster exit. Potential field contours from the near-field of the P5 HET[60] are included to display a characteristic external figure structure 191

Figure 5-8 Angular distributions of the residuals (left) and slope (right) of the ion current density linear extrapolation to vacuum conditions for the 105-V, 120-V, 150-V, and 300-V discharge at 10-mg/s and 20-mg/s anode flow rate 193

Figure 5-9 Angular distributions of the slope of the ion current density linear extrapolation to vacuum condition for experiment and a superposition of Gaussians at 20-mg/s (left) and 10-mg/s (right) anode flow rate 195

Figure 5-10 Discharge current, ion beam current, and the axial component of ion beam current with increasing background pressure for 300-V, 7-CFF and 150-V, 16-CFF operation at 10-mg/s and 20-mg/s anode flow rate 198

Figure 5-11 Thruster discharge current extrapolated to vacuum conditions as a function of discharge voltage from 105-V to 300-V at constant 10-mg/s and 20-mg/s anode flow rate 200

Figure 5-12 Thrust extrapolated to vacuum conditions as a function of discharge voltage from 105-V to 300-V at constant 10-mg/s and 20-mg/s anode flow rate …… 201

Figure 5-13 Total thruster efficiency, T/P, and total Isp as a function of discharge voltage from 105-V to 300-V at constant 10-mg/s and 20-mg/s anode flow rate …… 202

Figure 5-14 Total thruster efficiency, T/P, and total Isp as a function of discharge power from 105-V to 300-V at constant 10-mg/s and 20-mg/s anode flow rate …… 203

Figure 5-15 Thruster discharge current power spectra for 105-V to 300-V at 10-mg/s and 20-mg/s anode flow rate …… 205

Figure 5-16 Thruster cathode-to-ground potential power spectra for 105-V to 300-V discharge at 10-mg/s and 20-mg/s anode flow rate. …… 206

Figure 5-17 Dominant frequency from the discharge current power spectra and maximum peak-to-peak oscillation amplitude relative to the mean discharge current for 105-V to 300-V discharge at 10-mg/s and 20-mg/s anode flow rate …… 208

Figure 5-18 Ion current density profiles extrapolated to vacuum conditions and angular distributions of ion beam current on a 1-meter radius for 105-V to 300-V discharge at 20-mg/s (left) and 10-mg/s (right) anode flow rate …… 210

Figure 5-19 Integrated ion beam current and the axial component of ion beam current from vacuum current density profiles at 1 meter radius for 105-V to 300-V discharge at 20-mg/s and 10-mg/s anode flow rate …… 212

Figure 5-20 Langmuir probe traces of dI/dV on thruster centerline located 1-meter downstream of the exit plane for 105-V to 300-V discharge at 10-mg/s and 20-mg/s anode flow rate …… 214

Figure 5-21 RPA collected ion current traces and Normalized RPA ion energy per charge distributions on thruster centerline located 1-meter downstream of the exit plane for 105-V to 300-V discharge at 10-mg/s and 20-mg/s anode flow rate …… 215

Figure 5-22 Normalized ExB measurements of ion energy distributions on channel centerline located 1-meter downstream of the thruster exit plane for 105-V to 300-V discharge at 10-mg/s and 20-mg/s anode flow rate …… 218

Figure 5-23 Ion mass flow fractions (left), ion current fractions (middle), and ion species number fractions (right) of Xe^{+}, Xe^{+2}, and Xe^{+2} from ExB measurements of ion energy distribution on channel centerline 1-meter downstream of the exit plane for 105-V to 300-V discharge at 10-mg/s and 20-mg/s anode flow rate. Labels for increased CFF at 120-V operation are listed on ion current fractions, and may be used to determine the operating condition on traces of ion mass flow fractions and ion species number fractions ……...…. 219

Figure 5-24 Total thruster efficiency calculated with plume properties compared to total thruster efficiency based on thrust measurements for 105-V to 300-V discharge at 10-mg/s and 20-mg/s anode flow rate. ……...…. 221

Figure 5-25 Comparison of thrust to power ratio, total specific impulse, and total thruster efficiency calculated with plume properties and thrust measurements for 105-V to 300-V discharge at 20-mg/s anode flow rate 222

Figure 5-26 Comparison of thrust to power ratio, total specific impulse, and total thruster efficiency calculated with plume properties and thrust measurements for 105-V to 300-V discharge at 10-mg/s anode flow rate 222

Figure 5-27 Comparison of the voltage exchange parameter and the mass exchange parameter calculated with plume properties and thrust measurements for 105-V to 300-V discharge at 10-mg/s and 20-mg/s anode flow rate ……..... 223

Figure 5-28 Comparison of the energy efficiency (top), propellant efficiency (middle), and beam efficiency (bottom) as a function of discharge voltage for 105-V to 300-V at 10-mg/s and 20-mg/s anode flow rate …….…….…. 226

Figure 5-29 Comparison of the axial component of ion beam current (top), beam divergence half-angle (middle), and beam efficiency (bottom) as a function of voltage at 10-mg/s (left) and 20-mg/s (right) anode flow rate. Values calculated from Faraday probe measurements extrapolated to vacuum are compared to the values required to equate performance parameters based on plume measurements with those based on thrust measurements ……. 228

Figure 5-30 Thrust to power ratio, total specific impulse, and total thruster efficiency calculated with plume measurements based on the estimated axial component of ion beam current at the exit compared to calculations based on thrust measurements for 105-V to 300-V at 10-mg/s and 20-mg/s anode flow rate ..……...…. 229

Figure 5-31 Comparison of the factors affecting propellant efficiency as a function of discharge voltage for 105-V to 300-V at 10-mg/s and 20-mg/s anode flow rate. Partial efficiencies include the neutral-gain utilization (top), charge utilization (middle), and mass utilization (bottom). ……...…. 232

Figure 5-32 Comparison of the factors affecting the ratio of output moles of charge per input moles of propellant, χ, for 105-V to 300-V at 10-mg/s and 20-mg/s anode flow rate. Average ion charge (top), the value χ (middle), and the mass utilization (bottom) are shown as a function of discharge voltage ...…. 235

Figure 5-33 Comparison of the factors affecting energy efficiency as a function of discharge voltage for 105-V to 300-V at 10-mg/s and 20-mg/s anode flow rate. Partial efficiencies include the voltage utilization (top) and current utilization (bottom) 236

Figure 5-34 Comparison of jet power with the total power losses and the minimum power required for ionization as a function of discharge power for 105-V to 300-V at 10-mg/s and 20-mg/s anode flow rate 238

Figure 5-35 Comparison of the total power losses and the minimum power required for ionization (top) with the ionization cost per beam ion (bottom) as a function of discharge power for 105-V to 300-V at 10-mg/s and 20-mg/s anode flow rate 240

Figure 5-36 Comparison of the experimental anode electron current fraction (top) with the theoretical minimum electron current fraction (bottom) for ideal cascade ionization as a function of discharge voltage for 105-V to 300-V at 10-mg/s and 20-mg/s anode flow rate. Experimental and theoretical anode electron currents are normalized by the discharge current. The experimental electron current to the anode is compared to manifolds of anode electron current for constant ionization potential per beam ion of a singly-charged plasma (Q=1) during 10-A and 20-A operation. The theoretical minimum electron current to the anode is compared to manifolds of anode electron current for constant discharge current operation of a singly-charged plasma (Q=1) for the minimum xenon ionization potential of 12 eV/ion 242

Figure 5-37 Comparison of the factors affecting thrust to power as a function of discharge voltage for 105-V to 300-V at 10-mg/s and 20-mg/s anode flow rate. Discharge properties related to ion species composition (top), the axial component of ion beam current (upper middle), and the most probable ion acceleration potential (lower middle) are shown relative to the T/P (bottom) 246

Figure 6-1 Photographs of the 6-kW Hall thruster jet-mode plume structure for the low-current mode (top left) and high- current mode (bottom left) during 105-V, 20-mg/s operation. Contours of constant image intensity are shown for the low-current mode (top right) and the high-current mode (bottom right). Photos were taken with identical settings on a tripod mounted Nikon D200 DSLR using a 70 mm lens with manual focus at F/5, ISO-400, and exposure time of 1/2000 sec 254

Figure 6-2 Mapping of anode and cathode thruster operating characteristics at 100-V, 105-V, 110-V, 115-V, and 120-V discharge. Discharge current, thrust, T/P, and total thruster efficiency are shown for lines of constant discharge voltage as a function of cathode flow fraction during 10-mg/s (left column), 15-mg/s (middle column), and 20-mg/s (right column) anode mass flow rate operation. Operating characteristics are reported for facility background pressure in the range of 0.8×10^{-5} to 1.2×10^{-5} torr. Transitions from the operation in low-current to high-current mode are shown with arrows 256

Figure 6-3 Voltage exchange parameter and mass exchange parameter at 100-V (top), 105-V (middle), and 110-V (bottom) thruster operation for lines of increasing cathode flow during 10-mg/s, 15-mg/s, and 20-mg/s anode flow. Operating characteristics are reported for facility background pressure in the range of $0.8x10^{-5}$ to $1.2x10^{-5}$ torr. Transitions from the operation in high-current to low-current mode are shown with arrows, indicating the direction of increasing cathode flow fraction ……..……...…. 258

Figure 6-4 Thruster I-V characteristics at 10-mg/s anode flow rate. Lines of constant cathode flow rate operation are shown as a function of discharge voltage from 100-V to 300-V. Low discharge voltage operation is magnified from 100-V to 120-V discharge ……..……...…. 260

Figure 6-5 Comparison of discharge current oscillations in the low-current and high-current modes for 105-V, 20-mg/s, 16-CFF operation (top) and 120-V, 10-mg/s, 7-CFF operation (bottom) during a 5-ms time period ..……...…. 262

Figure 6-6 Comparison of discharge current oscillation spectra (top) and cathode to ground potential oscillation spectra (bottom) in the low-current and high-current modes for 105-V, 20-mg/s, 16-CFF operation (left) and 120-V, 10-mg/s, 7-CFF operation (right) from 0 to 100-kHz. ……..……...…. 263

Figure 6-7 Comparison of discharge current oscillation spectra in the high-current mode for 105-V, 20-mg/s, 16-CFF operation (top) and 120-V, 10-mg/s, 7-CFF operation (bottom) with variation in facility background pressure ..…. 264

Figure 6-8 Comparison of discharge current oscillation spectra in the low-current mode (top) and high-current mode (bottom) for 120-V, 10-mg/s operation at 5, 7, and 12-CFF ……..……...…. 266

Figure 6-9 Comparison of ion current density extrapolated to vacuum for high-current and low-current regimes. The current density at 105-V, 20-mg/s, 16-CFF is compared to the case of decreased anode flow at 10-mg/s (top), decreased cathode flow rate at 10-CFF (middle), and increased anode potential at 120-V (bottom). Integrated ion beam current, divergence angle, and discharge current are listed in the legends for vacuum conditions . 269

Figure 6-10 Langmuir probe traces of normalized dI/dV on thruster centerline and the natural logarithm located 1-m downstream of the exit plane for 105-V, 20-mg/s operation with cathode flow fraction ranging from 8-CFF to 16-CFF ... 271

Figure 6-11 Angular variation of electron temperature from 0° to thruster centerline (top). Langmuir probe traces of normalized dI/dV (middle) and the natural logarithm (bottom) located 1-m downstream of the exit plane for 100-V, 20-mg/s, 7-CFF in the high-current operating regime ……..……...…. 273

Figure 6-12 Electron temperature on thruster centerline located 1-meter downstream of the exit plane for 100-V, 105-V, and 110-V at 10-mg/s (top), 15-mg/s (middle), and 20-mg/s (bottom) with cathode flow fraction ranging from 8-CFF to 26-CFF. Transitions from operation in high-current mode to low-current mode are shown with arrows, indicating the direction of increasing cathode flow fraction 274

Figure 6-13 Normalized RPA ion energy per charge distributions on thruster centerline located 1-meter downstream of the exit plane for 105-V, 20-mg/s operation with cathode flow fraction ranging from 8-CFF to 16-CFF. The ion energy per charge has been corrected for local plasma potential at the probe 277

Figure 6-14 Comparison of ExB probe ion energy distributions on channel centerline located 1-meter downstream of the exit plane for high-current and low-current regimes. The ion energy distribution at 105-V, 20-mg/s, 16-CFF is compared to the case of decreased anode flow at 10-mg/s (top), decreased cathode flow rate at 10-CFF (middle), and increased anode potential at 120-V (bottom). Ion species peaks are for comparison, and do not account for additional ion acceleration from plasma potential to the ground reference at the probe entrance 280

Figure 6-15 Comparison of ExB probe and RPA measurements on channel centerline located 1-meter downstream of the exit plane for 105-V, 20-mg/s, 10-CFF operation in the high-current and low-current regimes. The ExB probe ion energy distributions (top), ExB probe ion species energy per charge distributions (middle), and the comparison of RPA and ExB probe ion energy per charge distributions (bottom) are normalized to the peak of the low-current profile for each diagnostic 282

Figure 6-16 Experimental and modeled thrust (left) and discharge current (right) of the 6-kW Hall thruster in the high-current mode and low-current mode as a function of facility background pressure for 105-V, 20-mg/s, 16-CFF (top), 105-V, 10-mg/s, 16-CFF (upper middle), 105-V, 20-mg/s, 10-CFF (lower middle), and 120-V, 20-mg/s, 16-CFF (bottom). The neutral entrainment factor is listed for all cases. The differences in current utilization, discharge current, and ion beam current are listed between low-current mode and high-current mode at vacuum conditions 285

Figure 6-17 Ratio of thrust T/P and total Isp with variation in cathode flow and auxiliary propellant for 105-V, 20-mg/s operation in the high-current and low-current regimes. The total combined flow to the cathode and auxiliary port is fixed and equivalent to 10-CFF, such that the total mass flow to the thruster is constant. Performance parameters are extrapolated to vacuum conditions 289

List of Tables

Table 1-1 Typical performance range of electric propulsion technologies and comparison to chemical propulsion systems. ……..……...……. 8

Table 3-1 RPA grid bias potentials and grid separation. ……..... 81

Table 3-2 Nested Faraday probe dimensions. …….……...…. 96

Table 4-1 Angular span of nested Faraday probe collector configurations. ……....….. 119

Table 4-2 Corrected and uncorrected collection areas of the nested Faraday probe ….. 127

Table 4-3 Normalized collected current for variation in guard ring bias potential for the 0.5 mm gap configurations …….. 132

Table 4-4 Geometry and area correction of the JPL and GRC nude Faraday probes 139

Table 4-5 Comparison of the JPL and GRC Faraday probes for variations in background pressure and thruster operation from Walker, *et al*. ……..... 141

Table 5-1 Operating conditions of the 6-kW Hall thruster. …….…..……. 177

Table 5-2 Comparison of the dominant discharge current frequency of the 6-kW Hall thruster from measurements at AFRL and PEPL. ……...……...……. 207

Table 5-3 Comparison of the integrated ion beam current of the 6-kW Hall thruster from measurements at AFRL and PEPL. …..…..…….……. 211

Table 6-1 Comparison of the ion and electron currents in the discharge of the 6-kW Hall thruster during low-current and high-current operation ……. 268

List of Appendices

Appendix A	Propagation of Measurement Uncertainty ……..…….	313
Appendix B	Tables of Thruster Performance, Telemetry, and Plume Data ……..	319
Appendix C	Tables of Thruster Operation with Mass Flow Variation …...…….....	322
Appendix D	Tables of Thruster Characteristics with Operating Regime …….….....	328

Nomenclature

Constants

$\mathcal{F}$	Faraday constant	[96,485 C/mol]
g	gravitational constant	[9.81 m/s^2]
k_b	Boltzmann constant	[1.38x10^{-23} J/K]
$\mathcal{M}$	molecular mass of propellant	[0.1313 kg/mol for Xe]
m_e	electron mass	[9.1094x10^{-31} kg/particle]
$\mathcal{N}_A$	Avogadro's number	[6.02x10^{23} particles/mole]

Variables

A	spherical shell surface area element in the plume	[m^2]
$A_{0,1,2}$	second order polynomial coefficients	[-]
A_C	projected cross-sectional area of the FP probe collector	[m^2]
$\overline{\mathbf{A}}_C$	side-wall surface area of the FP collector	[m^2]
A_{C1}	projected cross-sectional area of the nested FP inner collector	[m^2]
A_{C1+C2}	cross-sectional area of the nested FP inner and outer collectors	[m^2]
$A_{Effective}$	corrected cross-sectional collection area of the FP collector and gap	[m^2]
A_{en}	entrained area of ingested neutral flow	[m^2]
A_{Gap}	projected cross-sectional area of the FP gap	[m^2]
$\overline{\mathbf{A}}_{GR}$	side-wall surface area of the FP guard ring	[m^2]
B	magnitude of magnetic field (magnetic flux density)	[T]
$\bar{B}$	magnetic flux density vector	[T]

B_{ExB}	ExB probe magnetic field	[T]
d_{ExB}	distance between ExB probe parallel plate electrodes	[m]
$\vec{E}$	electric field vector	[V/m]
E_1	voltage exchange parameter	[-]
E_2	mass exchange parameter	[-]
$\vec{F}$	force vector	[V/m]
F	thrust density vector in the plume	[N/m^2]
f^*_j	normalized exit mass flow fraction of *j*th ion species	[-]
$f(v), f(V)$	distribution function, velocity or voltage	[s/m]
f_b	Hall thruster breathing-mode frequency	[Hz]
g	gap width between the FP collector and guard ring	[m]
h_C	height of the FP collector	[m]
h_{GR}	height of the FP guard ring	[m]
I_{Axial}	axial component of ion beam current parallel to thruster centerline	[A]
I_{Beam}	integrated ion beam current	[A]
I_{C1}	ion current to the inner collector of the nested FP	[A]
I_{C1+C2}	combined current to the inner and outer collectors of the nested FP	[A]
I_d	anode discharge current	[A]
I_F	number fraction of ionized propellant	[-]
$I_{NFP}(V_{Bias})$	ion current to the NFP with variable guard ring bias potential	[A]
I_{probe}	collected probe current	[A]
I_{sat}	Langmuir probe ion saturation current	[A]
I_{sp}	specific impulse	[s]
j	propellant charge state index = 0, 1, 2, 3 for $Xe^0, Xe^{+1}, Xe^{+2}, Xe^{+3}$	[-]
$J(\theta)$	current density in the plume at angular position θ	[A/m^2]
K_n	Knudsen number	[-]
L	characteristic length scale in the discharge	[m]

L_i	length of ionization in the discharge	[m]
m_{final}	final vehicle mass	[kg]
$m_{initial}$	initial vehicle mass	[kg]
m_{pay}	mass of delivered mission payload	[kg]
m_{prop}	mass of consumed propellant	[kg]
m_{PS}	propulsion system dry mass	[kg]
$\dot{m}(\theta)$	mass flux in the plume at angular position θ	[kg/m^2·s]
$\dot{m}_{en}$	entrained neutral mass flow rate	[kg/s]
$\dot{m}_j$	mass flow rate of *j*th propellant species	[kg/s]
$\dot{m}_i$	total ion mass flow rate	[kg/s]
$\dot{m}_T$	total propellant mass flow rate to the anode and cathode	[kg/s]
n_e	electron number density	[m^{-3}]
n_i	ion number density	[m^{-3}]
n_n	neutral number density	[m^{-3}]
n_o	neutral number density of the facility background gas	[m^{-3}]
p	corrected facility background pressure	[torr]
p_b	vacuum facility base pressure for air	[torr]
P_d	thruster discharge power	[W]
p_i	background pressure measured by an ionization gauge	[torr]
P_{jet}	jet power	[W]
P_{loss}	maximum power lost to ohmic heating, excitation, and radiation	[W]
P_{min}	minimum power lost to sustain ionization	[W]
Q	average charge of propellant ions	[-]
r	fraction of electron current to the anode, electron recycle fraction	[-]
(1-r)	current utilization efficiency	[-]
R	downstream measurement distance from the axis of rotation	[m]
R_C	outer radius of the FP collector	[m]

R_{CL}	channel centerline radius of the thruster ……..	[m]
R_{GR}	inner radius of the FP guard ring …….	[m]
R_L, R_R	downstream distance from the left or right ion point source to the FP	[m]
$R_{L,e}$	electron gyroradius (Larmar radius) ……	[m]
$R_{L,i}$	ion gyroradius (Larmar radius) ……	[m]
r_{min}	theoretical minimum fraction of electron current to the anode …….	[-]
r_p	probe radius …….	[m]
t	time ……..…….……	[s]
T	component of thrust vector parallel to thruster centerline……	[N]
T_b	temperature of background facility neutrals …….	[k]
T_e	electron temperature……	[k or eV]
$\vec{u}$	particle velocity vector ……..……	[m/s]
u_e	exhaust velocity of propellant mass…….……..	[m/s]
u_{ExB}	ion pass speed of the ExB probe ……...	[m/s]
V_a	most probable ion acceleration potential …….	[V]
$V_{a,j}$	acceleration potential of *j*th ion species……	[V]
V_{Bias}	probe bias potential …….……	[V]
V_{cg}	cathode potential relative to facility ground ……	[V]
V_d	anode discharge voltage ……..	[V]
V_{loss}	anode potential not utilized for ion acceleration ……..	[V]
V_{mp}	RPA most probable ion voltage relative to facility ground ……..	[V]
V_p	plasma potential……	[V]
v_j	speed of *j*th species……	[m/s]
v_n	thermal speed of neutral propellant in the discharge…….	[m/s]
v_e	speed of electrons in the discharge ……..…….	[m/s]
$\bar{\mathbf{v}}(\theta)$	mean velocity vector over velocity space d**v** at angular position θ ...	[m/s]
$\bar{v}(\theta)$	radial component of $\bar{\mathbf{v}}$ at position θ in spherical coordinates ……..	[m/s]

$\overline{v}$	average propellant velocity in the plume	[m/s]
$\overline{v^2}$	average propellant squared velocity in the plume	[m^2/s^2]
$\overline{v_i}$	average ion velocity in the plume	[m/s]
$\overline{v_i^2}$	average squared ion velocity in the plume	[m^2/s^2]
ΔV	velocity increment	[m/s]
w	ExB probe bias voltage resolution	[-]
x	measured quantity, independent variable	[-]
X	translation stage axis in measurement coordinate system	[-]
y	measurand, dependent variable	[-]
Y	translation stage axis in measurement coordinate system	[-]
y_j	normalized speed ratio of the *j*th species	[-]
Z_j	ion charge state of the *j*th ion species = 1, 2, 3 for Xe^{+1}, Xe^{+2}, Xe^{+3}	[-]
α	propulsion system specific power	[W/kg]
α_A	ion angle of divergence relative to channel centerline	[rad]
α_L, α_R	angle of incidence from the left and right point sources to the FP	[rad]
β	fractional loss of ion acceleration potential	[-]
$(1-\beta)$	voltage utilization efficiency	[-]
γ_j	secondary electron emission yield of *j*th ion species	[electrons / ion]
ε_B	effective ionization cost per beam ion	[eV/ ion]
$\varepsilon_{B,min}$	minimum ionization cost per beam ion	[eV/ ion]
ε_j	ionization potential of *j*th ion species	[eV/ ion]
ζ_{en}	thrust entrainment factor for facility neutral ingestion	[-]
η_E	energy efficiency	[-]
η_T	total thruster efficiency	[-]
θ	angular position, horizontal plane in spherical coordinate system	[rad]
κ_A	FP correction accounting for ion angle of incidence to the probe	[-]
κ_D	FP correction accounting for probe distance to channel centerline	[-]

κ_G	FP correction accounting for ion collection in the gap ……..…….	[m^2]
λ	plume momentum divergence half-angle, λ=0 on thrust axis……	[rad]
λ_D	electron Debye length ……	[m]
λ_{mfp}	mean free path of electron-neutral collisions …….	[m]
ξ_A	neutral entrainment area factor ……..	[-]
ρ	radial coordinate in spherical coordinate system ……..	[-]
σ_j	CEX collision cross section of the *j*th ion species …….	[$Å^2$]
$\sigma_{e\text{-}n}$	electron-neutral ionization cross section…….	[$Å^2$]
Φ_m	mass utilization efficiency, ion mass flow fraction at exit ……	[-]
$\Phi_{N\text{-}G}$	neutral-gain utilization efficiency……..	[-]
Φ_P	propellant efficiency……...	[-]
Φ_q	charge utilization efficiency …….……	[-]
χ	output moles of charge per input moles of propellant ……...	[-]
φ	angular position, vertical plane in spherical coordinate system…..…	[rad]
Ψ_B	beam efficiency …….	[-]
Ω_j	ion current fraction of the *j*th ion species …….…….	[-]

Operations

[p]	parameter measured or calculated as a function of background pressure
[R]	parameter measured or calculated as a function of measurement distance
[R_{CL}]	parameter calculated as a function of channel centerline radius
[θ]	parameter measured or calculated as a function of angular location
Δ( )	measurement error or propagated uncertainty
$< >_m$	mass-weighted average quantity in the plume ($0<\theta<\pi$)
$< >_{mv}$	momentum-weighted average quantity in the plume ($0<\theta<\pi$)
$< >_J$	current-weighted average quantity in the plume ($0<\theta<\pi$)

Acronyms

AFRL	Air Force Research Laboratory
AFB	Air Force Base
AIAA	American Institute of Aeronautics and Astronautics
BN	Boron Nitride
CCDD	Channel Centerline Diameters Downstream
CEX	Charge Exchange
CFF	Cathode Flow Fraction
EP	Electric Propulsion
FFT	Fast Fourier Transform
FP	Faraday Probe
FWHM	Full Width at Half Maximum
GEO	Geosynchronous Earth Orbit
GRC	Glenn Research Center
HET	Hall Effect Thruster
HWHM	Half Width at Half Maximum
JPL	Jet Propulsion Laboratory
I-V	Current-Voltage characteristic
ISO	International Organization for Standardization
Isp	Specific Impulse
LaB6	Lanthanum Hexaboride
LEO	Low Earth Orbit
LVDT	Linear Voltage Displacement Transducer
LVTF	Large Vacuum Test Facility
MPDT	Magnetoplasmadynamic Thruster
NASA	National Aeronautics and Space Administration
NFP	Nested Faraday Probe

NIST	National Institute of Standards and Technology
NSTAR	NASA Solar electric propulsion Technology Applications Readiness
PEPL	Plasmadynamics and Electric Propulsion Laboratory
PIT	Pulsed Inductive Thruster
PPT	Pulsed Plasma Thruster
RPA	Retarding Potential Analyzer
RZSS	AFRL Spacecraft Propulsion Branch
SEE	Secondary Electron Emission
SPT	Stationary Plasma Thruster
TAL	Thruster with Anode Layer
T/P	Thrust to Power ratio
UM	University of Michigan
VDF	Velocity Distribution Function

Abstract

During the early development stages of Hall thruster technology, plasma research and propulsion advancements centered primarily on 300-V, 1600-s specific impulse operation. Since the first Hall thruster firing on a Soviet satellite in 1972, extensive investigations of the plasmadynamic discharge phenomena and operating characteristics progressed the propulsion concept to a high level of performance suitable for a wide range of near-earth maneuvers and interplanetary missions. The expanded performance envelope is primarily a function of improvements in thruster lifetime, thermal margin, discharge stability, and power system capability. Advancements in Hall thruster propulsion systems enable a wider range of input parameters to the thruster, including the applied anode-to-cathode potential. Operation in the low discharge voltage regime is associated with a decline in total thruster efficiency. This dissertation is intended to investigate low-voltage Hall thruster physics, identify dominant performance loss mechanisms, and determine the discharge characteristics that drive efficiency.

A systematic, experimental investigation of low-voltage Hall thruster performance and plume properties led to the conclusion that reduced electron temperature in the discharge was correlated with diminished Joule heating losses and a lower ionization cost per beam ion. However, the reduced electron temperature also decreased the ionization rate coefficient, and corresponded to an escalation of electron current to the

anode to sustain ionization processes. In addition, divergence of the kinetic ion jet limited the component of axially directed thrust and reduced the total thruster efficiency. Two jet-mode Hall thruster operating regimes were discovered for low-voltage operation, corresponding to ionization instabilities in the discharge and additional electron current to the anode. These modes are methodically characterized and potential causes are hypothesized.

During the course of this research, corollary studies on Faraday probe design, facility effects, and data analysis techniques improved accuracy of current density profiles and far-field plume properties. Faraday probe uncertainty is difficult to quantify, and therefore is often employed for qualitative analysis of electric propulsion plumes. The reduction in Faraday probe measurement uncertainty and the increased capability to approximate on-orbit plume expansion are significant improvements for comparison with numerical simulations and analysis of thruster performance.

Chapter 1

Introduction

In the early 20th century, the dawn of charged particle physics inspired theoretical propulsion advantages using high velocity electrons created in cathode ray tubes. High exhaust velocity electron jets, as opposed to ions, were initially proposed since the nature of positively charged particles had not been fully established.[1] The first analytical studies of electric propulsion can be traced to Robert Goddard, who realized the advantages of ion propulsion and the necessity of beam neutralization with oppositely charged particles. Goddard's studies led to patents for particle ionization concepts[2] and acceleration mechanisms for space propulsion.[3]

While rocketry and chemical propulsion evolved with revolutionary technical advancements, electric propulsion remained a futuristic thought-experiment until the early 1950s. Through the first half of the 20th century, scientists and engineers focused on space propulsion for manned exploration, and dismissed the advantages of electric propulsion because of the mass prohibitive power requirements of pre-1950s technology. In 1951, Lyman Spitzer, the "father" of the U.S. fusion program and founder of the Princeton Plasma Physics Laboratory, proposed on-orbit spacecraft acceleration significantly less than previously envisioned and thereby presented viable motivation for electric propulsion development.[4] Analyses of low-thrust trajectory optimization

established the advantages of electric propulsion for certain missions compared to high-thrust chemical propulsion. These improvements in capability were realized during the dawn of the space race, and initiated technology development programs for ion prolusion systems.

1.1 Fundamentals of Space Propulsion

Electric propulsion technology is based on decoupling the available beam energy from the propellant, which leads to significant advantages over conventional chemical thrusters. In chemical propulsion systems, potential energy is stored in the propellant molecular bonds and is converted to kinetic energy through the combustion process. The molecular composition has a finite potential energy and therefore limits the maximum exhaust velocity. In contrast, the available beam energy in electric propulsion systems is limited by the external power sources.

Conservation of momentum of a rocket propulsion system is the foundation of all space mission designs, and establishes the framework from which all propulsion system requirements are determined. The rocket equation in Eq. (1-1) was derived by Konstantin Tsiolkovsky for an ideal, constant momentum system in the absence of external forces to express the fundamental relationship between the system mass and exhaust velocity. In this incarnation of the rocket equation, the final vehicle mass (m_{final}) is related to the initial vehicle mass ($m_{initial}$), where the velocity increment ΔV is a fundamental metric of the total change in velocity over the course of the maneuver.

$$\frac{m_{final}}{m_{initial}} = \frac{m_{pay} + m_{PS}}{m_{prop} + m_{pay} + m_{PS}} = e^{-\Delta V / u_e} \tag{1-1}$$

where

$$m_{initial} = m_{final} + m_{prop} = m_{pay} + m_{PS} + m_{prop} \tag{1-2}$$

Maneuver requirements typically dictate ΔV and the delivered payload mass (m_{pay}). For chemical propulsion systems with an upper limit on the chemical energy stored in the propellant, the maximum payload is typically a matter of maximizing the exhaust velocity (u_e). The exhaust velocity of electric propulsion systems is limited by available on-board power, and the propulsion system mass (m_{PS}) is the predominant limitation. In most electric propulsion systems, the power electronics comprise a significant fraction of the mass.

Based on the rocket equation, a simple model of the payload mass fraction may be formulated for electric propulsion devices according to Eq. (1-3) as a function of the maneuver trip time (t), the thruster efficiency (η_T), and the specific power (α).[5]

$$\frac{m_{pay}}{m_{initial}} = e^{-\Delta V/u_e} - \left(1 - e^{-\Delta V/u_e}\right)\frac{u_e^2}{2\eta_T \alpha t} \tag{1-3}$$

This model will be employed to demonstrate the fundamental differences between chemical propulsion and electric propulsion technologies. In Figure 1-1, the payload fraction trade-space is demonstrated as a function of exhaust velocity for variation in trip time, variation in specific power, and variation in thruster efficiency. In all cases, the maximum payload fraction is optimized at a specific exhaust velocity. The maximum exhaust velocity of state-of-the-art chemical propulsion systems is typically less than 5 km/s, and therefore these devices rarely operate near the optimal exhaust velocity to maximize the payload fraction for a given maneuver. Higher ΔV maneuvers typically optimize payload fraction at increased exhaust velocity.

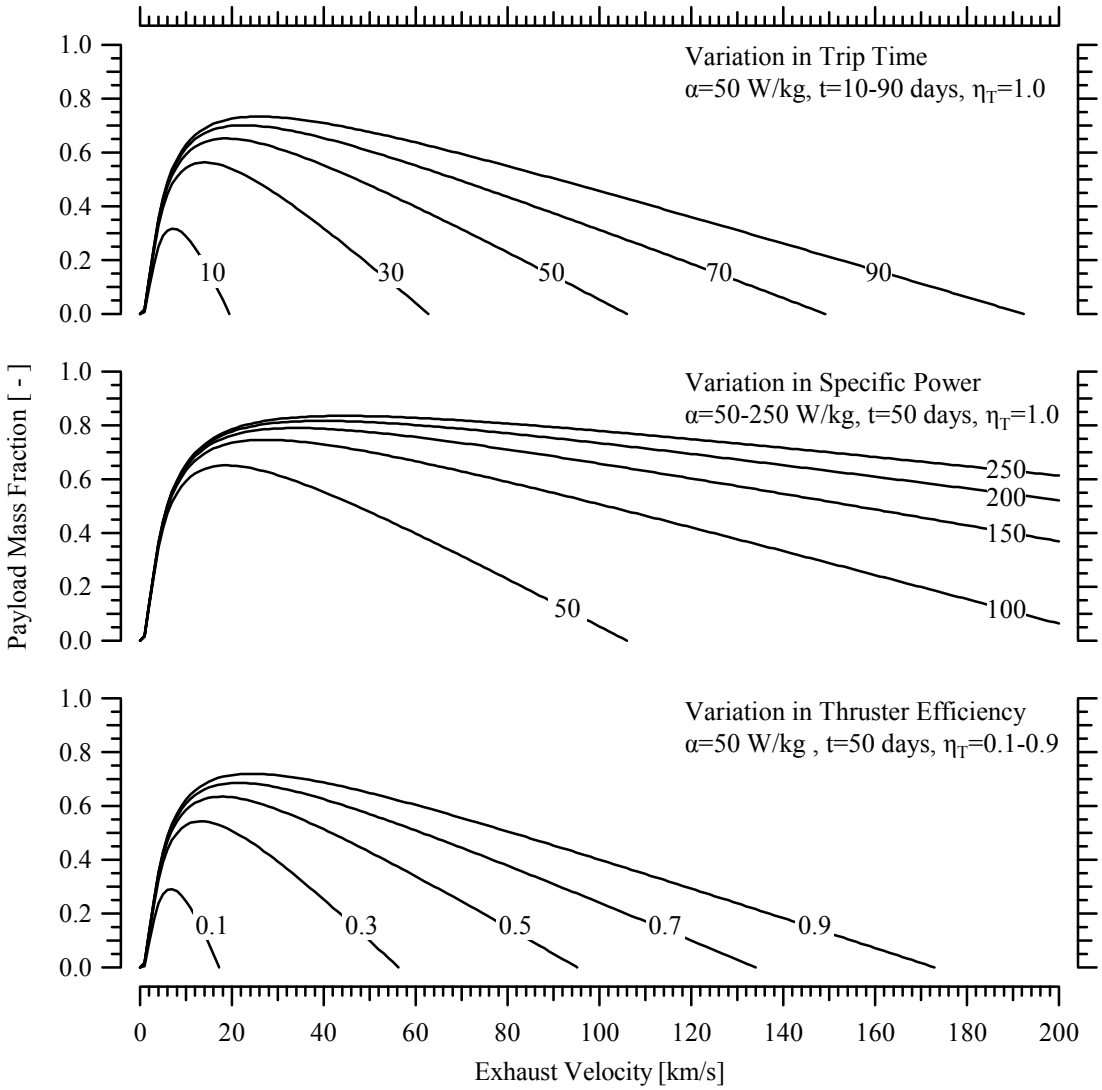

Figure 1-1 Trade-space of payload mass fraction as a function of exhaust velocity with variations in propulsion system metrics for a maneuver with ΔV=4000 m/s, (theoretical LEO to GEO transfer). Variations in maneuver time, specific power, and thruster efficiency are studied for the rocket equation.

In electric propulsion systems, the beam energy is decoupled from the propellant. This enables a wide range of exhaust velocities and enhances capability for optimization of payload fraction. The increased exhaust velocity corresponds to more efficient use of propellant, and thus has the potential to provide significant advantages to certain maneuvers. Some of these advantages include extended spacecraft lifetime, increased payload to orbit, and cost savings associated with a smaller launch vehicle. The costs

associated with these advantages make electric propulsion an attractive alternative for some mission classes.

The primary drawbacks of electric propulsion systems are the reduction in thrust and the long duration maneuver time required to realize the performance benefits. Therefore, electric propulsion technology is typically utilized for low thrust operations such as station-keeping, orbit-raising, repositioning, and attitude control. In some instances, such as interplanetary travel, electric propulsion may be a mission-enabling technology. The comparison with chemical thrusters and analysis of payload fraction optimization emphasizes that maximizing the exhaust velocity does not always correlate with the most advantageous thruster technology for a given maneuver.

Specific impulse (Isp) is a common performance metric used for comparison of the propulsion exhaust velocity. This parameter is defined for units of seconds in Eq. (1-4), and is a measure of the total impulse per unit weight of propellant.

$$I_{SP} \equiv \frac{\int T\, dt}{g \int \dot{m}_T\, dt} \approx \frac{u_e}{g} \tag{1-4}$$

The simplified formulation of Isp based on exhaust velocity does not account for the fraction of ionized propellant that contributes meaningful thrust in an electric propulsion device. Calculating Isp of electric propulsion technology based solely on the ion exhaust velocity may significantly over-predict the actual value based on the formal definition of total impulse per unit weight of propellant, and should be avoided.

1.2 Electric Propulsion Thruster Technologies

Electric propulsion thrusters are classified according to three categories based on the governing physics, including: electrothermal, electromagnetic, and electrostatic. The ionization processes, acceleration mechanisms, performance, and power levels vary for the device technology in each category. The fundamental characteristics and relevant applications of each thruster technology will be summarized in the following sections.

1.2 .1 Electrothermal Propulsion

The discharge energy input to electrothermal thrusters is applied to heating the propellant. These devices were the first electric propulsion concepts to be investigated in a laboratory setting[1,6], and are often developed through modification of existing chemical propulsion thrusters. Propellant is heated through the application of electrical energy to high temperatures, and accelerated through a converging-diverging nozzle. Electrothermal thruster variants include resistojets, which heat the working fluid with a heating element, and arcjets, which heat the fluid with an arc-discharge. These variants exhibit the lowest exhaust velocities among electric propulsion systems, and are subject to the high stagnation temperatures and frozen flow losses associated with chemical propulsion. Both resistojets and arcjets typically operate on hydrazine or a derivative, and have extensive flight heritage over several decades of operation.[7]

1.2 .2 Electromagnetic Propulsion

The governing physics of propellant ionization and acceleration in electromagnetic propulsion is determined by interactions with electric and magnetic

fields. These concepts are based on driving a current through the propellant and accelerating plasma based on a JxB force with applied or self-magnetic fields. In addition, electromagnetic thruster concepts include both pulsed and steady discharge operation. One of the primary advantages of electromagnetic propulsion concepts is that the electric fields are not used for direct acceleration of ionized particles. As a result, the thrusters are not space-charge limited and may operate at higher thrust densities.

Electromagnetic propulsion devices include magnetoplasmadynamic thrusters (MPDT), pulsed-inductive thrusters (PIT), and pulsed plasma thrusters (PPT). The power levels of these concepts range from the sub-kilowatt level for PPTs up to the megawatt level for MPDs. Several missions have employed PPTs on-orbit using a spark discharge across a solid propellant and generating thrust through a combination of the electrothermal and electromagnetic acceleration processes of the ablation products. The development status of MPD thrusters is less mature, primarily due to the high power levels required for efficient operation.

1.2 .3 Electrostatic Propulsion

Acceleration of propellant ions in electrostatic propulsion is accomplished through applied electric fields. These propulsion concepts include gridded ion thrusters, colloid thrusters, field emission electric propulsion (FEEP), and Hall effect thrusters (HET). Ion thrusters have been studied extensively in the United States since the 1960s, and have flown successfully on numerous missions. NASA's Solar electric propulsion Technology Application Readiness (NSTAR) thruster was the primary propulsion system

for the Deep Space 1 mission, and is the mission-enabling propulsion system of the Dawn spacecraft.[8]

Hall effect thrusters are the focus of this dissertation, and an overview of the governing physics will be presented in the following sections. Typical ranges for the specific impulse of the electric propulsion technologies described in Section 1.2 are listed in Table 1-1. This list is intended as an overview of current capability for nominal systems, and is not intended as a complete catalog of performance. As on-board power availability increases in magnitude and decreases in specific mass, the variation in optimal specific impulse and power operating regime necessitates reassessment of electric propulsion technologies for a given maneuver and mission.

Table 1-1 Typical performance of electric propulsion technologies and comparison to chemical propulsion systems[5,9,10]

Thruster Concept	Specific Impulse [s]
Chemical Monopropellant	150-225
Chemical Bipropellant	300-450
Electrothermal Propulsion	
Resistojet	300
Arcjet	500-1000
Electromagnetic Propulsion	
Magnetoplasmadynamic thruster	1000-5000
Pulsed Plasma Thruster	1000-1500
Pulsed Inductive Thruster	2000-8000
Electrostatic Propulsion	
Hall Effect Thruster	1000-8000
Ion Thruster	2000-10000

1.3 Hall Effect Thruster Overview

In the early 1960s, Hall thruster propulsion concepts were discovered independently in the United States and former Soviet Union. Initial success in development of ion thruster technology in the United States for the 5,000-s to 10,000-s range of Isp led to a concentration on the more mature electric propulsion device for high specific impulse applications. This range of Isp was largely a function of the high specific power levels anticipated for nuclear power generation.[11] By 1970, experimental efforts in the U.S. directed toward Hall thruster technology were minimal.[12]

Conversely, the Soviet achievements in Hall thruster devices were directed toward a more modest specific impulse range, and resulted in the inception of two variants based on the discharge channel design. These variants were classified as the thruster with anode layer (TAL) and stationary plasma thruster (SPT). The successful development of these Hall thruster devices continued in parallel, and resulted in numerous models of each design. In 1972, the first spaceflight of a Hall thruster was the SPT-60 onboard the Soviet Meteor spacecraft.[13] Over the following decades, more than 140 SPT devices were flown on Soviet missions.[14] The TAL variant was not initially utilized due to a higher power level design point that was not available on-orbit at that time.[15]

The end of the Cold War brought the advanced Hall thruster technology to the Western space propulsion community. In the early 1990s, the mature SPT and TAL devices were evaluated at NASA Lewis Research Center[16] and the Jet Propulsion Laboratory (JPL).[17,18] These qualification tests verified the revolutionary progression of

Soviet Hall thruster technology, and initiated extensive investigations throughout U. S. industry, academia, and government facilities.

1.3.1 Hall Thruster Physics

Hall thruster physics are governed by the charged-particle interactions between the applied electric field and the magnetic field topology. These devices are typically annular, and an applied voltage between the anode and cathode forms a potential profile that accelerates ionized propellant. In most cases, the anode is designed to inject propellant flow into the discharge channel. The magnetic field topology is typically shaped with an iron magnetic circuit and a series of electromagnets, although permanent magnets are feasible. Hall thruster coordinate geometry is classically defined with cylindrical coordinates, where the axial component is parallel to the direction of the thrust vector, the radial component is outward from the thruster centerline, and the azimuthal component follows the channel annulus.

The Hall thruster cathode serves two functions. One population of electrons neutralizes the ion beam and prevents charging of the system. The second population travels to the anode to ionize propellant and sustain plasma processes. The transport properties and dynamics of this second electron population are complex, and necessitate anomalous diffusion terms in Hall thruster numerical simulations.

In a Hall thruster discharge, the magnetic field is formed such that the primary component is in the radial direction and the peak is near the channel exit plane. The field strength is created such that the electron gyroradius ($R_{L,e}$) is much less than the characteristic channel length (L), and the ion gyroradius ($R_{L,i}$) is much larger. The

difference is caused by the large difference in mass between the species, and is expressed in Eq. (1-5).

$$R_{L,e} = \frac{\nu_n}{\Omega_B}\left(\frac{m_e \mathcal{N}_A}{\mathcal{F}}\right) << L << R_{L,i} = \left(\frac{2\mathcal{M}\, V_{a,1}}{\mathcal{F}\, \Omega_B^2}\right)^{1/2} \tag{1-5}$$

This design feature of Hall thrusters results in a magnetized electron population that travels around the annulus, and is referred to as the Hall current. The electron Hall current is produced by an ExB drift of the orthogonal electric and magnetic fields. The Hall motion increases the electron residence time in the channel and enhances propellant ionization, and is the basis for Hall thruster operation and designation. The ion population is unmagnetized due to their larger particle mass, and is axially accelerated by the electric field out of the discharge channel to generate thrust. The Hall thruster discharge maintains quasi-neutrality throughout the acceleration region and the plume, which enables a much higher density of accelerated current compared to ion thrusters. A more detailed analysis of the Hall thruster discharge physics and performance loss mechanisms will be discussed in Chapter 2.

1.3 .2 Hall Thruster Design Considerations and Operation

While the physical description of Hall thruster operation is straightforward, the discharge plasma processes and interrelated field effects complicate the design of high-performance Hall thrusters. Hall thruster design criteria are largely based on empirical scaling laws. Of particular importance are the magnetic field topology, discharge channel geometry, uniform propellant injection, and cathode coupling effects.

The SPT class of Hall thruster, also referred to as magnetic layer thruster, is the focus of this investigation. A conventional Hall thruster device is controlled with four operating parameters: discharge voltage, anode mass flow rate, cathode mass flow rate, and magnetic field through electromagnet current settings. An illustration of the Hall thruster components and operation is shown in Figure 1-2.

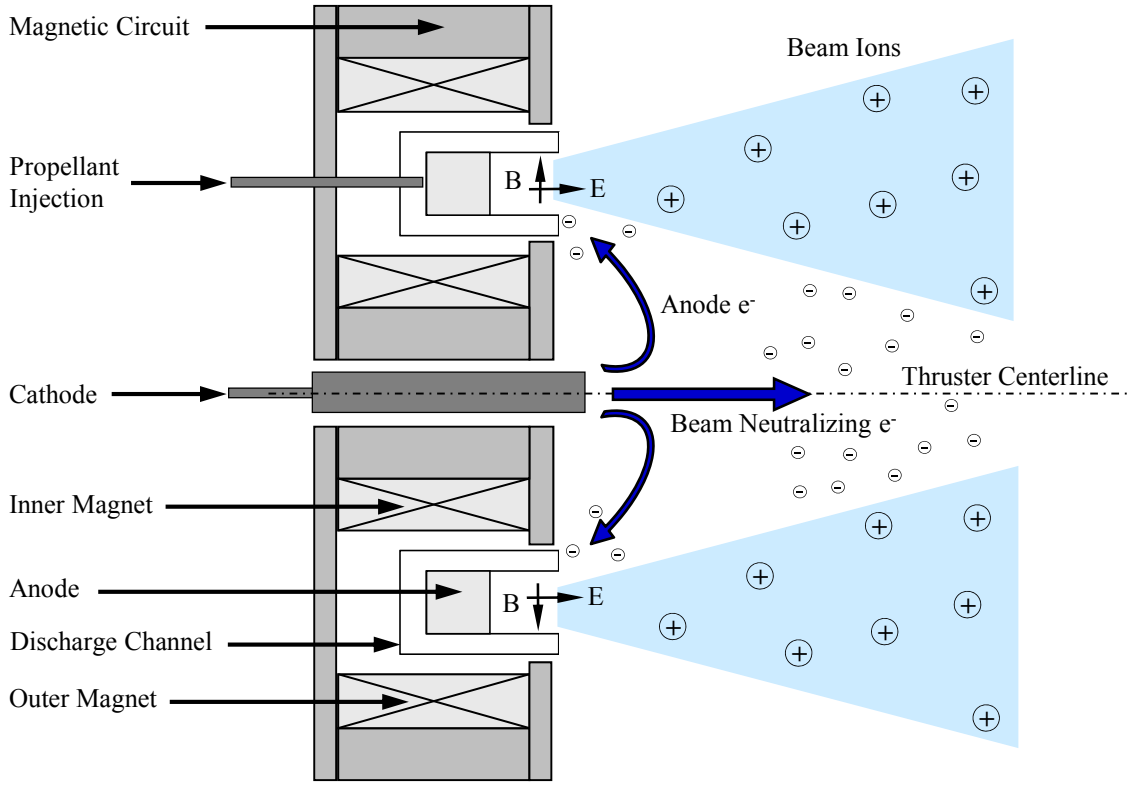

Figure 1-2 Cross-sectional illustration of a conventional magnetic layer Hall thruster with a centrally mounted cathode.

A discharge voltage on the order of hundreds of volts is applied to the anode-cathode circuit, and dictates the maximum acceleration potential of ionized propellant. The applied potential also has a strong influence on the electron temperature in the discharge, which is a dominant parameter for ionization and Joule heating processes. As

stated previously, the anode also serves as a gas distributor in many Hall thruster designs. The density of neutral propellant in the channel and the electromagnetic field profile form regions of ionization and acceleration in the discharge. Ionization of anode propellant typically occurs upstream of the exit, whereas a finite fraction of the cathode neutral flow and facility neutrals are ionized in the thruster near-field. Acceleration occurs near the discharge channel exit and often extends further downstream. Variation in the location of ionization relative to the potential profile results in the dispersion of beam ion energy.

The magnetic circuit is designed to generate a primarily radial component of magnetic field in the discharge channel that is orthogonal to the local electric field. Plasma lens magnetic field topology produces a concave field structure that creates a magnetic mirror, which has been shown to increase electron residence time in the discharge and augment ionization. To first order, the magnetic field lines are equipotential to the electric field lines and may be utilized to enhance ion beam focusing.

Cathode mass flow is often set at 7% of the anode flow rate during nominal Hall thruster operation, and is a parasitic loss required for cathode operation. In this investigation, the cathode flow rate will be shown to play an important role during low discharge voltage operation.

1.4 Motivation

During the early development stages of Hall thruster technology, plasma research and propulsion advancement centered primarily on 300-V, 1600-s specific impulse operation. Low discharge voltage operation corresponds to a decrease in the exhaust velocity due to the lower potential applied to ion acceleration, and subsequently results in

lower thruster Isp. With advancements in the power system capability, operation in this specific impulse regime may provide benefits for maneuvers optimizing at low propellant exhaust velocity due to constraints in trip time, discharge voltage, or specific power of the on-board power system.

Operation in the low discharge voltage regime is associated with a decline in total thruster efficiency. Below a threshold voltage, there is a decline in efficiency where the performance and plasmadynamic loss mechanisms are poorly understood. Understanding the physical processes affecting low-voltage performance and cultivating mitigating technologies has become a primary focus of current research.

There are a limited number of studies on the loss mechanisms associated with low-voltage Hall thruster operation, since most investigations to date have focused on high Isp performance for space exploration.[19] Manzella and Jacobson[20] evaluated low discharge voltage performance of the 2-kW NASA-120Mv2 and the 50-kW NASA-457M Hall thrusters, and identified decreased propellant ionization and reduced ion acceleration as primary loss mechanisms. The drop in efficiency was more pronounced in the smaller 2-kW thruster, which was attributed to an increase in axial electron leakage to the anode. Reducing discharge voltage below 130-V provided minimal increases in thrust-to-power (T/P), and efficiency was reduced due to decreasing Isp.

Several investigations have demonstrated that cathode position and coupling effects play a larger role during low-voltage operation. Sommerville and King[21] found thruster performance of the BPT-2000 was dependent on cathode position, and efficiency varied by as much as 12% absolute scale. To mitigate the effects of cathode position on thruster performance, recent investigations with an internal cathode have shown

advantages over the external configuration. Hofer, *et al.*[22] compared plume divergence and symmetry in a Busek BHT-8000 Hall thruster modified with a centrally mounted cathode. Reductions in plume divergence and enhanced symmetry in the near-field plasma structure were attributed to the internal cathode flow increasing plasma density and decreasing pressure gradients in the plume.

Further investigations are required to develop a better understanding of the interrelated processes driving discharge loss mechanisms during low-voltage Hall thruster operation. This dissertation is intended to investigate low-voltage Hall thruster physics, identify dominant performance loss mechanisms, and determine the discharge characteristics that drive efficiency.

1.5 Contributions of Research

A systematic, experimental investigation of low-voltage Hall thruster performance and plume properties resulted in several important contributions to the electric propulsion community. During the course of this research, corollary studies on Faraday probe design, facility effects, and data analysis techniques resulted in improved accuracy of current density profiles and far-field plume properties. These developments enabled the comprehensive examination of Hall thruster performance in an efficiency architecture that was designed to isolate loss mechanisms into processes related to conversion of the discharge power to jet kinetic energy, processes related to dispersion of the exhaust velocity distribution function (VDF), and divergence of the plasma jet. A systematic investigation of low-voltage Hall thruster performance and examination of the far-field plume provided a means to study discharge physics in the context of the

efficiency architecture. The major conclusions of this body of work are summarized below.

1. Characterization of low discharge voltage performance loss mechanisms

The low-voltage discharge properties of a 6-kW laboratory Hall thruster led to the conclusion that beam divergence and electron current to the anode were primary loss mechanisms reducing total efficiency during low discharge voltage operation. Contrary to conventional perceptions, the propellant utilization exhibited a minor increase during low-voltage operation due to a decrease in the production of multiply-charged ions. A relatively constant ion mass flow fraction with decreasing discharge voltage indicates the ion production rate per unit volume is approximately constant. Since low-voltage operation is associated with reduced electron temperature in the discharge channel and increased electron current to the anode, it suggests low-voltage HET operation is associated with a decline in Joule heating losses and a reduction in the ionization rate coefficient ($< \sigma_{e\text{-}n}\, v_e >$).

2. Estimation of the low-voltage ionization cost per beam ion

An effective discharge ionization cost based on the total energy losses and the number of beam ions revealed that the ionization cost is approximately 70 to 80 eV per beam ion during low discharge voltage operation. The ionization cost is shown to be directly proportional to discharge voltage. Although higher discharge voltage operation exhibited higher energy efficiency and additional ionization events per cathode electron, the effective ionization cost per beam ion increased. This was true for comparisons of both constant power and constant current thruster operation.

High-voltage operation leads to increased exhaust velocity and Isp, but is associated with diminishing gains in velocity as discharge voltage is increased ($u_e \sim V_d^{1/2}$). Thus, small increases in exhaust velocity require a large increase in discharge voltage and the energy losses per beam ion escalate. For comparison of constant current thruster operation, increased electron temperature during high discharge voltage operation led to additional Joule heating losses in the form of multiply-charged ions, excitation, and high-energy wall collisions. For comparison of constant power operation, a larger fraction of the discharge power is applied to accelerate fewer ions to high exhaust velocity during high-voltage operation. Conversely, during low-voltage operation a larger fraction of the discharge power is applied to ionization of propellant with fewer Joule heating losses.

3. Evaluation and characterization of low-voltage operating regimes

Two jet-mode Hall thruster operating regimes were investigated for low discharge voltage operation. The low-current mode corresponded to the I-V characteristic of nominal 300-V operation, whereas operation in the high-current mode produced significant increases in the discharge current magnitude and oscillation amplitude with equivalent thrust. Evaluation of the thruster performance and far-field plume demonstrated that electron current to the anode was the primary source of increased discharge current in the high-current regime. Injection of additional neutral flow in the thruster near-field damped the oscillations and maintained operation in the low-current mode. Improved understanding of this low-voltage operating regime may reduce the possibility of operation in the high-current regime on-orbit.

4. Reduction in uncertainty of integrated ion beam current and plume divergence

A comprehensive investigation of nude Faraday probe design and analytical technique was conducted with the AFRL nested Faraday probe. Enhanced understanding of Faraday probe ion current collection and methods for evaluating plume properties minimized the CEX facility effects on current density distributions and reduced the integrated ion beam current by ~20%. The corrected plume properties are in line with expected values of ion beam current based on Hall thruster performance and discharge properties. A key discovery was the ability to predict the amount of additional ion current on the collector side walls. This result eliminates the Faraday probe design criteria of 5 to 10 Debye lengths between the collector and guard ring. These studies indicate conventional Faraday probe designs with a ceramic base are more suitable for characterization of facility effects and current density mapping with a wide range of Debye lengths in the plume. Based on the results of this systematic investigation, the uncertainty of Faraday probe ion beam current measurements is estimated as ±3% and the uncertainty in the axial component of ion beam current is estimated as ±5% when the recommendations in Section 4.5 are followed. The reductions in measurement uncertainty and the increased capability to approximate on-orbit plume expansion are a significant improvement for comparisons with numerical simulations and analysis of Hall thruster performance.

5. External potential field structure effects on far-field current density profiles

A detailed study of the angular distribution of ion beam current in the plume of a low-power Hall device and a 6-kW Hall thruster exhibited angular regions of constant beam current in the far-field plume. This phenomenon was compared to numerical

simulations of the vacuum plume expansion in COLISEUM, and indicated the beam current profiles were largely formed by the external electric field structure. This underscores the importance of a high fidelity source model and known field topology near the thruster exit. Comparison of the low-power Hall ion source with the 6-kW laboratory model led to the hypothesis that different far-field characteristics between the thrusters was due to the location of facility neutral ionization and acceleration relative to the potential field.

6. Development of a self-consistent Hall thruster efficiency architecture

A Hall thruster performance architecture was developed based on separation of the total thrust directed along thruster centerline into mass-weighted and momentum-weighted terms. With this formulation, the total thruster efficiency equation was analytically decomposed to explicitly account for the effects of energy conversion losses, plume divergence, and the velocity distribution function of the propellant jet. This architecture employs performance measurements and bulk plume characteristics to experimentally determine physical processes and relationships that are difficult to measure directly. This technique enhanced the capability of using global thruster operating parameters to interpret performance loss mechanisms on a macroscopic level.

1.6 Organization

The framework of this dissertation is delineated in a natural progression. Chapter 2 will formalize the basis for analytical separation of total thruster efficiency into the product of energy efficiency, propellant efficiency, and beam efficiency. Loss mechanisms will be isolated in terms of energy losses that lead to Joule heating,

dispersion of the jet VDF, and loss of thrust due to plume divergence. While these processes are physically coupled, the effects on performance may be mathematically isolated. The framework will be referred to throughout the experimental investigations in Chapters 4, 5, and 6. The primary source of complication in this efficiency architecture is the high degree of uncertainty associated with conventional Faraday probe measurements and analysis.

Chapter 3 describes the experimental apparatus and facilities used in the investigations, and ends with a description of the nested Faraday probe. This diagnostic was designed specifically to study facility effects and Faraday probe design in order to minimize the uncertainty of far-field current density profiles. In Chapter 4, current density profiles of a low-power Hall device are measured in a systematic test matrix of background pressure, downstream distance, Faraday probe design configurations, and probe bias potential operation. The facility effects and probe design are evaluated to improve accuracy and reduce uncertainty of plume properties determined with a Faraday probe. This reduction in uncertainty greatly enhanced the analytical capabilities of the efficiency architecture developed in Chapter 2.

The loss mechanisms of low discharge voltage Hall thruster operation are studied in Chapter 5 through measurements of thrust, discharge oscillations, and an array of far-field plasma diagnostics. Nominal discharge voltage operation (300-V) is compared to intermediate (150-V) and low-voltage operation (120-V) for constant anode flow rate of 10-mg/s and 20-mg/s at 7-CFF. Operation below 120-V required increased cathode flow to optimize performance. Optimized performance at 120-V and 105-V are compared to the 7-CFF conditions, which established a framework for comparison of discharge

voltage, anode mass flow rate, and cathode mass flow rate. Performance characteristics of low-voltage operation are studied with the efficiency architecture developed in Chapter 2. Thruster utilization efficiencies will be related to plasma processes in the discharge to determine the dominant loss mechanisms inhibiting performance in the low-voltage Hall thruster operating regime.

During the course of low discharge voltage experiments with the 6-kW Hall thruster, discontinuities in thruster performance occurred for small variations in operating parameters. Minor changes in magnetic field or cathode flow rate resulted in an intense, visible transformation of the jet-mode plume structure. The existence of two discharge operating regimes led to classification as the high-current mode and low-current mode. This transformation corresponded to an abrupt escalation in the discharge current with constant thrust. In Chapter 6, the phenomenon is characterized with a systematic map of thruster operation for discharge voltages ranging from 100-V to 120-V, anode flow rates at 10-mg/s, 15-mg/s, and 20-mg/s, and cathode flow rate fractions of 7-25% of the anode flow. Performance characteristics and far-field plume properties were studied within the context of the efficiency architecture developed in Chapter 2 and the enhanced understanding of low-voltage loss mechanisms gained in Chapter 5. In Chapter 7, the major conclusions are summarized and recommendations for the course of future research are outlined.

Chapter 2

Hall Thruster Efficiency Architecture

Standardization of experimental methods, facilities, diagnostic apparatus, and efficiency analysis has previously been proposed in the electric propulsion community.[23] In this chapter, a Hall thruster efficiency architecture is formulated that is based on a consistent set of definitions, conservation of energy, conservation of mass and charge, and Newton's Second Law. The relationships between Hall thruster performance data, telemetry (V_d, I_d, and $\dot{m}_T$), and plume measurements are summarized and new correlations are developed.

This chapter formalizes the basis for analytical separation of total thruster efficiency into the product of energy efficiency, propellant efficiency, and beam efficiency, which are less than unity under all operating conditions. Separating utilization efficiencies in this manner isolates loss mechanisms in terms of energy losses that lead to Joule heating, dispersion of the jet VDF, and loss of thrust due to plume divergence. While these processes are physically coupled, the effects on performance may be mathematically isolated.

Historical perspective of early ion thruster analyses, methodologies developed in the former Soviet Union, and a brief description of contemporary efficiency models are discussed in relation to the presented architecture. The architecture is distinctive in

formulation of the axial component of thrust as the product of mass-weighted and momentum-weighted averaged quantities, and introduces a new definition of propellant utilization that incorporates multiple ion species and the effects of neutral propellant. Including cathode flow in the performance analysis is vital to accurately assess loss mechanisms over a wide range of thruster operation. While cathode flow rate is typically 7% of the anode flow, the characterization of low discharge voltage operation presented in Chapter 6 indicates total thruster efficiency optimizes at higher cathode flow rate. In addition, a fraction of this cathode flow may ionize and must be accounted for in far-field plume measurements.

Thruster performance parameters, including T/P and specific impulse, are formulated in terms of utilization efficiencies to provide a higher level of confidence in comparisons between plume measurements and thrust measurements. Analytical techniques for determining accurate plume averaged quantities will not be discussed in this chapter, since the performance model is mathematically self-consistent and is based on macroscopic thruster characteristics. Methods for evaluating global properties, assessing measurement uncertainty, and techniques to account for dispersion of the jet due to scattering and charge exchange ions in the plume will be discussed in Chapter 3.

2.1 Historical Perspective and Recent Methodologies

Investigations of ion acceleration and electron transport using Hall thruster technology began in the early 1960s in the United States and former Soviet Union.[24,25,26,27,28,29,30,31,32,33,34] The focus of US electric propulsion research shifted

primarily to ion thruster technology in the early 1970s[35], whereas investigations in the USSR continued Hall thruster advancements throughout the following decades.[12,15,36]

Analytical factorization of ion thruster efficiency was described as early as 1975 by Masek, *et al.*[37] in a review of ion thruster performance. Anode thrust efficiency was factored into the product of energy efficiency and propellant utilization efficiency using Newton's Second Law, with terms accounting for losses due to doubly-charged ions and beam divergence. However, the derivation was condensed and an explanation for the treatment of beam divergence and multiply-charged ions was not presented. The methodology was not widely adopted or cited in the ion thruster community and is absent in modern analysis.

In the 1990s, the manifestation of Russian Hall thruster technology in the Western and Japanese spacecraft communities catalyzed a resurgence of Hall thruster research.[16,17,18,38,39,40] Technology transfer that began in the early 1990s brought invaluable benefits and advancements to Western Hall thruster development, but much of the earlier Soviet progress in Hall thruster research that was published in the Russian language was not translated. The limited availability of translated documents from this extensive literature inevitably impeded the transmission of knowledge. As a result, several important contributions from Russian research have not been widely disseminated in the West, including the analytical factorization of anode thrust efficiency.

Factorization of Hall thruster efficiency was outlined in a manual on stationary plasma thrusters by Belan, Kim, Oranskiy, and Tikhononv from the Kharkov Aviation Institute in 1989.[41] This seminal document was later referenced and the performance methodology summarized by Bugrova *et al.*[42] without explicitly stating the nature of the

earlier derivation. Kim's highly cited 1998 publication[43] on processes that determine Hall thruster efficiency and other contemporary publications[44,45,46] continued the elaboration of the Kharkov Aviation Institute methodology. These approaches showed similarities to the analysis presented here, and demonstrated relationships between experimental variables and plasma phenomena that affect thruster performance.

A textbook by Grishin and Leskov[47] analyzed thruster performance based on energy efficiency and thrust efficiency. The ratio of thrust efficiency to energy efficiency was asserted to describe the velocity dispersion in magnitude and direction. This ratio will be derived from first principles in the following section, where it will become apparent that the ratio is equivalent to beam efficiency and propellant efficiency, which capture losses resulting from plume divergence, incomplete ionization, and the production of multiply-charged ions.

In the post-1990 era, numerous efficiency analysis frameworks and modifications have been proposed, [48,49,50,51,52,53,54] including notable studies by Komurasaki[55], Ahedo[56], and Hofer[19,57]. The differences between the proposed architecture with past ion thruster studies, the analytical factorization in Russian literature, and the post-1990 methodologies vary in each case. Dissimilarities arise due to varying levels of completeness regarding the treatment of multiply-charged ions, beam divergence, and the effect of neutral propellant on dispersion of the jet VDF. In some instances, the effects of these loss mechanisms are neglected or inserted as a utilization efficiency without rigorously factoring the term from the thrust efficiency equation. Utilization efficiencies in the performance model presented in this paper are analytically separated from the total thruster efficiency and are formulated to minimize the introduction of new terminology.

The primary differences with all previous methodologies is quantifying the effect of neutrals on the dispersion of the VDF in the neutral-gain utilization, and decomposing total thrust into the product of mass-weighted and momentum-weighted quantities.

2.2 Development of a Hall Thruster Efficiency Architecture

The following efficiency architecture builds on the development of past studies, and is proposed to enable experimental measurements of global thruster operating parameters that may be used to interpret performance loss mechanisms on a macroscopic level. While numerical simulations typically determine plasma properties throughout the plume and/or performance attributes based on a particle source model, this analysis employs performance measurements and bulk plume characteristics to experimentally determine physical processes and relationships that are difficult to measure directly.

The physical interpretation of propellant efficiency, energy efficiency, and beam efficiency will be discussed in the following sections. Propellant efficiency will be decomposed into mass and charge utilization efficiencies, and the neutral-gain utilization is introduced to characterize the effect of neutral propellant on dispersion of the VDF. Next, energy efficiency is separated into the product of voltage utilization and current utilization using the term χ. Beam efficiency will then be analyzed in terms of the distinction between momentum-weighted divergence and current-weighted plume divergence. Experimental parameter groups (E_1 and E_2) are established and thruster performance characteristics (T/P and Isp) are expressed in terms of utilization efficiencies. Assessment of T/P and Isp provides a higher degree of evaluation for

performance characterized with plume measurements compared to thrust based measurements.

2.2.1 Formulation of Thrust

The total thrust generated by a Hall thruster is primarily a function of electromagnetic forces, and to a much lesser degree gasdynamic forces. In this architecture, thrust is formulated from plume averaged quantities to correlate performance measurements with plasma diagnostics. Downstream of the primary ionization and acceleration regions, the total resultant thrust may be found from Eq. (2-1) through integration of the thrust density vector (**F**) throughout the plume, where $\hat{\rho}$ is the outward normal radial component in spherical coordinates.

$$T\,\hat{\rho} = \oiint \mathbf{F} \cdot \hat{\rho}\; \mathrm{d}A \tag{2-1}$$

This idealized description suffers from numerous experimental difficulties and uncertainties. Although Eq. (2-1) may be valid in the space environment, facility effects inherent in ground tests result in significant ion scattering in the plume and potentially increased thrust from neutral ingestion. Measurements of thrust density throughout the HET plume are extremely difficult, but may be viable using an impact target plate.[58]

The conventional inverted pendulum thrust stand measures the component of thrust directed along the thruster centerline axis. Careful thruster alignment and uniform propellant injection generally result in an axisymmetric plume with negligible deviations between the resultant thrust vector direction and the thruster centerline axis.

For an axisymmetric plume, the steady state scalar component of thrust (T) directed along thruster centerline is formulated in Eq. (2-2). The total thrust may be

factored into the product of total mass flow rate ($\dot{m}_T$), mass-weighted average velocity ($<\bar{v}>_m$), and momentum-weighted average cosine ($<\cos(\theta)>_{mv}$). This analytical separation of thrust is produced using the definitions in Eq. (2-3) through Eq. (2-12). Thrust is typically defined as the product of averaged quantities without mathematically separating terms from the thrust integral or specifying the nature of the average. Although the fraction of thrust generated by non-ionized propellant is negligible, a fraction of the cathode flow may be ionized and the total propellant flow is necessary to characterize performance over a wide range of thruster operation.

$$T = 2\pi R^2 \int_0^{\pi/2} \dot{m}(\theta)\ \bar{v}(\theta)\cos(\theta)\sin(\theta)d\theta = \dot{m}_T <\bar{v}>_m <\cos(\theta)>_{mv} \tag{2-2}$$

Hemispherical integration of the mass flux, $\dot{m}(\theta)$, in the direction $\hat{\rho}$ throughout the plume at constant radius in Eq. (2-3) is equal to the total mass flow rate supplied to the anode and cathode.

$$\dot{m}_T = 2\pi R^2 \int_0^{\pi/2} \dot{m}(\theta)\sin(\theta)d\theta \tag{2-3}$$

The average velocity vector, $\bar{v}$, is defined in Eq. (2-4) as the integral of the VDF over all velocity space for an axisymmetric plume at angular position θ and radius R. The radial component ($\hat{\rho}$) of propellant velocity in spherical coordinates, $\bar{v}$, is formulated in Eq. (2-5) and the radial component of ion velocity, $\bar{v}_i$, is formulated in Eq. (2-6) using ion mass flow fractions (f^*_j). This is the dominant velocity component for ions originating from the thruster discharge, and other velocity components in the plume are typically orders of magnitude less.

$$\overline{\mathbf{v}} = \iiint \mathbf{v}\ f(\mathbf{v})d\mathbf{v} \Big/ \iiint f(\mathbf{v})d\mathbf{v} \tag{2-4}$$

$$\overline{v} = \sum_{j=0} \frac{\dot{m}_j}{\dot{m}_T} v_j = \frac{\dot{m}_i}{\dot{m}_T} \sum_{j=0} f_j^*\ v_j \tag{2-5}$$

$$\overline{v_i} = \sum_{j=1} \frac{\dot{m}_j}{\dot{m}_i} v_j = \sum_{j=1} f_j^* v_j \tag{2-6}$$

The radial component terms of squared propellant velocity, $\overline{v^2}$, and of squared ion velocity, $\overline{v_i^2}$, are found using analogous expressions in Eqs. (2-7), (2-8), and (2-9).

$$\overline{v^2} = \iiint \mathbf{v}\cdot\mathbf{v}\ f(\mathbf{v})d\mathbf{v} \Big/ \iiint f(\mathbf{v})d\mathbf{v} \tag{2-7}$$

$$\overline{v^2} = \sum_{j=0} \frac{\dot{m}_j}{\dot{m}_T} v_j^2 = \frac{\dot{m}_i}{\dot{m}_T} \sum_{j=0} f_j^*\ v_j^2 \tag{2-8}$$

$$\overline{v_i^2} = \sum_{j=1} \frac{\dot{m}_j}{\dot{m}_i} v_j^2 = \sum_{j=1} f_j^* v_j^2 \tag{2-9}$$

The radial component of the average velocity vector, $\overline{v}$, in spherical coordinates is directed away from the intersection of thruster centerline with the exit plane. The mass-weighted average velocity, $<\overline{v}>_m$, is defined in Eq. (2-10) and simplified using Eq. (2-3). The mass-weighted average squared velocity, $<\overline{v^2}>_m$, is defined in Eq. (2-11) and simplified using Eq. (2-3).

$$<\overline{v}>_m = \frac{2\pi R^2 \int_0^{\pi/2} \dot{m}(\theta)\ \overline{v}(\theta)\sin(\theta)d\theta}{2\pi R^2 \int_0^{\pi/2} \dot{m}(\theta)\sin(\theta)d\theta} = \frac{2\pi R^2 \int_0^{\pi/2} \dot{m}(\theta)\ \overline{v}(\theta)\sin(\theta)d\theta}{\dot{m}_T} \tag{2-10}$$

$$< \overline{v^2} >_m = \frac{2\pi R^2 \int_0^{\pi/2} \dot{m}(\theta)\, \overline{v^2}(\theta) \sin(\theta)\, d\theta}{2\pi R^2 \int_0^{\pi/2} \dot{m}(\theta) \sin(\theta)\, d\theta} = \frac{2\pi R^2 \int_0^{\pi/2} \dot{m}(\theta)\, \overline{v^2}(\theta) \sin(\theta)\, d\theta}{\dot{m}_T} \tag{2-11}$$

The momentum-weighted average cosine, $< \cos(\theta) >_{mv}$, is defined in Eq. (2-12) and simplified using Eq. (2-10). The definition of thrust in Eq. (2-2) is naturally produced through the formulation of mass-weighted and momentum-weighted terms in Eq. (2-12).

$$< \cos(\theta) >_{mv} = \frac{2\pi R^2 \int_0^{\pi/2} \dot{m}(\theta)\ \overline{v}(\theta) \cos(\theta) \sin(\theta)\, d\theta}{2\pi R^2 \int_0^{\pi/2} \dot{m}(\theta)\ \overline{v}(\theta) \sin(\theta)\, d\theta} = \frac{T}{\dot{m}_T < \overline{v} >_m} \tag{2-12}$$

This formulation of thrust sets the foundation for the Hall thruster efficiency architecture outlined in the following sections. All far-field quantities are assumed steady state and are evaluated at constant radius from the exit plane. For hemispherical integration about a point source, the measurement distance must be multiple thruster diameters downstream of the exit. The definitions in Eq. (2-3) through (2-12) do not account for dispersion of the jet due to scattering and charge exchange collisions in the plume. These processes will have a different effect depending on the diagnostic, facility, background pressure, and distance from the thruster. To this point, an axisymmetic spherical plume with outward-normal particle velocity and negligible facility effects are the only approximations required. Analytical techniques to evaluate global properties and account for facility effects, probe measurement uncertainty, and geometric variations associated with hemispherical measurement and integration about a point source will be dealt with separately.

2.2.2 Decomposing Total Thruster Efficiency

In this architecture, the total thruster efficiency is mathematically separated into the product of energy efficiency, propellant efficiency, and beam efficiency. The analytical framework incorporates macroscopic performance parameters with global plume properties to isolate loss mechanisms related specifically to ionization and acceleration processes in the thruster discharge region.

The standard definition of total thruster efficiency (η_T) is expressed in terms of thruster telemetry and measured thrust in Eq. (2-13). The expression for thrust formulated in Eq. (2-2) is substituted into Eq. (2-13) and enables the separation of total thruster efficiency into three partial efficiencies.

$$\eta_T = \frac{T^2}{2\dot{m}_T P_d} = \frac{\left(\dot{m}_T < \bar{v} >_m < \cos(\theta) >_{mv}\right)^2}{2\dot{m}_T P_d} \tag{2-13}$$

In Eq. (2-14), performance loss mechanisms are isolated in terms of energy losses that lead to Joule heating of the plasma and channel walls, dispersion of the jet VDF, and loss of thrust due to plume divergence. The energy efficiency (η_E), propellant efficiency (Φ_P), and beam efficiency (Ψ_B) in Eq. (2-14) will be further decomposed in the following sections.

$$\eta_T = \left(\frac{\dot{m}_T < \overline{v^2} >_m}{2P_d}\right)\left(\frac{< \bar{v} >_m^2}{< \overline{v^2} >_m}\right)(< \cos(\theta) >_{mv})^2 = \eta_E \, \Phi_P \, \Psi_B \tag{2-14}$$

2.2.3 Propellant Efficiency

The term *propellant utilization efficiency* has been used in at least three different ways in the literature. Most commonly as (1) the ionization fraction of anode mass flow, as (2) the fraction of momentum carried by ions[12], or as (3) the ratio of output moles of charge to the input moles of propellant[59]. The presence of multiple ions species often increases this value greater than unity, and therefore is not suitable as a utilization efficiency metric.

Propellant efficiency in Eq. (2-15) is the mathematical relationship between the jet momentum and the jet kinetic energy. It contains all loss information associated with dispersion of the jet VDF due to incomplete ionization and the presence of multiple ion species with widely varying velocities. This ratio is unity for 100% ionization to a single ion species.

$$\Phi_P = \frac{< \overline{v} >_m^2}{< \overline{v^2} >_m} \tag{2-15}$$

Propellant efficiency is separated into the product of mass utilization (Φ_m), charge utilization (Φ_q), and neutral-gain utilization ($\Phi_{N\text{-}G}$) in Eq. (2-16). The influence of non-uniform velocity distribution on propellant efficiency is expressed in this way to maintain a consistent definition of mass utilization and charge utilization with previous methodologies[57], and isolate effects caused by non-ionized propellant exhausted from the plasma discharge.

$$\Phi_P = \left(\frac{< \overline{v_i} >_m^2}{< \overline{v_i^2} >_m} \right) \left(\frac{< \overline{v} >_m^2}{< \overline{v_i} >_m^2} \frac{< \overline{v_i^2} >_m}{< \overline{v^2} >_m} \right) = \Phi_q \Phi_m \Phi_{N\text{-}G} \tag{2-16}$$

2.2.3.1 Charge Utilization

The standard definition of charge utilization is formulated from the first term in brackets in Eq. (2-16). Charge utilization is defined in Eq. (2-17) using ion current fractions (Ω_j) and also in terms of ion species mass flow fractions (f^*_j). In this description of charge utilization, all ion species are considered to be created in the same zone whose length is small compared to the acceleration length, such that average ion species acceleration potential ($V_{a,j}$) is equivalent for all species, $V_a \approx$ constant. Terms of average ion exit velocity in Eq. (2-17) are determined using ion flow fractions in Eq. (2-6) and Eq. (2-9), and are related to the average ion acceleration potential and ion charge state (Z_j) through an expression based on conservation of energy in Eq. (2-18). The expression for charge utilization in Eq. (2-17) is formulated with ion current fractions by relating the current of each ion species with the ion species mass flow rate, $I_j = \dot{m}_j Z_j \left(\mathcal{F}/\mathcal{M}\right)$.

$$\Phi_q = \left(\frac{< \bar{v}_i >_m^2}{< \overline{v_i^2} >_m} \right) = \frac{\left(\sum_{j=1} \frac{\Omega_j}{\sqrt{Z_j}} \right)^2}{\sum_{j=1} \frac{\Omega_j}{Z_j}} = \frac{\left(\sum_{j=1} f_j^* \sqrt{Z_j} \right)^2}{\sum_{j=1} f_j^* Z_j} \tag{2-17}$$

$$v_j = \sqrt{2 Z_j V_{a,j} \left(\frac{\mathcal{F}}{\mathcal{M}} \right)} \tag{2-18}$$

In this form, charge utilization is unity for ionization to a single ion species. Losses due to complete ionization to a doubly-charged or triply-charged plasma state are manifested in the minimum power required to sustain ionization, and will be further discussed relative to the theoretical minimum anode electron current in Section 2.2.4.2 and with regard to the minimum power required to sustain ionization processes in Section 2.3.3.

It is important to note the distinction between ion current fractions Ω_j, ion mass flow fractions f^*_j, and ion species number fractions ζ_j. Ion current fractions are determined directly from ExB probe traces, and defined in Eq. (2-19). The ion species number fraction in Eq. (2-20) is based on particle number density, and is commonly reported for incorporation in numerical simulations. The ion mass flow fraction defined in Eq. (2-21) is a more suitable figure of merit for experimental plume studies, since it is related to the ion species flux in the plume.

$$\Omega_j = \frac{I_j}{\sum_{j=1} I_j} = \frac{f^*_j Z_j}{Q} \tag{2-19}$$

$$\zeta_j = \frac{n_j}{\sum_{j=1} n_j} = \frac{\Omega_j Z_j^{-3/2}}{\sum_{j=1} \Omega_j Z_j^{-3/2}} \tag{2-20}$$

$$f^*_j = \frac{\dot{m}_j}{\sum_{j=1} \dot{m}_j} = \frac{\Omega_j Z_j^{-1}}{\sum_{j=1} \Omega_j Z_j^{-1}} \tag{2-21}$$

where,

$$\sum_{j=1} \Omega_j = \sum_{j=1} \zeta_j = \sum_{j=1} f^*_j = 1 \tag{2-22}$$

The average ion charge, Q, is formulated in terms of ion mass flow fractions, ion current fractions, and ion species fractions in Eq. (2-23). Knowledge of Q enables a simplified relationship between Ω_j and f^*_j as expressed in Eq. (2-19).

$$Q = \sum_{j=1} f^*_j Z_j = \left(\sum_{j=1} \frac{\Omega_j}{Z_j} \right)^{-1} = \frac{\sum_{j=1} \zeta_j Z_j^{3/2}}{\sum_{j=1} \zeta_j Z_j^{1/2}} \tag{2-23}$$

2.2.3.2 Mass Utilization

The mass utilization and neutral-gain utilization are developed from the second term in brackets in Eq. (2-16). In Eq. (2-24) and (2-25), the relationship between ion and particle momentum and ion and particle kinetic energy are expressed in terms of ion mass flow fractions and normalized speed ratios.

$$\frac{\left[< \bar{v} >_m \Big/ < \bar{v}_i >_m \right]^2}{< \overline{v^2} >_m \Big/ < \overline{v_i^2} >_m} = \frac{\left[\sum_{j=0} \left(\frac{\dot{m}_j}{\dot{m}_T} v_j \right) \Big/ \sum_{j=1} \left(\frac{\dot{m}_j}{\dot{m}_i} v_j \right) \right]^2}{\sum_{j=0} \left(\frac{\dot{m}_j}{\dot{m}_T} v_j^2 \right) \Big/ \sum_{j=1} \left(\frac{\dot{m}_j}{\dot{m}_i} v_j^2 \right)} \tag{2-24}$$

which may be reduced to,

$$\frac{\left[< \bar{v} >_m \Big/ < \bar{v}_i >_m \right]^2}{< \overline{v^2} >_m \Big/ < \overline{v_i^2} >_m} = \frac{\left[\left(\frac{\dot{m}_i}{\dot{m}_T} \right) \left(\frac{\sum_{j=0} f_j^* y_j}{\sum_{j=1} f_j^* y_j} \right) \right]^2}{\left(\frac{\dot{m}_i}{\dot{m}_T} \right) \left(\frac{\sum_{j=0} f_j^* y_j^2}{\sum_{j=1} f_j^* y_j^2} \right)} = \left(\frac{\dot{m}_i}{\dot{m}_T} \right) \left[\frac{\left(\frac{\sum_{j=0} f_j^* y_j}{\sum_{j=1} f_j^* y_j} \right)^2}{\left(\frac{\sum_{j=0} f_j^* y_j^2}{\sum_{j=1} f_j^* y_j^2} \right)} \right] \tag{2-25}$$

The ratio of ion mass flow rate ($\dot{m}_i$) to total propellant mass flow rate ($\dot{m}_T$) that is factored in Eq. (2-25) is the mass utilization. Mass utilization is defined in Eq. (2-26) and expressed in terms of beam current (I_{Beam}) from a Faraday probe and the average ion charge from an ExB probe. If only the anode mass flow rate is used, it is possible for this term to be greater than unity when a significant fraction of the cathode flow is ionized in the plume.

$$\Phi_m = \frac{\sum_{j=1} \dot{m}_j}{\sum_{j=0} \dot{m}_j} = \frac{\dot{m}_i}{\dot{m}_T} = \frac{I_{Beam}}{\dot{m}_T Q} \frac{\mathcal{M}}{\mathcal{F}} \tag{2-26}$$

The mass utilization in a Hall thruster discharge is much larger than the number fraction (I_F) of ionized propellant. The number fraction of ionized propellant is shown in Eq. (2-27), and takes the form described elsewhere in the literature[19] when all ion species are accelerated over an equal potential profile such that the ion velocity ratio magnitudes are $|y_j|=(Z_j)^{1/2}$ for ($j \geq 1$).

$$I_F = \frac{\sum_{j=1} n_j}{\sum_{j=0} n_j} = \frac{\sum_{j=1} \frac{\dot{m}_j}{v_j}}{\sum_{j=0} \frac{\dot{m}_j}{v_j}} = \frac{1}{1+\left[(1-\Phi_m)\Big/\left(\Phi_m\, y_0 \sum_{j=1} \frac{f_j^*}{y_j}\right)\right]} \tag{2-27}$$

In Figure 2-1, the ionization number fraction of a singly-charged plasma (Q=1) is shown as a function of mass utilization ranging from 0.5 to 1.0 for lines of constant neutral velocity ratio (y_0). Variations in the ion species composition for a singly-charged plasma have a lesser effect on the ionization number fraction. For the axial neutral speed ranging from 100 m/s to 600 m/s, the neutral speed ratio $y_0=v_0/v_1$ may range from less than 0.01 for high-voltage operation up to 0.06 for low-voltage operation. In a typical Hall thruster discharge with 90% mass utilization, the ionization fraction ranges from approximately 10% to 30%. This value is consistent with internal ion number density measurements by Haas[60] and Reid[61], and agrees with the analysis by Hofer[19] for a multiply-charged plasma. It is important to note this fraction is based on plume averaged quantities, and may significantly fluctuate throughout the discharge channel in time and space with breathing mode oscillations and ionization instabilities. In addition, the formulation is expressed using the total mass flow rate, which will decrease the ionization number fraction by several percent compared to analyses using only the anode mass flow rate.

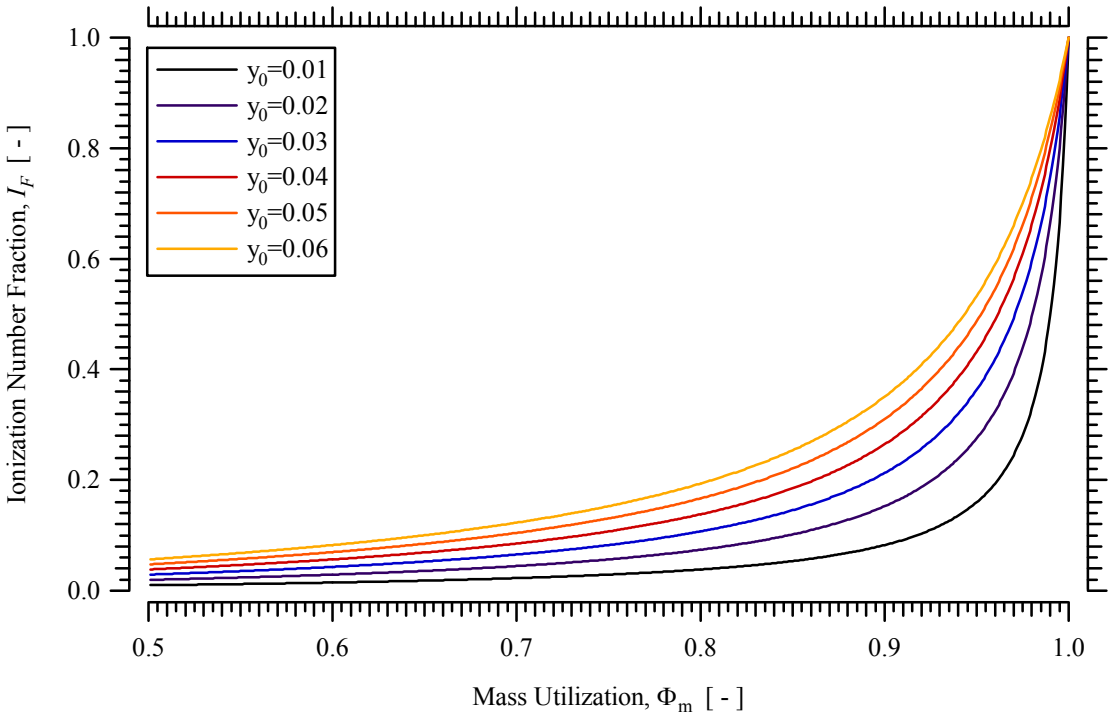

Figure 2-1 Ionization number fraction as a function of mass utilization with lines of constant neutral velocity ratio, y_0, for a singly-charged plasma ($Q = 1, f_2^* = f_3^* = 0$).

2.2.3.3 Neutral-gain Utilization

The neutral-gain utilization is isolated from mass utilization in Eq. (2-25), and characterizes the minimal dispersion of the jet VDF due to the axial injection speed and thermal speed of neutral propellant. Neutral-gain utilization is expressed in terms of thruster utilization efficiencies and global characteristics in Eq. (2-28). Second order terms with y_0 are neglected in Eq. (2-29), since $y_0^2 < 1 \times 10^{-3}$ for experimental measurements of $y_o < 0.05$.[62,63] The simplification elucidates that $\Phi_{N\text{-}G}$ is primarily a function of the neutral speed ratio and mass utilization. It is important to note that the neutral-gain utilization is a new metric in performance models, and the appropriate global measure of neutral speed is yet to be determined. Nevertheless, it is likely that an exit

plane measurement of axial neutral speed characterizes the minimal momentum of non-ionized propellant, and is a good starting point for characterizing the neutral-gain utilization.

$$\Phi_{N\text{-}G} = \left[\frac{\left(\frac{\sum_{j=0} f_j^* y_j}{\sum_{j=1} f_j^* y_j} \right)^2}{\left(\frac{\sum_{j=0} f_j^* y_j^2}{\sum_{j=1} f_j^* y_j^2} \right)} \right] = \frac{\left[1 + \frac{y_0 \left(1 - \Phi_m\right)}{\Phi_m \sqrt{\Phi_q Q}} \right]^2}{\left[1 + \frac{y_0^2 \left(1 - \Phi_m\right)}{\Phi_m Q} \right]} \tag{2-28}$$

$$\Phi_{N\text{-}G} \approx 1 + \frac{2 y_0 \left(1 - \Phi_m\right)}{\Phi_m \sqrt{\Phi_q Q}} \tag{2-29}$$

The neutral-gain utilization is always greater than unity and increases total thruster efficiency. However, effects that increase neutral-gain utilization result in significant detrimental losses to other utilization efficiencies. Ideal thruster operation would correspond to unity neutral-gain for 100% ionization or zero neutral speed for infinite neutral residence time in the channel.

The small gain in efficiency due to neutral-gain utilization is generally neglected, but may increase during low discharge voltage operation where the value of y_0 is increased and/or ionization is reduced. In addition, neutral-gain utilization may also increase for a high neutral thermal speed due to increased anode temperature or a large axial neutral speed due to poor anode propellant injection. In Figure 2-2, neutral-gain utilization is characterized for variations in y_0, Φ_m, and ion species composition. Neutral-gain utilization is shown to increase with reduced mass utilization and large neutral speed ratio. For the range of neutral speed ratio from y_0=0.01 to y_0=0.06, the neutral-gain utilization may increase up to 1.03 during low mass utilization operation.

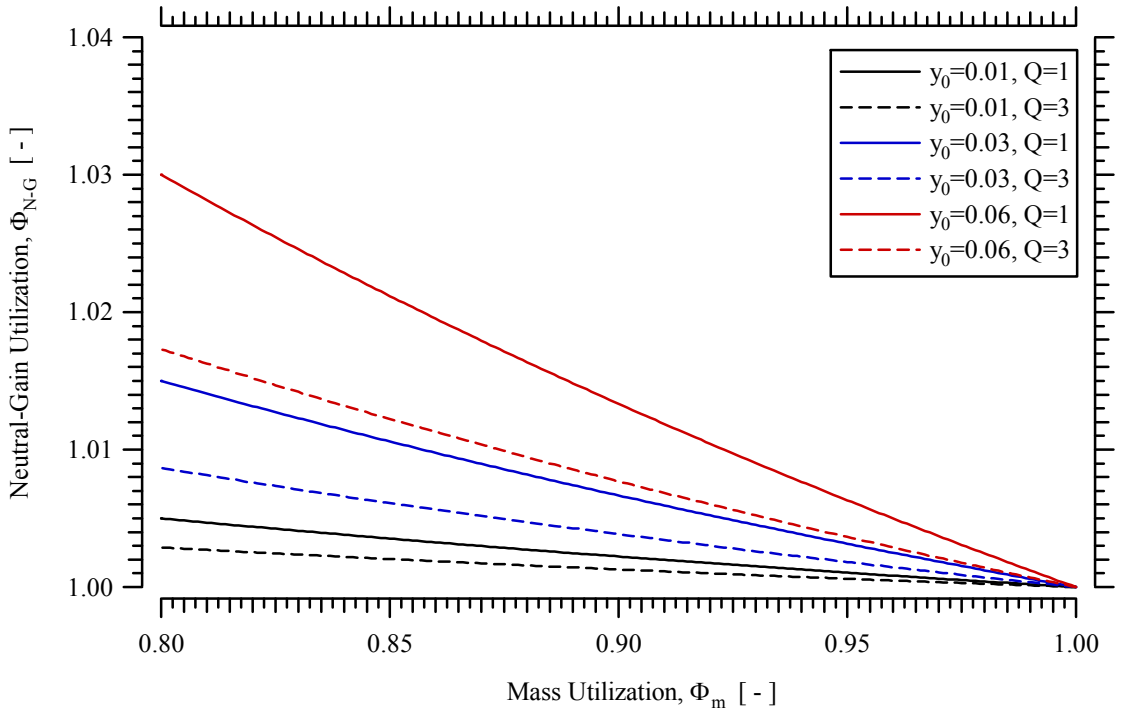

Figure 2-2 **Neutral-gain utilization as a function of mass utilization with variations in neutral speed ratio from y_0=0.01 to y_0=0.06 for Q=1 and Q=3, which are limiting cases for a trimodal ion population.**

The neutral-gain utilization is bracketed for a trimodal ion species composition for Q=1 and Q=3. High-performance Hall thruster operation with 90% singly-charged ions and 90% mass utilization corresponds to neutral-gain utilization of approximately 1.005 for estimates of $y_0 \approx 0.03$. Thus, minimizing the neutral-gain utilization is critical for high-performance operation, since it increases with decreased ionization and decreased neutral residence time in the discharge channel.

2.2.4 Energy Efficiency

Energy efficiency is factored in Eq. (2-30) and (2-31) as the product of voltage utilization (1-β) and current utilization (1-r). It is convenient to introduce χ, which is defined in Eq. (2-32) as the ratio of output moles of charge to input moles of propellant.

Although χ cancels in the energy efficiency term, it is shown in the following sections to reveal the physical nature of the voltage utilization and current utilization inherent in the total thruster efficiency.

$$\eta_E = \frac{\frac{1}{2}\,\dot{m}_T < \overline{v^2} >_m}{P_d} = \left[\frac{\frac{1}{2} < \overline{v^2} >_m}{\frac{\mathscr{F}}{\mathscr{M}} V_d}\right]\left[\frac{\dot{m}_T}{I_d}\frac{\mathscr{F}}{\mathscr{M}}\right] \tag{2-30}$$

$$\eta_E = \left[\chi\,(1-\beta)\right]\left[\frac{(1-r)}{\chi}\right] = (1-\beta)\,(1-r) \tag{2-31}$$

where, by definition

$$\chi = \frac{\sum_{j=1} \dot{m}_j\, Z_j}{\sum_{j=0} \dot{m}_j} = \frac{\sum_{j=1} \dot{m}_j \sum_{j=1} f_j^*\, Z_j}{\dot{m}_T} = \Phi_m\; Q \tag{2-32}$$

2.2.4.1 Voltage Utilization

The definition of voltage utilization is well established in Hall thruster performance models, and is often referred to as the acceleration efficiency.[43] The first term in brackets of Eq. (2-30) is transformed in Eq. (2-33) to an expression that contains explicit utilization of acceleration potential for each ion species, $V_{a,j}/V_d$.

$$\frac{\frac{1}{2} < \overline{v_i^2} >_m}{\frac{\mathscr{F}}{\mathscr{M}} V_d} \frac{< \overline{v^2} >_m}{< \overline{v_i^2} >_m} \approx \frac{\frac{1}{2}\Phi_m}{\frac{\mathscr{F}}{\mathscr{M}} V_d} \quad \sum_{j=1}\left(\frac{\dot{m}_j}{\dot{m}_i} v_j^2\right) = \Phi_m \sum_{j=1}\left(f_j^*\, Z_j \frac{V_{a,j}}{V_d}\right) \tag{2-33}$$

The ratio of average particle specific kinetic energy to average ion specific kinetic energy ($< \overline{v^2} >_m / < \overline{v_i^2} >_m$) in Eq. (2-33) is shown to be approximately equal to mass utilization in Eq. (2-34). The bracketed quantity in Eq. (2-34) is very close to unity under all reasonable conditions of Hall thruster operation due to the value $y_0^2 < 1 \times 10^{-3}$ in the

numerator. Thus, the approximation $<\overline{v^2}>_m/<\overline{v_i^2}>_m \approx \Phi_m$ is accurate to better than one in one thousand.

$$\frac{<\overline{v^2}>_m}{<\overline{v_i^2}>_m} = \frac{\sum_{j=0}\left(\frac{\dot{m}_j}{\dot{m}} v_j^2\right)}{\sum_{j=1}\left(\frac{\dot{m}_j}{\dot{m}_i} v_j^2\right)} = \Phi_m \left[1 + \frac{y_0^2 \left(1 - \Phi_m\right)}{\chi}\right] \approx \Phi_m \tag{2-34}$$

Ion mass flow fractions and estimation of each ion species acceleration potential with a high accuracy ExB probe measurement would enable a voltage utilization to be calculated for each ion species. The RPA measurement of most probable ion acceleration potential is generally a higher accuracy measurement, and thus is a more accurate representation of the global voltage utilization.

To simplify the analysis of voltage utilization, all ions are considered to be created in the same zone whose length is small compared to the acceleration length, such that $V_a \approx V_{aj} \approx$constant. Previous investigations by Kim[64] and King[65] found that species dependent energy to charge ratios varied by tens of volts using different types of energy analyzers. This variation in energy to charge ratio is less than 10% of the typical discharge voltage. According to Hofer[19], the approximation will have a negligible effect on accuracy since the plume is predominantly composed of singly ionized xenon. The velocity of neutrals and each ion species is approximated with a delta function distribution of velocities, such that the ion species kinetic energies are proportional to their charge and the ion velocity ratio magnitudes are $|y_j|=(Z_j)^{1/2}$. This approximation is consistent with other performance architectures.

Based on the approximation that all ion species have equivalent average ion acceleration potential, the first term in brackets of Eq. (2-30) may be expressed in terms

of the average voltage utilization efficiency and χ in Eq. (2-35). The average voltage utilization definition in Eq. (2-36) compares the most probable acceleration potential of ions with the applied anode potential, and is unity for ionization at the anode face if ions are accelerated through the entire anode-to-cathode potential.

$$\frac{\frac{1}{2}<\overline{v^2}>_m}{\frac{\mathscr{F}}{\mathscr{M}}V_d} \approx \Phi_m \frac{V_a}{V_d}\sum_{j=1}\left(f_j^* Z_j\right) = \Phi_m (1-\beta) Q = (1-\beta)\chi \tag{2-35}$$

$$(1-\beta) = \frac{V_a}{V_d} \tag{2-36}$$

2.2.4.2 Current Utilization

The second bracketed term in Eq. (2-30) is transformed in Eq. (2-37) to an expression containing the current utilization efficiency and χ. Ion beam current is related to χ as shown in Eq. (2-38).

$$\frac{\dot{m}_T}{I_d}\frac{\mathscr{F}}{\mathscr{M}} = \frac{\dot{m}_T(\mathscr{F}/\mathscr{M})\chi}{I_d}\frac{1}{\chi} = \frac{I_{Beam}}{I_d}\frac{1}{\chi} = \frac{(1-r)}{\chi} \tag{2-37}$$

$$I_{Beam} = \sum_{j=1}\dot{m}_j Z_j \frac{\mathscr{F}}{\mathscr{M}} = \dot{m}_T \chi \frac{\mathscr{F}}{\mathscr{M}} \tag{2-38}$$

Current utilization efficiency is the fraction of ion beam current relative to the total thruster discharge current, as calculated in Eq. (2-39). This utilization efficiency is also equivalent to the fraction of cathode electrons applied to beam neutralization, and is expressed in terms of the fraction of cathode electron current to the anode (r).

$$(1-r) = \frac{I_{Beam}}{I_d} \tag{2-39}$$

There is a theoretical minimum electron current (r_{min}) required to produce a cascade of ionization for a given ion species population. The analysis presented here is based on the model by Hruby, *et al.*[53] and is extended to include multiply-charged ions. The maximum number of electron-impact ionization collisions may be estimated based on the propellant species ionization potential (ε_i) and the applied anode to cathode potential (V_d). Each ionization event resulting in a singly-charged ion will correspond to a supplementary electron in the discharge in addition to the high energy ionizing electron. Likewise, creation of a doubly-charged ion will generate two supplementary electrons. The cascade ionization effect is illustrated in Figure 2-3, where each electron ionizes a neutral particle after it has gained sufficient energy from the potential field.

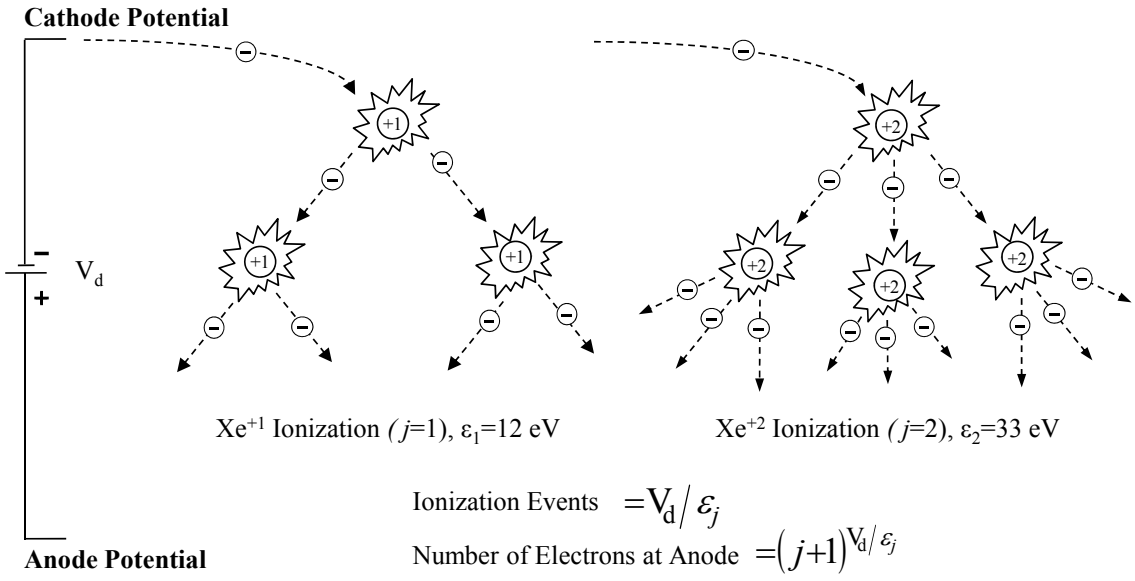

Figure 2-3 Illustration of electron-impact cascade ionization of singly-charged and doubly-charged ions in the Hall thruster discharge.

Knowledge of the ion species current fractions is sufficient information to determine the number of collisions required to produce each ion population. The total electron current produced by ionization of each ion species in the discharge allows an estimate of the minimum cathode electron current required for ionization. Thus, the cathode electron current required for a given ion species population is expressed in terms of the thruster discharge voltage, ion species ionization potential, and the ion mass flow fractions in Eq. (2-40).

$$r_{min} = \frac{\sum_{j=1} (j+1)^{-V_d/\varepsilon_j} \dot{m}_j Z_j \frac{\mathcal{F}}{\mathcal{M}}}{I_d} = \frac{(1-r)}{Q} \sum_{j=1} (j+1)^{-V_d/\varepsilon_j} f_j^* Z_j \qquad (2\text{-}40)$$

Experimental measurements show significantly larger electron current than the theoretical minimum. Although the maximum number of ionizing collisions per cathode electron from the anode to the cathode may be estimated as (V_d/ε_j), this number will decrease due to excitation, wall collisions, and recombination. A more plausible number of ionization collisions may be estimated by equating r_{min} in Eq. (2-40) with the experimentally determined fraction of anode electron current, and solving for (V_d/ε_j). This corresponds to approximately 1 to 4 ionization events per cathode electron, and reveals the increased electron current corresponding to significant Joule heating losses.

2.2.5 Beam Efficiency

Jet momentum losses due to beam divergence are quantified using the momentum-weighted average cosine in Eq. (2-41). This formulation is similar to the focusing efficiency[43], but is naturally expressed as a momentum-weighted average quantity from the formulation of thrust. The momentum-weighted average plume

divergence is equal to the ratio of the measured thrust component directed along the thruster centerline relative to the theoretical thrust achieved when all ions are traveling parallel to thruster centerline. Momentum losses associated with plume divergence may be calculated with knowledge of the total mass flow rate, measured thrust, and the mass-weighted average velocity.

$$\Psi_B = <\cos(\theta)>_{mv}^2 = \left(\frac{T}{\dot{m}_T <\bar{v}>_m} \right)^2 \tag{2-41}$$

The value $<\cos(\theta)>^2$ has been used in previous analyses[41,42,43] to describe plume focusing, but there has not been a consistent method to evaluate the effect of plume divergence on thruster performance. This is primarily due to the difficulty of measuring particle velocity throughout the plume. Charge divergence in the plume is indicative of the loss in thrust due to off-axis ion velocity, and is often used as an alternative for experimental characterization of performance losses due to plume divergence. The momentum-weighted average divergence in Eq. (2-42) is approximated as the charge-weighted average divergence in Eq. (2-43) for an axisymmetric plume.

$$<\cos(\theta)>_{mv}^2 = \left(\frac{2\pi R^2 \int_0^{\pi/2} \left(\frac{\dot{m}(\theta)\bar{v}(\theta)}{J(\theta)} \right) J(\theta)\cos(\theta)\sin(\theta)\,d\theta}{2\pi R^2 \int_0^{\pi/2} \left(\frac{\dot{m}(\theta)\bar{v}(\theta)}{J(\theta)} \right) J(\theta)\sin(\theta)\,d\theta} \right)^2 \tag{2-42}$$

$$<\cos(\theta)>_{mv}^2 \cong \left(\frac{2\pi R^2 \int_0^{\pi/2} J(\theta)\cos(\theta)\sin(\theta)\,d\theta}{2\pi R^2 \int_0^{\pi/2} J(\theta)\sin(\theta)\,d\theta} \right)^2 = <\cos(\theta)>_J^2 \tag{2-43}$$

Off-axis cosine losses integrated in the numerator of Eq. (2-43) quantify the axial component of beam current (I_{Axial}) that generates thrust. This formulation has been used

in past analyses[41,66], and creates a method where the plume divergence vector loss is evaluated in a scalar form. Beam efficiency (Ψ_B) is evaluated in Eq. (2-44) as a charge-weighted average cosine, which is equal to the square of the axial component of ion beam current relative to the total ion beam current as measured by a Faraday probe. The calculation of Ψ_B is complicated by the presence of charge exchange (CEX) collisions in the plume, which increase measured beam current at large angles from centerline and artificially increases divergence losses.

$$\Psi_B \cong <\cos(\theta)>_J^2 = \left(\frac{I_{Axial}}{I_{Beam}}\right)^2 \tag{2-44}$$

An effective plume divergence angle, λ, may be calculated as shown in Eq. (2-45). This angle is significantly less than the 95% divergence half-angle that is typically reported for evaluation of plume expansion.

$$\lambda = \cos^{-1}\left(<\cos(\theta)>_J\right) = \cos^{-1}\left(\frac{I_{Axial}}{I_{Beam}}\right) \tag{2-45}$$

Analysis of the ratio $\dot{m}(\theta)v(\theta)/J(\theta)$ introduced in Eq. (2-42) characterizes the properties that cause differences between momentum-weighted divergence and charge-weighted plume divergence. The ratio is evaluated at angular position θ in Eq. (2-46). Each particle species is approximated with a delta function velocity distribution and velocity ratios are calculated for the idealized case of ion creation at the same location. The ratio $\dot{m}(\theta)v(\theta)/J(\theta)$ is characterized using the dimensionless quantity γ, which describes differences associated with mass utilization and ion species population. The term γ is shown as a function of Φ_m, Φ_P, χ, and y_0 in Eq. (2-47).

$$\frac{\dot{m}(\theta)\bar{v}(\theta)}{J(\theta)} = \frac{\sum_{j=0}\dot{m}_j v_j}{\sum_{j=1}\dot{m}_j Z_j \left(\mathcal{F}/\mathcal{M}\right)}\bigg|_\theta = \frac{\dot{m}_T \Phi_m |v_1| \sum_{j=0} f_j^* y_j}{\dot{m}_T \Phi_m Q \left(\mathcal{F}/\mathcal{M}\right)}\bigg|_\theta = \left(2V_a \frac{\mathcal{M}}{\mathcal{F}}\right)^{1/2} \gamma\bigg|_\theta \qquad (2\text{-}46)$$

$$\gamma = \frac{\sum_{j=0} f_j^* \sqrt{y_j}}{Q} = \left(\frac{\Phi_P}{\chi}\right)^{1/2} \left[1 + \frac{y_0^2 \left(1-\Phi_m\right)}{\chi}\right]^{1/2} \approx Q^{-1/2} \qquad (2\text{-}47)$$

The term inside the brackets of Eq. (2-47) is near unity for $y_0^2 < 1\text{x}10^{-3}$, and variations in the neutral speed ratio have negligible effect on γ. In Figure 2-4, γ is shown for unity mass utilization, which cancels terms with y_0. The ratio is bounded for a trimodal ion population, and is shown to be primarily a function of average ion charge.

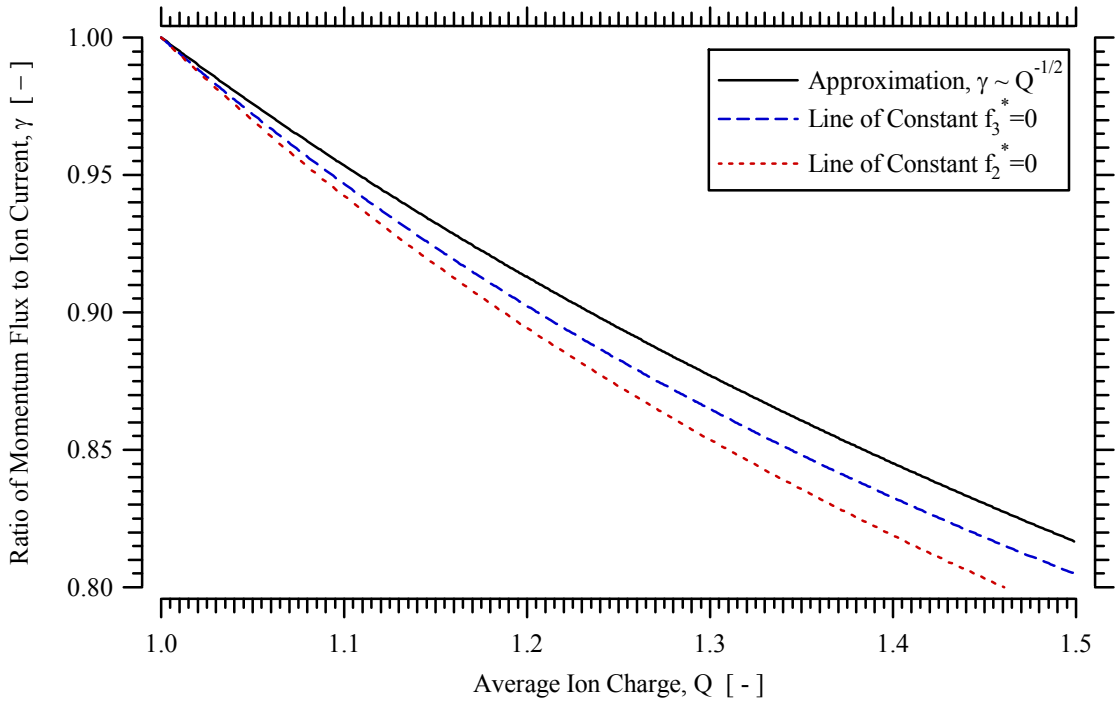

Figure 2-4 **Variation in γ due to ion species composition for Φ_m=1. Lines of constant f_2^*=0 and f_3^*=0 bound γ for a trimodal ion population, and are compared with the approximation $\gamma \approx Q^{-1/2}$.**

Variations in the magnitude of Q alter γ, however, the angular location of these variations is the dominant factor causing differences between momentum-weighted divergence and charge-weighted divergence. This effect is illustrated in Figure 2-5, which shows a representative angular distribution of ion current density and ion beam current for the 6-kW laboratory Hall thruster described in Chapter 3 operating at 300-V. The location of peak beam current in the plume is approximately 8° from thruster centerline, and variations in Q within the angular range of full width half maximum (FWHM) will have the greatest effect on plume divergence calculations. For the beam current in Figure 2-5, this range is approximately 3° to 21° from thruster centerline. Near and far-field plume measurements of the 6-kW Hall thruster in this investigation, the SPT-100[67], and the BHT-200[68] Hall thruster found that the ion species populations did not significantly change within ±15 degrees from thruster centerline, and the fraction of Xe^{+2} ions sharply increased by approximately 5% at ±20 degrees. These changes in ion species composition have a negligible effect on the value of $\langle\cos(\theta)\rangle_{mv}$, thus enabling the approximation of equivalence between momentum-weighted divergence and charge-weighted plume divergence as measured with a Faraday probe.

A more accurate determination of plume divergence may be estimated with Eq. (2-42) using the value of γ at each location in the plume. This approach requires estimation of the particle velocity ratios and ion species composition throughout the plume, and is likely to introduce more uncertainty in the calculation of divergence than the estimation based on charge-weighted methods.

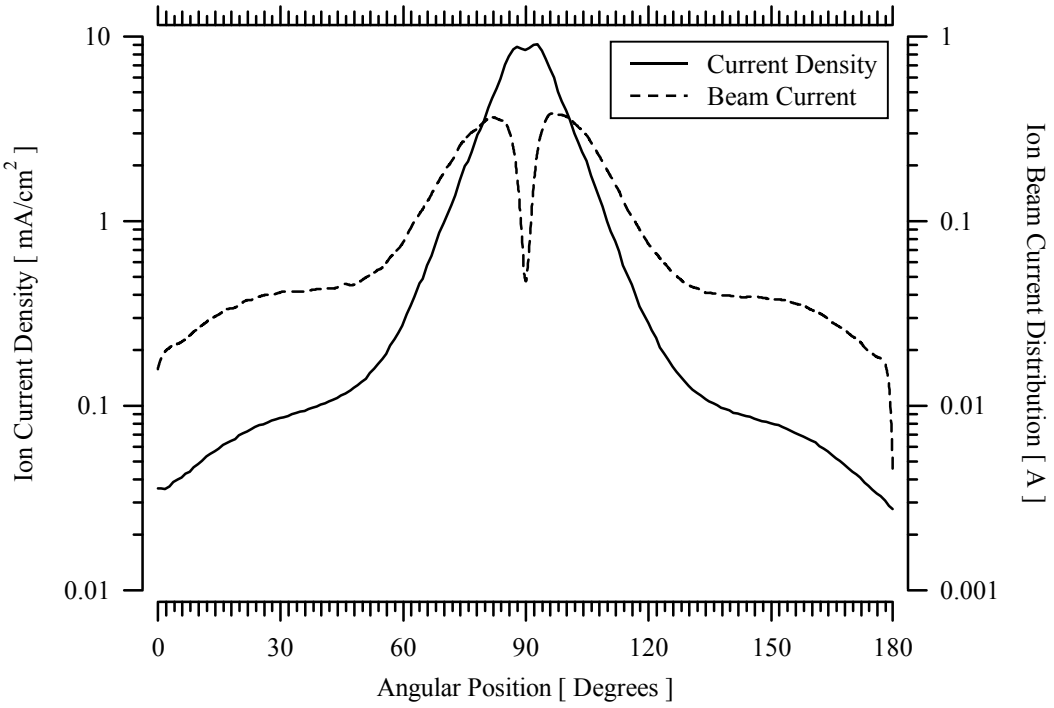

Figure 2-5 Representative distribution of beam current and current density at 1 meter radius as a function of angular position in the plume of a nominal 6-kW laboratory Hall thruster operating at 300-V, 20-mg/s described in Chapter 3.

2.3 Performance Parameters

2.3.1 Voltage Exchange and Mass Exchange Parameters

Two experimental parameters, denoted E_1 and E_2, may be written using the preceding utilization efficiencies to isolate changes in performance due to processes related to thrust or discharge current. The parameters are formed in Eq. (2-48) such that the product of E_1 and E_2 is equal to total thruster efficiency.

$$\eta_T = \Phi_P \, \eta_E \, \Psi_B = \left[\Phi_P \, \Psi_B (1-\beta) \chi\right] \left[\frac{(1-r)}{\chi}\right] = E_1 \, E_2 \tag{2-48}$$

Equations (2-49) and (2-50) show how these quantities are calculated by (1) plume measurements, and by (2) telemetry and thrust measurements. These parameters

provide insight about the relative magnitudes of the individual utilization efficiencies in the absence of specific plume measurements.

$$E_1 = \Phi_P \, \Psi_B (1-\beta) \chi = \frac{\frac{1}{2}\left[\frac{T}{\dot{m}_T}\right]^2}{V_d \frac{\mathcal{F}}{\mathcal{M}}} \tag{2-49}$$

$$E_2 = \frac{(1-r)}{\chi} = \frac{\dot{m}_T}{I_d} \frac{\mathcal{F}}{\mathcal{M}} \tag{2-50}$$

For fixed thruster telemetry inputs V_d and $\dot{m}_T$, the dimensionless experimental parameter E_1 separates changes in thruster efficiency directly to variations in thrust and E_2 isolates changes due to variations in discharge current. The quantity $E_1 \sim T^2$, and is a function of propellant efficiency, beam efficiency, voltage utilization, and χ. Experimental parameter E_1 relates losses in the applied acceleration potential to dispersion and divergence of the jet. The quantity $E_2 \sim I_d^{-1}$, and is a function of current utilization and χ. Experimental parameter E_2 relates the input flow of mass to the output flow of ion charge. The inverse of E_2 was used in the Soviet literature[69] as early as 1978 and termed the exchange parameter.[70,71] The naming convention used here describes the exchange of applied input parameters to operational thruster properties. Thus, E_1 is termed the voltage exchange parameter and E_2 is termed the mass exchange parameter. While ionization and acceleration processes are closely coupled, the form of the experimental parameters indicates that propellant efficiency, beam efficiency, and voltage utilization are principal in the formation of directed thrust. In the absence of diagnostics for the determination of plasma properties, these experimental parameter groups allow limits to be placed on self-consistent values for the average ion charge, mass utilization, and plume divergence.[72,73]

2.3.2 Specific Impulse and Thrust to Power Ratio

The loss mechanisms that affect T/P and Isp are expressed in terms of the experimental parameters and in terms of utilization efficiencies in Eqs. (2-51) and (2-52). These formulations indicate low current utilization and large χ will decrease T/P. Conversely, specific impulse is not directly affected by current utilization and increases for large χ.

$$\frac{T}{P_d} = E_2 E_1^{1/2} \left(\frac{2}{V_d} \frac{\mathscr{M}}{\mathscr{F}} \right)^{1/2} = (1-r)(1-\beta)^{1/2} \left(\frac{\Phi_P \, \Psi_B}{\chi} \right)^{1/2} \left(\frac{2}{V_d} \frac{\mathscr{M}}{\mathscr{F}} \right)^{1/2} \tag{2-51}$$

$$I_{sp} \, g = E_1^{1/2} \left(2V_d \frac{\mathscr{F}}{\mathscr{M}} \right)^{1/2} = (1-\beta)^{1/2} \left(\chi \, \Phi_P \, \Psi_B \right)^{1/2} \left(2V_d \frac{\mathscr{F}}{\mathscr{M}} \right)^{1/2} \tag{2-52}$$

The T/P formulation is similar to the one dimensional analysis used to estimate thrust of the SERT-II ion thrusters, which is equivalent to Eq. (2-51) for the idealized case where ($\Phi_P \, \Psi_B / \chi$) is unity.[74,75,76,77,78,79] An analogous expression was used to estimate thrust of the NSTAR ion thrusters on-board NASA's Deep Space 1 by including factors to estimate the effect of multiply-charged ions and beam cosine losses.[80] These factors were similar to those in the formulation of thrust by Masek, *et al.*[37] and were related to the ratio $(\Phi_P \, \Psi_B / \chi)^{1/2}$ for a bimodal ion population. The formulations of T/P and Isp in Eqs. (2-51) and (2-52) will be used in addition to the total efficiency to determine the efficacy of plume measurements in evaluating thruster performance.

2.3.3 Energy Losses and Ionization Cost of a Multiply-Charged Plasma

The fraction of cathode electron current flowing to the anode, r, increases as a result of Joule heating of the plasma and channel walls. A fraction of the Joule heating is

required to sustain propellant ionization, and the remaining energy is lost to dissipative plasma processes. The minimum electron current to the anode required to create a given ion species composition was established for the theoretical case of ideal electron-impact cascade ionization in Section 2.2.4.2. The minimum power required for ionization (P_{min}) is formulated in Eq. (2-53) based on the fractions of ion mass flow rate and the species ionization potentials (ε_j). This is distinct from the minimum electron current to the anode (r_{min}), since the electrons released in an ionization event may gain sufficient energy to ionize propellant and contributes to the overall power lost to ionization. An effective minimum ionization cost per beam ion ($\varepsilon_{B,\min}$) may be determined from this minimum power for a given set of discharge properties, as expressed in Eq. (2-54).

$$P_{\min} = \frac{\mathscr{F}}{\mathscr{M}} \sum_{j=1} \left(\dot{m}_j Z_j \varepsilon_j \right) = \frac{I_{Beam}}{Q} \sum_{j=1} \left(f_j^* Z_j \varepsilon_j \right) \tag{2-53}$$

$$\varepsilon_{B,\min} = \frac{P_{\min}}{I_{Beam}} Q = \sum_{j=1} \left(f_j^* Z_j \varepsilon_j \right) \tag{2-54}$$

Power in excess of P_{min} is lost by energy deposition to the anode, channel walls, and plasma interactions within the discharge. When P_{min} is combined with the total power loss estimates from energy efficiency, the value of P_{loss} places an upper limit on Joule heating losses to the anode and walls amounting to the power loss in Eq. (2-55).

$$P_{loss} = P_d - P_{jet} - P_{min} \tag{2-55}$$

A more conventional metric of energy loss is the total effective ionization cost per beam ion (ε_B). This parameter was previously described for ion thrusters with a singly-charged beam.[81] In Eq. (2-56), the equation has been adapted for Hall thrusters based on Eq. (2-54) to account for multiply-charged ions and the loss of ion acceleration voltage.

Expressing the effective ionization cost per beam ion in terms of utilization efficiencies indicates this parameter may increase during high discharge voltage Hall thruster operation due to increases in both V_d and Q.

$$\varepsilon_B = \frac{\left(P_d - P_{jet}\right)}{I_{Beam}} Q = V_d Q \left[\frac{1}{(1-r)} - (1-\beta) \right] \tag{2-56}$$

2.4 Application to Experimental Results

The efficiency architecture developed in this chapter will be used extensively to characterize low discharge voltage Hall thruster performance in Chapters 5 and Chapter 6. A complete set of plume diagnostics includes a Faraday probe for measurement of current density, an ExB probe for ion species composition, an RPA for the most probable ion acceleration potential, and a Langmuir probe measurement of plasma potential to correct the RPA. Coarse estimates of the axial neutral speed at the thruster exit plane from LIF measurements are sufficient to approximate the neutral-gain utilization in propellant efficiency.

Combining results from several plume diagnostics introduces significant uncertainty in estimates of utilization efficiencies and global plasma properties. Of the plasma diagnostics required for complete plume characterization, Faraday probe measurements typically have the highest degree of uncertainty. Minimizing this uncertainty is crucial to accurately evaluating performance and thruster loss mechanisms. In Chapter 4, a study of Faraday probe design and scattering effects in the plume reveals systematic error associated with conventional analysis techniques and demonstrates methods to minimize facility effects on measured current density.

Relationships for the propagation of uncertainty in the utilization efficiencies and performance parameters are listed in Appendix A, and are based on the ISO *Guide to the Expression of Uncertainty in Measurement*.[82] The relative error associated with each diagnostic is discussed in Chapter 3, and analysis of the uncertainty in Faraday probe measurements due to scattering is detailed in Chapter 4.

2.5 Summary

The separation of scalar thrust into mass-weighted and momentum-weighted terms enabled factorization of total thruster efficiency into the product of (1) energy efficiency, (2) propellant efficiency, and (3) beam efficiency. The analysis decomposed total efficiency from first principles, and formulated the relationships such that losses associated with energy conversion were analyzed separately from losses associated with dispersion of the jet VDF and beam divergence. Energy efficiency can never be unity in a Hall thruster discharge due to a finite flow of electrons that are recycled to the anode to sustain ionization processes. The effects of multiply-charged ions are included, and the neutral-gain utilization was introduced to account for the neutral speed. The momentum-weighted divergence loss term ($<\cos(\theta)>^2_{mv}$) contains all jet vector losses, and differences from the current-weighted divergence were characterized. Experimental energy losses in the discharge are described with the ionization cost per beam ion for a multiply-charged plasma, and a theoretical model of electron-impact cascade ionization was presented to characterize the minimum electron current required to sustain ionization. The performance architecture has similarities to previous analyses, including: the formulation

by Masek, *et al.*[37] in the ion thruster community, the framework by Belan, *et al.*[41] from the Kharkov Aviation Institute, and a contemporary methodology by Hofer. [19,57]

Chapter 3

Experimental Apparatus

A Hall thruster efficiency analysis was developed in Chapter 2 to enhance the physical understanding of Hall thruster operation and characterize loss mechanisms. Experimental measurements of thrust, ion current fractions, most probable ion acceleration potential, and current density in the plume are sufficient to develop a complete description of thruster performance. The uncertainty in Faraday probe measurements is typically larger than the other diagnostics, and often drives the relative error in utilization efficiencies and performance metrics to unacceptable levels. Minimizing uncertainty of Faraday probe current density measurements is critical for accurate interpretation of physical processes using the efficiency architecture. Chapter 4 details an investigation of Faraday probe design and scattering effects that was conducted with a low-power Hall device in Chamber 1 at AFRL. The experimental procedures and Faraday probe data analysis techniques were then applied to investigations of low discharge voltage Hall thruster operation in Chamber 3 at AFRL. This chapter describes the facilities, diagnostics, and apparatus used to study Faraday probes in Chamber 1 and investigate low discharge voltage characteristics in Chamber 3.

3.1 Vacuum Facilities

Chamber 3 is the high-power electric propulsion test facility at the AFRL/RZSS Spacecraft Propulsion Branch, with a larger size and greater pumping capacity than Chamber 1. The advantage of Chamber 1 is the diagnostic positioning capability, which enabled plume characterization in a hemispherical arc from 0° to 180° at a variable radius up to 60-cm from the axis of rotation. Faraday probe measurements in the plume of a low-power Hall device in Chamber 1 were studied to characterize facility effects on current density measurements over a wide range of downstream distances and background pressures. The knowledge and methods developed in that study were applied to investigations of a larger, 6-kW Hall thruster in Chamber 3. Far-field Faraday probe scans in Chamber 3 are conducted at a single, fixed measurement radius approximately 1-meter downstream of the exit plane. Although the scan radius in Chamber 3 is larger than the maximum distance studied in Chamber 1, the measurement distance is fewer thruster diameters downstream. In addition, the background pressure during thruster operation is higher in Chamber 3 due to order of magnitude increase in propellant mass flow. Therefore, facility effects are expected to be greater in the larger facility and improved understanding of background pressure on Faraday probe current density measurements is essential to research low-voltage Hall thruster operation in Chamber 3.

3.1.1 Chamber 1 at AFRL

Chamber 1 at AFRL is a stainless steel, cylindrical vacuum chamber 2.4-m in diameter and 4-m in length. A schematic is shown in Figure 3-1. All surfaces optically visible to the plasma plume were shielded with graphite felt. An Edwards DryStar

GV160 mechanical booster pump reached rough vacuum and lighter gases were removed with a Varian TV55 turbomolecular pump. Two CVi TorrMaster cryotubs circulated liquid nitrogen to cool 4 cryopanels, and achieved a maximum xenon pumping speed of 50,000 l/s. The thruster was located along the centerline of the chamber and fired towards the cryopanels at the opposing end.

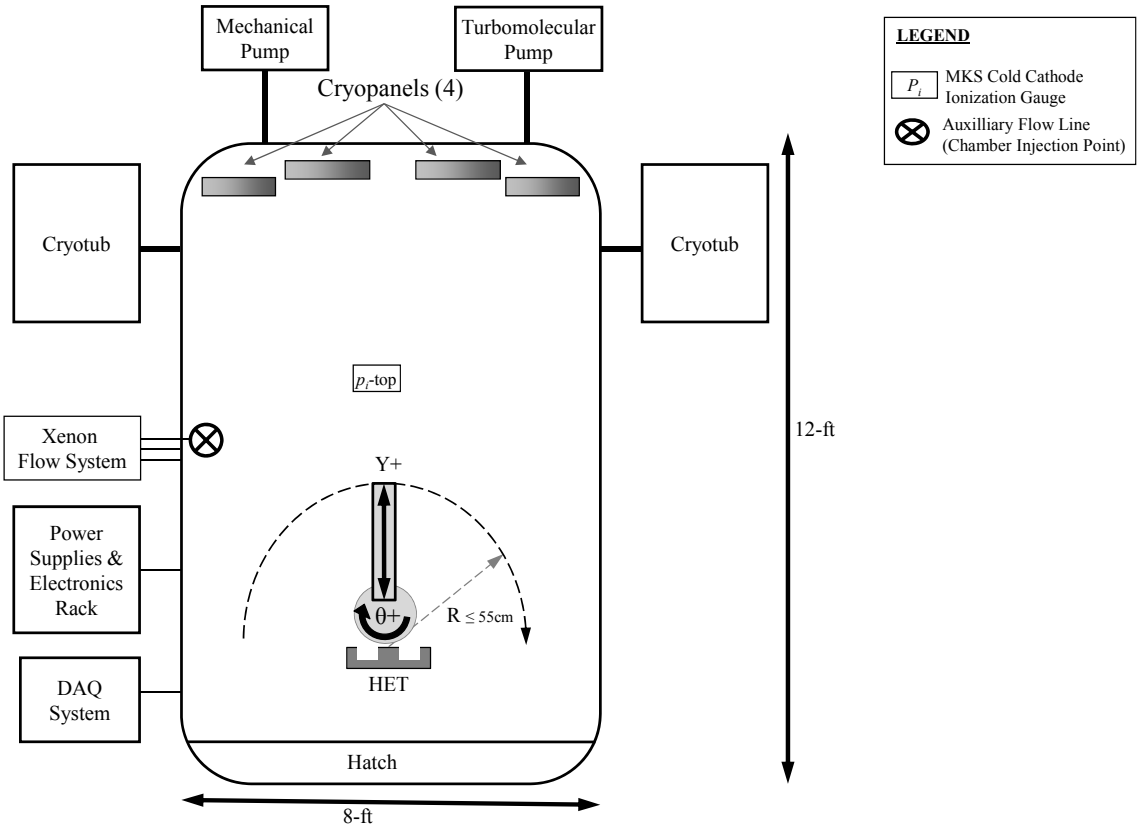

Figure 3-1 Chamber 1 schematic (not to scale).

An MKS Instruments cold cathode ionization gauge was located on the chamber ceiling above the thruster centerline approximately 1 meter downstream of the exit plane. Background pressure was corrected using a xenon correction factor of 2.87 along with the

facility base pressure of air using Eq. (3-1), which was conservatively estimated at $p_b \approx 1\text{x}10^{-7}$ torr.

$$p = \frac{p_i - p_b}{2.87} + p_b \tag{3-1}$$

Chamber background pressure was increased by injecting xenon through an auxiliary flow line located approximately 1-meter downstream of the thruster exit plane. Injected flow of approximately 9, 29, and 127-sccm corresponded to a corrected xenon background pressure of $3.2\text{x}10^{-6}$, $1.1\text{x}10^{-5}$, and $3.5\text{x}10^{-5}$ torr, respectively.

3.1.1.1 Power Electronics and Propellant Hardware

Prior to Faraday probe data collection, the low-power laboratory Hall device was fired for over 1 hour after initial start-up. Thruster discharge power was provided by a Sorenson DHP Series DC power supply. The heater and magnet coils were energized with Sorenson DLM 40-15 power supplies, and the cathode keeper supply was a Sorenson DCS 600-1.7E. During the HET ion source operation, the heater supply was limited to 3.0-A and the keeper current was limited to 0.5-A. Discharge current was monitored through a high accuracy current shunt with an uncertainty of ±0.5%. Thruster telemetry was monitored during Faraday probe sweeps, and exhibited negligible deviation from steady-state operation.

The propellant flow system was supplied with research grade xenon (99.999% purity) via ¼-inch stainless steel tubing. Anode flow was controlled with a 20-sccm Unit 7300 mass flow controller and cathode flow was regulated with a 10-sccm Unit 7300 mass flow controller. A 250-sccm Unit 8160 analog mass flow controller regulated auxiliary flow to increase facility backpressure. Flow controllers were set with a Unit

URS-100-5 analog control box. All flow controllers were calibrated with xenon prior to testing with a DH Instruments Molbloc/Molbox gas flow calibration system with an estimated uncertainty of ±0.5% as per the manufacturer's specifications.

3.1.1.2 Diagnostic Positioning System

Plume characterization of current density in Chamber 1 was conducted with the laboratory Hall device mounted near the center of the chamber, with the plume expanding approximately 3-m towards the cryopanels. The Faraday probe positioning system consisted of a translation stage for control of measurement radius and a rotation stage, which was centered beneath the exit plane on thruster centerline. In Figure 3-2, one end of the translation stage is shown mounted on top of the rotation stage, enabling current density scans from 0° to 180° at constant radius up to 60-cm from the axis of rotation at the exit plane.

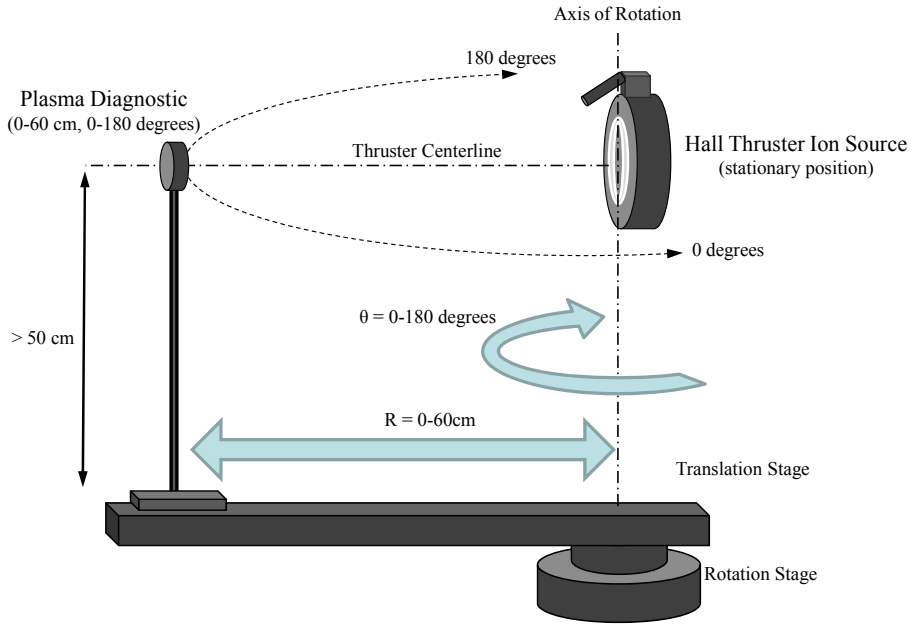

Figure 3-2 Diagnostic positioning system in Chamber 1 with R,θ-coordinate axis control.

The Faraday probe and laboratory thruster were mounted higher than 50-cm above the rotation and translation stages. A National Instruments MID-7604/7602 Power Drive interfaced with the rotation and translation stages, and data acquisition was controlled through LabView.

3.1.2 Chamber 3 at AFRL

The investigation of low-voltage Hall thruster operation was conducted in Chamber 3 at AFRL. Chamber 3, pictured in Figure 3-3, is a cylindrical, stainless steel, vacuum chamber 3.3-m in diameter and 8-m in length.

Figure 3-3 Chamber 3 at AFRL/RZSS.

As illustrated in Figure 3-4, the Hall thruster exit plane was located in the center of the chamber diameter and directed down the long axis approximately 7-m from the far end. All surfaces that are optically visible to the plasma plume are shielded with ½ inch thick, high purity, sulfur-free carbon plates. A dedicated dry Stokes mechanical pump reaches rough vacuum with a pumping speed of 450 l/s and a Pfeiffer Vacuum turbomolecular pump removes lighter gases. The facility utilizes eight helium-cooled cryopanels, resulting in a maximum xenon pumping speed of 140,000 l/s. The heat load to these cryopanels is moderated by shrouds coated with low emissivity paint, which are cooled by four IGC Polycold Cryogenic Refrigeration units. A conservative measurement of the ultimate base pressure is less than $1x10^{-7}$ torr.

Background pressure was monitored with two MKS Instruments cold cathode ionization gauges. The readings were corrected for xenon using Eq. (3-1), and were averaged to determine an effective facility background pressure. One gauge was located on the chamber ceiling above the thruster and the other was located behind the thruster on the side chamber wall, as shown in Figure 3-4. Corrected operating pressures were approximately $8.0x10^{-6}$, $1.3x10^{-5}$, and $1.5x10^{-5}$ torr for xenon flow rates of 10, 15, and 20-mg/s. Past studies have shown neutral entrainment at these pressure and flow rates have a negligible impact on thruster performance.[83,84] However, measurements of thrust, discharge current, and current density were conducted at several background pressures to characterize facility effects and minimize measurement uncertainty.

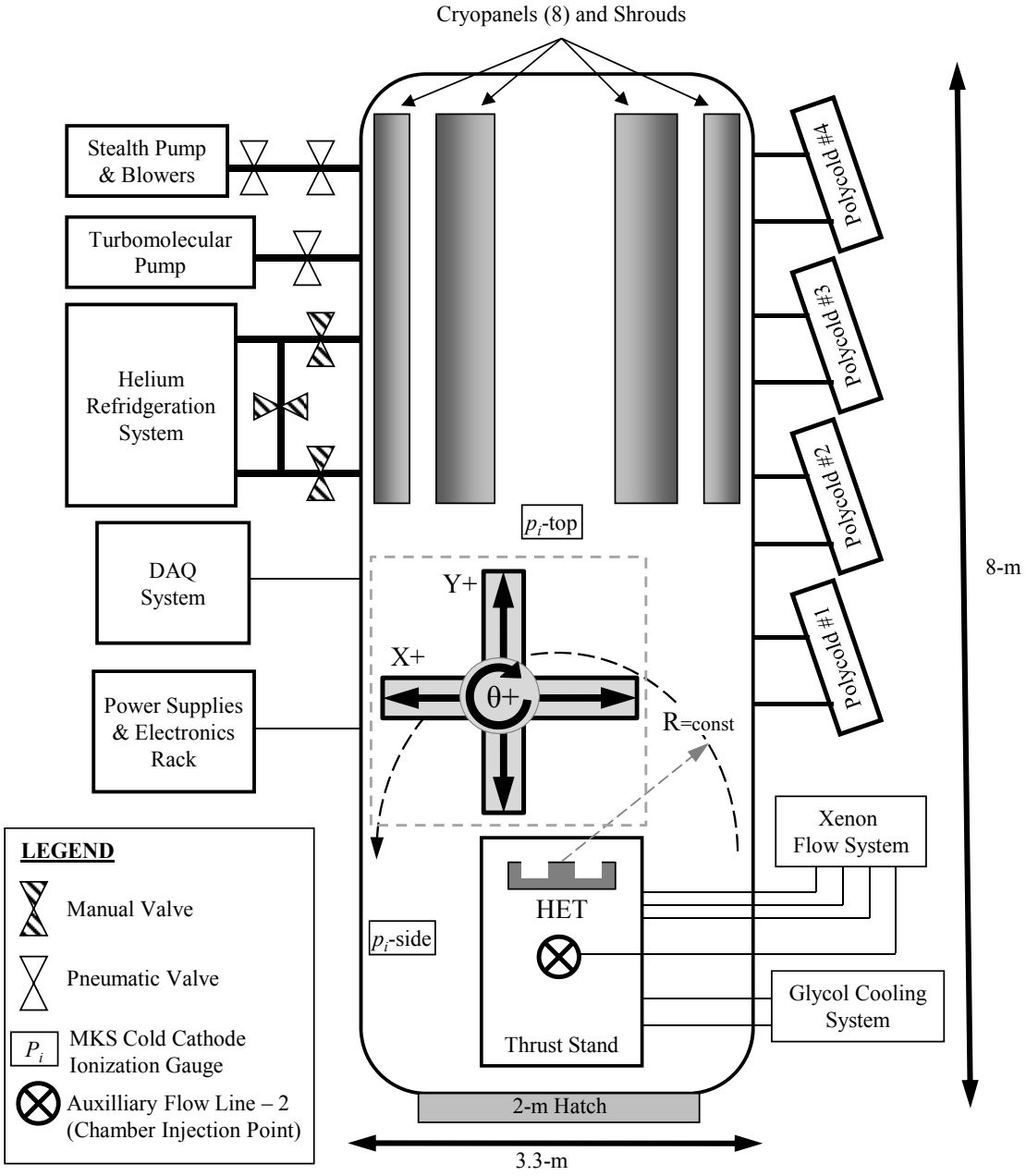

Figure 3-4 Chamber 3 schematic (not to scale).

3.1.2.1 Power Electronics and Propellant Hardware

Thruster discharge power was provided by a 1250-V, 80-A AMREL HPS1250-80 DC power supply in line with an RLC circuit to provide low pass filtering of the main discharge. The thruster body and thrust stand shroud were electrically connected to chamber ground. Coils were energized with Sorenson DLM 60-10 power supplies. The cathode heater was powered with an EMS 20-30 supply and the cathode keeper used a Sorenson LHP 300-3.5 power supply. The heater power supply was shut down during thruster operation. A schematic of the thruster and cathode power electronics are shown in Figure 3-5.

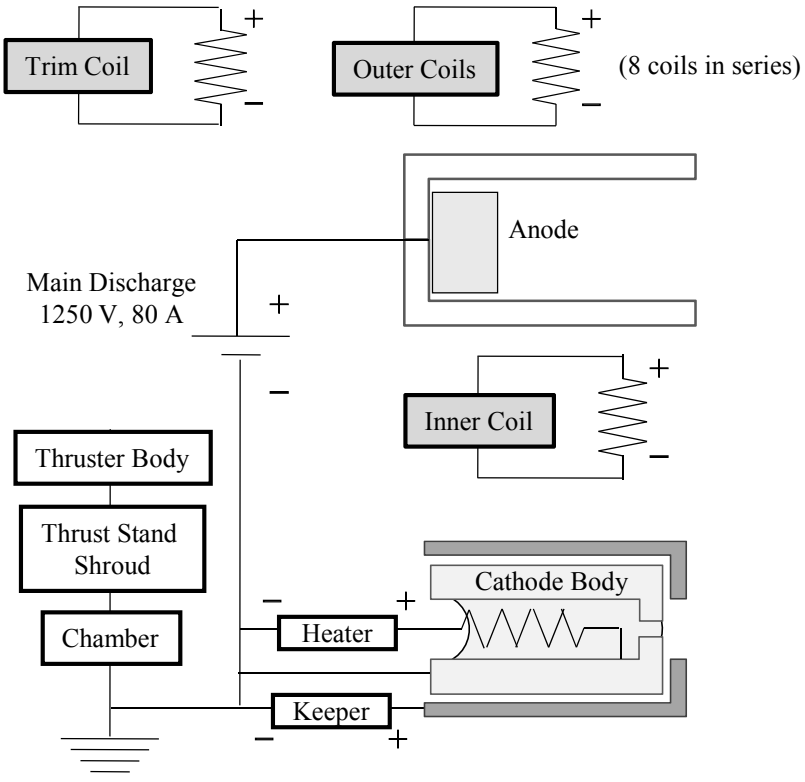

Figure 3-5 Electrical diagram of power electronics in Chamber 3 for the 6-kW Hall thruster and LaB6 cathode.

The propellant flow system was supplied with research grade xenon (99.999% purity) via ¼-inch stainless steel tubing. A schematic of the flow system is shown in Figure 3-6, which illustrates the dual anode and cathode flow control capability for high and low flow rate applications.

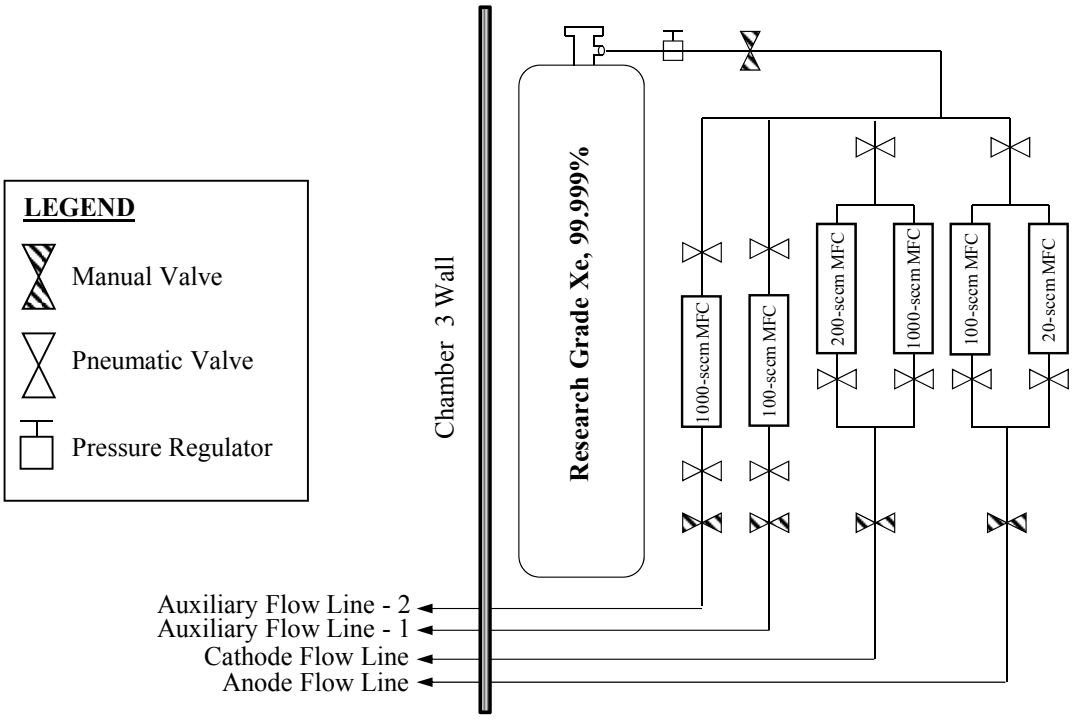

Figure 3-6 Schematic of the Chamber 3 propellant distribution system.

In these investigations, anode flow was controlled with a 1000-sccm Unit 1661 digital mass flow controller. Cathode flow was regulated with a 100-sccm Unit 8161 digital mass flow controller. Auxiliary flow line 1 was installed to enable propellant injection to the region surrounding the centrally mounted cathode keeper, and was adjusted with a 100-sccm Unit 8161 digital mass flow controller. Auxiliary flow line 2 utilizes a 1000-sccm Unit 1661 digital mass flow controller to increase the facility background pressure by injecting propellant at the chamber floor behind and below the

thruster, as illustrated in Figure 3-4. All mass flow controllers were calibrated with xenon prior to testing with a DH Instruments Molbloc/Molbox gas flow calibration system with an estimated uncertainty of ±0.5% according to the manufacturer's specifications.

3.1.2.2 Thruster Telemetry and Data Acquisition System

A National Instruments Compact FieldPoint system transmitted thrust and thruster telemetry data to a LabView code monitoring the total thruster efficiency and performance in real-time at ~1 Hz. DC thruster discharge current and electromagnet currents were monitored with high accuracy current shunts with an uncertainty of ±0.5%. All current shunts and Compact FieldPoint modules were calibrated prior to use, and the calibration curves incorporated into the LabView data acquisition program. For a given discharge voltage and flow rate, the magnet coil currents were adjusted for maximum total thruster efficiency. When peak efficiency was achieved, the magnet coils were further tuned for maximum T/P ratio. The efficiency optimization did not always correspond to minimum discharge current, since decreasing thrust would further reduce efficiency.

Discharge current oscillations were measured with a CM-10-MG current monitor with a conversion factor of 0.1-V/A. The current monitor was connected to a Tektronix DPO 4034 Digital Phosphor oscilloscope that is rated to 350 MHz. Discharge current was recorded in 100-ns intervals for 1-ms. Frequency analysis of the discharge oscillations was conducted in IGOR using the discrete Fourier transform FFT operation

with a Hanning window to smooth the ends of the data set. The dominant frequency is conservatively estimated to within 0.5-kHz.

3.1.2.3 Diagnostic Positioning Systems

Chamber 3 is equipped with two separate experimental positioning systems. The first is a rotational arm attached to the chamber ceiling above the thruster exit plane, illustrated in Figure 3-7, where the axis of rotation is perpendicular to thruster centerline.

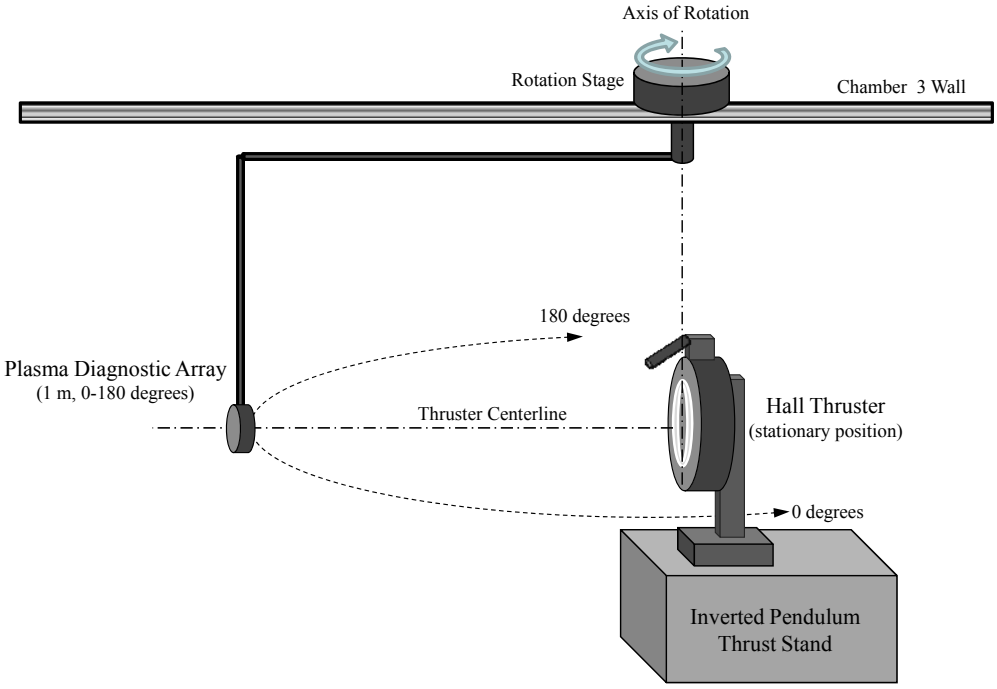

Figure 3-7 Diagnostic positioning system in Chamber 3 with θ-coordinate axis control.

The rotational arm was swept in a 1-meter arc from θ=0° to 180° and enabled discrete single point measurements or continuous measurements during low speed travel. Continuous measurements minimized mechanical arm vibrations caused by acceleration and deceleration, and prolonged probe life by decreasing transit time in the plume. The

rotation stage is an RNN-250 Thermionics Northwest, Inc. rotary platform mounted externally above the chamber via an FRH-450-1.33-8 custom feed-through assembly. Workstation control is executed with a National Instruments MID-7604 4/2 Axis Stepper Motor Drive.

A separate X-Y-θ positioning system was installed in Chamber 3 that allowed more detailed spatial mapping of the far-field plume and near-field region. The X-Y-θ motion control system is illustrated in Figure 3-8, where the measurement span is a 1-m by 1-m region and the probe is aligned in the thruster centerline horizontal plane. Probe orientation is achieved with a rotation stage that is mounted on a rigid post. The system is tuned for a specific weight to maintain holding torque and minimize vibrations during positioning. Graphite felt is wrapped over the stages and mount to decrease erosion and sputtering.

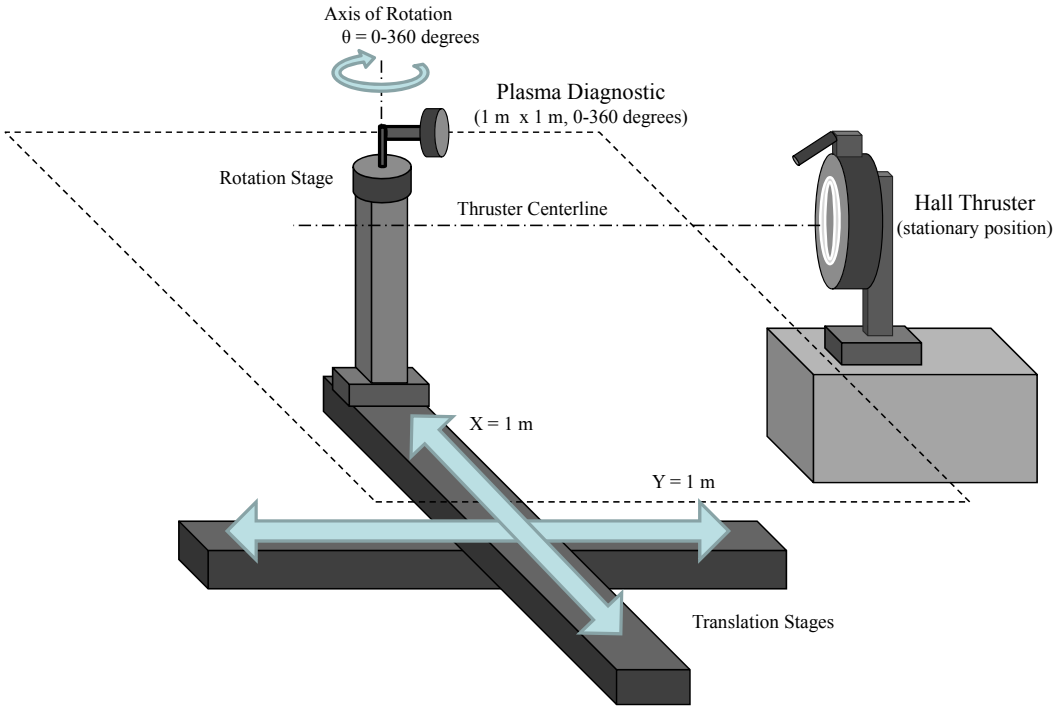

Figure 3-8 Diagnostic positioning system in Chamber 3 with X,Y,θ-coordinate axis control.

Translation in the X-Y coordinate axes was achieved with Aerotech ATS62100 Linear stages using NEMA 34 brushless servomotor drive systems. Diagnostic angular orientation using the θ–axis was controlled with an Aerotech ADRS mechanical-bearing rotary stage. The X-Y-θ stages were each connected to an NCDrive20 Amplifier, which were connected via FireWire (IEEE-1394) to the workstation. Position was managed with Aerotech A3200 Motion Control software.

3.2 Laboratory Hall Effect Thruster

Investigations of low discharge voltage operation in Chamber 3 were conducted with a nominal 6-kW Hall thruster, shown in Figure 3-9 and 3-10. The laboratory model was developed at AFRL in collaboration with JPL and the University of Michigan to serve as a standardized test-bed for research of Hall thruster physics. This 6-kW thruster model has similarities to the P5 and NASA173M thruster designs, and has been characterized at AFRL, PEPL, and JPL.[61,63,73,85,86,87,88]

The magnetic circuit consists of eight outer electromagnets, one inner electromagnet, and an internal trim coil for fine-tuning the magnetic field within the boron nitride (BN) discharge channel. A large channel diameter enabled the placement of a centrally mounted, high-current LaB6 hollow cathode designed by JPL. Auxiliary flow line 1 injected xenon flow through the thruster backplate and around the cathode keeper. This additional flow is utilized to inject a fraction of the cathode neutral flow into the near-cathode region. The schematic in Figure 3-11 illustrates the internal cathode configuration and auxiliary propellant flow injection.

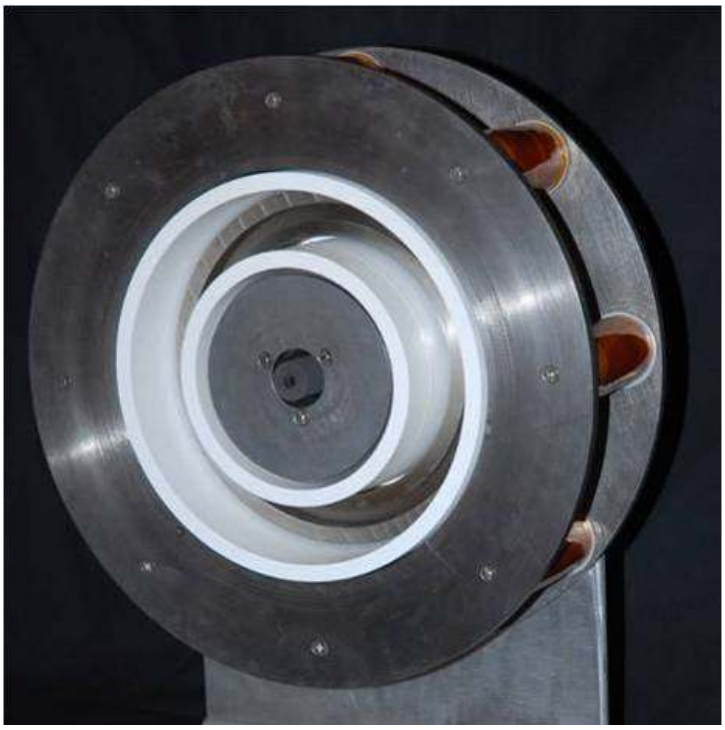

Figure 3-9 **Photograph of the 6-kW laboratory Hall thruster with a centrally mounted LaB6 hollow cathode.**

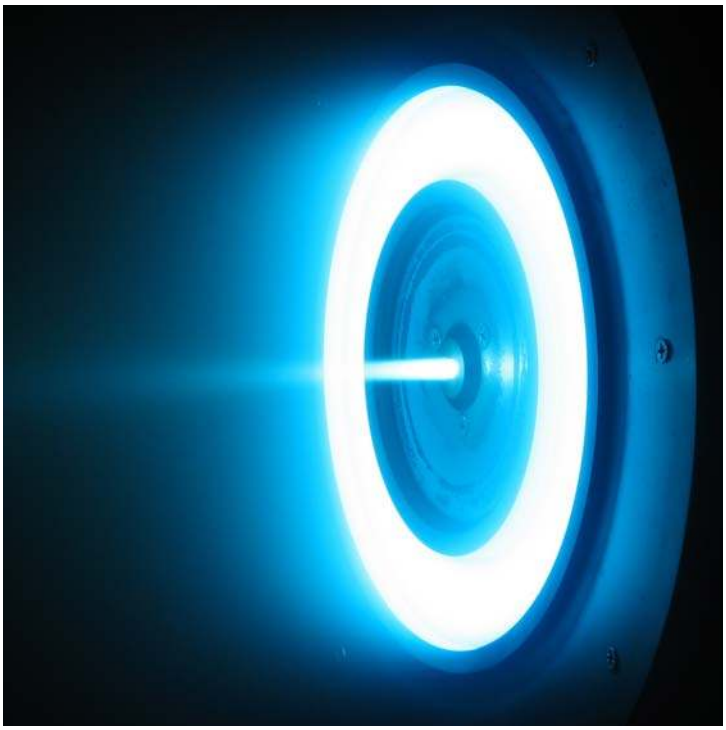

Figure 3-10 **Photograph of the 6-kW laboratory Hall thruster (courtesy of JPL).**

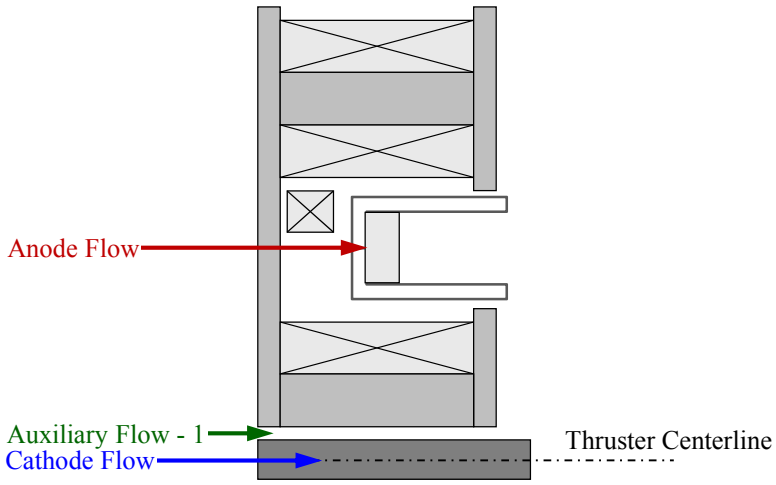

Figure 3-11 **Schematic of the 6-kW laboratory model Hall thruster illustrating locations of propellant injection at the anode, cathode, and auxiliary port.**

3.3 Performance and Plume Diagnostics

Prior to experimental measurements, the Hall thruster was run for approximately 3 hours after the initial chamber pump down to allow the system to reach thermal equilibrium. Subsequent thruster warm-up firings were conducted for 1 hour prior to experimental measurements to provide time for the system to out-gas and minimize drift in thrust measurements due to heating of the null coil.

3.3.1 Inverted Pendulum Thrust Stand

Thrust measurements were taken with a null-type, inverted pendulum thrust stand based on the NASA GRC design.[89] In Figure 3-12, the thruster is shown mounted to the thrust stand. The thrust stand internal wiring was enclosed within a copper shroud. Variation in the coil response due to thermal drift was minimized with coolant lines flowing diluted Glycol solution at 10º C. The thruster center of mass was balanced above

the inverted pendulum thrust stand mount, such that the thruster freely oscillated with minimal friction when the thrust stand electronics were off.

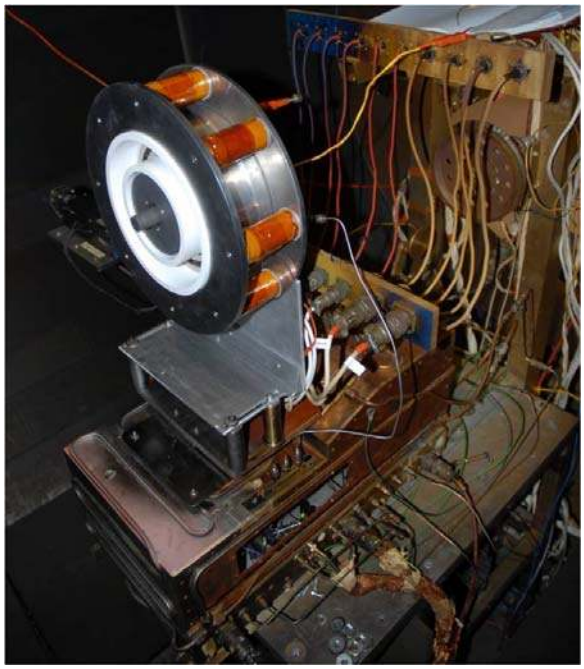

Figure 3-12 Photograph of a 6-kW Hall thruster mounted on the inverted pendulum thrust stand at AFRL/RZSS.

The null type thrust stand utilizes a PID controller with null coil feedback to maintain stationary thruster position. Thrust stand calibration was conducted with a set of five known weights in a pulley system assembly, and the null coil response was correlated to the exerted force. As the thrust stand and thruster reached thermal equilibrium, the calibration curves showed repeatability with less than 1% variation. The zero offset was recorded after each test point and used with the calibration slope to calculate thrust. Thrust stand calibrations were performed in several configurations to test the influence of electromagnet coils and cathode operation. Repeated tests showed consistent thruster performance to within 1%, signifying that the calibrations and zero

offsets were unaffected by these variables. In cases where the thrust stand was not calibrated after each operating condition, the zero position was found for each point in time based on a linear interpolation of the zero offset before firing and after shutdown. Inclination was managed with a stepper motor to balance the null coil response current around zero for the thruster on and off conditions. This minimized thermal drift in the null coil signal after shutdown and yielded a more reliable zero offset. At steady state conditions, thrust measurements varied by less than 0.5 mN. Due to the highly repeatable thrust measurements and minimal thermal drift, the overall uncertainty in thrust is conservatively estimated at ±2%.

3.3.2 Langmuir Probe

The Langmuir probe is an electrostatic diagnostic developed by Irving Langmuir in 1924.[90] In its simplest form, the Langmuir probe enables evaluation of several plasma properties based on the collected current response of a single electrode to an applied bias voltage. Local plasma potential, electron number density, and electron temperature may be discerned from the I-V characteristic over the range of probe ion saturation to the electron saturation regime.

When a large, negative bias potential is applied, electrons are repelled from the probe and all collected current is from ions. As the probe bias voltage is gradually increased, the floating potential may be determined when a balance between ion and electron current results in zero net probe current. Further increasing the probe bias voltage repels slow electrons while higher energy electrons overcome the sheath and generate a positive flow of current to the electrode. The local plasma potential is

distinguished as an inflection point, or "knee" in the I-V characteristic. Probe bias voltage greater than the plasma potential leads to transition to the electron saturation region, where nearly all electrons are collected by the probe and the sheath expands. Although the electrostatic theory of Langmuir probe operation is straightforward, the implementation and analysis is complicated by several factors, including sheath effects and perturbation of the local plasma under examination.

Langmuir probes are generally categorized according to shape and number of electrodes. Probe geometries range from spherical, planar, and cylindrical in nature with one to four or more electrodes. Multiple electrodes typically decrease plasma perturbation due to lower bias voltages at the expense of increased probe size and decreased spatial resolution. Analysis of the I-V characteristic is dependent on the length scales of plasma Debye length, Knudsen number, and probe geometry. The Knudsen number (K_n), defined in Eq. (3-2), is a dimensionless parameter characterizing particle collisions in the probe sheath. If the electron-neutral mean free path (λ_{mfp}) is greater than the probe radius (r_p) and the Knudsen number is greater than unity, the probe is in a collisionless regime. A Knudsen number less than unity corresponds to a continuum plasma and the probe is in a collisional regime.

$$K_n = \frac{\lambda_{mfp}}{r_p} \tag{3-2}$$

The size of the plasma sheath surrounding the probe is proportional to the electron Debye length (λ_D), defined in Eq. (3-3). The probe is in the "thick" sheath regime when the ratio of probe radius to Debye length is less than ~3. A "thin" sheath analysis is applicable for probe radius to Debye length greater than approximately ~10. The

transitional region between the "thick" and "thin" sheath regimes may be analyzed using the iterative Laframboise method.[91]

$$\lambda_D = 743\left(\frac{T_e}{n_e}\right)^{1/2} \tag{3-3}$$

The probes in this study are in the collisionless, thick sheath regime, often referred to as "orbital motion limited (OML)". A more detailed description of Langmuir probe theory and analysis is provided elsewhere in the literature.[92,93,94]

A single, cylindrical Langmuir probe was used to measure plasma potential near the RPA in order to accurately evaluate the far-field average ion acceleration potential. The Langmuir probe consisted of a 0.5 mm diameter, 10 mm length tungsten wire protruding from a 3.2 mm (1/8 inch) diameter alumina tube. Bias voltage relative to facility ground was applied to the wire electrode by a Keithley 2400 Sourcemeter and recorded with LabView on a data acquisition computer.

The single Langmuir probe was mounted to a diagnostic array and aligned toward the measurement axis of rotation shown in Figure 3-7. The electrode was positioned 1 meter downstream of the thruster exit plane, approximately 3-cm to the side of the RPA. Prior studies concluded the far-field plasma potential varies by only a few volts across large angles.[95] Due to the proximity of the Langmuir probe to the RPA, the difference in plasma potential between the Langmuir probe location and the RPA on the thruster centerline was estimated at less than one volt.

Plasma potential was estimated based on curve fitting to the "knee" in the measured I-V characteristic curve and also using the peak in the first derivative of collected current as a function of bias voltage. Both techniques are illustrated in Figure

3-13 for the 105-V, 20-mg/s thruster operating condition located 1 meter downstream of the exit plane on thruster centerline. The two methods differed in measured plasma potential by less than 2 V for all cases. The overall uncertainty in measured plasma potential at the RPA location was estimated at ±3 V, which includes error in data analysis and variation due to the Langmuir probe distance from the RPA.

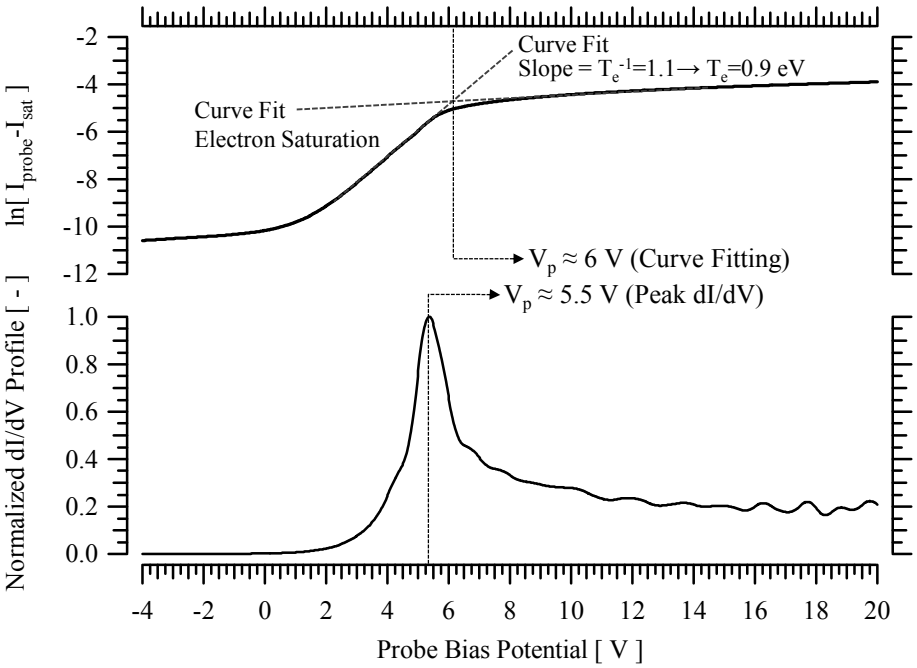

Figure 3-13 Langmuir probe trace comparing data analysis techniques used to determine plasma potential. The measurement was taken on thruster centerline 1-meter downstream of the 6-kW HET operating at 105-V, 20-mg/s in Chamber 3.

3.3.3 Retarding Potential Analyzer

A retarding potential analyzer (RPA) measured the ion voltage distribution by controlling the minimum ion energy per charge to a collector with a series of positively and negatively biased grids. Probe construction is illustrated in Figure 3-14 and is based on the gridded energy analyzer design described by Hutchinson. [96]

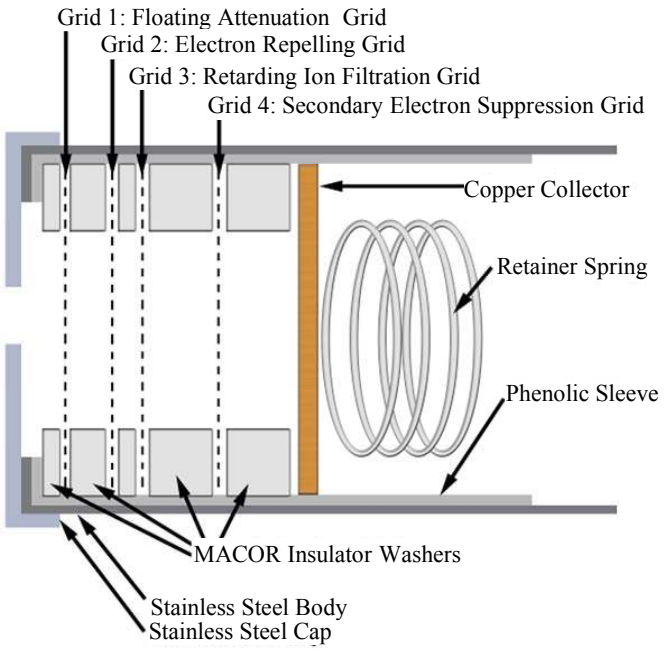

Figure 3-14 Cross-sectional illustration of the RPA showing the multi-grid design and particle filtration process.

The retarding grids filter ambient electrons and selected ions before they reach the copper collector of the RPA. The outer grid (Grid 1) exposed to the plume is floating to minimize the perturbation between the probe and ambient plasma. Grid 1 also provides additional attenuation of the plasma, which leads to reduced number density and increases the internal probe Debye length.[96] Grids 2 and 4 are biased to -30 V below thruster ground. Grid 2 repels electrons from the plume while Grid 4 suppresses secondary electrons from ion impacts with the upstream grids from reaching the collector. Grid 4 also minimizes SEE yield from high energy ion impacts with the copper collector. Positive potential applied to the ion retarding grid (Grid 3) generates a high pass filter for beam ions, where only ions above the grid threshold voltage reach the collector. The voltage applied to Grid 3 is swept over a specified range, and ion current to the collector is recorded as a function of the applied voltage to the ion repelling grid.

A phenolic sleeve inside the stainless steel body electrically isolates the grids. A stainless steel cap with a 1-cm diameter aperture was attached to the RPA body to reduce the incoming ion flux at high flow rates and avoid current saturation of the collector electronics.

The derivative of the measured I-V characteristic is proportional to the ion energy per charge distribution, shown in Eq. (3-4) for plasma with one ion species such that $I_{probe}=I_j$ and $f(V_{Bias})=f(V_{a,j})$.[96] In a singly-charged plasma, the dI/dV profile is proportional to the ion energy distribution function.

$$\frac{dI_{probe}}{dV_{Bias}} = \frac{dI_j}{dV_{a,j}} = -\left(\frac{A_C \mathcal{F}^2}{\mathcal{N}_A \mathcal{M}}\right) Z_j^2 \, n_j \, f(V_{a,j}) \tag{3-4}$$

In a Hall thruster discharge with multiple ion species, the magnitude of each ion species voltage distribution function is scaled differently depending on the species number density and Z_j^2. The magnitude of dI/dV in RPA traces is also complicated by the unknown open area fraction of the bias grids (A_c). Therefore, the absolute current density in the plume and corresponding distribution function magnitude are difficult to resolve, and complicate quantitative comparison of the collected current between different measurement locations, thruster operating conditions, and RPA designs. One approach to determine the open area fraction is to scale the current collected by the RPA with the local Faraday probe current density measurement.[97]

Although the distribution function magnitude has significant uncertainty, the location of the peak in the ion voltage distribution is a high fidelity measurement and repeated traces demonstrated excellent precision. The most probable ion potential in the dI/dV trace may be used to establish a local average ion acceleration potential of all ion

species. A sample RPA trace 1 meter downstream on thruster centerline during nominal 300-V, 20-mg/s thruster operation is shown in Figure 3-15. RPA data was processed in the IGOR Pro software environment. Raw collected current data was fitted with a cubic spline prior to differentiation to reduce signal noise of low bias voltage data points.

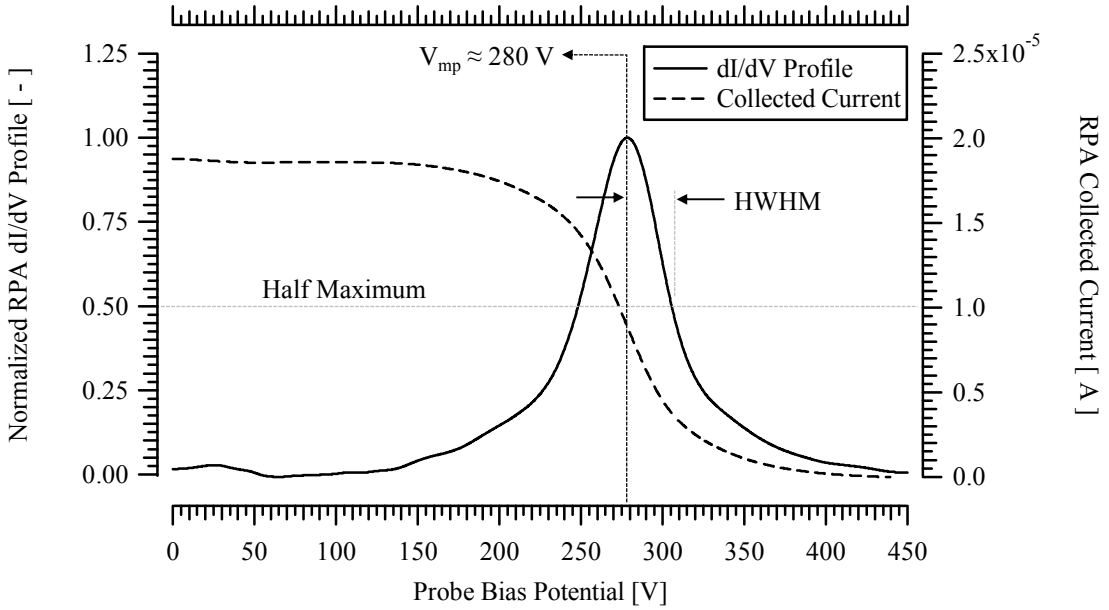

Figure 3-15 RPA trace showing the data analysis technique used to determine the most probable ion potential. The measurement was taken on thruster centerline 1-meter downstream of the 6-kW HET operating at 300-V, 20-mg/s in Chamber 3.

The most probable ion potential (V_{mp}) is corrected by the local plasma potential (V_p) in Eq. (3-5) to calculate the average ion acceleration potential (V_a). Average voltage utilization, defined in Eq. (2-36), is expressed in Eq. (3-6) with respect to RPA and Langmuir probe measurements.

$$V_a = V_{mp} - V_p = V_d - V_{loss} \tag{3-5}$$

$$(1-\beta) = \frac{V_{mp} - V_p}{V_d} = 1 - \frac{V_{loss}}{V_d} \tag{3-6}$$

In Figure 3-16, a potential diagram illustrates the correlation between measured values with the average ion acceleration potential. The dispersion in average ion acceleration potential was primarily due to CEX and elastic collisions in the plume, and variation in the location of propellant ionization with respect to the potential field. Ions with energy to charge ratio greater than the anode potential are created when a multiply-charged ion experiences a charge decreasing collision, thereby decreasing the ion charge state for constant ion kinetic energy.[98] The spread in the distribution is characterized with the half width at half-maximum (HWHM), which typically increased during high discharge voltage thruster operation. In these investigations, the HWHM ranged from 14 V to 23 V during 120-V and 300-V thruster operation, respectively.

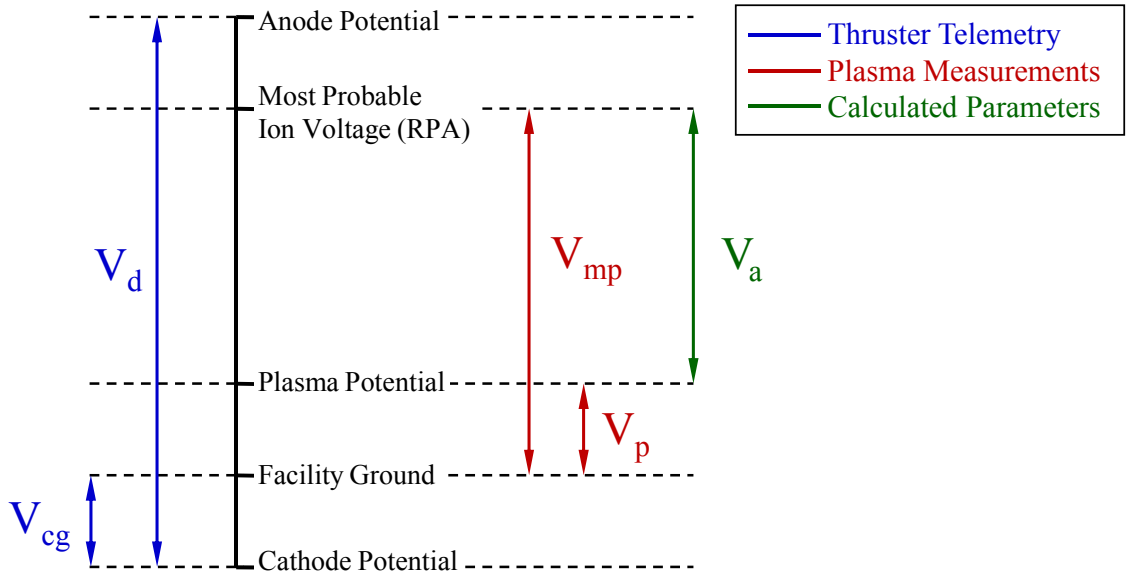

Figure 3-16 Potential diagram illustrating the relationship between measured voltages (V_d, V_{cg}), plume measurements (V_{mp}, V_p) and calculated potentials (V_a).

Retarding grids are composed of a 0.127-mm thick, photochemically etched 316 SS with an open area fraction of approximately 38% and separated by MACOR spacers. Since there are four grids in series, the attenuation is ~2% of the maximum collection area (0.38^4=0.02). Grid spacing is related to the upstream electron temperature and applied grid potential according to Eq. (3-7).

$$\frac{Grid\ Spacing}{\lambda_D} < 4 < \frac{2}{3}\left[\frac{2}{\exp(-1)}\right]^{1/4}\left(\frac{V_{Bias}}{T_e}\right)^{3/4} \tag{3-7}$$

To avoid space-charge limitations, the expression is formed such that the grid spacing between the ion repelling and upstream electron repelling grid is less than $4\lambda_D$.[96] A second function of Grid 1 is to decrease the plasma density upstream of Grid 2, which increases the Debye length and relaxes the separation distance required between Grid 2 and Grid 3 to satisfy the criteria in Eq. (3-7). For estimates of electron temperature in the Hall thruster plume ($T_e \approx 1$ eV), the potential difference between the ion and electron repelling grids must be greater than ~10 V to minimize space-charge limitations. The grid spacing and applied potentials are listed in Table 3-1.

Table 3-1 RPA grid bias potentials and grid separation

	Bias Potential (to facility ground) [V]	Separation [mm]
Grid 1: Floating Grid	Floating	3.35 (Grid 1-2)
Grid 2: Electron Repelling Grid	- 30 V	1.73 (Grid 2-3)
Grid 3: Ion Retarding Grid	0 to $1.5V_d$	6.55 (Grid 3-4)
Grid 4: Secondary Electron Suppression Grid	-30 V	6.55 (Grid 4 – Collector)

Electron repelling Grids 2 and 4 are biased to -30 V below facility ground by a BK Precision 1760 Triple Output DC power supply. The ion retarding grid is connected to a Keithley 2410 1100-V Sourcemeter and swept from 0 to ~500 V with respect to facility ground. During low discharge voltage thruster operation, the maximum sweep voltage was typically 150% of the applied anode potential to minimize time in the plume and avoid damage to the probe. A Keithley 485 Picoammeter recorded the RPA collected current with respect to facility ground. A circuit diagram is shown in Figure 3-17. Data acquisition of the applied ion retarding potential and collected RPA current was controlled on a computer running LabView.

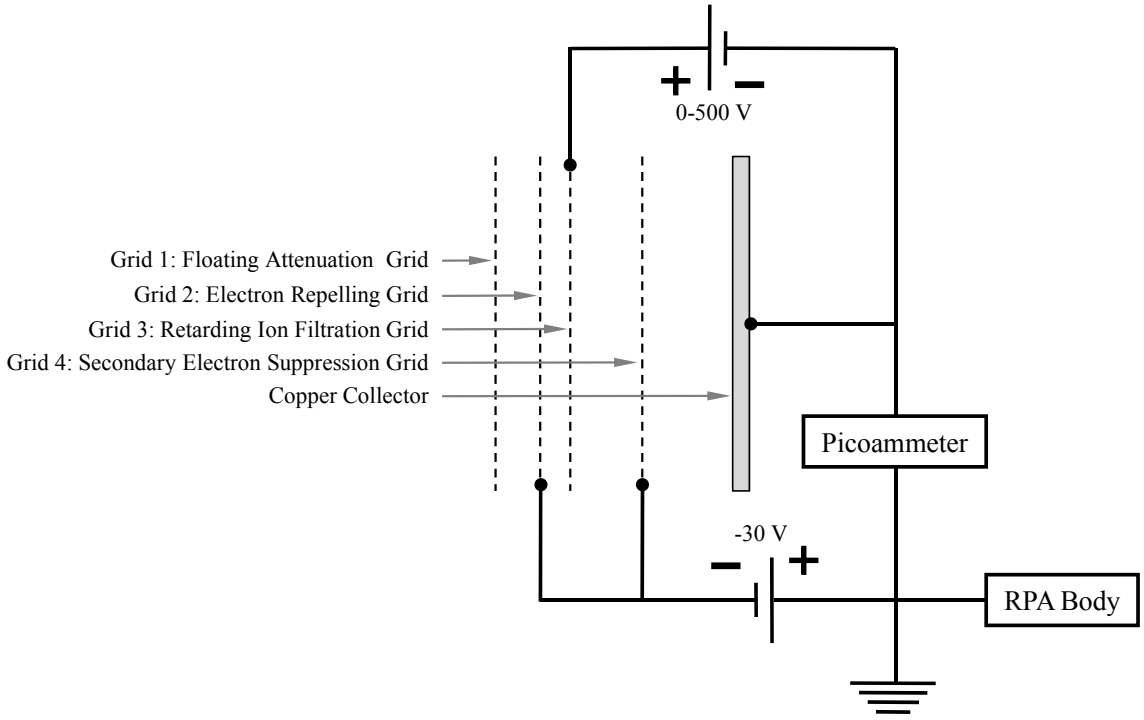

Figure 3-17 Electrical diagram of RPA grid power electronics and DAQ system.

This RPA design has been used extensively throughout the electric propulsion community at various facilities on several thrusters and over a wide throttle range. The ion voltage distribution has previously been compared to an electrostatic energy analyzer,

and exhibited a consistent most probable ion acceleration potential to within 8 V for a several measurements throughout the plume.[99] Measurement uncertainty in the most probable ion acceleration potential is typically estimated as ±10 V. Due to the low thruster discharge voltages studied in this investigation, the uncertainty in RPA most-probable ion potential is estimated as ±50% of the HWHM. This formulation gives rise to the uncertainty of ±11 V during 300-V thruster operation and decreases to approximately ±7 V and ±9 V during 120-V and 150-V operation, respectively. However, the HWHM increases to 28 V during 105-V thruster operation, which may be attributed to a broadening of the overlap between the ionization and acceleration regions within the discharge channel.

3.3.4 ExB Probe

In the ExB probe, perpendicular electric and magnetic fields establish an ion velocity filter and discern the relative ion species composition in the plume. This diagnostic, also known as a Wien filter, was first developed in 1898 to study anode rays by German physicist Wilhelm Carl Werner Otto Fritz Franz Wien.[100] The ion velocity filter is established by balancing the perpendicular electromagnetic forces in the Lorentz force equation, such that there is no net force acting on particles with a select velocity normal to the applied electric and magnetic fields. Ions with an entrance velocity different than the filter pass velocity (u_{ExB}) experience a non-zero drift force and are deflected from the collector. The Lorentz force is set to zero in Eq. (3-8) and the ExB pass speed is expressed in Eq. (3-9) as a function of the applied perpendicular electric and magnetic fields.

$$\vec{F} = \frac{\mathscr{F}}{\mathscr{N}_{\mathrm{A}}} Z(\vec{E} - \vec{u} \times \vec{B}) = 0 \tag{3-8}$$

$$u_{\mathrm{x}} = \frac{E_{\mathrm{y}}}{B_{\mathrm{z}}} = \frac{\mathrm{V_{Bias}} / \mathrm{d_{ExB}}}{\mathrm{B_{ExB}}} = u_{ExB} \tag{3-9}$$

where,

$$\begin{aligned} \vec{u} &= (u_{\mathrm{x}}, 0, 0) \\ \vec{E} &= (0, E_{\mathrm{y}}, 0) \\ \vec{B} &= (0, 0, B_{\mathrm{z}}) \end{aligned} \tag{3-10}$$

In many ExB probes, the magnetic field ($\mathrm{B_{ExB}}$) is fixed with permanent magnets and the electric field is varied between two parallel plate electrodes. The ExB probe functions solely as an ion velocity filter, and the measured ion velocity distribution is independent of mass and charge. Hall thruster plumes are typically composed of multiple ion species, where each ion species is created within a narrow region of the discharge channel such that the exit velocity is proportional to the square root of the ion charge state, $Z_j^{1/2}$. In Eq. (3-11), ExB probe ion pass velocity is related to the individual ion species velocity from Eq. (2-18) and the local plasma potential.

$$u_{\mathrm{ExB}} = \mathrm{v}_j + \sqrt{2\, \mathrm{Z}_j\, \mathrm{V_p} \left(\frac{\mathscr{F}}{\mathscr{M}} \right)} = \sqrt{2\, \mathrm{Z}_j \left(\mathrm{V_{a,}}_j + \mathrm{V_p} \right) \left(\frac{\mathscr{F}}{\mathscr{M}} \right)} \tag{3-11}$$

$$\mathrm{V_{Bias}} = \mathrm{B_{ExB}} \mathrm{d_{ExB}} \sqrt{2\, \mathrm{Z}_j \left(\mathrm{V_{a,}}_j + \mathrm{V_p} \right) \left(\frac{\mathscr{F}}{\mathscr{M}} \right)} \tag{3-12}$$

The local plasma potential must be included in this formulation due to the finite ion acceleration between the plasma potential at the inlet orifice and the facility ground used to reference the plate bias potential. Knowledge of the distance between the plates ($\mathrm{d_{ExB}}$) and the fixed magnetic field enables a relationship between the applied electrode

bias voltage (V_{Bias}) and the ion pass velocity as a function of particle species, charge, plasma potential, and the ion acceleration potential.

As opposed to the energy per charge distribution measured by the RPA, each ion species will correspond to individual peaks in the ExB velocity distribution and may be identified based on the respective ion mass and charge state. Ion current to the collector is expressed in Eq. (3-13) and is related to the ion species mass flow rate ($\dot{m}_j$) and ion species number density (n_j). Relationships between ion current fractions, ion mass flow fractions, and ion species number fractions that were described in Chapter 2 are formulated based on this correlation. The secondary electron emission yield term, γ_j, is neglected in this study, since the ExB probe collector assembly includes an electron suppression grid upstream of the collector.

$$I_j = \dot{m}_j Z_j \left(\frac{\mathcal{F}}{\mathcal{M}}\right)(1+\gamma_j) = n_j Z_j v_j A_c \left(\frac{\mathcal{F}}{\mathcal{N}_A}\right)(1+\gamma_j) \tag{3-13}$$

The ExB probe in this investigation was designed and manufactured by Plasma Controls, LLC. A schematic of the diagnostic and the ion filtration scheme is shown in Figure 3-18. In the Plasma Controls design, the distance between the parallel plate electrodes is 3.1 mm and the magnetic flux density is 0.344 T. The entrance collimator orifice is ~0.4 mm diameter, which provides an acceptance angle of approximately ±0.3°. The ExB probe was aligned in the plume using the X-Y-θ positioning system described in Section 3.1.2.3.

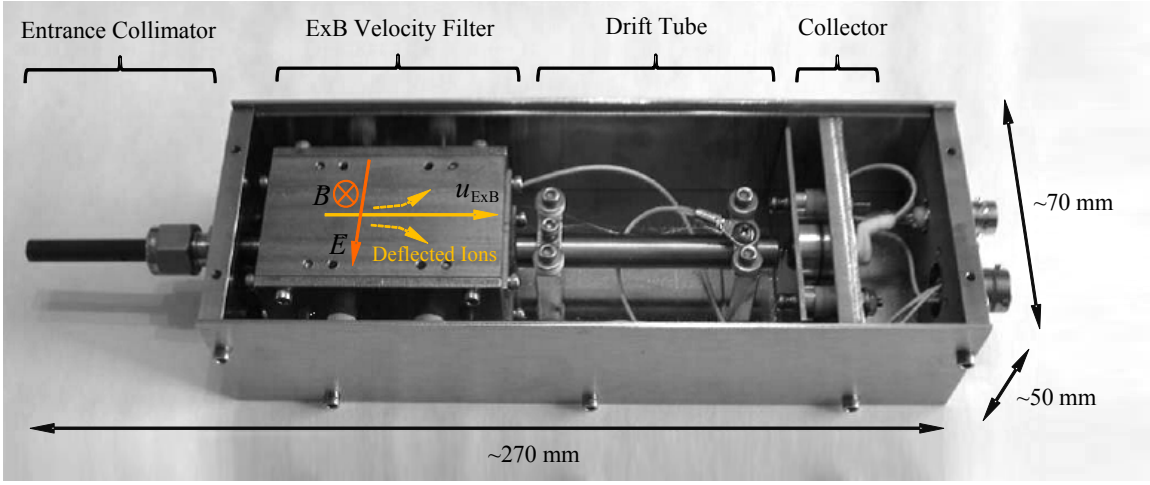

Figure 3-18 Photograph of the ExB probe build by Plasma Controls, LLC. The top cover is removed to illustrate the electromagnetic fields in ion velocity filter and regions of ion collimation, drift, and collection.

The ExB bias parallel plates were connected to a Keithley 2410 1100-V Sourcemeter and swept from 0 to ~50 V with respect to the probe body and facility ground. During low discharge voltage thruster operation, the maximum sweep voltage was set based on the expected probe bias potential required to measure Xe^{+3} ions. An electrical schematic is shown in Figure 3-19. A secondary electron suppression grid was biased to -30 V below thruster ground with a BK Precision 1760 Triple Output DC power supply. A Keithley 6485 Picoammeter recorded the collected current with respect to facility ground, with Average and Median filters enabled. Data acquisition was controlled on a computer running LabView, and voltage sweeps took several minutes each due to the signal averaging. No post-processing or smoothing was required.

Due to the extremely narrow acceptance angle, the signal strength was extremely sensitive to probe alignment during off-axis measurements. Aligning the probe for maximum signal strength during 300-V thruster operation did not correspond to the orientation for maximum signal strength during lower voltage operation. The optimum

probe alignment varied by as much as 3° between operating conditions, and was attributed to the changes in the location of ion acceleration. Although the signal magnitude was affected, the relative velocity distribution was constant and the ion current fractions were insensitive to this effect.

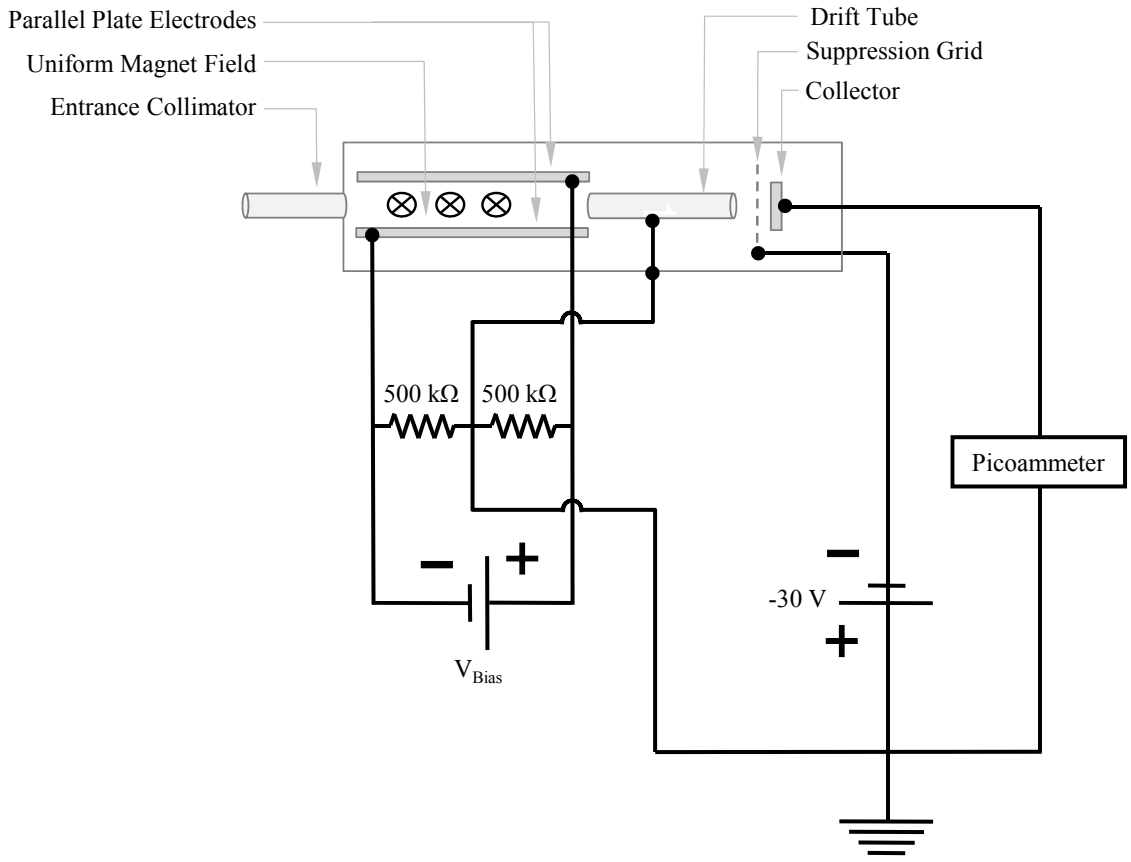

Figure 3-19 Electrical diagram of ExB probe power electronics and DAQ system.

Systematic studies of ExB probe spectra at various downstream distances and angles concluded that a single-point measurement on channel centerline provided an accurate assessment of the ion composition in the plume compared to a multipoint spatial map. [87,101] Due to the off-axis measurement sensitivity to probe orientation in this study, ExB probe measurements were conducted on channel centerline at several downstream

distances. In Figure 3-20, normalized ExB probe spectra are shown at 1.3-m on channel centerline during 300-V, 20-mg/s thruster operation. The ion velocity distributions showed excellent precision, and species current fractions were determined using the method of triangle fitting. A methodical comparison of various ExB analysis techniques by Shastry[101] demonstrated the method of triangle fitting captured the effects of peak width on the calculated ion species composition in accord with more complicated curve-fitting procedures.

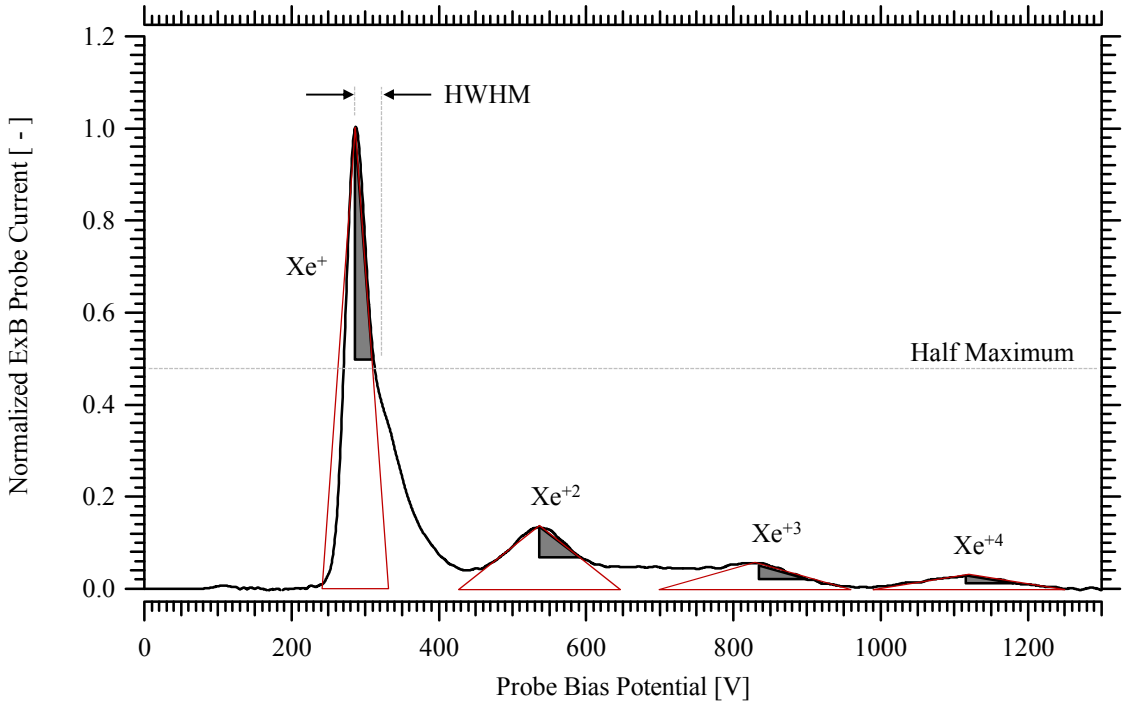

Figure 3-20 Normalized ExB probe trace showing the data analysis technique used to determine ion species fractions. The measurement was taken on thruster centerline 1.3 meters downstream of the 6-kW HET operating at 300-V, 20-mg/s in Chamber 3.

The method of triangle fitting is based on the approximation that the area under the curve of each ion species is proportional to the triangle formed by the peak height and the HWHM. Results using this approach were consistent with numerical integration of a

small subset of the data in this investigation, which further validated the technique. All ion species current fractions in this investigation are reported based on this analysis.

Uncertainty in ExB probe measurements are attributed to several factors, including: (1) equipment error in the power supply source voltage and current measured by the picoammeter, (2) uncertainty due to resolution of the ion velocity filter, (3) uncertainty in the probe calibration factors, (4) uncertainty in measured current due to pressure build-up within the probe, and (5) beam attenuation due to CEX collisions. Measurement uncertainty in the ion pass velocity will be discussed first, followed by uncertainty due to CEX collisions in the plume, and uncertainty in the collected current.

The ion pass velocity and measured energy distribution is a function of the ion velocity filter. The probe was calibrated by Plasma Controls with an 8-cm ion source with argon propellant, and the magnetic field was calculated as B_{ExB}=0.344±.005 T. The distance between the parallel plates were measured at AFRL as d_{ExB}=3.26±0.1 mm. The product of these terms based on measurements at AFRL and the calibration at Plasma Controls agreed to within 2%.

The range of plate electrode bias potential over which an ion may reach the collector is a function of probe geometry and ion energy. This resolution is estimated as ~1% of the ion acceleration potential ($0.01V_d$) using the approach developed by Kim[67], and is independent of ion mass or charge. Decreased probe resolution during high discharge voltage operation corresponded to an increase in the velocity range of ions capable of reaching the collector, which increased the peak collected current for a given ExB probe bias potential. This effect increased the signal magnitude, but is not expected to drastically change the energy distribution or relative species current fractions.

Based on the probe calibration uncertainty (±2%), probe resolution (±1%), and the manufacturer specified uncertainty in the Keithley 2410 (±0.03%), the overall uncertainty in ion pass voltage is ±4%. Normalized ExB energy distributions of several thruster operating conditions were plotted as a function of Xe^+ acceleration potential, and the Xe^+ peaks were consistent with energy per charge distributions measured using the RPA. While the ExB spectra provided information about the individual ion acceleration potential, the RPA is a more robust measurement and is used to calculate the global voltage utilization described in Chapter 2.

Beam attenuation due to CEX collisions is accounted for using a simplified model that has been shown to accurately modify the ion species current fractions for symmetric reactions between beam ions and a uniform background neutral density.[101] The CEX attenuation is calculated for a given ion species as shown in Eq. (3-14) and the respective CEX collision cross sections are listed in Eq. (3-15) through (3-17).

$$\left(\frac{I_{probe}[R]}{I_{probe}[R=0]}\right)_j = \exp\left(-n_o \sigma_j Z_j\right) \tag{3-14}$$

$$\sigma_1 = 87.3 - 13.6\log(V_d) \tag{3-15}$$

$$\sigma_2 = 45.73 - 8.9\log(2V_d) \tag{3-16}$$

$$\sigma_3 = 16.9 - 3.0\log(3V_d) \tag{3-17}$$

The model was stated to work best when the product of background pressure (in 10^{-5} torr) and downstream measurement distance (in meters) was ≤ 2. In this dissertation, the maximum ExB probe measurement was taken 1.3-m downstream of channel centerline and the maximum background pressure was 1.5×10^{-5} torr. The criterion

(1.3x1.5 < 2) was satisfied for ExB probe measurements at all thruster operating conditions. The measurement uncertainty of background pressure is ±20%, and inserting this range of uncertainty into the estimation of beam attenuation varied the current fraction calculations of Xe^{+1}, Xe^{+2}, and Xe^{+3} by approximately ±0.02, ±0.01, and ±0.005, respectively.

Figure 3-21 shows ExB probe traces from 1.0 to 1.3-m downstream of channel centerline for 150-V, 20-mg/s and 300-V, 10-mg/s operation. Variations in ion composition revealed the Xe^{+1} current fraction increased with downstream distance. Accounting for CEX beam attenuation reduced this effect on the ion current populations to less than 1%.

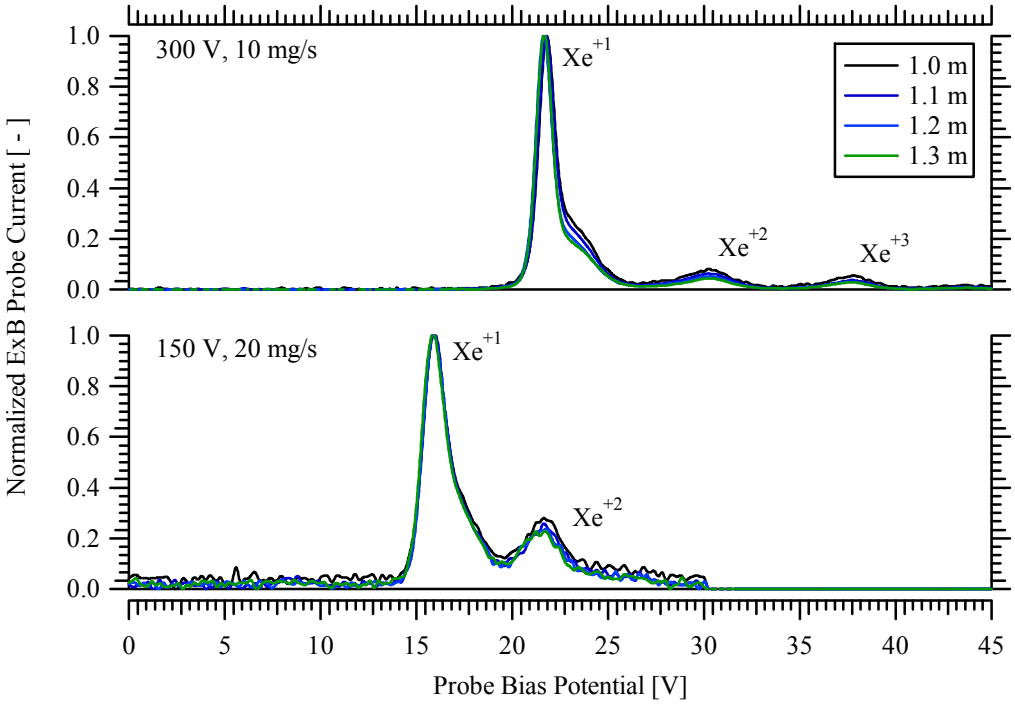

Figure 3-21 Normalized ExB probe traces on thruster centerline from 1.0-m to 1.3-m downstream of the 6-kW HET operating at 300-V, 10-mg/s and 150-V, 20-mg/s in Chamber 3.

Uncertainty in the collected current by the picoammeter was ~0.2% in the 2-nA to 2-A range, as specified by the manufacturer. As previously specified, uncertainty in collected current due to collector SEE was negligible due to the electron suppression grid.

Pressure build-up within the probe was characterized by repeated measurements in the plume. Iterative measurements during low-voltage thruster operation showed negligible variation between traces, and particle interactions within the probe due to increased internal pressure were considered negligible. Higher voltage thruster operation showed minimal changes after extended time in the plume. The variation manifested as a linear increase in the minimum collected current with time, and was an easily recognizable effect. This appeared to be related to discharge voltage as opposed to chamber background pressure or thruster mass flow rate, and was attributed to heating of the permanent magnet.

To account for possible variations in the permanent magnet properties and minimize uncertainty, higher power thruster operating conditions were conducted at the end of a testing cycle. In addition, the probe was repositioned outside of the beam at the first sign of thermal drift to allow the heat to dissipate for at least 12 hours. A graphite box was built to shield the probe body from direct plume impingement and minimize heating. Comparing a large set of measurements that exhibited negligible thermal drift for each high-power thruster operating condition resulted in consistent profiles and species current fractions. Thus, the overall effect of magnet heating and internal pressure on reported ion energy distributions should be minor.

The overall uncertainty in Xe^{+1}, Xe^{+2}, and Xe^{+3} current fractions is approximately ±4%, ±20%, and ±50%, respectively. These uncertainties are correlated, since the sum of

the current fractions is defined as unity. See Appendix A for a description of the propagation of current fraction uncertainty in calculations of charge utilization and average ion charge.

3.3.5 Faraday Probes

Faraday probes measure the ion beam current to a negatively biased surface. Equal bias potential is applied to the collector and guard ring to create a flat, uniform sheath across the collector surface that repels electrons. The geometric probe collection area is used to calculate current density throughout the plume, which may be integrated to determine the total ion beam current and plume divergence. Faraday probe measurements are prone to facility effects that cause increased current collection on the wings and may introduce significant error. Two Faraday probes are described in the following sections. The first is a conventional nude Faraday probe for far-field measurements in Chamber 3. The second probe was developed with adaptable geometry to study Faraday probe design and facility effects in Chamber 1. Measurement uncertainty and data analysis techniques accounting for probe design and facility effects will be discussed in Chapter 4.

3.3.5.1 Nude Faraday Probe

The far-field nude Faraday probe is a conventional design that has been used extensively for studies in Chamber 3 at AFRL. The Faraday probe electrical circuit and geometric dimensions are shown in Figure 3-22.

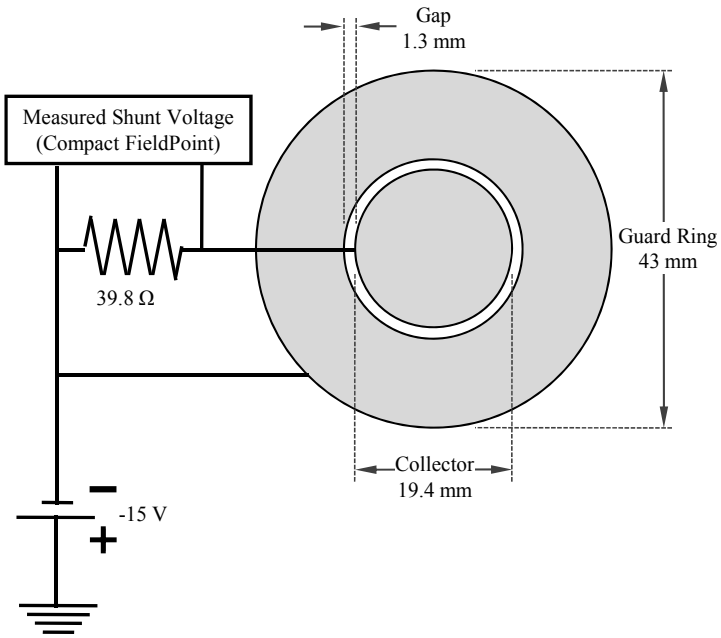

Figure 3-22 Electrical diagram of the nude Faraday probe power electronics and DAQ system.

The probe consists of a 19 mm outer diameter molybdenum collector electrode bordered by a 43 mm outer diameter annular guard ring. The collector to guard ring gap is 1.3 mm, which is typically designed to measure less than 10 Debye lengths in order to minimize electric field fringing effects above the collector electrode.[102] Bias potential to the collector and guard ring is fixed at -15 V below facility ground. Ion beam current to the collector was measured across a 39.8 ohm shunt resistor with a manufacturer specified uncertainty of ±0.5%. Measured voltage across the shunt resistor was recorded with the Compact FieldPoint system and data acquisition was controlled through LabView.

The nude Faraday probe was mounted to a diagnostic array and scanned at a constant 1-meter radius from θ=0° to 180° using the rotational arm shown in Figure 3-6. Ion beam current and the axial component of ion beam current are calculated for a hemispherical, axisymmetric plume about thruster centerline in Eq. (3-18) and (3-19). In

Chapter 4, it will be shown that the effective ion collection area is not equal to the geometric cross-sectional collector area.

$$I_{Beam} = 2\pi R^2 \int_0^{\pi/2} \frac{I_{probe}[\theta]}{A_{Effective}} \sin(\theta) d\theta \tag{3-18}$$

$$I_{Axial} = 2\pi R^2 \int_0^{\pi/2} \frac{I_{probe}[\theta]}{A_{Effective}} \cos(\theta)\sin(\theta) d\theta \tag{3-19}$$

In Eq. (3-18) and (3-19), the measured current densities from each side of the plume (0° to 90° and 90° to 180°) are integrated, and the reported beam currents are the average of the two sides. Repeated scans show excellent precision.

3.3.5.2 Nested Faraday Probe

A Faraday probe with three concentric rings was designed and fabricated to assess the effect of gap width and probe geometry in a systematic study of the Hall thruster plume. The nested Faraday probe consisted of two concentric collector rings and an outer guard ring, which enabled simultaneous current density measurements on the inner and outer collector. Two versions of the outer collector, also referred to as Collector 2, were fabricated to create gaps of 0.5-mm and 1.5-mm between the rings. For either version of Collector 2, the gap between Collector 1 and Collector 2 is always the same as the gap between Collector 2 and the guard ring. The collectors and guard ring are seated within a boron nitride shell and are different heights to form a highly concentric probe with uniform gap width, as illustrated in the diagram in Figure 3-23. Probe dimensions are listed in Table 3-2.

Table 3-2 Nested Faraday probe dimensions

	Collector 1	Collector 2		Guard Ring
		0.5 mm Gap	1.5 mm Gap	
Inner Diameter [mm]	-	7.06	9.16	20.27
Outer Diameter [mm]	6.11	18.91	17.06	29.93
Height [mm]	15.58	13.75	13.76	10.22
Collector 1 – 2 Gap [mm]	-	0.48	1.53	-
Collector 2 – Guard Ring Gap [mm]	-	0.68	1.61	-

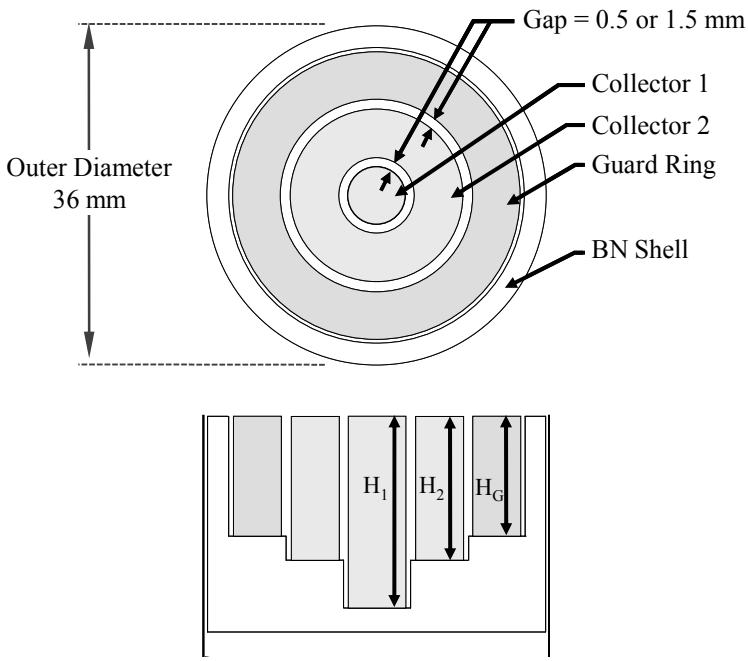

Figure 3-23 Top-view and cross-sectional diagrams of the AFRL nested Faraday probe.

Past experimental estimates of the electron temperature and ion number density in the plume of the low-power Hall thruster ion source studied in Chapter 4 indicated the Debye length ranged from 0.05 mm to ~1 mm throughout the plume from 20 cm to 50 cm downstream of the exit plane. Thus, the 0.5 mm gap configuration is less than or equal to

10 Debye lengths for all locations studied with the nested Faraday probe. The 1.5 mm gap configuration is greater than 10 Debye lengths, and is oversized to highlight effects of a gap width greater than the $10\lambda_D$ design criteria.

There are four probe collection geometries that may be studied using the nested Faraday probe. These configurations are shown in Figure 3-24 and referred to as:

1. Configuration 1 – Current to Collector 1 with a 0.5 mm gap
2. Configuration 2 – Combined current to Collector 1 and 2 with a 0.5 mm gap
3. Configuration 3 – Current to Collector 1 with a 1.5 mm gap
4. Configuration 4 – Combined current to Collector 1 and 2 with a 1.5 mm gap

For either the 0.5 mm or 1.5 mm gap configuration, the current collected by Collector 1 is compared to the combined current on Collector 1 and Collector 2 (termed Collector 1+2). Adding the collected current isolated effects caused by the inner gap to Collector 1 from effects caused by the outer gap to Collector 1+2. If the collected current were not added, Collector 2 may be influenced by effects between the inner gap (Collector 1 with Collector 2) and the outer gap (Collector 2 with the guard ring). This analysis allowed comparison of simultaneous measurements to different collection cross-sections with the same gap width.

The collectors were machined from arc-cast low-carbon grade 365 molybdenum, and the guard ring is grade 360 molybdenum. Differences in secondary electron emission between the collectors and guard ring due to electrode material and surface roughness should be minimal. Collection surfaces were machined to a standard 32 μ" AA finish.

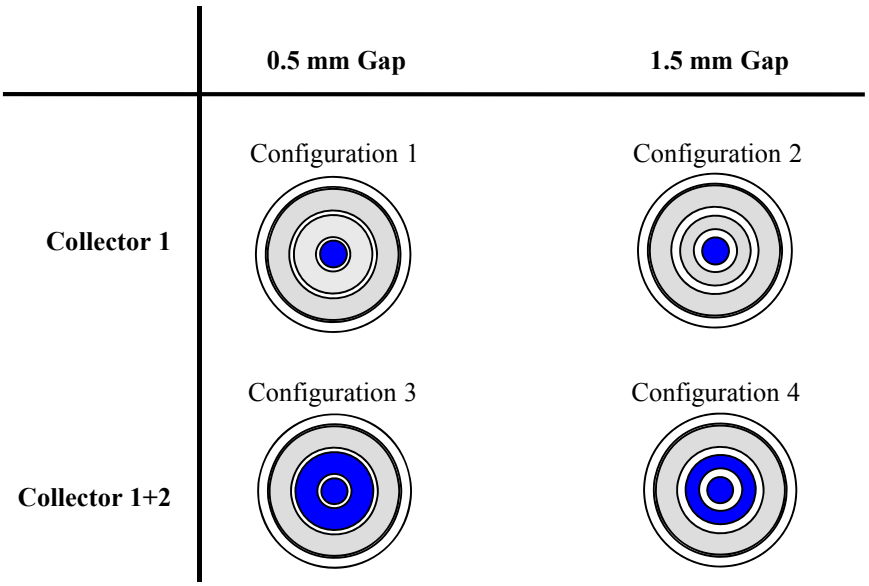

Figure 3-24 **Top view of the four collection area configurations of AFRL nested Faraday probe. Regions of blue are the current collecting surfaces orthogonal to the beam. The gap between Collector 1 and Collector 2 is equal to the gap between Collector 2 and the guard ring.**

A 20-cm long SS tube houses the BN shell and probe leads. This SS housing extends to the probe face and is grounded to create known boundary conditions for probe simulations. Trials with the SS housing allowed to float caused no change in collected current. All subsequent measurements were taken with the SS housing connected to chamber ground. The nested Faraday probe and SS housing are shown in Figure 3-25.

Figure 3-25 **Photograph of the AFRL nested Faraday probe shown in the 0.5 mm gap width configuration.**

Current density in the plume was measured in angular sweeps from 0° to 180° at 8, 12, 16, and 20 thruster diameters downstream of the Hall thruster exit plane using the positioning system described in Section 3.1.1.2. Unless otherwise specified, angular measurements were taken in 2° increments. Current density scans took approximately 6 minutes.

Collected current on both collectors and the guard ring were measured with an Agilent 34970A Data Acquisition / Switch Unit. An Agilent E3631A Triple Output DC power supply was used to bias the collectors and guard ring to the same potential. For measurements with dissimilar bias potentials on the collectors and/or guard ring, an Agilent 6614C DC power supply is used to bias the outermost ring(s). The schematic in Figure 3-26 shows the circuit diagram for the case of equal bias potential on all rings. A comparison of collected current with and without averaging the Agilent 34970A Data Acquisition / Switch Unit resulted in negligible change in collected current traces.

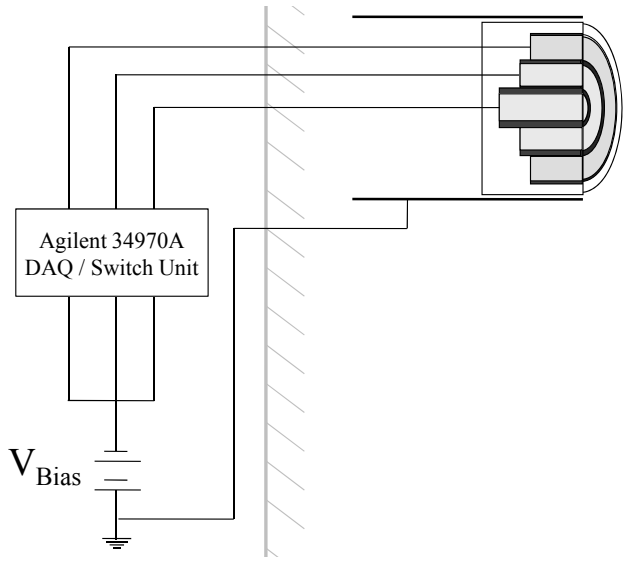

Figure 3-26 Electrical diagram of the nested Faraday probe power electronics and DAQ system.

The nested Faraday probe operation was characterized with variations in probe bias potential over a range of angular positions and downstream distances at several facility background pressures. A sample of the probe characterization is shown in Figures 3-27. A bias potential of -20 V with respect to facility ground was beyond the ion current saturation limit in all cases, and was used for all Faraday probe measurements unless otherwise noted.

The investigation of Faraday probe design, facility effects, and plume expansion in Chapter 4 will show that the uncertainty in the total ion beam current may be conservatively estimated as ±3% and the uncertainty in the axial component of ion beam current may be conservatively estimated as ±5%. These values are significantly less than typically reported, and are due to the plume characterization with facility background pressure, distance, and the thorough characterization of the nested Faraday probe. Uncertainty in the nude Faraday probe measurements conducted in Chamber 3 are estimated as ±10% and ±6% for the axial and total ion beam current, respectively. Although facility effects were well characterized in Chamber 3, the far-field measurements were conducted at a single downstream radius and did not allow for estimation of the plume expansion from CEX collisions with thruster neutrals and external potential field effects.

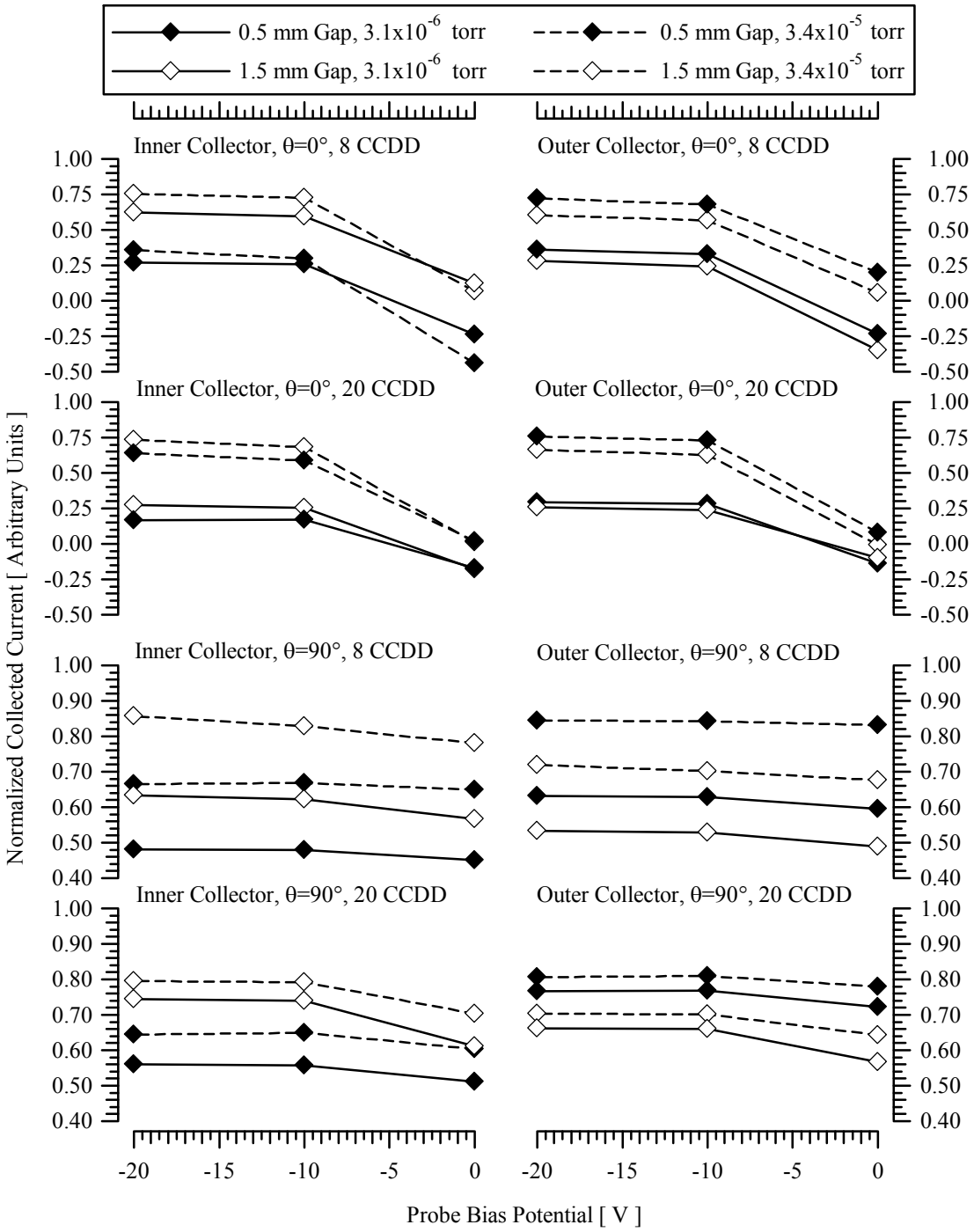

Figure 3-27 **Nested Faraday probe bias voltage characterization of the inner collector (left) and the outer collector (right) for the 0.5 mm and 1.5 mm gap configurations at 3.1×10^{-6} and 3.4×10^{-5} torr. Normalized current is shown at the location of largest Debye length in the plume at θ=0 degrees and the location of smallest Debye length in the plume at θ=90 degrees at 8 CCDD and 20 CCDD.**

3.4 Summary

This chapter described the facilities, diagnostics, and apparatus used to study Faraday probes in Chamber 1 and investigate low discharge voltage phenomena in Chamber 3. A comprehensive study of nude Faraday probes and facility effects on plume expansion is presented in Chapter 4. The results of this study are incorporated into the analysis of low discharge voltage Hall thruster operation and loss mechanisms in Chapter 5 and Chapter 6.

Chapter 4

Evaluation of Faraday Probe Design and Scattering Effects

Accurate measurement of current density in the Hall thruster plume is required to study ion beam divergence and to quantify electron current to the anode. Faraday probe current density measurements are typically used for qualitative evaluation of the plume profile as opposed to quantitative assessment, since calculations of total ion beam current are often greater than the thruster discharge current. In addition, beam divergence is artificially increased with distance from the exit plane due to particle scattering from the central core to the wings of the plume. These over-predictions are exacerbated at high background pressure and large angles from thruster centerline, and are attributed to facility effects that would not be present on-orbit.[103]

This chapter examines three aspects of far-field Faraday probe current density measurements, which include (1) considerations for measuring an axisymmetric, annular geometry as originating from a point source, (2) characterizing the effects of gap width and collector size, and (3) evaluating facility effects over a range of distance and pressure. The overarching goal is to reduce the measurement uncertainty, such that accurate calculations of ion beam current and plume divergence may be incorporated into the efficiency analysis described in Chapter 2. More importantly, the ion current density distributions in this investigation are studied to advance understanding of facility effects

on the Hall thruster plume, and thereby improve comparisons of ground-based experimental measurements with simulations of the on-orbit plume.

4.1 Past Investigations

A number of studies have investigated the effects of elevated background pressure, compared nude Faraday probe designs, and studied design modifications to minimize uncertainty due to CEX collisions in the plume. Manzella and Sankovic[104] found high background pressure increased ion current density on the wings, while the central core remained largely unaffected on measurements of several Hall thruster designs. Discharge current increased linearly with increasing pressure, which was attributed to neutral xenon ingested into the discharge channel. Ingested propellant is ionized and accelerated to create additional ion beam current in the plume and electron current to the anode, thereby increasing discharge current. The escalation of current density at high angles off thruster centerline was due to CEX collisions between fast moving ions and slow moving xenon from the background gas. The resulting slow moving ions are scattered from the central core to the outer wings.

Past investigations at PEPL evaluated Faraday probe design and facility background pressure on collected ion current. A comparison of two nude Faraday probe designs concluded the differences in measured current density were due to probe design and dissimilar secondary electron emission (SEE) properties of the collectors.[102,105] For tests using the P5 Hall thruster at several operating conditions, increasing facility backpressure increased the current density on the wings. The lower current, 4.3-A case showed the current distribution in the central core was unaffected by backpressure,

similar to results by Manzella and Sankovic.[104] However, the higher current 10-A case exhibited minor increases in the central core current density, and was attributed to ionization and acceleration of the background neutrals near the exit plane. These trends are consistent with far-field Faraday probe measurements using the SPT-140.[106]

Plasma potential in the region surrounding a nude Faraday probe has been measured to study the possibility of probe bias voltage acting as a point source potential sink, and thereby attracting low energy CEX ions.[107] Langmuir probe measurements near a nude Faraday probe resulted in potential variations of less than 3 V within 20-mm of the probe. It was concluded that CEX ions had a negligible attraction to the probe bias potential, and the random flux of low energy ions was insufficient to explain the increased current density at high background pressure and large off-axis angles. This conclusion was consistent with computational modeling of the ion flow around an axisymmetric Faraday probe. A hybrid-PIC model simulated the collected current for off-axis conditions present in a low-power HET plume, and found errors due to sheath expansion were minimal. [108]

To mitigate the collection of low energy ions created in CEX collisions, numerous filtering mechanisms have been investigated. One approach is to attach a collimator to the entrance of a nude Faraday probe to filter low energy ions that are created by CEX collisions in the plume.[109,110] Ions created by CEX collisions near the exit plane and directed to the probe are still collected. The CEX ion population resulting from collisions with the anode and cathode thruster neutrals is present on orbit, but CEX collisions with facility neutrals and the ions attributed to entrainment of facility neutral flow may also be collected.

Further efforts utilized a magnetic field to filter low energy CEX ions. A study by Rovey, *et al.*[111] compared results from a magnetically filtered Faraday probe, a boxed Faraday probe, and a nude Faraday probe to separately assess the effect of the magnetic filter and the boxed collimator that houses the filter. Similar to past results, the nude Faraday probe exhibited increased beam current and larger current density on the wings with increasing background pressure. The magnetically filtered and boxed Faraday probes resulted in decreased beam current and diminished current density on the wings with increasing background pressure. The central core measured by all three probes was unaffected by increased chamber pressure. These findings indicate the boxed collimator and magnetic filtering decrease low energy CEX ions collected by the Faraday probe. The downside of these approaches is that they do not selectively filter facility effects from the ionization of thruster neutrals downstream of the primary acceleration zone.

A different method for discerning CEX processes in the plume was demonstrated by de Grys, *et al.*[109] and more recently by Azziz[97], who compared Faraday probe measurements at individual locations in the plume at several background pressures and extrapolated the current density to vacuum conditions. This approach is a more advanced technique to experimentally assess CEX facility effects throughout the plume, and enables a more accurate estimation of the on-orbit ion current density distribution.

Despite extensive study of experimental methods and analytical techniques, Faraday probe measurements continue to be complicated by facility effects. Systematic measurement error will be discussed in Section 4.2 and the study of probe design will incorporate these uncertainties in Section 4.3. A detailed analysis of ion scattering and plume expansion will be discussed in Section 4.4 to evaluate the on-orbit beam properties

and assess measurement uncertainty. In Section 4.5, a summary of recommendations are outlined for high accuracy current density profiles.

4.2 Measurement Coordinate System Effects and Correction Factors

A detailed theoretical examination of the measurement coordinate geometry is necessary to isolate systematic trends due to probe design and facility effects in experimental measurements. This analysis is aimed at resolving the error caused by probe measurements with respect to a point source as opposed to the annular discharge geometry of a HET. The analysis is based on constant measurement radius from the probe axis of rotation as illustrated in Figure 3-7, where current density is integrated in a hemisphere around the point source. In the following axisymmetric analysis, the thruster is modeled as two point ion sources located at the centerline of the discharge channel. Figure 4-1 illustrates the probe angular location with respect to the thruster centerline, and is applicable to the measurement positioning systems in Figures 3-2 and 3-7.

Two geometric corrections will be analyzed in the following sections. The first correction accounts for variations in probe angle with respect to the point sources, which will affect the current collection area. The second correction deals with the differences in distance from the probe face to the two point sources, which will influence the R^2 term in the hemispherical integration of current density in Eq. (3-18) and (3-19). These effects will be combined in a generalized form based on the probe angular position θ, the probe distance from the axis of rotation R, and the channel centerline radius R_{CL}. The ratio of R/R_{CL} is incorporated to simplify the analysis and enable a more direct comparison between large and small thrusters.

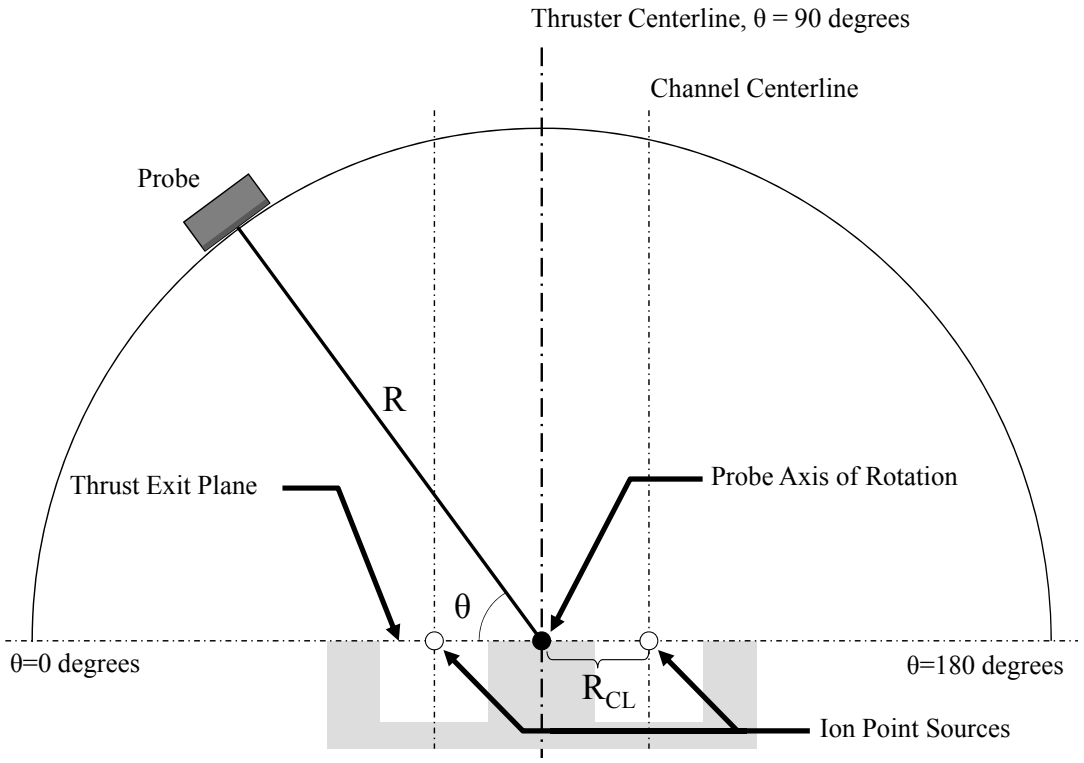

Figure 4-1 Coordinate system for probe distance and angular location with the thruster modeled as two point sources.

4.2.1 Angle of Beam Ions to Probe Face

In a single point source analysis, where the ion point source is located at the probe axis of rotation, the probe face is perpendicular to the source as it is swept in a 180° arc. Modeling the thruster as two point sources changes this probe orientation, and the probe face is only perpendicular to the point sources at 0° and 180°. The ion angle of incidence to the probe face changes with angular position and distance, and decreases the effective probe collection area of beam ions. In addition, the ion angle of incidence at a given location is different for each point source. The angles of incidence are calculated for the left and right point sources as α_L and α_R, and are used to evaluate cosine losses in the probe collection area. Figure 4-2 illustrates the defined angles and distances.

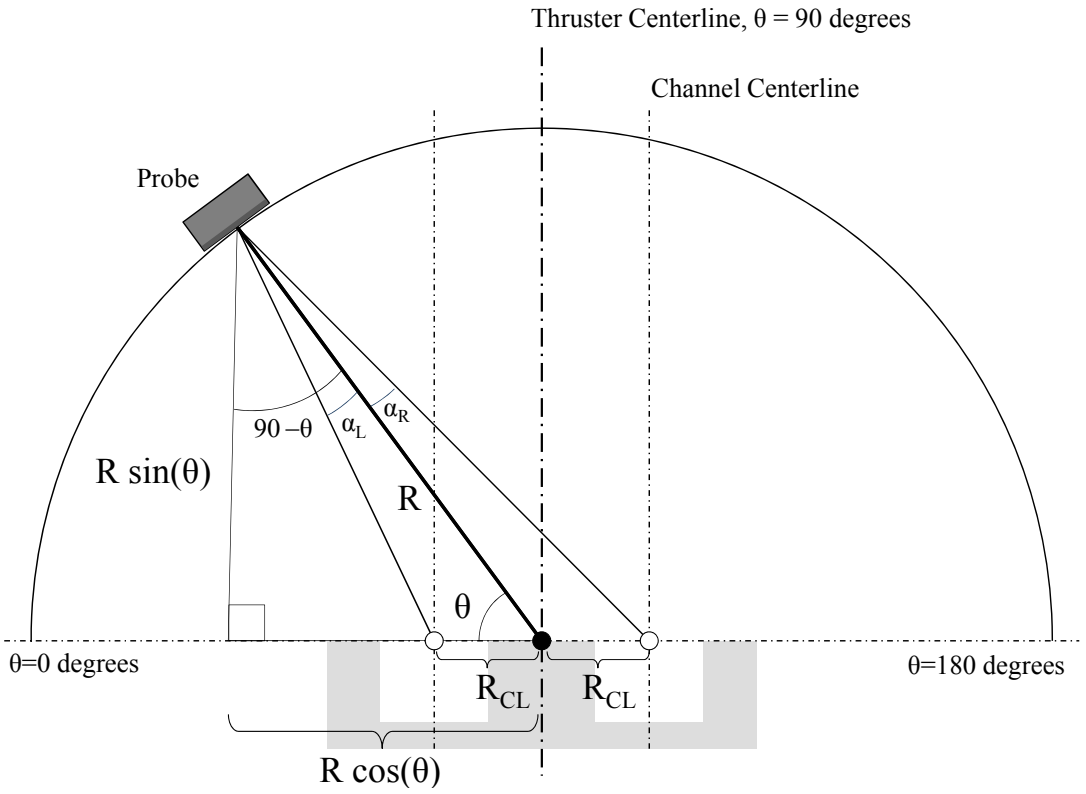

Figure 4-2 Diagram of ion angles of incidence and relevant distances for the probe angular orientation in a two point source system.

The angles α_L and α_R are found using basic trigonometry and are formulated in Eq. (4-1) and (4-2) based on the geometry shown in Figure 4-2.

$$\tan(90-\theta-\alpha_L)=\left(\frac{R\cos(\theta)-R_{CL}}{R\sin(\theta)}\right) \tag{4-1}$$

$$\tan(90-\theta+\alpha_R)=\left(\frac{R\cos(\theta)+R_{CL}}{R\sin(\theta)}\right) \tag{4-2}$$

Solving Eq. (4-1) for α_L and Eq. (4-2) for α_R yields a generalized equation for the left and right angles of incidence in Eq. (4-3).

$$\alpha_{L,R}[\theta,R,R_{CL}]=\pm\left(90-\theta-\tan^{-1}\left(\frac{\cos(\theta)\mp\frac{R_{CL}}{R}}{\sin(\theta)}\right)\right) \tag{4-3}$$

The probe collection area (A_C) is corrected for cosine losses using the average of α_L and α_R in Eq. (4-4). The area correction factor, κ_A, is defined in Eq. (4-5) as a function of θ, R, and R_{CL}.

$$A_C = \pi\left(R_C \cos\left(\frac{\alpha_L + \alpha_R}{2}\right)\right)^2 = \pi {R_C}^2 \kappa_A \tag{4-4}$$

where,

$$\kappa_A[\theta, R, R_{CL}] = \cos^2\left(\frac{\alpha_L + \alpha_R}{2}\right) \tag{4-5}$$

The ion angle of incidence is plotted in Figure 4-3 and the area correction, κ_A, is shown in Figure 4-4 as a function of angular position with contours of constant downstream measurement distance, R/R_{CL}. In Figure 4-3, the ion angle of incidence is largest on thruster centerline, and thus the cross-sectional probe collection area normal to the ion point sources is smallest in that region. Variation in collection area due to ion angle of incidence decreases rapidly with downstream distance, and the approximation of a point source measurement improves.

In Figure 4-5, the value of κ_A on thruster centerline is shown as a function of ($R/2R_{CL}$), which is the commonly reported metric of downstream thruster diameters (channel centerline diameters in this analysis). The correction factor asymptotically approaches unity with downstream measurement distance, and is greater than 99% for distances greater than 5 channel centerline diameters downstream (CCDD).

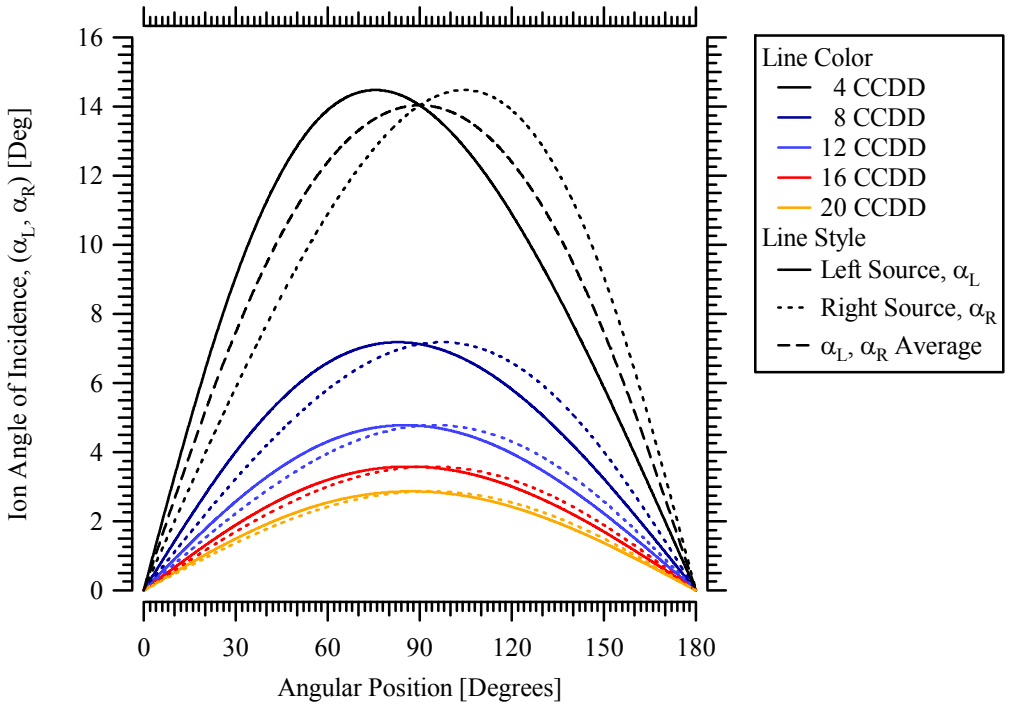

Figure 4-3 **Ion angle of incidence from the left and right point sources as a function of probe angular position with contours of constant $R/2R_{CL}$ = 4, 8, 12, 16, and 20 CCDD.**

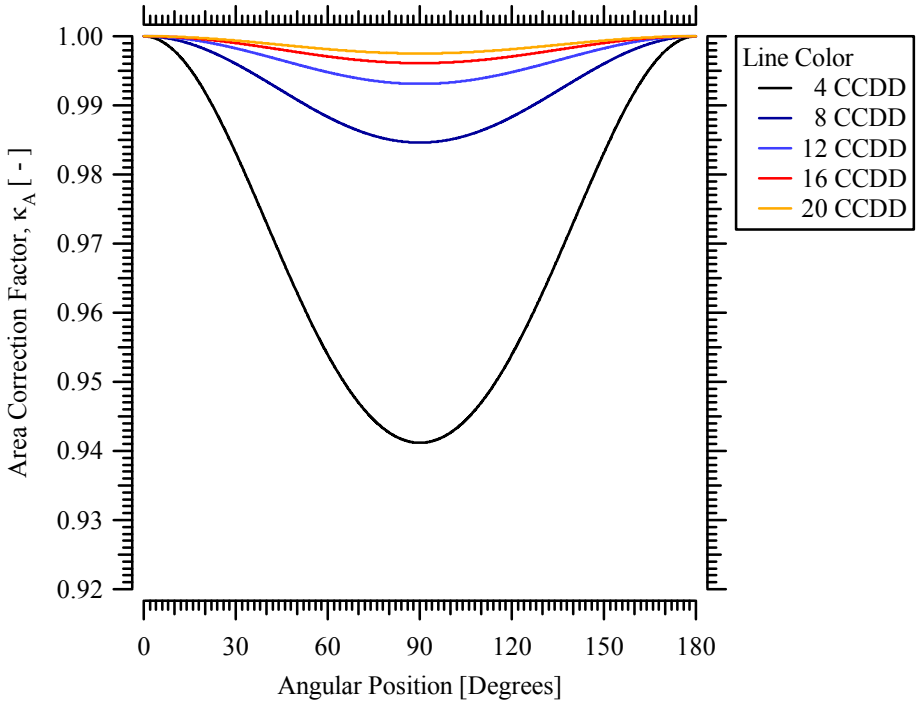

Figure 4-4 **Correction factor, κ_A, accounting for cosine losses in the probe collection area as a function of angular position with contours of constant $R/2R_{CL}$ = 4, 8, 12, 16, and 20 CCDD.**

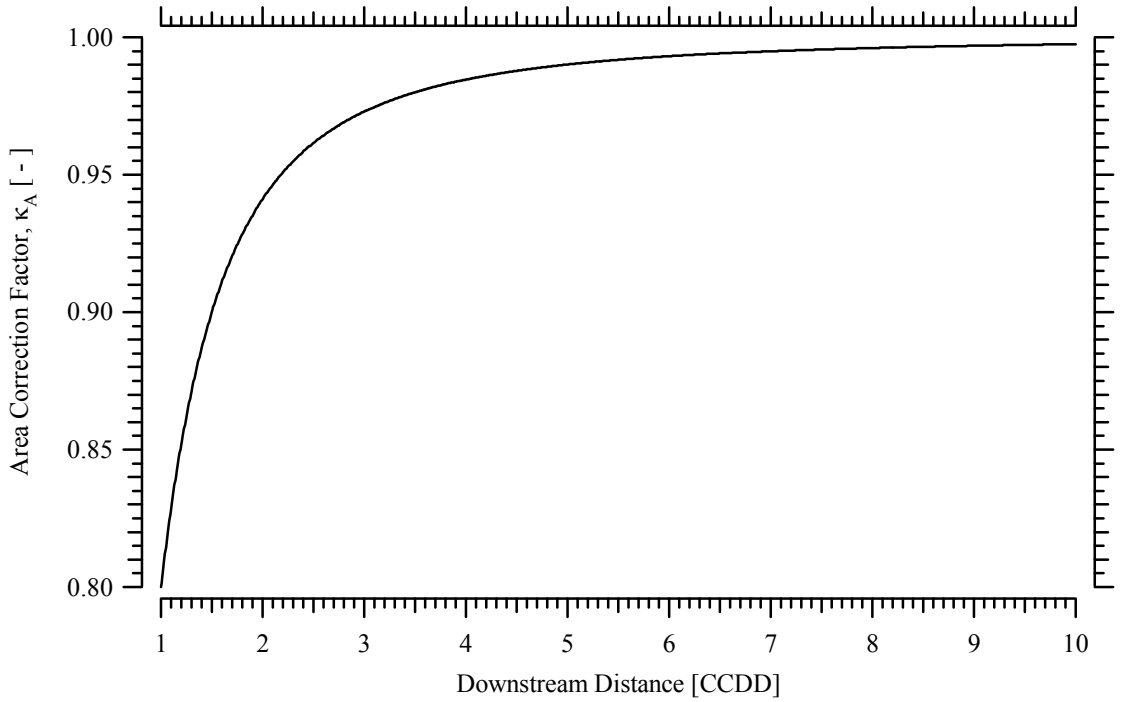

Figure 4-5 Correction factor, κ_A, accounting for cosine losses in the probe collection area on channel centerline (θ=90°) as a function of downstream thruster diameters ($R/2R_{CL}$).

For current density measurements taken in Chamber 1 and reported in the following sections of Chapter 4, the nearest measurement location is greater than 8 channel centerline diameters downstream of the ion source. Thus, the variation in probe collection area due to the angle of the probe face to the two point source ion beam was less than 0.5% for all measurement locations. The fixed measurement radius was approximately 6 CCDD in Chamber 3. It is recommended that the radius of far-field hemispherical measurements be greater than four downstream thruster diameters due to the sharp decline in κ_A when $R/2R_{CL}$ is less than three.

The change in probe collection area is only valid for beam ions originating near the exit plane. Charge exchange collisions downstream of the primary ionization region increase dispersion of ion velocity, and the correction is not relevant to this population.

In addition, the analysis does not account for channel width. This is of lesser concern, since minor variations in channel centerline radius will have a negligible effect on measurements taken beyond four thruster diameters.

4.2.2 Distance of Beam Ions to Probe Face

Differences in path length from the left and right point sources to the probe introduce error in the R^2 term in the axisymmetric plume integration. This effect is illustrated in Figure 4-6 using geometry analogous to Figure 4-2. The probe distances from the left and right point source are characterized as R_L and R_R. Similar to the analysis of ion angle of incidence, the path length will vary with probe angular position and is dissimilar for each point source. The exception is on thruster centerline, where the distance from the probe to each point source is equal and greater than the measurement radius of rotation, R.

The lengths R_L and R_R in Figure 4-6 are calculated with respect to the measurement distance in Eq. (4-6). The distance correction factor, $\kappa_{D,}$ is defined in Eq. (4-7) as a function of θ, R, and R_{CL}.

$$\frac{R_{L,R}[\theta, R, R_{CL}]}{R} = \sqrt{(\sin(\theta))^2 + \left(\cos(\theta) \mp \frac{R_{CL}}{R}\right)^2} \tag{4-6}$$

where,

$$\kappa_D[\theta, R, R_{CL}] = \left(\frac{1}{2}\left(\frac{R_L}{R} + \frac{R_R}{R}\right)\right)^2 \tag{4-7}$$

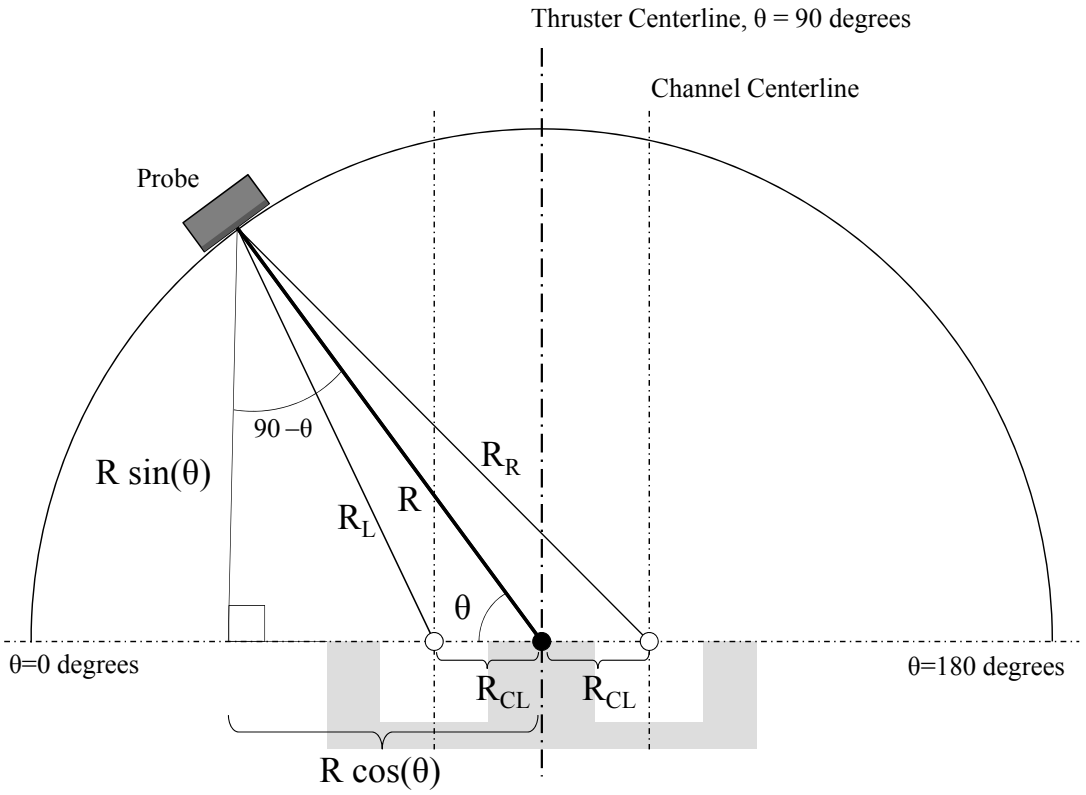

Figure 4-6 Diagram of the relevant angles and distances to characterize probe distance to the left and right ion point sources.

The distance ratios, R_L/R and R_R/R, are plotted in Figure 4-7 with contours of constant downstream distance, $R/2R_{CL}$. While the disparity in distance is greatest on the wings of the plume, the superposition of effects cancels differences from the left and right sides when averaged in the correction factor, κ_D. Conversely, the distance from the probe to the point sources is greater than R within the region of largest current density near thruster centerline, resulting in a net increase in the probe distance. In Figure 4-8, the distance correction factor is illustrated as a function of angular position and highlights the increased probe distance near thruster centerline.

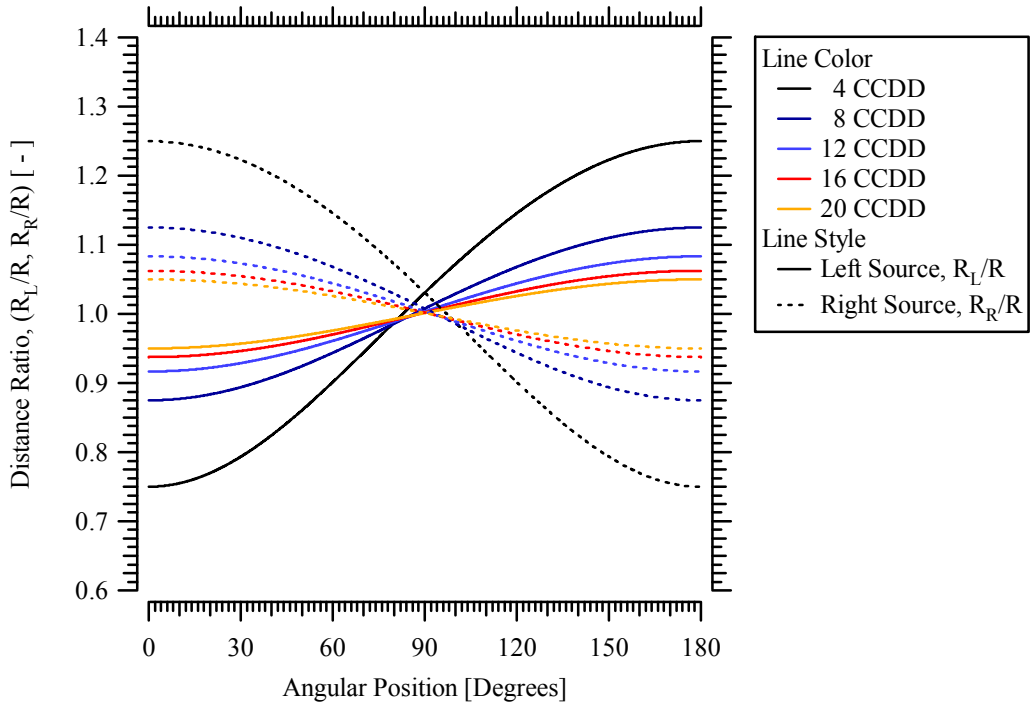

Figure 4-7 **Probe distance from the left and right point sources relative to the measurement radius, R, as a function of probe angular position with contours of constant $R/2R_{CL}$ = 4, 8, 12, 16, and 20 CCDD.**

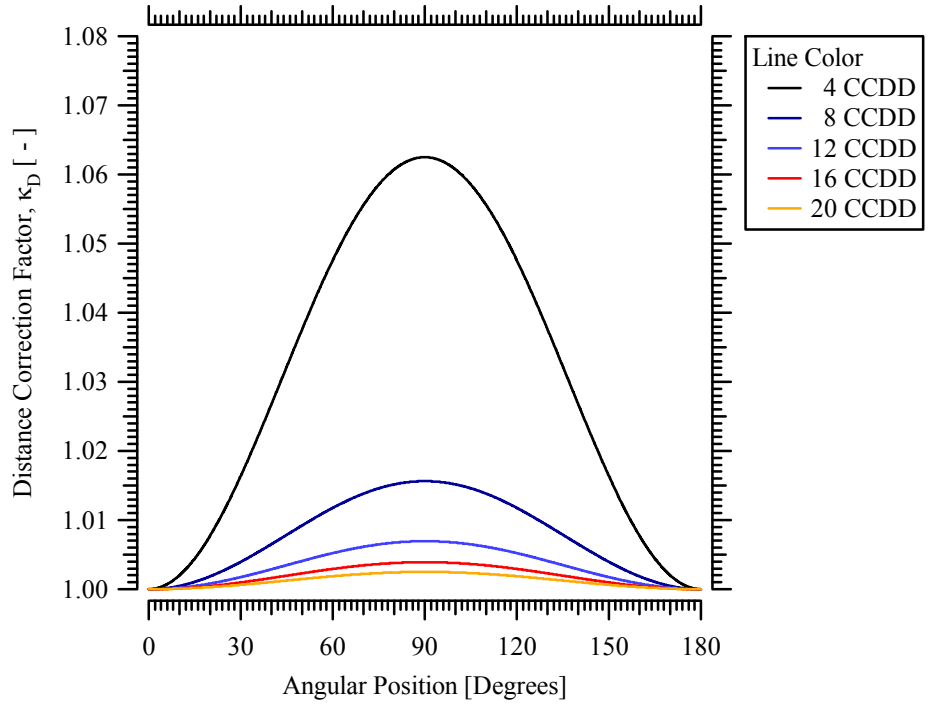

Figure 4-8 **Correction factor, κ_D, accounting for the probe distance to the left and right ion point sources as a function of angular position with contours of constant $R/2R_{CL}$ = 4, 8, 12, 16, and 20 CCDD.**

In Figure 4-9, the distance ratios R_L/R and R_R/R are displayed as a function of downstream thruster diameters at θ=0° and θ=90° for the left and right point sources. This distance ratio asymptotically approaches unity with downstream distance, and is approximately one on thruster centerline by 4 CCDD. Similar to the analysis in Section 4.2.1, the downstream measurement distance should be at least four thruster diameters to reduce these effects to less than 2% on thruster centerline.

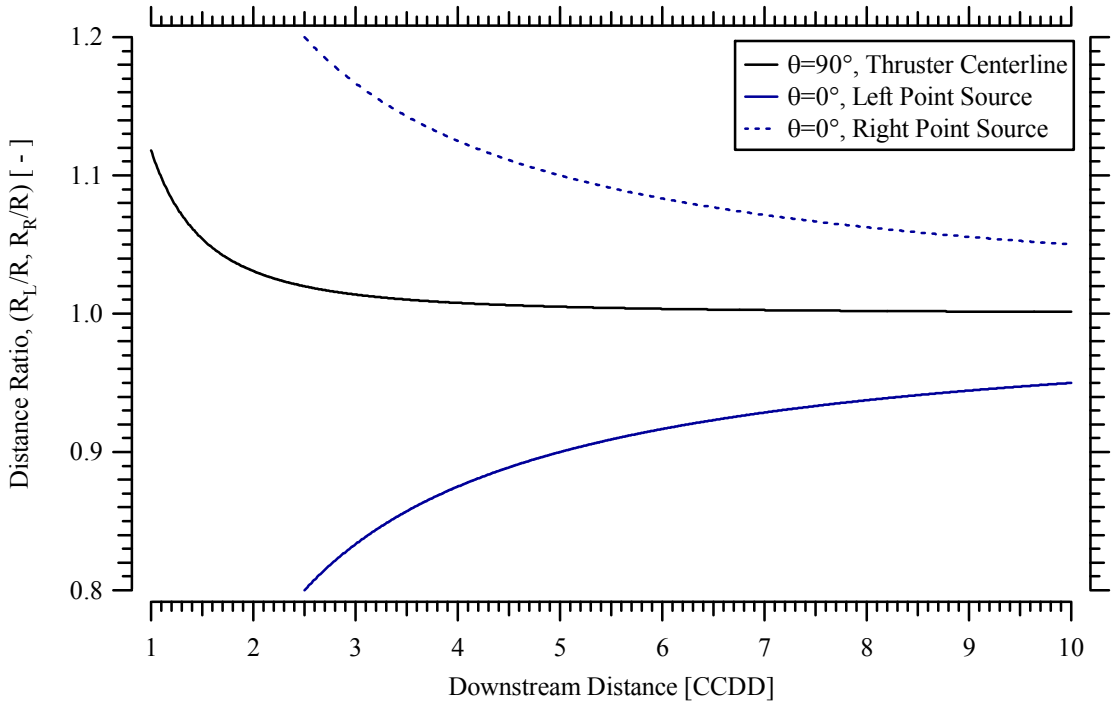

Figure 4-9 **Probe distance from the left and right ion point sources relative to the measurement radius, R, as a function of downstream thruster diameters ($R/2R_{CL}$) at θ=0° and θ=90°.**

4.2.3 Faraday Probe Angle and Distance Correction Factors

The combined effects of the area and distance correction factors are applied to all Faraday probe current density measurements using Eq. (4-8). For a Faraday probe scan at constant measurement radius R, the correction factors are a function of angular position, θ.

$$I_{Beam} = 2\pi R^2 \int_0^{\pi/2} \frac{I[\theta]}{A_C} \left(\frac{\kappa_D[\theta, R, R_{CL}]}{\kappa_A[\theta, R, R_{CL}]} \right) \sin(\theta)\, d\theta \tag{4-8}$$

The spatial correction ratio (κ_D/κ_A) is displayed as a function of probe angular position in Figure 4-10 for constant $R/2R_{CL}$. The overall effect is to increase current density in the central plume core, which will increase the integrated beam current.

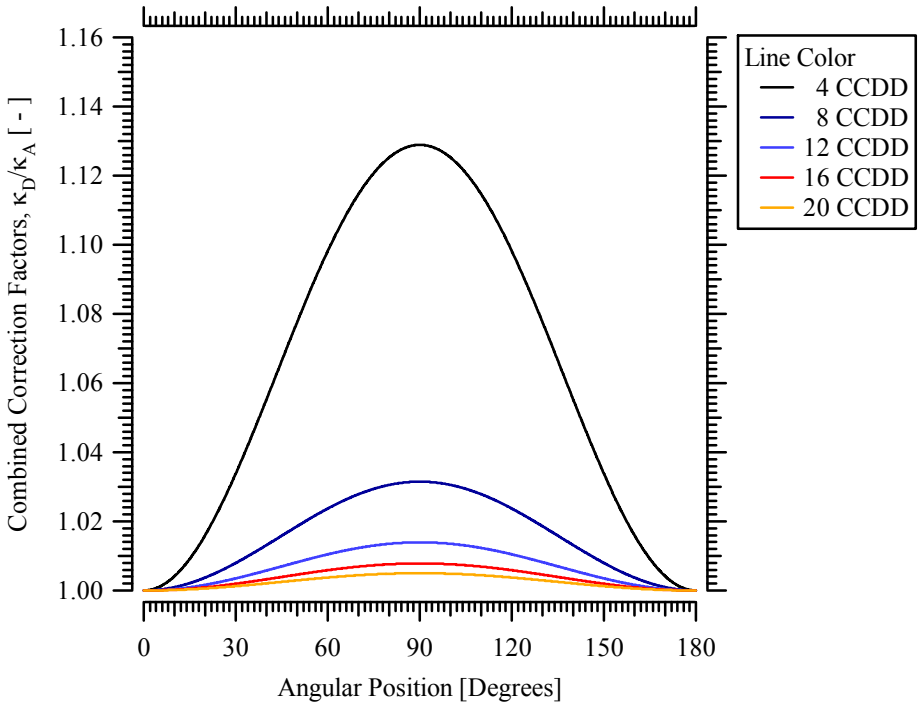

Figure 4-10 Combined effect of correction factors (κ_D/κ_A) accounting for the probe distance and angle with respect to the left and right ion point sources as a function of angular position with contours of constant $R/2R_{CL}$ = 4, 8, 12, 16, and 20 CCDD.

In Figure 4-11, the correction on thruster centerline is shown as a function of downstream thruster diameters. The overall correction accounting for spatial effects will be less than 2% for the analysis of Faraday probes throughout this chapter, since the closest measurement distance was greater than 8 CCDD ($R/R_{CL} \geq 16$). However, current density measurements in Chamber 3 are taken at approximately 6 CCDD, where the centerline correction is ~1.5%. Thus, including the spatial corrections minimizes a systematic source of error introduced from the hemispherical measurement system. All current density traces and beam current calculations in Chapter 4, Chapter 5, and Chapter 6 will incorporate the spatial corrections for ion angle of incidence and measurement distance.

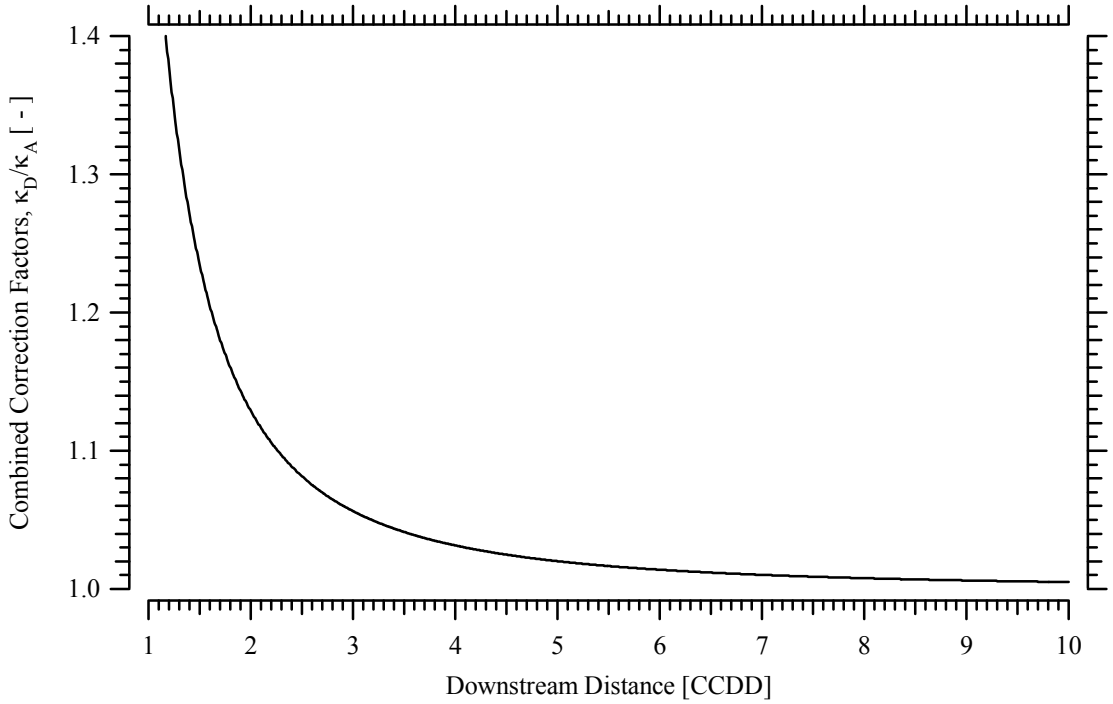

Figure 4-11 Combined effect of the correction factors (κ_D/κ_A) on channel centerline (θ=90°) as a function of downstream thruster diameters ($R/2R_{CL}$).

4.2.4 Additional Spatial Measurement Uncertainty

The preceding analyses accounted for systematic error associated with the measurement coordinate system, and introduced spatial corrections for a two point source model. These corrections quantified and minimized uncertainty due to the hemispherical integration about a point source. However, additional error may be introduced in Faraday probe measurements due to a large probe collection area.

A large collection area will increase the angular span, which results in decreased resolution and may lead to increased measurement error due to gradients in the current density over the probe collection area. The angular spans of the inner and outer nested Faraday probe collectors are listed in Table 2. Configuration 3 had the largest angular span of 2.7° at 8 CCDD. Measurements further downstream had a smaller angular span and the resolution increased. Overall uncertainty due to these effects is expected to be minimal over the small probe collection area of Collector 1.

Table 4-1 Angular span of nested Faraday probe collector configurations

Downstream Thruster Diameters, $R/2R_{CL}$	Collector 1 Angular Span [degrees]	Collector 2 Angular Span [degrees]	
		0.5 mm Gap	1.5 mm Gap
8	0.93	2.72	2.43
12	0.62	1.81	1.62
16	0.47	1.36	1.22
20	0.37	1.09	0.97

4.3 Examination of Faraday Probe Design and Geometry

The nested Faraday probe was developed for parametric investigation of the gap spacing and collection area. The design is described in Section 3.3.5.2, and has two concentric collectors for simultaneous measurements of current density over different size collection areas. The division of collected current between the inner and outer collector was further examined by adjusting the guard ring bias potential for a fixed collector bias potential. Facility effects are quantified and isolated from differences due to probe design by adjusting facility backpressure and measurement distance from the thruster exit plane. A detailed analysis of measurement uncertainty due to facility effects is outlined in Section 4.4. The test matrix facilitated a comprehensive study of Faraday probe design and advanced understanding of ion collection in the plume.

4.3.1 Comparison of Nested Faraday Probe Current Density Profiles

Normalized ion current density profiles of the four collector configurations are shown at 8, 12, 16, and 20 CCDD in Figure 4-12. All profiles are normalized to the peak current density of Configuration 1 at 8 CCDD. The current density measured by Collector 1 was consistently larger than Collector 1+2, and the 1.5 mm gap configurations measured a larger current density than the 0.5 mm gap configurations. These differences were uniform over the entire profile. Configuration 3 measured the maximum current density at a given scan radius, followed by Configurations 1, 4, and 2. This pattern is shown pictorially in Figure 4-12. Although the 1.5 mm gap is larger than 10 Debye lengths and may be expected to cause discrepancies between Configurations 3 and 4, the 0.5 mm gap configurations should measure equivalent current density profiles.

In the 0.5 mm gap configurations, the current density of Configuration 1 (Collector 1) is approximately 10% larger than the current density of Configuration 2 (Collector 1+2).

It should be noted that current density measurements using the 0.5 mm gap were taken separately from the 1.5 mm gap configuration. However, differences in operation of the ion source were minimal, and would not explain the large discrepancies of Configuration 1 compared to Configuration 2. Configuration 2 was the only probe configuration to measure a beam current less than the HET ion source discharge current.

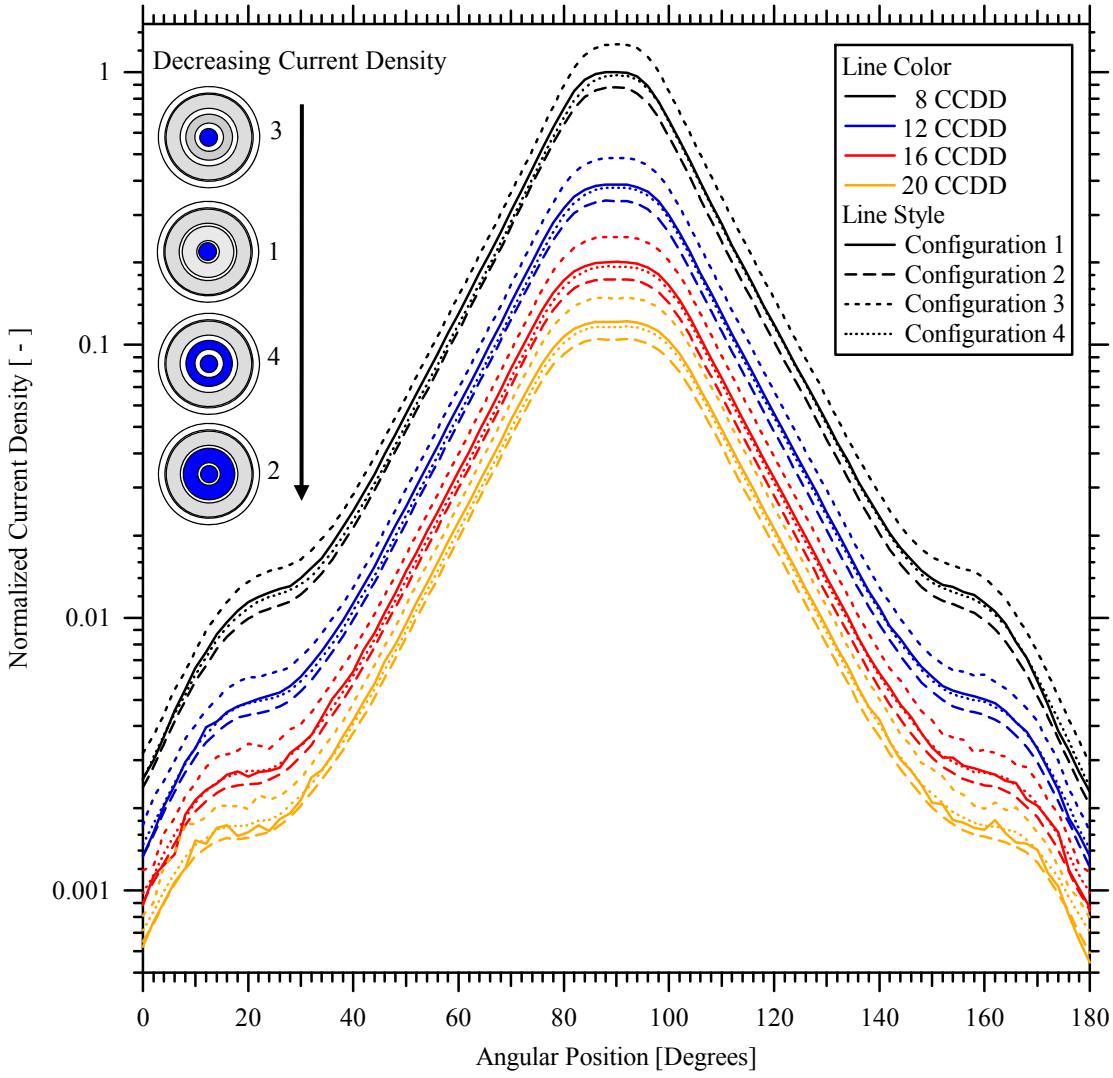

Figure 4-12 Normalized current density profiles from Collector 1 and Collector 1+2 for the 0.5 mm and 1.5 mm gap configurations measured at 8, 12, 16, and 20 CCDD with a facility background pressure of 3.1×10^{-6} torr.

In this investigation of probe geometric effects on collected current, it is assumed the current density is constant across the probe surface. For constant current density, the ratio of the collected current on the inner and outer collectors should be equivalent to the ratio of the current collection areas, as expressed in Eq. (4-9).

$$\frac{I_{C1+C2}[\theta]}{A_{C1+C2}} = \frac{I_{C1}[\theta]}{A_{C1}} \Leftrightarrow \frac{I_{C1+C2}[\theta]}{I_{C1}[\theta]} = \frac{A_{C1+C2}}{A_{C1}} \tag{4-9}$$

Ratios of probe collection area and ratios of collected current are shown for all background pressures and all distances in Figure 4-13. The ratios are calculated based on the collected current or area of the outer collector (Configuration 2 or 4) relative to the inner collector (Configuration 1 or 3). Dashed lines representing the Faraday probe collector area ratios are approximately 15% and 20% greater than the ratios of collected current for the 0.5 mm and 1.5 mm gap configurations, respectively. Fluctuations in the collected ion current ratio increase beyond ±50° from thruster centerline during low background pressure operation. However, ratios of collected ion current are relatively insensitive to variations in distance and pressure in the central core, which indicates the primary difference between current ratios and area ratios is a systematic error associated with the ion collection area. Variations on the wings are attributed to differences in probe resolution and the orders of magnitude decrease in collected current magnitude.

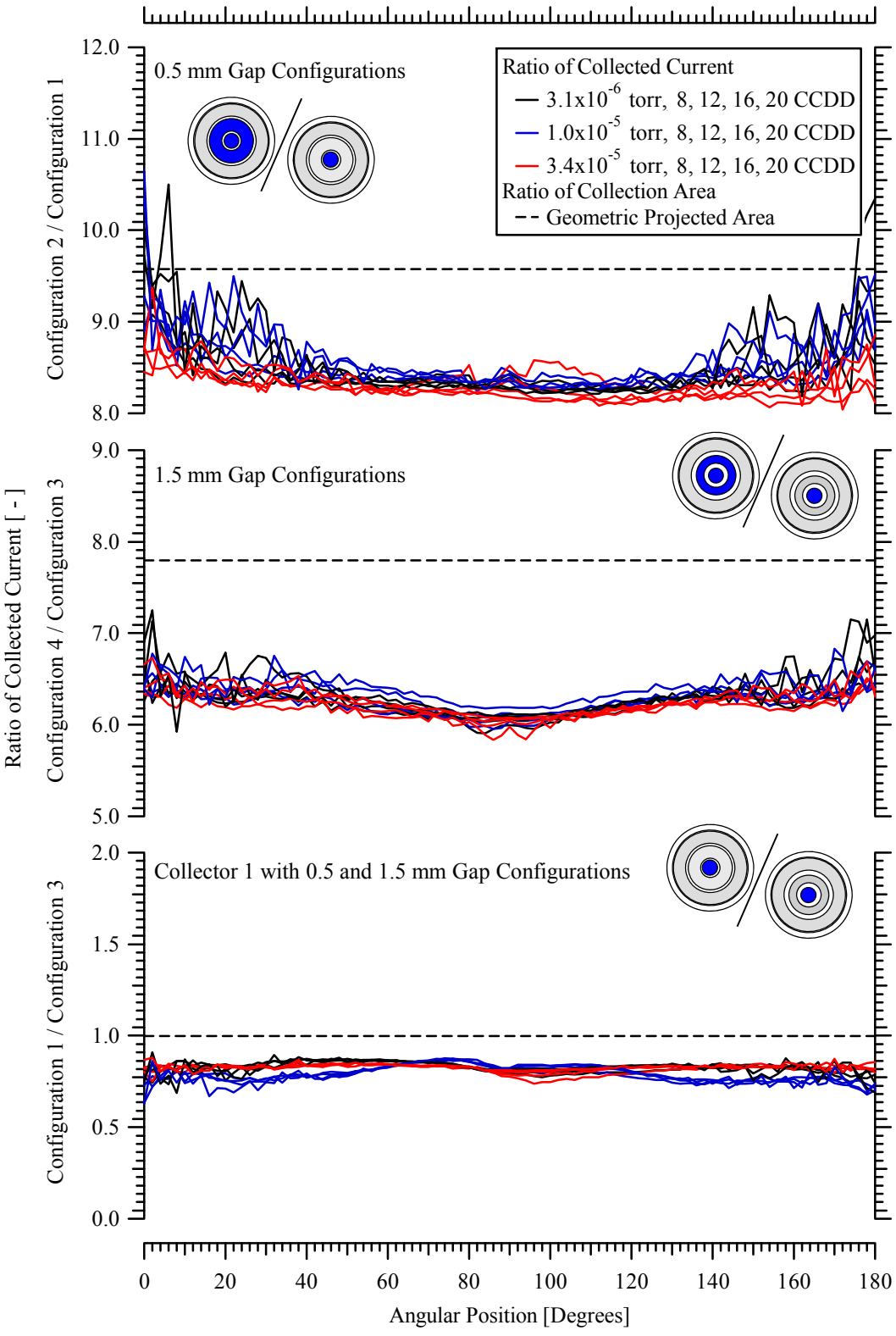

Figure 4-13 **Comparison of collector area ratios and collected current ratios of the 0.5 mm configuration (top), 1.5 mm configuration (middle), and Collector 1 (bottom) at 3.1×10^{-6}, 1.0×10^{-5}, and 3.4×10^{-5} torr measured at 8, 12, 16, and 20 CCDD as a function of probe angular position.**

Several patterns emerge from the comparison in Figure 4-13. The first is that the 1.5 mm gap configuration appears to have a larger systematic error than the 0.5 mm gap configuration. In addition, the ratio of the outer collector area relative to the inner collector area is over-predicted, thereby suggesting that the size of the collector plays a role in this systematic error. The effect of gap width on current to Collector 1 is studied as the ratio of Configuration 1 relative to Configuration 3. While these measurements were performed during different firings of the Hall thruster ion source, the increased gap width corresponds to an increase in the collected current. Identifying and correcting the systematic error will be the focus of the following section.

4.3.2 Gap Correction Factor for the Effective Projected Collection Area

Current density profiles and ratios of collected current compared to ratios of the probe collection area demonstrated that the gap width and probe size have an effect on Faraday probe measurements, and may cause differences of up to 20%. In addition to the trends derived from Figure 4-13, extensive experimental evidence has shown that Faraday probe measurements typically overestimate ion beam current in the Hall thruster plume. This phenomenon is typically attributed to additional ion current from CEX facility effects, but may also be a result of under-predicting the effective probe collection area.

In conventional nude Faraday probe design and analysis, the collection area is calculated as the geometric surface area of the collector ($A_C = \pi R_C^2$). The gap width is typically designed to be less than 5-10 Debye lengths to create a flat, uniform sheath over the collector surface.

One possible mechanism for variation from the geometric probe collection area is ions within the gap between the collector and guard ring. In this hypothesis, high energy beam ions entering the gap volume impact the ceramic base of the nested Faraday probe, and the resulting low energy ions are collected by the walls of the negatively biased electrodes. A fraction of this current is collected on the side walls of the collector, thereby increasing the collected ion current and causing an overestimate of the current density. This effect is shown in Figure 4-14. The orange region illustrates the increase in the projected collection area to account for ion current to the collector side wall.

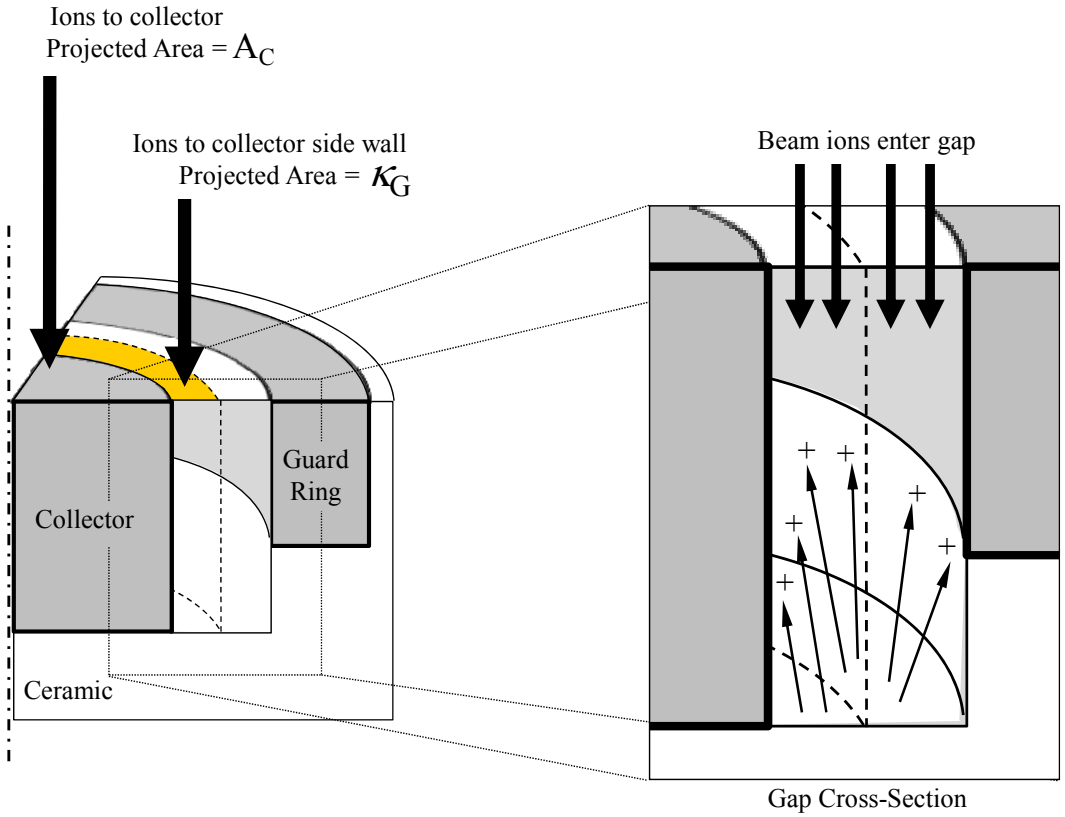

Figure 4-14 Illustration of ions collected by the side walls of the nested Faraday probe and the increase in projected collection area.

To correct for this increase in the effective probe collection area, a Faraday probe gap correction factor, κ_G, was developed to account for differences in collector diameter and gap width. This correction factor partitions the current collected in the gap volume based on the ratio of the side wall surface areas.

The geometric probe collection area is increased according to Eq. (4-10) to account for ions entering the gap volume that are collected by the collector side wall. The gap correction factor, κ_G, is defined in Eq. (4-11) as a function of the probe geometry shown in Figure 4-15.

$$A_{Effective} = \pi R_C^2 + \kappa_G \tag{4-10}$$

$$\kappa_G = A_{Gap}\left(\frac{\overline{A}_C}{\overline{A}_C + \overline{A}_{GR}}\right) = \pi\left(R_{GR}^2 - R_C^2\right)\left(\frac{2\pi R_C h_C}{2\pi R_C h_C + 2\pi R_{GR} h_{GR}}\right) \tag{4-11}$$

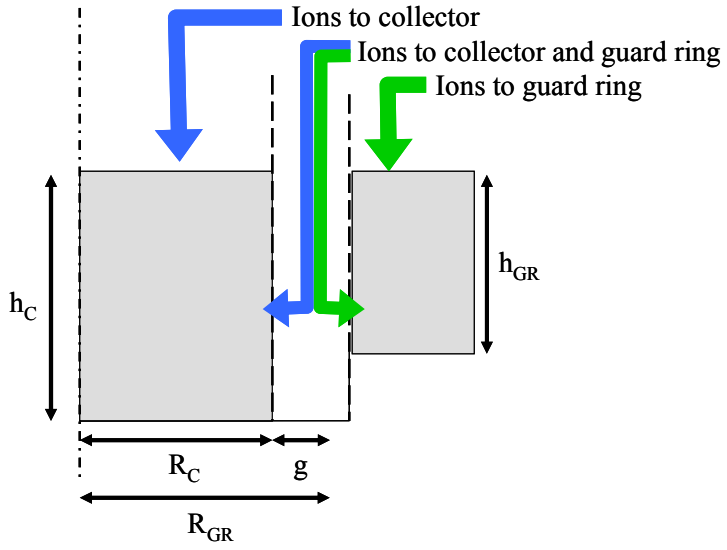

Figure 4-15 Diagram of the nude Faraday probe collector (outer radius R_c, height h_C), guard ring (inner radius R_{GR}, height h_{GR}) and gap width (g).

Based on this hypothesis, the effective probe collection area would show the greatest increase for designs with a large gap width and a large collector side wall surface area. The projected area of a 5-10 Debye length gap width may collect a significant fraction of the measured ion current, especially for a probe with a small collector diameter. It is important to note that the formulation in Eq. (4-10) is only applicable to conventional nude Faraday probes with a ceramic base in the gap volume. The area of probe designs with a conductive base would be expected to behave differently. This scenario will be studied in greater detail in Section 4.3.4.

Corrected and uncorrected collection areas of the four nested Faraday probe configurations are compared in Table 4-2. The gap correction factor increased the projected areas by approximately 10% to 55% to account for ion collection in the gap.

Table 4-2 Corrected and uncorrected collection areas of the nested Faraday probe

	Collection Area Corrected with κ_G	Uncorrected Collection Area
0.5 mm gap		
A_{C1} [cm^2]	Configuration 1 = 0.34	Configuration 1 = 0.29
A_{C1+C2} [cm^2]	Configuration 2 = 3.04	Configuration 2 = 2.81
A_{C1+C2}/A_{C1}	Area Ratio = 8.90	Area Ratio = 9.58
1.5 mm Gap		
A_{C1} [cm^2]	Configuration 3 =0.45	Configuration 3 =0.29
A_{C1+C2} [cm^2]	Configuration 4=2.79	Configuration 4=2.29
A_{C1+C2}/A_{C1}	Area Ratio = 6.18	Area Ratio = 7.80

The geometry with smallest collector diameter and the largest gap, Configuration 3, had the largest correction in projected area of approximately 55%. By comparison, the correction to Collector 1 with a 0.5 mm gap (Configuration 1) was approximately 17%. This substantial difference highlights the effect of a large gap on a small diameter

collector. The gap corrections were larger for the inner collector and larger for the 1.5 mm gap configurations. These trends mirror the patterns established in Figure 4-13.

The corrected area ratios of Configuration 2 relative to Configuration 1 and Configuration 4 relative to Configuration 3 are listed in Table 4-2. These values are compared to the ratio of collected ion current in Figure 4-16. The ratios of corrected probe collection area are within 5% of the ratios of collected ion current for all cases. Agreement between the ratios implies the gap correction factor is accurately partitioning ions in the gap between the collector and guard ring walls for all distances and pressures.

Profiles of ion current density using the corrected probe collection areas are shown in Figure 4-17. All four profiles exhibit excellent agreement and the current density of Configurations 2, 3, and 4 are indistinguishable throughout the plume. The current density of Configuration 1 is larger than the other profiles by a consistent margin. This may be caused by underestimation of the corrected collection area for this configuration, which would also account for the 5% larger corrected area ratio of the 0.5 mm configurations in Figure 4-16. Possible causes of this deviation include errors in machining tolerance and misalignment. Despite this variation, the uniform current density profiles of four different probe configurations is strong support that κ_G is accurately accounting for differences in probe geometry based on probe size and gap width. Therefore, the total ion beam current in this study is calculated using Eq. 4-12, which incorporates the corrections for measurement coordinate geometry and the collection of ions in the gap volume.

$$I_{Beam} = 2\pi R^2 \int_0^{\pi/2} \frac{I[\theta]}{A_C + \kappa_G} \left(\frac{\kappa_D[\theta, R, R_{CL}]}{\kappa_A[\theta, R, R_{CL}]} \right) \sin(\theta)\, d\theta \qquad (4\text{-}12)$$

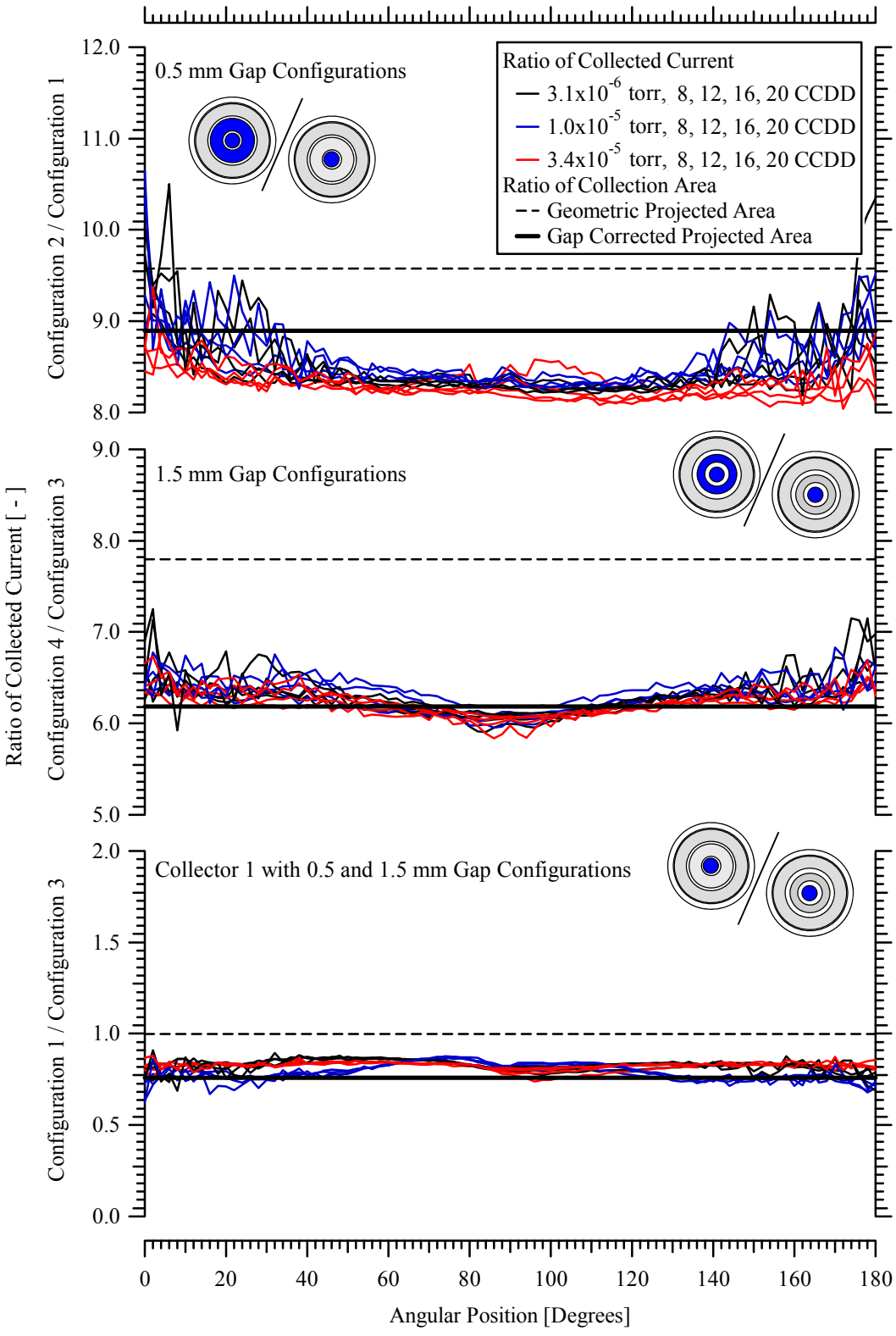

Figure 4-16 **Comparison of corrected and uncorrected collector area ratios and collected current ratios of the 0.5 mm configuration (top), 1.5 mm configuration (middle), and Collector 1 (bottom) at 3.1×10^{-6}, 1.0×10^{-5}, and 3.4×10^{-5} torr measured at 8, 12, 16, and 20 CCDD as a function of probe angular position.**

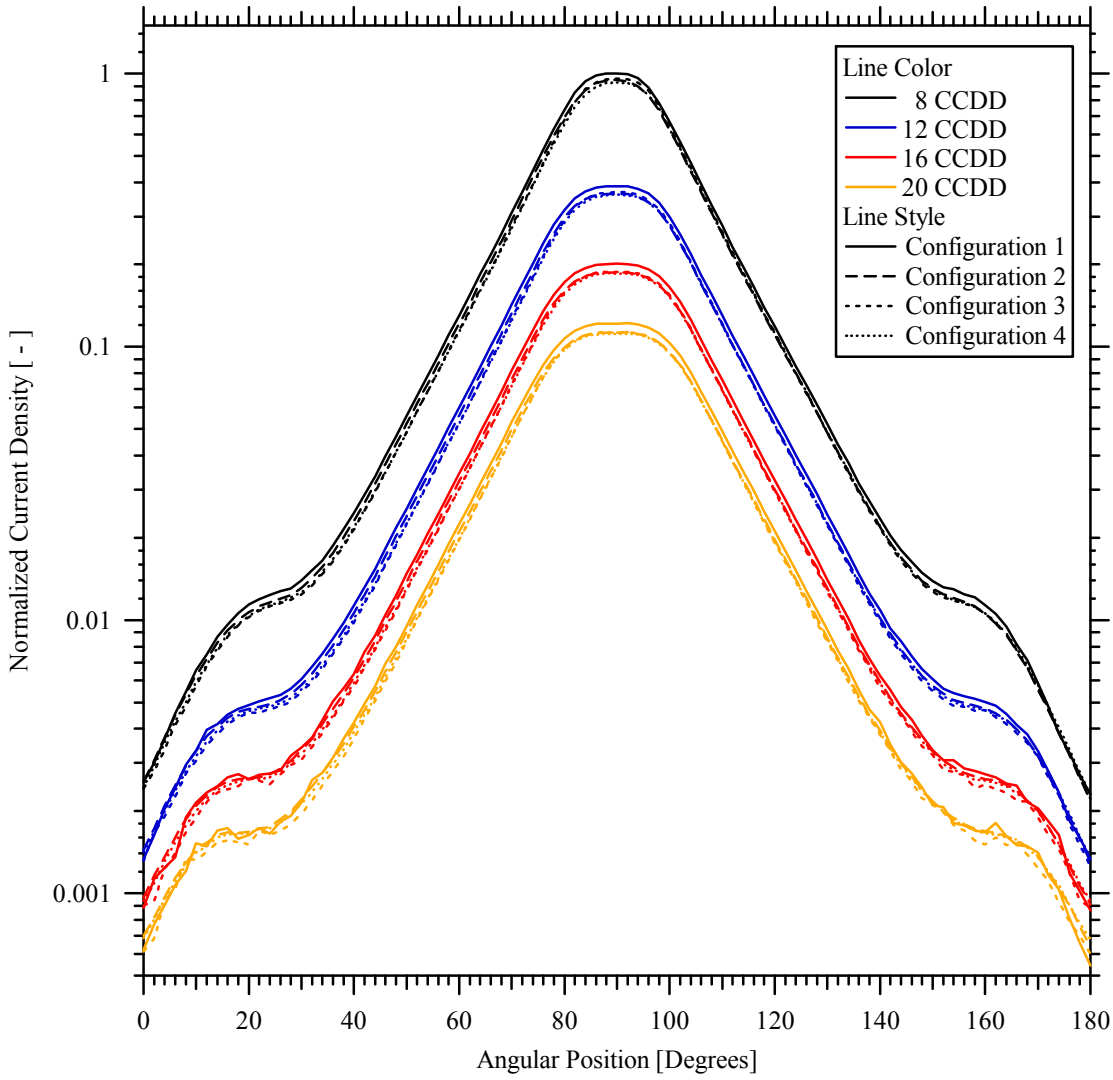

Figure 4-17 Normalized current density profiles, corrected with κ_G, from Collector 1 and Collector 1+2 for the 0.5 mm and 1.5 mm gap configurations measured at 8, 12, 16, and 20 CCDD with a facility background pressure of 3.1×10^{-6} torr.

The uniform current density traces between the 0.5 mm and 1.5 mm gap configurations in this study signals that fringing field effects above the gap may be a negligible effect, and the 5 to 10 Debye length design criteria may be unnecessary. This concept will be studied in the following section by varying the bias potential on the guard ring while holding a constant potential on the collector electrode.

4.3.3 Effects of Non-uniform Bias Potential

A non-uniform bias potential across the Faraday probe surface is used to study the current collected in the gap volume and how it is distributed to either the collector or guard ring. The following analysis is idealized and based on the model of ion collection by the side walls described in the previous section. With zero bias potential on the guard ring and -15 V on the collector, all current in the gap volume would be measured on the collector. In this case, the effective collection area would be the combined projected area of the collector and gap (A_C+A_{Gap}). With a large negative bias potential on the guard ring (<< -15 V) and -15 V on the collector, all current in the gap volume should be collected by the guard ring and the collector will measure less current. In this instance, the effective collection area would simply be the projected geometric area of the collector (A_C). For uniform current density over the probe collection area, the ratio of collected current at the highest and lowest guard ring bias potential should be equal to the ratio of the collecting areas. This formulation is shown in Eq. (4-13) and is similar to the rationale used in Eq. (4-9).

$$\frac{I_{NFP}\left[V_{Bias}=0\right]}{A_C+A_{Gap}}=\frac{I_{NFP}\left[V_{Bias}=-25\right]}{A_C}\Leftrightarrow\frac{I_{NFP}\left[V_{Bias}=0\right]}{I_{NFP}\left[V_{Bias}=-25\right]}=\frac{A_C+A_{Gap}}{A_C} \tag{4-13}$$

The equivalence in Eq. (4-13) is examined for the 0.5 mm gap version of the outer collector. Normalized collected current measured by Configuration 1 is displayed in Figure 4-18 and Configuration 2 is shown in Figure 4-19. For a fixed -15 V on the collector, the collected current as a function of guard ring bias potential is shown at θ=50° to 130° in 10° increments. In the study of Configuration 1, the inner gap between Collector 1 and 2 is studied, where Collector 2 is considered the guard ring. In the study

of Configuration 2, the outer gap between Collector 2 and the guard ring is studied, and the collector consists of the combined current from Collector 1 and Collector 2. These two cases show the variation in collected ion current when the respective guard ring bias voltage is varied from 0 V to -25 V. As predicted, the collector current saturates when the guard ring is biased to 0 V. When the guard ring bias voltage is decreased, the current to the collector decreases and asymptotes as the bias voltage approaches -25 V. In regions of the central core where the collected current has a negative slope at -25 V on the guard ring, the steady state value is estimated. Table 4-3 lists the normalized current of Configuration 1 and Configuration 2 at V_{Bias}=0 and -25 V on the respective guard rings.

Table 4-3 Normalized collected current for variation in guard ring bias potential for the 0.5 mm gap configurations

Probe Position [degrees]	Normalized Current to Collector 1 [A]			Normalized Current to Collector 1+2 [A]		
	V_{Bias} = 0V	V_{Bias}→Saturation	$\frac{I_{NFP}(0)}{I_{NFP}(-25)}$	V_{Bias} = 0V	V_{Bias}→Saturation	$\frac{I_{NFP}(0)}{I_{NFP}(-25)}$
50°	0.081	0.06	1.35	0.079	0.068	1.16
60°	0.19	~0.14	1.36	0.18	0.16	1.14
70°	0.43	~0.34	1.26	0.44	0.38	1.14
80°	0.88	~0.71	1.24	0.89	~0.76	1.16
90°	1.0	~0.80	1.25	1.0	~0.86	1.16
100°	0.85	~0.68	1.25	0.85	~0.74	1.14
110°	0.40	~0.31	1.29	0.40	0.34	1.14
120°	0.17	0.13	1.31	0.17	0.15	1.15
130°	0.078	0.058	1.34	0.075	0.065	1.15

The geometric area ratio of the 0.5 mm inner gap is based on the Collector 1 outer diameter and the Collector 2 inner diameter. This area ratio may be calculated as $\pi(7.06/2)^2/\pi\ (6.11/2)^2=1.33$. The geometric area ratio of the 0.5 mm outer gap is based on the Collector 2 outer diameter and the guard ring inner diameter, and may be calculated as $\pi(20.27/2)^2/\pi(18.91/2)^2=1.15$. In both configurations, the ratio of collected current is approximately equal to the ratio of the geometric collection areas. Similar trends were observed for the 1.5 mm gap configurations, but the larger gap distance required a larger negative bias potential on the guard ring to achieve current saturation.

These findings indicate ions in the gap volume were distributed according to the ratio in Eq. (4-13), and comprise a non-negligible fraction of the collected current. Ions collected in the gap increase the effective area of the Faraday probe, and necessitate a correction to the projected geometric collection area for measurements of current density in the plume. In addition, fringing field effects appear to have minimal importance in this study, since the collected current saturates for all distances as the guard ring bias potential approaches 0 V. It may be possible to relax the probe design criteria of 5 to 10 Debye lengths if the effective collection area can be determined by geometry.

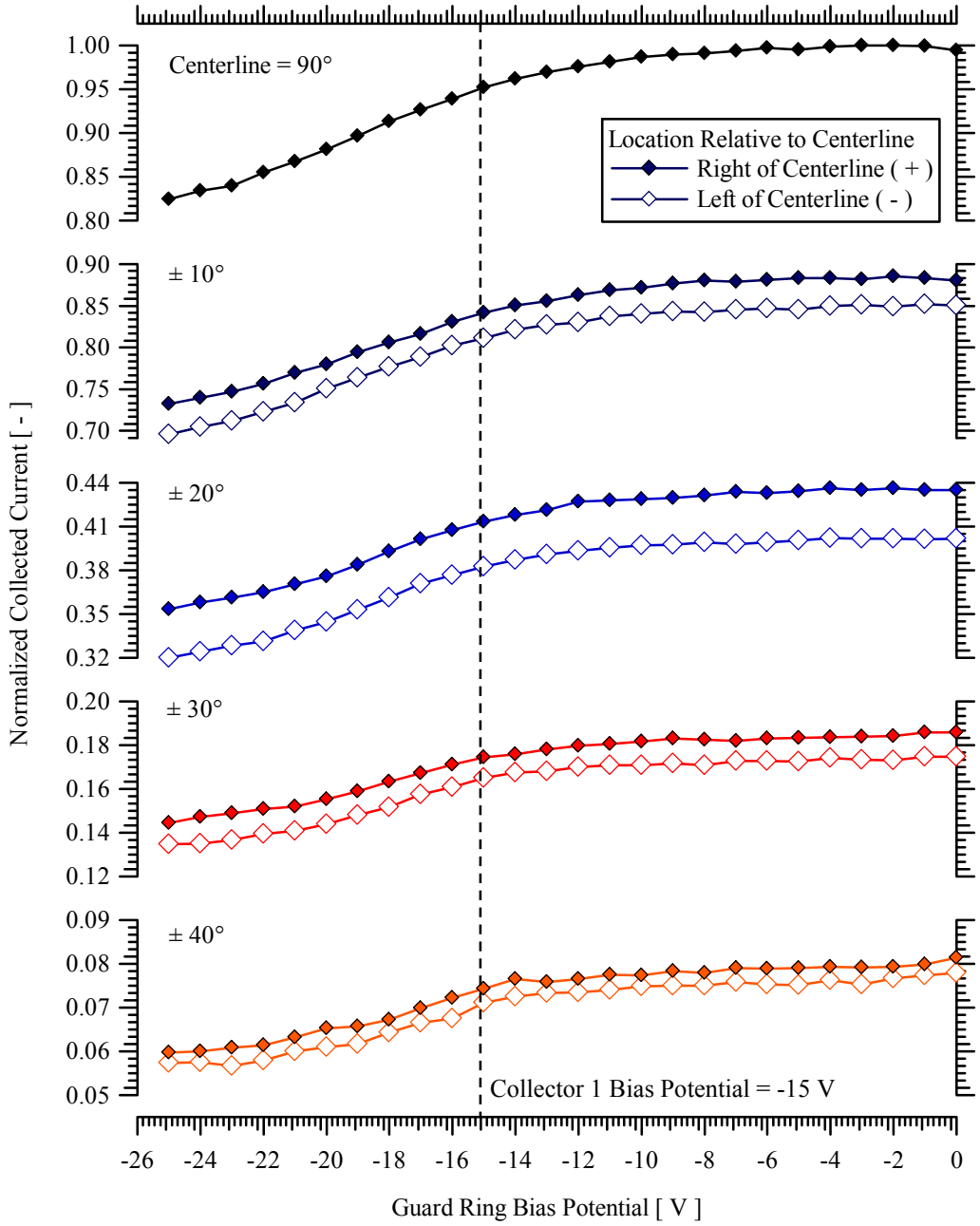

Figure 4-18 **Normalized current to Collector 1 in the 0.5 mm gap configuration (Configuration 1) as a function of bias potential on Collector 2 and the guard ring. Measurements are normalized to the maximum centerline current for 0 V on the guard ring, and are shown from θ=50° to 130° in 10° increments at 20 CCDD with a facility background pressure of 3.1×10^{-6} torr.**

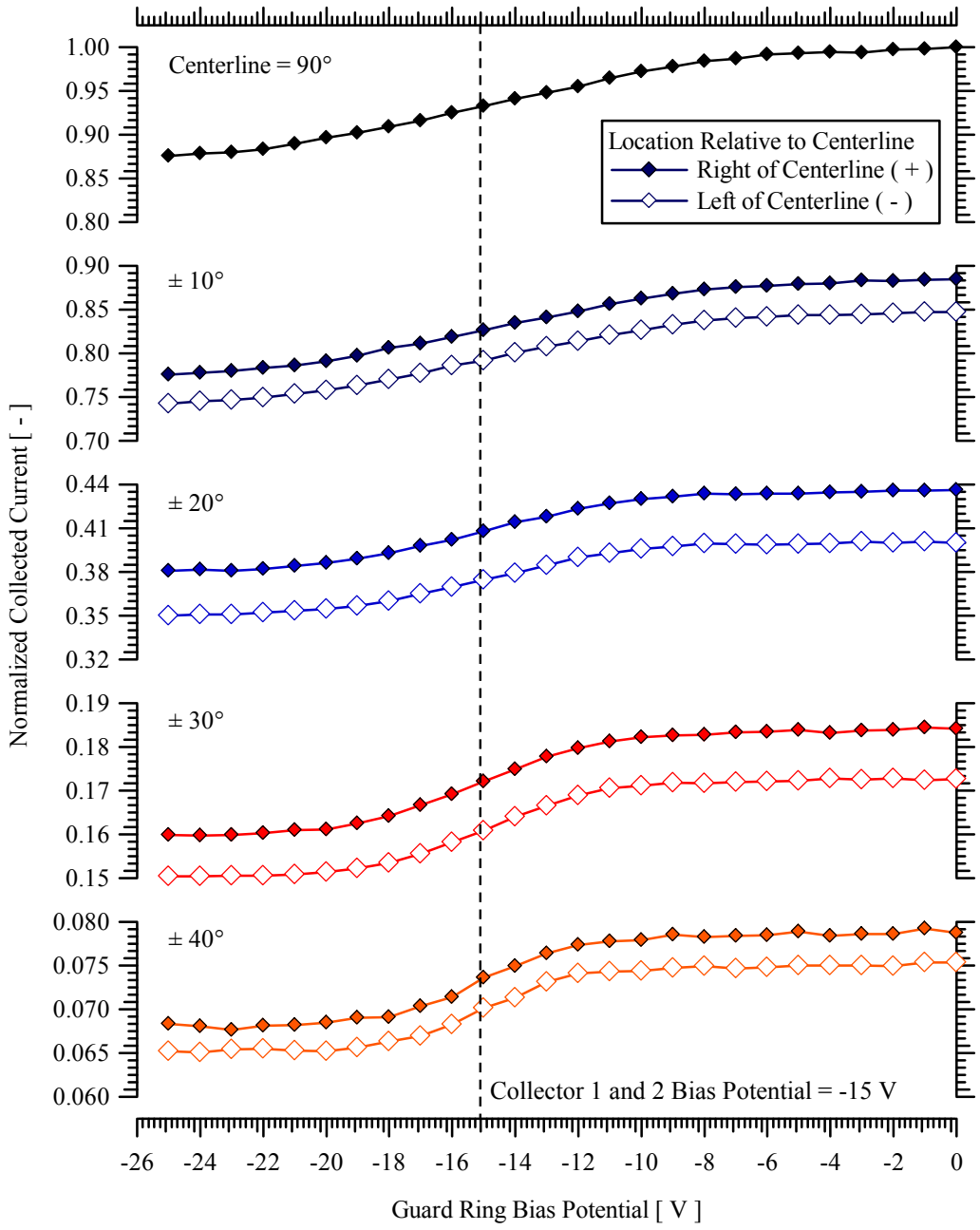

Figure 4-19 **Normalized current to Collector 1+2 in the 0.5 mm gap configuration (Configuration 2) as a function of bias potential on the guard ring. Measurements are normalized to the maximum centerline current for 0 V on the guard ring, and are shown from θ=50° to 130° in 10° increments at 20 CCDD with a facility background pressure of 3.1×10^{-6} torr.**

In Figure 4-20, the projected collection area is estimated for each configuration base on the guard ring bias potential. For 0 V applied to the guard ring, all ions in the gap volume are evaluated as current to the collector side walls and the collection area is estimated as the projected area of the collector and gap (A_C+A_{Gap}). For -25 V applied to the guard ring, all ions in the gap volume are evaluated as current to the guard ring side walls and the collection area is estimated as the projected area of the collector (A_C). The case of -15 V on the guard ring is evaluated using the gap correction factor ($A_C+\kappa_G$).

In the 0.5 mm gap configurations, the current density profiles show excellent agreement throughout the plume. Thus, for a probe design with a 5 to 10 Debye length gap, fringing fields have a negligible effect. In addition, the equivalent current density profiles show that the collection area may be estimated for variations in guard ring bias potential based on probe geometry. Measurements with 0 V or a large negative bias potential on the guard ring may be compared with standard Faraday probe current density measurements, where the guard ring bias potential is equal to the collector bias. This technique could verify current density profiles with three independent measurements of different collection areas for a given thruster operating condition. Consistent agreement using this approach should minimize measurement uncertainty associated with the probe collection area.

The 1.5 mm gap configurations exhibited effects that may be caused by fringing fields. Configurations 4 with 0 V on the guard ring showed increased current density on the wings. This is possible for increased sheath expansion as the Debye length increased, resulting in additional ion collection and under-prediction of the projected area.

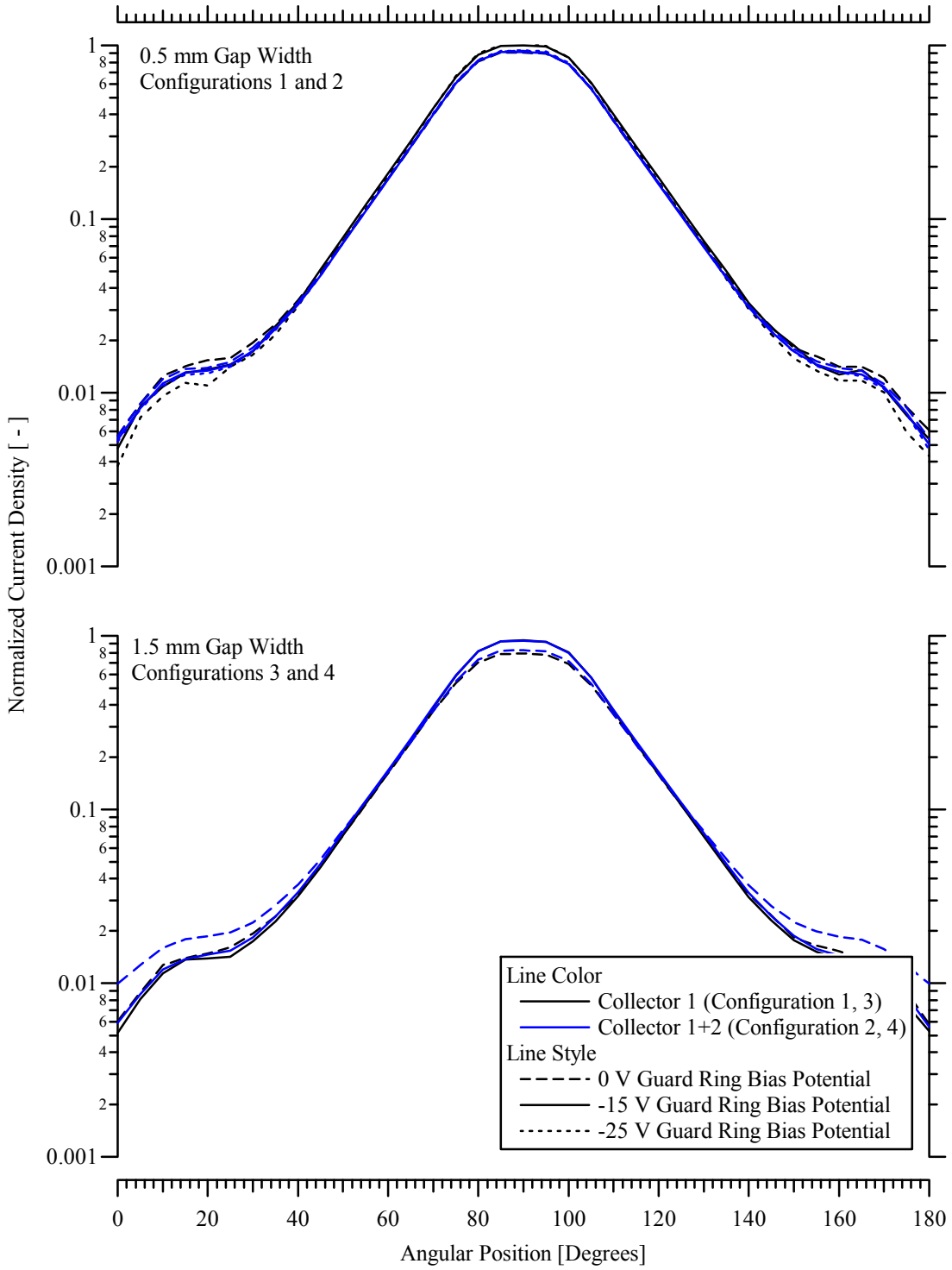

Figure 4-20 **Normalized current density profiles of the 0.5 mm and 1.5 mm gap configurations with -15 V on the collector and 0 V, -15 V, and -25 V on the guard ring at 20 CCDD. Measurements are normalized to the maximum centerline current of Configuration 1 with -15 V on the guard ring.**

Both Configurations 3 and 4 with 0 V on the guard ring measured slightly less current density in the central core compared to the profiles with -15 V on the guard ring. This indicates a small fraction of the ions in the gap are collected by the guard ring side walls, and the area approximation is overestimated. It is possible a more negative collector bias potential would minimize this difference.

According to these results, a gap width larger than 5 to 10 Debye lengths may introduce additional error in current density profiles if the collector and guard ring bias potential is not equivalent. The gap correction factor minimized these effects, which may enable this design criterion to be relaxed for equal bias potential on the guard ring and collector electrode. Therefore, this study characterizes the distribution of ions in the gap volume of a conventional nude Faraday probe design with a ceramic base, and supports the applicability of κ_G to estimate the projected probe collection area.

4.3.4 Applying the Gap Correction Factor to Past Results

Previous investigations comparing Faraday probe designs concluded disparities in measured current density were the result of differences between the collector SEE and probe geometry.[102,105] Collector material is not considered in this investigation, but past studies found negligible difference in current density between molybdenum, aluminum, and carbon collectors for equivalent probe geometry.[112]

The gap correction factor is applied to a past investigation of probe design at PEPL comparing the JPL nude Faraday probe and the GRC nude Faraday probe.[102,105] Relevant probe dimensions are shown in Table 4-4.

Table 4-4 Geometry and area correction of the JPL and GRC nude Faraday probes.[102]

	JPL Nude Faraday Probe Design	GRC Nude Faraday Probe Design
Collector Outer Diameter [mm]	23.1	19.4
Guard Ring Inner Diameter [mm]	25.4	22.2
Gap Width [mm]	1.15	1.40
Projected Geometric Area [cm^2]	4.19	2.96
Projected Area Corrected with κ_G [cm^2]	4.40	3.38

Applying the gap correction factor κ_G to the geometric area increases the JPL probe collection area by ~5% and the GRC probe by ~14%. However, the guard ring design of the JPL probe differs from the GRC probe and the AFRL nested Faraday probe. The collection area of the step in the JPL probe guard ring at the base of the gap is accounted for in the same manner as the guard ring side wall in the correction κ_G. Ion collection by the area behind the collector is expected to be minimal and is not accounted for in this limited analysis. Schematics of the probe design geometries are displayed in Figure 4-21 and Figure 4-22.

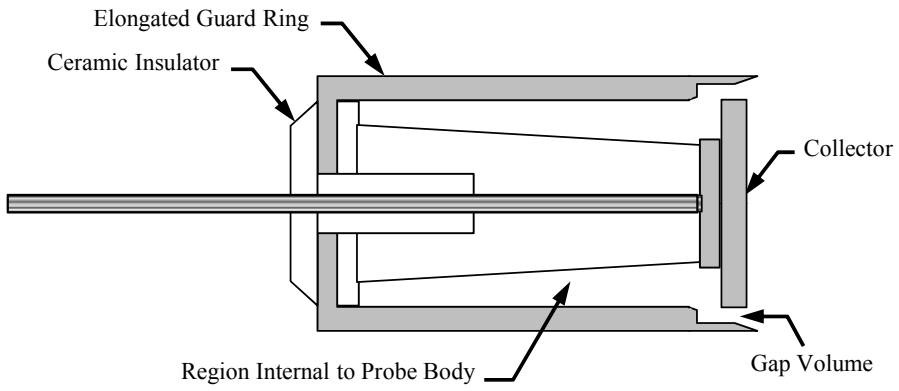

Figure 4-21 Diagram of the JPL nude Faraday probe.

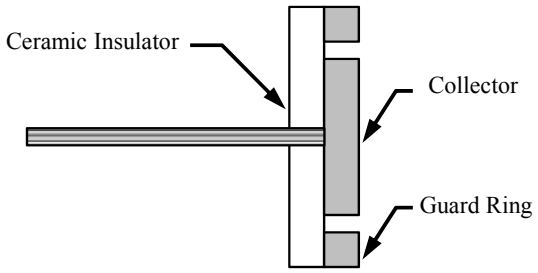

Figure 4-22 Diagram of the GRC nude Faraday probe.

The GRC probe measured a larger current density and total ion beam current for all operating conditions. The total ion beam current is shown in Figure 4-23 as a function of pumping speed for all thruster operating conditions tested. In all cases, the plume profiles were similar and the authors attributed the disparity in magnitude to collector SEE and an uneven sheath over the GRC probe. While both effects may influence the collected current, another possible explanation is the difference between the corrected and uncorrected collection areas.

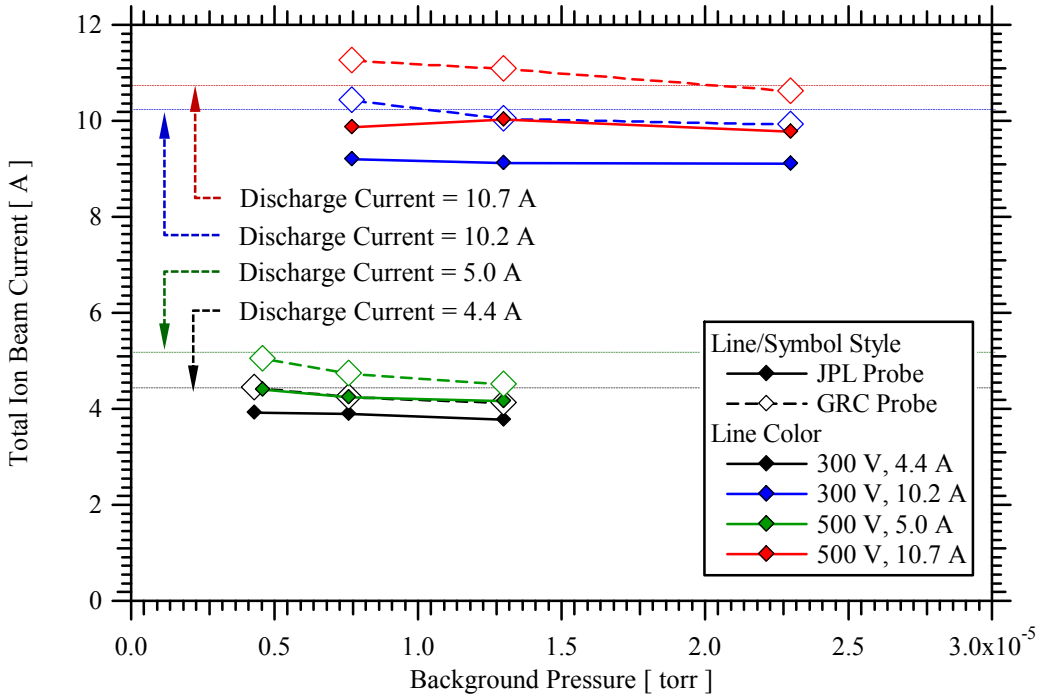

Figure 4-23 Total ion beam current of the NASA173M-v1 as a function of background pressure for the JPL and GRC nude Faraday probes from Walker, *et al.*[105]

Results from the investigation are listed in Table 4-5 for three facility pumping speed configurations. Pumping speeds in the Large Vacuum Test Facility (LVTF) were 70,000, 140,000, and 250,000 l/s, corresponding to 2, 4, and 7 operational cryopumps. Beam current values in Table 4-5 are calculated from reported values of I_{beam}/I_d.

Table 4-5 Comparison of the JPL and GRC Faraday probes for variations in background pressure and thruster operation from Walker, *et al.* [105]

# of LVTF Cryopumps	Background Pressure [torr]	Discharge Voltage [V]	Discharge Current [V]	Reported Ion Beam Current [A]		Gap Corrected Ion Beam Current [A]	
				JPL Probe	GRC Probe	JPL Probe	GRC Probe
2	$1.3x10^{-5}$	300	4.39	3.78	4.13	3.59	3.61
4	$7.6x10^{-6}$	300	4.37	3.89	4.24	3.70	3.71
7	$4.3x10^{-6}$	300	4.35	3.92	4.44	3.73	3.88
2	$2.3x10^{-5}$	300	10.23	9.10	9.92	8.66	8.68
4	$1.3x10^{-5}$	300	10.14	9.13	10.04	8.68	8.78
7	$7.7x10^{-6}$	300	10.22	9.20	10.42	8.75	9.11
2	$1.3x10^{-5}$	500	5.01	4.16	4.51	3.96	3.94
4	$7.6x10^{-6}$	500	4.93	4.24	4.73	4.03	4.14
7	$4.6x10^{-6}$	500	4.89	4.40	5.04	4.19	4.40
2	$2.3x10^{-5}$	500	10.62	9.77	10.62	9.30	9.29
4	$1.3x10^{-5}$	500	10.66	10.02	11.09	9.53	9.69
7	$7.7x10^{-6}$	500	10.72	9.86	11.26	9.38	9.84

The following analysis considers three cases and illustrates the results as the ratio of the total ion beam current of the JPL probe relative to the GRC probe.

Case 1: No area corrections. Beam current ratio corresponds to the ratio of reported values.

Case 2: Both areas corrected. Beam currents of both probes are modified according to the gap corrected area values in Table 4-4.

Case 3: Only the GRC probe collection area is corrected according to the gap corrected area value in Table 4-4.

Case 3 evaluates the uncorrected beam current of the JPL probe with the corrected beam current of the GRC probe. Due to the step in the guard ring and internal region of the JPL probe, the gap correction factor may not be suitable as presently formulated. The GRC probe guard ring configuration is a similar design to the AFRL nested Faraday probe, and the gap correction is more applicable.

The ratios of measured and corrected ion beam current from Table 4-5 are illustrated in Figure 4-24. For Case 1, beam current measured by the JPL probe is ~10% less than the ion current measured by the GRC probe. Case 2 shows the effect of correcting both probe collection areas for the gap width, and resulted in good agreement to within 3% for all thruster operating conditions at the high background pressures, corresponding to facility pumping speeds of 70,000 and 140,000 l/s. The correction appears to be more applicable in the highest background pressure case. In Case 3, the GRC probe and JPL probe beam currents exhibited very good agreement for all thruster operating conditions at the lowest facility background pressure of 250,000 l/s.

As the number of pumps was decreased, and hence the background pressure and CEX ion density increased, the JPL probe measured a higher beam current than the GRC probe. This may be due to the distribution of ions to the guard ring and collector walls within the JPL probe gap. At low background pressure, ions in the gap volume are collected primarily by the step in the guard ring since this is facing the incoming ions, and the ion collection area is approximately equal to the geometric probe collection area. The effect is illustrated in Figure 4-25. At higher background pressure, a significant fraction of the ions distributed within the gap volume are collected by the collector wall. This increases the effective collection area of the probe. In this hypothesis, the partition

of ions in the gap volume of the JPL probe is a function of background pressure and is not adequately described by the gap correction factor, κ_G. The geometric area of the JPL nude Faraday probe would be appropriate at low background pressure, but additional characterization may be required to determine the collection area at high facility background pressure.

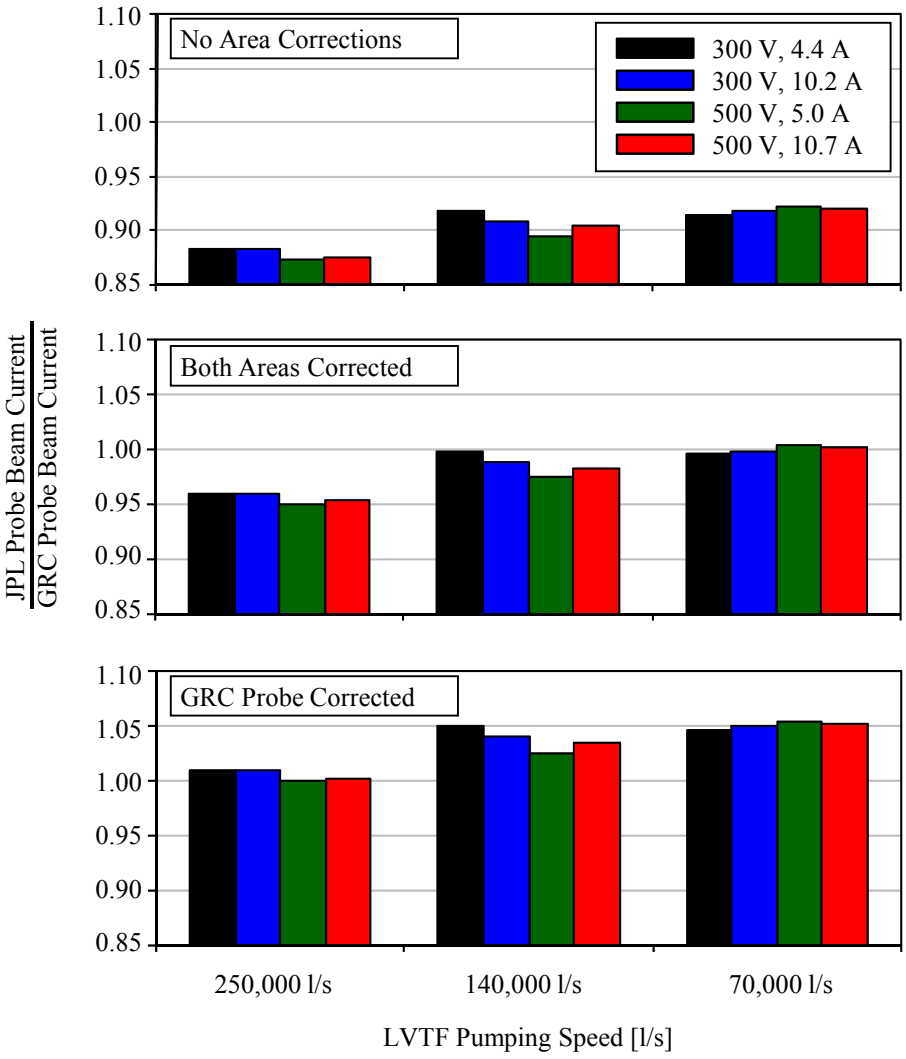

Figure 4-24 **Ratio of total ion beam current of the JPL nude Faraday probe relative to the GRC nude Faraday probe with variations in facility pumping speed for the case of no area corrections (Case 1, top), both probe collection areas corrected (Case 2, middle), and only the GRC probe collection area corrected (Case 3, bottom).**

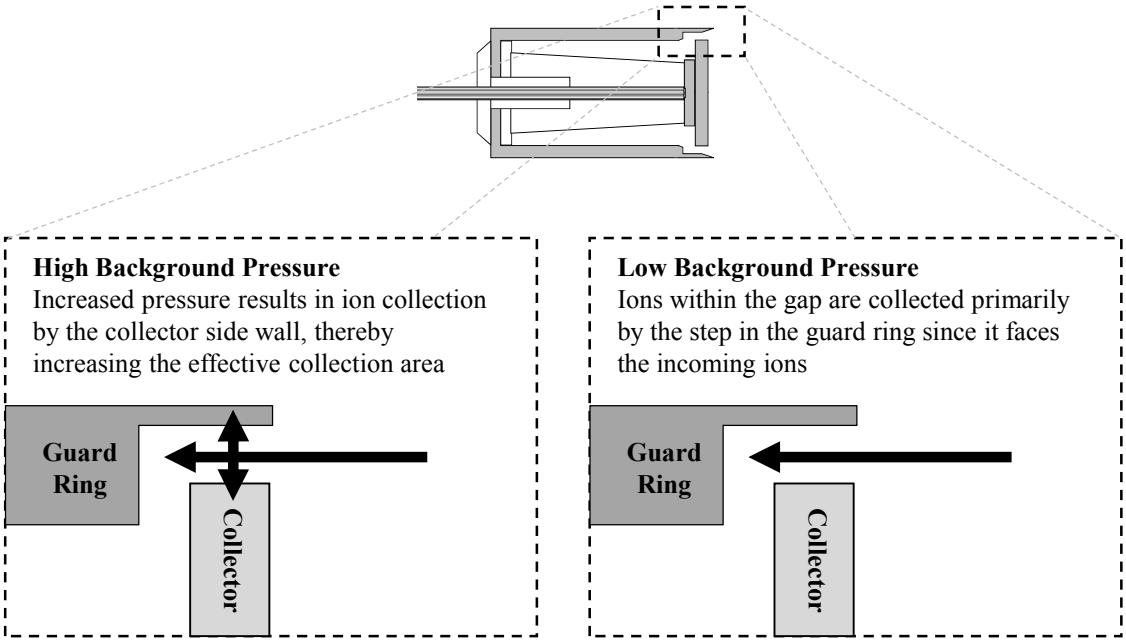

Figure 4-25 Illustration of the distribution of ions in the gap volume of the JPL Faraday probe for high and low facility background pressure.

Applying the gap correction factor to results from the investigations by Walker, *et al.*[102,105] revealed differences associated with Faraday probe design and the importance of accurately assessing ion collection in the gap. If the effective probe collection area of the JPL probe varies with background pressure, characterization of facility effects on current density measurements with the JPL probe may introduce unknown trends. Although the JPL Faraday probe may not require an area correction at low background pressures, the collection areas of the conventional GRC Faraday probe and the AFRL nested Faraday probe designs are less difficult to characterize and therefore are more suitable for investigations of beam divergence and facility effects when the Debye length varies throughout the plume.

4.4 Analysis of Plume Scattering and Facility Effects

Corrections for measurement location and Faraday probe design were proposed to minimize systematic error, but facility effects also introduce a significant source of uncertainty that requires characterization of the thruster and chamber based on background pressure and operating conditions. The methods developed in this section will incorporate the corrections developed in Sections 4.2 and 4.3, and focus solely on experimental techniques to further understanding of the measured current density and ion migration in the plume.

Far-field Faraday probe measurements are generally prone to facility effects, and presumed to have relatively large uncertainty in the current density magnitude. Past investigations have examined the wings with variations in background pressure, and several methods have been developed to reduce collection of low energy facility CEX ions in the plume. Nevertheless, the integrated ion beam current from far-field measurements is typically larger than the value reported from near-field measurements, and is often greater than the thruster discharge current. In some cases, the thruster anode flow is modified to maintain a constant discharge current as pressure is adjusted. While this approach mitigates increased thrust due to the neutral ingestion of facility neutrals, it requires variation of thruster operating conditions and is not an ideal comparison between different background pressures. In this investigation of facility effects with the nested Faraday probe, the HET anode and cathode propellant flow rates are fixed. Background pressure is regulated through auxiliary injection of xenon, as described in Section 3.1.1.

4.4.1 Determination of Vacuum Current Density Profiles

Numerous experimental designs and analytical techniques have been used to minimize facility effects on far-field Faraday probe current density measurements. Experimental approaches include various types of filters to reduce collection of low energy CEX ions and measuring the ram current density using a backward facing Faraday probe. Current density profiles corrected with the ram current density are sensitive to background pressure, and the measurements are complicated by the wake surrounding the probe.[40] Filtration designs have proven to minimize CEX facility effects, but do not account for increased discharge current or ion beam current due to neutral propellant ingestion. In addition, a fraction of the filtered ions are present on-orbit due to CEX collisions with anode and cathode neutrals. This population should not be removed for an ideal evaluation of on-orbit plume divergence and current density distribution.

Analytical techniques include subtracting the ambient current density at $\theta=0°$ from the entire plume profile, or extrapolating the exponential region ($30°<\theta<50°$) of the ion current density to the outer periphery ($50°<\theta<90°$). While these approaches provide a simple alternative to the experimental methods, they are limited in determining the spatial influence of facility effects throughout the plume. Subtracting a finite current density from the profile based on the value at $\theta=0°$ is based on the assumption that collection of ambient tank ions is uniform throughout the plume. The exponential extrapolation is based on the spatial decay of beam ions on the edges of the primary beam, but removes features of the outer periphery that may arise due to CEX collisions near the thruster exit. Neither of these techniques accurately captures the angular distribution of low energy ions that would be present on orbit.

Studying the ion current density at each angular location in the plume as a function of background pressure enables a more accurate characterization of facility effects. Extrapolating the current density at discrete angular locations to vacuum conditions isolates effects arising from facility CEX ions and neutral ingestion. This technique is shown for Configuration 1 in Figure 4-26 at 20 CCDD. Collected ion current is plotted in 10° increments as a function of facility background pressure. On thruster centerline at θ=90°, the collected current increased linearly with background pressure. However, at ±10° from centerline the slope appears to transition and transforms to a slightly negative linear slope at ±20° and ±30° from thruster centerline. The reverse trend occurs at approximately ±40° and results in a positive linear slope on the periphery from ±60° to ±90° from thruster centerline.

These variations in the slope of the collected ion current with facility background pressure are plotted as a function of angular position in Figure 4-27 at 8, 12, 16, and 20 CCDD. The transitions from positive to negative slope occur at approximately ±10° from thruster centerline for all downstream distances. Similarly, the transition from negative to positive slope occurs at approximately ±50° from thruster centerline for all downstream distances. Residuals show the degree of linearity at each angular location, and reveal that the transition at ±50° moves inwards toward the central core as downstream distance increases. This trend is indicative of the outward scattering of beam ions caused by CEX facility effects. Although increased background pressure increased the central core current density, the residuals indicate the angular location of ion migration from the central core within ±10° is largely unaffected by downstream distance.

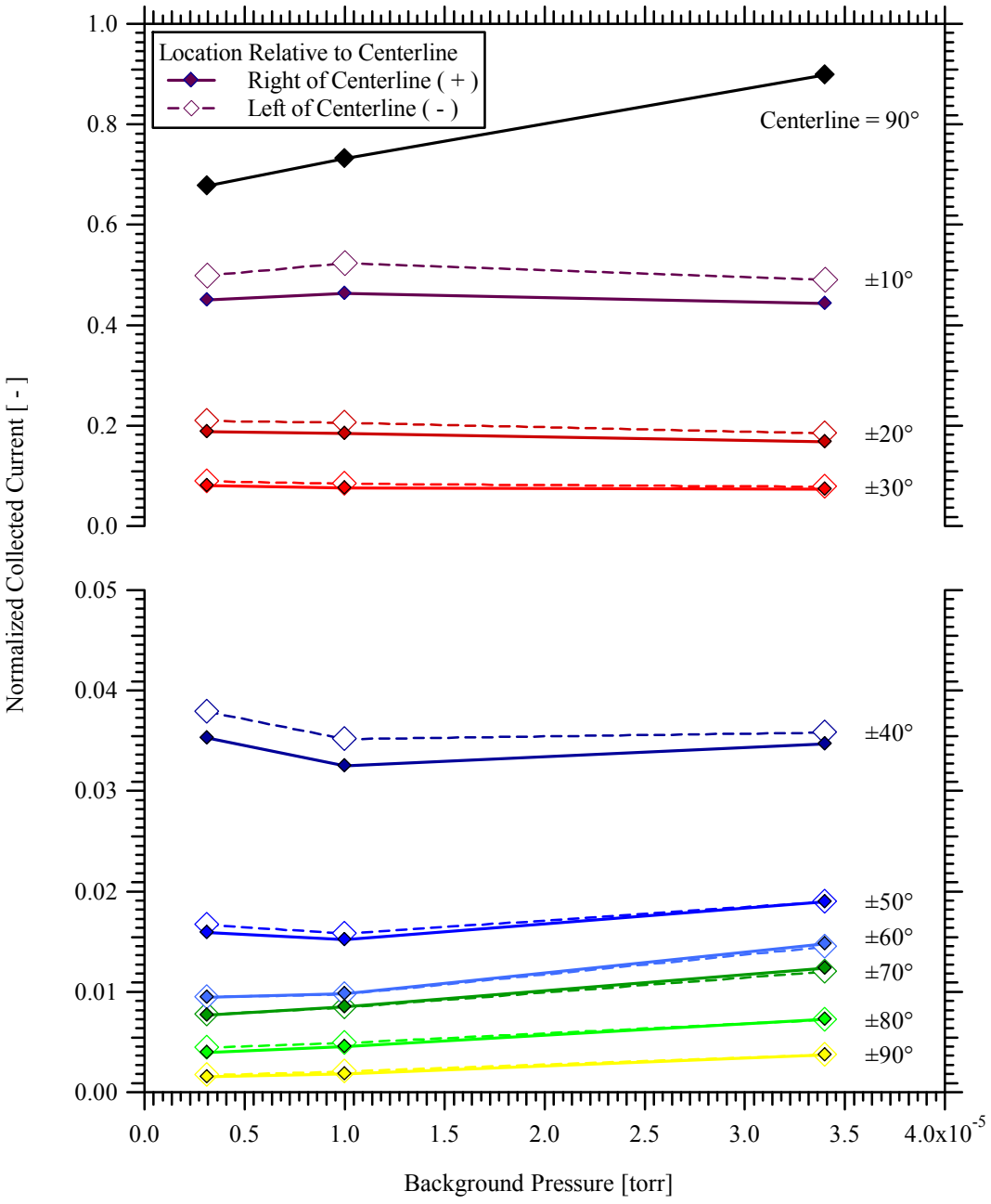

Figure 4-26 **Normalized collected ion current of the nested Faraday probe Configuration 1 as a function of background pressure at discrete angular locations in the plume at 20 CCDD. Measurements are normalized to the maximum collected current of the profile at 3.4×10^{-5} torr.**

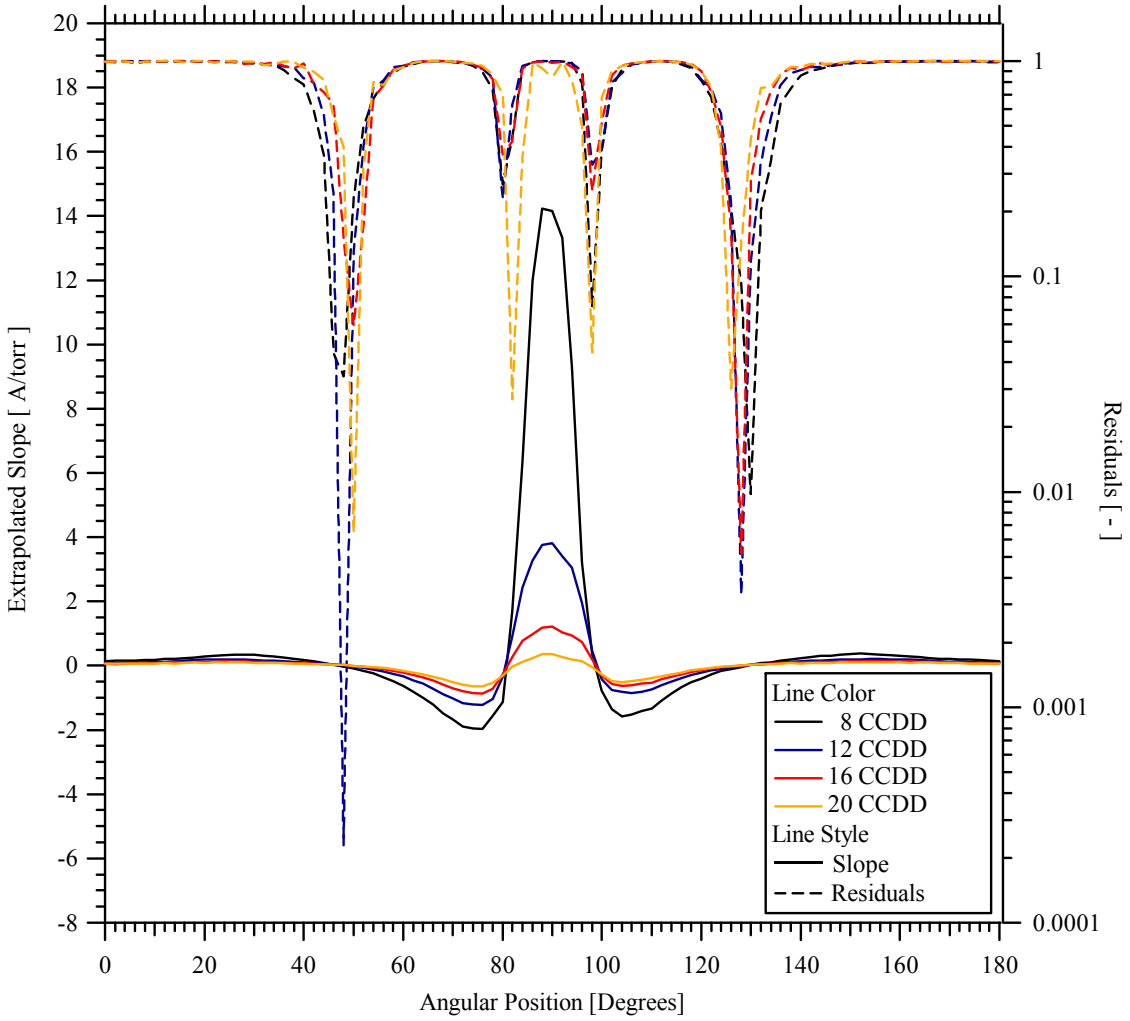

Figure 4-27 Residuals and slope of the extrapolated collected ion current of the nested Faraday probe Configuration 1 as a function of angular position at 8, 12, 16, and 20 CCDD.

The slope of the extrapolated collected ion current density in Figure 4-27 provides information about the angular location of increased current due to neutral ingestion and dispersion from beam scattering due to CEX collisions with facility neutrals. The slope appears to be dominated by two distinct effects in the plume. The first leads to a positive increase in the slope about thruster centerline, and is attributed to ionization and acceleration of ingested facility neutrals. CEX processes with facility

neutrals within the discharge channel may also lead to increased current density in the central core, but would not increase ion beam current or discharge current.

The second effect is broader and leads to a negative slope in the central core about thruster centerline. This is believed to be the result of CEX collisions with facility neutrals near the thruster exit downstream of the primary acceleration zone. In this case, no additional current is created and the primary ion beam is dispersed. The outer edge of this distribution corresponds to the location of minimum residuals at each operating condition.

These two effects are each modeled with a Gaussian distribution, and the modeled slope distribution is the superposition of these Gaussian best-fit curves. The choice of a Gaussian distribution is arbitrary, but may be appropriate for processes related to the thermalized facility neutral propellant population. The two fitted Gaussian curves, the modeled slope, and the experimental slope are compared in Figure 4-28 at 8 to 20 CCDD. The superposition of Gaussian distributions shows consistent agreement with the experimental distribution of slope for all downstream distances. Although the Gaussian distribution may not be the correct physical distribution, it provides a qualitative means of comparing effects and assessing variations in the experimental slope.

The following is a hypothesis of facility effects that satisfy the trends established in Figure 4-27 and Figure 4-28. The increase in slope about thruster centerline is caused by ionization of ingested neutrals and CEX collisions with facility neutrals in the discharge within the primary acceleration zone. The decrease in slope is the result of CEX collisions with facility neutrals downstream of the primary acceleration zone, which results in a secondary population of low energy ions and dispersion of the

primary ion beam. Facility neutrals may also undergo direct electron-impact ionization in this downstream region, but will cause a net increase in the collected ion current. The fitted Gaussian curves reveal details related to each effect.

The magnitude of the positive slope in the central core decreased with downstream distance as approximately R^2, and affected a slightly larger angular range of the plume. The decrease in slope with downstream distance is expected as the higher energy ions created by facility neutrals are scattered due to CEX collisions with facility neutrals. The width of the Gaussian attributed to downstream CEX collisions with facility neutrals was relatively constant with downstream distance in the far-field, and the magnitude decreased by approximately half from 8 CCDD to 20 CCDD. The residuals decline where the effects of ionization and acceleration of facility neutrals are approximately equal to the effects of CEX collisions with facility neutrals near the thruster exit. This analysis provides a qualitative characterization of the angular range and relative magnitude of facility effects in the plume. This hypothetical model will be further discussed in Section 5.1.2 regarding facility characterization of the 6-kW Hall thruster in Chamber 3.

The complete effects of background pressure on current density profiles are shown in Figure 4-29. These profiles show the escalation of ion current density in the central core with background pressure, which was attributed to ionization of ingested neutrals upstream of the primary acceleration region. Increased current density on the wings is primarily the result of ambient low energy facility ions and beam ion scattering from the central core due to CEX collisions.

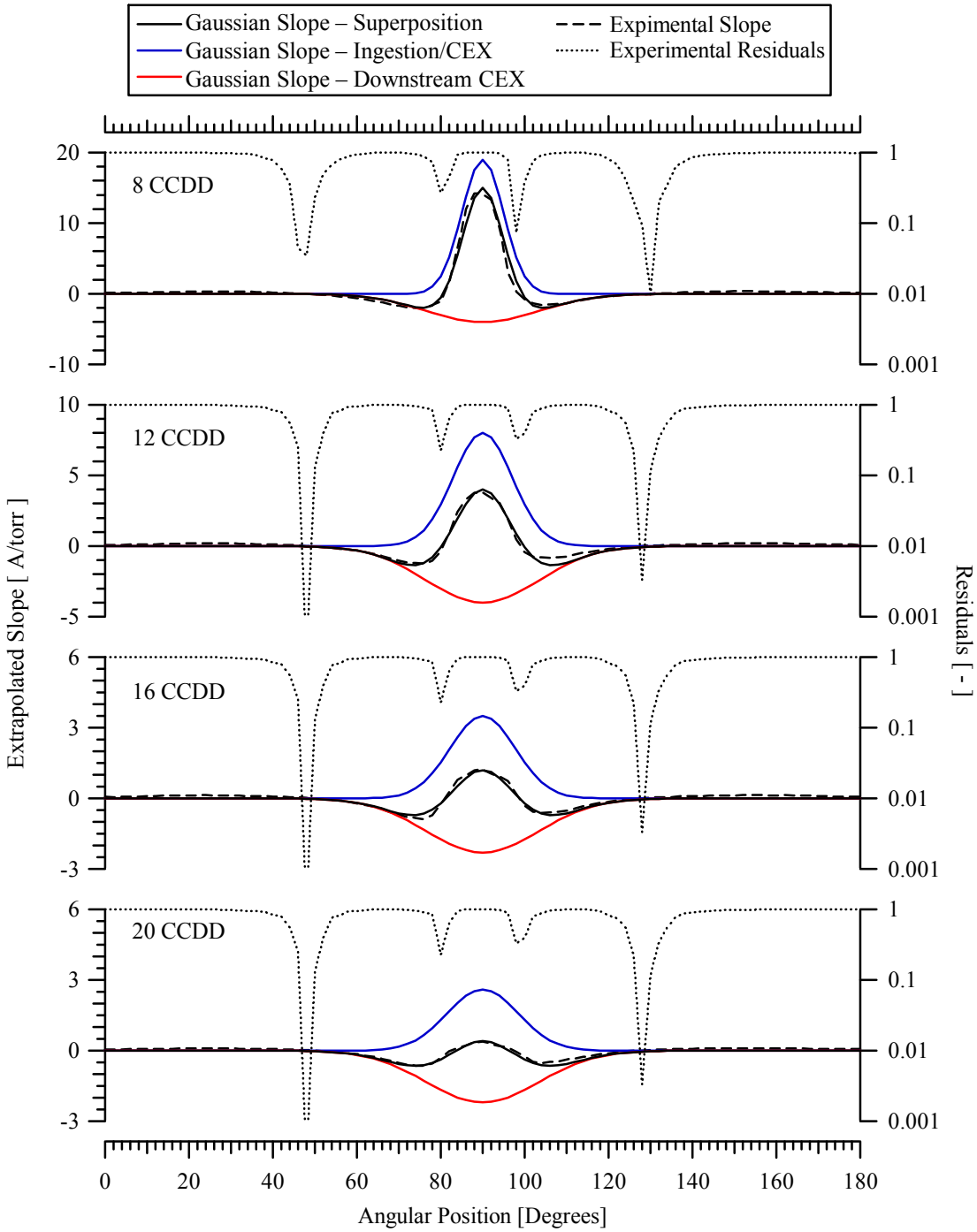

Figure 4-28 **Residuals and slope of the extrapolated collected ion current of the nested Faraday probe Configuration 1 as a function of angular position at 8, 12, 16, and 20 CCDD. A superposition of two Gaussian curves is fit to the experimental slope. Note the differences in scale of the Slope axes.**

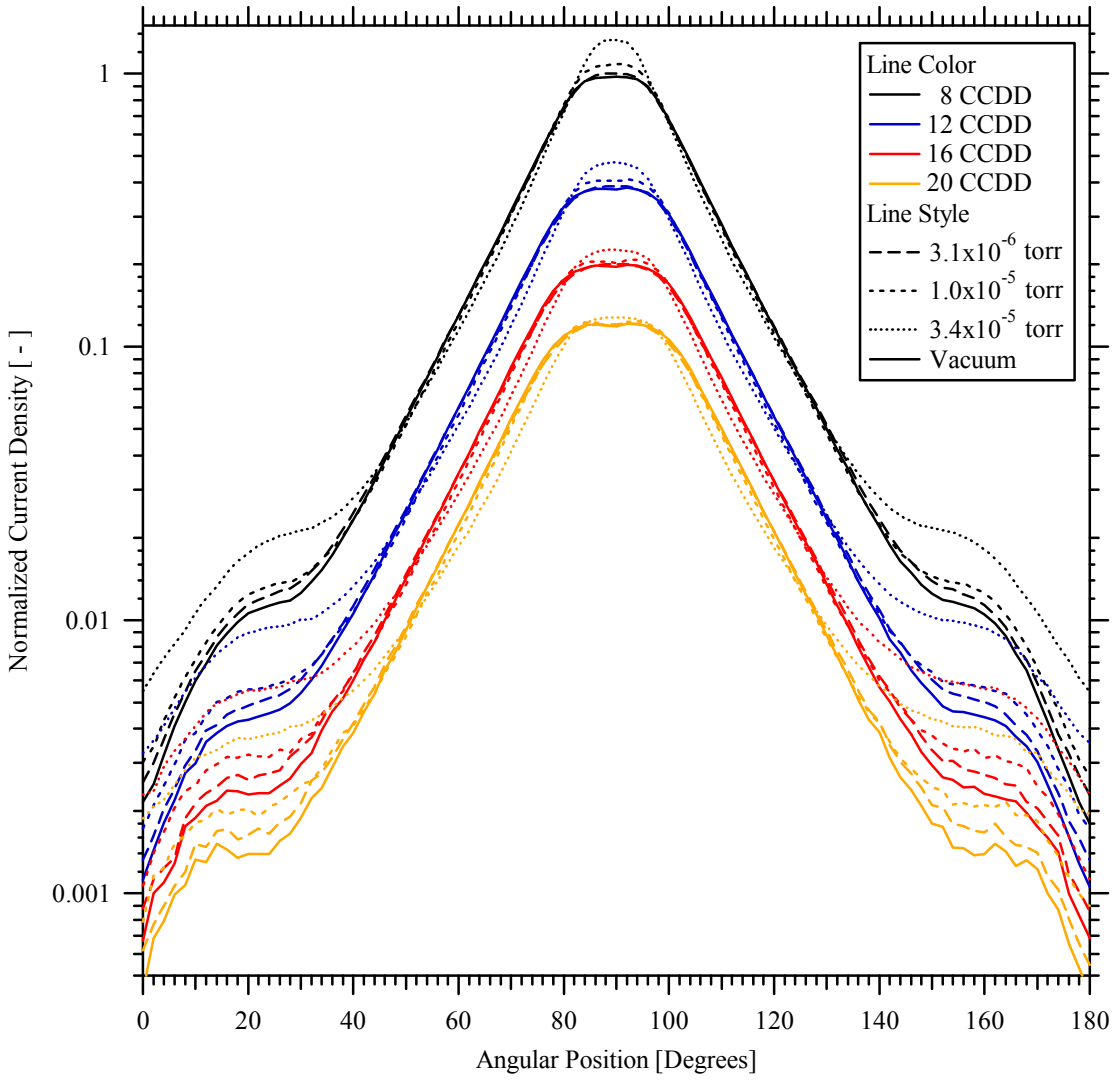

Figure 4-29 **Normalized ion current density profiles of the nested Faraday probe Configuration 1 as a function of angular position at 8, 12, 16, and 20 CCDD. The extrapolated vacuum profiles are compared to measurements at background pressures of 3.1×10^{-6}, 1.0×10^{-5}, and 3.4×10^{-5} torr. Current density profiles are normalized to the maximum extrapolated vacuum current density at 8 CCDD.**

Current density profiles of the four nested Faraday probe configurations are extrapolated to vacuum conditions for all downstream distances in Figure 4-30. These vacuum current density profiles isolate facility effects, and provide insight into the ion migration that would be present on-orbit. The configurations exhibit consistent profiles at all distances, and further increase confidence in the methods developed for

determination of on-orbit current density. As shown in Figure 4-17, the current density of Configuration 1 is slightly larger than the other configurations, and is attributed to measurement and/or alignment error of the inner collector.

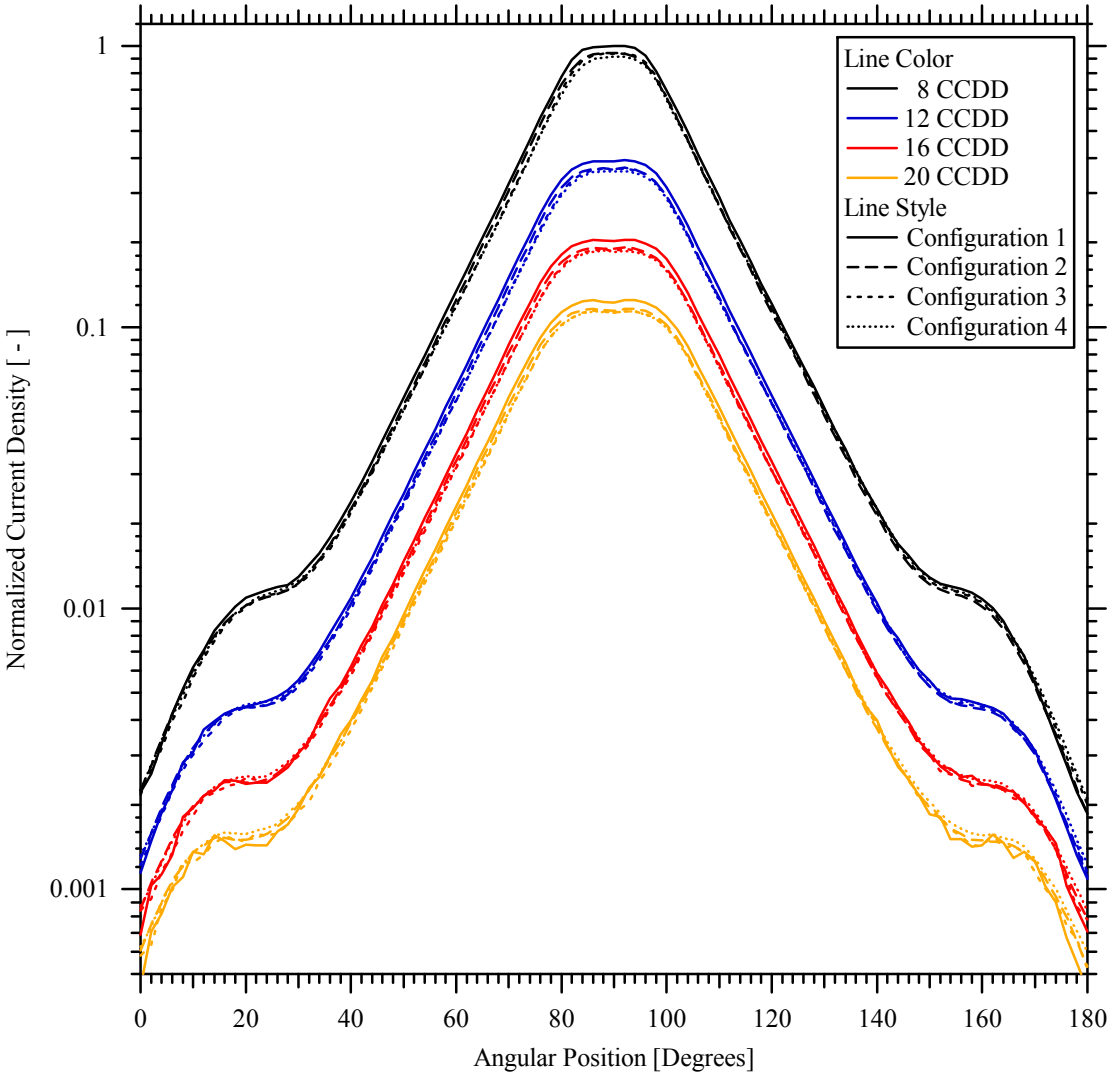

Figure 4-30 **Normalized ion current density profiles at vacuum conditions of the nested Faraday probe Configurations 1, 2, 3, and 4 as a function of angular position at 8, 12, 16, and 20 CCDD. Current density profiles are normalized to the maximum extrapolated vacuum current density of Configuration 1 at 8 CCDD.**

4.4.2 Analysis of Ion Migration in the Plume

Elimination of beam scattering generated by facility effects enables the study of ion migration in the plume and enhances comparisons with numerical simulations. Figure 4-31 shows profiles of vacuum current density per unit solid angle at 8, 12, 16, and 20 CCDD. The residuals are shown to illustrate the angular zones where the slope is approximately zero and background pressure has a minimal effect on the plume.

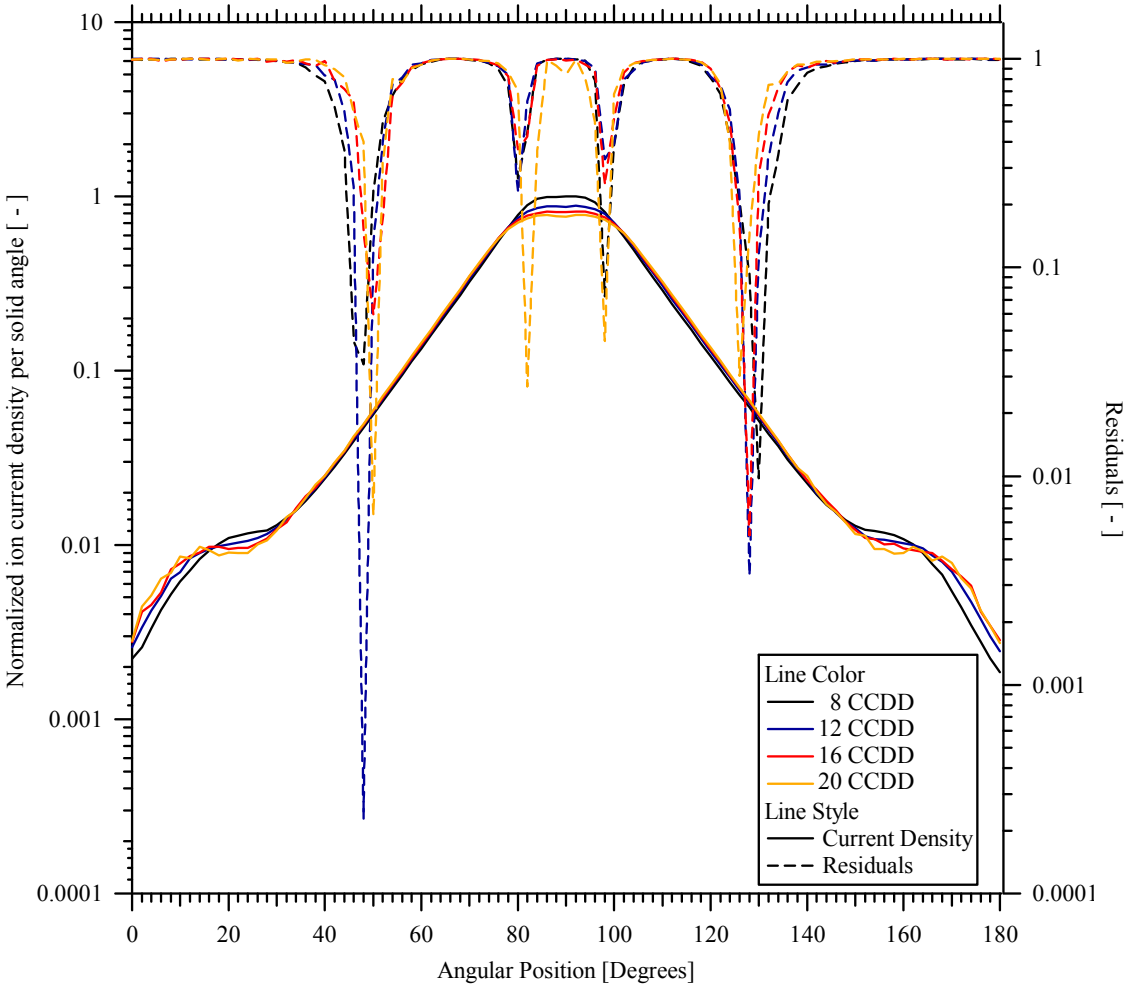

Figure 4-31 Normalized profiles of ion current density per solid angle at vacuum conditions and residuals of the nested Faraday probe Configuration 1 as a function of angular position at 8, 12, 16, and 20 CCDD. Profiles are normalized to the maximum extrapolated vacuum current per steradian at 8 CCDD.

Total ion migration in the plume may be studied in greater detail using the angular distribution of ion beam current through the surface of a spherical stripe, as shown in Figure 4-32. The angular distribution of ion beam current passing through a constant angular width stripe allows spatial analysis of beam current transport with distance and angle. Summing the ion beam current passing through the stripes within a given half-angle results in the ion beam current per steradian, and the sum from θ=0° to 180° is the total ion beam current. The ion current passing through a stripe will be referred to in units of amperes per 1° degree wide stripe [A/ unit stripe].

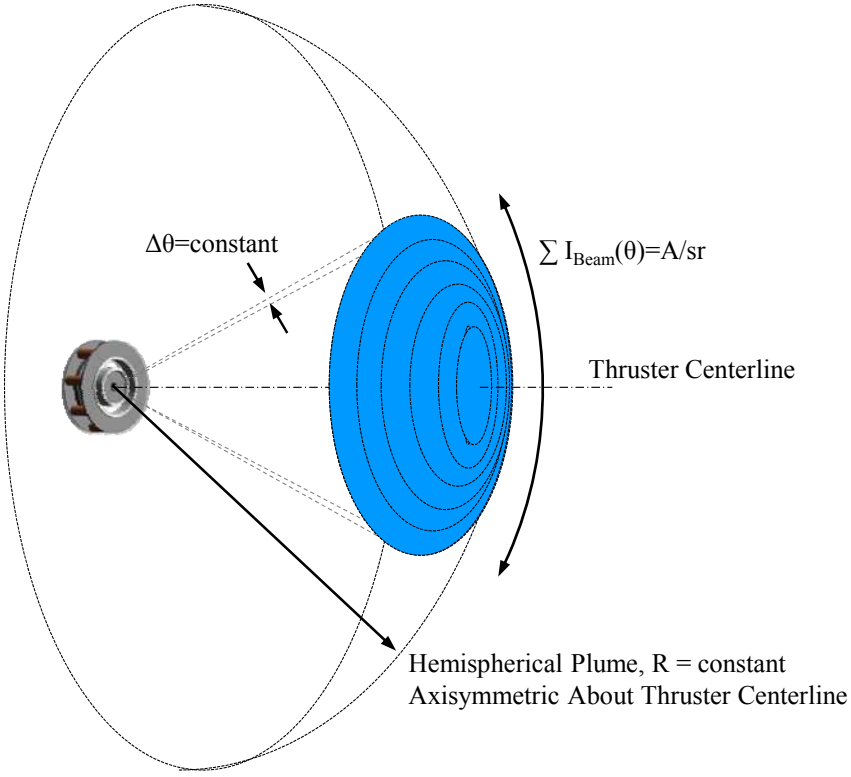

Figure 4-32 Diagram of the axisymmetric spherical stripe coordinate geometry for analysis of angular ion beam current distribution in the plume.

The trends in Figure 4-29 and Figure 4-31 are examined as the angular distributions of ion beam current in Figure 4-33. The vacuum ion beam current per stripe is shown as a function of angular position for 8, 12, 16, and 20 CCDD. The uppermost plot in Figure 4-33 shows the differences in ion beam current at 12, 16, and 20 CCDD relative to the ion beam current profile at 8 CCDD. The four lower plots show the difference in ion beam current at 3.1×10^{-6}, 1.0×10^{-5}, and 3.4×10^{-5} torr relative to the vacuum ion beam current profile at the four downstream distances studied. The relative differences in ion beam current per stripe are shown on a larger scale in Figure 4-34.

As seen in past studies, increased background pressure amplified the ion beam current on the wings. Increased ion beam current in the central core due to ingested facility neutrals increased at high pressure and decreased with downstream distance. Figures 4-33 and 4-34 highlight the significant impact facility effects have on the current density profiles relative to the vacuum conditions. In this study, deviations from the vacuum beam current distribution reached as much as 20% near the central core at 20 CCDD and the highest background pressure.

Facility pressure effects resulted in a larger deviation in beam current profiles at a constant distance compared to variations in vacuum profiles with downstream distance. However, these vacuum beam current profiles exhibit a consistent trend with downstream distance that warrants additional examination. The relative difference in vacuum ion beam current was zero for all downstream distances at three angular locations in the plume, not including the outer periphery at $\theta=0°$ and $180°$. Although the magnitude of the deviation from vacuum ion beam current at 8 CCDD increased with downstream distance, the angular locations of constant ion beam current were approximately equal to the zones where the residuals decreased and the extrapolated slope was zero.

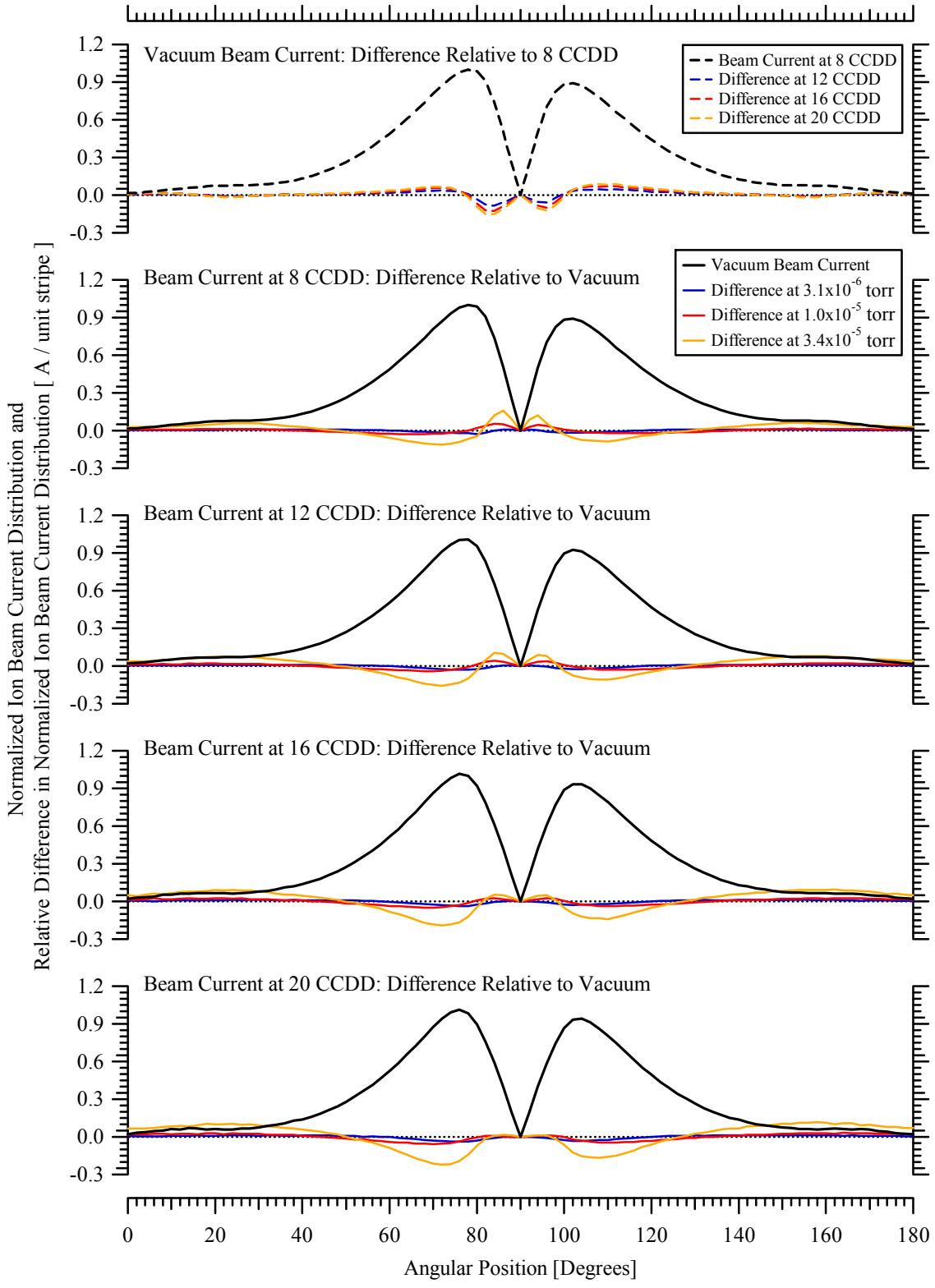

Figure 4-33 **Normalized vacuum profiles of ion beam current per unit stripe and relative difference in ion beam current distributions with variation in downstream distance and pressures as a function of angular position. All profiles are normalized to the maximum extrapolated vacuum beam current at 8 CCDD.**

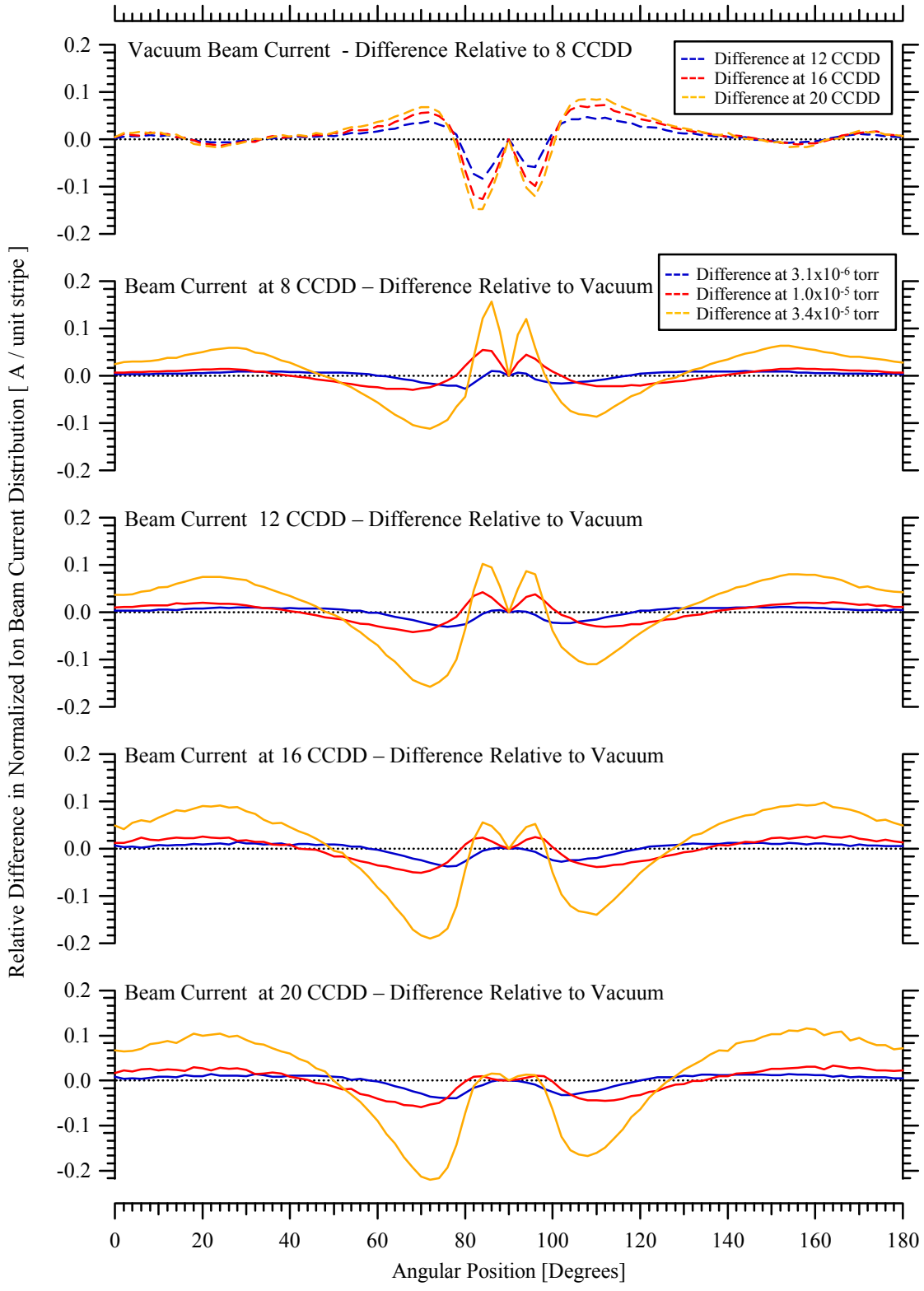

Figure 4-34 **Distributions of the relative difference in ion beam current per unit stripe with variation in downstream distance and pressures as a function of angular position. All profiles are normalized to the maximum extrapolated vacuum beam current at 8 CCDD.**

The differences in ion beam current relative to the profile at 8 CCDD are further magnified in Figure 4-35 from θ=0° to θ=90°. Regions of constant ion beam current in the plume are extremely consistent to within ±1°. These zones are located at θ=16°, θ=34°, and θ=78°. The relative difference in beam current per stripe at each downstream location is integrated as a function of angular position to evaluate the total transfer of beam current per steradian.

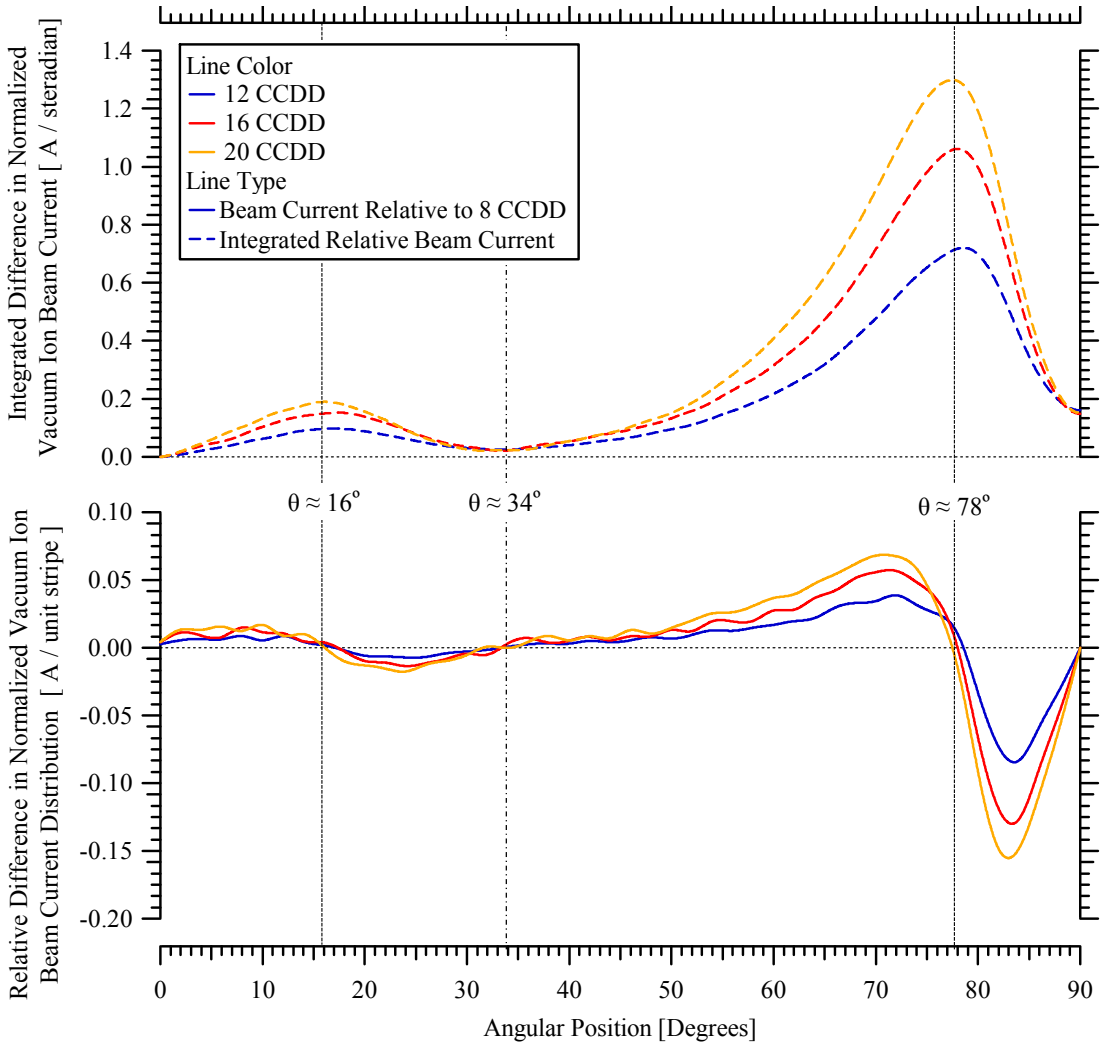

Figure 4-35 **Normalized difference in vacuum ion beam current at 12, 16, and 20 CCDD relative to the profile at 8 CCDD as a function of angular position. All profiles are normalized to the maximum extrapolated vacuum beam current at 8 CCDD.**

This plot indicates the overall transfer of ion beam current from 78° to 90° is transferred to the region between 34° and 78°. A negligible fraction of current migrates across the boundary at θ=34°, and suggests that the primary ion beam is approximately conserved within this angle for vacuum conditions at all downstream distances in the far-field plume. In a similar manner to the primary beam, the ion current from 16° to 34° is transferred to the region between 0° and 16° at all downstream distances. The variation of integrated vacuum ion beam current in the plume from 0° to 180° varied by less than 2% from the value at 8 CCDD.

4.4.3 Comparison of Ion Migration Results with Numerical Simulations

The experimental ion migration trends for vacuum conditions in Figure 4-35 are compared to preliminary numerical simulations[113] of the far-field plume using DRACO[114], an electrostatic Particle-In-Cell (PIC) module in COLISEUM.[115,116] DRACO uses a hybrid-PIC model of the plasma processes with a kinetic description of heavy particles and a fluid description for the electrons. Collisions are modeled with Monte Carlo Collision (MCC) methods[117,118] in a Cartesian mesh framework. DRACO supports the standard finite-difference PIC method and utilizes a Boltzmann field solver based on the assumption that the potential is directly related to the charge density. [119]

In these numerical simulations of the far-field plume, the ion source model is determined with a modified version of HPHall-2 using a three region mobility model.[120] HPHall-2 is an axisymmetric, hybrid fluid/PIC model of the Hall thruster discharge, where heavy particles are modeled with PIC methods[121] and electrons are modeled as a fluid.[122]

In this comparison of ion migration, elastic processes and CEX collisions with the background gas were not included in COLISEUM simulations of the far-field plume, and therefore the numerical simulations will be compared to the experimental vacuum profiles. Two simulations were performed in order to model the plume expansion, one with and one without CEX collisions with thruster neutrals. Comparisons of the experimental and simulated differences in vacuum ion beam current profiles relative to 8 CCDD are shown in Figure 4-36. While the ion current density profiles show significant discrepancies in plume structure, the differences in ion beam current per ring enable analysis of the ion migration in the far-field plume. Studies of the HPHall-2 source model indicate collisions with facility neutrals may influence the transport and plasma potential profile in the near-field plasma region.[120] The difference in potential profile between the ion source model and experiment are believed to be the cause of differences in the structure of ion migration in Figure 4-36.

Despite the differences in structure, the comparison of experimental and simulated results in Figure 4-36 reveals important details about Hall thruster plume expansion in a vacuum. Simulations including CEX collisions with thruster neutrals exhibited minimal difference from the simulations without CEX processes. The simulated results matched the experimental regions of minimal ion migration near θ=34° and θ=78°. In the simulation neglecting CEX collisions and elastic processes in the plume, the only source of ion migration is acceleration due to the external potential field structure. This indicates that far-field angular regions of constant vacuum ion beam current per ring may arise due to the external field, and CEX collisions with thruster neutrals play a lesser role within this half-angle and distance. This result is anticipated as

the density non-ionized thruster propellant decreases with downstream distance. If this is the case, characteristics of ion migration in the far-field plume are captured with the COLISEUM model despite possible differences in the near-field potential profile. This effect may be attributed to the fact that plasma potential gradients in the far-field plume are minimal compared to gradients in the near-field thruster plasma.

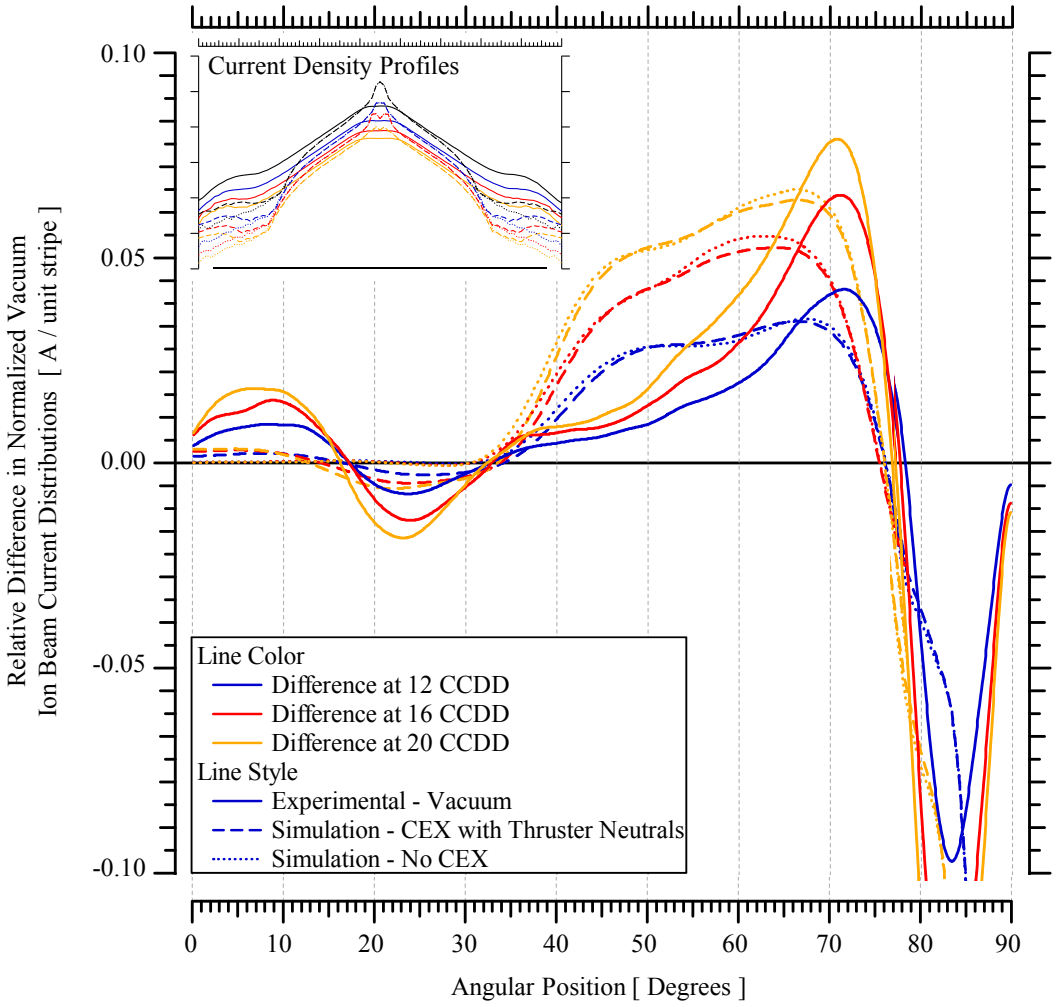

Figure 4-36 **Comparison of the simulated and experimental normalized differences in vacuum ion beam current at 12, 16, and 20 CCDD relative to the profile at 8 CCDD as a function of angular position. All profiles are normalized to the maximum extrapolated experimental vacuum beam current at 8 CCDD. The simulated and experimental normalized current density profiles are shown in the small window for reference.**

The simulation with CEX collisions recreated features of the experimental structure between θ=0° and θ=34°. The lack of structure within this region in the simulation without CEX collisions indicates this process may be related to CEX collisions with thruster neutrals. The mechanisms that result in the overall plume structure are not fully understood, and require additional simulation and analysis. This experimental analysis of ion migration in the Hall thruster ion source plume will be compared with plume measurements from the 6-kW thruster in Section 5.1.2.

4.4.4 Calculation of Vacuum Beam Divergence

This section will outline a method for determination of the vacuum ion beam divergence for incorporation in the Hall thruster efficiency architecture. To accurately assess plume divergence, it is necessary to characterize the migration of primary beam ions in the plume due to external fields and CEX collisions with anode and cathode neutrals. Although this scattering would be present on-orbit, beam divergence downstream of the primary ion acceleration zone where thrust is produced will cause an over-prediction of plume divergence losses in the Hall thruster efficiency architecture.

The systematic approach begins with the vacuum current density profiles described in Section 4.4.1. The axial component of these far-field distributions will be studied relative to the angle from channel centerline as opposed to thruster centerline. Figure 4-37 illustrates the reduction in plume divergence angle with respect to channel centerline, α_A, compared to the plume divergence angle with respect to thruster centerline, 90°-θ. The reference frame based on channel centerline reduces systematic error in plume divergence associated with beam ions in the central core, and is similar to

the methodology developed in Section 4.2 to reduce the systematic error of a point source measurement coordinate system.

In Figure 4-37, the cosine loss in beam current is fixed at α_A=0° in the central core and calculated with respect to channel centerline in the region beyond the central core to θ=90°. This piecewise function for α_A is expressed in Eq. 4-14.

$$\alpha_A[\theta, R, R_{CL}] = \begin{cases} \tan^{-1}\left(\dfrac{\cos(\theta) - \dfrac{R_{CL}}{R}}{\sin(\theta)}\right) & \text{for} \quad 0^\circ \le \theta \le \cos^{-1}\left(\dfrac{R_{CL}}{R}\right) \\ 0 & \text{for} \quad \cos^{-1}\left(\dfrac{R_{CL}}{R}\right) \le \theta \le 90^\circ \end{cases} \tag{4-14}$$

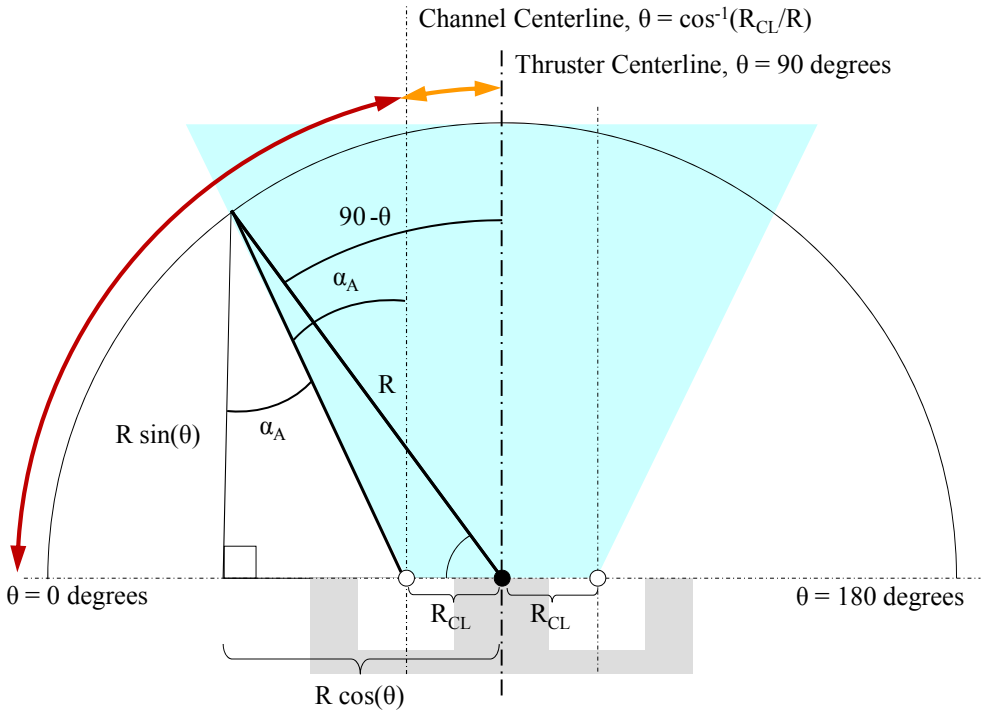

Figure 4-37 Diagram of the axial component of beam current relative to channel centerline.

The axial component of ion beam current is calculated in Eq. (4-15) using α_A, and includes the correction factors derived in Sections 4.2 and 4.3.

$$I_{Axial} = 2\pi R^2 \int_0^{\pi/2} \frac{I[\theta]\cos\left(\alpha_A[\theta, R, R_{CL}]\right)}{A_C + \kappa_G}\left(\frac{\kappa_D[\theta]}{\kappa_A[\theta]}\right)\sin(\theta)d\theta \tag{4-15}$$

The ratio of the axial component of ion beam current calculated in Eq. (4-15) relative to the total ion beam current determined from Eq. (4-12) is shown for all background pressures and all configurations of the nested Faraday probe in Figure 4-38. As downstream distance increases, the ratio decreases for all cases. This effect is expected from the analysis in Section 4.4.2, and is primarily attributed to divergence caused by the external potential field structure, CEX collisions with anode and cathode neutrals, and CEX collisions with facility neutrals for the profiles at finite background pressure.

The ratios of the axial component of ion beam current relative to the total ion beam current in Figure 4-38 are extrapolated as a 2nd order polynomial trend to the exit plane to more accurately assess the loss of divergence on thrust. While additional ion acceleration may occur further downstream, a majority of the thrust has been generated within one thruster diameter downstream of the discharge channel exit. Sixteen trendlines of I_{Axial}/I_{Beam} with respect to downstream distance correspond to the four probe configurations at four background pressures, including vacuum. All of the second order polynomial trendlines intersect at the exit plane value of ~0.94±0.01 for this thruster operating condition. This excellent agreement of four probe configurations over a wide range of facility background pressures and downstream distances indicates a high degree of accuracy and precision.

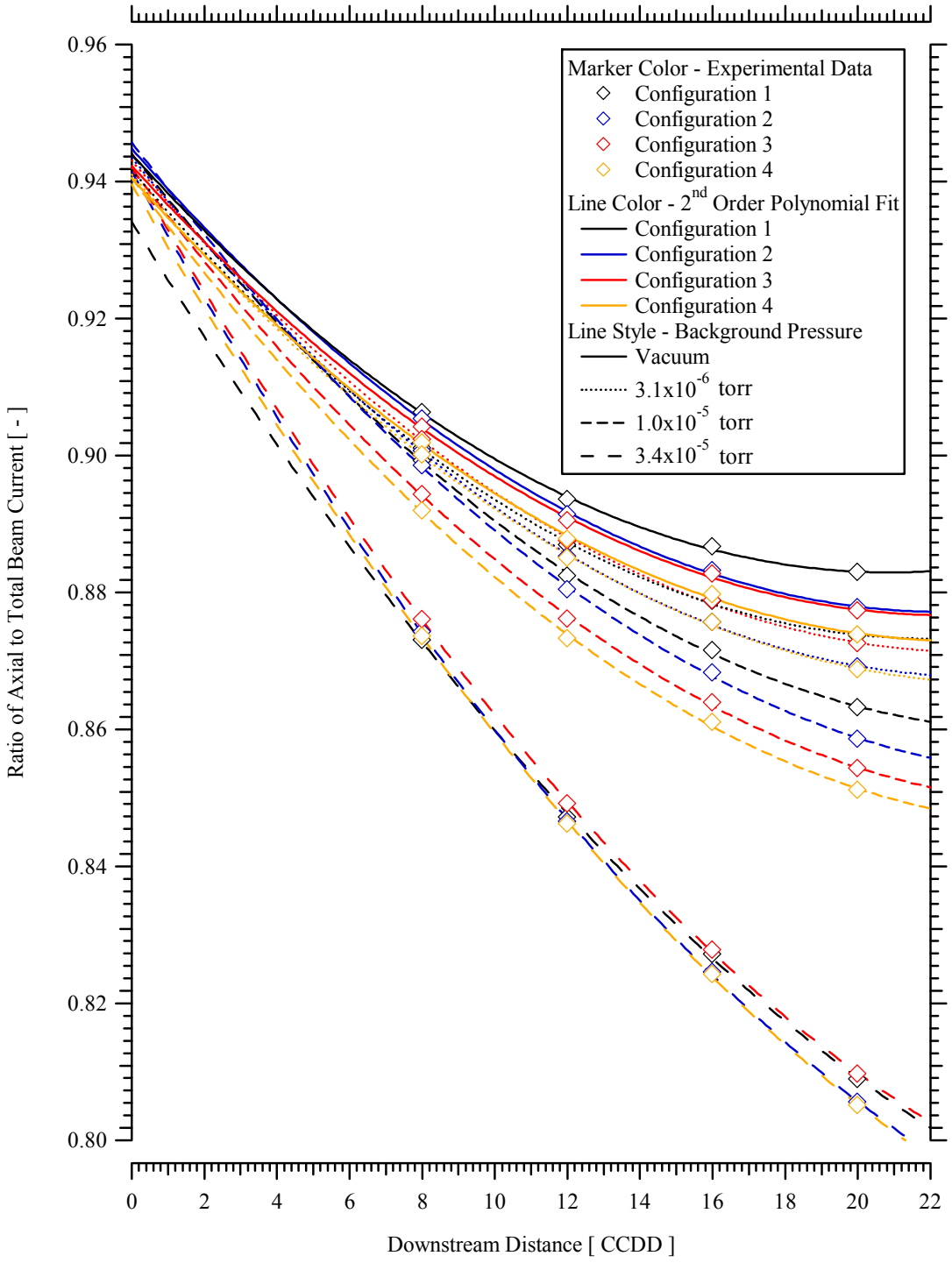

Figure 4-38 **Experimental data (markers) and 2nd order polynomial trendlines (lines) of the ratio of the axial component of ion beam current relative to the total ion beam current of the nested Faraday probe Configurations 1, 2, 3, and 4 as a function of downstream distance at background pressures of 3.1×10^{-6} torr, 1.0×10^{-5} torr, 3.4×10^{-5} torr, and the ratio extrapolated to vacuum. Experimental data deviates from the trendlines by less than ±0.1%.**

It should be noted that the ratio of I_{Axial}/I_{Beam} extrapolated to vacuum conditions showed a significant decline with downstream distance, albeit less than the reduction with increased facility background pressure. This reveals that a significant source of plume divergence is unrelated to facility effects. Based on these measurements, the ratio of I_{Axial}/I_{Beam} may diminish by more than 5% in the near-field plume before reaching a steady value in the far-field plume.

The coefficients of the 2nd order polynomial trendlines varied with background pressure. Further investigations also showed variations in the 2nd order polynomial coefficients with thruster operating conditions, although the excellent fit to a 2nd order polynomial was consistent. No universal function was found that correlated these coefficients to background pressure, discharge voltage, and mass flow rate. For a general 2nd order polynomial of the form $y(x)=A_2x^2+A_1x+A_0$, increased background pressure increased the coefficient A_1 and decreased the coefficient A_2. In this form, the coefficient A_0 is the ratio of the axial component of ion beam current relative to the total ion beam current at vacuum conditions.

Variations in the polynomial coefficients with discharge voltage and anode mass flow rate are more difficult to isolate and quantify due to the dependence on plume focusing and the location of ionization. Initial results indicate higher discharge voltage decreased the magnitude of both coefficients. This relationship is attributed to the more collimated beam that is typically seen during high-voltage operation.

The anode mass flow rate is believed to have two competing effects on divergence. Increased propellant flow rate corresponds to a narrower axial region of ionization and acceleration in the discharge, along with a more concentrated ion density

near channel centerline.[61] These effects lead to a decrease in divergence due to enhanced plume focusing, and would likely have a similar effect as discharge voltage on the polynomial coefficients. However, the increased neutral flow may also lead to increased CEX collisions with thruster neutrals downstream of the exit plane, thereby increasing ion scattering in the far-field plume.

A simple analytical model is deemed insufficient to fully characterize the influence of beam focusing and facility effects on plume divergence. Additional systematic investigations and numerical simulations with a high fidelity source model are required to determine these relationships.

4.5 Recommendations for High Accuracy Current Density Profiles

Based on the experimental results in Chapter 4, the best approach for high accuracy current density distributions is to characterize the plume with variations in facility background pressure and downstream distance. The analytical methods and experimental techniques described in Sections 4.2, 4.3, and 4.4 may be used to determine Hall thruster current density profiles and integrated ion beam current to a high degree of accuracy. In order to minimize measurement error of far-field Faraday probe measurements, the following guidelines are recommended for Faraday probe design, experimental approach, and analysis of results. Several of these guidelines are conventional practice or have been recommended in previous literature.[97,102]

1. Consider effects introduced by ion collection at the base of the gap volume when selecting a Faraday probe design. A ceramic base is recommended for investigations at variable or high background pressure.

2. Select a Faraday probe design with a 5 to 10 Debye length gap for a wide range of downstream distances and pressures. Select collector and guard ring material with minimal SEE coefficient, such as molybdenum, graphite, or tungsten.

3. Conduct Faraday probe current density measurements at a minimum of 3 facility background pressures to determine the vacuum current density profiles. The background pressures should range by at least one order of magnitude.

4. Conduct Faraday probe current density measurements at a minimum of 3 downstream distances to determine the axial component of ion beam current at the exit plane. For far-field measurements about a single axis of rotation using a spherical measurement coordinate system, the distance should be greater than 4 CCDD. For near-field measurements based on a cylindrical measurement coordinate system, spatial effects and cosine losses should be estimated and the maximum distance should be less than approximately one thruster diameter downstream using a dynamic window integration method[61] or similar technique.

5. Include the correction factors κ_A, κ_D and α_A to account for the point source measurement coordinate geometry and the annular thruster geometry.

6. Account for ions collected in the gap volume by increasing the effective ion collection area with κ_G.

7. For increased accuracy of far-field measurements, repeat Step 3 and Step 4 with 0 V and -30 V bias potential on the guard ring. Depending on conditions, the large negative bias potential may need to be adjusted to achieve minimum ion collection similar to Figures 4-18 and 4-19. For the case of 0 V on the guard ring, calculate the current density based on the combined projected geometric collector area and the total projected gap collection area (Area = $A_C + A_{Gap}$). For the case of -30 V on the guard ring, calculate current density based on the projected geometric collector area (Area = A_C). These measurements provide additional current density distributions using the same Faraday probe without venting the vacuum chamber between measurements. Consistent agreement between profiles is a sign of high accuracy distributions.

The guidlines provide a framework for determination of on-orbit current density profiles and minimize experimental measurement uncertainty. Following the recommendations in these guidelines is expected to minimize uncertainty in the total ion beam current to ±3% and the uncertainty in the axial component of ion beam current to ±5%. Ideally, the experimental current density profiles extrapolated to vacuum will enable comparison with numerical simulations in the absence of facility effects, thereby reducing the computational complexity and time.

Guideline 7 provides additional measurements that may be compared to the conventional measurement technique where the collector and guard ring are biased to the same potential. A probe meeting the 5 to 10 Debye length design criteria should result in

congruent current density profiles throughout the plume for each guard ring bias potential, and increases confidence in the accuracy of the gap correction factor.

Near-field measurements would seem to minimize the uncertainty associated with far-field measurements. However, these measurements introduce new difficulties, including perturbation of the plasma discharge, a wider range of Debye length in the measurement domain, and possibly SEE effects from the probe collector. In addition, ingestion and near-field CEX collisions with facility neutrals are expected to affect near-field measurements. Thus, the ion current density profiles should still be characterized for variations in distance and background pressure. A second set of spatial corrections for measurement geometry may also be necessary to reduce systematic error associated with cylindrical integration as distance from the exit plane increases.

4.6 Summary and Conclusions

The AFRL nested Faraday probe with two concentric collectors and an outer guard ring was designed and fabricated to investigate the effects of gap width and collection area on current density measurements in a Hall thruster plume. The probe was characterized over a range of background pressures and downstream distances to isolate effects specific to probe geometry. Correction factors accounting for variations in distance and angle of the Faraday probe collector surface to the ion beam were introduced through a theoretical analysis of the near-field plume with the Hall thruster modeled as two point sources. A gap correction factor was developed to adjust the effective probe collection area for ions collected by the walls in the gap volume. The correction is greatest for small collector areas with a large gap.

For nude Faraday probes of this design with a ceramic base, the gap correction factor is insensitive to background pressure and downstream distance from the thruster exit plane. A non-uniform bias potential was applied to the guard ring of the nested probe in 0.5 mm and 1.5 mm gap configurations, and showed the ability to collect nearly all of the ions in the gap volume on either the side wall of the guard ring or collector. Applying the correction factors to both the 0.5 mm and the 1.5 mm gap configurations resulted in equivalent plume profiles, total ion beam current, and plume divergence despite the 1.5 mm gap being 15-30 Debye lengths on thruster centerline. Thus, although the 1.5 mm gap configuration may introduce a non-uniform sheath over the Faraday probe collecting surface, the non-uniformity is primarily over the gap width and is accounted for by distributing the ions in the gap volume using the gap correction factor, κ_G.

The gap correction factor was applied to a past investigation comparing the JPL nude Faraday probe design with the GRC nude Faraday probe design. The GRC probe design is similar to the AFRL nested Faraday probe in that the base of the gap volume is a ceramic. At low background pressure, applying the gap correction factor to the GRC probe resulted in good agreement in total ion beam current compared to the JPL probe. Increased background pressure required application of the gap correction factor to both probes, and suggests the effective collection area of the JPL probe design is more sensitive to facility effects. This response is attributed to the conductive base in the gap volume of the JPL Faraday probe, and may complication characterization of facility effects over a range of distances and pressures.

Facility effects in this investigation were studied over a range of downstream measurement distances and background pressures for all nested Faraday probe configurations. The measured current density at each angular location in the plume was extrapolated to vacuum conditions, similar to past studies by Azziz[97] and deGrys[109]. Ion migration in the plume due to facility effects was studied and compared to plume expansion of the extrapolated vacuum current density profiles. This approach enabled a more accurate description of the on-orbit current density profiles using ground measurements. Variations in the ion current density with facility background pressure were studied as the superposition of two Gaussian curves. These curves provided qualitative information about the ionization of ingested neutrals and CEX collisions of facility neutrals in the near-field plume. Comparisons with numerical simulations indicate the primary beam had minimal ion migration beyond a fixed angular location at approximately ±55° from thruster centerline. This phenomenon may be a consequence of the external field structure of the Hall thruster ion source discharge.

The ratio of the axial component of ion beam current with respect to the total ion beam current was extrapolated with a 2nd order polynomial to the thruster exit plane, and resulted in consistent agreement to within 1% for all background pressures and probe configurations. Coefficients of the 2nd order polynomial fit varied with background pressure, thruster discharge voltage, and mass flow rate. The plume expansion requires additional investigation to accurately assess the loss of thrust due to ion beam divergence.

The experimental techniques and analytical methods in this investigation minimized facility effects and reduced the overall ion beam current by ~20%. Precision in total ion beam current measurements was within a 3% range for all nested Faraday

probe configurations after the corrections and facility effects were accounted for. Based on the results of this systematic investigation, the measurement uncertainty of Faraday probe ion beam current measurements is estimated as ±3% and the uncertainty in the axial component of ion beam current is estimated as ±5% when the recommendations in Section 4.5 are followed. The reductions in measurement uncertainty and the increased capability to approximate on-orbit plume expansion are a significant improvement for comparisons with numerical simulations and analysis of Hall thruster performance.

The far-field Faraday probe plume study of low discharge voltage Hall thruster performance in Chapter 5 and Chapter 6 was conducted at one downstream distance and five background pressures. Only one downstream distance was studied in Chamber 3 due to the limited range of measurement with respect to the chamber wall, and the furthest downstream distance was ~6 downstream thruster diameters. Thus, although the facility effects were accounted for, the ratio of I_{Axial}/I_{Beam} was not corrected for distance and is most likely under-predicted. This error will be discussed in Section 5.4. Since the axial component of ion beam current is only used for determination of the beam divergence in the Hall thruster efficiency architecture, the under-prediction will not affect calculations of energy efficiency or propellant efficiency. Divergence is considered to be the primary source of error in the efficiency analysis and will be discussed in further detail in the following chapter.

Chapter 5

Characterization of Low-Voltage Hall Thruster Operation

The loss mechanisms of low discharge voltage Hall thruster operation are investigated with an array of far-field plasma diagnostics, thrust measurements, and discharge oscillations. Performance characteristics of low-voltage operation are studied with the efficiency architecture developed in Chapter 2. Thruster utilization efficiencies will be related to plasma processes in the discharge to determine the dominant loss mechanisms inhibiting performance in the low-voltage Hall thruster operating regime.

In this chapter, nominal discharge voltage operation (300-V) is compared to intermediate (150-V) and low-voltage operation (120-V) for constant anode flow rate of 10-mg/s and 20-mg/s at 7-CFF. Thruster operation below 120-V discharge required increased cathode flow in order to optimize performance. Optimized performance at 120-V and 105-V are compared to the 7-CFF conditions, which established a framework for comparison of discharge voltage, anode mass flow rate, and cathode mass flow rate. The ten operating conditions are listed in Table 5-1. The data in this chapter is tabulated in Appendix B for vacuum conditions.

Table 5-1 Operating Conditions of the 6-kW Hall Thruster

Thruster Operating Conditions	
20-mg/s Anode Flow Operation	10-mg/s Anode Flow Operation
300-V, 20-mg/s, 7-CFF	300-V, 10-mg/s, 7-CFF
150-V, 20-mg/s, 7-CFF	150-V, 10-mg/s, 7-CFF
120-V, 20-mg/s, 7-CFF	120-V, 10-mg/s, 7-CFF
120-V, 20-mg/s, 16-CFF	120-V, 10-mg/s, 12-CFF
105-V, 20-mg/s, 16-CFF	105-V, 10-mg/s, 16-CFF

Facility effects on plume expansion are evaluated at nominal and low discharge voltage to study background neutral ingestion and near-field CEX collisions. Evaluation of facility effects was conducted for each operating condition at five background pressures by injecting neutral xenon behind and below the thrust stand at the base of the chamber. Magnetic fields were optimized for maximum thruster efficiency at each operating condition and held fixed as background pressure was varied.

During the course of low discharge voltage performance optimization, two operating regimes were discovered below 120-V corresponding to discontinuities in discharge current for small variations in operating parameters. Low discharge voltage optimization and physics of the operating regimes are the focus of Chapter 6.

5.1 Facility Effects on Thruster Performance and Beam Formation

Thrust and discharge current were recorded as a function of pressure to ascertain facility effects on thruster performance. Ion current density in the beam was measured at each background pressure to facilitate the plume analysis described in Chapter 4. In

Chamber 3, the maximum possible downstream distance was ~6 thruster diameters, and analysis of spatial measurement error in Section 4.2.1 indicated the minimum distance should be greater than 4 thruster diameters for spherical measurement coordinate geometry. In this investigation, far-field Faraday probe measurements were only taken at one downstream distance due to the limited range of measurement with respect to the chamber wall. Performance and plume expansion are analyzed to characterize differences in facility effects on nominal discharge voltage compared to low discharge voltage operation.

5.1.1 Thrust and Discharge Current

Variations in thruster characteristics with background pressure are shown in Figure 5-1 for 105-V and 300-V thruster operation. Experimental thrust and discharge current increased linearly with pressure. Extrapolation to vacuum conditions at 300-V, 20-mg/s resulted in thrust of 410 mN and discharge current of 20.5 A. Comparable performance was reported for this thruster model at the University of Michigan for vacuum conditions under equivalent operating conditions.[61] The values reported here are approximately 2.5% greater in thrust and 4.5% greater in discharge current. Differences are likely due to variations between thruster model reproductions and dissimilar magnet settings.

A model of the entrained facility neutral mass flow rate developed by Randolph[123] was adapted by Reid[61] for determination of thrust and discharge current with increased facility background pressure. In the adapted model by Reid, the entrainment area was approximated as a hemisphere encompassing the outer diameter of the thruster discharge

channel, and was used to estimate the entrained neutral mass flow rate as a function of pressure as shown in Eq. (5-1).

$$\dot{m}_{en} = A_{en}\, p\left(\frac{\mathscr{M}}{2\pi T_b k_b \mathscr{N}_A}\right)^{\frac{1}{2}} \tag{5-1}$$

This technique has adequately accounted for entrained neutral flow on this thruster during nominal discharge voltage operation[61], but appeared to underestimate the neutral entrainment area during low discharge voltage operation in this investigation. To remedy this effect, the effective area of ingested neutrals is scaled by a neutral entrainment area factor, ξ_A. In this analysis, the neutral entrainment area factor is evaluated at each operating condition to account for the increased discharge current over a range of facility background pressures. If all entrained neutral flow is ionized to Xe^+ ions, the vacuum discharge current may be calculated according to Eq. (5-2). This model is limited in that it accounts for all increases in discharge current as originating from ionization of ingested beam ions, and does not account for variations in electron current to the anode or multiply-charged ions. While a model based on variation in ion beam current in the plume may seem more appropriate, it is complicated by CEX collisions. For most Hall thruster operation, the increase in electron current to the anode is expected to be minimal, and will be resolved with the neutral entrainment area factor within the limited capability of this simple model.

$$I_d[p=0] = I_d[p] - \xi_A \dot{m}_{en}\left(\frac{\mathscr{F}}{\mathscr{M}}\right) \tag{5-2}$$

Thrust was estimated with Eq. (5-3) using the thrust entrainment factor[61], ζ_{en}, to account for ingested neutrals that are ionized and contribute to discharge current but

produce negligible directed thrust. When ζ_{en} is unity, all of the ingested neutrals that are ionized contribute to useful thrust.

$$T[p=0] = T[p]\left(1-\zeta_{en}\frac{\xi_A \dot{m}_{en}}{\dot{m}_T + \xi_A \dot{m}_{en}}\right) \tag{5-3}$$

This model of neutral ingestion is used to estimate macroscopic facility effects on performance, and highlight similarities and distinctions between experiments at AFRL and the University of Michigan. In this investigation, the neutral entrainment area factor is determined based on Eq. (5-2) for a given operating condition, such that the discharge current at all facility background pressures is approximately equal to the value extrapolated to vacuum conditions. This value of the neutral entrainment area factor is incorporated into Eq. (5-3), and an analogous iterative approach is used to determine the thrust entrainment factor.

The model shows good agreement with the vacuum extrapolated values of thrust and discharge current in Figure 5-1 for the 300-V and 105-V operating conditions. The area entrainment factor was unity for 20-mg/s operating conditions, and was therefore equivalent to the model used by Reid. The thrust entrainment factor is approximated as ζ_{en}=0.5 for nominal 300-V, 20-mg/s operation, which is consistent with the value reported for this operating condition at PEPL.[61]

The 300-V, 10-mg/s case exhibited different characteristics in the entrainment area factor and the thrust entrainment factor, corresponding to an extremely large entrainment collection area with minimal useful thrust generated by ionized facility neutrals. This may signal that the thruster sphere of influence extends further downstream for the lower anode flow rate operating condition, and therefore the near-

field ionization of facility neutrals has a much larger effect on discharge current. A second possibility is the creation of multiply-charged ions. However, this process is more likely during the 20-mg/s anode mass flow rate operation since the neutral density is larger, and hence the electron-neutral and electron-ion collision frequency is increased. A final consideration is increased electron current to the anode as the ionization of facility neutrals escalates with background pressure. This scenario is possible and warrants further investigation, but is beyond the scope of these experimental measurements. The discussion of low discharge voltage operating regimes in Chapter 6 will further characterize facility effects and near-field neutral density on Hall thruster discharge physics.

During 105-V operation, the neutral entrainment area factor was estimated as ξ_A=1.2 and ξ_A=1.0 for 10-mg/s and 20-mg/s operation, respectively. Thus the lower anode flow rate operation likely corresponded to larger effective collection area of entrained neutral flow. The thrust entrainment factor of the 105-V conditions was approximated as ζ_{en}=1.0 and ζ_{en}=0.8 for 10-mg/s and 20-mg/s operation, respectively. This value indicates that most of the ingested neutral flow ionized within the approximately hemispherical collection area contributes to thrust and is ionized downstream of the primary region of ion acceleration.

The linear increase in thrust and discharge current with background pressure was evident for all operating conditions listed in Table 5-1. The experimental parameters E_1 and E_2 allow a more detailed analysis of the overall effect of background pressure on total thruster efficiency for the operating conditions in Figure 5-1.

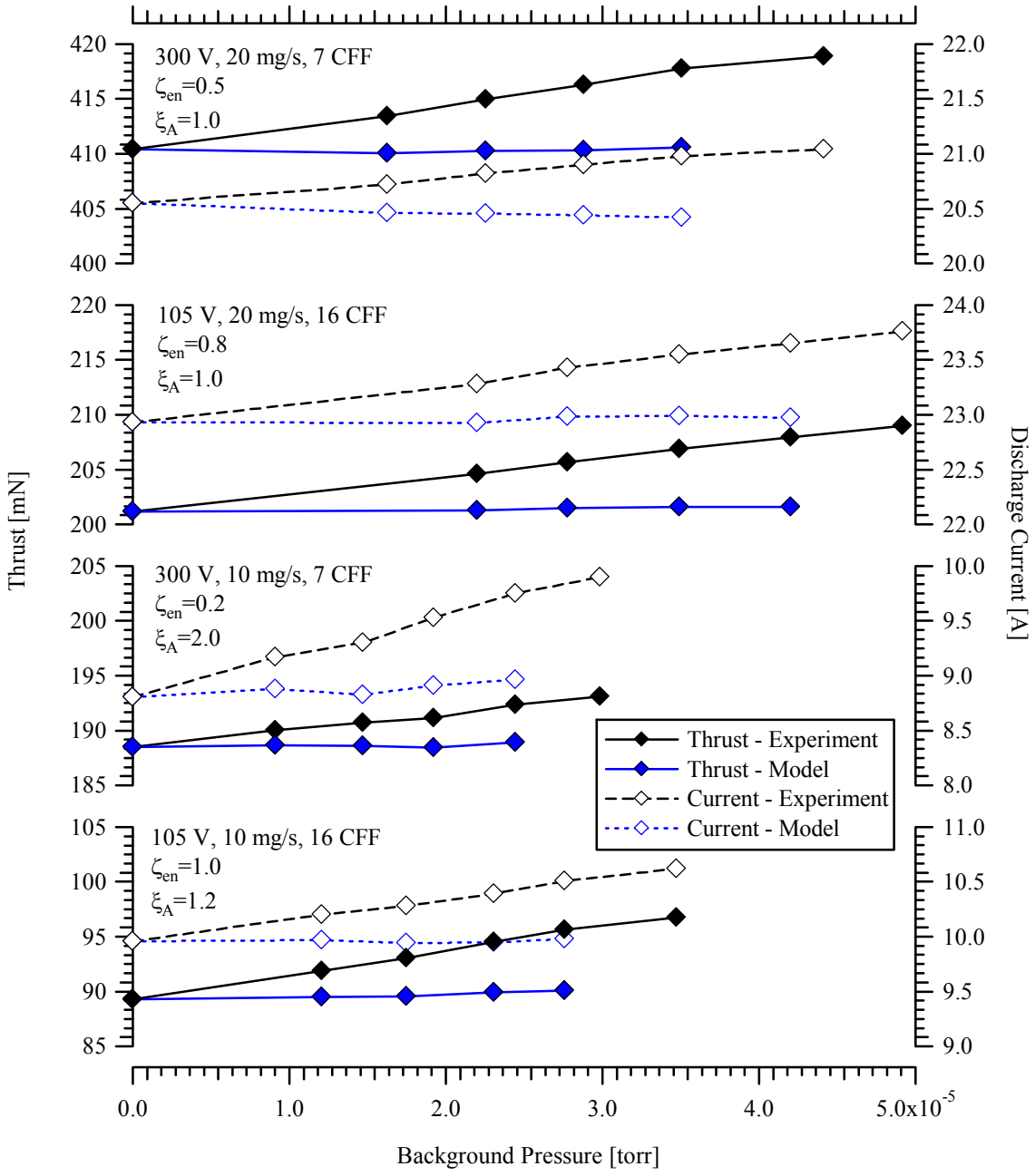

Figure 5-1 **Experimental and modeled thrust and discharge current of the 6-kW Hall thruster as a function of facility background pressure for 300-V, 7-CFF and 150-V, 16-CFF operation at 10-mg/s and 20-mg/s anode flow rate.**

In Figure 5-2, the parameters $E_1 \sim T^2$ and $E_2 \sim I_d^{-1}$ illustrate how high facility pressure increased efficiency for all cases in Figure 5-2, with the exception of the 300-V, 10-mg/s operating condition. At 300-V, 10-mg/s, the total thruster efficiency increased from η_T=0.59 at p=3.0x10^{-5} torr to the extrapolated value at vacuum of η_T=0.63. Taken with the trends in Figure 5-1, the 300-V, 10-mg/s operating condition is influenced in a different manner than the other operating conditions. This difference highlights the importance of characterizing facility effects on thrust and discharge current for each thruster operating condition. The 150-V operating conditions, which are not shown in Figures 5-1 and 5-2, exhibited negligible variation in efficiency with pressure due to a balanced increase in thrust and discharge current.

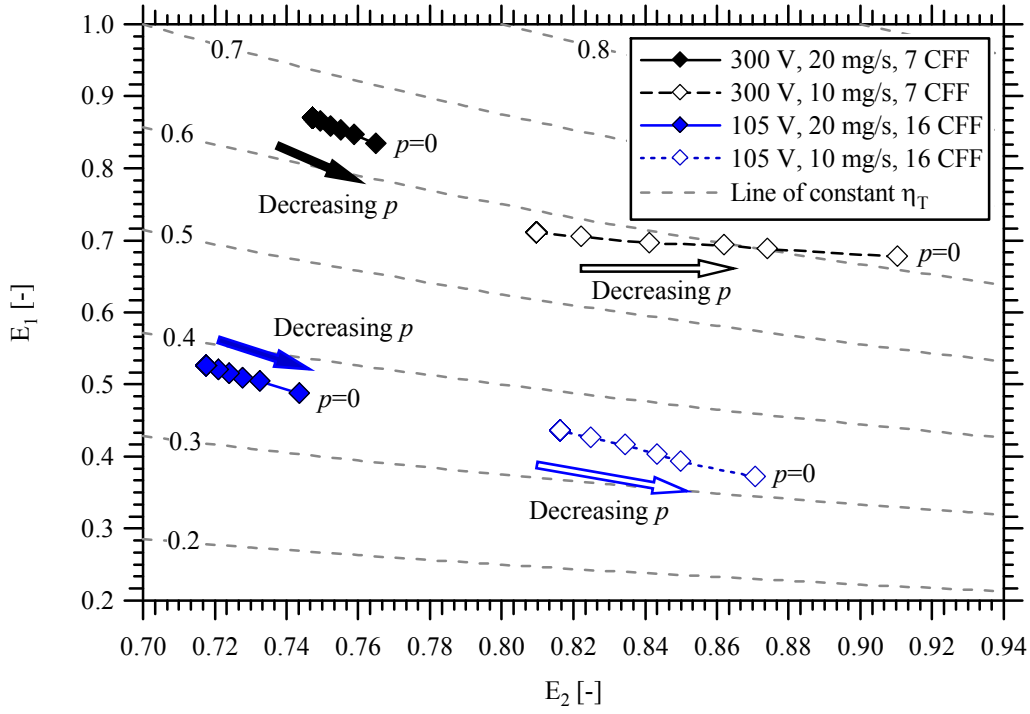

Figure 5-2 **Experimental parameters E_1 and E_2 with increasing background pressure for 300-V, 7-CFF and 150-V, 16-CFF operation at 10-mg/s and 20-mg/s anode flow rate. Arrows of decreasing pressure illustrate facility effects on total thruster efficiency, and extrapolated vacuum conditions are labeled as p=0.**

5.1.2 Ion Current and Plume Expansion

The effect of increased facility background pressure on formation and expansion of the ion beam is shown in Figure 5-3 for 300-V and 105-V operation at 20-mg/s. A highly collimated beam is formed during 300-V operation, whereas a more divergent beam is produced during 105-V operation. Differences in the plume structures on the periphery of the plume in the higher voltage case are typically attributed to ionization and acceleration further upstream in the discharge channel. Performance losses associated with increased divergence of low discharge voltage conditions will be discussed in Section 5.4.2.1.

The angular distributions of ion current density and ion beam current are extrapolated to vacuum conditions for the 300-V, 10-mg/s and 20-mg/s cases in Figure 5-4 and for the 105-V, 10-mg/s and 20-mg/s cases in Figure 5-5. The 105-V and 300-V vacuum current density profiles showed increased magnitude at 20-mg/s compared to 10-mg/s, but only minor difference in contour for constant discharge voltage operation.

The angular distribution of ion beam current per unit stripe at vacuum conditions is subtracted from the angular ion beam current distribution at each background pressure in order to feature the angular regions where increased facility background pressure alters the Hall thruster plume. The angular differences in ion beam current per unit stripe reveal several distinct features between the profiles of the 105-V and 300-V operating conditions. Although the 105-V conditions were operated at a higher pressure, the magnitude of the difference in angular ion beam current migration was consistently larger for the 300-V cases on the wings and in the central core.

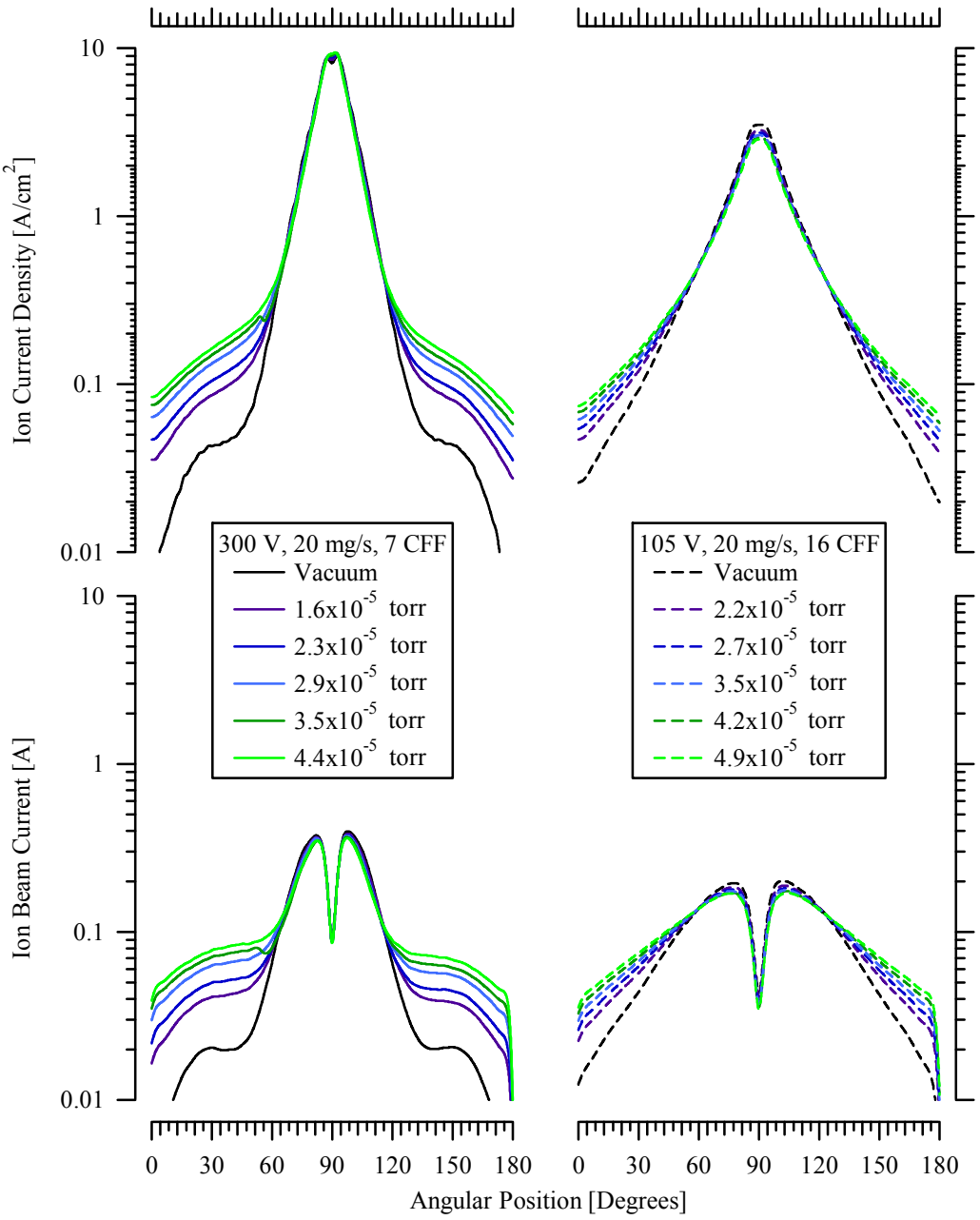

Figure 5-3 **Angular distributions of ion current density (top) and ion beam current (bottom) with increasing background pressure for 300-V, 7-CFF and 150-V, 16-CFF operation at 20-mg/s anode flow rate.**

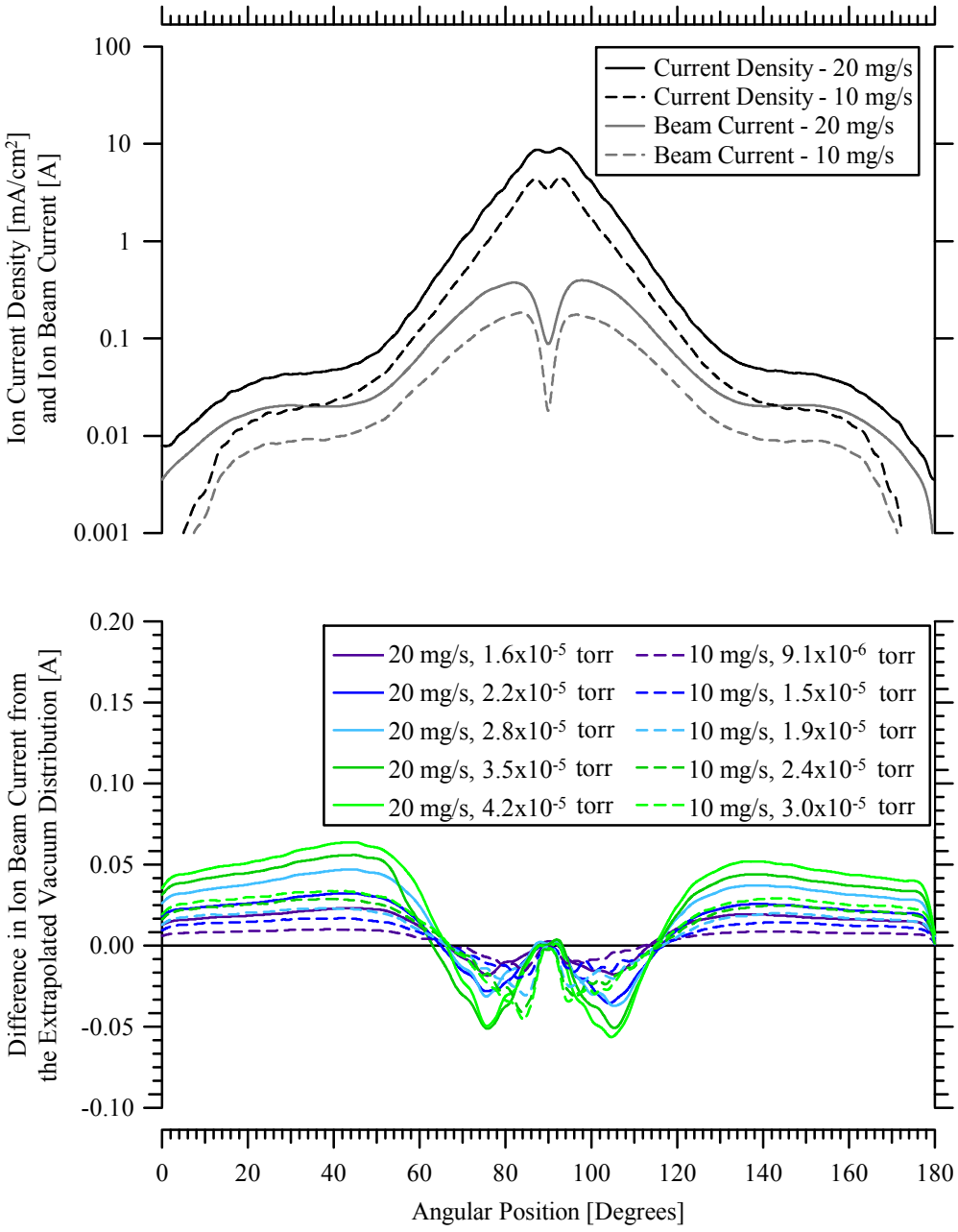

Figure 5-4 **Angular distributions of current density and ion beam current extrapolated to vacuum (top) and the angular difference in ion beam current from vacuum (bottom) with increasing background pressure for 300-V, 7-CFF at 10-mg/s and 20-mg/s anode flow rate.**

At 300-V for both the 10-mg/s and 20-mg/s conditions in Figure 5-4, the ion beam current per unit stripe was constant at approximately ±26° from thruster centerline. This is evident in the consistent intersection of the distributions through zero at this angle. A similar pattern is seen with increasing background pressure in Figure 5-5 for the 105-V operating conditions. However, the invariant central core of the 105-V, 20-mg/s case was located further from thruster centerline than the 105-V, 10-mg/s case. Ion beam current of the 20-mg/s anode mass flow rate was constant at approximately ±30° from thruster centerline, compared to approximately ±20° during 10-mg/s anode mass flow rate operation. Increased facility background pressure decreased the ion beam current within this central core and increased the ion beam current outside this region.

An angular region of constant ion beam current per unit stripe with increasing background pressure seen in Figure 5-4 and 5-5 is similar to the phenomena seen in Figure 4-36 for the angular region of constant vacuum ion beam current per unit stripe with increasing downstream distance. Although the 6-kW thruster studied Chapter 5 and the low-power Hall device studied in Chapter 4 exhibited similar plume characteristics, a distinct difference exists since the 6-kW thruster exhibited this angular region of constant ion beam current per unit stripe with increasing background pressure. The low-power Hall thruster did not follow this trend with pressure, as shown in Figure 4-33. In Chapter 4, comparison of experimental current density measurements with plumes simulated in COLISEUM indicated this effect may be a function of the external potential field profile in the plume. A hypothetical explanation of these differences will be outlined based on the discussion in Section 4.4.2, under the assumption that the external fields in the thruster are not affected by background pressure.

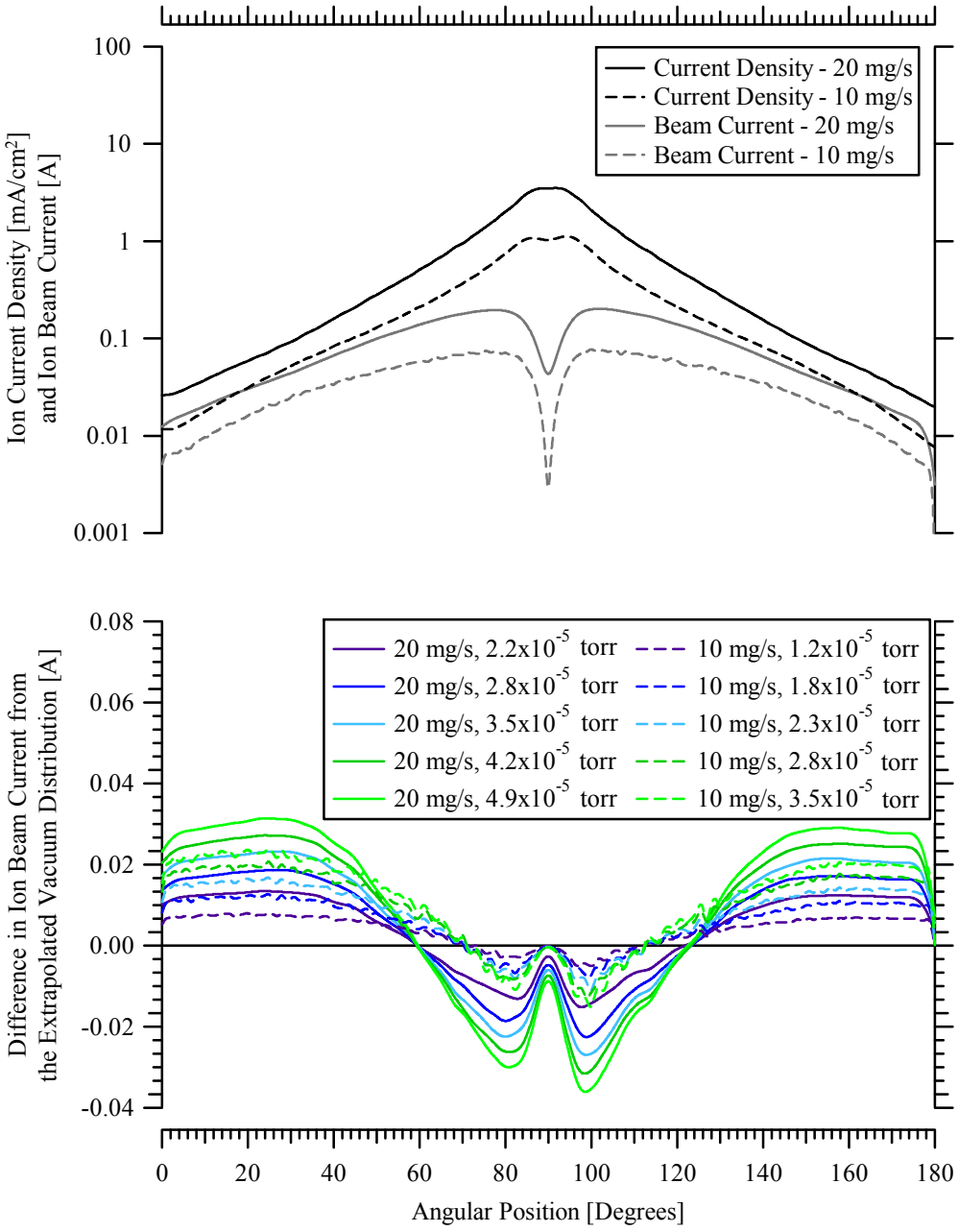

Figure 5-5 **Angular distributions of current density and ion beam current extrapolated to vacuum (top) and the angular difference in ion beam current from vacuum (bottom) with increasing background pressure for 105-V, 16-CFF at 10-mg/s and 20-mg/s anode flow rate.**

It is hypothesized that these differences stem from the location of ionization of ingested facility neutrals and CEX collisions with facility neutrals relative to the primary acceleration zone. In the case of the low-power Hall thruster ion source in Chamber 1, variations in the location of these facility effects with increasing neutral density would alter the acceleration of ionized facility neutrals by the external fields. If the low-power ion source has significant acceleration occurring in the near-field plume, the change in the creation point of ionized facility neutrals and the subsequent acceleration in the external field would alter the ion migration pattern as a function of background pressure. Thus, the magnitude of ionized facility neutrals and the angular locations of ion migration are affected by facility background pressure, as shown in Figure 4-34. These concepts are illustrated in Figure 5-6.

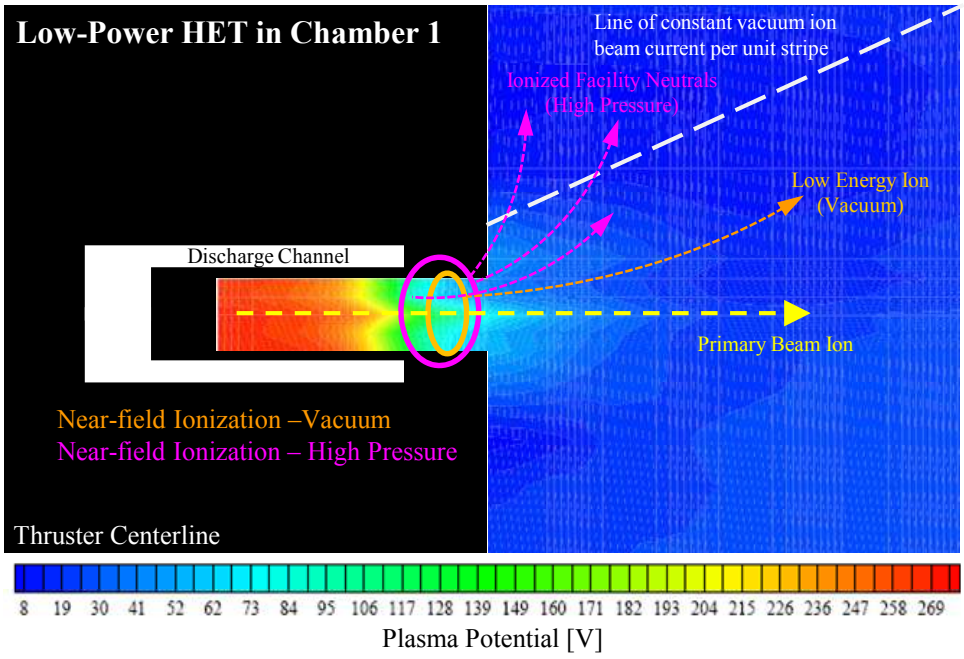

Figure 5-6 **Illustration of facility effects on the low-power Hall thruster in Chamber 1. Increased pressure alters the location of ionization of facility neutrals near the thruster exit and varies the effect of the external potential field on ionized facility neutral. Potential field contours from the near-field of the P5 HET[60] are included to display a characteristic external figure structure.**

The vacuum conditions studied in Chapter 4 have isolated and removed facility effects, and far-field plume expansion is primarily caused by CEX collisions with thruster and cathode neutrals. Under these vacuum conditions, the external field structure will influence the angular region in the far-field plume where the beam current per unit stripe is constant. In the far-field plume, ions will travel parallel to the line of constant beam current per unit stripe, and the net ion transport from CEX collisions entering this region from the central core is balanced by the ion flux exiting into the periphery.

The 6-kW Hall thruster in this study exhibited angular regions of constant ion beam current per unit stripe as facility background pressure was increased. Based on the previous hypothesis, this trend would indicate the locations of ionization and acceleration of facility neutrals is relatively constant with background pressure. Therefore, ionized facility neutrals see a similar external field regardless of background neutral density. As a result, the influence of the external field structure on the angular region in the far-field plume where beam current per unit stripe is constant will not change with background pressure. These concepts are illustrated in Figure 5-7.

Far-field measurements of this thruster at several distances would be expected to demonstrate an equivalent region of constant beam current per unit stripe, since the magnitude and gradients of the external field diminish with distance. Internal measurements of the 6-kW thruster operating at 300-V demonstrated the regions of ionization and acceleration occur within a few millimeters downstream of the exit plane, and the electron temperature sharply declined within this region.[61] These measurements are consistent with the stated hypothesis that facility neutrals are ionized and accelerated within a narrow region of the discharge in this thruster. Thus, the narrow width and

constant nature of the location of ionized facility neutrals causes an invariant angular location of ion beam current per unit stripe in the plume.

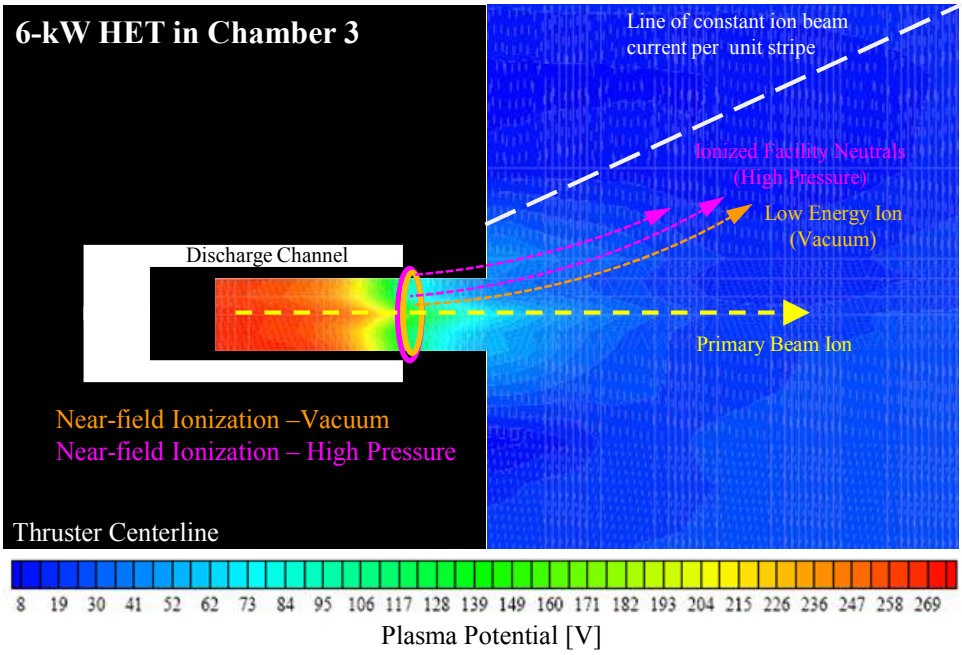

Figure 5-7 **Illustration of facility effects on the 6-kW Hall thruster in Chamber 3. Increased pressure has minimal effect on the location of ionization of facility neutrals near the thruster exit. Potential field contours from the near-field of the P5 HET[60] are included to display a characteristic external figure structure.**

Discharge oscillations of the breathing mode would also be expected to vary the location where facility neutrals are ionized. Oscillation measurements in Section 5.2.3 will demonstrate that oscillations are typically within ±10% of the discharge current with a breathing mode frequency of approximately 12-kHz at nominal 300-V, 6-kW conditions. Therefore, it is not unreasonable to venture that the variation in location of ionized facility neutrals is small during the predator-prey ionization processes.

The slope and residuals of the Faraday probe ion current density linear extrapolation to vacuum conditions are studied in Figure 5-8 to evaluate the ion plume

expansion of all operating conditions listed in Table 5-1. The locations of minimum residuals correspond to regions of approximately zero slope. Residuals of the 105-V and 300-V operating conditions in Figure 5-8 correspond to the angular locations of constant ion beam current per unit stripe in Figure 5-4 and Figure 5-5. Decreased residuals during 150-V and 300-V operation were located at approximately ±25° from thruster centerline for the 10-mg/s and 20-mg/s conditions. The minimum residuals of the 120-V, 7-CFF operating conditions were positioned at approximately ±21° from thruster centerline, and were equivalent to the location of minimum residuals for the 120-V, 10-mg/s, 12-CFF conditions. Increasing the cathode flow rate during 120-V, 20-mg/s operation increased the angular location of minimum residuals with respect to thruster centerline. These angular regions of minimum residuals, constant ion beam current per unit stripe, and approximately zero slopes are all attributed to the location of facility ion creation and external field effects, where the net ion transport of CEX ions entering this region from the central core is balanced by the ion flux exiting into the periphery.

The slopes of the extrapolated ion current density in Figure 5-8 provide a second source of information about neutral ingestion and beam scattering due to CEX collisions near the thruster exit. The slopes are modeled as the superposition of two Gaussian distributions related to facility effects in Figure 5-9. The first leads to a positive increase in the slope about thruster centerline, and is attributed to ionization and acceleration of ingested facility neutrals. CEX processes with facility neutrals within the discharge channel may also lead to increased current density in the central core, but would not increase ion beam current or discharge current.

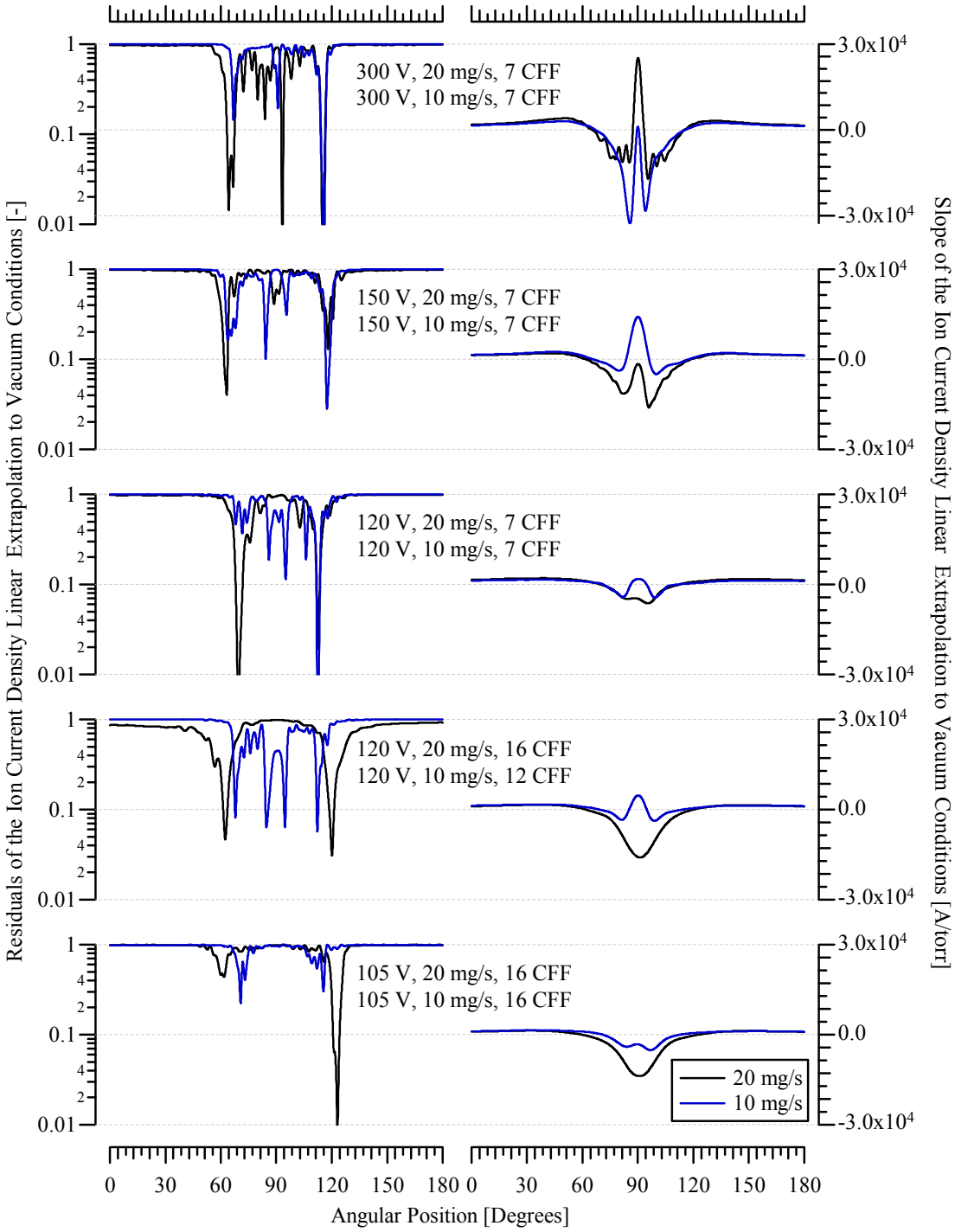

Figure 5-8 **Angular distributions of the residuals (left) and slope (right) of the ion current density linear extrapolation to vacuum conditions for the 105-V, 120-V, 150-V, and 300-V discharge at 10-mg/s and 20-mg/s anode flow rate.**

The second effect leads to a negative slope in the central core about thruster centerline, and is a feature of CEX collisions with facility neutrals near the thruster exit downstream of the primary acceleration zone. In this case, no additional current is created and the primary ion beam is dispersed. The outer edge of this distribution corresponds to the location of minimum residuals at each operating condition. Section 4.4.1 provides additional details about these populations and facility effects.

Facility effects are studied with fitted Gaussian curves in Figure 5-9, and the superposition is compared to the slope of experimental data. The hypothesis of facility effects and the excellent agreement of experimental data with the fitted Gaussian curves in Section 4.1.1 enable further analysis of the differences between nominal 300-V and low discharge voltage operation.

The Gaussian curves attributed to ionization of ingested neutrals decreased in magnitude and increased in width as discharge voltage was reduced from 300-V to 120-V at constant 7-CFF operation. These trends indicate ingested facility neutrals are ionized less frequently and possibly over a wider range of the potential field during low discharge voltage operation. The widths are relatively constant between 10-mg/s and 20-mg/s anode flow and the magnitude is slightly larger for the 10-mg/s conditions for a constant discharge voltage. Increased cathode flow at 20-mg/s resulted in a negligible increase in slope attributed to facility neutrals. However, the slope due to ingestion of neutrals was evident for 105-V and 120-V conditions at 10-mg/s. It is possible the near-field pressure of the higher anode flow rate operation minimized ingestion of facility neutrals and decreases the effect.

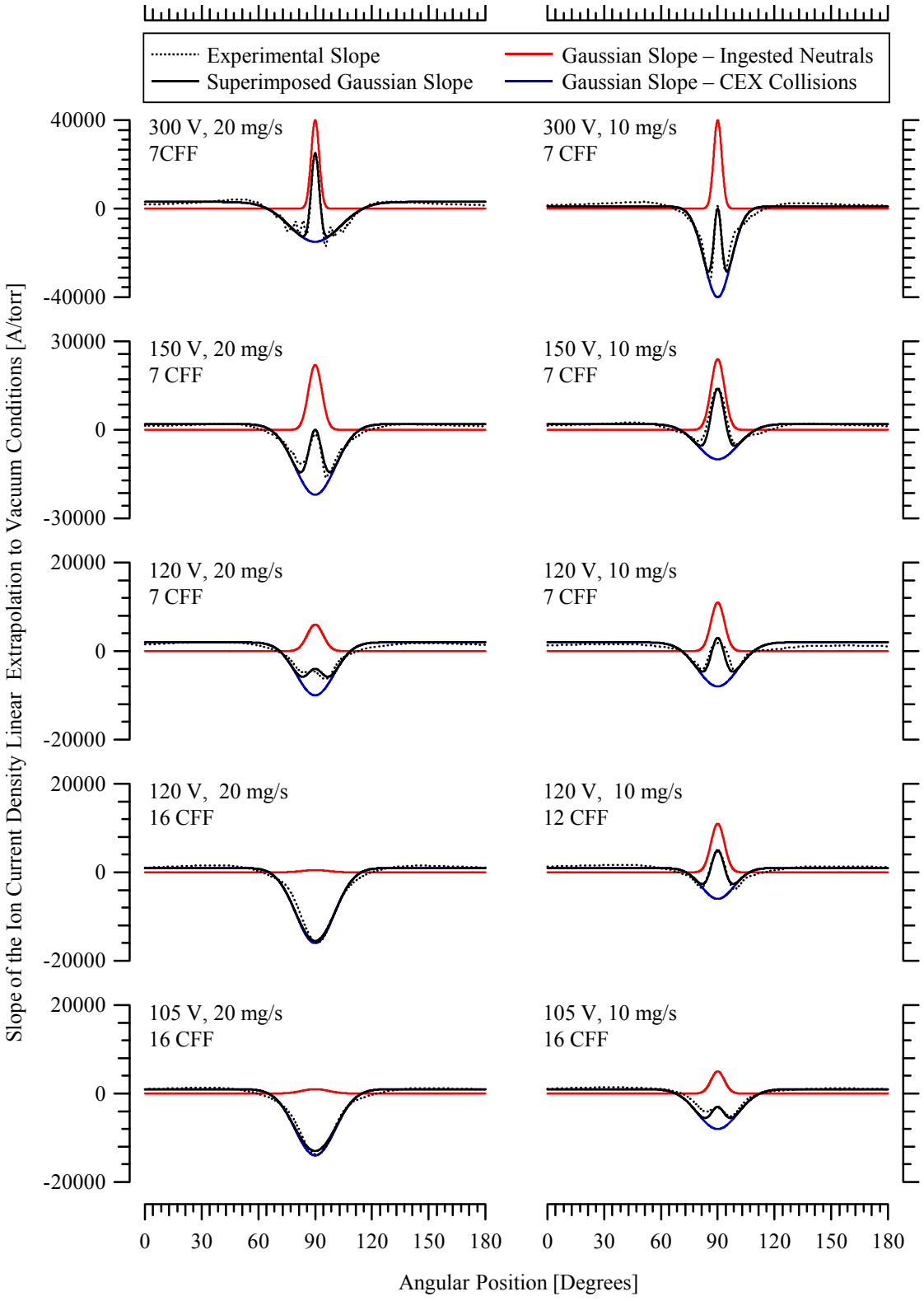

Figure 5-9 **Angular distributions of the slope of the ion current density linear extrapolation to vacuum condition for experiment and a superposition of Gaussians at 20-mg/s (left) and 10-mg/s (right) anode flow rate.**

The increase in thrust due to ingested facility neutrals was estimated with the neutral entrainment factor in Section 5.1.1. This value was greater at 105-V compared to 300-V and greater at 105-V, 10-mg/s anode flow than 105-V, 20-mg/s anode flow. The difference with discharge voltage is likely caused by the regions of ionization and acceleration occurring further downstream in the low-voltage case. While the 300-V operating conditions show a larger magnitude slope due to ingested neutrals, this population contributes less to the overall thrust since the facility ions are created further downstream of the acceleration region and have a larger dispersion.

The ionization of ingested neutrals decreased during high CFF operation at low discharge voltage. This may be the result of anode propellant ionization occurring further upstream or closer to the discharge channel centerline during increased cathode flow rate operation. The reduction of ingested neutrals would lead to a higher density of facility neutrals near the thruster exit and lead to increased plume dispersion as a result of CEX collisions with these particles. Thus in the absence of facility effects, increased cathode flow should decrease plume divergence during low discharge voltage operation. This hypothesis will be further analyzed in Section 5.4.2.1, where increased CFF during low discharge voltage operation will be shown to decrease plume divergence.

Effects of CEX collisions with facility neutrals near the thruster exit do not show a clear trend with discharge voltage or anode mass flow rate for 7-CFF operation. The Gaussian curve attributed to CEX collisions exhibited a slight increase in width as discharge voltage was decreased. However, differences emerge as cathode flow rate is increased above 7-CFF at 120-V operation. The 120-V, 20-mg/s, 16-CFF case displayed an increase in magnitude of the Gaussian curve, whereas the 120-V, 10-mg/s, 12-CFF

case resulted in a decrease in magnitude and width. Changes in the Gaussian slope attributed to facility CEX collisions at 105-V and 120-V may be related to the near-field pressure and the location of beam ion acceleration, both of which are expected to vary with anode and cathode flow rate.

Faraday probe measurements of ion beam current and the axial component of ion beam current for 300-V and 105-V cases are shown as a function of background pressure in Figure 5-10 with the experimental discharge current from Figure 5-1. The ion beam current increased with background pressure while the axial component of ion beam current is relatively constant 1-meter downstream in the far-field plume. The increase in ion beam current at 300-V is much greater than the increase in discharge current, and suggests a significant fraction of the beam current was created outside of the thruster sphere of influence. Study of the axial component of ion beam current is complicated by dispersion caused by CEX collisions near the thruster exit, and the methods developed in Section 4.4.4 are not possible with only one downstream measurement location. An estimate of the axial component of ion beam current and the divergence loss at the exit plane will be calculated using the difference in total efficiency from thrust measurements and plume measurements.

The results in this section illustrate the importance of characterizing facility effects for far-field plume measurements. Internal and near-field measurements would also be affected by ingestion and by CEX collisions with facility neutrals within the thruster sphere of influence. This phenomenon may be present in the near-field current density measurements using this thruster model at the University of Michigan[61] and at JPL[88]. These investigations found the near-field ion current density peaked downstream

of the primary ionization and acceleration zone. Therefore, performance and plume characterization with variations in background pressure and distance is highly recommended for all Hall thruster investigations.

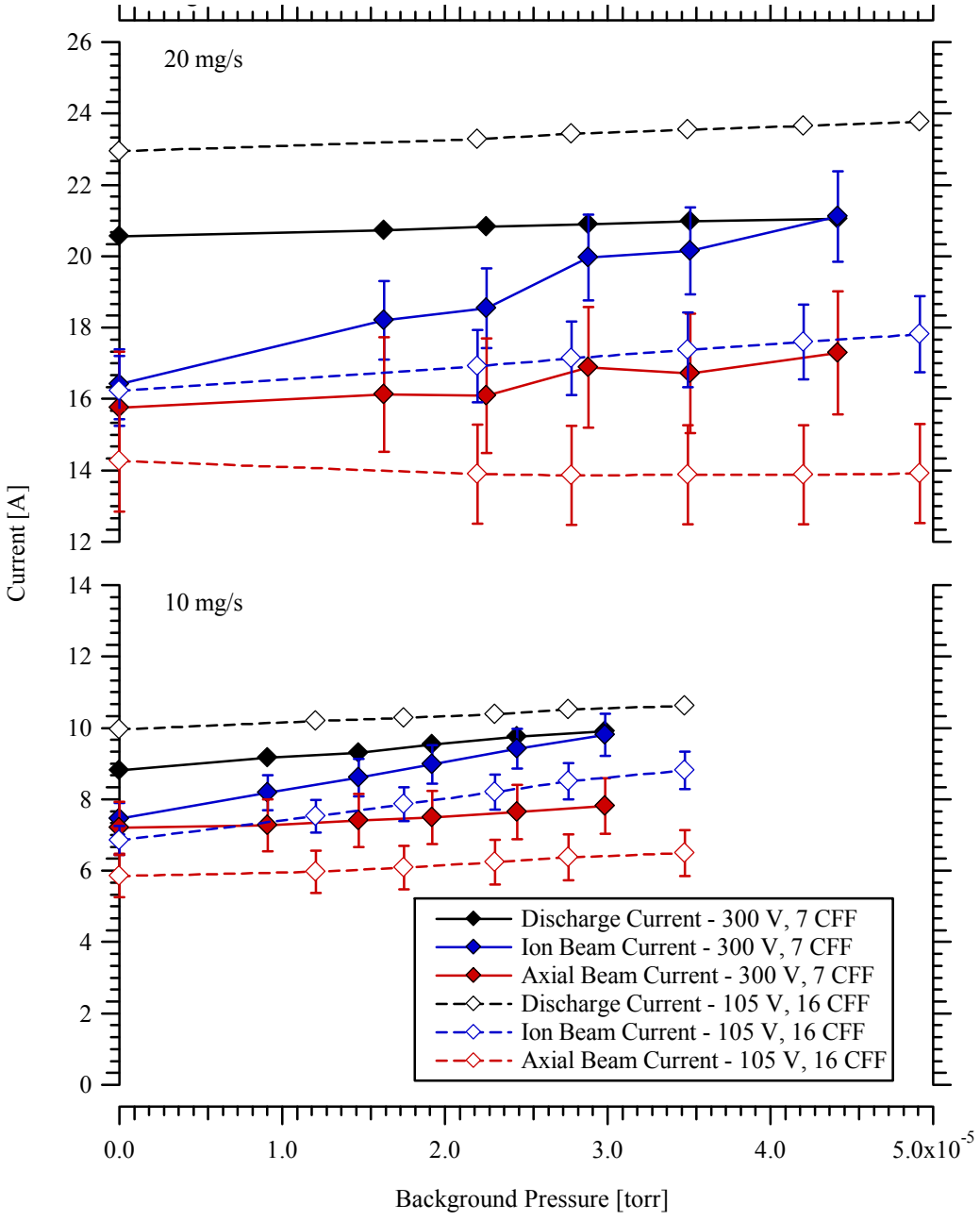

Figure 5-10 Discharge current, ion beam current, and the axial component of ion beam current with increasing background pressure for 300-V, 7-CFF and 150-V, 16-CFF operation at 10-mg/s and 20-mg/s anode flow rate.

5.2 Thruster Performance Measurements

Low discharge voltage Hall thruster operation is characterized with measurements of thrust, discharge current, and an array of plume diagnostics. All reported values of thrust, discharge current, and far-field current density profiles have been extrapolated to vacuum conditions using the techniques described in Section 5.1. Facility effects are expected to be minimal on far-field ExB, RPA, and Langmuir probe measurements. These diagnostics were only employed at the lowest facility operating pressure. However, variations in thruster operation due to ingestion and near-field CEX collisions with facility neutrals were not characterized, and may contribute to increased error in the reported values of most probable ion acceleration potential and average ion charge.

5.2.1 Current-Voltage Characteristics

The thruster I-V characteristics at vacuum conditions are shown in Figure 5-11 for constant anode flow operation at 10-mg/s and 20-mg/s. The thruster magnetic field and cathode flow rate were optimized for maximum total efficiency at the lowest background pressure. Discharge current decreased with increasing discharge voltage, which is typical for high-performance Hall thrusters operating below 300-V. At 120-V, 20-mg/s operation the increase in cathode flow rate from 7-CFF to 16-CFF caused a 5% increase in discharge current. A similar increase in CFF at 120-V, 10-mg/s caused a negligible variation in discharge current. Calculations of ion beam current in Section 5.3.1 will be used to assess whether this variation is due to an increase in ion current or a rise in electron current to the anode.

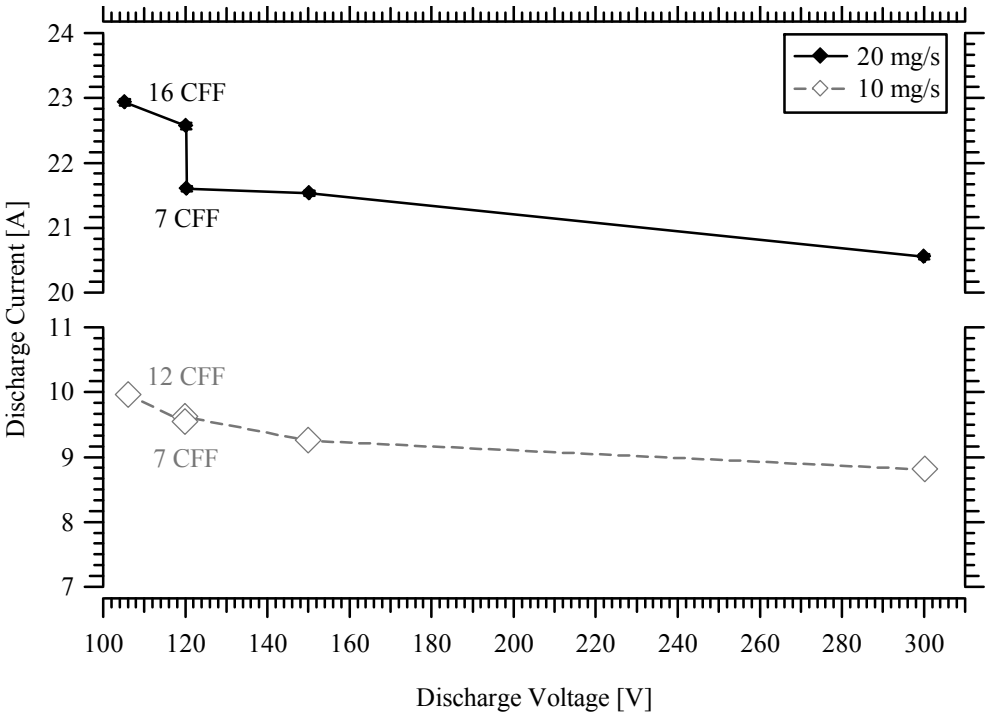

Figure 5-11 Thruster discharge current extrapolated to vacuum conditions as a function of discharge voltage from 105-V to 300-V at constant 10-mg/s and 20-mg/s anode flow rate.

5.2.2 Thrust and Performance

Measured thrust extrapolated to vacuum conditions is shown in Figure 5-12 for constant anode flow operation at 10-mg/s and 20-mg/s. Thrust increased with mass flow rate and the square root of discharge voltage according to Eq. (2-2). The increase in cathode flow rate at 120-V corresponded to a 9% increase in thrust along with the 5% increase in discharge current.

Performance trends are shown in Figure 5-13 as a function of discharge voltage, and reveal a 3 mN/kW increase in T/P at the 120-V, 20-mg/s, 16-CFF condition. The increase in cathode flow from 7-CFF to 16-CFF during 120-V, 20-mg/s operation also corresponded to a 1.5% increase in total thruster efficiency while total Isp was constant at 1040 seconds. The 120-V, 10-mg/s case exhibited a 2 mN/kW increase in T/P and

constant total efficiency with increased cathode flow from 7-CFF to 12-CFF. Total thruster efficiency and total specific impulse were greater for the higher anode mass flow rate operation at a given discharge voltage. Total thruster efficiency and total Isp did not reach a maximum over the discharge voltages in this data set. However, the T/P was maximized at approximately 87 mN/kW at 120-V discharge. The low-voltage performance mapping in Section 6.1 exhibited the maximum T/P to be 92 mN/kW for 105-V, 15-mg/s operation with greater than 25-CFF. The trends indicate T/P may be further augmented with additional increases in CFF. Although facility effects were not accounted for in the performance mapping in Section 6.1, the T/P varied by less than 2 mN/kW from the extrapolated vacuum value to the highest background pressure for all operating conditions in Table 5-1. These trends will be discussed in further detail in Chapter 6.

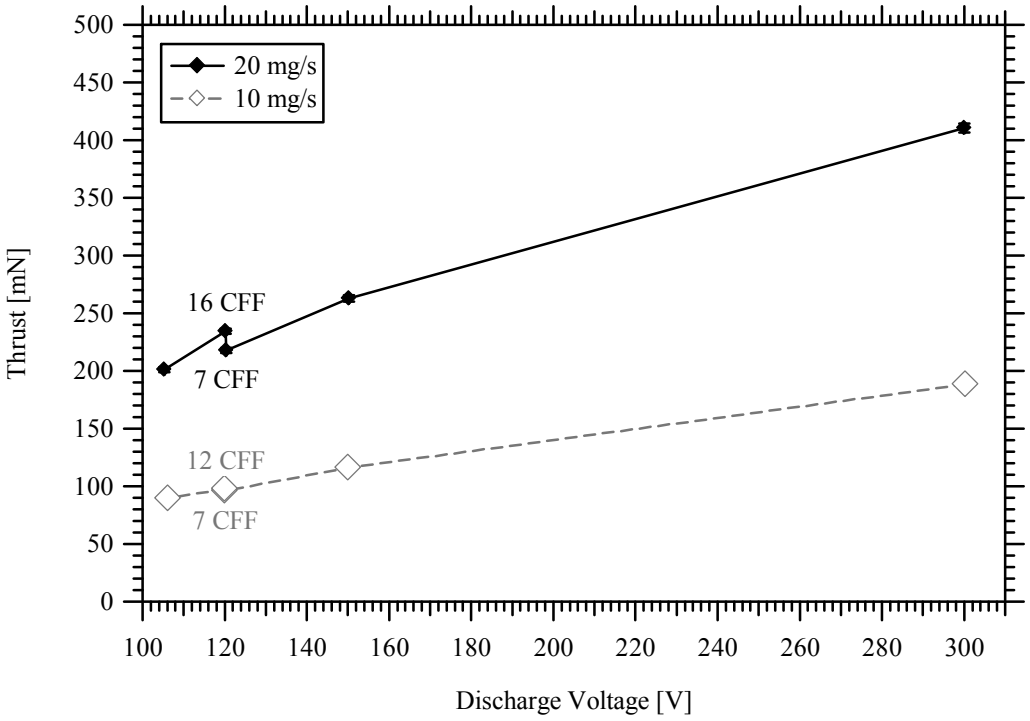

Figure 5-12 Thrust extrapolated to vacuum conditions as a function of discharge voltage from 105-V to 300-V at constant 10-mg/s and 20-mg/s anode flow rate.

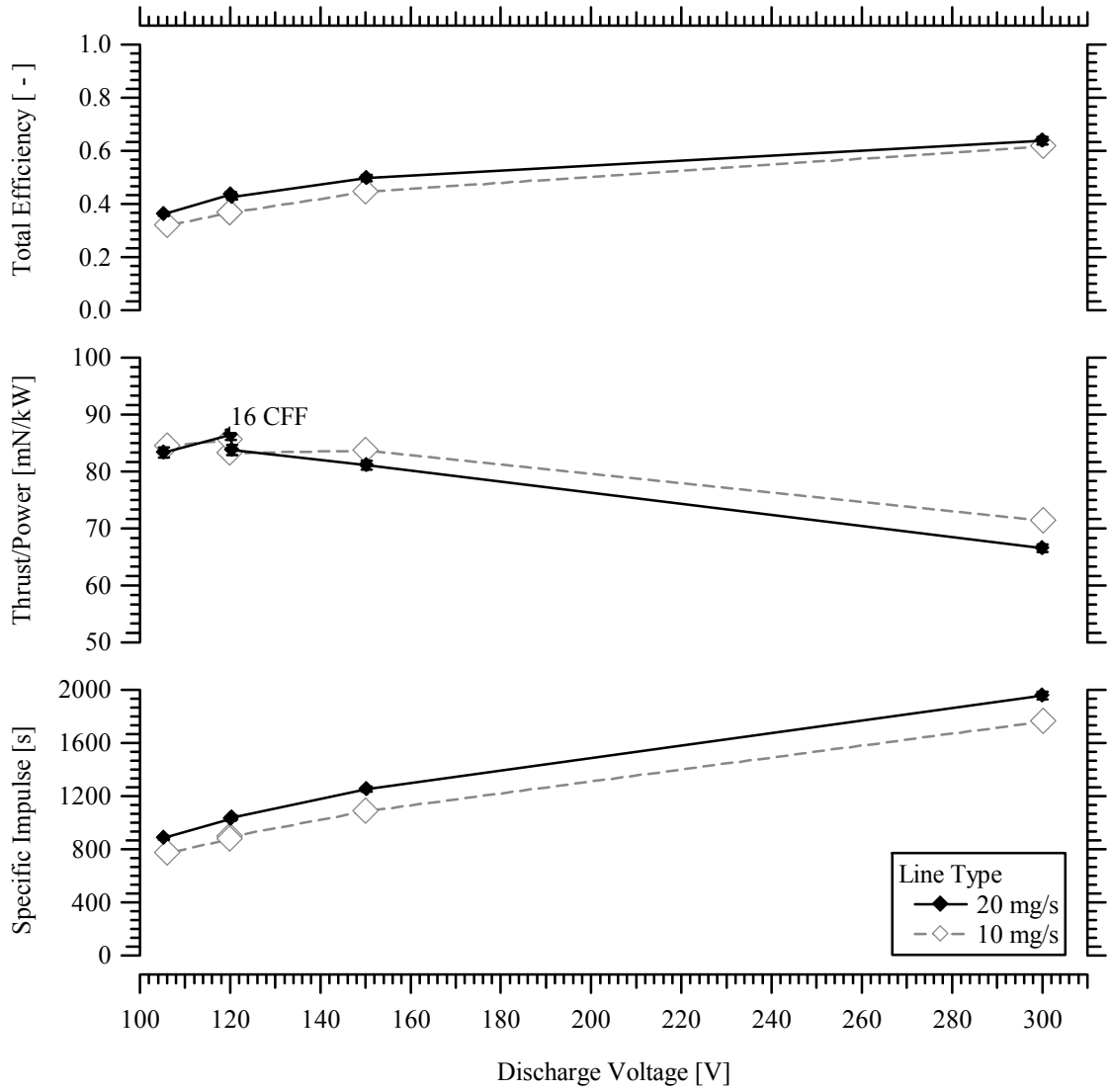

Figure 5-13 Total thruster efficiency, T/P, and total Isp as a function of discharge voltage from 105-V to 300-V at constant 10-mg/s and 20-mg/s anode flow rate.

Performance variations with discharge power are shown in Figure 5-14. The only comparison between constant discharge power conditions occurs at ~2.5 kW between the 300-V, 10-mg/s case and the 105-V to 120-V, 20-mg/s cases. Although total efficiency and total Isp are larger for the 10-mg/s cases at constant power, the T/P is ~15 mN/kW larger for the low discharge voltage conditions at 20-mg/s. The low discharge voltage loss mechanisms and the physical cause of increased T/P will be studied in Section 5.3.

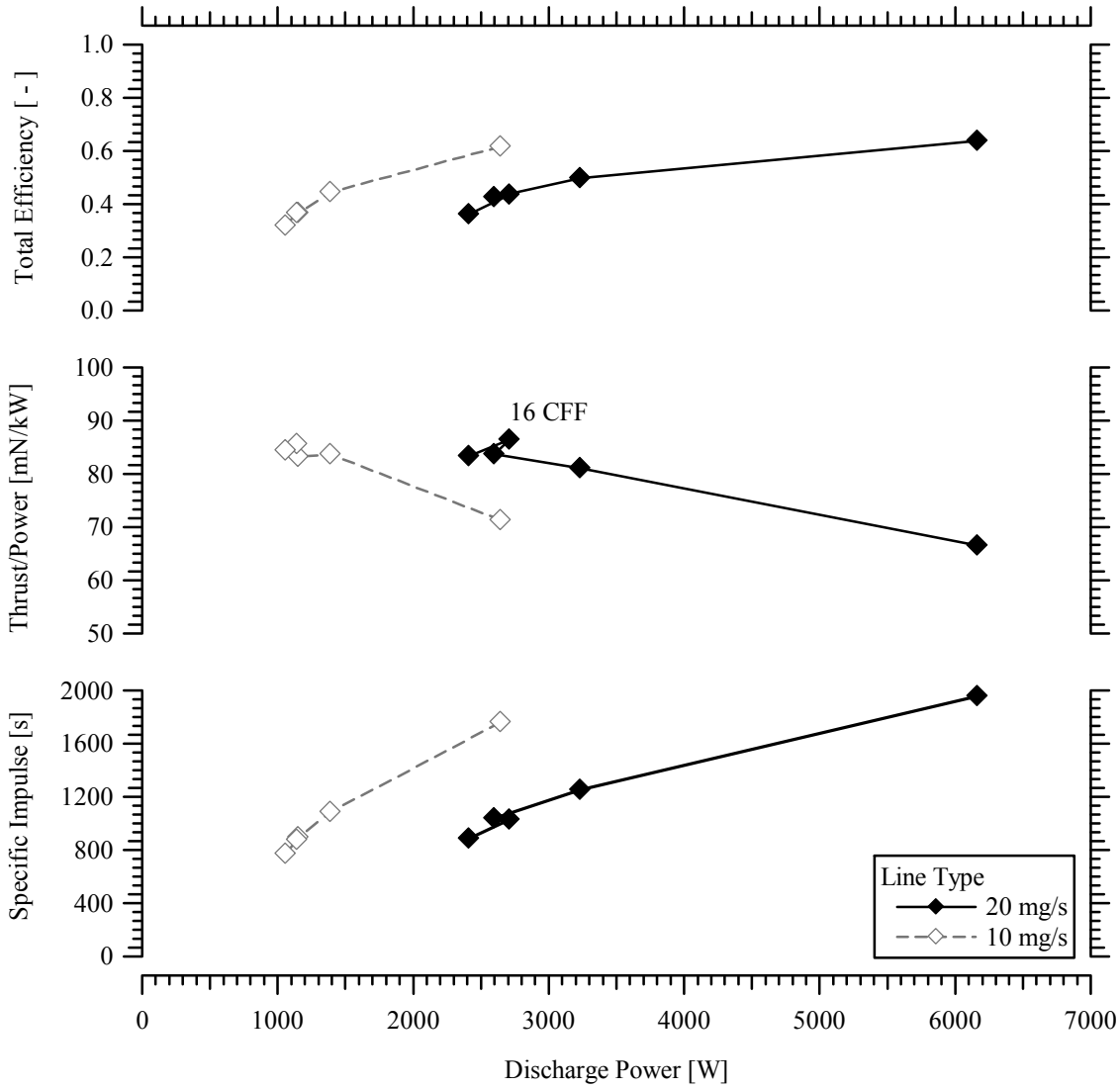

Figure 5-14 Total thruster efficiency, T/P, and total Isp as a function of discharge power from 105-V to 300-V at constant 10-mg/s and 20-mg/s anode flow rate.

5.2.3 Thruster Discharge Oscillations

Oscillations in discharge current and cathode-to-ground potential were monitored with a digital oscilloscope as described in Section 3.1.2.2. Accuracy of the dominant frequency at each thruster operating condition is estimated at ±0.5 kHz. Oscillations of the 120-V, 20-mg/s, 7-CFF case were not measured.

The discharge current power spectra and the cathode-to-ground potential power spectra are shown in Figure 5-15 and Figure 5-16 for 105-V to 300-V at 10-mg/s and 20-mg/s anode flow rate. Power spectra are displayed on the same scale, and show that the dominant frequency is more defined for the lower discharge voltage cases. In addition, the dominant cathode-to-ground potential frequency matches the frequency of peak discharge current power spectra.

The dominant frequency during nominal Hall thruster operating is the breathing-mode frequency. The breathing mode frequency is summarized by the "predator-prey" model[124], and is characterized by the cyclic exhaust and resupply of neutral propellant near the exit.[125] These oscillations are known to result in severe discharge fluctuations and show a dependence on the magnetic field. The predator-prey model in Eq. (5-4) predicts the breathing mode frequency (f_b) based on the velocity of neutral propellant (v_n), the length of the ionization zone (L_i), and the increase in ion velocity across this distance ($\overline{v_i}$). The velocity increment is generally estimated with the most probable ion acceleration potential and the neutral velocity is proportional to the anode temperature.

$$2\pi f_b \approx \frac{\sqrt{\overline{v_i}\, v_n}}{L_i} \tag{5-4}$$

Low discharge voltage operation has also been associated with the "rotating spoke" instability. These azimuthal oscillations have been studied as a function of the thruster I-V characteristic[126], and increase during low discharge voltage operation. The spoke may be created by coupling between ionization processes and density non-uniformities in the channel, and is believed to correspond to an azimuthal disturbance on the order of the critical ionization velocity (4.2-km/s for xenon).[127]

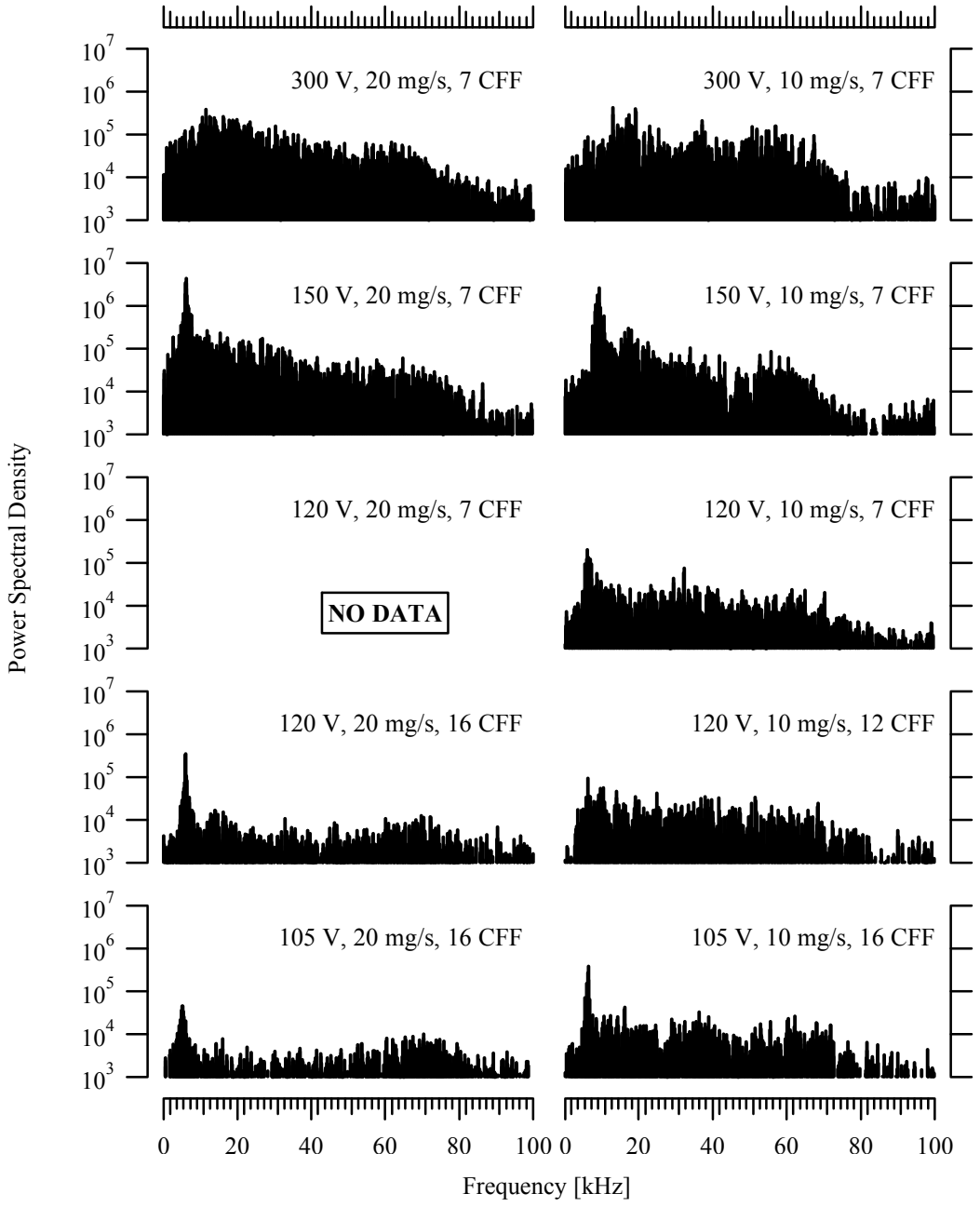

Figure 5-15 Thruster discharge current power spectra for 105-V to 300-V at 10-mg/s and 20-mg/s anode flow rate.

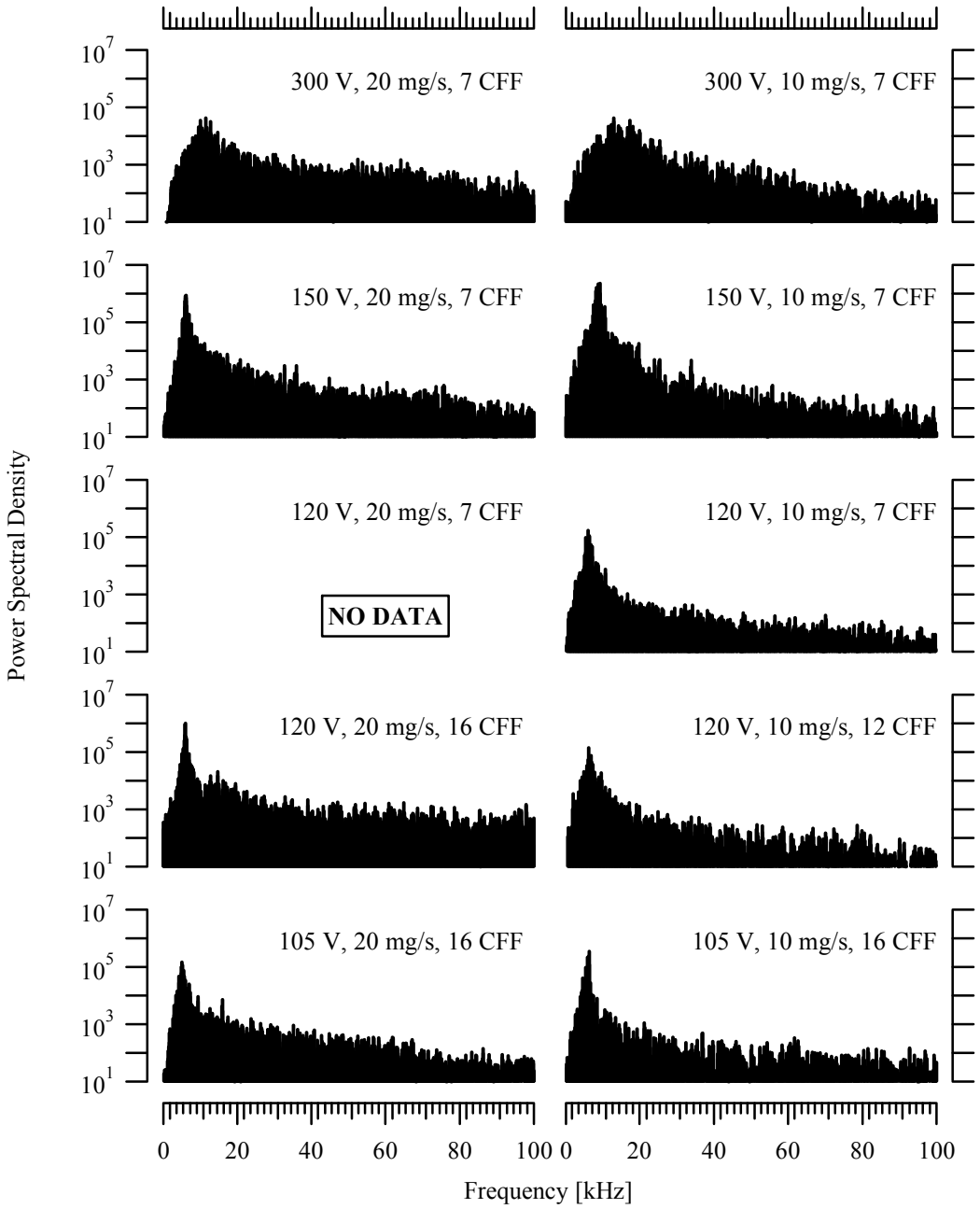

Figure 5-16 Thruster cathode-to-ground potential power spectra for 105-V to 300-V discharge at 10-mg/s and 20-mg/s anode flow rate.

The dominant discharge current frequency and mean peak-to-peak amplitude are shown in Figure 5-17. Discharge current oscillations are evaluated with comparable operation of this thruster model at PEPL in Table 5-2.[61] Nominal 300-V operation at AFRL exhibited a breathing mode frequency of approximately 12 to 13 kHz, which is significantly less than measured at PEPL where the trim coil was not powered. Differences are most likely caused by dissimilar magnetic field profiles, and are expected for comparisons of dissimilar trim coil settings.[128]

Table 5-2 Comparison of the dominant discharge current frequency of the 6-kW Hall thruster from measurements at AFRL and PEPL.

Thruster Operating Conditions	Dominant Frequency [kHz]	
	AFRL	PEPL[61]
300-V, 20-mg/s, 7-CFF	11.6	23
300-V, 10-mg/s, 7-CFF	13.2	16
150-V, 20-mg/s, 7-CFF	6.2	7.2
150-V, 10-mg/s, 7-CFF	9.4	7.9

Low discharge voltage operation corresponded to a decrease in the dominant frequency to approximately 6-kHz. If these oscillations are the breathing mode frequency as described in Eq. (5-4), the neutral thermal speed would be expected to scale with the anode temperature, which is approximately proportional to the square root of the discharge voltage. The ion speed is also proportional to the square root of discharge voltage. Based on these approximations and the increasing trend in dominant frequency with discharge voltage in Figure 5-17, the ionization length of the breathing mode frequency would be expected to increase by approximately 25% from 300-V to 105-V discharge.

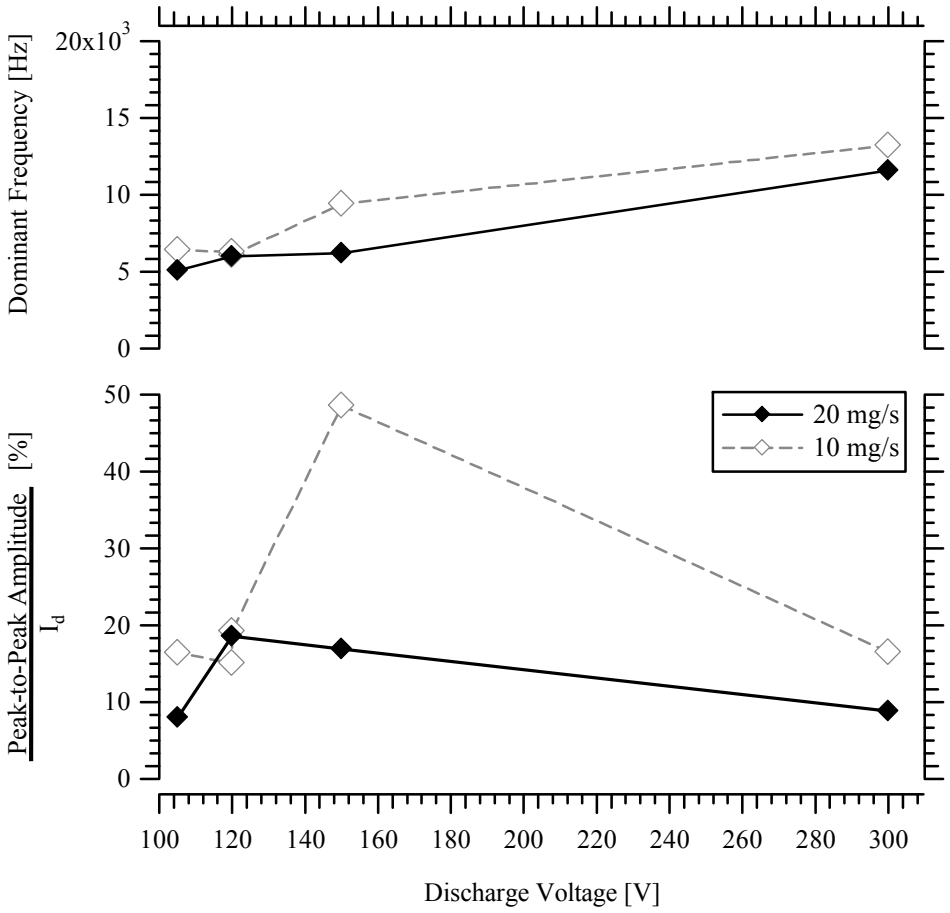

Figure 5-17 Dominant frequency from the discharge current power spectra and maximum peak-to-peak oscillation amplitude relative to the mean discharge current for 105-V to 300-V discharge at 10-mg/s and 20-mg/s anode flow rate.

The maximum peak-to-peak oscillation amplitudes are also displayed as a function of discharge voltage in Figure 5-17. Fluctuations were less than 20% of the discharge current for all operating conditions except the 150-V, 10-mg/s case. This specific operating condition also exhibited the largest oscillation amplitude in the investigation at PEPL for operation from 1-kW to 10-kW. The reason for increased oscillation amplitude at this condition is unknown. A more complete description of thruster discharge oscillations are described elsewhere in the literature.[129]

5.3 Far-field Plume Measurements

Investigation of the far-field Hall thruster plume beyond six thruster diameters was conducted for the operating conditions in Table 5-1 to study discharge properties for incorporation into the efficiency architecture developed in Chapter 2. Details concerning the plasma diagnostic designs and implementation are described in Chapter 3. This section describes ion current density profiles measured with a Faraday probe, ion voltage distributions on thruster centerline determined from RPA measurements of most probable ion potential and Langmuir probe measurements of local plasma potential, and ion species composition on channel centerline with an ExB probe. These diagnostics are required for the detailed analysis of Hall thruster loss mechanisms in Section 5.4.

5.3.1 Current Density Profiles and Ion Beam Current

Faraday probe current density profiles were analyzed using the techniques described in Chapter 4. Facility effects have been isolated and minimized through characterization at increased background pressure, and the primary mechanisms causing increased plume divergence during low-voltage operation are reduced plume focusing and CEX collisions with thruster neutrals.

The vacuum current density profiles and vacuum ion beam current distributions are shown in Figure 5-18. The beam structure is more collimated during high discharge voltage operation. Low anode mass flow rate operation at 10-mg/s corresponded to a more collimated plume at 150-V. It is unknown if the increased discharge oscillation amplitude at 150-V, 10-mg/s is related to the increased collimation at this condition.

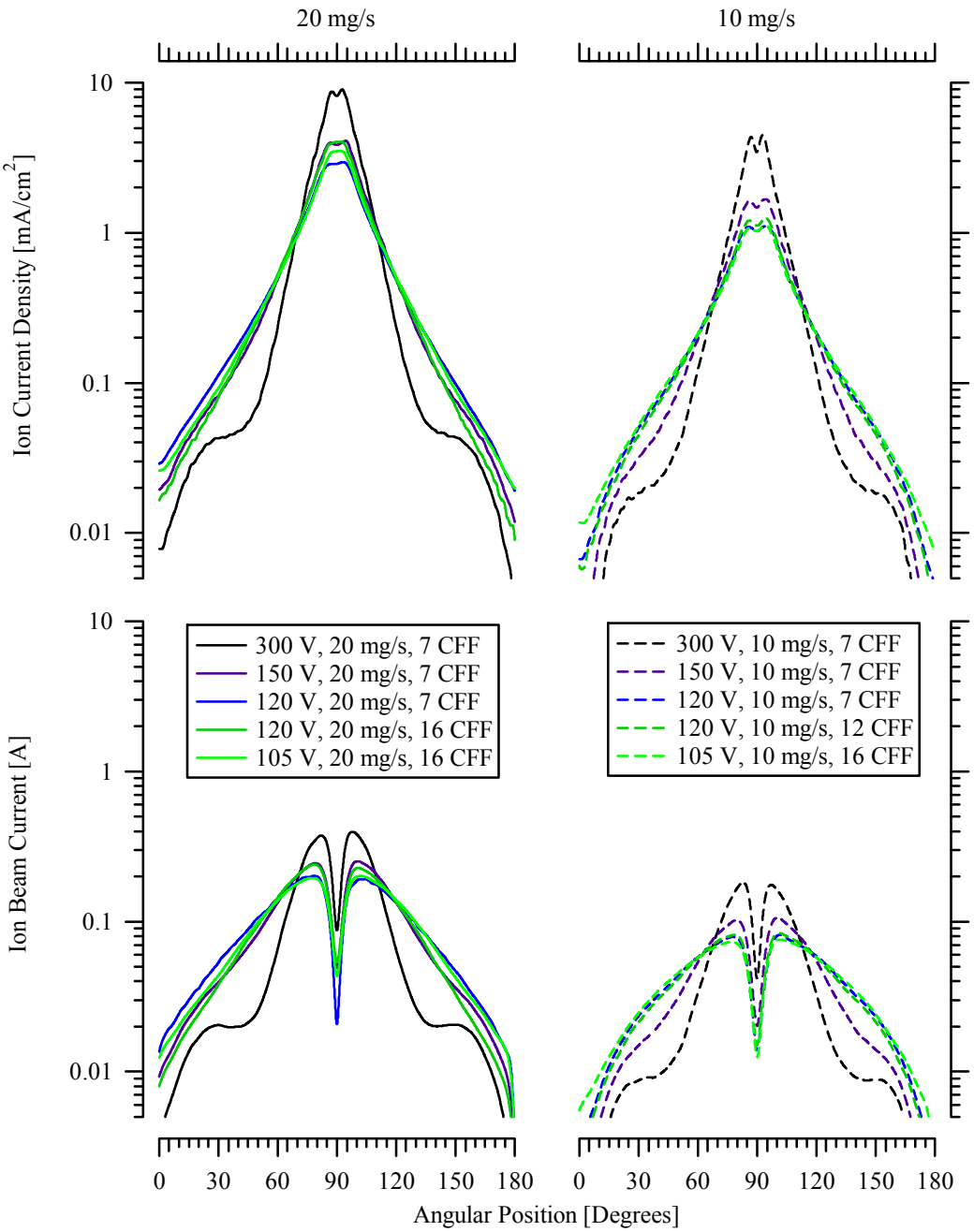

Figure 5-18 **Ion current density profiles extrapolated to vacuum conditions and angular distributions of ion beam current on a 1 meter radius for 105-V to 300-V discharge at 20-mg/s (left) and 10-mg/s (right) anode flow rate.**

Integrated ion beam current and the axial component of ion beam current are shown as a function of discharge voltage in Figure 5-19. The far-field vacuum ion beam current measurements at AFRL showed consistent agreement with near-field beam current values from PEPL for 150-V and 300-V operation at 10-mg/s and 20-mg/s anode flow. Table 5-3 lists the total ion beam current at these operating conditions from both facilities.

Table 5-3 Comparison of the integrated ion beam current of the 6-kW Hall thruster from measurements at AFRL and PEPL.

Thruster Operating Conditions	Integrated Ion Beam Current [A]	
	AFRL – Far-field	PEPL[61] – Near-field
300-V, 20-mg/s, 7-CFF	16.4	15.8
300-V, 10-mg/s, 7-CFF	7.4	7.4
150-V, 20-mg/s, 7-CFF	15.5	14.8
150-V, 10-mg/s, 7-CFF	6.9	6.8

Although the far-field measurements at AFRL resulted in a higher beam current during 20-mg/s operation, the ratio of ion beam current relative to the total discharge current was less than 2% larger at AFRL for both 300-V, 20-mg/s and 150-V, 20-mg/s operation. Therefore, these differences in ion beam current may be due to minor differences in propellant flow rate and/or magnetic field settings. In addition, it was suggested that the near-field measurements at PEPL may have underestimated the ion beam current at increased anode flow rate.[61] This proposition was based on a simplified model of ion beam current using Newton's Second Law and the ion charge flux, and evaluated with measurements of thrust, average ion acceleration potential, and ion species fractions.

The comparison with independent near-field measurements at PEPL and the systematic analysis of facility effects using techniques from Chapter 4 provide increased confidence in the values of total ion beam current in Figure 5-19. Since the current density was only measured at one downstream distance, the ratio of I_{Axial}/I_{Beam} is under-predicted and uncertainty in the axial component and total ion beam current are estimated as ±10% and ±6%. Assuming the total ion beam current is accurate and the axial component is under-predicted, an effective value for axial component of ion beam current will be estimated in Section 5.4.4 based on the difference between total efficiency measured by thrust measurements and total efficiency based on far-field plume measurements. Performance variations due to losses in current utilization, mass utilization, and beam efficiency will be calculated with the integrated values of ion beam current in Section 5.4.

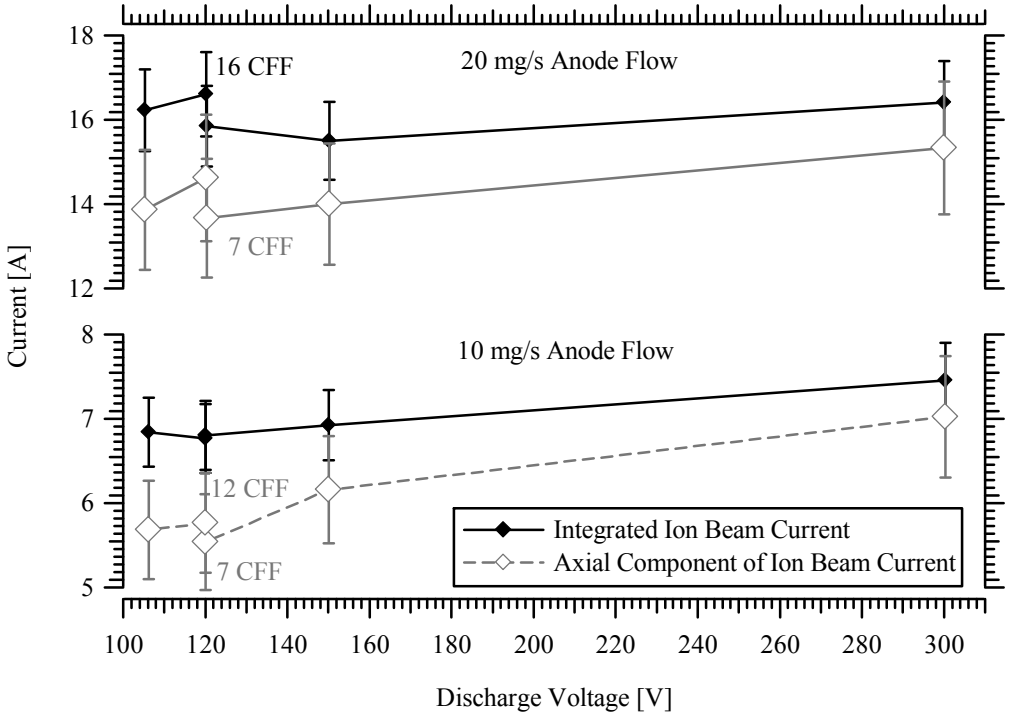

Figure 5-19 Integrated ion beam current and the axial component of ion beam current from vacuum current density profiles at 1 meter radius for 105-V to 300-V discharge at 20-mg/s and 10-mg/s anode flow rate.

5.3.2 Ion Energy per Charge Distributions

The ion energy per charge distribution was measured on thruster centerline 1 meter downstream of the thruster exit plane with an RPA and Langmuir probe. Plasma potential was calculated based on the peak of the 1st derivative of the Langmuir probe I-V characteristic. These values were compared with the curve fitting technique described in Section 3.3.2, and agreed to within 1-V. The overall error in plasma potential measurements was estimated as ±3 V.

Traces of dI/dV are shown for all operating conditions in Figure 5-20. Plasma potential decreased with thruster discharge voltage from approximately 12-V to 5-V at 300-V and 105-V operation, respectively. These values were used to shift the RPA ion voltage distribution for the small acceleration from plasma potential to the ground reference. At constant discharge voltage, the centerline plasma potential also decreased with anode mass flow rate for the 7-CFF conditions. Increased cathode flow fraction at 105-V and 120-V reversed the trend with anode flow, and resulted in a higher plasma potential for 10-mg/s operation.

Collected current on the RPA is shown in Figure 5-21 as a function of the ion energy per charge corrected for the local plasma potential. Profiles of the ion energy per charge are used to determine the most probable ion acceleration potential for calculation of voltage utilization. The most probable ion acceleration potential showed minimal variation with anode and cathode mass flow rate. Secondary peaks on the ion energy per charge distribution below ~50 V may be due to space-charge limitations between the RPA grids. Spatial measurements from 0° to 180° resulted in minimal variation in the most probable ion acceleration potential for a wide range of thruster operation.

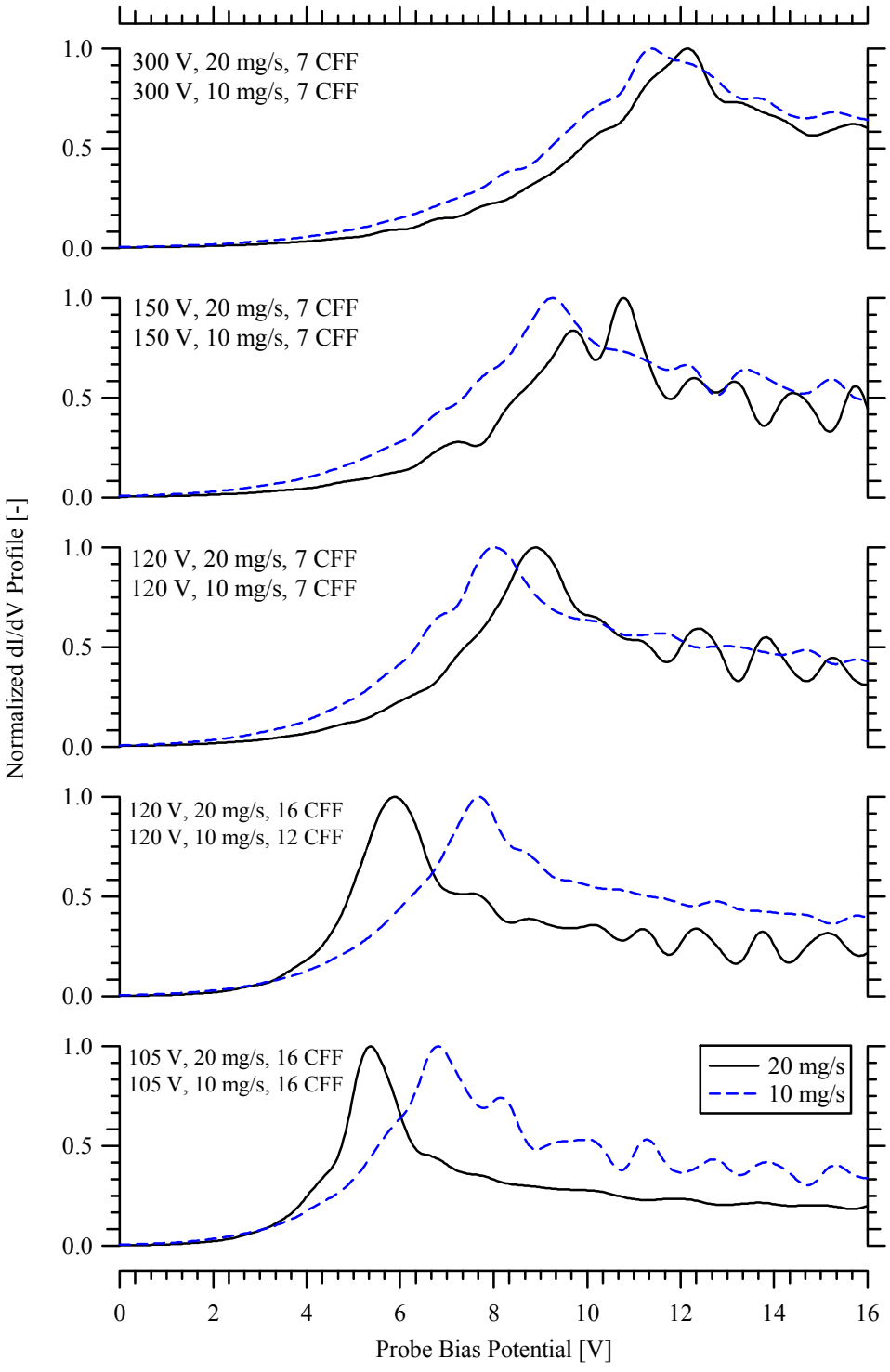

Figure 5-20 **Langmuir probe traces of dI/dV on thruster centerline located 1-meter downstream of the exit plane for 105-V to 300-V discharge at 10-mg/s and 20-mg/s anode flow rate.**

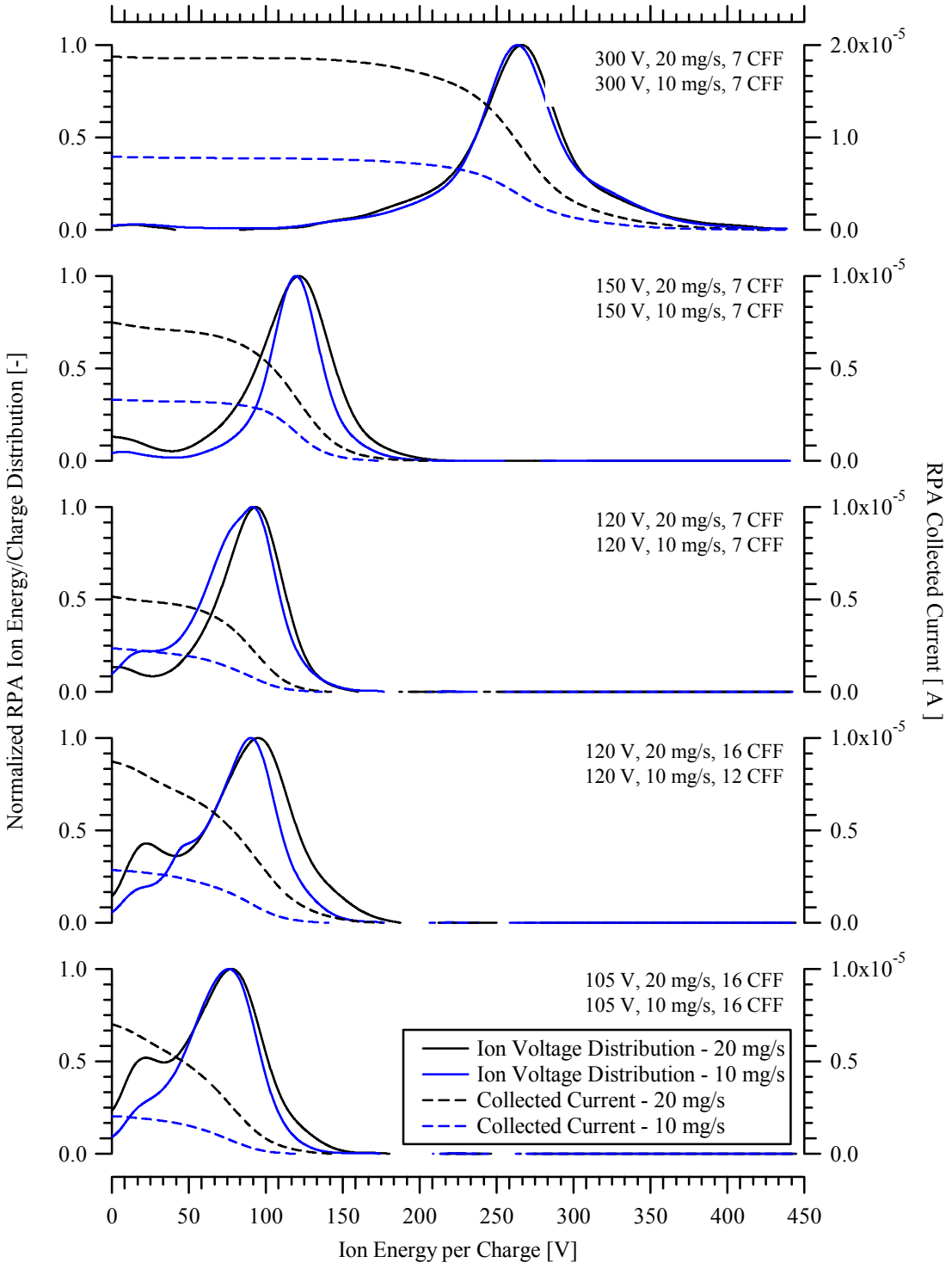

Figure 5-21 **RPA collected ion current traces and Normalized RPA ion energy per charge distributions on thruster centerline located 1-meter downstream of the exit plane for 105-V to 300-V discharge at 10-mg/s and 20-mg/s anode flow rate.**

5.3.3 Ion Species Current Fractions and Mass Flow Fractions

Ion energy distributions were measured with an ExB probe on channel centerline from 1.0 to 1.3-meters downstream of the thruster exit plane. The ion current fractions were corrected for beam attenuation due to CEX collisions in the plume, but still exhibited a minor decrease in the fraction of multiply-charged ions with downstream distance. These trends were consistent with past studies of ion composition using this thruster model[87,101], and were within the estimated uncertainty of ±4%, ±20%, and ±50% in Xe^{+1}, Xe^{+2}, and Xe^{+3} species current fractions, respectively. A more systematic characterization of pressure and temperature effects on the ion energy distributions and ion current fractions measured by this ExB probe model is recommended.

Normalized ion energy distribution profiles are shown in Figure 5-22 as a function of the Xe^{+} pass voltage for the operating conditions in Table 5-1. The fraction of multiply-charged ions decreased with discharge voltage and anode mass flow rate. The peak of Xe^{+2} ions also decreased in energy and increased in magnitude at higher anode flow conditions. Conversely, increased cathode flow rate at 120-V increased the peak of Xe^{+2} ions in addition to widening the ion species distributions.

The ion current fractions determined from ion energy distributions are shown with the calculated ion mass flow fractions and ion species number fractions in Figure 5-23. The 300-V ion compositions at 10-mg/s and 20-mg/s agreed with the current fractions on channel centerline reported at PEPL[61] to within the measurement uncertainty. The population of Xe^{+3} ions is negligible below 300-V, whereas the beam composition of Xe^{+2} ions was relatively constant with discharge voltage. Decreased production of

multiply-charged ions at low discharge voltage is typically attributed to decreasing electron temperature.

Increased anode mass flow rate also increased the production of multiply-charged ions. Although increased anode propellant flow has been shown to decrease the electron temperature magnitude, it also corresponds to an increase in the neutral density and subsequently the electron-neutral collision frequency. These collisions lead to an increased fraction of Xe^{+1} ions at high anode flow rate relative to the neutral population. This mechanism leads to a higher density of singly-charged xenon and therefore also increases the frequency of electron-ion collisions. The net result is an increase in the population of multiply-charged ions.

The increased electron-neutral and electron-ion collision frequency associated with higher anode flow was also evident with increased cathode flow rate at 120-V discharge. Although no Xe^{+3} ions were created at this low discharge voltage, the current fraction of Xe^{+2} ions increased by 50% at 10-mg/s, 12-CFF and by 15% at 20-mg/s, 16-CFF. The substantial increase from 7-CFF to 12-CFF at 120-V, 10-mg/s is likely due to the lower electron-neutral collision frequency of the 10-mg/s anode flow operation. This consequence of increased cathode flow fraction at low discharge voltage will be further discussed in Section 5.4 and Chapter 6.

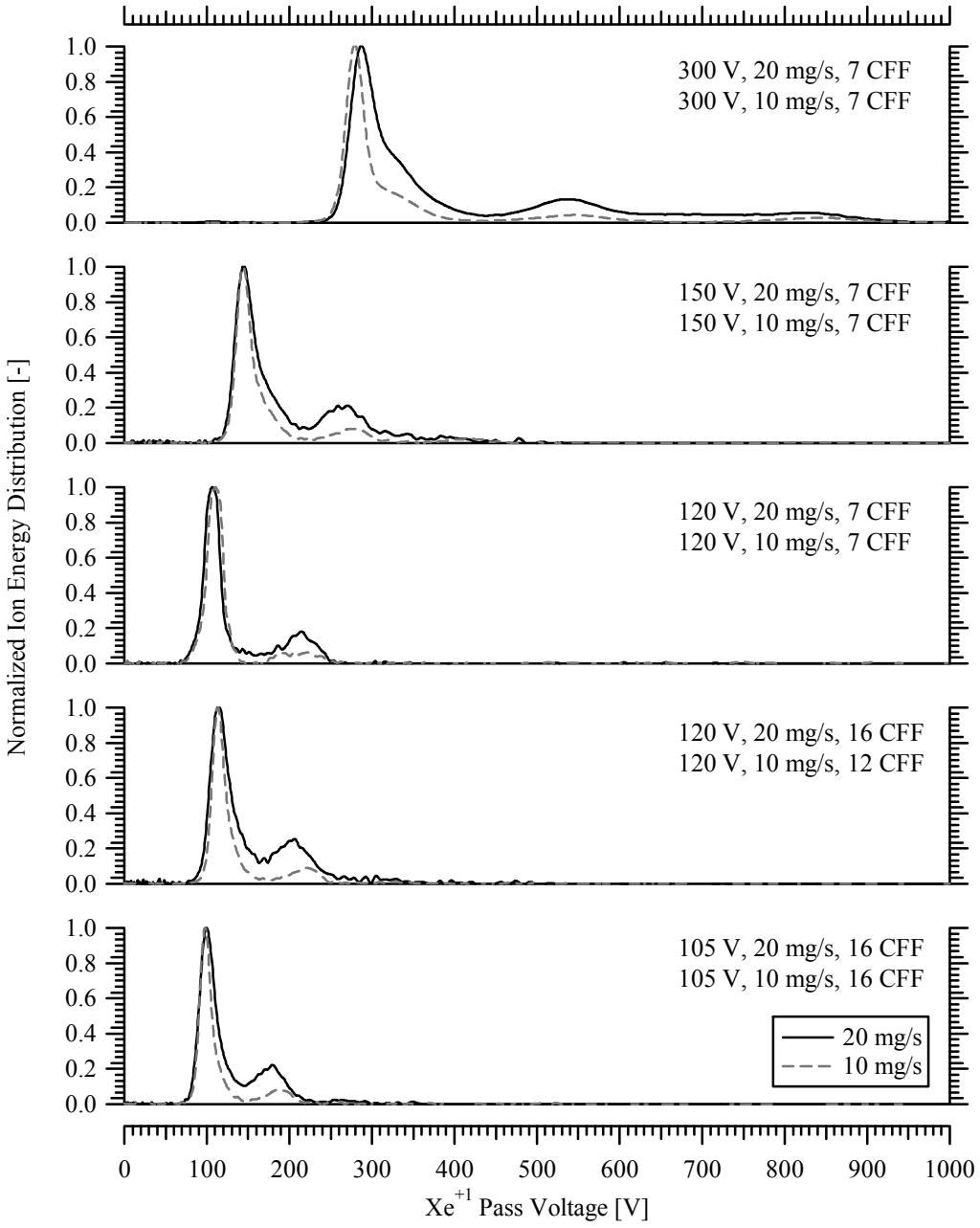

Figure 5-22 Normalized ExB measurements of ion energy distributions on channel centerline located 1-meter downstream of the exit plane for 105-V to 300-V discharge at 10-mg/s and 20-mg/s anode flow rate.

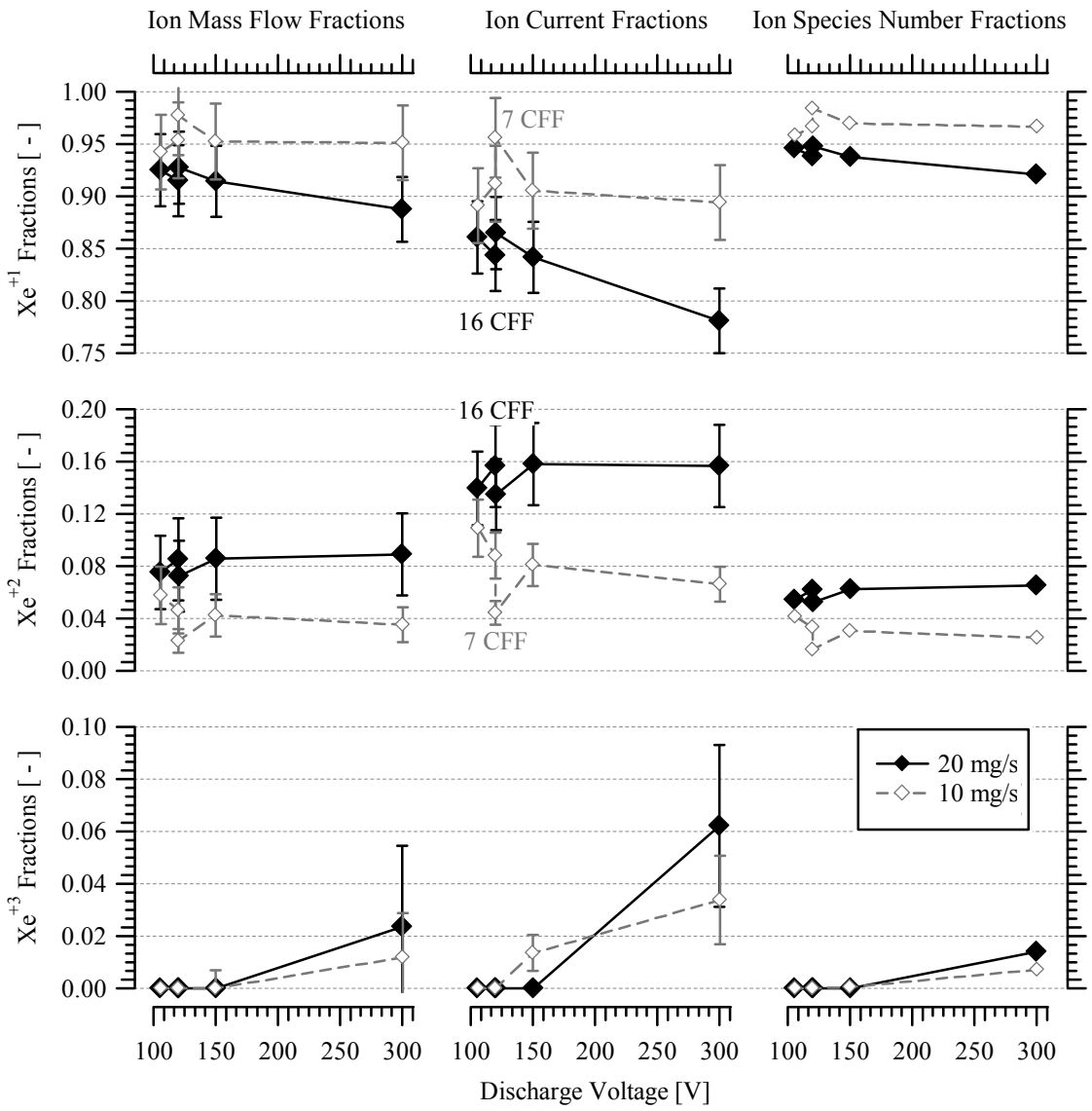

Figure 5-23 Ion mass flow fractions (left), ion current fractions (middle), and ion species number fractions (right) of Xe^{+}, Xe^{+2}, and Xe^{+2} from ExB measurements of ion energy distribution on channel centerline 1 meter downstream of the exit plane for 105-V to 300-V discharge at 10-mg/s and 20-mg/s anode flow rate. Labels for increased CFF at 120-V operation are listed on ion current fractions, and may be used to determine the operating condition on traces of ion mass flow fractions and ion species number fractions.

5.4 Low Discharge Voltage Hall Thruster Loss Mechanisms

The far-field plume properties and thrust measurements will be incorporated in the Hall thruster efficiency architecture developed in Chapter 2 to investigate the characteristics and physical loss mechanisms of low discharge voltage Hall thruster operation. This comprehensive analysis will first evaluate the total thruster efficiency calculated with plume measurements against performance calculated with measured thrust. Further comparison of T/P and total Isp calculated with the plume properties provides a second level of validation that is necessary to substantiate the physical mechanisms responsible for losses in thruster performance.

Following the comparison of thruster performance parameters with plume properties and thrust measurements, the individual utilization efficiencies will be studied to determine the dominant low discharge voltage losses. The implications of these losses will be discussed in relation to internal discharge processes.

5.4.1 Evaluation of Performance Parameters

The total thruster efficiency calculated with far-field plume measurements is compared to the value based on thrust measurements in Figure 5-24. Efficiencies calculated from thrust measurements and from plume properties followed the same trend with discharge voltage at 10-mg/s and 20-mg/s. However, total efficiency determined with thrust measurements was consistently larger by approximately 0.02 to 0.08. The discrepancies are within the margin of uncertainty for all operating conditions.

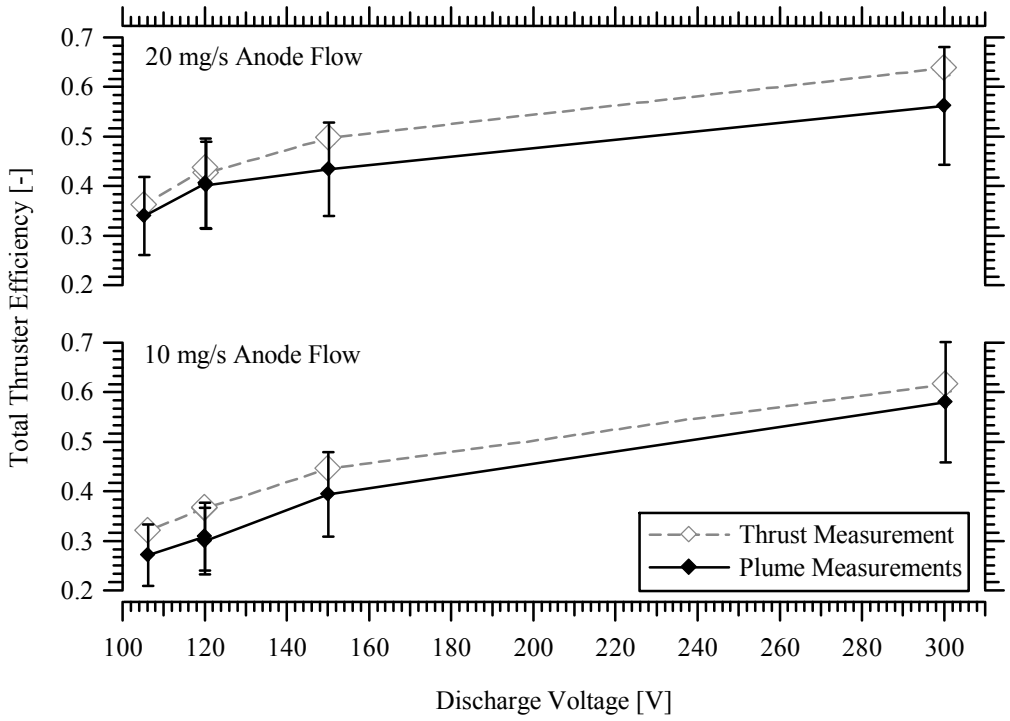

Figure 5-24 Total thruster efficiency calculated with plume properties compared to total thruster efficiency based on thrust measurements for 105-V to 300-V discharge at 10-mg/s and 20-mg/s anode flow rate.

This deviation in total thruster efficiency is analyzed as differences in T/P and total Isp in Figure 5-25 for 20-mg/s operation and in Figure 5-26 for 10-mg/s operation. In all cases, the performance parameters based on measured plume properties are under-predicted. Analysis of the voltage exchange parameter, E_1, and mass exchange parameter, E_2, in Figure 5-27 yields a second method of inspection. The error in total thruster efficiency is entirely contained in the voltage exchange parameter, which is apparent given that the mass exchange parameter is calculated with only discharge current and total mass flow rate. The relationship with E_1 provides a key as to the plume properties most likely to cause a systematic discrepancy in total thruster efficiency, and how these parameters relate to calculation of T/P and Isp.

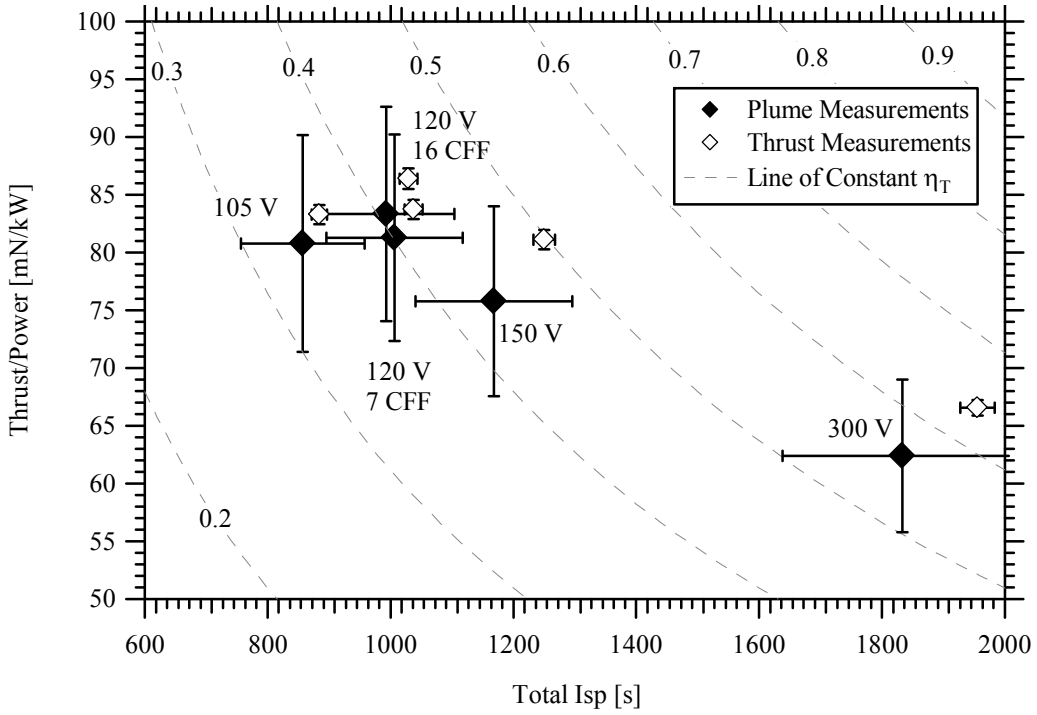

Figure 5-25 Comparison of thrust to power ratio, total specific impulse, and total thruster efficiency calculated with plume properties and thrust measurements for 105-V to 300-V discharge at 20-mg/s anode flow rate.

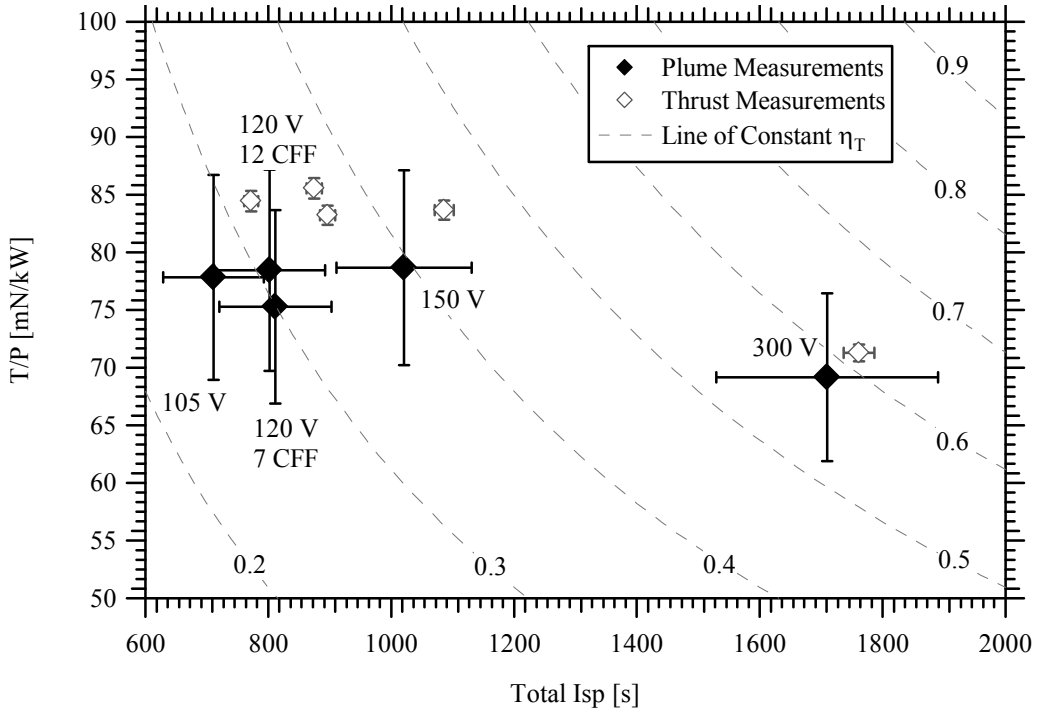

Figure 5-26 Comparison of thrust to power ratio, total specific impulse, and total thruster efficiency calculated with plume properties and thrust measurements for 105-V to 300-V discharge at 10-mg/s anode flow rate.

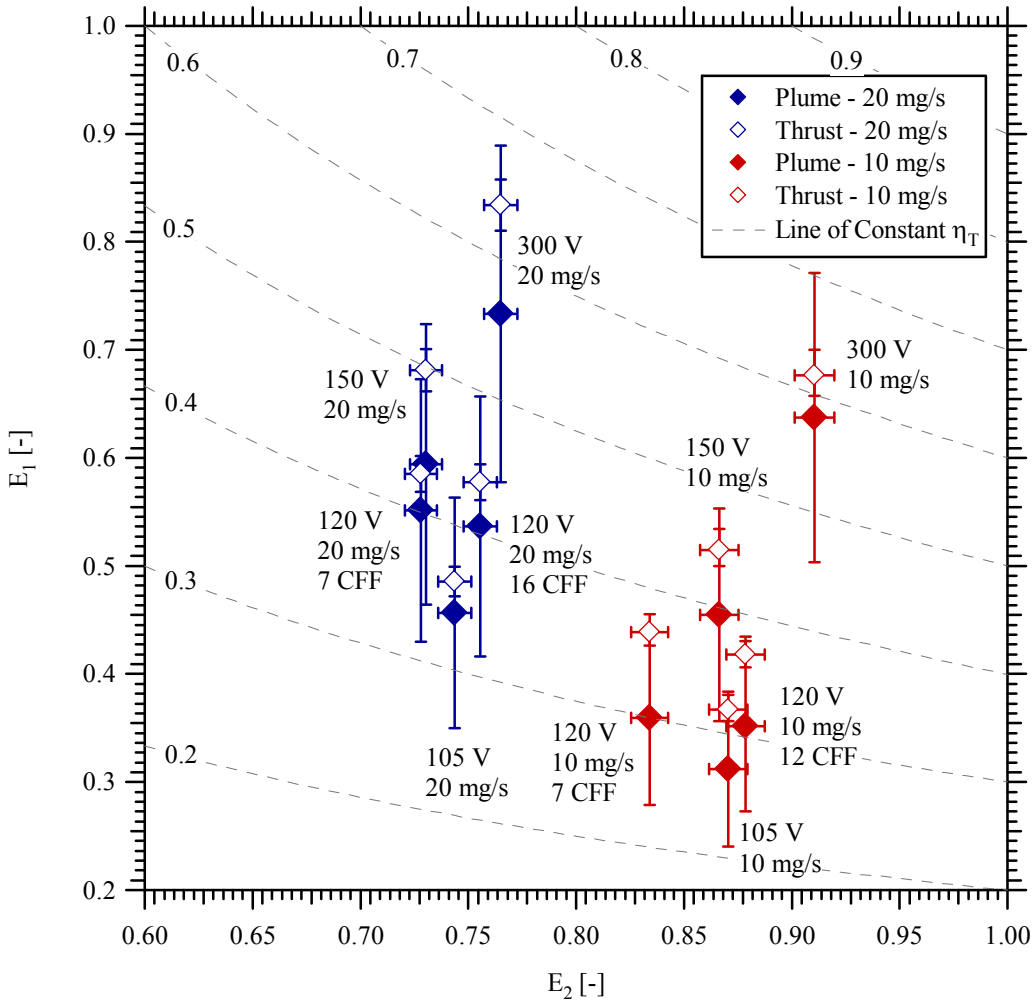

Figure 5-27 Comparison of the voltage exchange parameter and the mass exchange parameter calculated with plume properties and thrust measurements for 105-V to 300-V discharge at 10-mg/s and 20-mg/s anode flow rate.

Both T/P and Isp are proportional to the square root of E_1, which is a function of the product of voltage utilization, propellant efficiency, beam efficiency, and χ. Expressing T/P and Isp from Eq. (2-51) and Eq. (2-52) in terms of measured plume properties yields the relationships in Eq. (5-5) and Eq. (5-6). Terms with ion species fractions have been reduced to the simplest form without separating individual ion species contributions.

$$\frac{T}{P_d} = \left(\frac{V_a^{1/2} I_{Axial}}{V_d I_d} \right) \left(\frac{\Phi_q}{Q} \right)^{1/2} (\Phi_{N\text{-}G})^{1/2} \left(2 \frac{\mathcal{M}}{\mathcal{F}} \right)^{1/2} \tag{5-5}$$

$$I_{sp}\, g = \left(\frac{V_a^{1/2} I_{Axial}}{\dot{m}_T} \right) \left(\frac{\Phi_q}{Q} \right)^{1/2} (\Phi_{N\text{-}G})^{1/2} \left(2 \frac{\mathcal{M}}{\mathcal{F}} \right)^{1/2} \tag{5-6}$$

These formulations indicate that either the RPA most probable ion acceleration potential or the axial component of ion beam current are the beam properties causing discrepancy in T/P and Isp calculated with plume measurements. This conclusion is based on the minimal value of the neutral gain utilization and the correlation between average ion charge with charge utilization. The neutral-gain utilization is typically less than 1.02 for SOTA Hall thrusters, and accounting for the maximum difference in total thruster efficiency of 0.08 is highly unlikely. Secondly, the ratio (Φ_q/Q) is always less than unity and reached a minimum value of 0.93 at 300-V, 20-mg/s. Increasing this ratio to unity was not enough to match T/P and Isp calculated with Eq. (5-5) and Eq. (5-6) to the values based on thrust measurements. Therefore, this analysis reveals the most probable ion acceleration potential or the axial component of ion beam current are the most likely parameters reducing performance calculations.

While the under-estimations of T/P and Isp may be the result of a number of systematic errors and measurement uncertainties in thrust and far-field plume measurements, the simplest and most likely cause is an under-prediction of the axial component of ion beam current. The ratio of this value relative to the total ion beam current was shown to increase toward the exit plane in Section 4.4.3. This phenomenon was not fully understood nor accounted for in this experimental study of low discharge voltage operation.

Due to the squared nature of the axial component of ion beam current in beam efficiency, small errors in this parameter may result in large variations in the total efficiency, T/P, and Isp. The under-prediction of I_{Axial} that propagates into errors in beam efficiency and divergence will not affect calculations of energy efficiency or propellant efficiency, and will not complicate analysis of low discharge voltage loss mechanisms.

5.4.2 Performance Utilization Efficiencies

Total thruster efficiency calculated with plume measurements in Figure 5-24 is factored into the beam efficiency, propellant efficiency, and energy efficiency in Figure 5-28. These three partial efficiencies will be further decomposed into individual utilization efficiencies of mass, charge, neutral-gain, voltage, and current utilization to study performance loss mechanisms in Section 5.4.2.2 and Section 5.4.2.3.

Beam efficiency decreased with discharge voltage from 300-V to 105-V in Figure 5-28. Increased divergence during low-voltage operation is typically attributed to ionization and acceleration further downstream in the discharge channel. Increased cathode flow fraction at 120-V discharge increased the beam efficiency for both 10-mg/s and 20-mg/s operation. This increase in beam efficiency was accompanied by a decrease in propellant efficiency and an increase in T/P with constant total thruster efficiency in Figure 5-25 and Figure 5-26. Due to the presumed under-estimation of the axial component of ion beam current, the beam efficiency is expected to be greater than the values in Figure 5-28. The performance implications of an underestimation in the axial component of ion beam current in plume divergence and beam efficiency will be studied in Section 5.4.2.1.

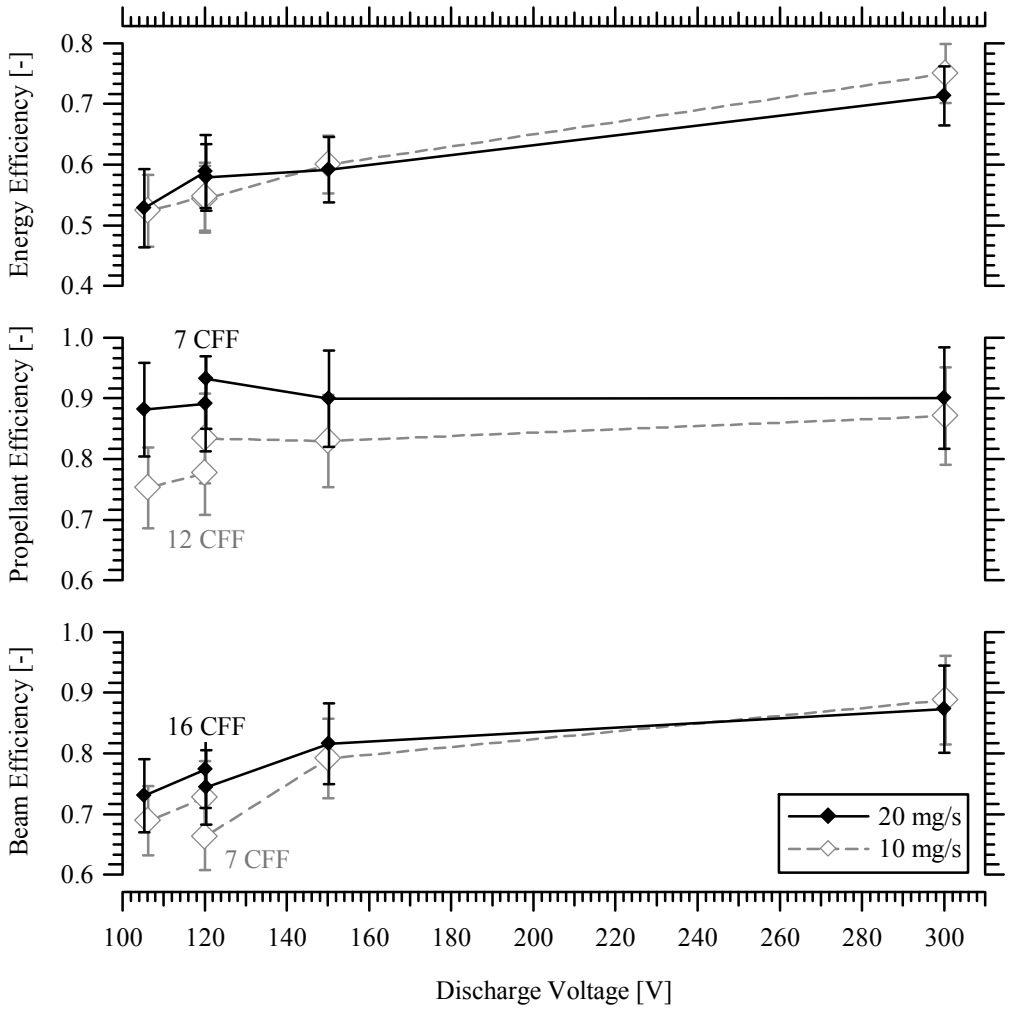

Figure 5-28 Comparison of the energy efficiency (top), propellant efficiency (middle), and beam efficiency (bottom) as a function of discharge voltage for 105-V to 300-V at 10-mg/s and 20-mg/s anode flow rate.

The propellant efficiency was relatively constant from 120-V to 300-V discharge, and exhibited a slight increase at 120-V. Past investigations of low discharge voltage operation stated a reduction in the propellant utilization was a primary loss.[20] The differences due to formulation and terminology are presented in Section 5.4.2.2. Low-voltage efficiency losses associated with reduced ion mass flow fraction and multiply-charged ions will be studied with the minor increase in performance associated with the neutral-gain utilization.

Energy efficiency decreased by approximately 0.2 from 300-V to 105-V, and represents a dominant loss during low discharge voltage operation. Energy losses declined in a linear manner as discharge voltage was decreased, and were relatively constant between 10-mg/s and 20-mg/s anode flow operation. A more detailed analysis of energy loss mechanisms with respect to voltage utilization and current utilization is presented in Section 5.4.2.3.

5.4.2.1 Beam Efficiency

In Figure 5-29, the axial component of ion beam current calculated with far-field Faraday probe current density measurements at vacuum conditions is compared to the value required to equate the performance parameters in Figure 5-25 and Figure 5-26. The effect on performance parameters using the estimated value of I_{Axial} at vacuum conditions and the thruster exit is shown in Figure 5-30. The imposed conformity in T/P, total Isp, and total thruster efficiency calculated with thrust measurements and plume measurements in Figure 5-30 is based on the approximation that all discrepancies are due to the under-estimation of I_{Axial} at the exit plane.

The analyses in Figure 5-29 show that the axial component of ion beam current at the exit is under-estimated for all operating conditions. Underestimation of I_{Axial} at vacuum conditions is up to 8% of the ion beam current, which is within the range predicted in Figure 4-38. The maximum deviation in the axial component of ion beam current as fraction of the total ion beam current occurred for low-voltage conditions at 10-mg/s and for high-voltage conditions at 20-mg/s.

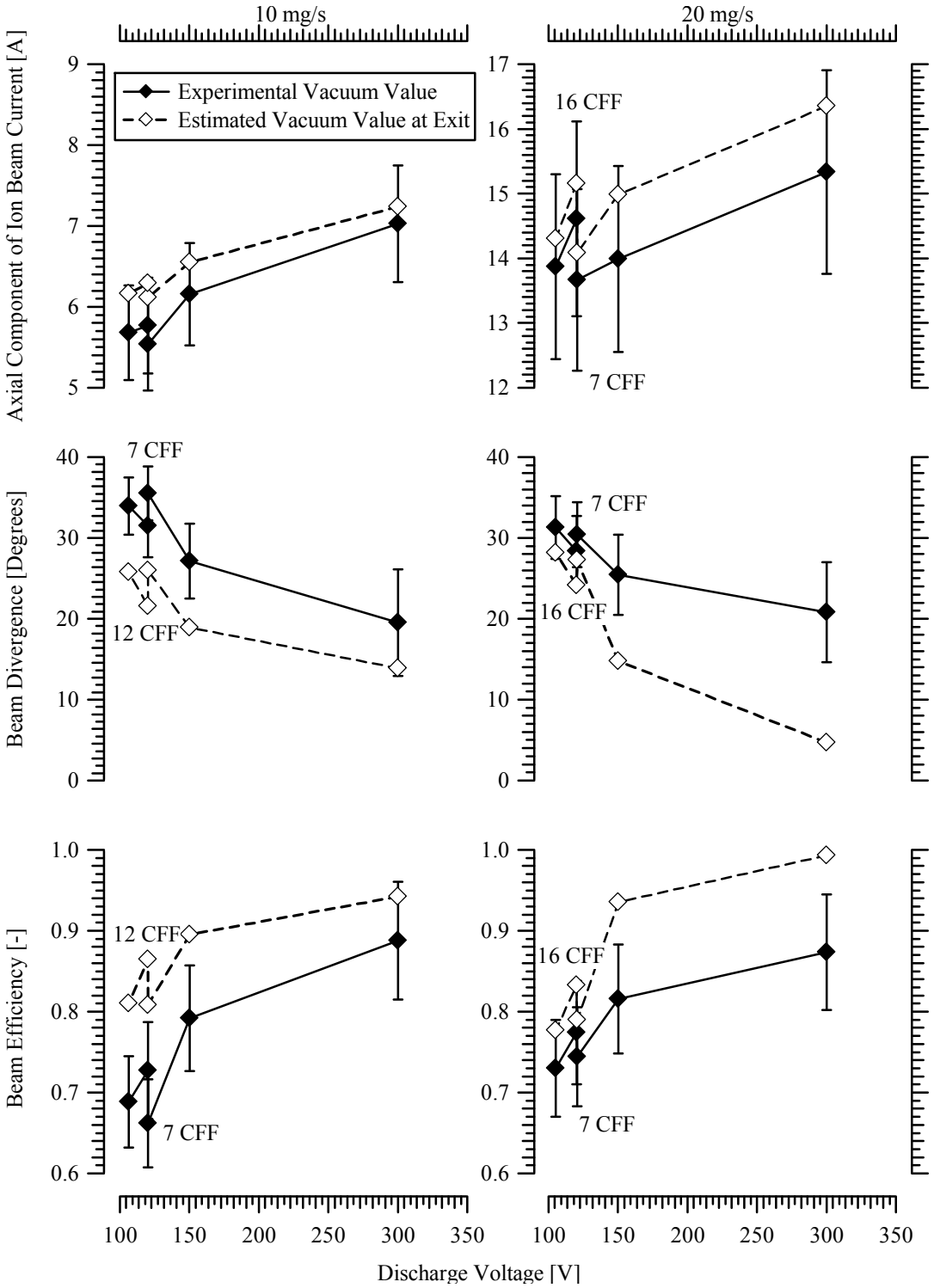

Figure 5-29 Comparison of the axial component of ion beam current (top), beam divergence half-angle (middle), and beam efficiency (bottom) as a function of voltage at 10-mg/s (left) and 20-mg/s (right) anode flow rate. Values calculated from Faraday probe measurements extrapolated to vacuum are compared to the values required to equate performance parameters based on plume measurements with those based on thrust measurements.

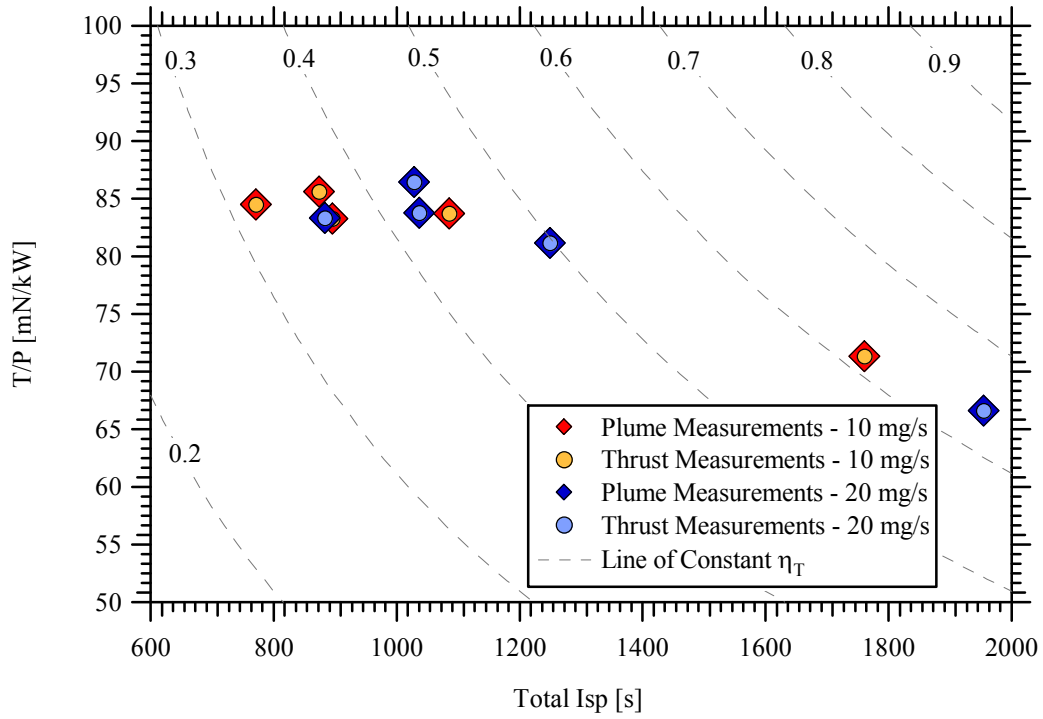

Figure 5-30 Thrust to power ratio, total specific impulse, and total thruster efficiency calculated with plume measurements based on the estimated axial component of ion beam current at the exit compared to calculations based on thrust measurements for 105-V to 300-V at 10-mg/s and 20-mg/s anode flow rate.

The plume divergence half-angle decreases by approximately 3° to 10° using the axial component of ion beam current estimated at the exit. The only operating condition outside of this range was 300-V, 20-mg/s, which decreased from a half-angle of 21° to 5°. This significant variation is partially attributed to the non-linear calculation of divergence as an inverse cosine function in Eq. (2-45). Although near-field current density measurements of this thruster model at PEPL estimated the plume divergence at ~21° for 300-V, 20-mg/s, there are several factors that should be considered when determining loss of thrust due to the divergent Hall thruster beam. Ionization of ingested facility neutrals and CEX collisions with facility neutrals will produce a more divergent population of ions than the primary beam ions. These divergent ion populations would

be expected to increase estimates of near-field plume divergence in a manner similar to far-field measurements, and necessitates characterization of facility effects similar to the analysis in Section 5.1. Therefore, the loss of thrust due to divergence of beam ions may be over-predicted by both near-field and far-field measurements, and the true divergence of beam ions at the end of the primary acceleration zone at 300-V, 20-mg/s may be in the range of 5° to 10°.

Based on these results, it is recommended that the loss of thrust due to divergence of beam ions should be estimated with near-field Faraday probe measurements in the downstream vicinity of the primary acceleration zone. These plume measurements should be characterized over a range of facility background pressures and downstream distances. The cosine losses on the inner and outer width of the annular beam should be estimated with respect to the edges of the discharge channel wall. This examination should isolate facility effects, characterize variations due to CEX collisions with thruster and cathode neutrals, and reduce cosine losses in the very near-field plume caused by the channel centerline measurement coordinate system. A comparison and agreement with far-field Faraday probe measurements using the recommendations in Section 4.5 would provide a high degree of confidence in the integrated ion beam current and divergence losses.

The beam efficiency in Figure 5-29 shows divergence increases during low discharge voltage operation, and causes a 10% to 20% decline in total efficiency from the nominal 300-V operation. Increased cathode flow at 120-V resulted in a 2° to 4° reduction in divergence half-angle at 20-mg/s and 10-mg/s, respectively. This reduced divergence corresponded to a 0.03 to 0.06 increase in beam efficiency. These gains were

similar for the divergence calculated with the axial component of ion beam current estimated at the exit plane.

The primary discrepancy in performance parameters calculated with plume measurements compared to thrust measurements is attributed to the axial component of ion beam current, and the losses in energy efficiency and propellant efficiency should be unaffected by this term. The effect of this discrepancy was estimated, and a predicted value for vacuum exit plane conditions is within the range of plausible values for jet divergence.

5.4.2.2 Propellant Efficiency

In this investigation, propellant efficiency is the product of mass utilization, charge utilization, and neutral-gain utilization. This terminology of propellant efficiency and the formulation is unique to the architecture developed in Chapter 2. Primary differences include the study of performance gains due to neutral propellant, including the total anode and cathode mass flow rate in the mass utilization, and incorporating the three utilization efficiencies into a measure of the propellant efficiency of the discharge. The rationale behind defining propellant efficiency with mass utilization, charge utilization, and neutral-gain utilization is to unite global effects causing dispersion of the jet VDF over a wide range of thruster operation. This model describes the performance advantages and losses associated with non-ionized particles and multiply-charged ions in the beam, and therefore enabled a more detailed examination of the ionization processes in the plasma discharge. The three components of propellant efficiency are shown in Figure 5-31.

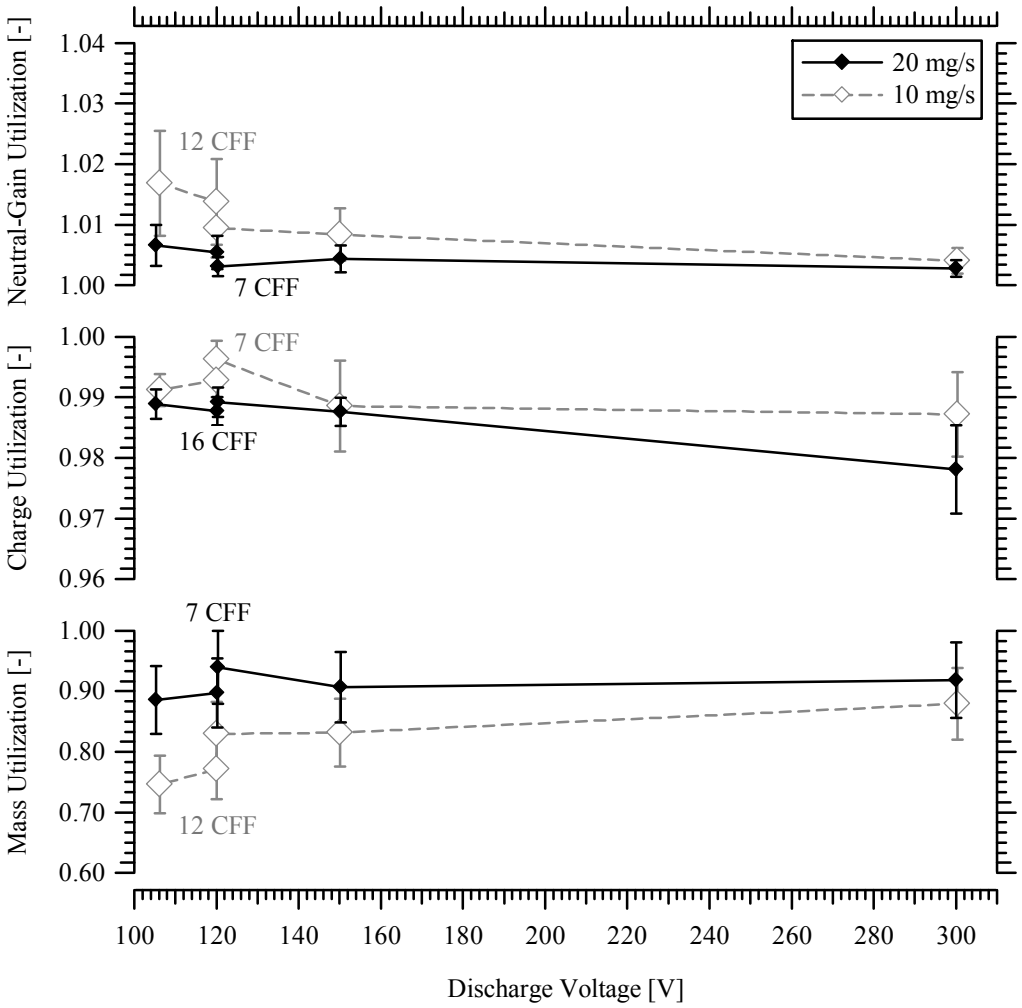

Figure 5-31 Comparison of the factors affecting propellant efficiency as a function of discharge voltage for 105-V to 300-V at 10-mg/s and 20-mg/s anode flow rate. Partial efficiencies include the neutral-gain utilization (top), charge utilization (middle), and mass utilization (bottom).

Charge utilization is near unity for all operating conditions in Figure 5-31, and is indicative of a beam composed primarily of a single ion species. Decreased charge utilization during higher voltage operation is predominantly due to creation of Xe^{+3} ions. The ion fraction of Xe^{+2} was relatively constant with discharge voltage, as shown in Figure 5-23. Increased anode flow operation resulted in an increase in the fraction of multiply-charged ions and a decrease in the charge utilization. This was attributed to the

increased electron-neutral collision frequency and corresponding increase in the electron-ion collision frequency when the neutral density increased during 20-mg/s operation. The charge utilization decreased with an increase in cathode flow fraction during 120-V operation, and is due to a parallel line of reasoning.

Mass utilization was the dominant factor in propellant utilization, since the charge utilization and neutral-gain utilization were near unity for all operating conditions. The ion mass flow fraction was relatively constant with variation in discharge voltage from 120-V to 300-V at 7-CFF. The mechanism behind increased charge utilization with increased anode flow may also explain the trends in mass utilization. Mass utilization at 20-mg/s is larger than the value at 10-mg/s due to the increased electron-neutral collision frequency during high anode flow rate operation. The decrease in mass utilization with increased cathode flow rate is due to the increase in total mass flow to the thruster, and a lower ionization rate of propellant injected from the cathode. Not accounting for propellant flow to the cathode in the ion mass flow fraction resulted in a mass utilization greater than unity for the 120-V and 105-V conditions at 20-mg/s. This suggests ionization of cathode neutrals is significant during low discharge voltage operation, and must be accounted for when analyzing and comparing thrust and plume properties in this range of operation.

The neutral-gain utilization is shown to have a minimal effect on total thruster efficiency of the 6-kW thruster in this investigation. This term is a gross approximation of the finite thrust generated by non-ionized particles exiting the discharge, and is estimated from the velocity of thermalized neutrals according to Eq. (2-29). Although the uncertainty of this utilization is greater than 50%, it quantifies global trends with

variations in discharge voltage and provides a benchmark for comparisons with investigations at other facilities. Performance is augmented by a larger amount during low discharge voltage operation at 10-mg/s, and is due to the increased fraction of thermalized neutral flow exiting the discharge. While the total thruster efficiency is increased by approximately 2% at 105-V, 10-mg/s, 16-CFF, it is accompanied by a decline in mass utilization to approximately 0.75. This consequence illustrates the importance of minimizing neutral-gain utilization for high-performance thruster operation.

In Figure 5-32, variations in the fraction of input moles of propellant relative to the output moles of charge, χ, are shown as a function of the mass utilization and average ion charge. The quantity χ and mass utilization have been termed "propellant utilization" in past analyses.[12,59] This comparison illustrates how increases in multiply-charged ions during high discharge voltage operation can increase χ above unity, and make the term ill-suited as a point of reference for efficiency. Mass utilization was shown to be the predominant factor in propellant utilization in Figure 5-31, but is less influential as charge utilization decreases during high discharge voltage operation. Therefore, descriptions of propellant utilization based on the value of χ and mass utilization will be approximately equivalent to the formulation of propellant efficiency in this architecture during low discharge voltage operation where the fraction of multiply-charged ions is small. As discharge voltage increases and charge utilization decreases, the value of χ and mass utilization will grow increasingly large relative to propellant efficiency as defined in Chapter 2.

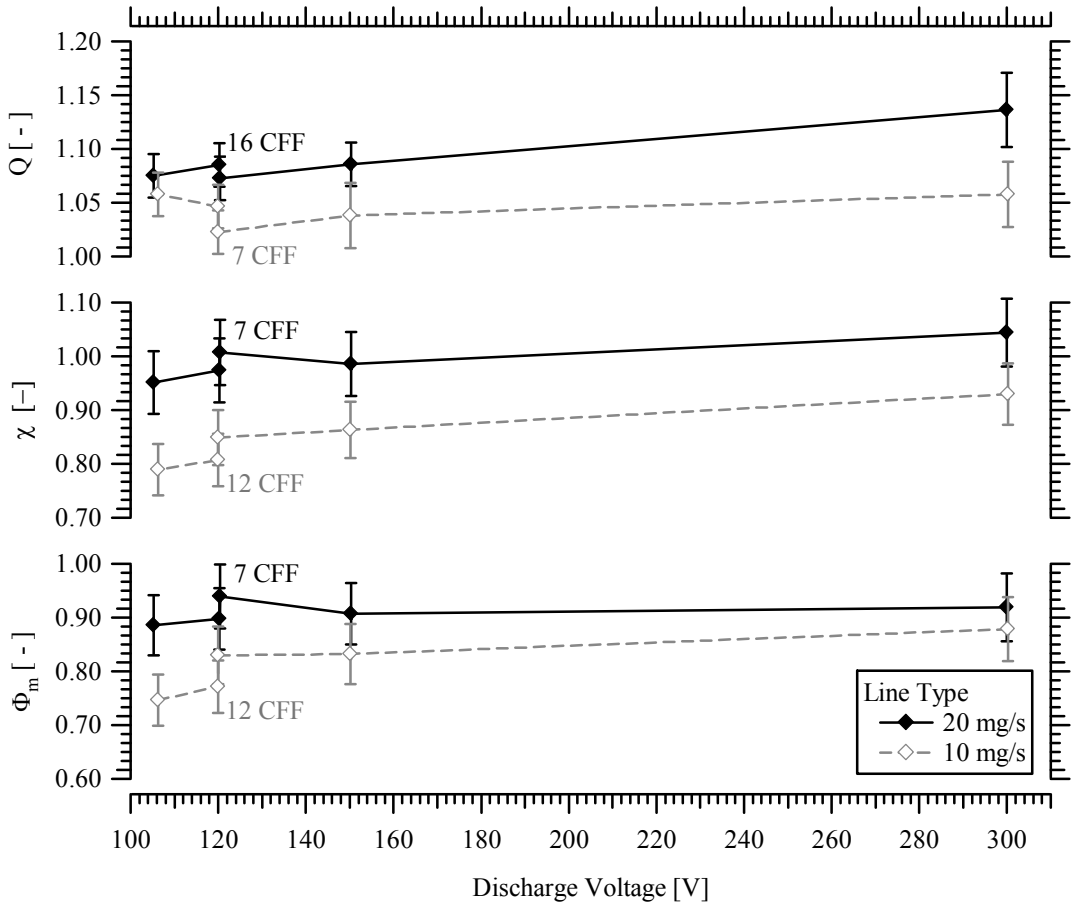

Figure 5-32 Comparison of the factors affecting the ratio of output moles of charge per input moles of propellant, χ, for 105-V to 300-V at 10-mg/s and 20-mg/s anode flow rate. Average ion charge (top), the value χ (middle), and the mass utilization (bottom) are shown as a function of discharge voltage.

5.4.2.3 Energy Efficiency

Energy losses are studied using the power associated with the ion jet kinetic energy from plume measurements relative to the input discharge power. The voltage utilization and current utilization are shown in Figure 5-33, and characterize losses in energy efficiency as resulting from electron current to the anode and loss of ion acceleration potential. Energy efficiency was shown to be a dominant loss mechanism during low discharge voltage operation in Figure 5-28.

Voltage utilization exhibits a steady decline as discharge voltage is reduced from 300-V to 105-V. This reduction in voltage utilization from 300-V is approximately equal to the ionization potential of xenon relative to the discharge voltage (ε_1/V_d). The voltage utilization magnitude and the decline with discharge voltage is equivalent for 10-mg/s and 20-mg/s operation. This implies the anode sheath was relatively insensitive to anode flow rate. Variations in cathode flow during 120-V operation had negligible effect on voltage utilization.

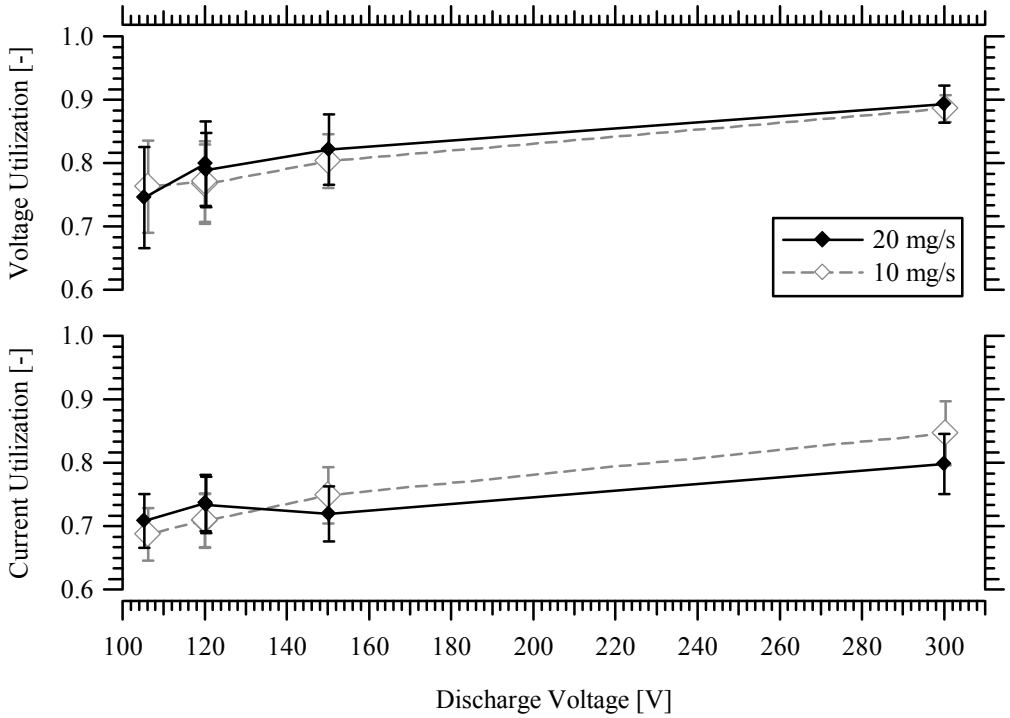

Figure 5-33 Comparison of the factors affecting energy efficiency as a function of discharge voltage for 105-V to 300-V at 10-mg/s and 20-mg/s anode flow rate. Partial efficiencies include the voltage utilization (top) and current utilization (bottom).

Current utilization is a measure of the ion beam current relative to the thruster discharge current, and losses are associated with increased electron flow to the anode due to Joule heating processes in the discharge. Joule heating losses manifest as ionization, excitation, radiation, and ohmic heating of the anode and channel walls. The fraction of cathode electron current to the anode increased during low-voltage operation, and represents a significant loss mechanism. The physics of these Joule heating losses will be studied in relation to thruster performance and ionization cost per beam ion in the following section.

5.4.3 Ionization Processes and Joule Heating Losses

The conversion of applied discharge power to jet kinetic power and the total power losses in energy efficiency are studied using the formulations in Section 2.3.3. Thruster performance will be studied as a function of constant anode mass flow operation and constant power operation. In Figure 5-34, the jet power increased linearly for lines of constant anode flow rate, which is approximately equivalent to lines of constant ion beam current throughput. For constant anode flow rate, the total power losses and the minimum power required to sustain ionization were relatively constant with increasing discharge voltage. Increased ion beam current throughput increased the energy losses, and therefore the power losses associated with 20-mg/s operation were greater than the power losses of 10-mg/s operation. Doubling the anode mass flow rate from 10-mg/s to 20-mg/s resulted in approximately double the power loss. This indicates decreased performance during low discharge voltage operation is associated with the constant power losses becoming a larger fraction of the applied discharge power.

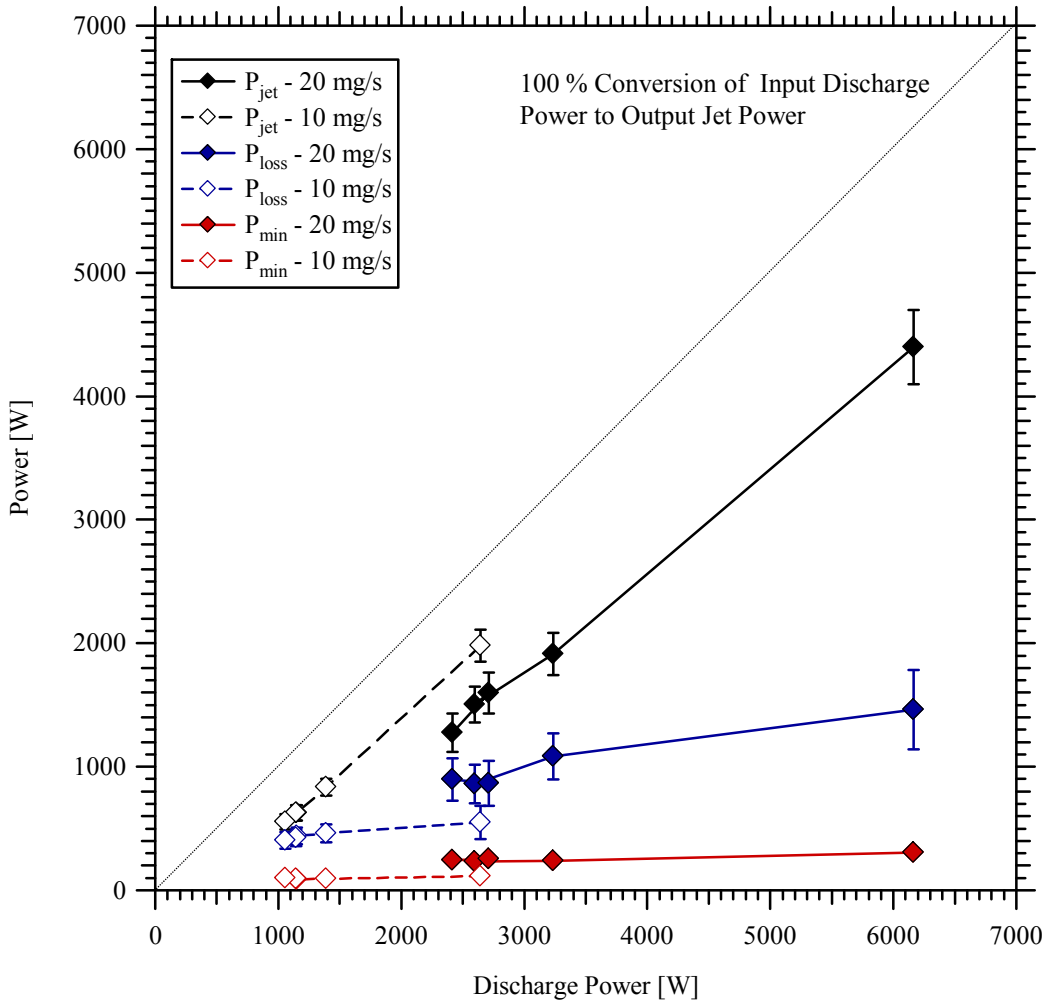

Figure 5-34 Comparison of jet power with the total power losses and the minimum power required for ionization as a function of discharge power for 105-V to 300-V at 10-mg/s and 20-mg/s anode flow rate.

The only comparison of constant power density throughput is for approximately 2.7-kW operation, where the 300-V, 10-mg/s case shows lower total power losses than the 120-V cases at 20-mg/s. This emphasizes the higher performance associated with increased exhaust velocity at higher discharge voltage, which is also more advantageous for the decrease in beam divergence losses.

Variations in power losses with ion beam current throughput and constant power operation is elucidated using the ionization cost per beam ion in Figure 5-35. The

minimum ionization cost and the effective ionization cost per beam ion are compared to the power losses from Figure 5-34. For constant anode flow rate operation, the ionization cost per beam ion parallels the power loss as discharge power increases. However, comparison of the constant power operation at ~2.7 kW shows that low discharge voltage operation has a lower ionization cost of ~70 to 80 eV per beam ion. Using Eq. 2-54, the theoretical minimum ionization cost is relatively constant at ~20 eV/ion, and is based solely on the ion species composition.

The trends in ionization cost per beam ion with discharge power may be a function of the neutral density in the discharge and the electron temperature. For constant power operation, high discharge voltage corresponds to a large electron temperature and leads to the production of multiply-charged ions, excitation, and high energy wall collisions. These loss mechanisms deplete the high energy electrons that would ionize neutral propellant and result in increased ionization cost per beam ion. Conversely, low discharge voltage operation corresponds to a lower electron temperature, and the energy per beam ion lost to ohmic heating, excitation, radiation, and other forms of Joule heating are reduced. However, the electron-neutral collision frequency is proportional to the square root of electron temperature, and eventually the reduction in Joule heating losses associated with low discharge voltage operation is balanced by the reduction in the electron-neutral collision frequency. Therefore, the nature of ionization processes leads to an optimum discharge voltage and propellant flow rate for minimum ionization cost per beam ion in the discharge.

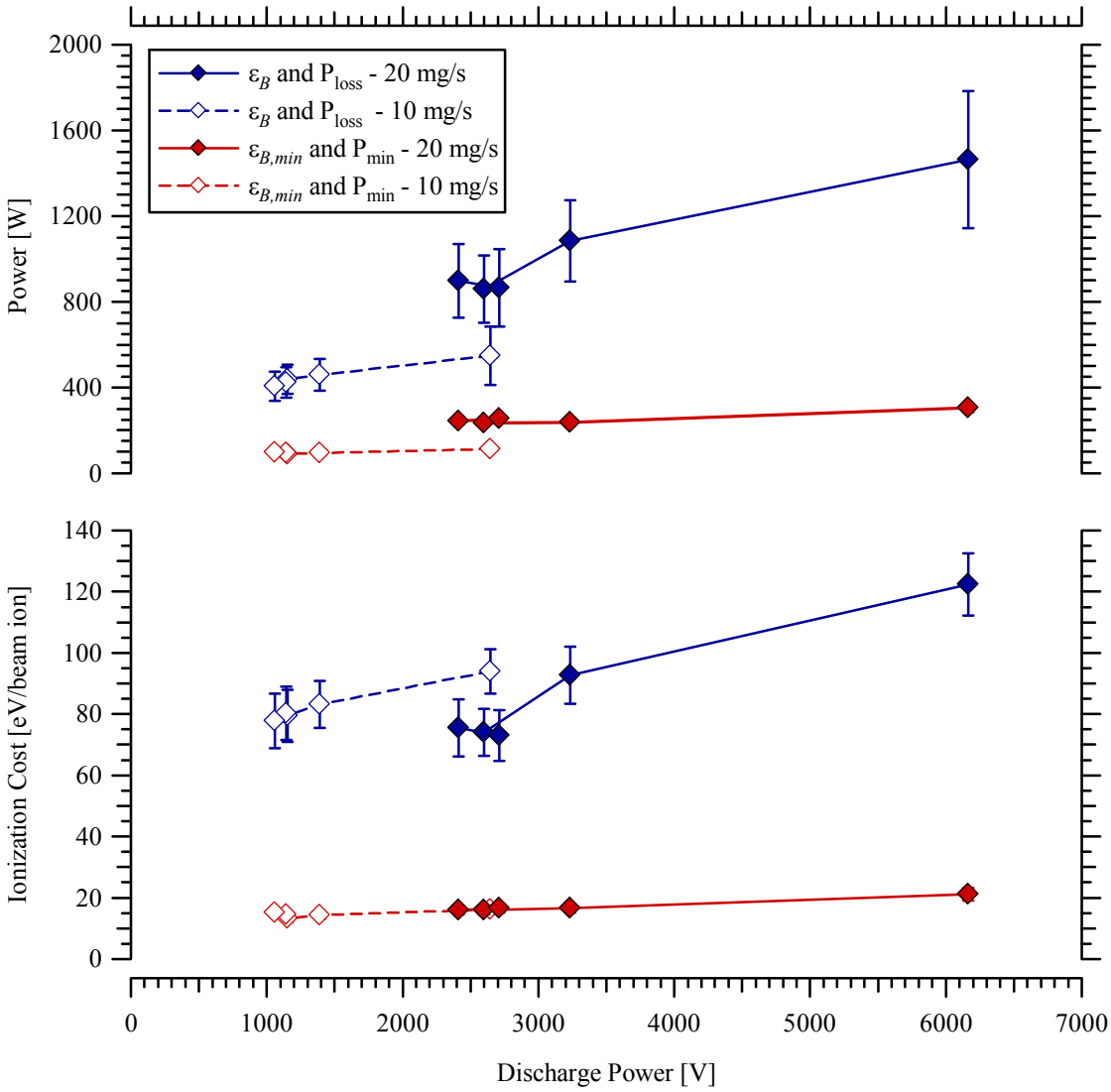

Figure 5-35 Comparison of the total power losses and the minimum power required for ionization (top) with the ionization cost per beam ion (bottom) as a function of discharge power for 105-V to 300-V at 10-mg/s and 20-mg/s anode flow rate.

The relationship of ionization cost per beam ion with respect to the fraction of electron current to the anode is studied in Figure 5-36. Experimental anode electron current fractions from Faraday probe measurements are compared to the theoretical minimum value for ideal electron-impact cascade ionization over the cathode-to-anode potential field. Manifolds of anode electron current are shown for a singly-charged

plasma with variations in discharge current and ionization potential per beam ion. These manifolds are derived by setting the value of r_{min}=r in Eq. (2-40) and solving for the anode electron current. The manifold approximation of a singly-charged plasma is meant to illustrate global trends in anode electron current with ionization cost as opposed to indicating an effective ionization cost associated with an experimental measurement. The effect of multiply-charged ions on ionization cost per beam ion is accounted for in Figure 5-35.

The minimum anode electron currents for ideal cascade ionization of 10-mg/s and 20-mg/s operation follow the trends for 10-A and 20-A operation. Deviations from the trendline are due to minor differences in discharge current and the ion species composition of experimental measurements. The theoretical minimums are approximately three orders of magnitude less than experimental results, and increase sharply below approximately 150-V discharge.

The experimental anode electron current fraction of 10-mg/s operation parallels the manifold for 10-A from 105-V to 150-V, and indicates a constant ionization cost per beam ion analogous to the trend in Figure 5-35. Increasing discharge voltage to 300-V at 10-mg/s resulted in an escalation of the ionization cost per beam ion, and the anode electron current fraction did not follow the manifold trend of the 105-V to 150-V operation. This signals Joule heating losses are increasing and additional anode electron current is required to sustain ionization and compensate for the lost energy. Based on the manifold trendlines, the anode electron current fraction during 300-V, 10-mg/s operation would be approximately 10% of the discharge current without the additional Joule heating losses.

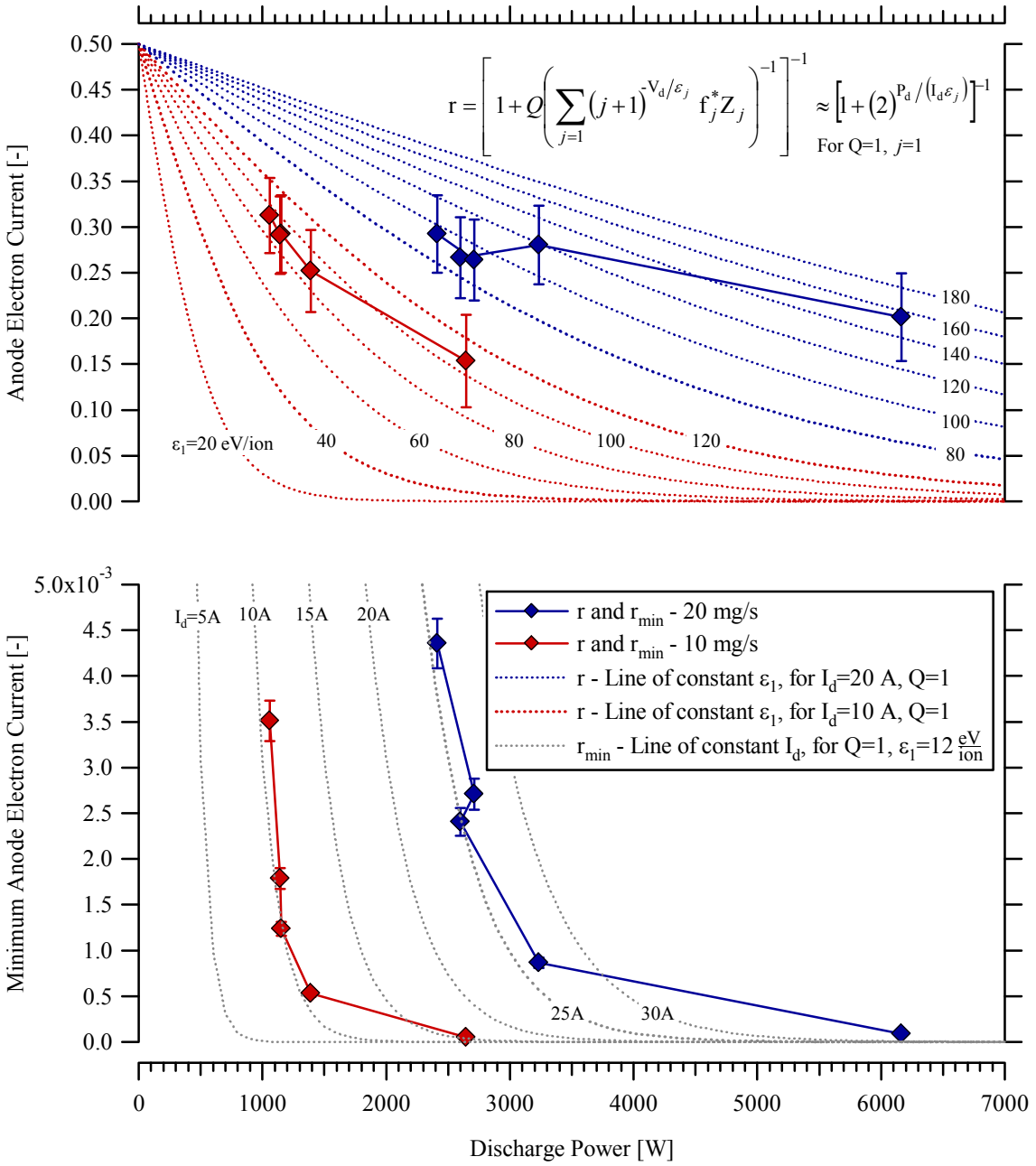

Figure 5-36 **Comparison of the experimental anode electron current fraction (top) with the theoretical minimum electron current fraction (bottom) for ideal cascade ionization as a function of discharge voltage for 105-V to 300-V at 10-mg/s and 20-mg/s anode flow rate. Experimental and theoretical anode electron currents are normalized by the discharge current. The experimental electron current to the anode is compared to manifolds of anode electron current for constant ionization potential per beam ion of a singly-charged plasma (Q=1) during 10-A and 20-A operation. The theoretical minimum electron current to the anode is compared to manifolds of anode electron current for constant discharge current operation of a singly-charged plasma (Q=1) for the minimum xenon ionization potential of 12 eV/ion.**

A large increase in the effective ionization cost is also seen for the 150-V and 300-V conditions at 20-mg/s anode flow rate, and corresponds to a significant increase in the recycled electron current fraction. Thus, Joule heating losses in the discharge cause an increase in the ionization cost per beam ion and thereby necessitate a larger anode electron current fraction.

For constant anode and cathode flow rate operation, the variation in mass utilization in Figure 5-31 is significantly less than the decline in current utilization in Figure 5-33. In a simple qualitative analysis of thruster ionization processes for variations in discharge voltage, the mass utilization (Φ_m) is representative of the ion production rate for electron impact ionization shown in Eq. 5-7 and the electron current fraction to the anode (r) is representative of variations in the electron density in the discharge channel. For nearly constant mass utilization with discharge voltage, the ion production rate will be approximately constant. The increased electron current during low voltage operation would correspond to increased electron density (n_e) in the channel, which would be balanced by a reduction in the ionization rate coefficient ($< \sigma_{e\text{-}n}\, v_e >$) for constant neutral density (n_n) and constant ion production rate (dn_i/dt).

$$\frac{dn_i}{dt} = n_e n_n < \sigma_{e-n}\, v_e > \tag{5-7}$$

In this investigation, the mass utilization hence ion production rate was relatively constant with decreasing discharge voltage. In contrast, the relationship in Eq. (5-7) suggests that the ionization rate coefficient is the parameter that is reduced as opposed to the commonly reported reduction in propellant efficiency.

The primary factors contributing to energy losses are the creation of multiply-charged ions, anode and channel wall collisions, and excitation. Generation of multiply-

charged ions and neutral excitation are likely unavoidable losses associated with higher discharge voltage operation. One area of improvement may be in reducing wall losses. An important aspect of Hall thruster design is the discharge channel geometry, which has conventionally been sized for 300-V operation. Different scaling laws relating the channel surface area to volume may govern low discharge voltage operation, and lead to decreased wall losses. Low-voltage operation is typically associated with ionization and acceleration further downstream in the discharge channel, which would also reduce the surface area of ion wall losses.

The T/P of typical Hall thrusters maximizes below 200-V discharge and at a total efficiency less than the optimal value, as seen in Figure 5-13 and Figure 5-14. However, thrust and Isp have been shown to increase with discharge voltage up to 1000-V. The previous analysis of energy losses demonstrated how ionization processes lead to an optimum range of discharge voltage and propellant flow rate for minimum ionization cost per beam ion in the discharge. The ion acceleration profile and magnetic field topology determine the divergence loss in the plume. Together, these discharge properties determine the T/P characteristics described in Eq. (5-5).

Low-voltage loss mechanisms will be studied in Figure 5-37 by separately analyzing the discharge properties associated with T/P in Eq. (5-5), which include with most probable ion acceleration potential, the axial component of ion beam current, and the properties associated with propellant efficiency. The ion species composition is primarily Xe^+ during low-voltage operation, and the increased fraction of multiply-charged ions at higher discharge voltages reduces the T/P by a small fraction. The reduction in T/P due to decreasing propellant efficiency during high-voltage operation is

magnified when the anode mass flow rate is increased and the fraction of multiply-charged ions amplifies. The axial component of ion beam current relative to the discharge current decreased significantly during low-voltage operation due to an increase in electron current to the anode and divergence losses. Although the voltage utilization decreased during low-voltage operation, the square root of the most probable ion acceleration potential relative to the discharge voltage increases. This is a direct result of the conversion of applied potential energy to acceleration of beam ions over the potential profile. This quantity is the primary driver for increased T/P ratio during low discharge voltage operation, and is insensitive to anode mass flow rate. The idealized case of ion acceleration over the entire potential profile is shown in Figure 5-37, and demonstrates that loss mechanisms in voltage utilization have a relatively minor effect on T/P.

The product of terms in Eq. (5-5) produced a maxima in T/P at approximately 120-V to 150-V discharge in Figure 5-37. The discharge voltage and propellant flow rate where T/P maximizes is established by ionization processes affecting the axial component of ion beam current and the ion species composition. Thus, the primary cause of a peak in T/P during low discharge voltage operation is the ratio of the axial component of ion beam current relative to the discharge current. A theoretical maximum T/P is shown for the case of a singly-charged plasma (Q=1) with ion acceleration over the entire potential profile (V_a=V_d), where all of the discharge current is due to ion beam current directed along the thrust axis (I_{Axial}=I_d). The significant difference between the theoretical maximum value and the case of ideal ion acceleration from the anode face demonstrates that divergence losses and electron current to the anode are the primary loss mechanisms reducing T/P during low discharge voltage operation.

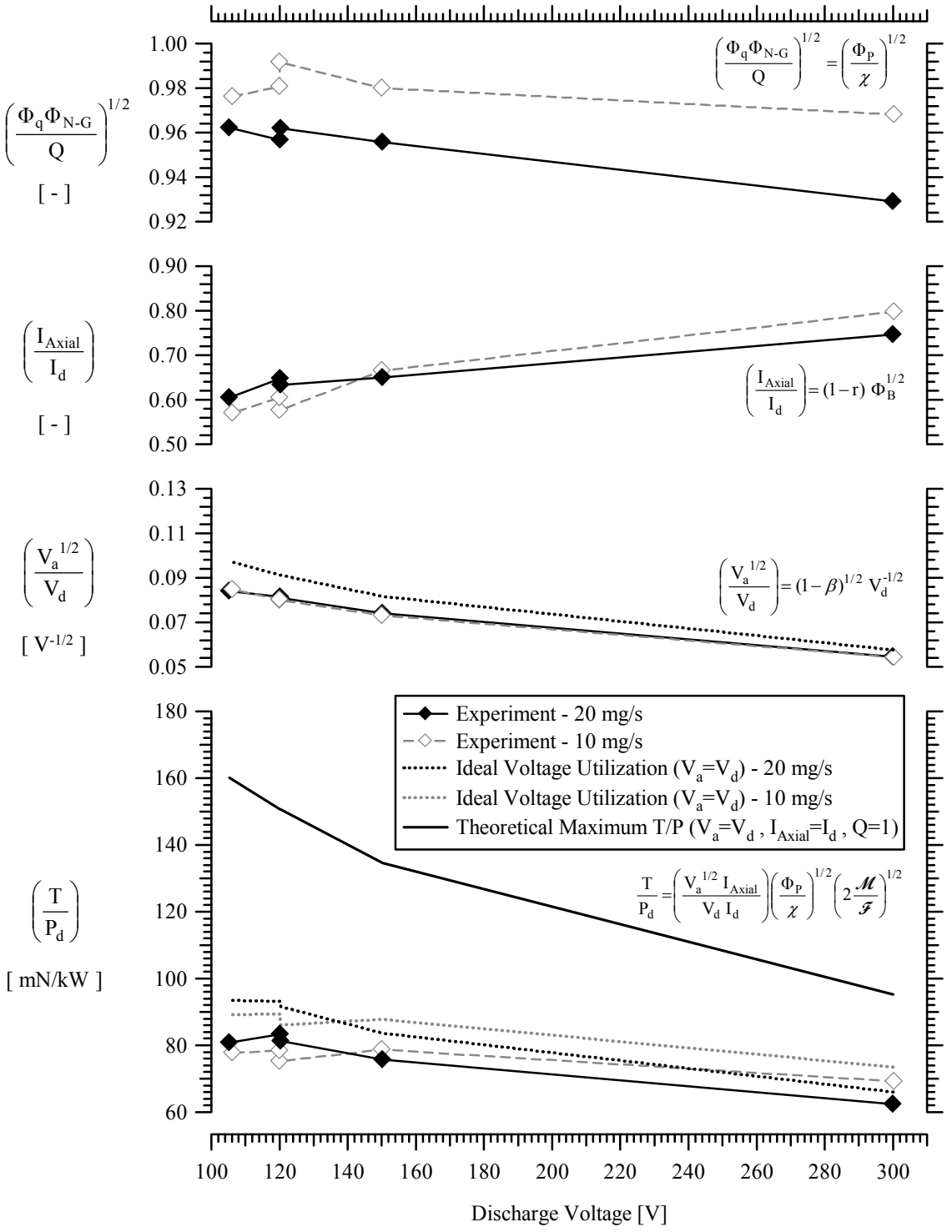

Figure 5-37 Comparison of the factors affecting thrust to power as a function of discharge voltage for 105-V to 300-V at 10-mg/s and 20-mg/s anode flow rate. Discharge properties related to ion species composition (top), the axial component of ion beam current (upper middle), and the most probable ion acceleration potential (lower middle) are shown relative to the T/P (bottom).

5.5 Summary

The low discharge voltage characteristics of a 6-kW thruster were evaluated with measurements of thrust and the far-field plume properties. Facility effects on thrust, discharge current, and ion current density measurements in the plume were isolated and analyzed to estimate the on-orbit performance from ground-based measurements. Loss mechanisms were studied using the Hall thruster efficiency architecture developed in Chapter 2 and related to propellant ionization and acceleration processes for variations in discharge voltage from 105-V to 300-V, anode mass flow rate at 10-mg/s and 20-mg/s, and increased cathode flow fraction during low-voltage operation.

Facility effects on performance were assessed over a range of background pressures using the analytical techniques developed in Chapter 4. Angular regions of constant ion beam current per unit stripe were found in the plume of the 6-kW thruster with increasing background pressure. These regions were similar to the phenomenon seen with increasing distance during vacuum conditions for the low-power Hall thruster in Section 4.4. Differences between the thrusters were attributed to variation in the location of ionization of facility neutrals as background pressure increased. The creation of facility ions in the 6-kW thruster was hypothesized to occur in a relatively compact region that did not reposition with background pressure. This effect led to angular regions of constant ion beam current per unit stripe caused by the external field that did not vary in angular location with background pressure.

Increased thrust and discharge current due to entrained neutral flow was characterized for 105-V and 300-V operation over a range of facility background pressures. The neutral entrainment factor at 300-V was consistent with values found for

similar operation at PEPL.[61] The angular distribution of slope in the ion current density distribution with background pressure was studied as the superposition of two Gaussian curves. The qualitative analysis indicated that ionization of ingested facility neutrals was reduced during low discharge voltage operation, and the primary effect was to disperse the plume through CEX collisions with background neutrals. However, unity neutral entrainment factor suggests that nearly all of the ionized ingested propellant contributed to thrust for a hemispherical entrainment area.

The vacuum ion beam current at 150-V and 300-V discharge from far-field measurements at AFRL showed consistent agreement with near-field measurements from the University of Michigan. Incorporating the ion beam properties into the efficiency architecture resulted in an under-prediction of total efficiency, T/P, and total Isp compared to the values calculated based on thrust measurements. Discrepancies were likely caused by underestimation of the axial component of ion beam current, since Faraday probe measurements were only taken at one downstream location. Results from Chapter 4 demonstrated the significant divergence that occurs in the plume downstream of the primary acceleration zone, even for current density profiles extrapolated to vacuum conditions. The axial component of ion beam current required to equate performance parameters calculated with beam properties compared to thrust measurements resulted in physically plausible divergence half-angles. Plume characterization with downstream distance and facility background pressure was recommended for all near-field and far-field Faraday probe current density measurements.

Beam divergence and electron current to the anode were found to be dominant loss mechanisms inhibiting low discharge voltage total thruster efficiency. Increased

cathode flow reduced beam divergence losses and increased T/P at the expense of mass utilization. Propellant utilization showed a slight increase during low discharge voltage operation due to the decrease in multiply-charged ions and a minimal increase in the neutral-gain utilization. Reduced voltage utilization was primarily due to the xenon ionization potential becoming a larger fraction of the applied anode-to-cathode potential.

A model of electron-impact cascade ionization with an ionization cost of 12 eV/ion showed the minimum fraction of electron current to the anode was two orders of magnitude less than the experimental value, and indicates the effective ionization cost during low-voltage operation was approximately 70 to 80 eVion. Manifolds of constant ionization cost per beam ion were studied relative to the experimental and theoretical fraction of electron current to the anode. Although the higher discharge voltage operation had a higher current utilization, the ionization cost was increased due to the increased voltage required to accelerate ions to high exhaust velocity. Trends in the low-voltage ionization cost for constant power and constant ion beam current operation were attributed to decreased Joule heating as electron temperature decreased, which also corresponded to a reduction in the electron-neutral collision frequency and therefore reduced propellant ionization.

Low discharge voltage operation corresponded to a decrease in the dominant frequency from approximately 12-kHz at 300-V to approximately 6-kHz at 105-V. The decrease in the breathing-mode frequency during low-voltage operation is consistent with reduced ion and neutral velocity. If these low-voltage oscillations are the breathing mode frequency as described in Eq. (5-4), the ionization length would be expected to increase by approximately 25% from 300-V to 105-V operation. An increase in the range of

propellant ionization during low-voltage operation is consistent with the reduced ionization rate coefficient for approximately constant ion production rate per unit volume. These macroscopic trends are based on global far-field parameters, and further examination of the near-field and internal plasma characteristics is required to study spatial and/or temporal variations during low-voltage Hall thruster operation.

Analysis of the beam properties affecting T/P established that the conversion of applied discharge potential to the axial acceleration of ions was responsible for a large increase in T/P at low discharge voltage. Interactions between the reduction of the axial component of ion beam current relative to discharge current and the conversion of anode potential to axial ion acceleration created a maxima in T/P during low-voltage operation.

In summary, high-voltage operation leads to increased exhaust velocity and Isp, but is associated with diminishing gains in velocity as discharge voltage is increased and the energy losses per beam ion escalate. A majority of the discharge power is applied to ion acceleration during high-voltage operation and the increased electron temperature leads to additional Joule heating losses. During low-voltage operation, the discharge power is applied to ionization of a larger fraction of propellant. The reduced electron temperature during low-voltage operation leads to a decline in the Joule heating losses and lower ionization rate coefficient. Therefore, increased electron current to the anode required to sustain ionization as the ionization rate coefficient declines was a dominant loss mechanisms during low-voltage operation.

Chapter 6

Low Discharge Voltage Thruster Operating Regimes

Early investigations in the former Soviet Union observed and characterized Hall thruster discharge oscillations, which are considered an inherent process associated with Hall thruster technology.[126,130] The oscillations are often related to ionization instabilities and density gradients that are dependent on the thruster operation, including variations in: discharge voltage, anode mass flow rate, cathode mass flow rate and location, propellant type, thruster geometry, PPU characteristics, and magnetic field topology. An exceptional overview of these Hall thruster discharge oscillations ranging from approximately 1-kHz up to over 60-MHz was described by Choueiri.[129]

Several recent investigations have studied the complex fluctuating Hall thruster discharge, and analyzed thruster operating modes dependent on the thruster operation and design. A systematic study of oscillation behavior from 2-kHz to 100-kHz by Chesta detailed the influence of azimuthal density non-uniformities and probe perturbations, and revealed that the interactions of these effects with the natural Hall thruster discharge dynamics may cause instabilities.[131] A study by Azziz on the BHT-1500 characterized two operating modes that were sensitive to magnetic field, termed the jet-mode and collimated mode.[97] These modes were attributed to the location of ionization within the discharge channel, and exhibited variations in ion current density and ion energy

distribution in the plume. Extensive studies of Hall thruster dynamics and oscillation behaviors have been conducted throughout the literature, however, the nature of these effects is extremely complex and difficult to quantify.

During the course of low discharge voltage experiments with the 6-kW Hall thruster, discontinuities in thruster performance occurred for small variations in operating parameters. Minor changes in magnetic field or cathode flow rate resulted in an intense, visible transformation of the jet-mode plume structure. This transformation corresponded to an abrupt escalation in the discharge current with constant thrust and amplification of the discharge oscillations. The transition was achieved with a hysteresis effect, such that identical operation set-points may generate vastly different discharge properties. It has been well documented that low discharge voltage operation is associated with increased oscillation behavior and variation in thruster performance.[125,126,132,133] Since the specific nature of the oscillations in this study are unknown, the existence of two discharge operating regimes led to classification as the high-current mode and low-current mode.

In this chapter, the phenomenon is characterized with a systematic map of thruster operation for discharge voltages ranging from 100-V to 120-V, anode mass flow rates at 10-mg/s, 15-mg/s, and 20-mg/s, and cathode flow rate fractions of 7% to 25% of the anode flow. Performance characteristics and far-field plume properties were studied in Chamber 3 with the diagnostics described in Chapter 3 and the efficiency architecture developed in Chapter 2. Although the exact nature of the operating regimes remains uncertain, the discharge characteristics are evaluated and potential physical causes are discussed. Data from this chapter is tabulated in Appendix C and Appendix D.

6.1 Visualization of Low Discharge Voltage Operating Regimes

The transition between low discharge voltage operating regimes corresponded to a sudden transformation of the jet-mode plume structure. The plume transformed from an extended, diffuse jet during high-current mode to a more compact jet located further upstream during low-current mode operation. The Hall thruster jet-mode is characterized by a visible jet-like plume profile extending several thruster diameters downstream of the exit, and is distinguished from a diffuse glow discharge by a significantly lower discharge current. Both jet-mode regimes in this study exhibited substantially lower discharge current than operation in the diffuse glow discharge mode. High resolution images of the operating regimes are shown in Figure 6-1, and contours of constant image intensity more clearly show the extended plume structure in the high-current mode compared to the low-current mode. This qualitative visualization illustrates the extended plume features discernible by eye in laboratory experiments.

During operation near the transition point between the two states, the thruster showed visible signs of flickering and instability. Performance measurements were not taken in this unstable transition regime due to uncertainties in thrust measurements for indeterminate pulsing. The thruster operated in a stable jet-mode in both the high-current and low-current states. As stated previously, the transformation between thruster operating regimes revealed characteristics of hysteresis, where a large cathode flow rate and magnetic field were required to transition from the high-current to low-current regimes. Once the transition to low-current mode occurred, the cathode flow and magnetic field could be decreased while maintaining the decreased current operation.

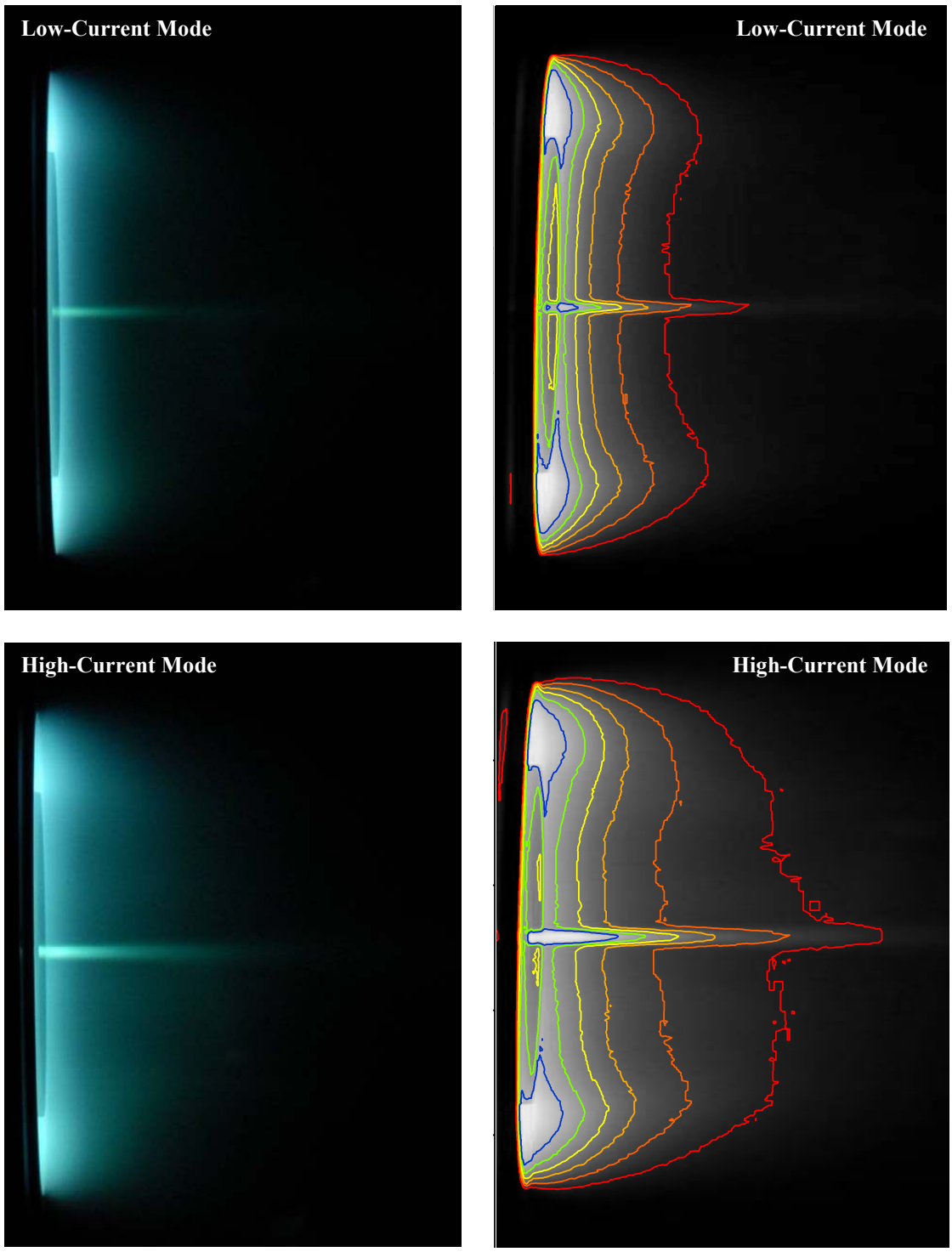

Figure 6-1 **Photographs of the 6-kW Hall thruster jet-mode plume structure for the low-current mode (top left) and high- current mode (bottom left) during 105-V, 20-mg/s operation. Contours of constant image intensity are shown for the low-current mode (top right) and the high-current mode (bottom right). Photos were taken with identical settings on a tripod mounted Nikon D200 DSLR using a 70-mm lens with manual focus at F/5, ISO-400, and exposure time of 1/2000 sec.**

The extended contours of constant image intensity during high-current mode indicate that excitation and ionization are occurring further downstream in the discharge. In addition, the cathode plume appears more intense and protracts much further from the exit plane. Further investigations are required to develop a better understanding of the interrelated processes driving low discharge voltage Hall thruster operation. In the following sections, the plume properties, performance characteristics, and discharge oscillations will be studied.

6.2 Mapping Thruster Operation for Anode and Cathode Flow Rate

The low discharge voltage thruster operation is examined from 100-V to 120-V in a systematic map of discharge voltage, anode mass flow rate, and cathode mass flow rate. In Figure 6-2, the thruster operating characteristics are shown for lines of constant discharge voltage as a function of cathode flow fraction at anode flow rates of 10-mg/s, 15-mg/s, and 20-mg/s. This data set has not been extrapolated to vacuum conditions, and magnetic fields were adjusted for maximum efficiency.

At a critical cathode flow fraction, the discharge current dropped by approximately 10%. This reduction is emphasized with arrows, and occurs across the operating transition from the high-current mode to the low-current mode for 100-V to 110-V thruster operation. The performance map features the thruster operating parameters where the low-current mode is achievable for an optimal magnetic field configuration.

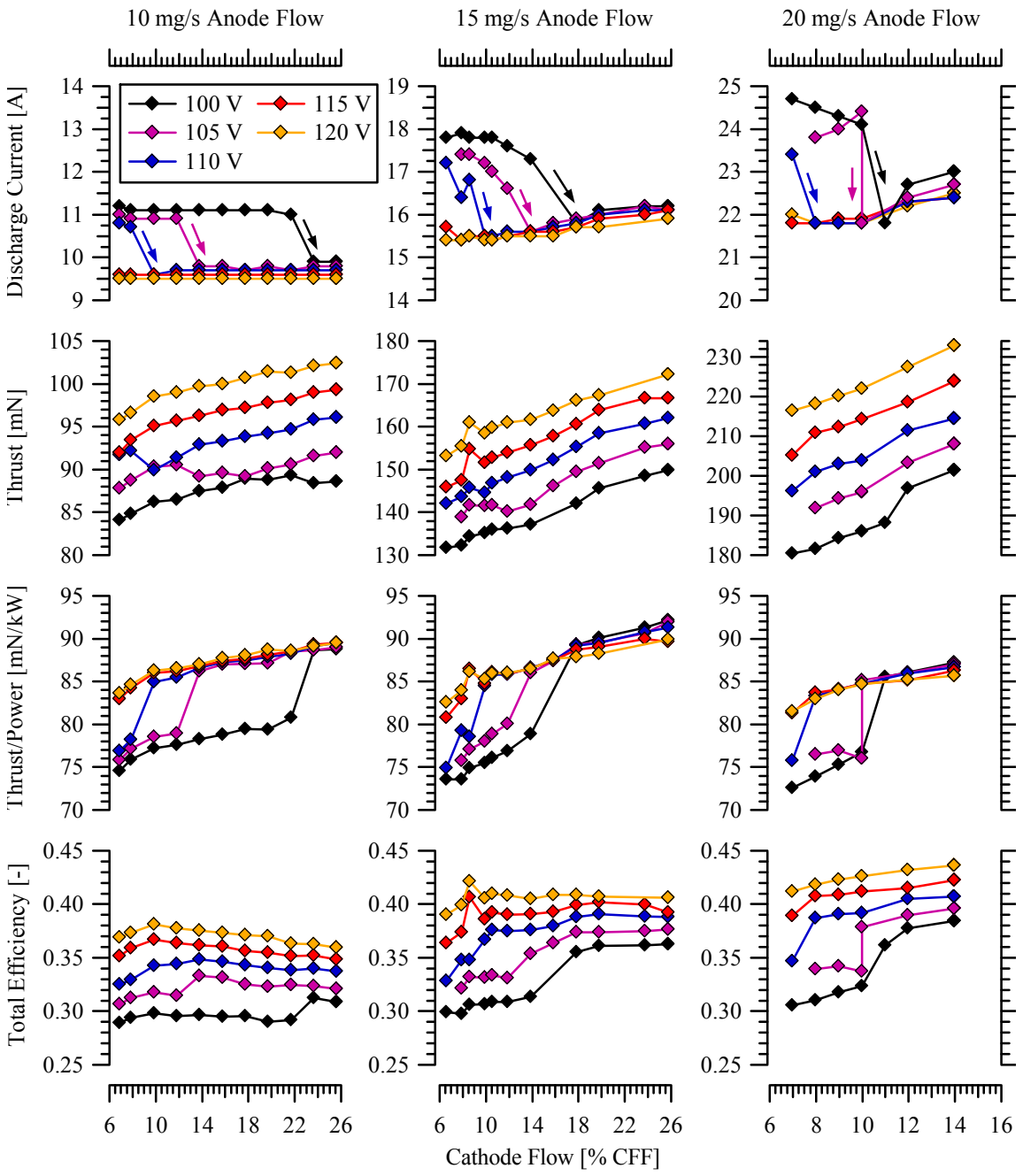

Figure 6-2 **Mapping of anode and cathode thruster operating characteristics at 100-V, 105-V, 110-V, 115-V, and 120-V discharge. Discharge current, thrust, T/P, and total thruster efficiency are shown for lines of constant discharge voltage as a function of cathode flow fraction during 10-mg/s (left column), 15-mg/s (middle column), and 20-mg/s (right column) anode mass flow rate operation. Operating characteristics are reported for facility background pressure in the range of 0.8×10^{-5} to 1.2×10^{-5} torr. Transitions from the operation in low-current to high-current mode are shown with arrows.**

Two points should be addressed regarding this performance map. The high-current operating regime also existed for 115-V and 120-V thruster operation in a span of magnetic field settings, but the thruster was capable of operation in the low-current mode for the full range of cathode flow rates studied. Conversely, thruster operation reported in the high-current mode below 110-V was unable to transition to low-current mode, such as during 100-V, 10-mg/s anode flow rate below 24-CFF.

Thrust was relatively constant between the low-current and high-current mode. The linear increase in thrust with cathode flow is attributed to neutral ingestion and acceleration of cathode propellant. As a result of the decline in discharge current associated with the low-current operating regime, the T/P and total thruster efficiency improved. Further increases in CFF generated additional neutral ingestion, and led to further increases in total efficiency for the 20-mg/s operating conditions. The highest T/P occurred for 15-mg/s operation at 26-CFF, however, the trend in the 20-mg/s data set indicates the T/P may also be increased to similar levels if CFF is increased beyond 14-CFF up to 26-CFF. For low-voltage operation where the ionization and acceleration regions are located further downstream than nominal 300-V operation, an optimal anode and cathode flow rate may lead to a decline in discharge energy losses in the channel with enhanced downstream ionization, and result in a maximum η_T with high T/P ratio.

The thruster operation and performance effects may be studied in a comprehensive manner using E_1 and E_2 in Figure 6-3. Lines of constant 10-mg/s anode flow operation showed that increased CFF causes a constant decrease in $E_1 \sim (T/\dot{m}_T)^2$. The transition from high-current mode to low-current mode followed this trend with minimal change in η_T for all 10-mg/s data.

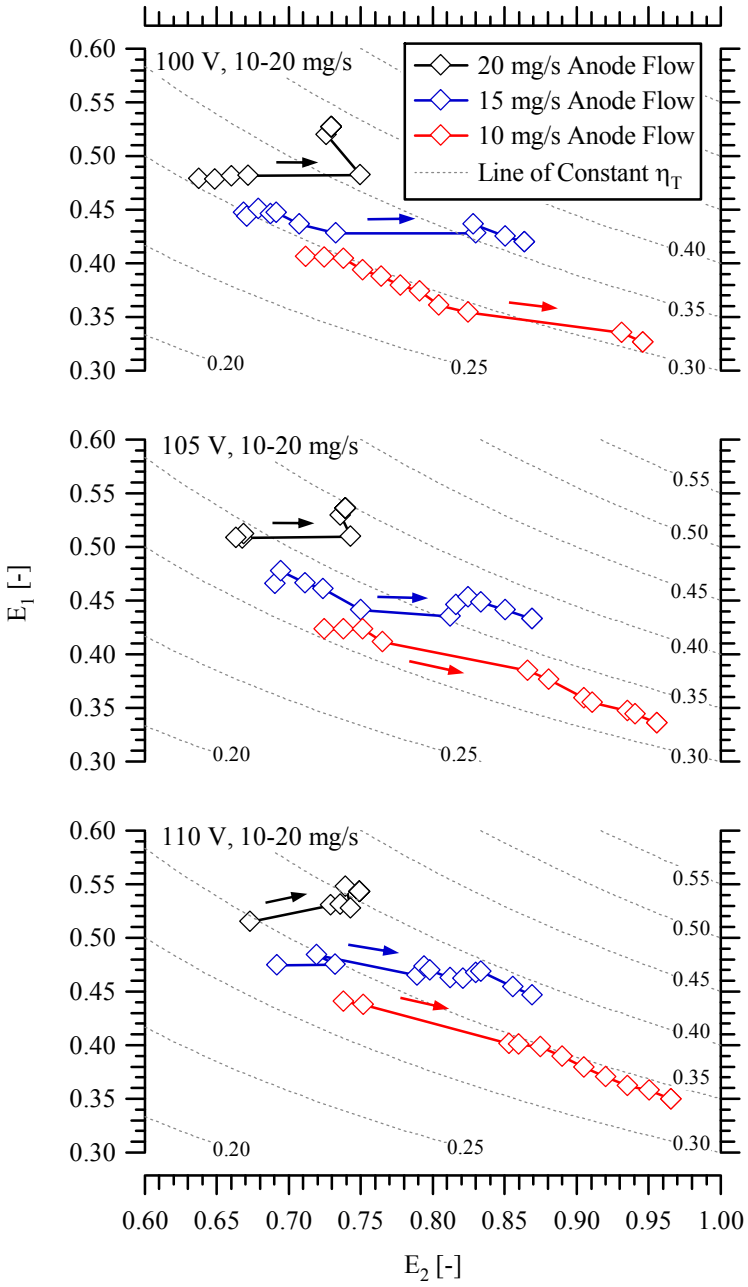

Figure 6-3 **Voltage exchange parameter and mass exchange parameter at 100-V (top), 105-V (middle), and 110-V (bottom) thruster operation for lines of increasing cathode flow during 10-mg/s, 15-mg/s, and 20-mg/s anode flow. Operating characteristics are reported for facility background pressure in the range of 0.8×10^{-5} to 1.2×10^{-5} torr. Transitions from the operation in high-current to low-current mode are shown with arrows, indicating the direction of increasing cathode flow fraction.**

Global observations of low discharge voltage operation from Figure 6-2 and Figure 6-3 are summarized below.

1. For constant discharge voltage and anode flow rate, decreasing cathode flow fraction to a critical level led to operation in the high-current mode, corresponding to a step increase in discharge current with approximately constant thrust.

2. Lower discharge voltage operation required a larger cathode flow fraction for thruster operation in the low-current regime (24-CFF at 100-V, 10-mg/s compared to 10-CFF at 110-V, 10-mg/s).

3. Lower anode flow rate operation required a larger cathode flow fraction for thruster operation in the low-current mode (24-CFF at 100-V, 10-mg/s compared to 12-CFF at 100-V, 20-mg/s).

4. The greatest difference in thruster performance between low-current mode and high-current mode occurred for low-voltage, high anode flow operation (greatest total efficiency gain of 5.5% at 100-V, 20-mg/s compared to 1.5% gain at 110-V, 10-mg/s).

5. For constant anode mass flow and constant CFF above the critical value for low-current operation, increasing discharge voltage from 100-V to 120-V resulted in improved T/P and nearly constant total efficiency.

In Figure 6-4, the low-voltage I-V characteristics with variations in cathode flow fraction are compared to thruster operation at 7-CFF from 100-V to 300-V for 10-mg/s anode flow rate. The low-current mode follows the trend of nominal thruster operation, and the high-current mode is a low discharge voltage anomaly. Thus, reduced cathode flow rate during low-voltage operation leads to a performance detriment. Since thrust is relatively constant during the transition from low-current mode to high-current mode, the simplest mechanism for increased discharge current is an escalation in electron current to the anode. This hypothesis will be evaluated in Sections 6.3 and Section 6.4.

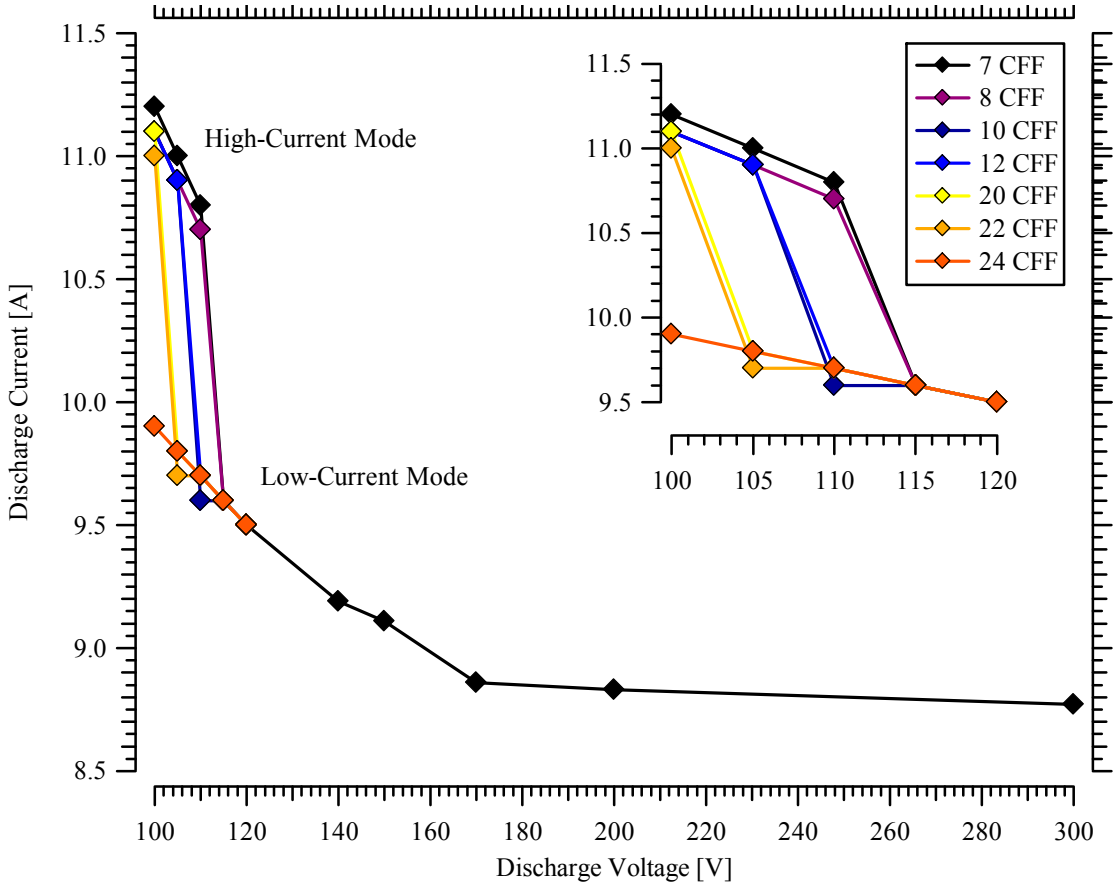

Figure 6-4 **Thruster I-V characteristics at 10-mg/s anode flow rate. Lines of constant cathode flow rate operation are shown as a function of discharge voltage from 100-V to 300-V. Low discharge voltage operation is magnified from 100-V to 120-V discharge.**

6.3 Discharge Oscillations of Low-Voltage Operating Regimes

In addition to a significant variation in the discharge current magnitude, the high-current mode may be identified by a significant increase in the amplitude of discharge oscillations. The substantial change in discharge current oscillation amplitude is shown in Figure 6-5 for 105-V, 20-mg/s, 16-CFF and 120-V, 10-mg/s, 7-CFF. The low discharge voltage, high flow rate condition was chosen because it exhibited the largest change in thruster performance between the high-current and low-current modes. The 120-V, 10-mg/s, 7-CFF case was chosen because it is opposite the 105-V case in terms of higher voltage, lower anode flow, and lower cathode flow fraction. In addition, the low-current regime performance characteristics of these operating points were analyzed in Chapter 5. For equivalent comparison of high-current and low-current operation, the magnetic field settings are identical between operating regimes and equivalent to the magnetic field settings used for these operating conditions in Table 5.1.

The power spectra of discharge current and cathode-to-ground potential oscillations are shown in Figure 6-6 for the 105-V and 120-V cases shown in Figure 6-5. Although the oscillation amplitude increased from low-current to high-current mode, the dominant frequency was constant. In addition, the peak frequencies in discharge current oscillations match the cathode-to-ground potential oscillations. Subsequent peaks are harmonics of the dominant frequency. These trends demonstrate there is significant cathode coupling during high-current operation. These trends are consistent with all oscillation measurements of the high-current and low-current regimes.

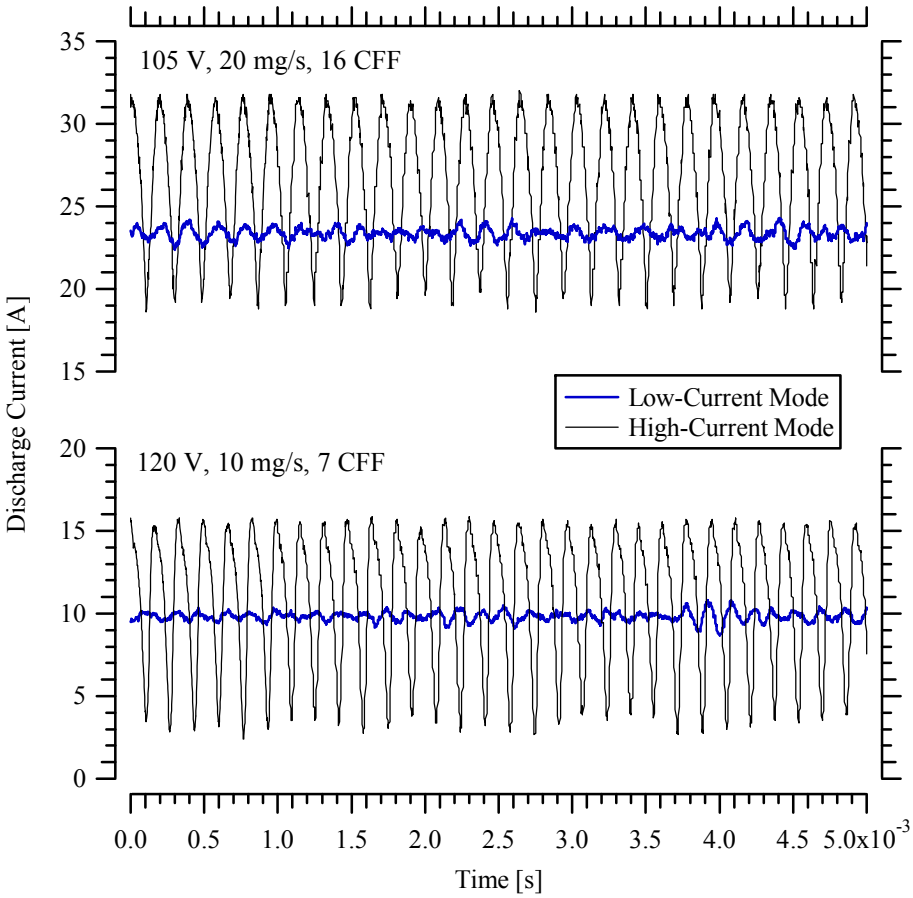

Figure 6-5 **Comparison of discharge current oscillations in the low-current and high-current modes for 105-V, 20-mg/s, 16-CFF operation (top) and 120-V, 10-mg/s, 7-CFF operation (bottom) during a 5-ms time period.**

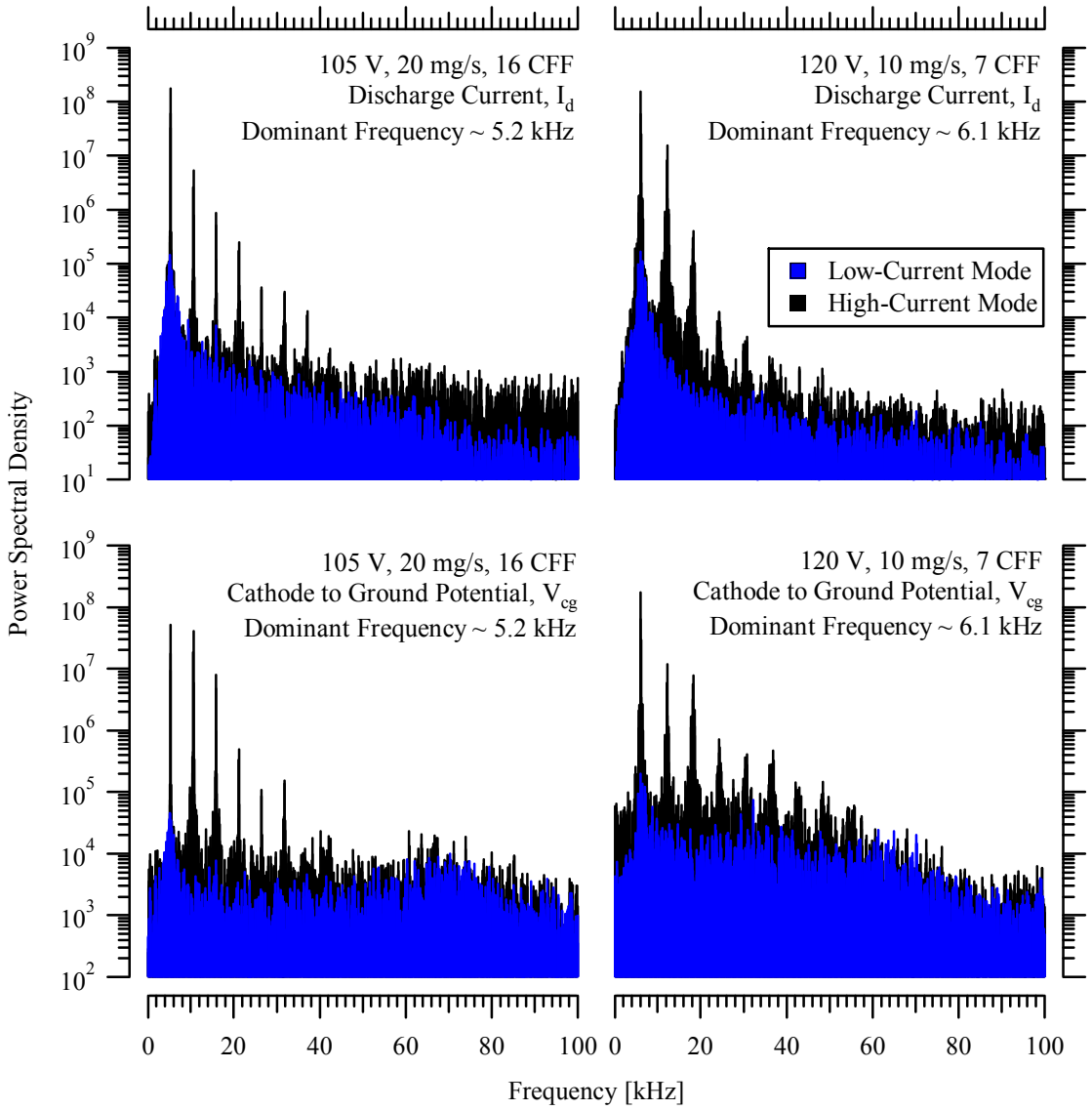

Figure 6-6 **Comparison of discharge current oscillation spectra (top) and cathode to ground potential oscillation spectra (bottom) in the low-current and high-current modes for 105-V, 20-mg/s, 16-CFF operation (left) and 120-V, 10-mg/s, 7-CFF operation (right) from 0 to 100-kHz.**

The stimulus of these oscillations is unknown. Possibilities include the Hall thruster breathing mode, the rotating "spoke" instability associated with low discharge current operation, oscillations manifested from cathode operation, or power supply induced discharge oscillations. The three former possibilities are associated with

ionization instabilities. The constant frequency of oscillations between high-current and low-current modes indicates one of the instabilities is amplified.

One key is that increased cathode flow eliminates the high-current operation, and may be due to increased neutral density near the thruster or cathode exit. In this case, increased facility background pressure should have a similar effect on the high-current operating regime. This is studied in Figure 6-7 for the 105-V, 20-mg/s, 16-CFF case and 120-V, 10-mg/s, 7-CFF case.

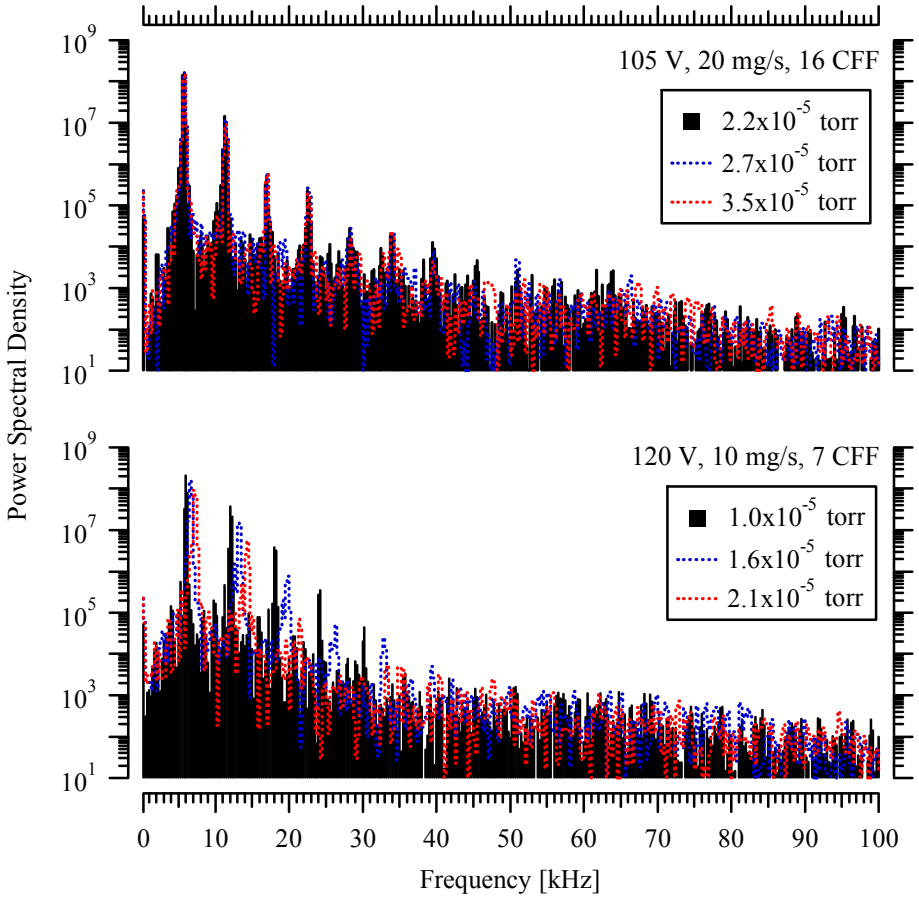

Figure 6-7 **Comparison of discharge current oscillation spectra in the high-current mode for 105-V, 20-mg/s, 16-CFF operation (top) and 120-V, 10-mg/s, 7-CFF operation (bottom) with variation in facility background pressure.**

In the 105-V case, increased facility background pressure ranging from $2.2x10^{-5}$ to $3.5x10^{-5}$ torr did not affect the discharge oscillations. However, the 120-V case exhibited a 1-kHz increase in the dominant frequency and a reduction in magnitude of spectra harmonics. Further increasing the background pressure up to ~$4.0x10^{-5}$ torr caused the thruster to transition to the low-current operating regime, and is further evidence that increased neutral density near the exit minimizes the discharge oscillations.

In the breathing mode "predator-prey model", the discharge frequency is inversely proportional to the ionization length, proportional to the square root of the neutral velocity, and proportional to the square root of the ion velocity increment. If the oscillations are related to the breathing mode, the increased dominant frequency in Figure 6-7 may be associated with a decrease in the ionization length.

Since the high-current operating regime of the 120-V, 10-mg/s, 7-CFF case appeared to be more sensitive to increased neutral density near the exit, this operating condition is studied in further detail for variations in CFF in Figure 6-8. The dominant frequency of the high-current mode increased from 5.8 kHz up to 6.3 kHz when cathode flow was increased from 5-CFF to 12-CFF. The low-current mode exhibited negligible variation in the dominant frequency as cathode flow fraction was increased.

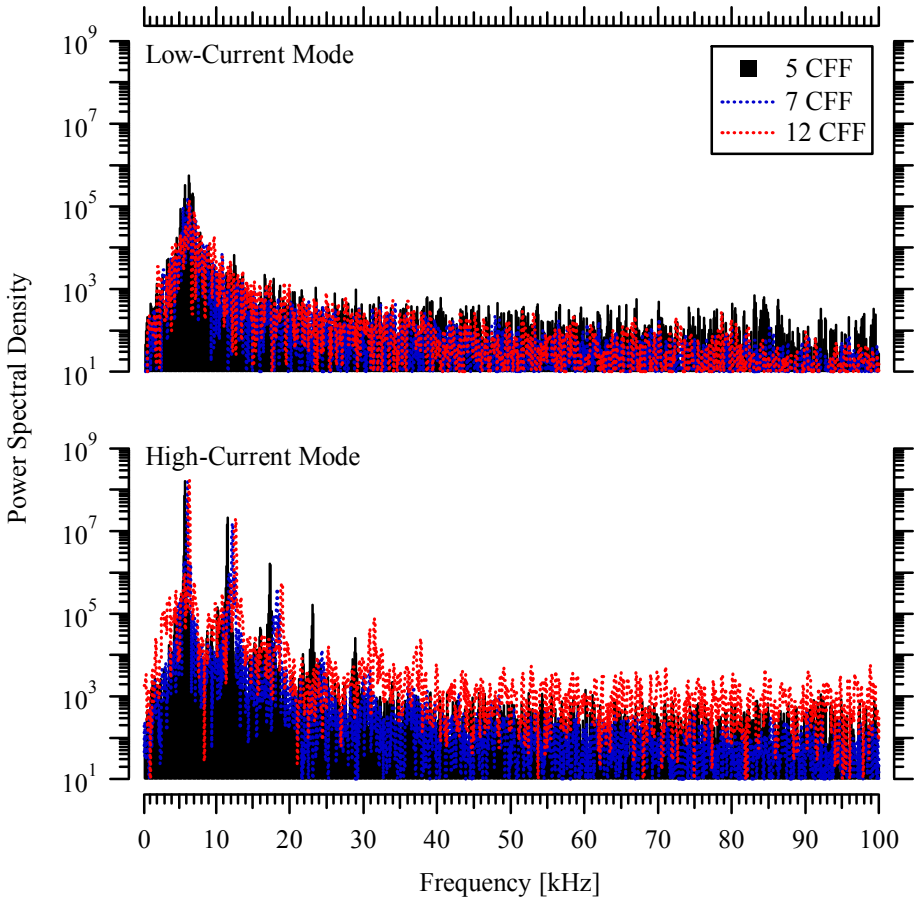

Figure 6-8 **Comparison of discharge current oscillation spectra in the low-current mode (top) and high-current mode (bottom) for 120-V, 10-mg/s operation at 5, 7, and 12-CFF.**

The trends in performance and discharge oscillations indicate high-current operation is associated with amplification of ionization instabilities, and these instabilities may be minimized with additional neutral flow near the thruster exit. As demonstrated in Section 6-2, the primary effect on thruster performance was a decrease in the discharge current. Far-field plume properties will be studied in Section 6-4 to further examine the low discharge voltage Hall thruster operating regimes.

6.4 Far-field Plume Measurements

Examination of the far-field plume properties was conducted with a nude Faraday probe, RPA, Langmuir probe, and ExB probe as described in Chapter 3 and employed in Chapter 5. The 105-V, 20-mg/s, 16-CFF case will be used as a benchmark for the high-current and low-current modes due to the stable thruster operation in each regime over a wide range of background pressures. Variations in anode flow rate, cathode flow rate, and discharge voltage will be studied relative to this operating condition.

6.4.1 Ion Beam Current and Plume Divergence

The angular distributions of ion current density at vacuum conditions for the low-current mode and high-current mode are shown in Figure 6-9. The benchmark 105-V, 20-mg/s, 16-CFF condition in each regime is evaluated with operation at 10-mg/s anode flow, with operation at 10-CFF, and with operation at 120-V discharge. The minimal cathode flow required for low-current mode is 10-CFF. Plume properties are listed in Table 6-1 to more clearly discern differences in the current density profiles.

Integrated ion beam current, discharge current, and divergence half-angle are compared for low-current and high-current modes in Table 6-1. The high-current mode was associated with an increase in electron current to the anode ($r\ I_d$) in all cases, which resulted in reduced current utilization. The increase in anode electron current suggests Joule heating losses and/or electron leakage are increased in the high-current mode.

Table 6-1 Comparison of the ion and electron currents in the discharge of the 6-kW Hall thruster during low-current and high-current operation.

Operating Conditions	Operating Regime	Current [A]			Current Utilization, (1-r)	Divergence Half-Angle, λ [degrees]
		I_d	I_{Beam}	r I_d		
105-V, 20-mg/s, 16-CFF	Low-current	22.9	16.2	6.7	0.71	31°
105-V, 20-mg/s, 16-CFF	High-current	27.1	18.0	9.1	0.66	36°
105-V, 10-mg/s, 16-CFF	Low-current	10.0	6.8	3.2	0.68	34°
105-V, 10-mg/s, 16-CFF	High-current	12.0	7.7	4.3	0.64	33°
105-V, 20-mg/s, 10-CFF	Low-current	22.1	15.8	6.3	0.72	31°
105-V, 20-mg/s, 10-CFF	High-current	26.8	16.9	9.9	0.63	33°
120-V, 20-mg/s, 16-CFF	Low-current	22.6	16.6	6.0	0.74	28°
120-V, 20-mg/s, 16-CFF	High-current	25.9	16.6	9.3	0.64	33°

The variation in anode flow rate resulted in approximately equivalent reduction in current utilization. However, the divergence decreased during the high-current mode for 105-V, 10-mg/s, 16-CFF operation. During the low-current operation studied in Chapter 5, the 10-mg/s case corresponded to a lower mass utilization and higher neutral-gain utilization. This was attributed to a reduction in the electron-neutral collision frequency resulting from decreased neutral density in the channel. In addition, the performance mapping in Section 6.2 indicated that a lower anode flow rate required a larger CFF for operation in the low-current regime. These observations suggest the increased neutral density and electron-neutral collision frequency associated with higher anode mass flow rate reduced the cathode flow rate required for low-current operation. However, the additional electron current fraction during 105-V, 10-mg/s, 16-CFF in the high-current mode may be ionizing anode propellant further upstream than the 20-mg/s case. These concepts will be further evaluated with far-field ExB probe measurements of ion energy distributions in Section 6.4.3.

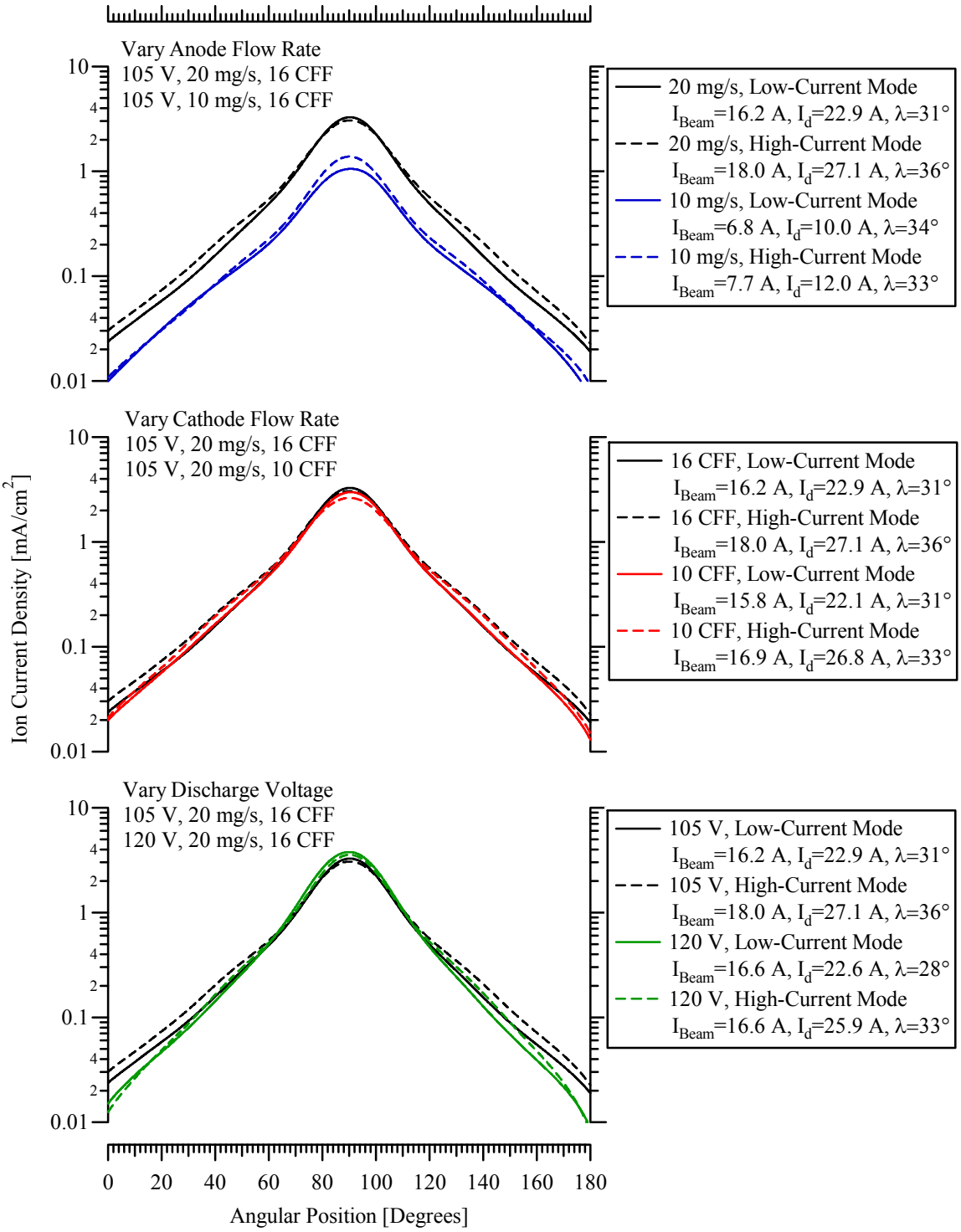

Figure 6-9 **Comparison of ion current density extrapolated to vacuum for high-current and low-current regimes. The current density at 105-V, 20-mg/s, 16-CFF is compared to the case of decreased anode flow at 10-mg/s (top), decreased cathode flow rate at 10-CFF (middle), and increased anode potential at 120-V (bottom). Integrated ion beam current, divergence angle, and discharge current are listed in the legends for vacuum conditions.**

Decreasing cathode flow rate from 16-CFF to 10-CFF produced more anode electron current in the high-current mode, and led to further reduction in the current utilization. Although the increase in ion beam current during high-current operation was approximately 1.7-A for the 105-V, 20-mg/s, 16-CFF and 105-V, 20-mg/s, 10-CFF cases, the higher cathode flow fraction exhibited a larger divergence in the far-field plume. It is expected that the higher neutral density near the thruster exit plane from cathode flow led to increased CEX collisions with beam ions.

During 120-V discharge operation, high-current operation yielded minimal change in the ion beam current. Thus, the 3.3 A increase in discharge current was entirely due to electron current to the anode, and caused a large decline in current utilization.

The global result of the high-current mode appears to be increased beam divergence, increased anode electron current, and increased ion beam current. While these effects vary slightly depending on the thruster operation, it is consistent with an escalation of Joule heating losses in addition to ionization and/or an acceleration profile further downstream in the discharge channel.

6.4.2 Plasma Potential and Electron Temperature

Far-field Langmuir probe measurements of plasma potential and electron temperature on channel centerline are shown in Figure 6-10 for 105-V, 20-mg/s operation from 8-CFF to 16-CFF in the high-current and low-current modes. The trends in these profiles are representative of the other low-voltage operating conditions.

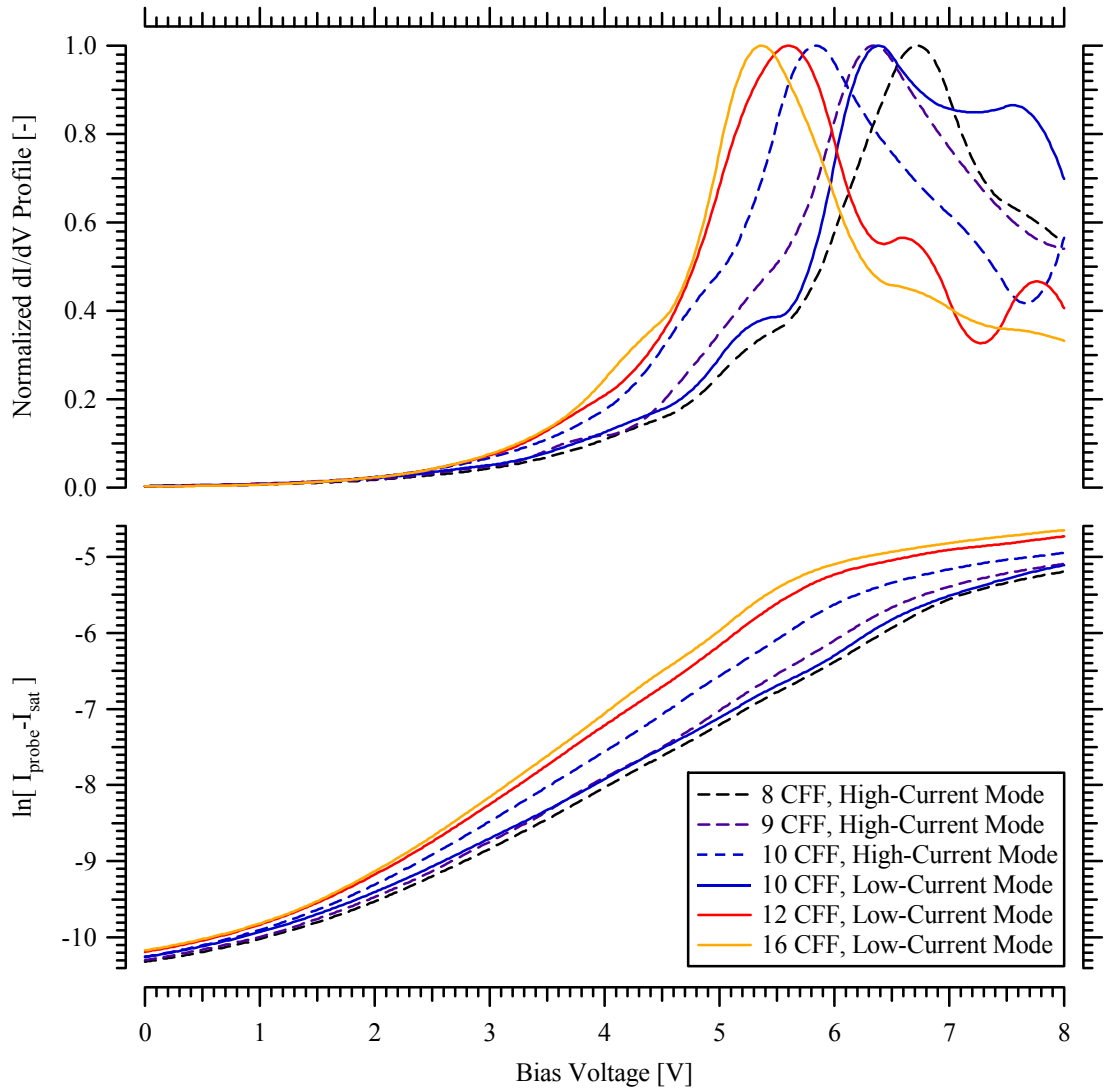

Figure 6-10 Langmuir probe traces of normalized dI/dV on thruster centerline and the natural logarithm located 1-m downstream of the exit plane for 105-V, 20-mg/s operation with cathode flow fraction ranging from 8-CFF to 16-CFF.

As cathode flow fraction was increased, the far-field plasma potential decreased. At 10-CFF, the transition to low-current mode corresponded to a ~0.5 V increase in plasma potential. Although the variations in plasma potential were within the measurement uncertainty, this trend was consistent for all operating conditions between the low-current and high-current regimes. During high-current operation, the dI/dV profiles exhibited significant fluctuations for probe bias potentials in the electron

saturation region. These fluctuations are likely caused by the significant discharge oscillations during high-current operation, and are magnified with probe sheath expansion in the electron saturation regime.

Electron temperature followed a similar trend with cathode flow fraction, as evidenced by the slope of the natural logarithm profile from approximately 2-V to 5-V bias potential in Figure 6-10. The increase in plasma potential during the transition to low-current mode was accompanied by an increase in the far-field electron temperature.

Angular variations in the far-field electron temperature were minimal, as shown in Figure 6-11 for 100-V, 20-mg/s operation in the high-current regime. Although the plasma potential decays on the periphery of the plume, the electron temperature was extremely constant. This measurement is associated with an uncertainty of approximately 50%, but allows a qualitative perspective on the repeatability and angular variation in electron temperature throughout the plume during high-current operation.

Variations in far-field electron temperature on thruster centerline are shown in Figure 6-12 for 100-V, 105-V, and 110-V at 10-mg/s, 15-mg/s, and 20-mg/s over the range of cathode flow rates studied in Section 6.2. Arrows show the transitional cathode flow fraction where the thruster is capable of operating in low-current mode. In Figure 6-12, the increase in electron temperature was largest for low anode flow rate operation. Electron temperature during 100-V operation exhibited the greatest sensitivity to anode flow rate, and showed negligible variation between high-current and low-current regimes at 20-mg/s anode flow rate. It is noted that further increasing cathode flow led to reductions in electron temperature, which was accompanied by a similar decline in plasma potential.

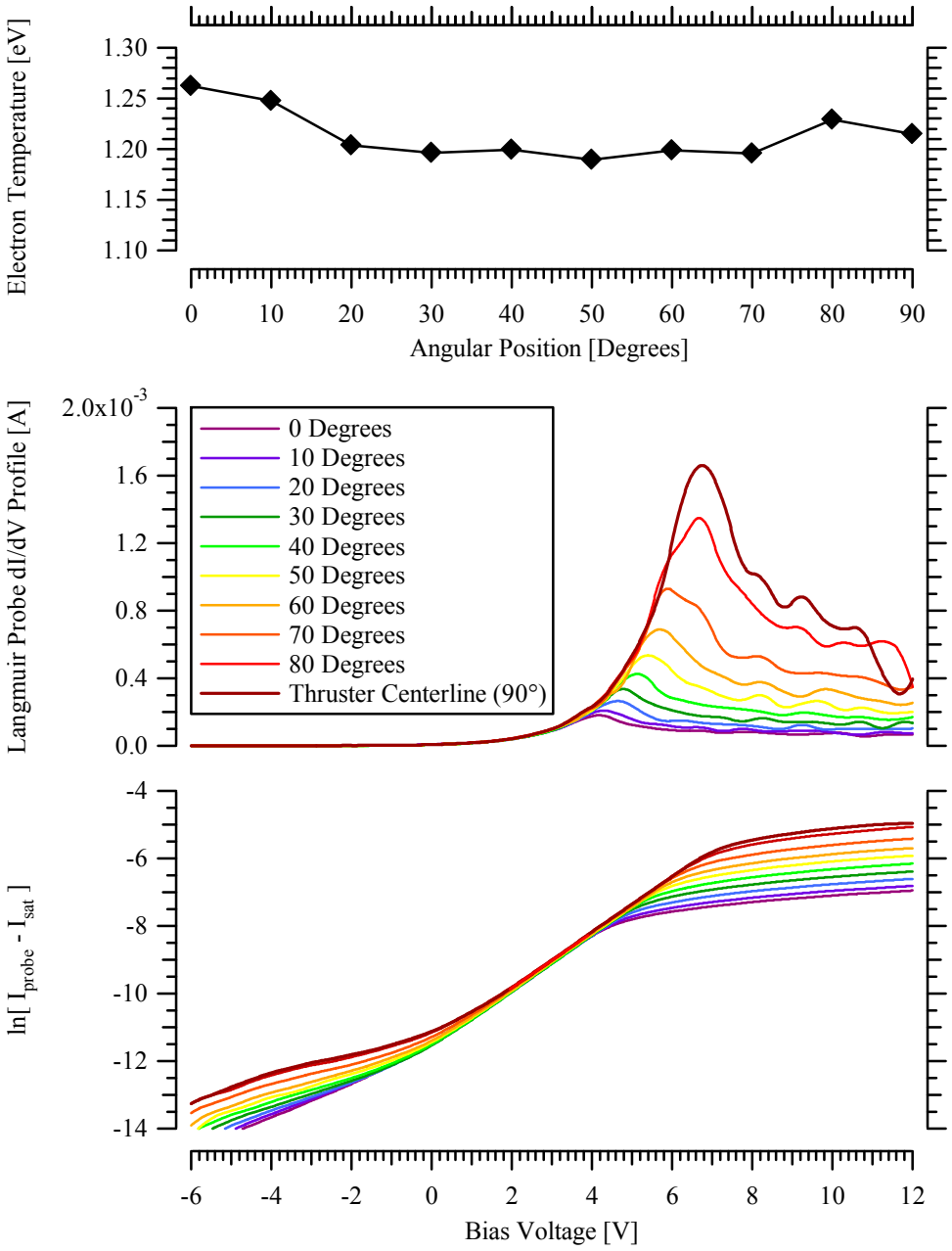

Figure 6-11 **Angular variation of electron temperature from 0° to thruster centerline (top). Langmuir probe traces of normalized dI/dV (middle) and the natural logarithm (bottom) located 1-meter downstream of the exit plane for 100-V, 20-mg/s, 7-CFF in the high-current operating regime.**

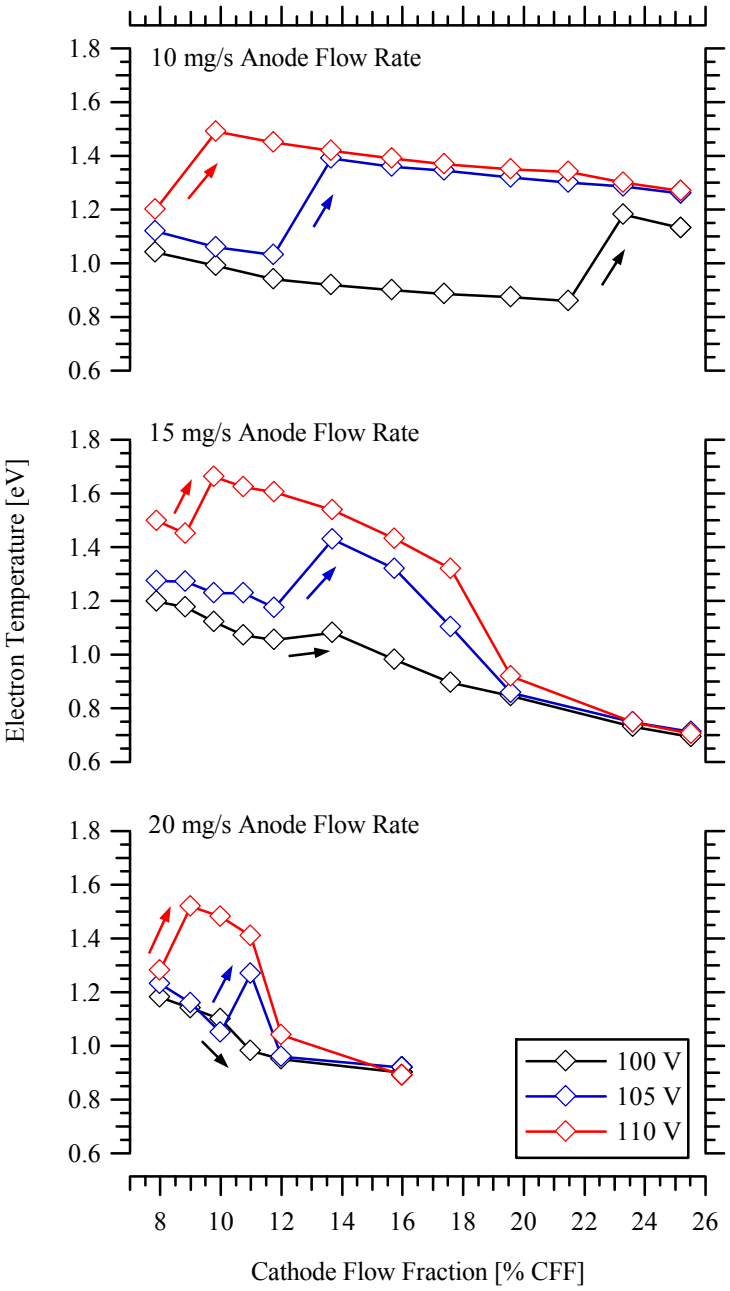

Figure 6-12 **Electron temperature on thruster centerline located 1-meter downstream of the exit plane for 100-V, 105-V, and 110-V at 10-mg/s (top), 15-mg/s (middle), and 20-mg/s (bottom) with cathode flow fraction ranging from 8-CFF to 26-CFF. Transitions from operation in high-current mode to low-current mode are shown with arrows, indicating the direction of increasing cathode flow fraction.**

The region of decaying electron temperature is where the total efficiency and T/P maximized for low discharge voltage operation conditions in Figure 6-2. In Chapter 5, this optimization was attributed to a reduction in Joule heating, specifically excitation and wall losses. At a critical cathode flow rate, the decreasing electron energy will reduce the ionization rate coefficient to a point where the performance benefits associated with reduced energy losses are balanced by the decline in ionization. There may be a correlation between the high T/P measured in Figure 6-2 with the minimum electron temperature occurring at 15-mg/s and greater than 18-CFF. Very large cathode flow rates above the fractions in this investigation may enable higher T/P, since the 15-mg/s and 20-mg/s operating conditions did not demonstrate a decrease in total efficiency in Figure 6-2 and the electron temperature continued to decline with cathode flow in Figure 6-12.

6.4.3 Distributions of Ion Energy and Ion Energy per Charge

Thus far, the transition from the high-current to low-current regime has been associated with decreased electron current to the anode, with increased electron temperature, and increased plasma potential in the far-field plume. The operating modes will be further studied using ExB probe and RPA distributions of ion energy and ion energy per charge.

In Figure 6-13, the RPA profile of ion energy per charge displays the most probable ion acceleration potential for 105-V, 20-mg/s operation from 8-CFF to 16-CFF. Variation in cathode flow had a negligible effect on the most probable ion acceleration potential, and appeared to have a minimal effect on the beam ion acceleration. The most significant variations occur on the high energy side of the ion energy per charge profile

between 90-V and 140-V. Ions with energy per charge ratio greater than the most probable ion acceleration potential are typically attributed to propellant ionized near the anode face or to multiply-charged ions that experienced a charge-reducing CEX collision downstream of the acceleration zone, thereby generating a high energy Xe^{+}. Thruster operation from 8-CFF to 10-CFF exhibited a substantial fraction of the energy per charge distribution greater than the discharge voltage, which would imply the high energy ions were at one time multiply-charged. The effect is exacerbated at 10-CFF in the high-current mode, at the transition to the low-current operating regime. Secondary peaks in the ion energy per charge distribution located at ~20 V are most likely due to space-charge limitations within the RPA grids. These peaks consistently formed for the lowest electron temperature conditions when the probe bias potential resulted in grid spacing greater than approximately $10\lambda_d$ according to Eq. (3-7).

In the 105-V, 20-mg/s, 10-CFF case during low-current operation, the distribution of low energy ions is less than the other operating conditions. During operation in the low-current regime, it is expected that increased cathode flow rate would increase the neutral density near the thruster exit and result in more low energy ions generated downstream of the primary beam. This population is created by a combination of CEX collisions and/or direct ionization of thruster and cathode neutrals in the near-field plume. Insensitivity of the most probable ion acceleration potential with cathode flow fraction displayed in Figure 6-13 was representative of the other operating conditions. Voltage utilization varied by less than 2% with variations in cathode flow fraction.

The significant “breathing” or large oscillations of plasma exhaust in the high-current mode would be expected to correspond to a wider dispersion in ion velocity due

to the wide fluctuations in neutral density in the discharge. Thus, the increased divergence during high-current operation in Figure 6-9 and the increased fraction of low energy ions during high-current operation may be attributed to ionization during the abatement and resupply of neutral propellant downstream of the peak acceleration zone during the large discharge fluctuations.

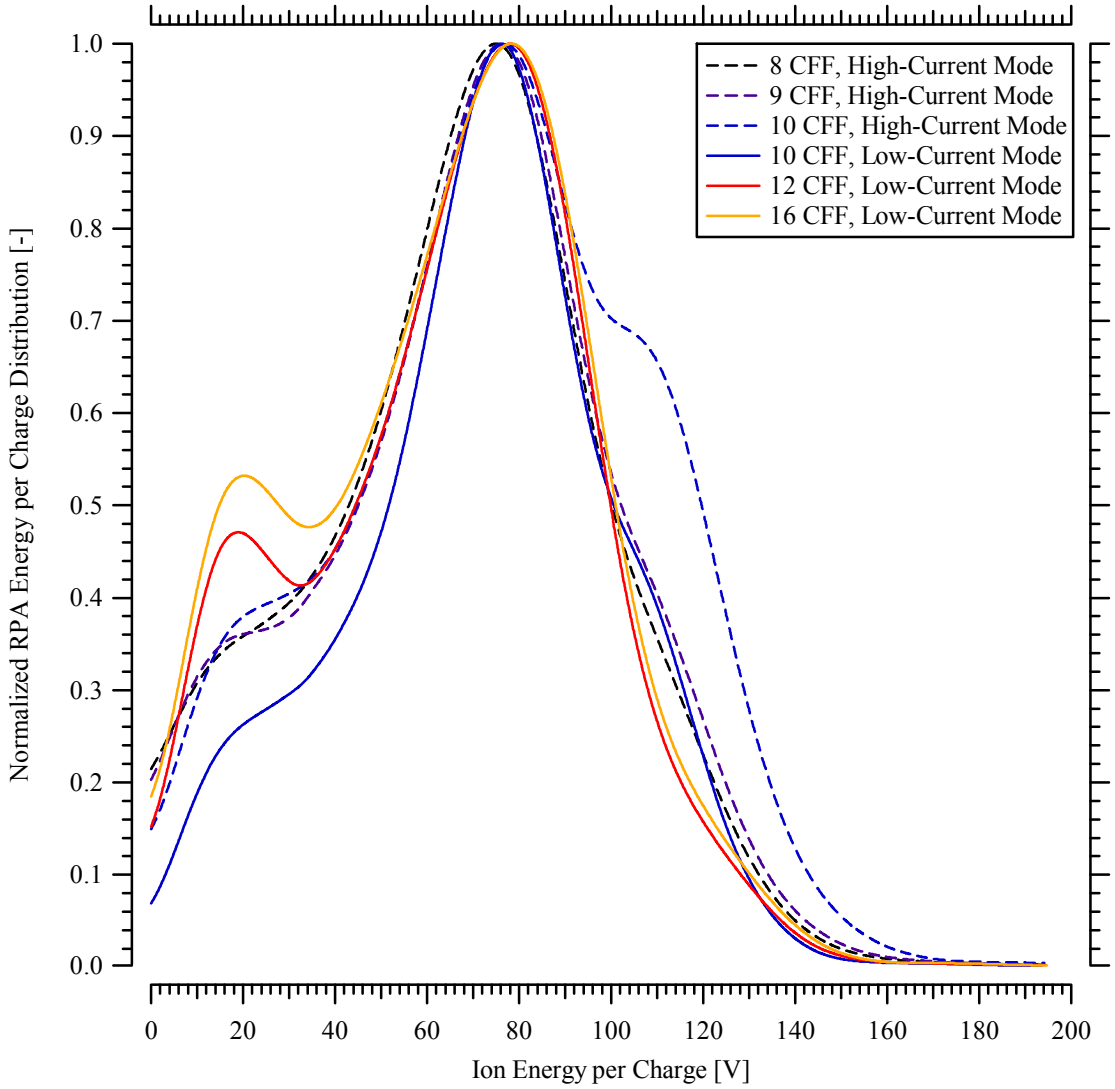

Figure 6-13 **Normalized RPA ion energy per charge distributions on thruster centerline located 1-meter downstream of the exit plane for 105-V, 20-mg/s operation with cathode flow fraction ranging from 8-CFF to 16-CFF. The ion energy per charge has been corrected for local plasma potential at the probe.**

In Figure 6-14, ion energy distributions of the benchmark 105-V, 20-mg/s, 16-CFF operation in the high-current and low-current regimes is evaluated with operation at 10-mg/s anode flow, with operation at 10-CFF, and with operation at 120-V discharge. In the high-current operating regime, the ion energy distributions show significant deviations from the distribution of the nominal low-current mode. These variations were extremely repeatable and exhibited minimal variation with downstream distance from 1.0 to 1.3-meters. The uncertainty of ion energy distributions in the high-current mode are estimated as equal to the low-current mode.

Examination of the benchmark 105-V, 20-mg/s, 16-CFF operation shows that the primary Xe^{+} peak remains in the same location, but is drastically reduced in magnitude. The peak of the high-current regime occurs between the Xe^{+} peak and the Xe^{+2} peak of the low-current regime. Although the population of high energy Xe^{+} ions was expected to increase during high-current operation based on the RPA ion energy per charge distribution, the radical transformation of the ion energy distribution indicates a significant number of ionization processes are occurring in the discharge. Extracting quantitative information about the ion species composition from these distributions is not possible. Instead, the ion energy distributions will be used for a qualitative comparison between operating regimes and between thruster operating parameters.

In Section 6.4.1, the study of 105-V, 16-CFF operation at 10-mg/s and 20-mg/s anode flow rate led to the concept that increased neutral density in the channel and electron-neutral collision frequency contributed to the observed high-current and low-current phenomenon. The comparison of anode flow rate conditions demonstrated equivalent reductions in current utilization during the high-current mode, and the primary

difference between operating regimes was an increase in beam divergence in the 20-mg/s case and a small decrease in divergence in the 10-mg/s case. The 105-V, 10-mg/s, 16-CFF case exhibited the least variation between high-current and low-current operating regimes in Figure 6-14, which is consistent with a minimal change in beam divergence listed in Table 6-1. Increased neutral flow in the discharge at 20-mg/s during high-current operation caused the primary peak to shift to a higher energy and also resulted in the creation of higher energy particles significantly greater than the Xe^{+2} ion population of the low-current regime. While the primary peak is likely a combination of high energy Xe^{+} ions and low energy Xe^{+2} ions, the highest energy spectra contains a significant fraction of Xe^{+3} ions.

The comparison of 16-CFF with 10-CFF during 105-V, 20-mg/s operation reveals minimal difference between the ion energy distributions in the low-current regime. During operation in the high-current regime, the distributions differ mainly in the larger magnitude of high energy ions in the 16-CFF case. Increased neutral density from the larger cathode flow rate would heighten the probability of a CEX collision with a primary beam ion. However, a significant fraction of the cathode flow must also be ionized and accelerated with the primary beam ions to increase the primary peak of the 16-CFF case relative to the rest of the distribution. The high-current operation of 105-V and 120-V at constant total flow rate of 20-mg/s, 16-CFF reveals that the distributions are similar in the distribution of ion energy. However, the ion energy distributions are difficult to compare when the ion species velocities overlap and the relative magnitude varies depending on the charge state. Comparison of these profiles is limited without estimating the contribution of each species to the overall distribution.

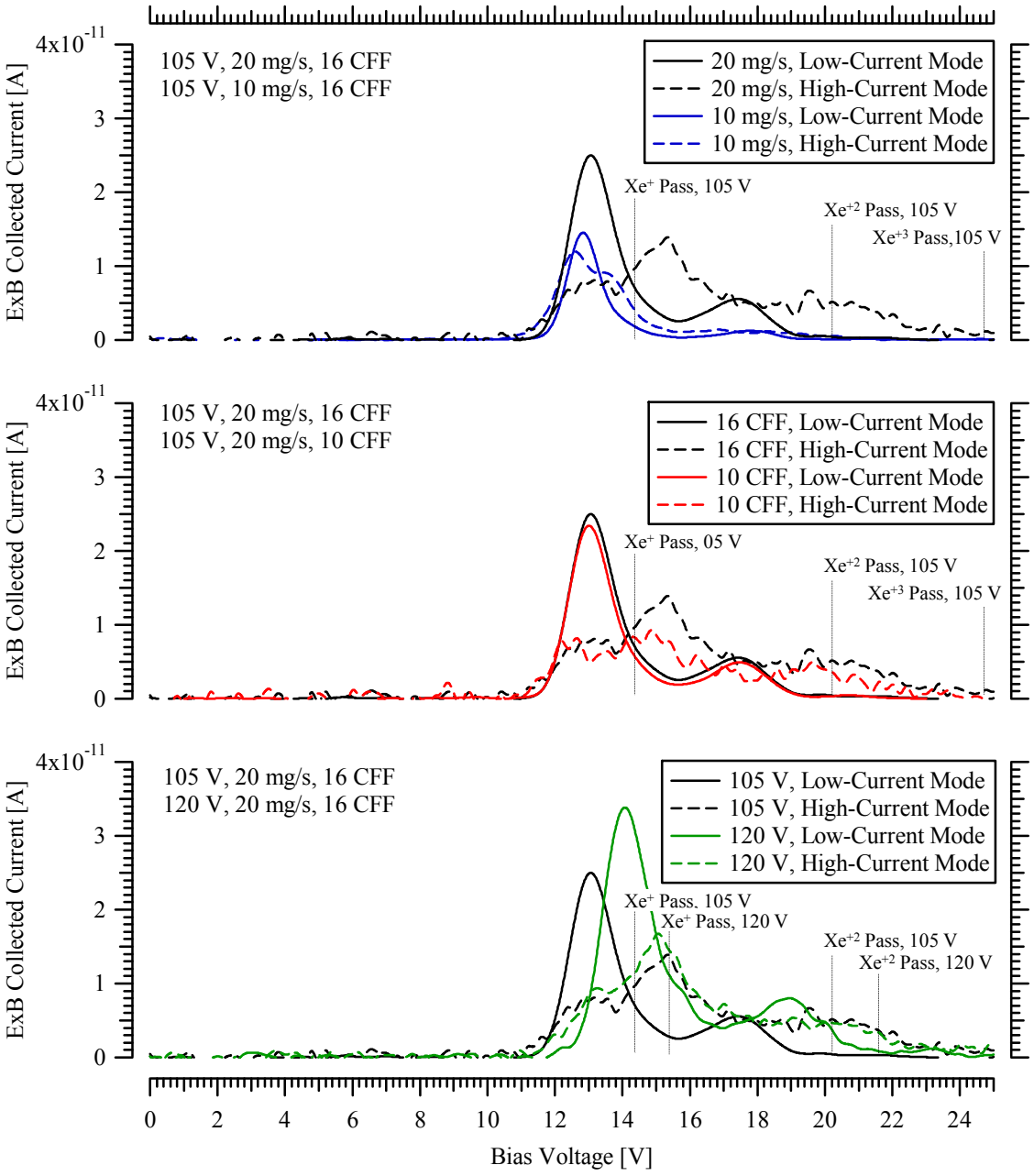

Figure 6-14 **Comparison of ExB probe ion energy distributions on channel centerline located 1-meter downstream of the exit plane for high-current and low-current regimes. The ion energy distribution at 105-V, 20-mg/s, 16-CFF is compared to the case of decreased anode flow at 10-mg/s (top), decreased cathode flow rate at 10-CFF (middle), and increased anode potential at 120-V (bottom). Ion species peaks are for comparison, and do not account for additional ion acceleration from plasma potential to the ground reference at the probe entrance.**

To more accurately assess the fraction of multiply-charged ions compared to high energy Xe^{+} ions, the ion energy distribution of the 105-V, 20-mg/s, 10-CFF case for high-current and low-current mode will be decomposed into energy distributions of the individual ion species. In Figure 6-15, the ExB probe ion energy distributions are normalized according to the peak of the low-current operating mode, and partitioned into ion species distributions of Xe^{+} ions and Xe^{+2} ions. The magnitude of the Xe^{+2} ion distribution is approximately proportional to $Z_j^{1/2} V_d$ according to Eq. (3-13). In addition, the ExB pass voltage of Xe^{+2} ions has been corrected for the increased velocity of the higher charge state.

The location where the ion energy distribution was divided is somewhat arbitrary, but was chosen based on an iterative approach to match the low energy side of the combined ion energy per charge distribution of the high-current and low-current regimes. The separation point is labeled on the figure for each operating regime. This matching of low energy distributions is comparable to the RPA ion energy per charge measurements. The ion pass voltage of the RPA and ExB distributions have been corrected for local plasma potential near the RPA, and differences in the plasma properties surrounding the ExB probe are considered minor compared to the large uncertainty associated with this qualitative examination. Superposition of Xe^{+} and Xe^{+2} ion energy per charge distributions from ExB measurements produced reasonable agreement with RPA measurements of energy per charge in Figure 6-15.

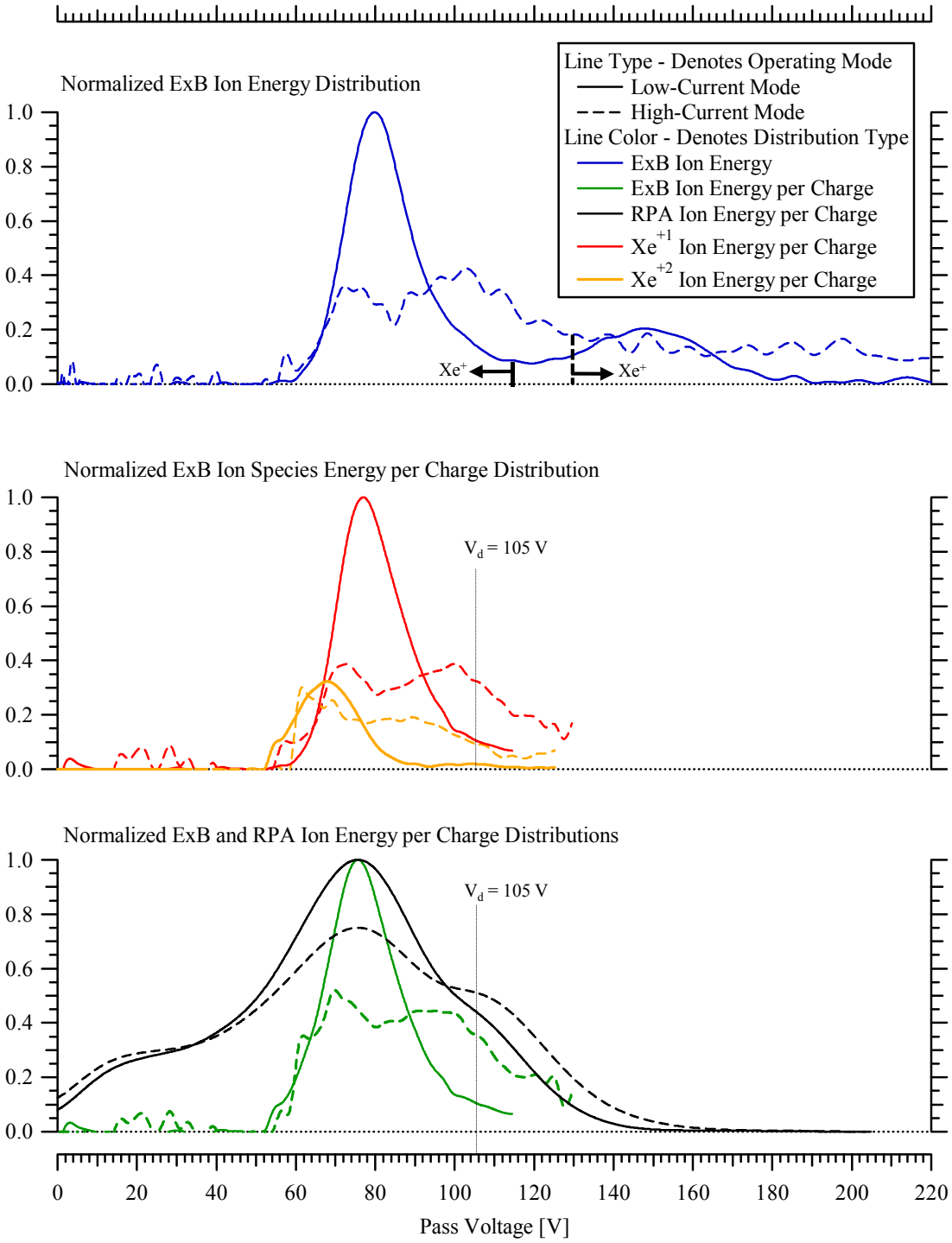

Figure 6-15 **Comparison of ExB probe and RPA measurements on channel centerline located 1-meter downstream of the exit plane for 105-V, 20-mg/s, 10-CFF operation in the high-current and low-current regimes. The ExB probe ion energy distributions (top), ExB probe ion species energy per charge distributions (middle), and the comparison of RPA and ExB probe ion energy per charge distributions (bottom) are normalized to the peak of the low-current profile for each diagnostic.**

The distributions of ion energy and ion energy per charge will aid in the assessment of low discharge voltage operating regimes, and enable a more comprehensive evaluation of the beam composition. Two mechanisms may contribute to the observed transformation of ion energy and ion energy per charge distributions during operation in the high-current regime. The first mechanism involves two distinct primary beam ion populations fluctuating in time with the discharge oscillations. One population is associated with ionization at approximately the same point in the potential field as the nominal low-current regime. The second population would correspond to ionization closer to the anode face and further upstream of the potential profile. The Xe^{+} ion species energy per charge distribution indicates there may be two distinct peaks in this population. Although not as distinct, the Xe^{+2} ion species energy per charge distribution also exhibits the possibility of two populations. Although the ions may be accelerated over a larger potential field, these populations would not be expected to produce ions with energy per charge greater than the discharge voltage.

The second source for generation of high energy ions is due to charge-reducing CEX collisions of multiply-charged ions downstream of the primary acceleration region. This would create two distinct populations in space, but would necessitate a large fraction of Xe^{+3} ions in the discharge channel and subsequent CEX collisions to create a population of high energy Xe^{+2} ions. This mechanism for production of high energy Xe^{+2} ions is expected to have an extremely low probability, and therefore would indicate the first mechanism is more likely.

For this operating condition, it is believed that the large dispersion in ion species energy per charge distributions during high-current operation is caused by variations in

the ionization zone relative to the acceleration profile. The large ionization instabilities and current oscillations lead to the cyclic exhaust and resupply of neutral propellant in the discharge. Electron current to the anode increases during the high-current mode, and may be due to electron leakage to the anode or to sustain ionization processes. Thrust may be approximately constant if a comparable fraction of propellant is accelerated over the most probable potential profile during one discharge oscillation.

Based on the hypothesis that the ion energy distribution is created by the discharge oscillations and an increase in fraction of multiply-charged ions, the effect of increased neutral density near the thruster exit will be evaluated in Section 6.5.

6.5 Variation in Near-field Neutral Density

In Section 6.2, the low discharge voltage operating regimes were studied with variations in the cathode flow fraction. However, the performance mapping was not extrapolated to vacuum conditions. Due to the sensitivity on the near-field neutral density, the facility effects on thrust and discharge current are studied for the benchmark operation at 105-V, 20-mg/s, 16-CFF in the high-current and low-current regimes. Discharge variations are evaluated with operation at 10-mg/s anode flow, with operation at 10-CFF, and with operation at 120-V discharge.

In Figure 6-16, the thrust increased with facility background pressure for all cases in the low-current and high-current mode. The key distinction is that discharge current decreases with background pressure in the high-current mode, and is likely related to the decline in discharge oscillations at higher background pressure in Figure 6-7. This demonstrates that the differences between the low discharge voltage operating regimes is largest at vacuum conditions.

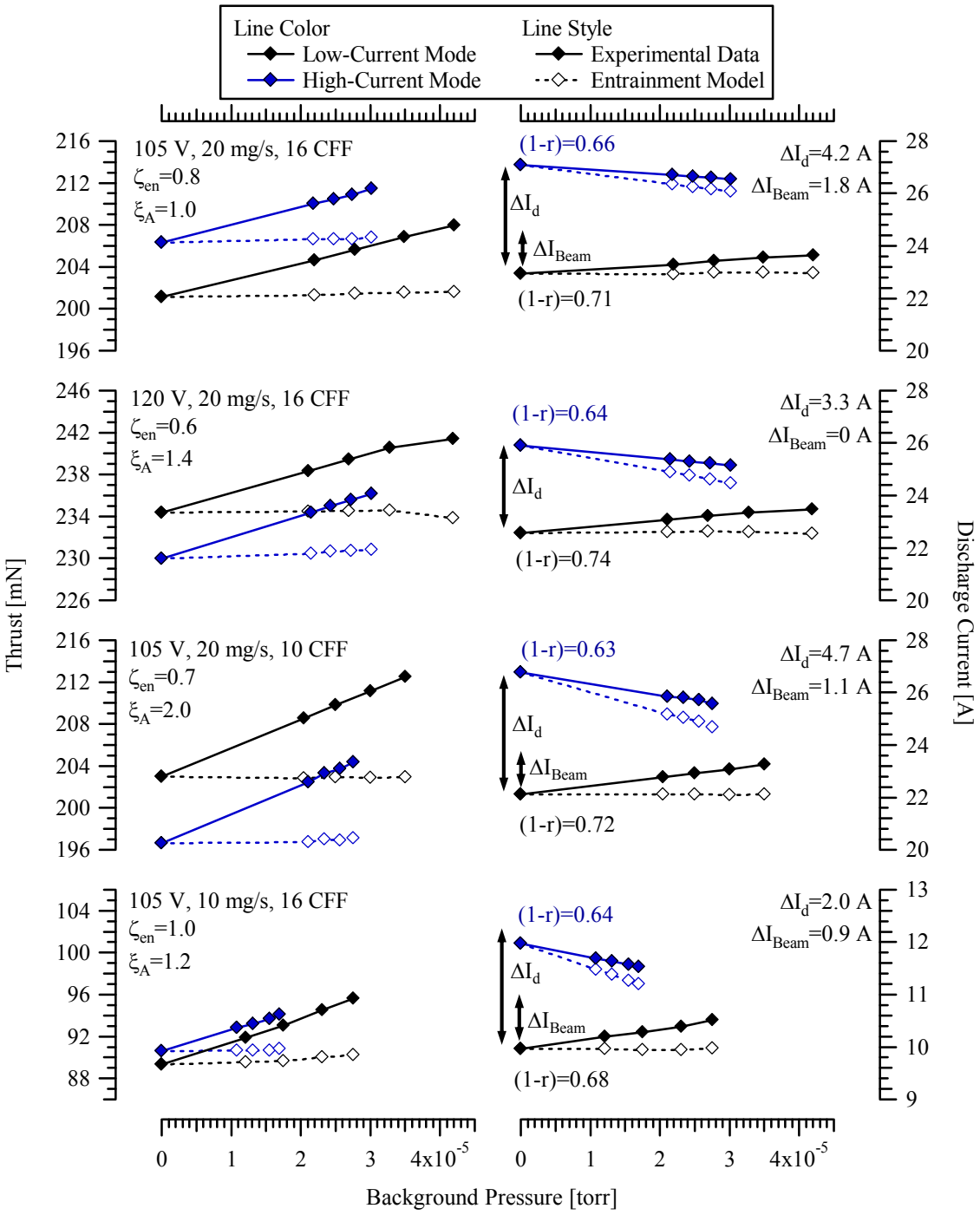

Figure 6-16 **Experimental and modeled thrust (left) and discharge current (right) of the 6-kW Hall thruster in the high-current mode and low-current mode as a function of facility background pressure for 105-V, 20-mg/s, 16-CFF (top), 105-V, 10-mg/s, 16-CFF (upper middle), 105-V, 20-mg/s, 10-CFF (lower middle), and 120-V, 20-mg/s, 16-CFF (bottom). The neutral entrainment factor is listed for all cases. The differences in current utilization, discharge current, and ion beam current are listed between low-current mode and high-current mode at vacuum conditions.**

Due to the decline in discharge current with background pressure in the high-current regime, the entrainment area factor was held constant between the low-current and high-current modes for a given thruster operating condition. Increases in thrust exhibited an equal and constant slope with background pressure between the high-current and low-current operating mode, and signals that the thrust generated by neutral entrainment of facility neutrals is not affected by the operating regime. Therefore, the increase in discharge current due to ionization of ingested facility neutrals is expected to be constant between low-current and high-current mode. Differences in the high-current mode discharge current at each facility background pressure from the value extrapolated to vacuum may be attributed to decreased electron current to the anode associated with a reduction in high-current mode discharge oscillations. Based on this metric, the high-current operating regime demonstrates increased electron current to the anode with reduced near-field neutral density. In this context, the variation in anode electron current with background pressure is greatest for the 105-V, 20-mg/s, 10-CFF, high-current operating condition. The difference in this case was ~3 A, and was also the transitional cathode flow fraction where the thruster was capable of operation in the low-current regime. This transition point corresponds to the greatest difference in current utilization, electron temperature in the far-field, and ion energy per charge distribution in the far-field plume between low-current and high-current mode.

The neutral entrainment area factor is equal to or greater than unity for all low discharge voltage operating conditions. In the low-current regime, these low-voltage operating conditions generate a negligible fraction of multiply-charged ions, and so this is not considered a cause of increased entrainment area factor. The phenomenon is

attributed to the under-prediction of entrainment area as a hemisphere and possibly effects associated with increased electron current to the anode at high background pressure. The systematic study of low-voltage loss mechanisms in Chapter 5 demonstrated that current utilization was a dominant loss mechanism, but the electron current to the anode decreased at higher anode mass flow rates. Based on that result, an increase in the near-field facility neutral density may be expected to reduce the recycled electron current and thereby increase the entrainment area factor. Therefore, the effective collection area of ingested neutrals is believed to be under-predicted by the hemispherical approximation during low discharge voltage operation.

The thrust entrainment factor was largest for the case with the lowest total flow rate, and was less than unity in all cases. It is unclear why thrust of the 105-V, 20-mg/s, 16-CFF high-current regime is greater than the low-current regime. Divergence of the high-current mode was larger for this operating condition, but the magnitude of the axial component of ion beam current was 0.7 A less in the low-current mode.

A second method of evaluating increased neutral density near the thruster exit is by injecting a fraction of the cathode flow through the auxiliary port, as illustrated in Figure 3-11. Auxiliary flow was injected around the keeper to study whether the low-voltage discharge behavior was due to processes internal to the cathode or external to the cathode exit. The auxiliary flow serves to increase the flow surrounding the cathode keeper and is expected to create a more diffuse cloud of neutral propellant. This thruster operation was studied in detail using the far-field diagnostics and characterized with variations in facility background pressure to determine the performance in vacuum. The 105-V, 20-mg/s, 10-CFF operating condition was studied for the case of 5-CFF and 2-

CFF, where the remaining flow fraction was injected through the auxiliary port such that the total mass flow rate was equivalent to 10-CFF. The 10-CFF case was chosen since it is the minimum cathode flow rate required for operation in the low-current regime at 105-V, 20-mg/s. In addition, this operating condition has demonstrated the greatest differences between low-current mode and high-current mode.

Variations in thruster performance with auxiliary flow injection are displayed in Figure 6-17. At vacuum conditions, the total efficiency is reduced by approximately 1% for operation at 2-CFF. However, operation in the low-current regime would not be possible for this low cathode flow fraction without the auxiliary flow rate of 8-CFF surrounding the keeper. Based on plume diagnostics, the decreased performance with reduced cathode flow fraction is associated with a minimal increase in current utilization and a decrease in beam divergence.

In the low-current regime, operation at each auxiliary flow condition demonstrated relatively constant T/P with decreasing background pressure, and is likely due to a constant neutral entrainment area. Conversely, the high-current regime shows significant reductions in performance at vacuum. This is attributed to the reduction in neutral propellant available to minimize the discharge oscillations, and is likely caused by a greater fraction of electron current to the anode.

The primary advantage of the auxiliary flow injection was to enable a wider operational envelope where the thruster was in the low-current regime. This included both magnetic field topology and cathode flow rate. In this study, the magnetic field was held constant. However, performance and beam divergence may improve with optimized magnet settings. For this operating condition, the auxiliary flow could be reduced to 7-

CFF when 2-CFF was supplied to the cathode. Although this did not improve performance, the addition of auxiliary flow may be considered a safeguard to maintain low discharge voltage operation in the low-current regime. Just as the high-current mode may be mitigated at increased background pressures, it may arise on-orbit in the vacuum of space for operating conditions that did not cause the high-current mode in ground-based experiments. Further study is required to more accurately characterize the thruster operation and discharge properties with auxiliary flow. An accurate study of facility background pressure effects would be critical for this examination.

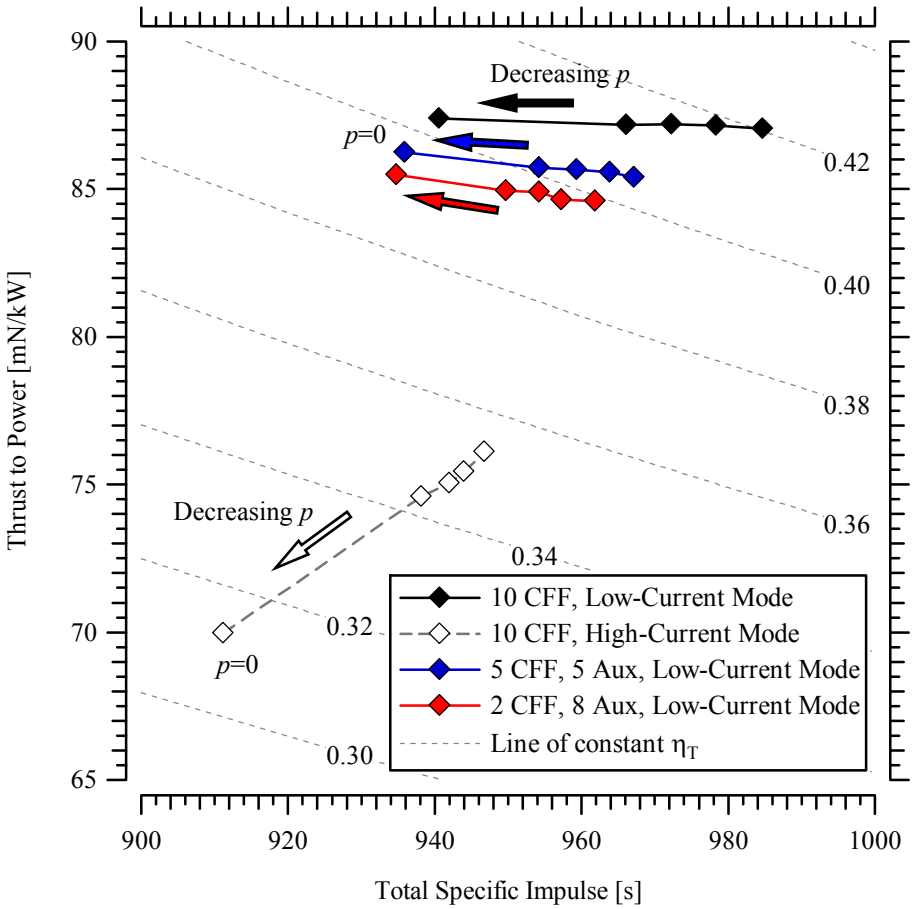

Figure 6-17 Ratio of thrust T/P and total Isp with variation in cathode flow and auxiliary propellant for 105-V, 20-mg/s operation in the high-current and low-current regimes. The total combined flow to the cathode and auxiliary port is fixed and equivalent to 10-CFF, such that the total mass flow to the thruster is constant. Performance parameters are extrapolated to vacuum conditions.

6.6 Potential Causes of Low Discharge Voltage Operating Regimes

The presence of two discharge current regimes was demonstrated to be a low-voltage phenomenon. As previously stated, discharge oscillations in the high-current mode may be caused by (1) breathing mode oscillations, (2) the azimuthal rotating "spoke" instability, (3) cathode induced instabilities, or (4) discharge power supply instabilities. Each scenario will be evaluated and discussed in the following sections.

6.6.1 Thruster Ionization Instabilities

A constant discharge frequency between the low-current and high-current operating regimes indicates that the oscillations are a natural phenomena of the discharge that is driven unstable by a local depletion of neutral density near the exit. The dominant frequency of ~5 kHz is within the frequency range of the breathing mode oscillations and the azimuthal "rotating spoke" instability described by Choueiri.[129]

The rotating spoke oscillations arise during low discharge voltage operation, and are generated by coupling between ionization processes and density non-uniformities in the channel. These instabilities were observed during the early years of Hall thruster research[127], and were believed to correspond to an azimuthal disturbance on the order of the critical ionization velocity (4.2-km/s for xenon). For the 6-kW thruster in this investigation, the critical ionization velocity of xenon would correspond to an azimuthal cycle around the annulus on the order of ~8 kHz.

The dominant breathing mode frequency during nominal Hall thruster operation is the breathing-mode frequency, and is due to the cyclic exhaust and resupply of neutral propellant near the exit. These oscillations are known to result in severe discharge

fluctuations and show a dependence on the magnetic field. Based on the "predator-prey" model, the breathing mode frequency is estimated at ~7 kHz for the 6-kW thruster in this investigation during low discharge voltage operation (<120-V).

Recent time-resolved studies of the BHT-600 Hall thruster discharge showed discrete toroidal plasma emissions corresponding to the breathing mode frequency.[134] Regions between the dense plasma structures contained approximately 75% lower plasma density during nominal 200-V discharge operation. The electron temperature and plasma potential varied with the breathing mode oscillations, and appeared to be driven by electron dynamics and the electromagnetic field. The resulting fluctuations and gradients in plasma potential associated with the propagating toroidal plasma may be a significant fraction of the anode potential during low-voltage operation.

Both the breathing mode oscillations and the spoke instabilities are related to ionization processes near the thruster exit, and the coupling between these oscillations is unknown. The mechanism for electron current to the anode and the nature of cross-field electron transport is beyond the scope of this investigation. The concept of discrete toroidal plasma emissions and the interactions of intense ionization instabilities external to the discharge channel necessitate simulation of the electron dynamics and a more sophisticated interrogation of the near-field region.

6.6.2 Cathode Induced Discharge Oscillations

Low-voltage Hall thruster operation may be more susceptible to cathode coupling effects due to the increased fraction of propellant ionization cost and cathode-to-ground potential with respect to the applied anode potential. Furthermore, the results of this

study indicate the thruster may be more sensitive to ionization instabilities and plasma potential fluctuations near the thruster exit during low-voltage operation.

The thruster sensitivity to cathode flow indicates the transition between high-current and low-current regimes may be triggered by cathode coupling or a cathode operating effect. One possibility is the gradual transition from cathode spot-mode to plume-mode, which is a function of cathode flow rate, the local magnetic field, and plasma properties near the exit orifice. Plume-mode operation is associated with an increase in electron temperature, cathode coupling voltage, and plasma potential oscillations near the cathode exit.[135,136,137] Plasma potential oscillations and energetic ion production during cathode plume-mode are the result of ionization instabilities near the cathode exit plane.[138] These instabilities typically increase with decreasing cathode flow and off-nominal magnetic field.

A recent investigation by Goebel, *et al.*[138] reported that large plasma potential oscillations and energetic ion production in the near-cathode region may be reduced by increased cathode flow or injection of neutral gas downstream of the cathode exit plane. They speculated cold neutral flow either damped the large potential oscillations and/or produced additional ionization to reduce the instabilities. In the low discharge voltage investigation in this dissertation, increased neutral density near the cathode exit may have mitigated the cathode induced plasma potential oscillations and stabilized the ionization instabilities. This moderation resulted in low-current thruster operation. Similar to the study by Goebel[138], auxiliary neutral flow injection near the cathode exit plane enabled a lower cathode flow rate required to maintain low-current thruster operation. This supports the concept of cold, dense neutral flow in the near-cathode region stabilizing

plasma oscillations and instabilities, and increasing the thruster and cathode operational envelope.

It is uncertain whether the thruster operation coincides with the cathode transition from spot-mode to plume-mode. The high-current mode in Figure 6-1 exhibited an intense, collimated plume extending into the cathode, which is characteristic of the plume-mode operation. In comparison, the low-current mode in Figure 6-1 showed a luminous spot of intense ionization near the cathode orifice, indicative of the spot-mode operation. Although the cathode potential and discharge current oscillations were fluctuating at the same frequency in high-current regime, it remains unclear if this is a cause or consequence of the plasma discharge oscillations. Further cathode characterization and examination of the near-cathode electron temperature and plasma potential is necessary to determine the cathode operating envelope during Hall thruster operation. Regardless of the specific cathode operating mode, plasma potential oscillations and energetic ion production have been shown to increase as cathode flow is reduced. Therefore, a critical magnitude of plasma perturbations near the cathode exit may affect thruster performance prior to the onset of plume-mode operation.

Several issues develop if the cathode operation is responsible for transition between the low discharge voltage operating regimes. The centrally-mounted cathode is surrounded by the iron magnetic circuit and is located in a region with minimal axial magnetic field. Although cathode operation has shown sensitivity to the axial magnetic field in past studies, it seems unlikely that the minimal variation in magnetic field topology would have a strong influence on the magnetic field in this region. Past cathode coupling studies performed on the BPT-4000[139] and also with this thruster model[88] at

discharge voltage >300-V concluded cathode flow rate had a negligible effect on performance. A more systematic study is required to determine if the cathode operating condition is affecting low discharge voltage performance and initiating severe discharge oscillations in the high-current regime.

6.6.3 Discharge Power Supply Oscillations

Extensive investigations in the former Soviet Union established that the Hall thruster discharge oscillations may be affected by the external supply and electrical circuit.[126,130] In this investigation, a ~500 Hz RLC filter was removed from the circuit with negligible change in the low-voltage thruster operation or discharge characteristics. While it does not rule out oscillations induced by the discharge power supply, it suggests that the operating regimes are a low discharge voltage plasmadynamic phenomenon associated with the thruster or cathode. In addition, a qualitative assessment of the low-voltage characteristics of this thruster model at PEPL demonstrated features in discharge current magnitude and oscillations that were consistent with the low-current and high-current operating regimes. Differences between facilities may be attributed to a different thruster model, discharge power supply circuitry, or variation in the centrally mounted cathode.

6.7 Summary

A systematic mapping of low discharge voltage Hall thruster performance revealed the existence of two operating regimes. The regimes were classified as high-current mode and low-current mode, and corresponded to a visible transformation of the

jet-mode plume structure. A large increase in the amplitude of discharge current oscillations manifested as a ~10% increase in the discharge current magnitude. The discharge regimes were highly dependent on cathode coupling and magnetic field topology.

Evaluation of the thruster performance and far-field plume demonstrated that electron current to the anode was the primary source of increased discharge current in the high-current regime. Analysis of the ion energy distributions and ion energy per charge distributions revealed that the high-current regime corresponded to increased multiply-charged ions and wide dispersion in the ion species energy distributions. This phenomenon may be caused by the cyclic exhaust and resupply of neutral propellant in the discharge. Increased neutral flow to the near-cathode region by additional cathode flow injection, through an auxiliary port, or by increased facility background pressure was shown to enable thruster operation in the more efficient low-current mode. A qualitative assessment of potential causes led to the hypothesis that the high-current operating mode is a result of (1) instability associated with the breathing mode and/or the rotating spoke instability, or (2) instability initiated by large radial plasma potential fluctuations and ionization instabilities near the cathode exit due to operation in the cathode plume-mode. Although the exact nature of the low-voltage operating regimes remains uncertain, the discharge characteristics are systematically evaluated and mitigation strategies are demonstrated.

Chapter 7

Summary and Concluding Remarks

The investigation of low-voltage Hall thruster operation in this dissertation contributed to the scientific understanding of discharge performance loss mechanisms in the electric propulsion community. During the course of this research, corollary studies on Faraday probe design, facility effects, and data analysis techniques resulted in improved accuracy of current density profiles and far-field plume properties. These developments enabled the comprehensive examination of Hall thruster performance in an efficiency architecture that was designed to isolate loss mechanisms into processes related to conversion of the discharge power to jet kinetic energy, processes related to dispersion of the exhaust VDF, and divergence of the plasma jet. A systematic investigation of low-voltage Hall thruster performance and examination of the far-field plume provided a means to study discharge physics in the context of the efficiency framework. The major conclusions of this research are summarized in the following sections and recommendations for future efforts are proposed to resolve unexplained findings.

7.1 Low Discharge Voltage Hall Thruster Loss Mechanisms

The low- voltage discharge properties of a 6-kW laboratory Hall thruster were characterized with measurements of thrust and interrogation of the far-field plume. Facility effects on thrust, discharge current, and ion current density profiles were assessed, and the on-orbit attributes were determined by linear extrapolation to vacuum conditions. Synthesizing the plume properties and performance parameters into the Hall thruster efficiency architecture led to the conclusion that beam divergence and electron current to the anode were primary loss mechanisms reducing total efficiency during low discharge voltage operation. Contrary to conventional perceptions, the propellant utilization exhibited a minor increase during low-voltage operation due to a decrease in the production of multiply-charged ions. At low anode potential, increasing the neutral density near the thruster exit decreased beam divergence losses and improved T/P at the expense of diminishing mass utilization.

Energy efficiency was monitored as a function of electron current to the anode in current utilization and as a function of the most probable ion acceleration potential in voltage utilization. Reduced voltage utilization was primarily due to the xenon ionization potential becoming a larger fraction of the applied anode potential. Losses in energy efficiency were manifested in Joule heating losses associated with excitation, ohmic heating of the channel walls, ionization of multiply-charged ions, and radiation. A theoretical model of the minimum anode electron current required to sustain discharge ionization for a given ion species composition was estimated for ideal electron-impact cascade ionization. This model evinced that the minimum fraction of anode electron

current for a xenon ionization cost of 12 eV/ion was two orders of magnitude less than indicated by Faraday probe measurements.

An effective discharge ionization cost based on the total energy losses and number of beam ions revealed a more accurate estimation was approximately 70 to 80 eV per beam ion during low discharge voltage operation. In terms of the cascade ionization model, this effective ionization cost correlates to one or two ionization events per cathode electron over the entire anode-to-cathode potential profile. Nevertheless, in this framework the low discharge voltage operating conditions corresponded to a lower ionization cost per beam ion than nominal 300-V conditions for comparisons of both constant power and constant current. Although the higher discharge voltage operation exhibited higher energy efficiency and additional ionization events per cathode electron, the effective ionization cost per beam ion was increased due to the increased potential applied to accelerate ions to high exhaust velocity.

It has been well established that T/P increases during low voltage operation, but is correlated with a decline in total thruster efficiency. Examination of the discharge properties and performance loss mechanism affecting T/P established that the conversion of applied discharge potential to the axial acceleration of beam ions was responsible for a large increase in T/P during low discharge voltage operation. This trend is directly caused by the ratio of ion velocity to discharge voltage, and is inversely proportional to the manner in which Isp increases with discharge voltage. The ratio of T/P would increase indefinitely with reductions in discharge voltage if not for the decline in the axial component of ion beam current relative to discharge current. Consequently, these competing effects lead to a maximum T/P in the low-voltage operating regime.

To summarize, high-voltage operation leads to increased ion exhaust velocity and Isp, but is associated with diminishing gains in velocity as discharge voltage is increased and the energy losses per beam ion escalate. A majority of the discharge power is applied to ion acceleration during high-voltage operation and the increased electron temperature leads to additional Joule heating losses. During low-voltage operation, the discharge power is applied to ionization of a larger fraction of propellant. The reduced electron temperature during low-voltage operation leads to a decline in the Joule heating losses, but is also associated with a lower ionization rate coefficient in the discharge. This decline in the ionization rate coefficient causes a reduction in the axial component of ion beam current, and requires increased electron current to the anode to sustain ionization during low-voltage operation. These interrelated electron temperature processes dominate low discharge voltage operation, and continued reductions in the applied anode-to-cathode potential initiate further escalation of electron current to the anode and divergence losses as ions are created further downstream of the potential profile.

7.2 Low Discharge Voltage Hall Thruster Operating Regimes

Two jet-mode Hall thruster operating regimes were investigated for low discharge voltage operation. The low-current mode corresponded to the I-V characteristic of nominal discharge voltage operation, whereas operation in the high-current mode produced significant increases in the discharge current magnitude and oscillation amplitude. The regimes were characterized through a systematic mapping of low discharge voltage Hall thruster performance with variations in the applied anode-to-

cathode potential, anode mass flow rate, and cathode mass flow rate. Evaluation of the thruster performance and far-field plume demonstrated that electron current to the anode was the primary source of increased discharge current in the high-current regime. Analysis of the ion energy distributions and ion energy per charge distributions revealed that the high-current regime corresponded to increased multiply-charged ions and wide dispersion in the ion species energy distributions. The increased dispersion was attributed to the cyclic exhaust and resupply of neutral propellant in the discharge, and may signal instability associated with the "predator-prey" model of breathing mode oscillations.

Several mechanisms for the transition to high-current mode were evaluated, including (1) instability associated with the breathing mode and/or the rotating spoke instability, or (2) instability initiated by large radial plasma potential fluctuations and ionization instabilities near the cathode exit due to operation in the cathode plume-mode. The discharge oscillations declined with increased neutral flow near the thruster exit, and eventually enabled operation in the low-current regime. Conversely, oscillations in the high-current regime were amplified as neutral density in the near-field was decreased. Injection of additional auxiliary flow in the thruster near-field is recommended as a safeguard to maintain low discharge voltage operation in the low-current regime, and reduce the possibility of operation in the high-current regime on-orbit.

7.3 Facility Effects and Formation of the Jet-Mode Plume Structure

An evaluation of facility effects on performance and plume properties was initiated to more accurately assess low discharge voltage loss mechanisms in the Hall

thruster efficiency architecture developed in Chapter 2. Thrust and discharge current were characterized over a range of facility background pressures and extrapolated to vacuum conditions. This approach was the starting point for a simple model designed to estimate the effective entrainment area of ionized facility neutrals and the contribution to useful thrust of this population. Low discharge voltage operation typically corresponded to an entrainment area larger than a hemispherical approximation, and was attributed to a physical increase in the thruster sphere of influence as opposed to an artificial increase in electron current to the anode with facility background pressure.

A detailed study of the angular distribution of ion beam current in the plume of a low-power Hall thruster was conducted with variations in distance and background pressure using four configurations of the nested Faraday probe. This comprehensive set of plume data was analyzed as the angular distribution of ion beam current per unit stripe, and exhibited angular regions of constant beam current in the far-field plume for vacuum conditions. This phenomenon was compared to numerical simulations of the vacuum plume expansion in COLISEUM, and indicated the angular beam current profiles were largely formed by the external potential field structure. This underscores the importance of a high fidelity ion source model and field topology near the thruster exit.

Similar angular regions of constant ion beam current per unit stripe were evident in the 6-kW thruster over a large range of background pressures and the vacuum conditions for each operating condition studied. This led to the hypothesis that locations of facility neutral ionization and acceleration in the 6-kW thruster occurred within a relatively compact region, and do not vary relative to the potential field as background pressure is increased. Therefore, the angular regions of constant ion beam current were

constant with increasing background pressure for this thruster model and were shaped by acceleration of ions through the external electric field. The low-power Hall device only exhibited the phenomenon during vacuum conditions with increased downstream distance, and was speculated to differ from the 6-kW thruster operation as a result of variation in the location of facility neutral ionization and acceleration as background pressure increased.

Angular distributions of the slopes corresponding to the linear extrapolation of ion current density to vacuum conditions was studied as the superposition of two Gaussian curves. These Gaussian curves provided qualitative information about the ionization of ingested neutrals and CEX collisions of facility neutrals in the near-field plume. The highly qualitative analysis indicated that ionization of ingested facility neutrals was reduced during low discharge voltage operation, and the primary effect was to disperse the plume through CEX collisions with background neutrals. However, unity neutral entrainment factor also suggested that nearly all of the ionized ingested propellant contributed to thrust.

7.4 Evaluation of Faraday Probe Design and Analysis

A comprehensive investigation of nude Faraday probe design and analytical techniques was conducted with the AFRL nested Faraday probe. Enhanced understanding of Faraday probe ion current collection and methods for evaluating plume properties minimized CEX facility effects on current density distributions and reduced the integrated ion beam current by ~20%. The corrected plume properties are in line with expected values of ion beam current based on Hall thruster performance and discharge

properties. Precision in total ion beam current measurements was within a 3% range for all nested Faraday probe configurations.

A key discovery was the ability to predict the amount of additional ion current on the collector side walls. The gap correction factor was proposed to adjust the effective probe collection area for ions collected by the walls in the gap volume. This correction was applied to a past investigation comparing the JPL nude Faraday probe design with the GRC nude Faraday probe design. Based on the analysis in this dissertation, the ion collection area of the JPL probe requires minimal correction in a low background pressure environment. However, the effective collection area of the JPL probe design is more sensitive to facility effects and is believed to increase with facility background pressure. This response is attributed to the conductive base in the gap volume of the JPL Faraday probe, and may complicate characterization of facility effects over a range of distances and pressures. In contrast, the more conventional GRC nude Faraday probe and the AFRL nested Faraday probe design feature a ceramic base, which demonstrated a constant gap correction factor over a wide range of background pressure and downstream distance from the thruster exit plane. Therefore, the conventional Faraday probe design with a ceramic base is more suitable for characterization of facility effects and plasma studies with a range of Debye lengths in the plume.

To further illustrate the nature of the gap correction factor, a dissimilar bias potential was applied to the collector and guard ring of the nested probe. Depending on the potential difference between the guard ring and collector, this study demonstrated the ability to collect nearly all of the ions in the gap volume on the side wall of the guard ring or the side wall of the collector. Correct application of the correction factors to both the

0.5 mm and the 1.5 mm gap configurations resulted in equivalent plume profiles, integrated beam current, and plume divergence despite the 1.5 mm gap being 15 to 30 Debye lengths on thruster centerline. Thus, although the 1.5 mm gap configuration may introduce a non-uniform sheath over the Faraday probe collecting surface, the non-uniformity is primarily over the gap width and appears to be accounted for by distributing the ions in the gap volume using the gap correction factor, κ_G.

Facility effects in this investigation were studied over a range of downstream measurement distances and background pressures for all nested Faraday probe configurations. Current density profiles were extrapolated to vacuum conditions, and enabled a more accurate description of the on-orbit current density profiles using ground measurements. The ratio of the axial component of ion beam current with respect to the total ion beam current was extrapolated with a 2^{nd} order polynomial to the thruster exit plane. Coefficients of the 2^{nd} order polynomial fit varied with background pressure, thruster discharge voltage, and mass flow rate. This methodology resulted in consistent agreement to within 1% for all background pressures and probe configurations.

For the low-power Hall thruster ion source in this investigation, the axial component of ion beam current at vacuum conditions decreased by approximately 5% to 10% from the exit plane to the far-field plume. This was attributed to CEX collisions with thruster neutrals and divergence by the external potential field structure. Although ion beam current may be accurately estimated in the far-field plume, the axial component of ion beam current requires additional investigation to accurately assess the loss of thrust due to ion beam divergence. This recommendation applies to near-field measurements as well, since these measurements introduce complications associated with perturbation of

the discharge, a reduction in the Debye length, and possibly SEE effects. In addition, ingestion and near-field CEX collisions with facility neutrals are expected to affect near-field measurements. Thus, characterization of ion current density profiles with variations in distance and background pressure are advised.

Based on the results of this systematic investigation, the measurement uncertainty of Faraday probe ion beam current measurements is estimated as ±3% and the uncertainty in the axial component of ion beam current is estimated as ±5% when the recommendations in Section 4.5 are followed. The reductions in measurement uncertainty and the increased capability to approximate on-orbit plume expansion are a significant improvement for comparisons with numerical simulations and analysis of Hall thruster performance.

7.5 Development of a Hall Thruster Efficiency Architecture

A Hall thruster performance architecture was developed based on separation of the total thrust directed along thruster centerline into mass-weighted and momentum-weighted terms. With this formulation, the total thruster efficiency equation was analytically decomposed to explicitly account for the effects of energy conversion losses, plume divergence, and the velocity distribution function of the propellant jet. Thruster efficiency was defined as the product of (1) energy efficiency, (2) propellant efficiency, and (3) beam efficiency. The performance architecture has similarities to previous analyses formulated by Masek, *et al.*[37] in the ion thruster community, Belan, *et al.*[41] from the Kharkov Aviation Institute, and a contemporary methodology by Hofer.[19,57] The terminology and definitions of voltage utilization, current utilization, mass utilization,

and charge utilization were preserved from past architectures to facilitate comparison with former and future investigations in the electric propulsion community.

Energy efficiency comprised losses due to ionization processes and losses that manifested as Joule heating of the thruster, and contains no information about the vector properties of the jet. Energy efficiency can never be unity in a Hall thruster discharge due to a finite flow of electrons that are recycled to the anode to sustain ionization processes. A theoretical minimum electron current to the anode was estimated for ideal electron-impact cascade ionization with the propellant ionization potential. Experimental energy losses in the discharge were described with the ionization cost per beam ion for a multiply-charged plasma.

Propellant efficiency incorporated losses from dispersion in the jet composition, and is unity for 100% ionization to a single ion species. The fraction of non-ionized propellant and the ion species composition were characterized with mass utilization and charge utilization. The effect of neutrals on dispersion of the jet VDF in propellant efficiency is introduced in the neutral-gain utilization. This term quantifies the finite thrust generated by non-ionized propellant exhausted from the discharge, and may increase total thruster efficiency by over 2%.

The beam efficiency accounts for divergence of the jet, and is ideal when the ion velocity vectors are parallel to the thrust axis. Plume divergence was defined as a momentum-weighted term, and the approximation as a charge-weighted term was characterized. Although facility effects were accounted for in the study of low discharge voltage loss mechanisms, the ratio of I_{Axial}/I_{Beam} was not corrected for distance and appeared to be under-predicted. This resulted in over-prediction of beam divergence

losses, and was considered to be the primary source of error in the efficiency analysis in this dissertation. The axial component of ion beam current required to equate performance parameters calculated with beam properties compared to thrust measurements resulted in plausible divergence half-angles.

7.6 Recommendations for Future Work

The advancements and conclusions in this body of work yield a number of unanswered questions that warrant further investigation. In the following section, several fundamental issues are addressed with an emphasis on recommendations for the course of future research.

7.6.1 Analysis of Joule Heating Discharge Loss Mechanisms

The aim of this dissertation was to evaluate the physics governing low discharge voltage Hall thruster loss mechanisms. In this investigation, increased electron current to the anode was the dominant loss mechanism during low-voltage Hall thruster operation. However, a theoretical analysis of the electron current required to sustain ionization for a typical Hall thruster ion species composition was two orders of magnitude less than observed in experimental measurements. Understanding the Joule heating losses in the Hall thruster discharge is critical to assess the energy losses and investigate plasmadynamic effects. This multifaceted subject requires a combination of numerical simulations and experimental investigations.

The interrelated electron temperature and Joule heating processes were hypothesized to dominate low discharge voltage Hall thruster operation. Increased

electron temperature leads to enhanced ionization in the discharge, but is also correlated with increased excitation, ohmic heating of the channel walls, radiation, and the creation of multiply-charged ions. These processes are determined by the propellant type and injection, discharge channel geometry, and operating conditions. While each of these subjects has been studied, the effect of channel geometry on low-voltage operation is unknown. As electron temperature decreases with applied anode potential, high energy wall collisions are believed to play a lesser role. The ramifications of wall surface area, channel length, and channel volume on the Joule heating processes during low-voltage thruster operation merits further study. This may be accomplished through performance characterization in addition to numerical analysis of thermal pathways and experimental temperature measurements using embedded or wall-mounted probes. In addition, LIF measurements of specific excitation states and estimation of the energy losses associated with these processes would enhance understanding of the nature and cause of electron current to the anode. Merging this information with knowledge of the electromagnetic fields in a numerical model may provide significant insight into low discharge voltage Hall thruster operation.

7.6.2 Interpretation of Low Discharge Voltage Operating Regimes

The low-voltage Hall thruster discharge oscillations and ionization instabilities described in Chapter 6 were highly sensitive to the near-field neutral density. Potential causes of these oscillations were discussed, but the exact nature remains unknown. Time-resolved internal and near-field interrogation of the plasma potential and electron temperature would greatly enhance the knowledge of this low discharge voltage

phenomenon. In addition, a detailed study of the thruster and cathode discharge oscillations would focus the investigation, and enhance understanding of the instabilities. Discharge current and cathode potential oscillations in the high-current regime were related, but the investigation did not resolve which one was driving the instabilities. Recognizing the character of this cathode coupling may assist future cathode and thruster development efforts.

Although the power supply circuit response was not believed to drive the discharge oscillations in the high-current regime, the possibility should be investigated in greater detail. The high-current mode oscillations were more severe as background pressure decreased, and thus the regime is more apt to arise on-orbit than in vacuum facilities on the ground. While conventional power processing units are designed for nominal 200-V to 400-V Hall thruster operation, the possibility that the power supply may have highly deleterious effects on low discharge voltage Hall thruster performance is of significant value.

One valuable experiment involves seeding the injected neutral flow with argon or another noble gas to study the processes that exacerbate or damp the discharge instabilities. This investigation may be accomplished through LIF or far-field plume measurements with ion energy diagnostics, such as an electrostatic energy analyzer or ExB probe. Injecting neutral propellant is a successful mitigation strategy to preserve thruster operation in the low-current regime, but understanding the discharge physics driving oscillations in the high-current regime may prove highly advantageous for the inception and development of future technologies.

7.6.3 Validation of Faraday Probe Experimental Methods and Analysis

The examination of Faraday probe design led to development of several experimental methods and analytical techniques that resulted in highly precise current density profiles and plume properties. Consistent agreement of beam properties measured with four nested Faraday probe configurations was the rationale for a high degree of accuracy, and was the justification for reducing ion beam current measurement uncertainty to ±3%. Implementing these advancements in the Hall thruster performance architecture further supported the methodologies, and highlighted the complexity of assessing the axial component of ion beam current in a Hall thruster discharge.

Further experimental validation at other facilities with different Faraday probe designs, thruster models, and operating conditions is recommended. Specifically, a comprehensive map of current density profiles with variations in facility background pressure, distance, and thruster operating conditions is compulsory to study the decline in the axial component of ion beam current in the near-field plume.

Numerical simulation of Faraday probe ion collection is suggested to verify the theory of ion collection in the gap volume. In addition, these simulations should assess the claim that a 5 to 10 Debye length gap between the collector and guard ring is unnecessary if a version of the gap correction factor is applied. While this is simply a conventional design criterion, understanding the nuances of Faraday probe ion collection area is essential for proper assessment of current density measurements. In addition, for experimental plume studies encompassing a wide range of Debye lengths, such as near-field measurements, the gap correction factor may allow implementation of a guard ring that reduces fringing field effects.

7.6.4 Improvements in Characterization of Global Performance Quantities

The performance architecture developed in Chapter 2 is an analytical tool that is not meant to predict Hall thruster physics or plasma properties in the same manner as a computational model. Rather, the analysis employs performance measurements and bulk plume characteristics to experimentally determine physical processes and relationships that are difficult to measure directly. In this investigation, the procedure has been reduced to the minimal and most basic measurements Thus, while the architecture may quantify global voltage utilization based on a single measurement of the most probable acceleration potential on thruster centerline, more elaborate plume averaging techniques and incorporation of the ion energy per charge distribution may be advantageous. These types of improvements are encouraged and expected.

Incorporation of the finite effect of neutral flow on thruster performance is not conventional, and the neutral-gain utilization is a new concept. Although it may be negligible in most instances, thrusters with a high fraction of thermalized neutral flow or poor propellant injection may experience performance benefits of several percent. Therefore, a rudimentary estimate of the exit exhaust velocity of neutral flow is recommended for future performance studies. A simplified study of the thrust generated by hot neutral flow in the absence of a plasma discharge is recommended to quantify the thrust of this non-ionized propellant. Based on this value, the velocity of this population may be estimated and compared to LIF measurements of the neutral flow at the exit plane of a Hall thruster discharge. While the overall effect is expected to be minor, it provides a more accurate representation of Hall thruster performance characteristics for comparison over a wide range of discharge voltage and discharge power.

Not accounting for the total flow to the anode and cathode in the estimation of ionization fraction and thruster performance led to over 100% mass utilization for some low-voltage operating conditions. Based on the improvements in estimation of ion beam current used in that calculation, it is believed a fraction of the cathode flow is ionized in addition to a majority of the anode flow. Thus, the total mass flow rate should be used for estimation of total thruster efficiency, utilization efficiencies, and total specific impulse to more precisely characterize thruster loss mechanisms over a wide operational envelope.

Appendix A

Propagation of Measurement Uncertainty

The interrelated expressions for utilization efficiencies and thruster performance parameters necessitate careful examination of the uncertainty. In several expressions, including the total thruster efficiency and propellant efficiency, measured quantities used to calculate the utilization efficiencies will cancel when combined to compute a new term, and the uncertainty should not be considered. The propagation of uncertainty is based on the NIST Technical Note 1297,[140] which is a summary of the comprehensive ISO *Guide to the Expression of Uncertainty in Measurement*.[82]

For uncorrelated terms where the covariance is zero, the propagation of uncertainty is calculated using the square root of the sum of the squared relative error according to Eq. (A-1), where y is the measurand and x is the independent variable.

$$\left(\frac{\Delta(\mathrm{y})}{\mathrm{y}}\right)^2 = \sum_{j=1}\left(\frac{\boldsymbol{\delta}\mathrm{y}}{\boldsymbol{\delta}\mathrm{x}_j}\right)^2\left(\frac{\Delta(\mathrm{x}_j)}{\mathrm{x}_j}\right)^2 \tag{A-1}$$

$$\mathrm{y} = f(x_1, x_2, \ldots) + constant \tag{A-2}$$

For correlated terms, the estimation of uncertainty is more difficult. These variables include the species current fractions (where $\sum\Omega_j = 1$) along with the axial

component and total integrated ion beam current. The error associated with these terms is examined in closer detail to analytically determine the range of uncertainty.

The average ion charge in Eq. (A-3) and the charge utilization in Eq. (A-4) are formulated in terms of the ion current fractions and the respective uncertainty of each ion species. The uncertainties of average ion charge and charge utilization are reduced to a function of uncertainty in the ion current fractions in Eq. (A-5) and (A-6).

$$Q \pm \Delta(Q) = \left(\sum_{j=1} \frac{\Omega_j \pm \Delta(\Omega_j)}{Z_j} \right)^{-1} \tag{A-3}$$

$$\Phi_q \pm \Delta(\Phi_q) = \frac{\left(\sum_{j=1} \frac{\Omega_j \pm \Delta(\Omega_j)}{\sqrt{Z_j}} \right)^2}{\left(\sum_{j=1} \frac{\Omega_j \pm \Delta(\Omega_j)}{Z_j} \right)} \tag{A-4}$$

$$\pm \frac{\Delta(Q)}{Q} = \frac{1}{1 + Q \sum_{j=1}^{Z} \left(\mp \Delta(\Omega_j) \right) \frac{(Z - j)}{j Z}} - 1 \tag{A-5}$$

$$\pm \frac{\Delta(\Phi_q)}{\Phi_q} \approx \frac{1 + 2 \left(\frac{Q}{\Phi_q} \right)^{1/2} \sum_{j=1}^{Z} \left(\pm \Delta(\Omega_j) \right) \left(\frac{1}{\sqrt{j}} - \frac{1}{\sqrt{Z}} \right)}{1 + Q \sum_{j=1}^{Z} \left(\pm \Delta(\Omega_j) \right) \frac{(Z - j)}{j Z}} - 1 \tag{A-6}$$

These conservative formulations of relative error are derived by estimating the deviation when the uncertainty is subtracted from the current fraction of lower ion charge states and is added to the fraction of the highest charge state. Thus, for a bimodal ion population the uncertainty in the Xe^+ current fraction is subtracted from Ω_1 and added to Ω_2. The ion charge state, Z, in Eq. (A-5) and (A-6) corresponds to the highest measured

charge state. The approximation in Eq. (A-6) is a result of neglecting second order uncertainty terms, and is expected to reduce the overall uncertainty by less than one in one thousand.

In many of the utilization efficiency and performance parameter calculations, the effect of multiply-charged ions reduces to the ratio of charge utilization with respect to average ion charge. Since these quantities are correlated, it is preferable to analytically estimate the range of uncertainty. The expression in Eq. (A-7) is also formulated by neglecting second order error effects, and the range of uncertainty is less than would be computed for treatment of Q and Φ_q separately based on Eq. (A-5) and (A-6).

$$\frac{\Delta\left(\Phi_q/Q\right)}{\left(\Phi_q/Q\right)} \approx 2\left(\frac{\Phi_q}{Q}\right)^{-1/2}\sum_{j=1}^{Z}\left(\frac{1}{\sqrt{j}}-\frac{1}{\sqrt{Z}}\right)\Delta\left(\Omega_j\right) \tag{A-7}$$

The correlated error between the axial ion current and total ion beam current is difficult to quantify due to facility effects. Systematic error associated with probe collection area will cancel, and the error associated with particle scattering and facility effects will be larger for the axial component of beam current. While the individual uncertainties were estimated as ±3% and ±5%, the uncertainty of the ratio is estimated as ±5% in Eq. (A-8) based on experimental measurements over a range wide range of distances and background pressures in Chapter 4. This uncertainty in Eq. (A-8) is increased to ±10% if the ratio is not characterized as a function of distance and facility background pressure.

$$\frac{\Delta\left(I_{Axial}/I_{Beam}\right)}{\left(I_{Axial}/I_{Beam}\right)} \approx .05 \tag{A-8}$$

All other parameters are considered uncorrelated, and relative errors are propagated based on the uncertainty of experimental measurements and/or the uncertainty of correlated values in Eq. (A-3) through (A-8). Uncertainty in divergence angle in Eq. (A-13) is based on the method of partial derivatives to propagate error, where the term in brackets is the partial derivative of the inverse cosine of the ratio of axial to total ion beam current.

$$\frac{\Delta(\Phi_m)}{\Phi_m} = \sqrt{\left(\frac{\Delta(I_{Beam})}{I_{Beam}}\right)^2 + \left(\frac{\Delta(Q)}{Q}\right)^2 + \left(\frac{\Delta(\dot{m}_T)}{\dot{m}_T}\right)^2} \tag{A-9}$$

$$\frac{\Delta(\Phi_{N\text{-}G})}{\Phi_{N\text{-}G}-1} \approx \sqrt{\left(\frac{\Delta(y_0)}{y_0}\right)^2 + 4\left(\frac{\Delta(\Phi_m)}{\Phi_m}\right)^2 + \frac{1}{4}\left(\frac{\Delta(Q)}{Q}\right)^2 + \frac{1}{4}\left(\frac{\Delta(\Phi_q)}{\Phi_q}\right)^2} \tag{A-10}$$

$$\frac{\Delta(\Phi_P)}{\Phi_P} \approx \sqrt{\left(\frac{\Delta(I_{Beam})}{I_{Beam}}\right)^2 + \left(\frac{\Delta(\dot{m}_T)}{\dot{m}_T}\right)^2 + \left(\frac{\Delta(\Phi_{N\text{-}G})}{\Phi_{N\text{-}G}-1}\right)^2 + \left(\frac{\Delta(\Phi_q/Q)}{(\Phi_q/Q)}\right)^2} \tag{A-11}$$

$$\frac{\Delta(\Psi_B)}{\Psi_B} = \sqrt{4\left(\frac{\Delta(I_{Axial}/I_{Beam})}{(I_{Axial}/I_{Beam})}\right)^2} \tag{A-12}$$

$$\frac{\Delta(\lambda)}{\lambda} = \sqrt{\left[\frac{\delta\left(\cos^{-1}\left(\frac{I_{Axial}}{I_{Beam}}\right)\right)}{\delta\left(\frac{I_{Axial}}{I_{Beam}}\right)}\right]^2 \left(\frac{\Delta(I_{Axial}/I_{Beam})}{\lambda}\right)^2} = \frac{\left(\frac{\Delta(I_{Axial}/I_{Beam})}{\lambda}\right)}{\sqrt{1-\left(\frac{I_{Axial}}{I_{Beam}}\right)^2}} \tag{A-13}$$

$$\frac{\Delta(1-\beta)}{(1-\beta)} = \sqrt{\left(\frac{\Delta(V_a)}{V_a}\right)^2 + \left(\frac{\Delta(V_d)}{V_d}\right)^2} \tag{A-14}$$

$$\frac{\Delta(1-r)}{(1-r)} = \sqrt{\left(\frac{\Delta(I_{Beam})}{I_{Beam}}\right)^2 + \left(\frac{\Delta(I_d)}{I_d}\right)^2} \tag{A-15}$$

$$\frac{\Delta(\eta_E)}{\eta_E} = \sqrt{\left(\frac{\Delta(V_a)}{V_a}\right)^2 + \left(\frac{\Delta(V_d)}{V_d}\right)^2 + \left(\frac{\Delta(I_{Beam})}{I_{Beam}}\right)^2 + \left(\frac{\Delta(I_d)}{I_d}\right)^2} \tag{A-16}$$

Thruster performance metrics and experimental parameter groups may be calculated using thrust measurements or plume measurements. Expressions for uncertainty based on thrust measurements are listed in Eq. (A-17) to (A-20). Uncertainty using plume measurements are listed in Eq. (A-21) to (A-24). The mass exchange parameter is computed based solely on telemetry data, and relative error is calculated using Eq. (A-25).

$$\frac{\Delta(E_1)}{E_1} = \sqrt{4\left(\frac{\Delta(T)}{T}\right)^2 + 4\left(\frac{\Delta(\dot{m}_T)}{\dot{m}_T}\right)^2 + \left(\frac{\Delta(V_d)}{V_d}\right)^2} \tag{A-17}$$

$$\frac{\Delta(I_{sp})}{I_{sp}} = \sqrt{\left(\frac{\Delta(\dot{m}_T)}{\dot{m}_T}\right)^2 + \left(\frac{\Delta(T)}{T}\right)^2} \tag{A-18}$$

$$\frac{\Delta(T/P_d)}{(T/P_d)} = \sqrt{\left(\frac{\Delta(V_d)}{V_d}\right)^2 + \left(\frac{\Delta(I_d)}{I_d}\right)^2 + \left(\frac{\Delta(T)}{T}\right)^2} \tag{A-19}$$

$$\frac{\Delta(\eta_T)}{\eta_T} = \sqrt{\left(\frac{\Delta(V_d)}{V_d}\right)^2 + \left(\frac{\Delta(I_d)}{I_d}\right)^2 + \left(\frac{\Delta(\dot{m}_T)}{\dot{m}_T}\right)^2 + 4\left(\frac{\Delta(T)}{T}\right)^2} \tag{A-20}$$

$$\frac{\Delta(E_1)}{E_1} = \sqrt{4\left(\frac{\Delta(\dot{m}_T)}{\dot{m}_T}\right)^2 + 4\left(\frac{\Delta(I_{Axial})}{I_{Axial}}\right)^2 + \left(\frac{\Delta(V_d)}{V_d}\right)^2 + \left(\frac{\Delta(V_a)}{V_a}\right)^2 + \left(\frac{\Delta(\Phi_{N\text{-}G})}{\Phi_{N\text{-}G}-1}\right)^2 + \left(\frac{\Delta(\Phi_q/Q)}{(\Phi_q/Q)}\right)^2} \tag{A-21}$$

$$\frac{\Delta(I_{sp})}{I_{sp}} = \sqrt{\left(\frac{\Delta(\dot{m}_T)}{\dot{m}_T}\right)^2 + \left(\frac{\Delta(I_{Axial})}{I_{Axial}}\right)^2 + \frac{1}{4}\left(\frac{\Delta(V_a)}{V_a}\right)^2 + \frac{1}{4}\left(\frac{\Delta(\Phi_{N\text{-}G})}{\Phi_{N\text{-}G}-1}\right)^2 + \frac{1}{4}\left(\frac{\Delta(\Phi_q/Q)}{(\Phi_q/Q)}\right)^2} \tag{A-22}$$

$$\frac{\Delta(T/P_d)}{(T/P_d)} = \sqrt{\left(\frac{\Delta(V_d)}{V_d}\right)^2 + \left(\frac{\Delta(I_d)}{I_d}\right) + \left(\frac{\Delta(I_{Axial})}{I_{Axial}}\right)^2 + \frac{1}{4}\left(\frac{\Delta(V_a)}{V_a}\right)^2 + \frac{1}{4}\left(\frac{\Delta(\Phi_{N\text{-}G})}{\Phi_{N\text{-}G} - 1}\right)^2 + \frac{1}{4}\left(\frac{\Delta(\Phi_q/Q)}{(\Phi_q/Q)}\right)^2}$$

(A-23)

$$\frac{\Delta(\eta_T)}{\eta_T} = \sqrt{\left(\frac{\Delta(\dot{m}_T)}{\dot{m}_T}\right)^2 + \left(\frac{\Delta(V_d)}{V_d}\right)^2 + \left(\frac{\Delta(I_d)}{I_d}\right) + 4\left(\frac{\Delta(I_{Axial})}{I_{Axial}}\right)^2 + \left(\frac{\Delta(V_a)}{V_a}\right)^2 + \left(\frac{\Delta(\Phi_{N\text{-}G})}{\Phi_{N\text{-}G} - 1}\right)^2 + \left(\frac{\Delta(\Phi_q/Q)}{(\Phi_q/Q)}\right)^2}$$

(A-23)

$$\frac{\Delta(E_2)}{E_2} = \sqrt{\left(\frac{\Delta(\dot{m}_T)}{\dot{m}_T}\right)^2 + \left(\frac{\Delta(I_d)}{I_d}\right)^2} \qquad \text{(A-25)}$$

Appendix B

Tables of Thruster Performance, Telemetry, and Plume Data

Table B-1 Thrust, telemetry, and far-field plume properties of the 6-kW laboratory Hall thruster at 105-V to 300-V during 20-mg/s anode flow rate operation. Thrust, discharge current, and cathode potential have been extrapolated to vacuum conditions.

Test Point	Thruster Discharge Properties				Propellant Mass Flow Rate		Electromagnet Settings			Thrust and Far-field Plume Properties							
	V_d [V]	I_d [A]	P_d [W]	V_{cg} [V]	Anode [mg/s]	Cathode [mg/s]	Inner [A]	Outer [A]	Trim [A]	T [mN]	V_{mp} [V]	V_p [V]	I_{Beam} [A]	I_{Axial} [A]	Ω_1 [-]	Ω_2 [-]	Ω_3 [-]
1	300.0	20.55	6166	-8.7	20.0	1.4	3.0	3.0	-1.1	410.4	280	12.0	16.4	15.3	0.78	0.16	0.06
2	150.3	21.53	3236	-7.3	20.0	1.4	2.7	2.7	-0.7	262.5	134	10.5	15.5	14.0	0.84	0.16	-
3	120.4	21.60	2600	-6.3	20.0	1.4	2.8	2.8	-0.7	217.8	104	9.0	15.8	13.7	0.87	0.13	-
4	120.2	22.57	2713	-6.0	20.0	3.2	2.7	2.4	-0.9	234.4	102	6.0	16.6	14.6	0.84	0.16	-
5	105.3	22.93	2415	-6.0	20.0	3.2	2.7	2.5	-0.9	201.2	84	5.5	16.2	13.9	0.86	0.14	-

Table B-2 Thrust, telemetry, and far-field plume properties of the 6-kW laboratory Hall thruster at 105-V to 300-V during 10-mg/s anode flow rate operation. Thrust, discharge current, and cathode potential have been extrapolated to vacuum conditions.

Test Point	Thruster Discharge Properties				Propellant Mass Flow Rate		Electromagnet Settings			Thrust and Far-field Plume Properties							
	V_d [V]	I_d [A]	P_d [W]	V_{cg} [V]	Anode [mg/s]	Cathode [mg/s]	Inner [A]	Outer [A]	Trim [A]	T [mN]	V_{mp} [V]	V_p [V]	I_{Beam} [A]	I_{Axial} [A]	Ω_1 [-]	Ω_2 [-]	Ω_3 [-]
6	300.3	8.81	2644	-12.5	10.2	0.7	2.8	2.7	-0.75	188.5	278	12.0	7.5	7.0	0.90	0.07	0.03
7	150.1	9.25	1389	-10.0	10.2	0.7	2.2	2.2	-0.75	116.2	130	9.5	6.9	6.2	0.91	0.08	0.01
8	120.0	9.61	1154	-8.7	10.2	0.7	2.4	2.0	-0.8	95.6	100	8.0	6.8	5.5	0.96	0.04	-
9	120.1	9.54	1144	-8.6	10.2	1.2	2.4	2.0	-0.8	97.9	100	7.5	6.8	5.8	0.91	0.09	-
10	105.7	9.96	1055	-8.2	10.2	1.6	2.6	2.4	-0.9	89.3	88	7.0	6.8	5.7	0.89	0.11	-

Table B-3 Performance parameters and utilization efficiencies of the 6-kW laboratory Hall thruster from 105-V to 300-V discharge during 20-mg/s anode flow rate operation, based on thruster properties extrapolated to vacuum conditions.

Test Point	Performance Based on Thrust Measurements				Performance Based on Plume Measurements					Plume and Discharge Properties				Efficiency Architecture Utilization Efficiencies							
	η_T [-]	T/P [mN/kW]	Total Isp [s]	E_1 [-]	η_T [-]	T/P [mN/kW]	Total Isp [s]	E_1 [-]	λ [deg]	Q [-]	E_2 [-]	χ [-]	ε_B [eV/ion]	(1-r) [-]	(1-β) [-]	η_E [-]	Φ_m [-]	Φ_q [-]	$\Phi_{N\text{-}G}$ [-]	Φ_P [-]	Ψ_B [-]
1	0.64	66.6	1955	0.83	0.56	62.4	1833	0.73	20.8	1.14	0.77	1.04	122	0.80	0.89	0.71	0.92	0.98	1.00	0.90	0.87
2	0.50	81.1	1251	0.68	0.43	75.8	1168	0.59	25.4	1.09	0.73	0.99	93	0.72	0.82	0.59	0.91	0.99	1.00	0.90	0.82
3	0.43	83.7	1037	0.58	0.40	81.3	1007	0.55	30.4	1.07	0.73	1.00	74	0.73	0.79	0.58	0.94	0.99	1.00	0.93	0.74
4	0.44	86.4	1030	0.58	0.41	83.3	993	0.54	28.4	1.09	0.76	0.97	73	0.74	0.80	0.59	0.90	0.99	1.01	0.89	0.77
5	0.36	83.3	884	0.49	0.34	80.1	857	0.46	31.3	1.08	0.74	0.95	76	0.71	0.75	0.53	0.89	0.99	1.01	0.88	0.73

Table B-4 Performance parameters and utilization efficiencies of the 6-kW laboratory Hall thruster from 105-V to 300-V discharge during 10-mg/s anode flow rate operation, based on thruster properties extrapolated to vacuum conditions.

Test Point	Performance Based on Thrust Measurements				Performance Based on Plume Measurements					Plume and Discharge Properties				Efficiency Architecture Utilization Efficiencies							
	η_T [-]	T/P [mN/kW]	Total Isp [s]	E_1 [-]	η_T [-]	T/P [mN/kW]	Total Isp [s]	E_1 [-]	λ [deg]	Q [-]	E_2 [-]	χ [-]	ε_B [eV/ion]	(1-r) [-]	(1-β) [-]	η_E [-]	Φ_m [-]	Φ_q [-]	$\Phi_{N\text{-}G}$ [-]	Φ_P [-]	Ψ_B [-]
6	0.62	71.3	1761	0.68	0.58	69.2	1710	0.64	19.6	1.06	0.91	0.93	94	0.85	0.89	0.75	0.88	0.99	1.00	0.87	0.89
7	0.45	83.7	1086	0.51	0.39	78.7	1021	0.45	27.2	1.04	0.87	0.86	83	0.75	0.80	0.60	0.83	0.99	1.01	0.83	0.79
8	0.37	83.2	897	0.44	0.30	75.3	812	0.36	35.5	1.02	0.83	0.85	79	0.71	0.77	0.54	0.83	1.0	1.01	0.83	0.66
9	0.37	85.5	875	0.42	0.31	78.4	803	0.35	31.5	1.05	0.88	0.81	80	0.71	0.77	0.55	0.77	0.99	1.01	0.78	0.73
10	0.32	84.5	772	0.37	0.27	77.8	711	0.31	33.9	1.06	0.87	0.79	78	0.69	0.76	0.52	0.75	0.99	1.02	0.75	0.69

Appendix C

Tables of Thruster Operation with Mass Flow Variation

Table C-1 Thrust, telemetry, and performance of the 6-kW laboratory Hall thruster at 100-V for 10-mg/s, 15-mg/s, and 20-mg/s anode flow rate operation. Thrust, discharge current, and cathode potential have not been extrapolated to vacuum conditions.

Test Point	Thruster Discharge Properties				Propellant Mass Flow Rate			Electromagnet Settings			Thrust and Performance						Facility Pressure [torr]
	V_d [V]	I_d [A]	P_d [W]	V_{cg} [V]	Anode [mg/s]	Cathode [mg/s]	CFF [%]	Inner [A]	Outer [A]	Trim [A]	T [mN]	T/P [mN/kW]	Total Isp [s]	η_T [-]	E_1 [-]	E_2 [-]	
181	100.7	11.2	1126	-7.9	10.15	0.7	7	2.2	2.1	-0.6	84.1	73.8	791	0.29	0.46	0.67	7.7E-06
186	100.7	11.1	1117	-8.0	10.15	0.8	8	2.3	2.2	-0.6	84.8	74.9	790	0.29	0.47	0.67	7.7E-06
191	100.6	11.1	1120	-7.8	10.15	1.0	10	2.3	2.2	-0.6	86.2	75.9	789	0.29	0.49	0.67	8.0E-06
196	100.4	11.1	1115	-7.8	10.15	1.2	12	2.3	2.2	-0.6	86.5	76.5	777	0.29	0.49	0.67	8.0E-06
201	100.7	11.1	1118	-7.8	10.15	1.4	14	2.3	2.2	-0.6	87.5	77.2	773	0.29	0.50	0.67	8.4E-06
206	100.5	11.1	1115	-7.7	10.15	1.6	16	2.3	2.2	-0.6	87.9	77.8	763	0.29	0.51	0.67	8.4E-06
211	100.8	11.1	1119	-7.7	10.15	1.8	17	2.3	2.2	-0.6	88.9	78.4	761	0.29	0.52	0.67	8.7E-06
216	100.8	11.1	1118	-7.6	10.15	2.0	20	2.3	2.2	-0.6	88.8	78.5	746	0.29	0.51	0.67	8.7E-06
260	100.5	11.0	1108	-7.8	10.15	2.2	21	2.3	2.2	-0.6	89.3	79.4	738	0.29	0.52	0.68	8.7E-06
217	100.7	9.9	998	-8.2	10.15	2.4	23	2.5	2.4	-0.9	88.4	87.0	720	0.31	0.51	0.75	9.1E-06
226	100.8	9.9	996	-8.2	10.15	2.6	25	2.5	2.3	-0.9	88.6	87.5	711	0.30	0.51	0.76	9.1E-05
57	100.6	17.8	1795	-8.7	15.20	1.0	7	3.0	2.0	-0.8	131.7	72.6	827	0.29	0.51	0.63	1.2E-05
139	100.5	17.9	1799	-7.8	15.15	1.2	8	3.0	2.3	-0.9	132.3	72.7	826	0.29	0.51	0.62	1.3E-05
160	100.7	17.8	1790	-7.7	15.15	1.3	9	3.0	2.3	-0.9	134.3	74.1	831	0.30	0.53	0.63	1.3E-05
150	100.5	17.8	1789	-7.5	15.15	1.5	10	3.0	2.4	-0.9	135.1	74.6	828	0.30	0.54	0.63	1.3E-05
155	100.4	17.8	1785	-7.3	15.15	1.6	11	3.0	2.4	-0.9	136.0	75.2	827	0.30	0.54	0.63	1.3E-05
165	100.7	17.6	1773	-7.3	15.15	1.8	12	3.0	2.4	-0.9	136.2	75.8	820	0.30	0.54	0.63	1.1E-05
168	100.6	17.3	1743	-7.3	15.15	2.1	14	3.2	2.2	-0.9	137.2	77.7	812	0.31	0.55	0.64	1.3E-05
172	100.8	15.8	1596	-7.0	15.15	2.7	18	2.8	2.3	-0.9	142.1	87.9	814	0.35	0.59	0.70	1.1E-05
231	100.4	16.1	1617	-6.7	15.15	3.0	20	2.5	2.1	-0.9	145.6	89.1	820	0.36	0.62	0.69	1.1E-05
250	100.4	16.2	1630	-6.9	15.15	3.6	24	2.5	2.1	-0.9	148.5	90.1	810	0.36	0.65	0.69	1.2E-05
251	100.4	16.2	1631	-7.1	15.15	3.9	26	2.5	2.1	-0.9	149.9	91.0	804	0.36	0.66	0.69	1.2E-05
58	100.6	24.7	2484	-7.7	20.04	1.4	7	2.6	2.2	-0.4	180.4	72.1	860	0.30	0.55	0.60	1.4E-05
121	100.3	24.5	2453	-7.0	20.04	1.6	8	3.0	2.3	-0.5	181.6	73.4	856	0.31	0.55	0.60	1.5E-05
126	100.7	24.3	2443	-6.8	20.04	1.8	9	3.0	2.3	-0.5	184.3	74.8	861	0.32	0.57	0.61	1.5E-05
131	100.6	24.1	2428	-6.5	20.04	2.0	10	3.0	2.3	-0.5	186.0	75.9	862	0.32	0.58	0.61	1.5E-05
242	100.9	21.8	2200	-6.6	20.04	2.2	11	3.0	2.5	-0.5	188.1	84.6	864	0.36	0.59	0.68	1.5E-05
236	100.7	22.7	2291	-6.4	20.04	2.4	12	2.5	2.3	-0.9	196.8	85.2	895	0.37	0.65	0.65	1.5E-05
241	100.5	23.0	2315	-6.2	20.04	2.8	14	2.5	2.2	-0.9	201.5	86.3	900	0.38	0.68	0.64	1.5E-05

Table C-2 Thrust, telemetry, and performance of the 6-kW laboratory Hall thruster at 105-V for 10-mg/s, 15-mg/s, and 20-mg/s anode flow rate operation. Thrust, discharge current, and cathode potential have not been extrapolated to vacuum conditions.

Test Point	Thruster Discharge Properties				Propellant Mass Flow Rate			Electromagnet Settings			Thrust and Performance						Facility Pressure [torr]
	V_d [V]	I_d [A]	P_d [W]	V_{cg} [V]	Anode [mg/s]	Cathode [mg/s]	CFF [%]	Inner [A]	Outer [A]	Trim [A]	T [mN]	T/P [mN/kW]	Total Isp [s]	η_T [-]	E_1 [-]	E_2 [-]	
180	105.3	11.0	1163	-8.2	10.15	0.7	7	2.2	2.1	-0.6	87.8	74.6	826	0.30	0.48	0.68	7.7E-06
185	105.5	10.9	1155	-8.4	10.15	0.8	8	2.3	2.2	-0.6	88.7	75.8	826	0.31	0.49	0.68	7.7E-06
190	105.5	10.9	1152	-8.1	10.15	1.0	10	2.3	2.2	-0.6	90.3	77.4	826	0.31	0.51	0.68	8.0E-06
195	105.2	10.9	1143	-8.1	10.15	1.2	12	2.3	2.2	-0.6	90.5	78.2	813	0.31	0.51	0.69	8.0E-06
200	105.6	9.8	1038	-8.5	10.15	1.4	14	2.5	2.4	-0.9	89.2	84.5	788	0.33	0.50	0.76	8.4E-06
205	105.1	9.8	1032	-8.4	10.15	1.6	16	2.5	2.3	-0.9	89.6	85.4	778	0.33	0.50	0.76	8.4E-06
210	105.6	9.7	1025	-8.5	10.15	1.8	17	2.6	2.3	-0.6	89.2	85.6	763	0.32	0.50	0.77	8.7E-06
215	105.5	9.8	1034	-8.4	10.15	2.0	20	2.4	2.3	-0.6	90.1	85.9	757	0.32	0.51	0.76	8.7E-06
259	105.5	9.7	1028	-8.4	10.15	2.2	21	2.4	2.2	-0.6	90.6	86.8	749	0.32	0.51	0.77	8.7E-06
218	105.4	9.8	1031	-8.2	10.15	2.4	23	2.3	2.0	-0.6	91.6	87.7	747	0.32	0.52	0.76	9.1E-06
225	105.5	9.8	1035	-8.2	10.15	2.6	25	2.3	2.2	-0.6	92.0	87.7	738	0.32	0.53	0.76	9.1E-05
138	105.3	17.4	1835	-8.1	15.15	1.2	8	3.0	2.3	-0.9	138.8	74.8	867	0.32	0.54	0.64	1.3E-05
144	105.7	17.4	1844	-7.7	15.15	1.3	9	3.0	2.3	-0.9	141.7	76.0	877	0.33	0.56	0.64	1.3E-05
149	105.5	17.2	1810	-7.6	15.15	1.5	10	3.0	2.4	-0.9	141.5	77.2	867	0.33	0.56	0.65	1.3E-05
154	105.6	17.0	1798	-7.5	15.15	1.6	11	3.0	2.4	-0.9	141.6	77.8	861	0.33	0.56	0.65	1.3E-05
164	105.5	16.6	1753	-7.9	15.15	1.8	12	3.7	2.6	-1.0	140.2	78.6	845	0.33	0.55	0.67	1.1E-05
167	105.7	15.6	1644	-7.4	15.15	2.1	14	3.2	2.2	-0.9	141.8	85.1	840	0.35	0.56	0.72	1.3E-05
264	105.8	15.8	1671	-7.1	15.15	2.4	16	2.7	2.2	-0.9	146.1	86.4	850	0.36	0.60	0.70	1.1E-05
173	105.3	15.9	1679	-6.9	15.15	2.7	18	2.5	2.2	-0.9	149.5	88.1	856	0.37	0.63	0.70	1.1E-05
230	105.6	16.0	1685	-6.9	15.15	3.0	20	2.6	2.2	-0.9	151.4	88.9	852	0.37	0.64	0.70	1.1E-05
249	105.6	16.2	1709	-7.0	15.15	3.6	24	2.5	2.1	-0.9	155.1	89.8	845	0.37	0.67	0.69	1.2E-05
252	105.3	16.1	1700	-7.1	15.15	3.9	26	2.5	2.1	-0.9	155.9	90.8	836	0.37	0.68	0.69	1.2E-05
120	105.4	23.8	2505	-7.1	20.04	1.6	8	3.1	2.4	-0.7	191.9	75.9	905	0.34	0.59	0.62	1.5E-05
125	105.2	24.0	2521	-6.8	20.04	1.8	9	2.9	2.4	-0.7	194.3	76.4	908	0.34	0.61	0.61	1.5E-05
134	105.6	24.4	2572	-6.6	20.04	2.0	10	2.8	2.3	-0.8	195.8	75.6	907	0.34	0.61	0.60	1.5E-05
133	105.6	21.8	2301	-6.5	20.04	2.0	10	3.0	2.3	-0.8	196.0	84.4	908	0.38	0.61	0.68	1.4E-05
235	105.5	22.4	2359	-6.4	20.04	2.4	12	2.7	2.3	-0.9	203.3	85.4	925	0.39	0.66	0.66	1.5E-05
240	105.3	22.7	2395	-6.3	20.04	2.8	14	2.6	2.2	-0.9	208.0	86.2	930	0.39	0.69	0.65	1.5E-05

Table C-3 Thrust, telemetry, and performance of the 6-kW laboratory Hall thruster at 110-V for 10-mg/s, 15-mg/s, and 20-mg/s anode flow rate operation. Thrust, discharge current, and cathode potential have not been extrapolated to vacuum conditions.

Test Point	Thruster Discharge Properties				Propellant Mass Flow Rate			Electromagnet Settings			Thrust and Performance						Facility Pressure [torr]
	V_d [V]	I_d [A]	P_d [W]	V_{cg} [V]	Anode [mg/s]	Cathode [mg/s]	CFF [%]	Inner [A]	Outer [A]	Trim [A]	T [mN]	T/P [mN/kW]	Total Isp [s]	η_T [-]	E_1 [-]	E_2 [-]	
179	110.4	10.8	1197	-5.6	10.15	0.7	7	2.2	2.1	-0.6	91.7	75.7	863	0.32	0.50	0.69	7.7E-06
184	110.2	10.7	1184	-8.8	10.15	0.8	8	2.3	2.2	-0.6	92.2	76.9	859	0.32	0.51	0.69	7.7E-06
189	110.2	9.6	1057	-9.0	10.15	1.0	10	2.7	2.4	-0.6	89.9	83.5	822	0.34	0.48	0.78	8.0E-06
194	110.2	9.7	1066	-8.7	10.15	1.2	12	2.4	2.3	-0.6	91.4	84.4	821	0.34	0.50	0.77	8.0E-06
199	110.6	9.7	1072	-8.6	10.15	1.4	14	2.3	2.2	-0.6	92.9	85.5	821	0.34	0.51	0.77	8.4E-06
204	110.2	9.7	1071	-8.4	10.15	1.6	16	2.2	2.2	-0.6	93.3	86.0	810	0.34	0.52	0.77	8.4E-06
209	110.6	9.7	1071	-8.4	10.15	1.8	17	2.2	2.2	-0.6	93.8	86.4	803	0.34	0.52	0.77	8.7E-06
214	110.5	9.7	1069	-8.4	10.15	2.0	20	2.2	2.0	-0.6	94.2	87.1	792	0.34	0.53	0.77	8.7E-06
258	110.6	9.7	1071	-8.4	10.15	2.2	21	2.1	2.0	-0.6	94.7	87.4	783	0.33	0.53	0.77	8.7E-06
219	110.8	9.7	1076	-8.4	10.15	2.4	23	2.1	2.0	-0.6	95.8	88.1	781	0.34	0.55	0.77	9.1E-06
224	110.7	9.7	1075	-8.4	10.15	2.6	25	2.2	2.0	-0.6	96.1	88.4	771	0.33	0.55	0.77	9.1E-05
76	110.2	17.2	1892	-8.4	15.20	1.0	7	3.0	2.2	-0.8	142.0	74.3	892	0.32	0.54	0.65	1.1E-05
137	110.5	16.4	1814	-8.4	15.15	1.2	8	3.2	2.7	-0.8	143.6	78.0	896	0.34	0.55	0.68	1.3E-05
143	110.5	16.8	1860	-7.9	15.15	1.3	9	2.9	2.0	-0.5	145.8	77.6	902	0.34	0.57	0.66	1.3E-05
148	110.4	15.5	1706	-7.5	15.15	1.5	10	3.0	2.3	-0.9	144.6	83.7	887	0.36	0.56	0.72	1.3E-05
153	110.4	15.5	1714	-7.4	15.15	1.6	11	2.9	2.3	-0.9	146.8	84.6	893	0.37	0.58	0.72	1.3E-05
163	110.6	15.6	1728	-7.5	15.15	1.8	12	2.8	2.3	-0.9	148.1	84.7	892	0.37	0.59	0.71	1.0E-05
169	110.9	15.6	1733	-7.4	15.15	2.1	14	2.7	2.2	-0.9	149.8	85.5	887	0.37	0.60	0.71	1.3E-05
263	110.8	15.7	1738	-7.2	15.15	2.4	16	2.6	2.2	-0.9	152.2	86.6	885	0.38	0.62	0.71	1.1E-05
174	110.2	15.8	1746	-7.1	15.15	2.7	18	2.5	2.2	-0.9	155.3	88.0	889	0.38	0.65	0.70	1.1E-05
229	110.6	16.0	1766	-6.8	15.15	3.0	20	2.6	2.2	-0.9	158.4	88.7	892	0.39	0.67	0.70	1.1E-05
248	110	16.1	1775	-7.0	15.15	3.6	24	2.5	2.2	-0.9	160.7	89.6	875	0.38	0.69	0.69	1.2E-05
253	110.2	16.1	1778	-7.0	15.15	3.9	26	2.5	2.2	-0.9	162.0	90.2	869	0.38	0.70	0.69	1.2E-05
80	110.7	23.4	2592	-7.4	20.04	1.4	7	2.9	2.4	-0.8	196.2	75.0	934	0.34	0.59	0.63	1.4E-05
119	110.7	21.8	2412	-6.7	20.04	1.6	8	2.8	2.4	-0.4	201.0	82.6	948	0.38	0.62	0.68	1.4E-05
124	110.7	21.8	2411	-6.6	20.04	1.8	9	2.8	2.4	-0.4	203.0	83.4	948	0.39	0.63	0.68	1.5E-05
129	110.3	21.8	2406	-6.6	20.04	2.0	10	2.8	2.4	-0.4	203.8	84.0	944	0.39	0.64	0.68	1.5E-05
234	110.3	22.3	2461	-6.5	20.04	2.4	12	2.7	2.3	-0.9	211.4	85.2	962	0.40	0.68	0.66	1.5E-05
239	110.4	22.4	2469	-6.4	20.04	2.8	14	2.6	2.3	-0.9	214.4	86.2	958	0.40	0.70	0.66	1.5E-05

Table C-4 Thrust, telemetry, and performance of the 6-kW laboratory Hall thruster at 115-V for 10-mg/s, 15-mg/s, and 20-mg/s anode flow rate operation. Thrust, discharge current, and cathode potential have not been extrapolated to vacuum conditions.

Test Point	Thruster Discharge Properties				Propellant Mass Flow Rate			Electromagnet Settings			Thrust and Performance						Facility Pressure [torr]
	V_d [V]	I_d [A]	P_d [W]	V_{cg} [V]	Anode [mg/s]	Cathode [mg/s]	CFF [%]	Inner [A]	Outer [A]	Trim [A]	T [mN]	T/P [mN/kW]	Total Isp [s]	η_T [-]	E_1 [-]	E_2 [-]	
178	115.5	9.6	1104	-9.3	10.15	0.7	7	2.5	2.2	-0.6	92.0	82.1	866	0.35	0.48	0.78	7.7E-06
183	115.5	9.6	1111	-9.0	10.15	0.8	8	2.3	2.2	-0.6	93.4	83.0	870	0.35	0.50	0.78	7.7E-06
188	115.2	9.6	1111	-8.8	10.15	1.0	10	2.2	2.2	-0.6	95.1	84.5	869	0.36	0.52	0.77	8.0E-06
193	115.6	9.6	1108	-8.8	10.15	1.2	12	2.2	2.0	-0.6	95.7	85.4	860	0.36	0.52	0.78	8.0E-06
198	115.6	9.6	1105	-8.8	10.15	1.4	14	2.2	2.0	-0.6	96.3	86.1	851	0.36	0.53	0.78	8.4E-06
203	115.5	9.6	1109	-8.6	10.15	1.6	16	2.1	2.0	-0.6	96.9	86.4	841	0.36	0.53	0.78	8.4E-06
208	115.5	9.6	1106	-8.6	10.15	1.8	17	2.1	2.0	-0.6	97.2	86.9	831	0.35	0.54	0.78	8.7E-06
213	115.6	9.6	1108	-8.6	10.15	2.0	20	2.1	2.0	-0.6	97.8	87.3	822	0.35	0.54	0.78	8.7E-06
257	115.4	9.6	1105	-8.7	10.15	2.2	21	2.3	2.0	-0.6	98.1	87.4	811	0.35	0.55	0.78	8.7E-06
220	115.5	9.6	1114	-8.5	10.15	2.4	23	2.0	2.0	-0.6	99.0	87.9	806	0.35	0.56	0.77	9.1E-06
223	115.6	9.6	1111	-8.5	10.15	2.6	25	2.1	1.9	-0.6	99.3	88.5	797	0.34	0.56	0.78	9.1E-05
77	115	15.7	1809	-8.1	15.20	1.0	7	3.0	2.3	-0.9	145.9	79.7	916	0.36	0.54	0.71	1.1E-05
140	115.4	15.4	1780	-7.6	15.15	1.2	8	2.7	2.5	-0.7	147.4	81.9	920	0.37	0.56	0.72	1.2E-05
142	115.5	15.5	1793	-7.6	15.15	1.3	9	2.9	2.3	-1.0	154.8	85.3	958	0.40	0.61	0.72	1.3E-05
147	115.4	15.5	1784	-7.5	15.15	1.5	10	2.7	2.3	-0.8	151.6	84.1	930	0.38	0.59	0.72	1.3E-05
152	115.3	15.4	1779	-7.5	15.15	1.6	11	2.7	2.2	-0.9	152.8	85.0	929	0.39	0.60	0.72	1.3E-05
162	115.7	15.5	1791	-7.7	15.15	1.8	12	2.7	2.2	-0.9	154.0	85.1	928	0.39	0.61	0.72	1.0E-05
170	115.3	15.6	1796	-7.5	15.15	2.1	14	2.6	2.2	-0.9	155.7	85.8	922	0.39	0.62	0.71	1.3E-05
262	115.7	15.6	1803	-7.4	15.15	2.4	16	2.6	2.2	-0.9	157.8	86.7	918	0.39	0.64	0.71	1.1E-05
175	115.3	15.7	1813	-7.3	15.15	2.7	18	2.6	2.2	-0.9	160.6	87.7	919	0.39	0.66	0.71	1.1E-05
228	115.8	15.9	1846	-6.9	15.15	3.0	20	2.6	2.2	-0.9	163.9	87.9	923	0.40	0.69	0.70	1.1E-05
247	115.7	16.0	1854	-7.0	15.15	3.6	24	2.6	2.2	-0.9	166.6	88.9	907	0.39	0.71	0.69	1.2E-05
254	115.4	16.1	1855	-7.0	15.15	3.9	26	2.6	2.2	-0.9	166.6	88.9	894	0.39	0.71	0.69	1.2E-05
79	115.7	21.8	2517	-7.0	20.04	1.4	7	2.9	2.4	-0.8	205.1	80.8	976	0.39	0.61	0.68	1.4E-05
118	115.5	21.8	2523	-6.8	20.04	1.6	8	2.8	2.4	-0.8	210.8	82.8	994	0.40	0.65	0.67	1.4E-05
123	115.3	21.9	2522	-6.7	20.04	1.8	9	2.8	2.4	-0.8	212.3	83.4	992	0.41	0.66	0.67	1.4E-05
128	115.5	21.9	2531	-6.6	20.04	2.0	10	2.8	2.4	-0.8	214.3	83.9	993	0.41	0.67	0.67	1.5E-05
233	115.1	22.3	2564	-6.6	20.04	2.4	12	2.7	2.4	-0.9	218.6	84.6	994	0.41	0.70	0.66	1.4E-05
238	115.9	22.4	2596	-6.4	20.04	2.8	14	2.7	2.4	0.9	223.9	85.6	1000	0.42	0.73	0.66	1.5E-05

Table C-5 Thrust, telemetry, and performance of the 6-kW laboratory Hall thruster at 120-V for 10-mg/s, 15-mg/s, and 20-mg/s anode flow rate operation. Thrust, discharge current, and cathode potential have not been extrapolated to vacuum conditions.

Test Point	Thruster Discharge Properties				Propellant Mass Flow Rate			Electromagnet Settings			Thrust and Performance						Facility Pressure [torr]
	V_d [V]	I_d [A]	P_d [W]	V_{cg} [V]	Anode [mg/s]	Cathode [mg/s]	CFF [%]	Inner [A]	Outer [A]	Trim [A]	T [mN]	T/P [mN/kW]	Total Isp [s]	η_T [-]	E_1 [-]	E_2 [-]	
177	120.6	9.5	1148	-9.3	10.15	0.7	7	2.2	2.0	-0.6	95.8	82.5	901	0.36	0.50	0.78	7.7E-06
182	120.2	9.5	1145	-9.1	10.15	0.8	8	2.2	2.0	-0.6	96.6	83.4	900	0.37	0.51	0.78	7.7E-06
187	120.2	9.5	1147	-8.9	10.15	1.0	10	2.1	2.0	-0.6	98.5	85.0	900	0.37	0.53	0.78	8.0E-06
192	120.4	9.5	1143	-8.7	10.15	1.2	12	2.1	2.0	-0.6	99.0	85.6	889	0.37	0.53	0.79	8.0E-06
197	120.6	9.5	1145	-8.8	10.15	1.4	14	2.1	2.0	-0.6	99.7	86.1	881	0.37	0.54	0.79	8.4E-06
202	120	9.5	1139	-8.8	10.15	1.6	16	2.2	2.0	-0.6	100.0	86.9	869	0.37	0.55	0.79	8.4E-06
207	120.4	9.5	1143	-8.7	10.15	1.8	17	2.1	2.0	-0.6	100.7	87.2	862	0.37	0.55	0.79	8.4E-06
212	120.3	9.5	1144	-8.6	10.15	2.0	20	2.0	2.0	-0.6	101.4	87.8	852	0.37	0.56	0.78	8.7E-06
256	120.4	9.5	1150	-8.9	10.15	2.2	21	2.5	2.4	-0.9	101.3	86.7	838	0.36	0.56	0.78	8.7E-06
221	120.6	9.5	1150	-8.7	10.15	2.4	23	2.0	1.9	-0.6	102.1	87.9	831	0.36	0.57	0.78	9.1E-06
222	120.4	9.5	1147	-8.4	10.15	2.6	25	2.0	2.0	-0.6	102.4	88.3	821	0.36	0.57	0.78	9.1E-06
56	120.4	15.4	1848	-8.8	15.20	1.0	7	3.0	2.3	-1.0	153.1	81.9	962	0.39	0.57	0.73	1.2E-05
135	120.2	15.4	1846	-7.8	15.15	1.2	8	2.7	2.3	-1.0	155.4	83.3	970	0.40	0.59	0.72	1.2E-05
141	120.6	15.5	1870	-7.7	15.15	1.3	9	2.6	2.3	-0.8	161.0	85.2	996	0.42	0.64	0.72	1.3E-05
146	120.6	15.4	1854	-7.7	15.15	1.5	10	2.6	2.3	-0.8	158.4	84.6	971	0.40	0.61	0.72	1.3E-05
151	120.7	15.4	1863	-7.6	15.15	1.6	11	2.5	2.3	-0.8	159.7	84.9	971	0.40	0.62	0.72	1.3E-05
161	120.7	15.5	1868	-7.8	15.15	1.8	12	2.5	2.3	-0.8	160.9	85.3	969	0.40	0.63	0.72	1.0E-05
171	120.6	15.5	1868	-7.7	15.15	2.1	14	2.6	2.2	-0.9	161.6	85.6	957	0.40	0.64	0.72	1.3E-05
261	120.5	15.5	1869	-7.6	15.15	2.4	16	2.6	2.2	-0.9	163.7	86.8	952	0.40	0.66	0.72	1.1E-05
176	120.4	15.7	1888	-7.4	15.15	2.7	18	2.6	2.2	-0.9	166.1	87.1	951	0.41	0.68	0.71	1.1E-05
243	120.7	15.7	1900	-7.3	15.15	3.0	20	2.7	2.2	-0.9	167.3	87.2	942	0.40	0.69	0.71	1.4E-05
255	120.5	15.9	1918	-7.2	15.15	3.9	26	2.6	2.4	-0.9	172.2	88.8	924	0.40	0.73	0.70	1.2E-05
59	120.7	22.0	2660	-8.0	20.04	1.4	7	2.7	2.2	-0.9	216.5	80.8	1030	0.41	0.66	0.67	1.4E-05
117	120.6	21.8	2627	-7.0	20.04	1.6	8	2.8	2.4	-0.8	218.1	82.3	1028	0.41	0.67	0.68	1.4E-05
122	120.2	21.8	2619	-6.9	20.04	1.8	9	2.8	2.4	-0.8	220.1	83.3	1028	0.42	0.68	0.68	1.4E-05
127	120.3	21.8	2627	-6.8	20.04	2.0	10	2.8	2.4	-0.8	222.0	83.8	1028	0.42	0.69	0.67	1.4E-05
232	120.2	22.2	2673	-6.9	20.04	2.4	12	2.7	2.4	-0.9	227.4	84.5	1035	0.43	0.73	0.66	1.4E-05
237	120.8	22.5	2714	-6.5	20.04	2.8	14	2.7	2.4	-0.9	232.8	85.1	1040	0.43	0.76	0.66	1.5E-05

Appendix D

Tables of Thruster Characteristics with Operating Regime

Table D-1 Thrust, telemetry, and far-field plume properties of the 6-kW laboratory Hall thruster at 105-V, 16-CFF during 10-mg/s and 20-mg/s anode flow rate operation as a function of facility background pressure and operating regime.

Test Point	Operating Mode	Thruster Discharge Properties				Propellant Mass Flow Rate			Electromagnet Settings			Thrust, Total Efficiency, and Far-field Plume Properties									Facility Pressure [torr]
		V_d [V]	I_d [A]	P_d [W]	V_{cg} [V]	Anode [mg/s]	Cathode [mg/s]	CFF [%]	Inner [A]	Outer [A]	Trim [A]	T [mN]	V_{mp} [V]	V_p [V]	I_{Beam} [A]	I_{Axial} [A]	λ [deg]	(1-r) [-]	η_T [-]	T/P [mN/kW]	
5	Low-Current	105.3	22.9	2415	-6.0	20.0	3.2	16	2.7	2.5	-0.9	201.2	-	-	16.2	13.9	31.4	0.71	0.36	83.3	Vacuum
	Low-Current	105.3	23.3	2451	-6.0	20.0	3.2	16	2.7	2.5	-0.9	204.6	84	5.5	16.9	13.9	34.8	0.73	0.37	83.5	2.2E-05
	Low-Current	105.3	23.4	2467	-5.9	20.0	3.2	16	2.7	2.5	-0.9	205.7	-	-	17.1	13.9	36.0	0.73	0.37	83.4	2.8E-05
	Low-Current	105.3	23.6	2480	-5.9	20.0	3.2	16	2.7	2.5	-0.9	206.9	-	-	17.4	13.9	37.0	0.74	0.37	83.4	3.5E-05
	Low-Current	105.3	23.7	2490	-5.8	20.0	3.2	16	2.7	2.5	-0.9	208.0	-	-	17.6	13.9	37.9	0.74	0.37	83.5	4.2E-05
	Low-Current	105.3	23.8	2502	-5.8	20.0	3.2	16	2.7	2.5	-0.9	209.0	-	-	17.8	13.9	38.7	0.75	0.38	83.5	4.9E-05
14	High-Current	105.8	27.1	2867	-5.6	20.0	3.2	16	2.6	2.4	-0.9	206.3	-	-	18.0	14.6	35.7	0.66	0.32	72.0	Vacuum
	High-Current	105.8	26.7	2825	-5.6	20.0	3.2	16	2.6	2.4	-0.9	210.0	84	5.5	19.8	15.1	40.2	0.74	0.34	74.4	2.2E-05
	High-Current	105.8	26.7	2820	-5.7	20.0	3.2	16	2.6	2.4	-0.9	210.5	-		20.0	15.2	40.8	0.75	0.34	74.6	2.5E-05
	High-Current	105.8	26.6	2814	-5.7	20.0	3.2	16	2.6	2.4	-0.9	210.9	-		20.3	15.2	41.2	0.76	0.34	74.9	2.7E-05
	High-Current	105.8	26.6	2809	-5.7	20.0	3.2	16	2.6	2.4	-0.9	211.5	-		20.5	15.3	41.7	0.77	0.34	75.3	3.0E-05
	High-Current	105.8	26.5	2798	-5.7	20.0	3.2	16	2.6	2.4	-0.9	212.1	-		20.8	15.4	42.2	0.79	0.35	75.8	3.5E-05
10	Low-Current	106.2	10.0	1058	-8.2	10.2	1.6	16	2.6	2.4	-0.9	89.3	-		6.8	5.7	33.9	0.69	0.32	84.5	Vacuum
	Low-Current	106.2	10.2	1083	-8.4	10.2	1.6	16	2.6	2.4	-0.9	91.9	88	7.0	7.5	6.0	37.5	0.74	0.33	84.8	1.2E-05
	Low-Current	106.2	10.3	1092	-8.5	10.2	1.6	16	2.6	2.4	-0.9	93.0	-	-	7.9	6.1	39.2	0.76	0.34	85.2	1.7E-05
	Low-Current	106.2	10.4	1103	-8.6	10.2	1.6	16	2.6	2.4	-0.9	94.5	-	-	8.2	6.2	40.5	0.79	0.34	85.7	2.3E-05
	Low-Current	106.2	10.5	1116	-8.7	10.2	1.6	16	2.6	2.4	-0.9	95.6	-	-	8.5	6.4	41.6	0.81	0.35	85.7	2.8E-05
	Low-Current	106.2	10.6	1128	-8.8	10.2	1.6	16	2.6	2.4	-0.9	96.7	-	-	8.8	6.5	42.5	0.83	0.35	85.8	3.5E-05
11	High-Current	105.4	12.0	1262	-9.0	10.2	1.6	16	2.6	2.4	-0.9	90.6	-	-	7.7	6.4	33.1	0.64	0.28	71.8	Vacuum
	High-Current	105.4	11.7	1232	-8.9	10.2	1.6	16	2.6	2.4	-0.9	92.8	84	7.0	7.7	6.2	36.3	0.66	0.30	75.3	1.1E-05
	High-Current	105.4	11.6	1226	-9.0	10.2	1.6	16	2.6	2.4	-0.9	93.2	-	-	7.7	6.2	37.0	0.66	0.30	76.0	1.3E-05
	High-Current	105.4	11.6	1219	-8.9	10.2	1.6	16	2.6	2.4	-0.9	93.6	-	-	7.7	6.1	37.5	0.67	0.30	76.8	1.6E-05
	High-Current	105.4	11.5	1215	-8.9	10.2	1.6	16	2.6	2.4	-0.9	94.1	-	-	7.8	6.1	38.1	0.67	0.31	77.4	1.7E-05

Table D-2 Thrust, telemetry, and far-field plume properties of the 6-kW laboratory Hall thruster at 120-V, 7-CFF during 10-mg/s and 20-mg/s anode flow rate operation as a function of facility background pressure and operating regime.

Test Point	Operating Mode	Thruster Discharge Properties				Propellant Mass Flow Rate			Electromagnet Settings			Thrust, Total Efficiency, and Far-field Plume Properties									Facility Pressure [torr]
		V_d [V]	I_d [A]	P_d [W]	V_{cg} [V]	Anode [mg/s]	Cathode [mg/s]	CFF [%]	Inner [A]	Outer [A]	Trim [A]	T [mN]	V_{mp} [V]	V_p [V]	I_{Beam} [A]	I_{Axial} [A]	λ [deg]	(1-r) [-]	η_T [-]	T/P [mN/kW]	
3	Low-Current	120.4	21.6	2600	-6.3	20.0	1.4	7	2.8	2.8	-0.7	217.8	-	-	15.8	13.7	30.4	0.73	0.43	83.7	Vacuum
	Low-Current	120.4	22.3	2687	-6.7	20.0	1.4	7	2.8	2.8	-0.7	223.2	104	9.0	18.1	14.6	36.2	0.81	0.43	83.1	2.0E-05
	Low-Current	120.4	22.5	2707	-6.8	20.0	1.4	7	2.8	2.8	-0.7	224.7	-	-	18.7	14.8	37.5	0.83	0.44	83.0	2.6E-05
	Low-Current	120.4	22.7	2733	-6.9	20.0	1.4	7	2.8	2.8	-0.7	226.2	-	-	19.3	15.1	38.5	0.85	0.44	82.7	3.1E-05
	Low-Current	120.4	22.9	2758	-6.9	20.0	1.4	7	2.8	2.8	-0.7	227.9	-	-	19.9	15.3	39.5	0.87	0.44	82.6	3.9E-05
	Low-Current	120.4	23.1	2779	-7.0	20.0	1.4	7	2.8	2.8	-0.7	229.2	-	-	20.5	15.6	40.2	0.89	0.44	82.5	4.7E-05
16	High-Current	119.7	24.8	2972	-7.0	20.0	1.4	7	2.6	2.6	-0.8	225.0	-	-	18.3	15.5	32.2	0.74	0.40	75.7	Vacuum
	High-Current	119.7	24.8	2972	-7.0	20.0	1.4	7	2.6	2.6	-0.8	225.0	104	9.0	19.3	15.5	36.5	0.78	0.40	75.7	2.0E-05
	High-Current	119.7	24.8	2972	-7.0	20.0	1.4	7	2.6	2.6	-0.8	225.0	-	-	19.4	15.5	37.0	0.78	0.40	75.7	2.2E-05
	High-Current	119.7	24.8	2972	-7.0	20.0	1.4	7	2.6	2.6	-0.8	225.0	-	-	19.5	15.5	37.4	0.79	0.40	75.7	2.4E-05
	High-Current	119.7	24.8	2972	-7.0	20.0	1.4	7	2.6	2.6	-0.8	225.0	-	-	19.7	15.5	37.8	0.79	0.40	75.7	2.7E-05
8	Low-Current	120.0	9.6	1154	-8.7	10.2	0.7	7	2.4	2.0	-0.8	96.0	-	-	6.8	5.5	35.5	0.71	0.37	83.2	Vacuum
	Low-Current	120.0	9.9	1184	-9.4	10.2	0.7	7	2.4	2.0	-0.8	99.0	100	8.0	7.6	5.8	39.6	0.77	0.38	83.6	1.2E-05
	Low-Current	120.0	9.9	1190	-9.7	10.2	0.7	7	2.4	2.0	-0.8	100.4	-	-	7.9	6.0	41.2	0.80	0.39	84.3	1.7E-05
	Low-Current	120.0	10.0	1204	-10.1	10.2	0.7	7	2.4	2.0	-0.8	101.8	-	-	8.2	6.1	42.5	0.82	0.39	84.6	2.2E-05
	Low-Current	120.0	10.1	1217	-10.3	10.2	0.7	7	2.4	2.0	-0.8	103.3	-	-	8.6	6.2	43.6	0.85	0.40	84.9	2.6E-05
	Low-Current	120.0	10.3	1231	-10.6	10.2	0.7	7	2.4	2.0	-0.8	104.3	-	-	8.9	6.4	44.5	0.87	0.40	84.7	3.2E-05
13	High-Current	119.6	11.9	1428	-9.7	10.2	0.7	7	2.2	2.0	-0.5	102.3	-	-	7.9	6.5	35.3	0.67	0.34	71.6	Vacuum
	High-Current	119.6	11.4	1359	-9.7	10.2	0.7	7	2.2	2.0	-0.5	102.7	100	8.0	7.9	6.2	38.3	0.70	0.36	75.6	1.0E-05
	High-Current	119.6	11.2	1335	-9.7	10.2	0.7	7	2.2	2.0	-0.5	103.0	-	-	7.9	6.1	39.5	0.71	0.36	77.2	1.3E-05
	High-Current	119.6	11.0	1319	-9.7	10.2	0.7	7	2.2	2.0	-0.5	103.1	-	-	7.9	6.1	40.1	0.72	0.37	78.2	1.6E-05
	High-Current	119.6	10.9	1301	-9.6	10.2	0.7	7	2.2	2.0	-0.5	103.0	-	-	7.9	6.0	40.6	0.73	0.37	79.1	1.8E-05
	High-Current	119.6	10.8	1287	-9.6	10.2	0.7	7	2.2	2.0	-0.5	103.1	-	-	7.9	5.9	41.2	0.73	0.38	80.1	2.0E-05

Table D-3 Thrust, telemetry, and far-field plume properties of the 6-kW laboratory Hall thruster at 120-V, 20-mg/s, 16-CFF operation as a function of facility background pressure and thruster operating regime.

Test Point	Operating Mode	Thruster Discharge Properties				Propellant Mass Flow Rate			Electromagnet Settings			Thrust, Total Efficiency, and Far-field Plume Properties									Facility Pressure [torr]
		V_d [V]	I_d [A]	P_d [W]	V_{cg} [V]	Anode [mg/s]	Cathode [mg/s]	CFF [%]	Inner [A]	Outer [A]	Trim [A]	T [mN]	V_{mp} [V]	V_p [V]	I_{Beam} [A]	I_{Axial} [A]	λ [deg]	(1-r) [-]	η_T [-]	T/P [mN/kW]	
4	Low-Current	120.2	22.6	2713	-6.0	20.0	3.2	16	2.7	2.4	-0.9	234.4	-	-	16.6	14.6	28.4	0.74	0.44	86.4	Vacuum
	Low-Current	120.2	23.1	2773	-5.9	20.0	3.2	16	2.7	2.4	-0.9	238.3	102	6.0	18.7	15.3	34.8	0.81	0.44	86.0	2.1E-05
	Low-Current	120.2	23.2	2791	-5.8	20.0	3.2	16	2.7	2.4	-0.9	239.4	-	-	19.3	15.5	36.3	0.83	0.44	85.8	2.7E-05
	Low-Current	120.2	23.4	2807	-5.8	20.0	3.2	16	2.7	2.4	-0.9	240.5	-	-	19.9	15.8	37.5	0.85	0.44	85.7	3.3E-05
	Low-Current	120.2	23.5	2822	-5.8	20.0	3.2	16	2.7	2.4	-0.9	241.4	-	-	20.4	16.0	38.5	0.87	0.44	85.5	4.2E-05
	Low-Current	120.2	23.6	2837	-5.7	20.0	3.2	16	2.7	2.4	-0.9	242.3	-	-	19.7	15.4	38.7	0.84	0.45	85.4	4.9E-05
15	High-Current	119.7	25.9	3101	-5.9	20.0	3.2	16	2.6	2.4	-0.9	230.0	-	-	16.6	14.0	32.6	0.64	0.37	74.2	Vacuum
	High-Current	119.7	25.4	3037	-5.9	20.0	3.2	16	2.6	2.4	-0.9	234.3	102	6.0	19.4	15.2	38.5	0.76	0.39	77.2	2.1E-05
	High-Current	119.7	25.3	3028	-5.9	20.0	3.2	16	2.6	2.4	-0.9	235.0	-	-	20.1	15.5	39.4	0.79	0.39	77.6	2.4E-05
	High-Current	119.7	25.2	3020	-5.9	20.0	3.2	16	2.6	2.4	-0.9	235.6	-	-	20.4	15.6	39.9	0.81	0.40	78.0	2.7E-05
	High-Current	119.7	25.2	3010	-5.9	20.0	3.2	16	2.6	2.4	-0.9	236.2	-	-	20.6	15.7	40.4	0.82	0.40	78.4	3.0E-05
	High-Current	119.7	25.1	3003	-5.9	20.0	3.2	16	2.6	2.4	-0.9	236.8	-	-	20.9	15.8	40.8	0.83	0.40	78.9	3.3E-05

Table D-4 Thrust, telemetry, and far-field plume properties of the 6-kW laboratory Hall thruster as a function of facility pressure for 105-V, 20-mg/s anode flow operation with a total combined flow to the cathode and auxiliary port equivalent to 10-CFF.

Test Point	Operating Mode	Thruster Discharge Properties				Propellant Mass Flow Rate			Electromagnet Settings			Thrust, Total Efficiency, and Far-field Plume Properties									Facility Pressure [torr]
		V_d [V]	I_d [A]	P_d [W]	V_{cg} [V]	Anode [mg/s]	Cathode [mg/s]	Aux [mg/s]	Inner [A]	Outer [A]	Trim [A]	T [mN]	V_{mp} [V]	V_p [V]	I_{Beam} [A]	I_{Axial} [A]	λ [deg]	(1-r) [-]	η_T [-]	T/P [mN/kW]	
17	Low-Current	105.3	22.1	2330	-5.9	20.0	2.0	0.0	3.0	2.3	-0.8	203.0	-	-	15.8	13.5	31.4	0.72	0.40	87.1	Vacuum
	Low-Current	105.3	22.8	2399	-5.9	20.0	2.0	0.0	3.0	2.3	-0.8	208.5	84	7.0	17.8	14.3	36.4	0.78	0.41	86.9	2.0E-05
	Low-Current	105.3	22.9	2413	-5.8	20.0	2.0	0.0	3.0	2.3	-0.8	209.8	-	-	18.2	14.5	37.4	0.80	0.41	86.9	2.5E-05
	Low-Current	105.3	23.1	2429	-5.8	20.0	2.0	0.0	3.0	2.3	-0.8	211.1	-	-	18.8	14.7	38.3	0.81	0.42	86.9	3.0E-05
	Low-Current	105.3	23.3	2448	-5.8	20.0	2.0	0.0	3.0	2.3	-0.8	212.5	-	-	19.2	14.9	39.1	0.83	0.42	86.8	3.5E-05
19	Low-Current	105.3	22.3	2349	-6.0	20.0	1.0	1.0	3.0	2.3	-0.8	202.0	-	-	15.5	13.2	31.6	0.69	0.41	86.0	Vacuum
	Low-Current	105.3	22.9	2409	-6.1	20.0	1.0	1.0	3.0	2.3	-0.8	205.9	84	7.0	17.6	14.1	36.9	0.77	0.42	85.5	2.1E-05
	Low-Current	105.3	23.0	2424	-6.1	20.0	1.0	1.0	3.0	2.3	-0.8	207.0	-	-	18.2	14.4	38.0	0.79	0.42	85.4	2.5E-05
	Low-Current	105.3	23.2	2438	-6.2	20.0	1.0	1.0	3.0	2.3	-0.8	208.0	-	-	18.8	14.6	38.9	0.81	0.42	85.3	3.0E-05
	Low-Current	105.3	23.3	2451	-6.2	20.0	1.0	1.0	3.0	2.3	-0.8	208.7	-	-	19.2	14.8	39.6	0.82	0.42	85.2	3.5E-05
20	Low-Current	105.3	22.5	2367	-6.1	20.0	0.4	1.6	3.0	2.3	-0.8	201.7	-	-	15.7	13.3	32.4	0.70	0.42	85.2	Vacuum
	Low-Current	105.3	23.0	2420	-6.4	20.0	0.4	1.6	3.0	2.3	-0.8	205.0	84	7.0	17.7	14.1	37.1	0.77	0.43	84.7	2.1E-05
	Low-Current	105.3	23.1	2432	-6.4	20.0	0.4	1.6	3.0	2.3	-0.8	205.9	-	-	18.3	14.4	38.2	0.79	0.43	84.7	2.5E-05
	Low-Current	105.3	23.3	2448	-6.5	20.0	0.4	1.6	3.0	2.3	-0.8	206.6	-	-	18.8	14.6	39.1	0.81	0.43	84.4	3.0E-05
	Low-Current	105.3	23.4	2461	-6.5	20.0	0.4	1.6	3.0	2.3	-0.8	207.6	-	-	19.3	14.8	39.9	0.82	0.43	84.4	3.7E-05
21	Low-Current	105.3	22.3	2353	-6.0	20.0	0.4	1.4	3.0	2.3	-0.8	199.4	-	-	15.6	13.2	32.3	0.70	0.41	84.8	Vacuum
	Low-Current	105.3	22.9	2409	-6.4	20.0	0.4	1.4	3.0	2.3	-0.8	203.0	84	7.0	17.8	14.1	37.5	0.78	0.42	84.3	2.1E-05
	Low-Current	105.3	23.0	2422	-6.5	20.0	0.4	1.4	3.0	2.3	-0.8	203.7	-	-	18.2	14.2	38.4	0.79	0.42	84.1	2.5E-05
	Low-Current	105.3	23.1	2435	-6.6	20.0	0.4	1.4	3.0	2.3	-0.8	204.5	-	-	18.6	14.4	39.3	0.80	0.42	84.0	3.0E-05
	Low-Current	105.3	23.3	2448	-6.7	20.0	0.4	1.4	3.0	2.3	-0.8	205.4	-	-	19.2	14.7	40.1	0.83	0.42	83.9	3.5E-05
18	High-Current	105.3	26.8	2818	-6.3	20.0	2.0	0.0	3.0	2.3	-0.8	196.7	-	-	16.9	14.2	32.7	0.63	0.31	69.8	Vacuum
	High-Current	105.0	25.9	2714	-6.4	20.0	2.0	0.0	3.0	2.3	-0.8	202.5	86	6.0	19.0	15.0	37.9	0.74	0.34	74.6	2.1E-05
	High-Current	105.0	25.8	2709	-6.4	20.0	2.0	0.0	3.0	2.3	-0.8	203.3	-	-	19.3	15.1	38.4	0.75	0.35	75.0	2.3E-05
	High-Current	105.0	25.7	2701	-6.5	20.0	2.0	0.0	3.0	2.3	-0.8	203.7	-	-	19.5	15.2	38.8	0.76	0.35	75.4	2.6E-05
	High-Current	105.0	25.6	2685	-6.5	20.0	2.0	0.0	3.0	2.3	-0.8	204.3	-	-	19.7	15.2	39.2	0.77	0.35	76.1	2.8E-05

Bibliography

[1] Choeuiri, E. Y., "A Critical History of Electric Propulsion: The First 50 Years (1906-1956)," *Journal of Propulsion and Power*, Vol. 20, No. 2, March-April 2004.

[2] Goddard, R. H., "Method and Means for Producing Electrically-Charged Particles," U.S. Patent No. 1,137,964, application filed April 1913, granted May 1915.

[3] Goddard, R. H., "Method and Means for Producing Electrified Jets of Gas," U.S. Patent No. 1,163,037, application filed October 1917, granted December 1920.

[4] Spitzer, L., "Interplanetary Travel Between Satellite Orbits," *Journal of the American Rocket Society*, Vol. 22, March-April, 1952, pp. 92-96.

[5] Humble, R. W., Henry, G. N., Larson, W. J., *Space Propulsion Analysis and Design*, Primis Custom Publishing, New York, 1995.

[6] Glushko, V. P., *Tsiolkovskii I Kosmonavtika*, Vetsnik Akademii Nauk, Moscow, 1976, pp. 106-109 (in Russian).

[7] Cassady, R. J., "Overview of Major U.S. Industrial Programs in Electric Propulsion," Proceedings of the 37th AIAA/ASME/ASEE Joint Propulsion Conference, AIAA-2001-3226, Salt Lake City, UT, July 2001.

[8] Brophy, J. R., Etters, M. A., Gates, J., Garner, C. E., Klatte, M., Lo, C. J., Marucci, M. G., Mikes, S., Pixler, G., Nakazono, B., "Development and Testing of the Dawn Ion Propulsion System," Proceedings of the 42nd AIAA/ASME/ASEE Joint Propulsion Conference, AIAA-2006-4319, Sacramento, CA, July 2006.

[9] Dailey, C. L., Lovberg, R. H., "The PIT MkV Pulsed Inductive Thruster," NASA-CR-1911555, 1993.

[10] Marrese-Reading, C. M., Frisbee, R., Sengupta, A., Cappelli, M. A., Tverdoklebov, S., Semenkin, S., Boyd, I., "Very High Isp Thruster with Anode Layer (VHITAL): An Overview," Space Conference and Exhibit, AIAA-2004-5910, San Diego, CA, September 28-30, 2004.

[11] Kauffman, H. R., "Technology of Closed-Drift Thrusters," *AIAA Journal*, Vol. 23, No. 1, 1985, pp. 78-878.

[12] Zhurin, V. V., Kaufman, H. R., Robinson, R. S., "Physics of Closed Drift Thrusters," *Plasma Sources Sci. Technol*., Vol. 8, 1999.

[13] Morozov, A. I., "The Conceptual Development of Stationary Plasma Thrusters," *Plasma Physics Reports*, Vol. 29, No. 3, 2003, pp. 235-250. Translated from Fizika Plazmy, Vol. 29, No. 3, 2003, pp. 261-276.

[14] Kim, V., Popov, G., Arkhipov, B., Murashko, V., Gorshkov, O., Koroteyev, A., Garkusha, V., Semenkin, A., Tverdokhlebov, S., "Electric Propulsion Activity in Russia," IEPC-2001-05, Proceedings of the 27th International Electric Propulsion Conference, Pasadena, CA, 15-19 October, 2001.

[15] Kim, V., Kozubsky, K. N., Murashko, V. M., Semenkin, A. V., "History of Hall Thrusters Development in USSR," IEPC-2007-142, Proceedings of the 30th International Electric Propulsion Conference, Florence, Italy, 17-20 September 2007.

[16] Sankovic, J. M., Hamley, J. A., Haag, T. W., "Performance Evaluation of the Russian SPT-100 Thruster at NASA LeRC," NASA-TM-106401, 1993.

[17] Brophy, J. R., "Stationary Plasma Thruster Evaluation in Russia", JPL Publication 92-4, NASA-CR-192823, March 15, 1992.

[18] Garner, C. E., Brophy, J. R., Polk, J. E., Semenkin, S., Garkusha, V., Tverdokhlebov, S., Marrese, C., "Experimental Evaluation of Russian Anode Layer Thrusters," Proceedings of the 30th AIAA/ASME/SAE/ASEE Joint Propulsion Conference, AIAA-1994-3010, Indianapolis, IN, June 27-29, 1994,.

[19] Hofer, R. R., "Development and Characterization of High-Efficiency, High Specific Impulse Xenon Hall Thrusters," Doctoral Dissertation, University of Michigan, Ann Arbor, Michigan, Published as NASA/CR-2004-213099, 2004.

[20] Manzella, D., Jacobson, D., "Investigation of Low-Voltage/High-Thrust Hall Thruster Operation," Proceedings of the 39th AIAA/ASME/ASEE Joint Propulsion Conference, AIAA-2003-5004, Huntsville, AL, July 2003.

[21] Sommerville, J. D., King, L. B., "Effect of Cathode Position on Hall-Effect Thruster Performance and Cathode Coupling Voltage," Proceedings of the 43rd AIAA/ASME/SAE/ASEE Joint Propulsion Conference, AIAA-2007-5174, Cincinnati, OH, July 8-11, 2007.

[22] Hofer, R. R., Johnson, L. K., Goebel, D. M., Fitzgerald, D. J., "Effects of an Internally-Mounted Cathode on Hall Thruster Plume Properties," Proceedings of the 42nd AIAA/ASME/SAE/ASEE Joint Propulsion Conference, AIAA-2006-4482, Sacramento, CA, July 9-12, 2006.

[23] Semenkin, A., Kim, V., Gorshkov, O., Jankovsky, R., "Development of electric propulsion standards – current status and further activity," IEPC-2001-70, Proceedings of the 27th International Electric Propulsion Conference, Pasadena, CA, 15-19 October, 2001.

[24] Morozov, A. I., "About Plasma Acceleration by Magnetic Fields," *Journal of Experimental and Theoretical Physics*, Vol. 32, N2, pp. 305, 1957 (In Russian).

[25] Yushmanov, E. E., *Radial Distribution of the Potential in Cylindrical Trap with Magnetron Ion Injection, In Book: Plasma Physics and the Problem of Controlled Fusion*, M. A. Leontovich, Ed. Moscow, USSR: USSR Academy of Science, 1958, Vol. 4, (In Russian).

[26] Zharinov, A. V., "Electric Double Layer in Strong Magnetic Field," Kurchatov Inst. Rep., Moscow, USSR, 1961 (In Russian).

[27] Lary, E.C., Meyerand, R. G. Jr., Salz, F., "Ion Acceleration in a gyro-dominated neutral plasma: Theory and experiment," *Bulletin of the American Physical Society*, Vol. 7, pg. 441, July 1962.

[28] Seikel, G. R., Reshotko, E., "Hall-current Ion Accelerator," *Bulletin of the American Physical Society*, Vol. 7, pg. 414, July 1962.

[29] Janes, G. S., Dotson, J., Wilson, T., "Electrostatic Acceleration of Neutral Plasmas – Momentum Transfer Through Magnetic Fields," Proceedings of the Third Symposium on Advanced Propulsion Concepts (Gordon and Breach Science Publishers, Inc., New York, 1963), pp. 153 – 175.

[30] Brown, C. O., Pinsley, E. A., "Further Experimental Investigations of a Cesium Hall-Current Accelerator," *AIAA Journal*, Vol. 3, No. 5, 1965, pp. 853-859.

[31] Morozov, A. I., "Investigation of the stationary electromagnetic plasma acceleration", Doctoral Thesis, Institute of Atomic Energy named after I. V. Kourchatov, Moscow, 1965 (In Russian).

[32] Janes, G. S., Lowder, R. S., "Anomalous Electron Diffusion and Ion Acceleration in a Low-Density Plasma", *Physics of Fluids*, Vol. 9, No. 6, 1966.

[33] Zharinov, A. V., Popov, Y. S., "Acceleration of plasma by a closed Hall current," *Soviet Physics – Technical Physics*, Vol. 12, No. 2, August 1967, pp. 208-211 (In Russian).

[34] Morozov, A. I., "Effect of Near-wall Conductivity in Magnetized Plasma," *Journal of Applied Math Technical Physics*, Vol. 3, pg. 19-22, 1968 (In Russian).

[35] Kaufman, H. R., "Technology of Closed-Drift Thrusters," *AIAA Journal*, Vol. 23, No. 1, 1985, pp. 78-87.

[36] Morozov, A. I., "The Conceptual Development of Stationary Plasma Thrusteres", *Plasma Physics Reports*, Vol. 29, No. 3, pg. 235-250, 2003 (Translated from Fizika Plazmy, Vol. 29, No. 3, pg. 261-276, 2003).

[37] Masek, T. D., Ward, J. W., Kami, S., "Primary Electric Propulsion Thrust Subsystem Definition," AIAA 11th Electric Propulsion Conference and Exhibit, AIAA 75-405, New Orleans, LA, 19-21 March, 1975.

[38] Meyer, R. M., Manzella, D. H., "SPT Thruster Plume Characteristics", Proceedings of the 23rd International Electric Propulsion Conference, Seattle, WA, 13-16 September, 1993,.

[39] Garner, C. E., Polk, J. E., Goodfellow, K. D., Brophy, J. R., "Performance Evaluation on Life Testing of the SPT-100," IEPC-93-096, Proceedings of the 23rd International Electric Propulsion Conference, Seattle, WA, 13-16 September, 1993.

[40] King, L. B., Gallimore, A. D., Marrese, C. M., "Transport-Property Measurements in the Plume of an SPT-100 Hall Thruster," *Journal of Propulsion and Power*, Vol. 14, No. 3, 1998, pp. 327-335.

[41] Belan, N. V., Kim, V. P, Oransky, A. I., Tikhonov, V. B., *Stationary Plasma Engines*, Khar'kov Karh'kovskiy Aviatsionnyy Institut, 1989, pp. 164 - 166. (in Russian)

[42] Bugrova, A. I., Kim, V. P, Maslennikov, N. A., Morozov, A. I., "Physical Properties and Characteristics of Stationary Plasma Thrusters with Closed Electron Drift", IEPC-91-079, Proceedings of the 22nd International Electric Propulsion Conference, Viareggio, Italy, 1991.

[43] Kim, V., "Main Physical Features and Processes Determining the Performance of Stationary Plasma Thrusters", *Journal of Propulsion and Power*, Vol. 14, No. 5, September – October, 1998.

[44] Morozov, A. I., Bugrova, A. I., Desyatskov, A. V., Ermakov, Y. A., Kozintseva, M. V., Lipatov, A. S., Pushkin, A. A., Khartchevnikov, V. K., Churbanov, D. V., "ATON-Thruster Plasma Accelerator," *Plasma Physics Reports*, Vol. 23, No. 7, pp. 587-597, 1997 (Translated from Fizika Plazmy, Vol. 23, No. 7, pp. 635-645, 1997)

[45] Bugrova, A. I., Lipatov, A. S., Morozov, A. I., Baranov, S. V., "Effect of the Ratio of Differently Charged Ions on the Integral Parameters of Stationary Plasma Thrusters of the ATON Type," *Technical Physics Letters*, Vol. 31, No. 11, pp. 943-946, 2005 (Translated from Pis 'ma v Zhurnal Tekhnicheskoi Fiziki, Vol. 31, No. 21, pp. 87-94, 2005)

[46] Bouchoule, A., Boeuf, J. P., Heron, A., Duchemin, O., "Physical Investigations and Developments of Hall Plasma Thrusters", *Plasma Physics and Controlled Fusion*, 46 (2004), B407-B421.

[47] Grishin, S. D., Leskov, L. V., *Electrical Rocket Engines of Space Vehicles*, Publishing House "Mashinostroyeniye", Moscow, 1989, pp. 12.

[48] Raitses, Y., Fisch, N. J., "Parametric Investigations of a Nonconventional Hall Thruster," *Physics of Plasmas*, Vol. 8, No. 5, pp. 2579-2586, 2001.

[49] Sasoh, A., "Generalized Hall Acceleration," *Journal of Propulsion and Power*, Vol. 10, No. 2, 1994, pp. 251-254.

[50] Bober, A., "Numerical Analysis of Hall Thruster Firing Tests," *Journal of Propulsion and Power*, Vol. 23, No. 3, May-June 2007, pp. 537-543.

[51] Linnell, J. A., Gallimore, A. D., "Efficiency Analysis of a Hall Thruster Operating with Krypton and Xenon," *Journal of Propulsion and Power*, Vol. 22, No. 6, 2006, pp. 1402-1418.

[52] Fife, J. M., Martinez-Sanchez, M., "Two-Dimensional Hybrid Particle-In-Cell Modeling of Hall Thrusters," IEPC-95-240, Proceedings of the 24th International Electric Propulsion Conference, Moscow, Russia, 19-23 September 1995.

[53] Hruby, V., Monheiser, J., Pote, B., Rostler, P., Kolencik, J., and Freeman, C., "Development of low power Hall thrusters," 30th Plasmadynamics and Lasers Conference, AIAA 1999-3534, Norfolk, VA, 28 June – 1 July, 1999.

[54] Jameson, K. K., Goebel, D. M., Hofer, R. R., Watkins, R. M., "Cathode coupling in Hall Thrusters," IEPC-2007-278, Proceedings of the 30th International Electric Propulsion Conference, Florence, Italy, 17-20 September, 2007.

[55] Komurasaki, K., Arakawa, Y., "Hall Current Ion-Thruster Performance," *Journal of Propulsion and Power*, Vol. 8, No. 6, 1992, pp. 1212-1216.

[56] Ahedo, E., Gallardo, J. M., Martinez-Sanchez, M., "Model of the Plasma Discharge in a Hall Thruster with Heat Conduction," *Physics of Plasmas*, Vol. 9, No. 9, pg. 4061-4070, 2002.

[57] Hofer, R. R., and Gallimore, A.D., "High-specific impulse Hall Thrusters, Part 2: Efficiency Analysis," *Journal of Propulsion and Power*, Vol. 22, No. 4, 2006, pp. 732-740.

[58] Chavers, G., Chang-Diaz, F., Breizman, Boris, Bengston, R., "Momentum Flux Measurements Using an Impact Thrust Stand," 46th APS Annual Meeting of the Division of Plasma Physics, Meeting ID: DPP04, Savannah, GA, 15-19 November 2004.

[59] Raitses, Y., Ashkenazy, J., and Guelman, M., "Propellant Utilization in Hall Thrusters," *Journal of Propulsion and Power*, Vol. 14, No. 2, 1998, pp. 247-253.

[60] Haas, J. M., "Low-Perturbation Interrogation of the Internal and Near-field Plasma Structure of a Hall Thruster Using a High-speed Probe Positioning System," Doctoral Dissertation, University of Michigan, Ann Arbor, Michigan, 2001.

[61] Reid, B. M., "The Influence of Neutral Flow Rate in the Operation of Hall Thrusters," Doctoral Dissertation, University of Michigan, Ann Arbor, Michigan, 2009.

[62] Hargus, W. A. Jr., Cappelli, M. A., "Interior and Exterior Laser-Induced Fluorescence and Plasma Measurements within a Hall Thruster," *Journal of Propulsion and Power*, Vol. 18, No. 1, 2002, pp. 159-168.

[63] Smith, T. B., Huang, W., Reid, B. M., Gallimore, A. D., "Near-field Laser-Induced Fluorescence Velocimetry of Neutral Xenon in a 6 kW Hall Thruster Plume," IEPC-2007-252, Proceedings of the 30th International Electric Propulsion Conference, Florence, Italy, 17-20 September, 2007.

[64] Kim, S. W., Gallimore, A. D., "Plume Study of a 1.35-kW SPT-100 Using an ExB Probe," *Journal of Spacecraft and Rockets*, Vol. 39, No. 6, 2002, pp. 904-909.

[65] King, L. B., "Transport-property and mass spectral measurements in the exhaust plume of a Hall effect space propulsion system," Doctoral Dissertation, University of Michigan, Ann Arbor, MI, 1998.

[66] Goebel, D. M., Katz, I., *Fundamentals of Electric Propulsion: Ion and Hall Thrusters*. (John Wiley & Sons, New York, 2007).

[67] Kim, S. W., "Experimental Investigations of Plasma Parameters and Species-Dependent Ion Energy Distribution in the Plasma Exhuast of a Hall Thruster," Doctoral Dissertation, University of Michigan, Ann Arbor, Michigan, 1999.

[68] Beal, B. E.. "Clustering of Hall Effect Thrusters for High Power Electric Propulsion Applications," Doctoral Dissertation, University of Michigan, Ann Arbor, Michigan, 2004.

[69] Morozov, A. I., *Physical Principles of Cosmic Electric Propulsion Engines*, Moscow: Atomizdat, 1978.

[70] Morozov, A. I., Balebanov, V. M., Bugrova, A. I., Lipatov, A. S., Khartchevnikov, V. K., "ATON-Thruster Plasma Accelerator," 4th All-Russian Seminar on Problems of Theoretical and Applied Electron Optics, Proceedings of SPIE, Vol. 4187, 2000.

[71] Bugrova, A. I., Lipatov, A. S., Morozov, A. I., Churbanov, D. V., "On Similarity Criterion for Plasma Accelerators of the Stationary Plasma Thruster Type," *Technical Physics Letters*, Vol. 28, No. 10, pp. 821-823, 2002 (Translated from Pis 'ma v Zhurnal Tekhnicheskoi Fiziki, Vol. 28, No. 19, pg. 56-61, 2002)

[72] Larson, C. William, Brown, Daniel L., and Hargus, William A. Jr., "Thrust efficiency, energy efficiency and the role of the VDF in Hall thruster performance analysis," 43rd AIAA/ASME/SAE/ASEE Joint Propulsion Conference and Exhibit, AIAA 2007-5270, Cincinnati, OH, 8-11 July, 2007.

[73] Brown, Daniel L., Larson, C. William, Haas, James M., and Gallimore, Alec D., "Analytical extraction of plasma properties using a Hall thruster efficiency architecture," IEPC-2007-188, Proceedings of the 30th International Electric Propulsion Conference, Florence, Italy, 17-20 September 2007.

[74] Mirels, H., Rosenbaum, B. M., "Analysis of One-Dimensional Ion Rocket," NASA TN D-266, 1960.

[75] Kaufman, H. R., "One-Dimensional Analysis of Ion Rockets," NASA TN D-261, 1960.

[76] Byers, D. C., "Angular Distribution of Kaufman Ion Thruster Beams," NASA TN D-5844, 1970.

[77] Nieberding, W. C., Lesco, D. J., Berkopec, F. D., "Comparative In-Flight Thrust Measurements of the SERT II Ion Thruster," AIAA 8th Electric Propulsion Conference and Exhibit, AIAA 75-405, Stanford, CA, August 31–September 2, 1970.

[78] Kerslake, W. R., Goldman, R. G., Nieberding, W. C., "SERT II: Mission, Thruster Performance, and In-Flight Thrust Measurements," *Journal of Spacecraft*, Vol. 8, No. 3, March 1971, pp. 213-224.

[79] Banks, B., Rawlin, V., Weigand, A., Walker, J., "Direct Thrust Measurement of a 30-cm Ion Thruster," NASA TM X-71646.

[80] Brophy, J. R., "NASA's Deep Space 1 Ion Engine (plenary)," *Review of Scientific Instruments*, Vol. 73, No. 2, Feb. 2002, pp. 1071-1078.

[81] Masek, T. D., "Plasma Properties and Performance of Mercury Ion Thrusters," *AIAA Journal*, Vol. 9, pp. 205-212, 1971.

[82] *Guide to the Expression of Uncertainty in Measurement*, Joint publication of the BIPM, IEC, IFCC, ISO, IUPAC, IUPAP, and OIML; prepared by ISO Technical Advisory Group 4 (TAG 4), Working Group 3 (WG 3), October, 1993.

[83] Hofer, R. R., Peterson, P. Y., Gallimore, A. D., "Characterizing Vacuum Facility Backpressure Effects on the Performance of a Hall Thruster," IEPC-01-045, 27th International Electric Propulsion Conference, Pasadena, CA, Oct 14-19, 2001.

[84] Walker, M. L. R., "Effects of Facility Backpressure on the Performance and Plume of a Hall Thruster," Doctoral Dissertation, Department of Aerospace Engineering, Univ. of Michigan, Ann Arbor, MI, 2005.

[85] Reid, B. M., Gallimore, A. D., "Langmuir Probe Measurements in the Discharge Channel of a 6-kW Hall Thruster," Proceedings of the 44th AIAA Joint Propulsion Conference, AIAA-2008-4920, Hartford, CT, July 20-23, 2008.

[86] Reid, B. M., Gallimore, A. D., "Plasma Potential Measurements in the Discharge Channel of a 6-kW Hall Thruster," Proceedings of the 44th AIAA Joint Propulsion Conference, AIAA-2008-5185, Hartford, CT, July 20-23, 2008.

[87] Reid, B. M., Shastry, R., Gallimore, A. D., Hofer, R. R., "Angularly-Resolved ExB Probe Spectra in the Plume of a 6-kW Hall Thruster," Proceedings of the 44th AIAA Joint Propulsion Conference, AIAA-2008-5287, Hartford, CT, July 20-23, 2008.

[88] Jameson, K. K., "Investigation of Hollow Cathode Effects on Total Thruster Efficeincy in a 6-kW Hall Thruster," Doctoral Dissertation, Department of Aerospace Engineering, Univ. of California, Los Angeles, CA, 2008.

[89] Haag, T. W., "Thrust Stand for High-Power Electric Propulsion Devices," *Review of Scientific Instruments*, Vol. 62, No. 5, May 1991, pp. 1186-1191.

[90] Mott-Smith, H. M., Langmuir, I., "Langmuir Probe Theory," *Physical Review*, Vol. 28, pp. 727, 1926.

[91] Laframboise, J. G., "Theory of Spherical and Cylindrical Langmuir Probes in a Collionless, Maxwellian Plasma at Rest," UTIAS Report No. 100, June, 1966.

[92] Ruzic, D. N., *Electric Probes for Low Temperature Plasmas*, American Vacuum Society Monograph Series (AVS Education Committee), New York, 1994.

[93] Chen, F. F., "Langmuir Probe Analysis for High Density Plasmas," *Physics of Plasmas*, Vol. 8, No. 6, pp. 3029-3041, June 2001.

[94] Herman, D. A., "The Use of Electrostatic Probes to Characterize the Discharge Plasma Structure and Identify Discharge Cathode Erosion Mechanisms in Ring-Cusp Ion Thrusters," Doctoral Dissertation, Department of Aerospace Engineering, Univ. of Michigan, Ann Arbor, MI, 2005.

[95] Gulszinski, F. S., "Examination of the Structure and Evolution of Ion Energy Properties of a 5 kW Class Laboratory Hall Effect Thruster at Various Operational Conditions," Doctoral Dissertation, Department of Aerospace Engineering, Univ. of Michigan, Ann Arbor, MI, 1999.

[96] Hutchinson, I. H., *Principles of Plasma Diagnostics*, 2nd Edition, Cambridge Univ. Press, New York, 1990.

[97] Azziz, Y., "Experimental and Theoretical Characterization of a Hall Thruster Plume," Doctoral Dissertation, Department of Aeronautics and Astronautics, Massachusetts Institute of Technology, Cambridge, MA, 2007.

[98] Pollard, J. E., Diamant, K. D., Khayms, V., Werthman, L., King, D. Q., de Grys, K. H., "Ion Flux, Energy, and Charge-State Measurements for the BPT-4000 Hall Thruster," Proceedings of the 44th AIAA Joint Propulsion Conference, AIAA-2001-3351, Salt Lake City, UT, 8-11 July, 2001.

[99] Beal, B. E., Gallimore, A. D., "Energy Analysis of a Hall Thruster Cluster," IEPC-2003-035, Presented at the 28th International Electric Propulsion Conference, Toulouse, France, March 17-21, 2003.

[100] Wien, W.,Verhandl. Deut. Physik. Ges. 16, 165 (1897); Ann. Der Physik 65, 440 (1898).

[101] Shastry, R., Hofer, R. R., Reid, B. M., Gallimore, A. D., "Method for Analyzing ExB Probe Spectra from Hall Thruster Plumes," Proceedings of the 44th AIAA Joint Propulsion Conference, AIAA-2008-4647, Hartford, CT, July 20-23, 2008.

[102] Walker, M. L. R., Hofer, R. R., Gallimore, A. D., "Ion Collection in Hall Thruster Plumes," *Journal of Propulsion and Power*, Vol. 22, No. 1, 2006, pp. 205-209.

[103] Boyd, I. D., "Review of Hall Thruster Plume Modeling," *Journal of Spacecraft and Rockets*, Vol. 38, No. 3, 2001, pp. 381-387.

[104] Manzella, D. H., Sankovic, J. M., "Hall Thruster Ion Beam Characterization," NASA TM-107034, Aug. 1995.

[105] Walker, M. L. R., Hofer, R. R., Gallimore, A. D., "The Effects of Nude Faraday Probe Design and Vacuum Facility Backpressure on the Measured Ion Current Density Profile of Hall Thruster Plumes," Proceedings of the 38th AIAA/ASME/SAE/ASEE Joint Propulsion Conference and Exhibit, AIAA-2002-4253, Indianapolis, IN, 7-10 July, 2002.

[106] Hargus Jr., W. A., Fife, J. M., Mason, L., Jankovsky, R. S., Haag, T. W., Pinero, S., "Preliminary Performance Results of the High Performance Hall System SPT-140," Proceedings of the 36th AIAA/ASME/SAE/ASEE Joint Propulsion Conference and Exhibit, AIAA-2000-3250, Huntsville, AL, 16-19 July, 2000.

[107] Walker, M.L.R., Victor, A.L., Hofer, R.R., Gallimore, A.D., "Effect of Backpressure on Ion Current Density Measurements in Hall Thruster Plumes," *Journal of Propulsion and Power*, Vol. 21, No. 3, May-June 2005.

[108] Boerner, J. J., "Computational Simulation of Faraday Probe Measurements," Doctoral Dissertation, Department of Aerospace Engineering, Univ. of Michigan, Ann Arbor, MI, 2008.

[109] de Grys, K.H., Tilley, D.L., Aadland, R.S., "BPT Hall Thruster Plume Characteristics," Proceedings of the 35th AIAA/ASME/SAE/ASEE Joint Propulsion Conference and Exhibit, AIAA-99-2283, Los Angeles, CA, 20-24 June, 1999.

[110] Hofer, R. R., Walker, M. L. R., Gallimore, A. D., "A Comparison of Nude and Collimated Faraday Probes for Use with Hall Thrusters," IEPC-01-020, Presented at the 27th International Electric Propulsion Conference, Pasadena, CA, Oct 14-19, 2001.

[111] Rovey, J.L., Walker, M.L.R., Gallimore, A.D., Peterson, P.Y., "Evaluation of a Magnetically-Filtered Faraday Probe for Measuring the Ion Current Density Profile of a Hall Thruster," Proceedings of the 40th AIAA/ASME/SAE/ASEE Joint Propulsion Conference and Exhibit, AIAA-2004-3948, Fort Lauderdale, FL, 11-14 July, 2004.

[112] Engelman, S.F., Fife, J.M., "Hemispherical Measurements of the SPT-140 Plume," Proceedings of the 38th AIAA/ASME/SAE/ASEE Joint Propulsion Conference and Exhibit, AIAA-2002-4255, Indianapolis, IN, 7-10 July, 2002.

[113] Simulations provided courtesy of Scharfe, M., March, 2009.

[114] Brieda, L., Pierru, J., Kafafy, R., Wang, J., "Development of the DRACO Code for Modeling of Electric Propulsion Plume Interactions," Proceedings of the 40th AIAA/ASME/SAE/ASEE Joint Propulsion Conference and Exhibit, AIAA-2004-3633, Fort Lauderdale, FL, 11-14 July, 2004.

[115] Fife, J. M., Gibbons, M. R., Hargus Jr., W. A., VanGilder, D. B., Kirtley, D. E., Johnson, L. K., "The Development of a Flexible, Usable Plasma Interaction Modeling System," Proceedings of the 38th AIAA/ASME/SAE/ASEE Joint Propulsion Conference and Exhibit, AIAA-2002-4267, Indianapolis, IN, 7-10 July, 2002.

[116] Gibbons, M. R., Kirtley, D. E., VanGilder, D. B., Fife, J. M., "Flexible Three-Dimensional Modeling of Electric Thrusters in Vacuum Chambers," Proceedings of the 39th AIAA/ASME/SAE/ASEE Joint Propulsion Conference and Exhibit, AIAA-2003-4872, Huntsville, AL, 20-23 July, 2003.

[117] Birdsall, C. K., "Particle-in-Cell Charge-Particle Simulations, Plus Monte Carlo Collisions with Neutral Atoms, PIC-MCC," *IEEE Transactions on Plasma Science*, Vol. 19, No. 2, pp. 65-85.

[118] Bird, G. A., *Molecular Gas Dynamics and the Direct Simulation of Gas Flows*, Oxford University Press, Oxford, 2003.

[119] Spicer, R. L, "Validation of the DRACO Particle-in-Cell Code Using Busek 200-W Hall Thruster Experimental Data," Masters Thesis, Department of Aerospace Engineering, Virginia Polytechnic Institute and State University, Blacksburg, VA, 2008.

[120] Hofer, R. R., Katz, I., Mikellides, I. G., Goebel, D. M., Jameson, K. K., Sullivan, R. M., Johnson, L. K., "Efficacy of Electron Mobility Models in Hybrid-PIC Hall Thruster Simulations," Proceedings of the 44th AIAA/ASME/SAE/ASEE Joint Propulsion Conference and Exhibit, AIAA-2008-4924, Hartford, CT , 21-23 July, 2008.

[121] Birdsall, C., Langdon, A., *Plasma Physics Via Computer Simulations*, Institute of Physics Pub. Philadelphia, 2000.

[122] Parra, F. I., Ahedo, E., Fife, J. M., Martinez-Sanchez, M., "A Two-Dimensional Hybrid Model of the Hall Thruster Discharge," *Journal of Applied Physics*, 100, 023304, 2006.

[123] Randolph, T, Kaufman, H., Kozubsky, K., Zhurin, V., Day, M., "Facility Effects on Stationary Plasma Thruster Testing," IEPC-93-93, Presented at the 23rd International Electric Propulsion Conference, Seattle, WA, Sept. 13-16, 1993.

[124] Fife, J. M., "Hybrid-PIC Modeling and Electrostatic Probe Survey of Hall Thrusters," Doctoral Dissertation, Department of Aeronautics and Astronautics, Massachusetts Institute of Technology, Cambridge, MA, 1998.

[125] Boeuf, J. P., Garrigues, L., "Low Frequency Oscillations in a Stationary Plasma Thruster," *Journal of Applied Physics*, Vol. 84, No. 7, October, 1998.

[126] Esipchuck, Y., Morozov, A., Tilinin, G., Trofimov, A., *Sov. Phys. Tech. Phys*., Vol. 18, pp. 928, 1974.

[127] Janes, G. S., Lowder, R. S., *Phys. of Fluids*, Vol. 9, pp. 1115, 1962.

[128] Hofer, R. R., and Gallimore, A.D., "High-specific impulse Hall Thrusters, Part 1: Influence of Current Density and Magnetic Field," *Journal of Propulsion and Power*, Vol. 22, No. 4, 2006, pp. 721-731.

[129] Choueiri, E. Y., "Plasma Oscillations in Hall Thrusters," *Physics of Plasmas*, Vol. 8, No. 4, April 2001.

[130] Tilinin, G., *Sov. Phys. Tech. Phys*., 22, 974, 1977.

[131] Chesta, E., Lam, C. M., Meezan, N. B., Schmidt, D. P., Cappelli, M. A., "A Characterization of Plasma Fluctuations within a Hall Discharge," *IEEE Transactions on Plasma Science*, Vol. 29, No. 4, August 2001.

[132] Meezan, N. B., Hargus Jr., W. A., Cappelli, M. A., "Optical and Electrostatic Characterization of Oscillatory Hall Discharge Behavior," AIAA-98-3502, Cleveland, OH, July 13-15, 1998.

[133] Gascon, N., Perot, C., Bonhomme, G., Caron, X., Bechu, S., Lasgorceix, P., Izrar, B., Dudeck, M., "Signal Processing and Non-Linear Behavior of a Stationary Plasma Thruster: First Results," AIAA-99-2427, Los Angeles, CA, June 20-24, 1999.

[134] Lobbia, R. B., Gallimore, A. D., "A Method of Measuring Transient Plume Properties," Proceedings of the 44th AIAA Joint Propulsion Conference, AIAA-2008-4650, Hartford, CT, July 20-23, 2008.

[135] Foster, J. E., Williams, G. J., Patterson, M. J., "Characterization of an Ion Thruster Neutralizer," *Journal of Propulsion and Power*, Vol. 23, No. 4, July-August 2007.

[136] Yu-Cai, F., Wilbur, P.J., "The Influence of Stray Magnetic Fields on Ion Beam Neutralization," IEPC-82-1945, Presented at the 16th International Electric Propulsion Conference, New Orleans, LA, 1982.

[137] Patterson, M.J., Mohajeri, K., "Neutralizer Optimization," IEPC-91-151, Presented at the 22nd International Electric Propulsion Conference, Viareggio, Italy, 1991.

[138] Goebel, D. M., Jameson, K. K., Katz, I., Mikellides, I. G., "Plasma Potential Behavior and Plume Mode Transitions in Hollow Cathode Discharges," IEPC-2007-277, Presented at the 30th International Electric Propulsion Conference, Florence, Italy, September 17-20, 2007.

[139] Tilley, D. L., de Grys, K. H., Myers, R. M., "Hall Thruster – Cathode Coupling," Proceedings of the 35th AIAA/ASME/ASEE Joint Propulsion Conference, AIAA-99-2865, Los Angeles, CA, June 20-24, 1999.

[140] Taylor, B. N., Kuyatt, C. E., "Guidelines for Evaluating and Expressing the Uncertainty of NIST Measurement Results," NIST Technical Note 1297, 1994 Edition.